Trinity College Dublin
Coláiste na Tríonóide, Baile Átha Cliath
The University of Dublin

School of Engineering

Department of Mechanical, Manufacturing and Biomedical Engineering

Modelling and Optimisation of Axial Fans for Thermal Management of Data Centre Systems

Wenguang Zhao

Supervisor: Prof. Tim Persoons

15th April 2025

A dissertation submitted in partial fulfilment
of the requirements for the degree of
Doctor of Philosophy

Declaration

I hereby declare that this dissertation is entirely my own work and that it has not been submitted as an exercise for a degree at this or any other university.

I have read and I understand the plagiarism provisions in the General Regulations of the University Calendar for the current year, found at https://www.tcd.ie/calendar/.

I have also completed the Online Tutorial on avoiding plagiarism 'Ready Steady Write', located at https://libguides.tcd.ie/academic-integrity/ready-steady-write.

Signed: Wenguang Zhao Date: 15th April 2025

Abstract

The rapid expansion of data centres, driven by the increasing demand for digital services and advancements in technologies such as artificial intelligence (AI), has led to substantial increases in energy consumption, heat generation, and noise levels. To manage the heat produced by electronic components in compact chassis, smaller, higher rotational-speed axial fans have played a vital role in data centre cooling systems. However, their aerodynamic and aeroacoustic performance is not well understood, resulting in suboptimal designs and excessive noise. This research investigates the aerodynamic and aeroacoustic characteristics of small axial fans used in electronics cooling, aiming to enhance noise control and improve efficiency. By integrating high-fidelity and reduced-order modelling approaches with innovative passive noise reduction techniques, this research seeks to develop quieter and more energy-efficient cooling systems to meet the demands of modern data centres.

The first part of this research employs high-fidelity simulations, including large eddy simulation (LES) and the Ffowcs Williams-Hawkings (FW-H) acoustic analogy, to uncover flow physics and noise generation mechanisms. Under normal operating conditions, the fan exhibits coherent flow structures influenced by asymmetric inlet-rotor interactions, while stall conditions lead to chaotic flow separations with high leading-edge turbulence. Tonal noise dominates under normal conditions, while broadband noise is prevalent during stall. The analysis highlights that the tip vortices and asymmetric inlet-rotor interaction significantly contribute to noise generation. These insights form the foundation for subsequent low-fidelity models and noise control strategies.

The second part of this research is dedicated to developing reduced-order models (ROMs) for rapid aerodynamic and aeroacoustic predictions. The aerodynamic ROM combines blade element theory with the vortex panel solver XFOIL, incorporating tip clearance effects to enhance accuracy. Validation against experimental data shows prediction errors below 7.1%, with computational efficiency surpassing steady-state Reynolds-averaged Navier-Stokes (RANS) simulations by over three orders of magnitude. This ROM is further extended to counter-rotating (CR) dual-impeller fans, providing reliable predictions across various fan designs. To improve the ROM's capability for high-solidity cascade blades, a source vortex panel method (SVPM) is

developed to replace XFOIL. For noise prediction, the ROM integrates both broadband and tonal noise models, including Amiet's theory for leading-edge and trailing-edge noise, as well as Lowson's model for blade interaction noise. The ROM demonstrates excellent accuracy in predicting tonal and broadband noise levels, showing strong agreement with LES data and experimental results. With discrepancies below 6 dB for tonal noise and 2.8 dB for overall sound pressure levels, this ROM proves to be valuable for fan system design and optimisation.

The third part of this research explores innovative passive noise control methods aimed at maintaining or enhancing aerodynamic performance. This includes developing novel acoustic liners to absorb fan noise emissions in the near field and blade modification strategies to mitigate noise generated by blade tip vortices. For the acoustic liners, compact micro-slit panel absorbers (C-MSPAs) are designed and optimised to target low-frequency noise with minimal aerodynamic impact. When applied to an 80 mm counter-rotating (CR) fan, the C-MSPAs achieve noise reductions exceeding 6 dB at target tonal and broadband frequencies. They outperform standard industrial acoustic foam by more than 1.5 dB, with only a 0.5% deviation in aerodynamic performance compared to the reference fan. Additionally, to better understand and mitigate noise induced by blade tip vortices, stereoscopic particle image velocimetry (SPIV) is used to investigate tip leakage flow structures in a simplified fixed-blade endwall configuration. The results reveal jet-like tip leakage flow characteristics, including a strong tip leakage vortex (TLV) influenced by the angle of attack and tip clearance size. These findings provide valuable insights into TLV formation and evolution. Building on this understanding, optimised winglet designs are introduced to suppress tip leakage vortices and improve flow behaviour. Experimental and numerical analysis shows that optimised suction-side winglets reduce tonal and broadband noise by up to 3.6 dB and enhance fan efficiency by 1.8%. These innovations demonstrate their effectiveness in reducing noise without compromising fan performance.

In conclusion, this thesis provides a comprehensive understanding of axial fan aerodynamics and aeroacoustics while delivering practical noise control solutions. The findings contribute to the development of quieter, more efficient electronics cooling systems and offer valuable insights for future research and industry applications.

Acknowledgements

First and foremost, I would like to express my deepest gratitude to my supervisor, Prof. Tim Persoons, for his invaluable guidance, support, and encouragement throughout my PhD journey. His mentorship has been inspiring, providing me with the freedom to explore new ideas and the confidence to overcome challenges.

I extend my sincere thanks to Dr. Sahan Wasala for his insightful discussions. His expertise in aeroacoustics has greatly improved my work. I also thank Prof. John Kennedy for his invaluable feedback on my research into acoustic measurements and acoustic metamaterials. A sincere thank you to Prof. Stephen Spence for his support at the beginning of my PhD journey. I am grateful to everyone in the Mechanical Workshop for helping to manufacture my experimental setup, especially Gerard Byrne for his hands-on assistance in the lab. His practical knowledge has been invaluable in completing my experiments. I also thank my colleagues and friends at Trinity for their support, encouragement, and camaraderie over the years. Their friendship has made my time at Trinity memorable and enjoyable.

I express my gratitude to Prof. Justin A. Weibel at Purdue University for his continuous support on the NSF I/UCRC Cooling Technologies Research Center (CTRC) project. I also thank Prof. Mark Drela at the Massachusetts Institute of Technology for sharing the XFOIL and MISES codes. I am grateful to Prof. Kenneth S. Brentner at Pennsylvania State University for sharing the PSU-WOPWOP code. Lastly, I thank Prof. Damiano Casalino at Delft University of Technology for providing the CAD model of the benchmark case of the unmanned aerial vehicle rotor.

I acknowledge the financial support from the NSF I/UCRC CTRC at Purdue University under the project 'Thermal Management and Aeroacoustics of Air Cooled Electronics Enclosures' (2021-2023), Trinity College Dublin, and the China Scholarship Council (202006090041). I also acknowledge the support of the DJEI/DES/SFI/HEA Irish Centre for High-End Computing (ICHEC) for the provision of computational facilities and support. I thank Seagate Technology LLC for sharing their research data.

Last but not least, I would like to extend my heartfelt thanks to my family for their constant support, love, and encouragement throughout my academic journey. I dedicate this thesis to my parents, who brought me into this world and have always supported me.

Contents

Abstract iii

List of Figures xxviii

List of Tables xxx

Nomenclature xxxi

Chapter 1 Introduction 1

1.1 The importance of axial fans for thermal management challenges 1

1.2 Goals and objectives of the thesis 8

1.3 Outline of the thesis 11

Chapter 2 State of the Art 13

2.1 Small-sized electronics cooling fans 13

2.1.1 Fan structure 13

2.1.2 Performance characteristics 15

2.1.3 Scaling laws 17

2.2 Fan noise sources 18

2.2.1 Airfoil self-noise 19

2.2.2 Rotor self-noise 22

2.2.3 Rotor interaction noise 23

2.2.4 Characteristics of noise generation mechanisms 25

2.3 Aerodynamic prediction 26

2.3.1 Governing equations for incompressible flow 27

2.3.2 Turbulence resolving and modelling 28

2.3.3 Large eddy simulation 29

2.3.4 Reynolds-averaged Navier-Stokes models 32

2.3.5 Panel method 33

2.3.6 Blade element theory 35

2.4 Aeroacoustic prediction 38

2.4.1 Ffowcs Williams and Hawkings (FW-H) acoustic analogy 38

2.4.2 Trailing-edge noise 40

2.4.3 Leading-edge noise . . . 44
2.4.4 Rotor interaction noise . . . 45
2.5 Comparison of prediction methods . . . 47
2.6 Fan optimisation and noise control . . . 49
2.6.1 Geometric modifications . . . 50
2.6.2 Acoustic liners . . . 53
2.7 Summary . . . 54

Part I High-Fidelity Modelling **57**

Chapter 3 Large Eddy Simulation for Aerodynamic and Aeroacoustic Characterisation of Electronics Cooling Axial Fans under Various Operating Conditions **59**
3.1 Introduction . . . 60
3.2 Experimental methodology . . . 64
3.2.1 Selection of the test fan . . . 64
3.2.2 Aerodynamic measurements . . . 64
3.2.3 Aeroacoustic measurements . . . 66
3.3 Numerical methodology . . . 70
3.3.1 Computational domain . . . 70
3.3.2 Numerical scheme and boundary conditions . . . 70
3.3.3 Noise prediction . . . 72
3.3.4 Grid development and refinement . . . 73
3.4 Validation of the numerical model . . . 76
3.5 Aerodynamic analysis . . . 79
3.5.1 Flow features . . . 79
3.5.2 Flow field analysis and statistics . . . 86
3.5.3 Force analysis . . . 91
3.6 Aeroacoustic analysis . . . 93
3.6.1 Overview of far-field noise . . . 93
3.6.2 Contribution of fan components . . . 94
3.6.3 Analysis of wall pressure fluctuations . . . 97
3.7 Summary . . . 101

Part II Reduced-Order Modelling **105**

Chapter 4 On the Fast Prediction of the Aerodynamic Performance of Electronics Cooling Fans Considering the Effect of Tip Clearance **107**
4.1 Introduction . . . 108

4.2 Proposed analytical method . . . 109
4.3 Experimental setup . . . 113
4.4 Computational study . . . 113
4.4.1 Computational setup and validation . . . 113
4.4.2 Effect of tip clearance on fan performance . . . 115
4.5 Validation of the reduced-order model . . . 120
4.5.1 Determination of the optimal correction factor . . . 120
4.5.2 Verification and validation of the results . . . 120
4.6 Summary . . . 122

Chapter 5 Reduced-Order Model for Predicting Aerodynamic Performance of Dual Impeller Fans in Data Centre Cooling Systems 125
5.1 Introduction . . . 126
5.2 Fan configuration and experimental setup . . . 127
5.3 Extension of reduced-order model . . . 128
5.4 Computational study . . . 130
5.5 Results and discussion . . . 132
5.5.1 Model validation . . . 132
5.5.2 Effect of stator . . . 133
5.5.3 Effect of radial flow . . . 134
5.5.4 Limitations . . . 136
5.6 Summary . . . 137

Chapter 6 Development and Assessment of an Inviscid Source Vortex Panel Method for Low-Reynolds Number Airfoil Cascades 139
6.1 Introduction . . . 140
6.2 Methodology . . . 142
6.2.1 Conformal mapping . . . 142
6.2.2 Potential flow system equation . . . 143
6.2.3 Velocity and pressure transformation . . . 146
6.3 Results . . . 147
6.4 Summary . . . 153

Chapter 7 Fast Prediction Methods for Broadband and Tonal Noise of Electronics-Cooling Axial Fans 155
7.1 Introduction . . . 156
7.2 Blade element theory for fan aerodynamics . . . 160
7.3 Broadband noise prediction . . . 161
7.3.1 Coordinates transformation and Doppler effect . . . 162
7.3.2 Leading-edge noise prediction . . . 163

7.3.3 Trailing-edge noise prediction . . . 165
7.3.4 Overall broadband noise . . . 167
7.4 Tonal noise prediction . . . 168
7.5 Validation and discussion . . . 170
7.5.1 Test case description . . . 170
7.5.2 Comparison of aerodynamic prediction . . . 171
7.5.3 Results of broadband noise prediction . . . 172
7.5.4 Results of tonal noise prediction . . . 177
7.5.5 Comparison of total noise prediction . . . 179
7.5.6 Effect of turbulence inflow on broadband noise . . . 180
7.6 Summary . . . 181

Part III Optimisation and Noise Control 185

Chapter 8 Compact Micro-Slit Panel Absorbers for Enhanced Low-Frequency Noise Control 187
8.1 Introduction . . . 188
8.2 Concept, analytical prediction and optimisation . . . 190
8.2.1 Concept of C-MSPAs . . . 190
8.2.2 Analytical methods . . . 192
8.2.3 Optimisation of C-MSPAs . . . 195
8.3 Sound absorption of C-MSPAs under normal incidence . . . 198
8.3.1 Experimental and numerical setup . . . 198
8.3.2 Results . . . 200
8.3.3 Sensitivity analysis . . . 203
8.4 Transmission loss of C-MSPAs under grazing incidence . . . 205
8.4.1 Methodology . . . 205
8.4.2 Results . . . 207
8.5 Experimental investigation of C-MSPAs for counter-rotating fan noise reduction . . . 208
8.5.1 Experimental setup and test conditions . . . 208
8.5.2 Results . . . 211
8.6 Summary . . . 216

Chapter 9 Investigation of Tip Leakage Flow via Stereoscopic Particle Image Velocimetry (SPIV) in a Fixed Blade-Endwall Configuration 219
9.1 Introduction . . . 220
9.2 Experimental methodology . . . 222
9.2.1 Experimental setup . . . 222

9.2.2 Test conditions . . . 226
9.2.3 PIV processing and data analysis . . . 228
9.3 Results and discussion . . . 229
9.3.1 Upstream flow conditions . . . 229
9.3.2 Topology of the tip leakage flow . . . 230
9.3.3 Effect of angle of attack . . . 232
9.3.4 Effect of tip clearance size . . . 232
9.3.5 Effect of velocity . . . 235
9.3.6 Comparison with CFD . . . 236
9.4 Summary . . . 238

Chapter 10 Winglet Designs for Optimised Performance of Small Axial Fans 241
10.1 Introduction . . . 242
10.2 Experimental methodology and key findings . . . 244
10.2.1 Designing winglets for axial fans . . . 245
10.2.2 Key findings from the experimental investigation . . . 246
10.3 Numerical methodology . . . 247
10.3.1 Computational domain and boundary conditions . . . 247
10.3.2 Grid independence study . . . 248
10.4 Discussion: Flow enhancement and noise reduction mechanisms in winglet designs . . . 249
10.4.1 Aerodynamic performance curve comparison . . . 250
10.4.2 Flow field analysis . . . 251
10.4.3 Mean flow quantities . . . 254
10.4.4 Noise spectrum comparison . . . 257
10.5 High-fidelity simulations . . . 259
10.6 Summary . . . 262

Chapter 11 Conclusions and Outlook 265
11.1 Conclusions . . . 265
11.1.1 High-fidelity modelling for flow physics and noise generation of axial fans . . . 265
11.1.2 Reduced-order modelling for fast prediction of aerodynamics and aeroacoustics of axial fans . . . 266
11.1.3 Novel passive noise control methods for axial fans . . . 268
11.2 Outlook . . . 270

References 302

APPENDICES **305**

Appendix A Experimental Measurements and Uncertainty Analysis **305**
A.1 Experimental methodology for aerodynamics 305
A.1.1 Experimental configurations 305
A.1.2 Performance curve calculation 308
A.1.3 Uncertainty analysis for flow measurements 309
A.2 Experimental methodology for aeroacoustics 310
A.2.1 Experimental configurations 310
A.2.2 Experimental calculations and corrections 313
A.2.3 Uncertainty analysis for noise measurements 318

Appendix B Development of the ROM code LONAT **321**
B.1 Work flow of the reduced-order model 321
B.1.1 Pre-processing 323
B.1.2 Flow solver 323
B.1.3 Noise solver 323
B.1.4 Post-processing 324

Appendix C ROM Code Validation for 2D Airfoil Trailing Edge Noise Prediction **325**
C.1 Validation against BANC experiments 325
C.1.1 Aerodynamic validation 326
C.1.2 Aeroacoustic validation 327
C.1.3 Directivity of trailing edge noise emission 329
C.2 Validation against NASA experiments 330

Appendix D ROM Code Validation for 3D UAV Rotor **333**
D.1 Aerodynamic validation 335
D.2 Aeroacoustic validation 338

Appendix E Derivations of the Source Vortex Panel Method for Airfoil Cascades **341**
E.1 Velocity components of potential flow 341
E.2 Flow tangency boundary condition 344
E.3 Kutta condition 345

Appendix F Geometrical Parameters of the Compact Micro-Slit Panel Absorbers (C-MSPAs) **347**

Appendix G Comparison of the Noise Level of the Baseline Fan Under Different Loading Conditions **349**

List of Figures

1.1 Typical data centre server room, sourced from *The Irish Times* [10]. 2
1.2 Examples of server cooling systems: (a) Air-cooled IBM E980 5U server with multiple axial fans, adapted from Ref. [11]; (b) Hybrid air/liquid-cooled Intel server board S2600BP with a liquid cooling block and multiple axial fans, adapted from Ref. [12]. 2
1.3 Axial fan cooled-heatsink assembly, sourced from *Electronics Cooling* [16]. 3
1.4 Noise effects on human health, adapted from Ref. [25]. 4
1.5 Comparison of different modelling approaches for electronics cooling fans, based on the results from this thesis. The trade-offs between accuracy and computational cost are highlighted. (U)RANS: (Unsteady) Reynolds-averaged Navier-Stokes; LES: Large eddy simulation; DNS: Direct numerical simulation; VPM: Vortex panel method. 7
1.6 Outline of the thesis. 11

2.1 Exploded view of a single-impeller axial fan used in electronics cooling applications. 14
2.2 Exploded view of a counter-rotating (CR) dual-impeller fan utilised in HDD enclosures within data centers. 15
2.3 Schematic of P-Q curve for a small-sized axial flow fan. Created based on the experimental data from the present thesis. 16
2.4 Typical noise level curve of a small-sized axial fan under different loading conditions: (a) Overall sound pressure level and (b) Narrowband sound pressure level spectrm at the free delivery condition. Created based on the experimental data from the present thesis. 17
2.5 Typical radiation patterns for monopole, dipole and quadrupole sources, adapted from Ref. [49]. 19
2.6 Schematic of flow structures around airfoil for each Re regime, adapted from Wang *et al.* [62]. 20
2.7 Schematic of a turbulent boundary layer which leads to the generation of trailing edge noise [52]. 21
2.8 Schematic of laminar boundary layer which leads to the generation of vortex shedding noise [52]. 21

2.9 Schematic of airfoil bluntness which leads to the generation of vortex shedding noise [52]. 21

2.10 Schematic of flow separation which leads to the generation of stall noise [52]. 22

2.11 Schematic of tip vortex generation which leads to the generation of tip noise [52]. 22

2.12 Schematic illustrating the solid blade section and the surrounding fluid volume displaced by the blade, which generates thickness noise. 23

2.13 Schematic illustrating the steady loading generated by the positive and negative blade forces, which results in steady loading noise. 23

2.14 Schematic noise spectrum of an airfoil, adapted from Blake [61]. 25

2.15 Schematic noise spectrum of an axial fan, adapted from Wright [78]. . . . 25

2.16 Schematic of the energy spectrum of turbulent flow as a function of wavenumber k, adapted from Hirsch [84] and Al-Am [85]. 29

2.17 Schematic of the filtering operation in large eddy simulation, showing (a) the spatial filtering operation in physical space and (b) the cut-off wavenumber in Fourier space, adapted from [83]. 30

2.18 Schematic of panel orientation in the panel method, showing the airfoil divided into linear panels. 34

2.19 Velocity and force triangles of a 2D airfoil. 36

2.20 Schematic of the blade element method, adapted from Ref. [73]. 37

2.21 Sample C_l and C_d curves as a function of angle of attack α with and without Viterna extrapolation [101] for a NACA 0012 airfoil at $Re = 5 \times 10^4$. 37

2.22 Flow chart of aerodynamic and aeroacoustic prediction methods. 48

3.1 Experimental setup for testing the aerodynamic performance of the fan. 65

3.2 Comparison of the fan performance curve with $N = 9000$ r/min, obtained from the experimental setup and the reference data provided by the manufacturer. 66

3.3 The set-up for acoustic noise measurements. 67

3.4 Comparison of the noise levels of the fan, the fan operating without blades (unloaded motor noise), and the background noise. The measurements were taken at microphone location M4 (90°) at 0 mmH_2O with a fan speed of 9000 r/min. 68

3.5 Comparison of sound pressure levels (SPL) $\overline{L_p}$ for the fan noise measurements between TCD and Seagate Technology under different backpressure conditions: (a) free delivery condition of 0 mmH_2O, and (b) stall condition of 18 mmH_2O. The dashed lines represent the first ten harmonics of the blade passing frequency f_{BPF}. The noise levels are measured at a distance of 1 m from the fan rotor (as shown in Fig. 3.3), and the SPL ($\overline{L_p}$) is calculated using Eq. 37. 70

3.6 Computational domain. 71

3.7 Grid system and close-up views of the grid refinements in the upstream and downstream regions of the fan, the blade tip region, and the trailing edge (TE) and leading edge (LE) regions. 74

3.8 The values of y^+ (a), x^+ and z^+ (b) for all fan surfaces. 74

3.9 LES index of quality for a rotor cut plane (a), a stator cut plane (b), and an axial cut plane (c). 75

3.10 Verification of numerical accuracy: (a) Comparison of flow rate Q and OASPL results. (b) SPL spectra comparison. Results are shown for coarse, medium, and fine mesh resolutions. The dashed lines represent the first ten harmonics of the blade passing frequency f_{BPF}. The noise levels are measured at a distance of 1 m from the fan rotor (as shown in Fig. 3.3), and the SPL ($\overline{L_p}$) is calculated using Eq. 37. 76

3.11 Comparison of the fan performance (P-Q) curve under different backpressure conditions with $N = 9000$ r/min. As the RANS simulations diverged at the stall condition, two extra operating conditions (*i.e.*, 3 mmH_2O and 9 mmH_2O) are included to show the performance of the RANS model. 77

3.12 Comparison of fan noise measurements at TCD and LES results under different backpressure conditions with $N = 9000$ r/min. (a) and (b) show the narrowband and 1/3 octave band sound pressure level (SPL) $\overline{L_p}$ at 0 mmH_2O, (c) and (d) show the narrowband and 1/3 octave band SPL at 6 mmH_2O, (e) and (f) show the narrowband and 1/3 octave band SPL at 12 mmH_2O, and (g) and (h) show the narrowband and 1/3 octave band SPL at 18 mmH_2O. The dashed lines represent the blade passing frequency (f_{BPF}) and its harmonics. The noise levels are measured at a distance of 1 m from the fan rotor (as shown in Fig. 3.3), and the SPL ($\overline{L_p}$) is calculated using Eq. 37. 78

3.13 Instantaneous snapshot of iso-surfaces of the Q-criterion (10^8 s^{-2}) under four different backpressure conditions: 0 mmH_2O (a), 6 mmH_2O (b), 12 mmH_2O (c), and 18 mmH_2O (d). The iso-surfaces are colored based on the normalised helicity (NH). The fan is viewed from the front. An animated sequence is provided as supplementary material, available at Elsevier Storage Repository: Animation 3.13. 79

3.14 Comparison of inlet vortex structures under different backpressure conditions: normal operating conditions of 0 mmH_2O (a), 6 mmH_2O (b), 12 mmH_2O (c), and stall condition of 18 mmH_2O (d). The fan is viewed from the top. 81

3.15 Tip flow topology at the blade tip region for the normal operating condition (0 mmH_2O): (a) Instantaneous snapshot of the Q-criterion with 10^8 s^{-2}. (b) Average Q-criterion with 10^8 s^{-2}. And for the stall condition (18 mmH_2O): (c) Instantaneous snapshot of the Q-criterion with 10^8 s^{-2}. (d) Average Q-criterion with 10^8 s^{-2}. The fan is viewed from the top. . . 82

3.16 Surface streamlines and friction coefficient distribution. The results for the suction side (SS) of blade are shown in (a-d): (a) 0 mmH_2O, (b) 6 mmH_2O, (c) 12 mmH_2O, and (d) 18 mmH_2O. The results for the pressure side (PS) of blade are shown in (e-h): (e) 0 mmH_2O, (f) 6 mmH_2O, (g) 12 mmH_2O, and (h) 18 mmH_2O. 84

3.17 Boundary layer flow vectors at the rotor blade surface of 25% span for a favorable pressure gradient (FPG) at 0 mmH_2O (a) and a large adverse pressure gradient (APG) at 18 mmH_2O (b). x_a and y_a are the local airfoil coordinates. The airfoil is normalised by the chord length c. 84

3.18 Boundary layer shape factor for the suction side of the blade at 50% span and 99% span under 0 mmH_2O and 18 mmH_2O. LSB: laminar separation bubble. S: separation. R: reattachment. 85

3.19 Instantaneous blade-to-blade snapshots of the vorticity magnitude at the blade tip region (99% span) under different backpressure conditions: 0 mmH_2O (a), 6 mmH_2O (b), 12 mmH_2O (c), and 18 mmH_2O (d). An animated sequence is provided as supplementary material, available at Elsevier Storage Repository: Animation 3.19. 87

3.20 Instantaneous blade-to-blade snapshots of the vorticity magnitude at the blade mid-span region (50% span) under different backpressure conditions: 0 mmH_2O (a), 6 mmH_2O (b), 12 mmH_2O (c), and 18 mmH_2O (d). An animated sequence is provided as supplementary material, available at Elsevier Storage Repository: Animation 3.20. 88

3.21 Turbulent kinetic energy at the rotor leading edge (LE) slice (a-d) and the rotor trailing edge (TE) slice (e-h) under four different backpressure conditions: 0 mmH_2O (a) and (e), 6 mmH_2O (b) and (f), 12 mmH_2O (c) and (g), and 18 mmH_2O (d) and (h). 89

3.22 Root-mean-square (RMS) of the pressure fluctuation at the blade mid-span region (50% span), the blade tip region (99% span), and the near shroud region (104% span) under four different backpressure conditions: 0 mmH_2O (a), 6 mmH_2O (b), 12 mmH_2O (c), and 18 mmH_2O (d). 90

3.23 Fast Fourier transform (FFT) of the thrust on one rotor and stator blade of the fan under different backpressure conditions: 0 mmH_2O (a) and 18 mmH_2O (b). 91

3.24 Comparison of far-field noise under different backpressure conditions with $N = 9000$ r/min: (a) directivity of overall SPL and (b) spectrum of SPL. The dashed lines indicate the blade passing frequency (f_{BPF}) and its harmonics. The noise levels are measured at a distance of 1 m from the fan rotor (as shown in Fig. 3.3), and the SPL ($\overline{L_p}$) is calculated using Eq. 37. 93

3.25 Comparison of the overall sound pressure level (OASPL) under two backpressure conditions: 0 mmH_2O (a) and 18 mmH_2O (b). 95

3.26 Average sound pressure level (SPL) comparison under two backpressure conditions: 0 mmH_2O and (a) 18 mmH_2O (b). The dashed lines indicate the blade passing frequency (f_{BPF}) and its harmonics. The noise levels are measured at a distance of 1 m from the fan rotor (as shown in Fig. 3.3), and the SPL ($\overline{L_p}$) is calculated using Eq. 37. 96

3.27 Root-mean-square (RMS) value of the wall surface pressure at the fan under two different backpressure conditions, *i.e.*, 0 mmH_2O (a) and 18 mmH_2O (b). The RMS pressure magnitude highlights regions with significant pressure fluctuations on the fan surface, indicating potential noise sources. However, it is important to note that these values do not directly represent the strength of noise radiation in the far-field. 97

3.28 Root-mean-square (RMS) value of the wall surface pressure in different frequency bands under two backpressure conditions: (a-c) for 0 mmH_2O — low frequency (LF), medium frequency (MF), and high frequency (HF); (d-f) for 18 mmH_2O — LF, MF, and HF. LF: 500 – 1600 Hz, MF: 1600 – 5000 Hz, HF: 5000 – 12800 Hz. The RMS pressure magnitude in dB highlights regions with significant pressure fluctuations on the blade surface across different frequency bands, indicating potential noise sources. However, it is important to note that these values do not directly represent the strength of noise radiation in the far-field. 98

3.29 Comparison of the power spectral density (PSD) of the wall pressure fluctuation at two spanwise locations for the leading edge (2% c) and trailing edge (98% c) points under the normal operating condition (0 mmH_2O): (a) 50% span and (b) 99% span, and under the stall condition (18 mmH_2O): (c) 50% span and (d) 99% span. 100

3.30 Logical flow of Part I and its connection to the subsequent parts. The insights used to inform Part II (Chapters 4–7) are highlighted in red, while the insights used to inform Part III (Chapters 8–10) are highlighted in blue. The chapters in Part I are connected to Part II and Part III through the grey lines. 103

4.1 Velocity triangles for a typical fan blade element. An imaginary ideal stator is fitted to reduce the pressure loss ($\rho {v_u}^2/2$) due to the rotational velocity component v_u. 110

4.2 Effect of the correction factor M_{AR} on fan performance prediction for an arbitrarily selected 5-bladed fan [23, 30]. 112

4.3 Computational domain (a) and grid (b). 114

4.4 Results of grid independence analysis. 115

4.5 Performance comparison between the CFD results with/without an ideal stator, the reference, the experiments, and the prediction with optimal M_{AR}. 116

4.6 A schematic in the meridional view illustrating the procedure for changing tip clearance by altering the shroud radius. Tip clearance ratio (T_R) is defined $T_R = \frac{t}{R_t}$. 116

4.7 Fan P-Q curves (a) and Efficiency curves (b) obtained by CFD simulations under different tip clearances at the nominal speed of 9000 r/min. The baseline (B/L) case has a tip clearance ratio of 2.5%. 117

4.8 Swirl strength contour at 7000 s^{-1} coloured by the normalised helicity (NH) at Q = 2.02 m^3/min for a tip clearance ratio T_R = 2.5%. 118

4.9 Vortical structures in a blade-to-blade view in the tip gap (from 90% of the blade tip radius to the shroud radius) at different tip clearance ratios varying from 0% to 12.7% computed at Q = 2.02 m^3/min. Green polylines denote the airfoil profiles at the blade tip, and black dots indicate the onsets of the main tip leakage vortex. 119

4.10 Fan sectional blade efficiency curves calculated at 26 different blade spanwise locations from the hub to the tip of the blade. Results were obtained by CFD simulations for Q = 2.02 m^3/min under different tip clearances. 119

4.11 Optimal correction factors for CFD cases and for eight different commercial fans as a function of the tip clearance ratio. The correlation equation was fitted based on the CFD cases. 122

5.1 (a) Test dual impeller fan and (b) experimental setup according to ANSI / AMCA 210-16 [211] and ISO 5167-2:2003 [234]. 127
5.2 Velocity triangles for a typical CR fan blade section. The diagram in the blue dashed box illustrates the definition of w as the vectorial mean of w_1 and w_2. 129
5.3 Computational domain (a) and grid system(b). 131
5.4 Results of the grid independence analysis. 132
5.5 Meridional view of the computational domain (a) with stator and (b) without stator. P. 1 – P. 4 indicate the analysed planes, slightly offset from the interface planes. 133
5.6 The result comparisons of (a) fan P-Q curve and (b) efficiency curve obtained from different sources at the speed of N_1 = 14200 r/min and N_2 = 15000 r/min. 133
5.7 The result comparisons of (a) fan P-Q curves and (b) swirl velocity distributions in P. 3, in the presence and absence of stator at the speed of N_1 = 14200 r/min and N_2 = 15000 r/min. $C_1 - C_3$ indicate three typical working conditions in (a) and the averaged axial velocity $\bar{v}$ (·····) was shown in (b). 134
5.8 The contour of radial velocity distribution of R1, S1 and R2 domain in meridional view. Positive radial velocity is defined as pointing from the hub to the shroud, and vice versa. The blade profiles are represented by the green curves. 135
5.9 The radial velocity distribution from hub to shroud of (a) P. 2 near R1 (b) P. 4 near R2 at three different pressures. Span was normalised based on $(r - r_{hub})/(r_{shroud} - r_{hub})$ and ratio of radial to axial velocity was obtained by $v_r/\bar{v}$. 135
5.10 ROM prediction with confidence range incorporating uncertainties stemming from the radial flow effect, at the speed of N_1 = 14200 r/min and N_2 = 15000 r/min. 136

6.1 Schematic illustrating the concept of Howell's [242] conformal mapping technique. 143
6.2 Panel distribution around a transformed airfoil. 145
6.3 Geometry definitions of the i^{th} panel. 145

6.4 Validation of SVPM pressure coefficients against theoretical results in [252]. The airfoil profile and pressure distribution of a theoretical cascade are characterised by $\alpha = 16°$, $\beta_1 = 53.5°$, and $\sigma_c = 1.01$. 147
6.5 Comparison of the pressure coefficients between experimental data [239, 249–251] and SVPM predictions for eleven different cascade cases as outlined in Table 6.1. 149
6.6 Comparison of the lift coefficients between experimental data [250] and SVPM predictions at three different solidities ($\sigma_c = 0.5, 0.75$ and 1) with $Re = 2.45 \times 10^5$ and $\beta_1 = 45°$ for the NACA 65-410. 150
6.7 Effect of the solidity on lift coefficients for the NACA 65-410. 151
6.8 Interference factor for lift coefficients obtained using the inviscid method for the NACA 65-410. 151
6.9 Comparison of lift coefficients for the NACA 65-410 airfoil involves the isolated airfoil with XFOIL, modified results using IF, a cascade with SVPM, and experimental data. 152
6.10 Comparison of pressure coefficients for the NACA 65-410 airfoil involves the isolated airfoil with XFOIL, modified results using IF, a cascade with SVPM, and experimental data. 152
6.11 Contour plots of the pressure coefficient C_p with streamlines for a NACA 65-410 airfoil at three different angles of attack ($\alpha = 0°, 6.3°$ and $14°$) with $\sigma_c = 0.75$, $Re = 2.45 \times 10^5$ and a constant stagger angle of $\zeta = 0°$. 152
6.12 Contour plots of the pressure coefficient C_p with streamlines for a NACA 65-410 airfoil at three different angles of attack ($\alpha = 0°, 6.3°$ and $14°$) with $\sigma_c = 0.75$, $Re = 2.45 \times 10^5$ and a constant inlet flow angle of $\beta_1 = 45°$. . . 153

7.1 Schematic of the blade element theory for a fan blade, where each spanwise element is treated as a two-dimensional airfoil. 160
7.2 Velocity and force triangles for each blade element in a fan system. The coordinate system is defined in the airfoil frame, where m' and r' are normalized by the sectional radius r. 161
7.3 Coordinates transformation of the observer locations from the global frame to the airfoil frame. 163
7.4 Comparison of sectional thrust (a), torque (b), and efficiency (c) between prediction and LES [210]. 172
7.5 Comparison of turbulence spectrum models against LES data [210] for 50% span location. The turbulence spectrum models used in ROM include the von Kármán spectrum ('vK') and Liepmann spectrum ('Lp'). . 174
7.6 Comparison of far-field leading-edge noise prediction against experimental data and LES data [210] in one-third octave bands. 174

7.7 Comparison of PSD of wall pressure fluctuations (Φ_{pp}) at 98% of the chord on suction side between prediction and LES [210] for 50% span location (a) and five different span locations (b). The WPS models used in the ROM include Goody ('G'), Rozenberg ('R'), Kamruzzaman ('K'), Catlett ('C'), Hu ('H'), Lee ('L'), and modified Lee ('L_{mod}'). 175

7.8 Comparison of trailing-edge noise prediction against experimental data and LES data [210]. The WPS models used in the ROM include Goody ('G'), Rozenberg ('R'), Kamruzzaman ('K'), Catlett ('C'), Hu ('H'), Lee ('L'), and modified Lee ('L_{mod}'). 177

7.9 Contour plots of (a) leading-edge noise, (b) trailing-edge noise, and (c) total broadband noise in one-third octave contours along the blade. . . . 177

7.10 Comparison of tonal noise prediction against experimental data and LES data [210] for the first five harmonics of the blade passing frequency (BPF).178

7.11 Comparison of different noise source contributions to the tonal noise for the first five harmonics of the blade passing frequency (BPF). The investigated noise sources include the asymmetric inlet-rotor interaction noise (IRI), rotor-stator interaction noise (RSI) on rotor blade and stator. . 179

7.12 Comparison of total far-field noise prediction against experimental data and LES data [210] in narrowband (a), and one-third octave bands (b). The uncertainties in turbulence intensity ±1.93% and length scale ±18.8 mm are considered in the ROM. The gray dashed lines in (a) represent the harmonics of the blade passing frequency (BPF). 180

7.13 Effect of turbulence intensity I on leading-edge noise (a) and trailing-edge noise (b) in one-third octave bands. 181

7.14 Effect of turbulence length scale on leading-edge noise in one-third octave bands. The length scale L_f is normalized by the chord length c = 26 mm. 181

7.15 Logical flow of Part II and its connection to the subsequent parts. Insights from Part II that inform Part III are highlighted in green, while contributions from Part I are emphasized using a similar style as in Fig. 3.30. This visualisation underscores the integration of findings across parts, demonstrating a cohesive framework for advancing low-noise fan design. 183

8.1 Schematic of the concept of the compact micro-slit absorbers. The comparison is made for a single-layer, dual-cell between (a) A standard micro-slit panel absorber (SD-MSPA), (b) A compact micro-slit panel absorber (C-MSPA). For normal incidence sound waves, the figure indicates incident (inc.) and reflected (refl.) waves. 191

8.2 Experimental setup of the impedance tube method [283] and numerical model based on the 3D FEM method. 198
8.3 Experimental, numerical and analytical results of the sound absorption coefficient of the compact micro-slit absorbers under normal incidence targeting different frequency ranges: (a) NI-1: 600 Hz, (b) NI-2: 600 and 1200 Hz, and (c) NI-3: 1000–2000 Hz. Three analytical models used for impedance prediction are compared: the equivalent fluid (EF) model [273, 274], the Maa model [170, 182, 183], and the Randeberg and Vigran (RV) model. 201
8.4 Comparison of the sound absorption coefficient between the standard micro-slit panel absorber (SD-MSPA) and the compact micro-slit panel absorber (C-MSPA) under normal incidence. For SD-MSPA, the geometrical parameters are d = 1.00 mm, t = 10.91 mm, D = 16.00 mm, W = 38.00 mm, while for C-MSPA, these are d = 1.00 mm, t = 10.95 mm, D = 16.00 mm, W = 38.00 mm, respectively. 202
8.5 Comparison of the sound absorption coefficient between the three C-MSPAs (*i.e.* NI-1, NI-2, NI-3) and six commercially available acoustic foams made of porous materials (*e.g.*, melamine foam and polyurethane foam). 202
8.6 Comparison of the sound absorption bandwidth (sound absorption coefficient > 0.8) of C-MSPAs and other compact broadband MPP-type absorbers. 204
8.7 Sensitivity analysis of the NI-1 C-MSPA for the sound absorption coefficient under normal incidence. The analysis examines four geometrical parameters: (a) slit width d, (b) thickness t, (c) air cavity depth D, and (d) porosity ϕ using the EF model. The baseline values for NI-1 case are d = 0.73 mm, t = 4.06 mm, D = 28.00 mm, and ϕ = 1.85% (*i.e.*, W = 38 mm) as shown in Table F.1. Each parameter is varied with a constant step size while keeping the others constant. 205
8.8 Numerical model of the compact micro-slit absorbers under grazing incidence. The 3D finite element method (FEM) thermoviscous solver was employed to simulate the detailed geometry of the annular rings of C-MSPAs in COMSOL Multiphysics 6.1. 206
8.9 Numerical and analytical results of the transmission loss of the compact micro-slit absorbers under grazing incidence targeting different frequency ranges: (a) GI-1: 600 Hz, (b) GI-2: 1200 Hz, and (c) GI-3: 900–1800 Hz. 208
8.10 Experimental setup of the compact micro-slit absorbers for the counter-rotating fan noise reduction. 209

8.11 Experimental results of the sound pressure level (SPL) and noise reduction performance (ΔSPL) of the compact micro-slit absorbers for loudspeaker white noise without flow. The acoustic spectra comparisons among the baseline, the acoustic foam, and the C-MSPAs are shown for three distinct cases: (a) GI-1: 600 Hz, (c) GI-2: 1200 Hz, and (e) GI-3: 900–1800 Hz. The noise reduction in one-third octave bands with respect to the baseline is presented for the same cases: (b) GI-1, (d) GI-2, and (f) GI-3.211

8.12 Experimental results of the sound pressure level (SPL) and noise reduction performance (ΔSPL) of the C-MSPAs for CR fan noise with flow. The acoustic spectra comparisons among the baseline, the acoustic foam, and the C-MSPAs are shown for three distinct cases: (a) GI-1: 600 Hz, (c) GI-2: 1200 Hz, and (e) GI-3: 900–1800 Hz. The noise reduction in one-third octave bands with respect to the baseline is presented for the same cases: (b) GI-1, (d) GI-2, and (f) GI-3. For GI-1 and GI-2, the fan speed is set to 76% PWM, while for GI-3, the fan speed is set to 46% PWM.213

8.13 Experimental results of the sound directivity of the C-MSPAs for the loudspeaker and counter-rotating fan noise. The sound pressure levels at different angles are measured and plotted in limited 1/3 octave bandwidth for three distinct cases: (a), (d) GI-1: 561–707 Hz (centered at 603 Hz), (b), (e) GI-2: 1122–1414 Hz (centered at 1250 Hz), and (c), (f) GI-3: 890–1781 Hz. The first row (a), (b), (c) is for the loudspeaker noise, while the second row (d), (e), (f) is for the counter-rotating fan noise. 215

8.14 Pressure-flow rate (P-Q) curves of the counter-rotating fan under the baseline case, acoustic foam and C-MSPA case. 217

9.1 Sectional view of the low-speed close-loop water tunnel at Trinity College Dublin (TCD) adopted from Jackson [302], showing the location of the test section. 223

9.2 Experimental setup for stereoscopic particle image velocimetry (SPIV) measurements in the fixed blade-endwall configuration. Streamline-shaped holders (not shown here, only shown in Fig. 9.3) are used to mount the flat-plate endwall. 224

9.3 Photo of the SPIV experimental setup in the water tunnel at TCD. 224

9.4 Transparency of the high-transparency SLA-printed NACA 0012 blade: (a) Illuminated by the laser sheet in the tip gap region, showing uniform light intensity around the tip gap flow field. (b) Illuminated by the laser sheet in a spanwise section, showing uniform light intensity except for two shielded areas above pressure side due to the leading and trailing edges. 226

9.5 Schematic of the tip gap between the high-transparency SLA-printed NACA 0012 blade and the flat-plate endwall. t is the tip gap size, e is the distance between the blade tip and the laser sheet t_{sheet} ($e = t - z_{\text{sheet}}$), x is the stream-wise direction, y is the normal direction, and z is the span-wise direction. The rotational axis is at the 30% chord of the blade ($x = 0.3c,\ y = 0$). 227

9.6 Upstream flow field near the sharp flat-plate endwall: (a) Velocity profile, (b) Turbulence intensity. The data is taken near the blade leading edge ($x/c = -0.1$ and $y/c = 0$) but without the blade in place. The velocity is normalised by the freestream velocity U_∞, and the distance from the endwall is normalised by the boundary layer thickness $\delta \approx 19$ mm (about $0.38c$), extracted from the velocity profile at 99% of the freestream velocity. 229

9.7 Tip leakage flow at a tip clearance size of 5 mm ($t/c = 10\%$), an angle of attack of 16° and a freestream velocity of around 1 m/s ($Re = 5 \times 10^4$). (a) Normalised velocity magnitude (U/U_∞), (b) Normalised 2D divergence $\text{div}(u, v)$. 230

9.8 Tip leakage flow at a tip clearance size of 5 mm ($t/c = 10\%$), an angle of attack of 16° and a freestream velocity of 1 m/s ($Re = 5 \times 10^4$): (a) averaged velocity u/U_∞, (b) velocity fluctuations σ_u/U_∞, (c) averaged velocity v/U_∞, (d) velocity fluctuations σ_v/U_∞, (e) averaged velocity w/U_∞, (f) velocity fluctuations σ_w/U_∞. 231

9.9 Effect of angle of attack on the tip leakage flow at a tip clearance size of 5 mm ($t/c = 10\%$) and a freestream velocity of 1 m/s ($Re = 5 \times 10^4$). (a), (c), (e) are the velocity magnitude (U/U_∞), (b), (d), (f) are the 2D divergence $\text{div}(u, v)$ of the tip leakage flow for angles of attack of 4° (top), 8° (middle), 12° (bottom), respectively. 233

9.10 Effect of tip clearance size on the tip leakage flow at an angle of attack of 16° and a freestream velocity of 1 m/s ($Re = 5 \times 10^4$). (a), (c) are the velocity magnitude (U/U_∞), (b), (d) are the 2D divergence $\text{div}(u, v)$ of the tip leakage flow for tip clearance sizes of 2.5 mm ($t/c = 5\%$) and 10 mm ($t/c = 20\%$), respectively. 234

9.11 Effect of Reynolds number on the tip leakage flow at a tip clearance size of 5 mm ($t/c = 10\%$) and an angle of attack of 16°. (a), (c), (e) are the velocity magnitude (U/U_∞), (b), (d), (f) are the 2D divergence $\text{div}(u, v)$ of the tip leakage flow for Reynolds numbers of 2.5×10^4 (top), 7.5×10^4 (middle), 1×10^5 (bottom), respectively. 235

9.12 The 2D divergence div(m', θ) for a fan blade tip flow based on CFD simulation results from Zhao *et al.* [31] (See Chapter 4). Four tip gap sizes are considered: (a) t/c = 3.65%, (b) t/c = 7.31%, (c) t/c = 10.96%, (d) t/c = 18.27%. The fan operates at a mid-span Reynolds number of around 5×10^4, with a tip radius of 37.35 mm and an effective angle of attack of around 8°. Only one blade out of five is shown for clarity. m' is the normalised axial coordinate, and θ is the normalised circumferential coordinate. 237

9.13 Comparison of the TLV trajectory between CFD (Fig. 9.12) and SPIV results (an example is shown in Fig. 9.9 (d)) at an angle of attack of 8° and a Reynolds number of around 5×10^4. The TLV trajectory is extracted from the 2D divergence plot of the CFD results of the fan blade tip flow and the SPIV results of the NACA 0012 blade tip flow. The figures are rotated to align the streamwise direction with the horizontal axis. 238

10.1 Winglet parameters tested. Hatching shows the original airfoil shape at the blade tip. 'W' denotes winglet. 'SS', 'PS', and 'TS' denote suction side, pressure side, and two sides, respectively. 'F', 'M', and 'R' denote front, middle, and rear winglets, respectively. '01', '02', and '03' represent sharp, moderate smooth, and smooth-edged winglets, respectively. Figure credit: J. Hickey [209]. 246

10.2 Computational domain and grid system. 248

10.3 Grid independence verification for the zero pressure rise case. 249

10.4 Comparison of performance curves between the baseline fan and four suction side winglet designs. 250

10.5 Iso-surfaces of the Q-criterion at 10^8 s^{-2} for the baseline fan under $P = 0$ Pa and $N = 7050$ r/min, colored by the vorticity magnitude. 252

10.6 Comparison of the iso-surfaces of the Q-criterion at 10^8 s^{-2} for the baseline fan and the optimised winglet designs under $P = 0$ Pa and $N = 7050$ r/min: (a) baseline fan, (b) full-length winglet design (W.SS.4.8mm.02), (c) front winglet design (W.SS.F.4.8mm.02), (d) middle winglet design (W.SS.M.4.8mm.02), and (e) rear winglet design (W.SS.R.4.8mm.02). The iso-surfaces are projected to a blade-to-blade view, with only one blade shown for clarity. 253

10.7 Comparison of the skin friction coefficient distribution and surface streamlines on the suction side of blade surfaces for the baseline fan and the optimised winglet designs under $P = 0$ Pa and $N = 7050$ r/min: (a) baseline fan, (b) full-length winglet design (W.SS.4.8mm.02), (c) front winglet design (W.SS.F.4.8mm.02), (d) middle winglet design (W.SS.M.4.8mm.02), and (e) rear winglet design (W.SS.R.4.8mm.02). 254

10.8 Spanwise distribution of sectional blade efficiency for the baseline fan and optimised winglet designs under $P = 0$ Pa and $N = 7050$ r/min, highlighting the sectional performance improvement achieved by the winglet designs. s represents the normalised spanwise location of the blade, with 0 and 1 indicating the hub and blade tip, respectively. 255

10.9 Comparison of the surface pressure coefficient (a) and boundary layer displacement thickness distribution on the suction side (b) between the baseline fan and the optimised winglet design at 75% span under $P = 0$ Pa and $N = 7050$ r/min. 256

10.10 Experimental noise spectrum comparison between the baseline fan and the four optimised winglet designs under $P = 0$ Pa and $N = 7050$ r/min. The dashed lines represent first ten harmonics of the blade passing frequency. Figure plotted by W. Zhao based on the experimental data obtained by J. Hickey [209]. 257

10.11 LES noise spectrum comparison between the baseline fan and the four optimised winglet designs under $P = 0$ Pa and $N = 7050$ r/min. The dashed lines represent first ten harmonics of the blade passing frequency. 260

10.12 LES tip vortex structures comparison between the baseline fan and the optimised winglet design under $P = 0$ Pa and $N = 7050$ r/min: (a) baseline fan, (b) front winglet design (W.SS.F.4.8mm.02). 261

10.13 LES surface pressure fluctuation comparison between the baseline fan and the optimised winglet design under $P = 0$ Pa and $N = 7050$ r/min: (a) baseline fan, (b) front winglet design (W.SS.F.4.8mm.02). 261

A.1 Experimental setup for testing the aerodynamic performance of the fan according to ANSI/AMCA 210-16 [211] and ISO 5167-2:2003 [307]. . . . 306

A.2 Schematic of a 1:2 scaled ISO standardised test facility. The fan is mounted in the plenum chamber, with the microphone array positioned at a distance of 1 m from the fan. The backpressure is controlled by an adjustable rear aperture slider. 311

A.3 A 1:2 scaled ISO standardised test facility developed at Trinity College Dublin. 312

A.4 Background noise correction factor K_1 for the baseline fan in ISO 10302 plenum box [215]. The selected valid frequency range [500 Hz, 10 kHz] are highlighted in green with a correction factor $K_1 < 0.2$ dB. 314
A.5 Sound power level comparison (top) and the environmental correction factor K_2 (bottom) for the laboratory environment. The valid limit of ±4 dB is highlighted in gray dashed lines. 315
A.6 Sound pressure level (SPL) in (a) narrowband and (b) one-third octave band of the raw measurement (Exp. raw), background noise (BG), and corrected measurement (Exp. corr.) for the reference fan under $P = 0$ Pa and $N = 7050$ r/min. 316
A.7 Sound pressure level (SPL) in narrowband of the raw measurement (Exp. raw) and the corrected measurement (Exp. corr.) for the reference fan under $P = 0$ Pa and $N = 7050$ r/min. 318

B.1 Flow chart of the Low-Order Noise Analysis Tool (LONAT). 322
B.2 Surface pressure of a fan blade, predicted by LONAT. 324

C.1 The set-up of BANC-III measurements. 326
C.2 Pressure coefficient validation against BANC-III results. 327
C.3 Comparison between experimental data [309] and six WPS models for the wall pressure spectrum predictions. 328
C.4 Comparison between experimental data [309] and six WPS models for the far-field noise predictions in 1/3 octave band. 329
C.5 Setup for calculating trailing edge noise directivity. 330
C.6 Directivity of acoustic emission from trailing edge for case 1, predicted by Lee's WPS model and Amiet's model. 330
C.7 The setup of NASA measurements. 331
C.8 Comparison between experimental data [52], BPM predictions [52], and six WPS models for far-field noise predictions in 1/3 octave bands. . . . 332

D.1 The geometry of the two-bladed APC-96 UAV propeller ($N = 5000$ r/min, $R_t = 150$ mm), adapted from Ref. [55]. 333
D.2 Chord and twist distributions of the APC-96 UAV blades shown in Fig. D.1. 334
D.3 Schematic of the chordwise and spanwise elements of the APC-96 rotor. 336
D.4 Effect of the number of spanwise elements on the propeller forces. 336
D.5 Effect of the number of spanwise elements on the far-field noise predictions. 336
D.6 Aerodynamic results comparison between measurements, LBM/VES and reduced-order model prediction. 337
D.7 Surface pressure distribution of one blade of the APC-96 UAV rotor. . . . 337

D.8 Comparison between measurements [55], LBM/VLES [55] and predicted broadband results based on different wall pressure models. 338
D.9 Comparison between measurements [55], LBM/VLES [55] and predicted results based on Rozenberg's wall pressure model. 339

G.1 Comparison of the noise level of the baseline fan under different loading conditions: (a) Overall sound pressure level and (b) Narrowband sound pressure level. 349

List of Tables

1.1 Duration (in hours) of allowable exposures based on Occupational Safety and Health Administration (OSHA) [18] and National Institute for Occupational Safety and Health (NIOSH) [19] criteria. PEL = permissible exposure limit; REL = recommended exposure limit. 4

2.1 Aeroacoustic noise sources and source characteristics ('T' = tonal, 'BB' = broadband). 19

2.2 Parameters for six semi-empirical wall pressure spectrum models. 43

2.3 Comparison of computational time of different modelling methods. . . . 48

2.4 Fan optimisation and noise control strategies for various axial fan applications. 50

3.1 Parameters for the selected single impeller fan. 65

3.2 Predicted overall aerodynamic and aeroacoustic results by LES under different backpressure conditions. 77

4.1 Optimal correction factors M_{AR} and prediction errors E comparing to CFD results. Tip clearance ratio (T_R) is defined $T_R = t/R_t$. 121

4.2 Optimal correction factors M_{AR} and prediction errors E compared to experimental results for eight different commercial fans. 121

6.1 Test cases for low-Reynolds number cascade experiments. 148

7.1 Calibrated momentum thickness Reynolds number (Re_θ) range for wall pressure spectrum (WPS) models. APG: adverse pressure gradient; ZPG: zero pressure gradient; FPG: favorable pressure gradient. 167

7.2 Comparison of the averaged aerodynamic quantities between prediction and LES [210]. 172

8.1 Impedance models for micro-slit panel absorbers (C-MSPAs). 193

9.1 Review of studies for blade tip flow. 221

9.2 Comparison cases between CFD simulations of fan blade tip flow (c = 26mm, See Chapter 4) and SPIV measurements of NACA 0012 blade tip flow (c = 50mm). Both blades have a mid-span Reynolds number of around 5×10^4 and an effective angle of attack of around 8°. 236

A.1 Uncertainty analysis of the measured parameters. 310
A.2 Uncertainty budget for determinations of σ_{R0} for the noise measurements. The entire band of frequencies [500 Hz, 10 kHz] is considered to calculate the combined uncertainty. 319
A.3 Combined uncertainty for noise measurements. 319

C.1 Test conditions for BANC-III experiments. 326
C.2 Test conditions for NASA experiments. 331

D.1 Design parameters for the APC-96 rotor. 334

F.1 Optimised geometrical parameters of the C-MSPAs under normal incidence. The parameters include the diameter of the micro-slit (d), the thickness of the micro-slit (t), the diameter of the micro-slit array (D), and the width of the micro-slit array (W). The optimised parameters are presented for three test cases: NI-1: 600 Hz, NI-2: 600 & 1200 Hz, and NI-3: 1000–2000 Hz. The overall absorber dimensions are 40 mm × 30 mm × 40 mm ($L_A \times D_A \times H_A$) and the wall thickness is h = 1 mm. 347
F.2 Optimised geometrical parameters of the C-MSPAs under grazing incidence. The parameters include the diameter of the micro-slit (d), the thickness of the micro-slit (t), the diameter of the micro-slit array (D), and the width of the micro-slit array (W). The optimized parameters are presented for three test cases: GI-1: 600 Hz, GI-2: 1200 Hz, and GI-3: 900–1800 Hz. The overall dimensions of the annular rings are 60 mm length, 30 mm thickness (inner diameter of R_{in} = 77 mm and outer diameter of R_{out} = 117 mm). 348

Nomenclature

Symbols

$\mathbf{A}$	Left-hand side matrix of the linear equation system of potential flow
$\mathbf{b}$	Right-hand side matrix of the linear equation system of potential flow
$\mathbf{M}_\beta$, $\mathbf{M}_\theta$, $\mathbf{M_r}$	Coordinates transformation matrix
$\mathcal{L}$	Aeroacoustic transfer function, [-]
$\mathrm{div}(u, v)$	Normalised 2D divergence, [-]
$\vec{F}$	Unsteady force, [N]
$\vec{x_a}$	Airfoil frame coordinates, [m]
$\vec{x}$	Global fan frame coordinates, [m]
AR	Aspect ratio, [-]
B	Number of rotor blades, [-]
c	Chord length, [mm]
c_0	Speed of sound in air, [m/s]
C_d	Drag coefficient, [-]
C_f	Skin friction coefficient, [-]
C_l	Lift coefficient, [-]
C_p	Pressure coefficient, [-]
D	Air cavity depth, [m]
D	Diameter, [m]
D	Drag force, [N]
$d\eta$	Blade sectional efficiency, [-]
dF_d	Drag force, [N]

dF_l	Lift force, [N]
dp/dx	Static pressure gradient, [Pa/m]
dQ	Blade sectional torque, [Nm]
dT	Blade sectional thrust, [N]
f	Frequency, [Hz]
f_r	Fan rotational frequency, [Hz]
FS	Frequency scaling factor, [-]
G	Clauser's shape factor, δ/θ, [-]
$G(f)$	Weight function, [-]
G_{pp}	Single-sided PSD, [dB/Hz]
H	von Kármán shape factor, δ^*/θ, [-]
h	Non-dimensional spacing, $h = s/c$, [-]
I	Turbulence intensity, [-]
I'	Modified turbulence intensity, [-]
k	Interference factor, [-]
k	Wavenumber, [m^{-1}]
L_p	Sound pressure level, [dB]
M	Torque, [Nm]
M_{AR}	Correction factor, [-]
Ma	Mach number, [-]
Ma_r	Tangential Mach number, [-]
N	Fan speed, [r/min]
n	Fan speed, $N/60$, [r/s]
P	Static-to-total pressure, [mmH_2O]
p	Sound pressure, [Pa]
p_{ref}	Reference pressure, 2×10^{-5} [Pa]
P_{elec}	Electrical power, [W]
Q	Volumetric flow rate, [m^3/min]

r	Radius, [m]
R_t	Tip radius, [m]
R_T	Ratio of timescales, [-]
Re	Chord-based Reynolds number, $Re = Uc/\nu$, [-]
Re_δ	Reynolds number based on δ, $\delta U_e/\nu$, [-]
S	Number of stator blades (struts), [-]
s	Blade span, [m]
s	Spacing (pitch) between airfoils in cascade, [m]
S_{pp}	Double-sided PSD, [dB/Hz]
T	Thrust, [N]
t	Thickness of the slit, [m]
t	Tip gap size, [mm]
T_R	Tip clearance ratio, t/r_t, [-]
TL	Transmission loss, [dB]
u, v, w	Velocity components in x, y, z directions, [m/s]
U_∞	Freestream velocity, [m/s]
U_c	Convection velocity, [m/s]
U_e	Velocity at the boundary-layer edge, [m/s]
V_∞	Freestream velocity, [m/s]
x, y, z	Coordinates in the global frame, [m]
Z	Acoustic impedance, [kg/m^2/s]

Greek Symbols

α	Angle of attack, [°]
α_0	Absorption coefficient, [-]
α_i	Induced angle of attack, [°]
β	Blade twist angle, [°]
δ	Boundary layer thickness, $\delta = \int_0^\infty (1 - u/U_e)\, dy$, [m]
δ^*	Boundary layer displacement thickness, $\delta^* = \int_0^\infty u/U_e dy$, [m]

δ_θ	Boundary layer momentum thickness, $\delta_\theta = \int_0^\infty u/U_e\,(1 - u/U_e)\,dy$, [m]
η	Efficiency, [-]
Γ	Gamma function, [-]
Γ	Total circulation, [m^2/s]
γ	Strength of point vortex per unit length, [m/s]
ν	Kinematic viscosity, [m^2/s]
Ω	Rotational speed, [1/s]
ω	Angular frequency, [1/s]
Φ	Non-dimensional fan flow rate coefficient, [-]
Φ	Power spectral density, [Pa^2 s]
ϕ	Effective inflow angle, [°]
ϕ	Panel porosity, [-]
Φ_{pp}	Wall pressure spectrum, [dB/Hz]
Φ_{ww}	Turbulence spectrum, [dB/Hz]
Ψ	Non-dimensional fan pressure coefficient, [-]
ρ	Fluid density, [kg/m^3]
σ	Standard deviation, unit depends on the quantity of interest
σ	Strength of point source per unit length, [m/s]
σ_c	Solidity of airfoil cascades $\sigma_c = c/s$, [-]
τ_w	Wall shear stress, [Pa]
θ	Azimuth angle of the observer, [°]
ζ	Stagger angle, [°]
u_t	Friction velocity, $\left(\tau_w/\rho\right)^{1/2}$, [m/s]

Subscripts and Superscripts

∞	Freestream condition
u, v, w	Velocity components in x, y, z directions
x, y, z	Coordinates in the global frame
1	Inlet condition

2	Outlet condition
b	Blade
BPF	Blade passing frequency
eff	Effective
h	Hub
max	Maximum
min	Minimum
ref	Reference
rms	Root mean square
t	Tip

Acronyms and Abbreviations

AOA	Angle of attack
APG	Adverse pressure gradient
BEMT	Blade element momentum theory
BET	Blade element theory
BOASPL	Broadband OASPL
BPF	Blade passing frequency
BPM	Brooks Pope and Marcolini
C-MSPA	Compact micro-slit panel absorber
CAA	Computational aeroacoustics
CFD	Computational fluid dynamics
CR	Counter-rotating
DES	Detached eddy simulation
DNS	Direct numerical simulation
EF	Equivalent fluid
FEA	Finite element analysis
FEM	Finite element method
FG	Feedback generator

FPG	Favorable pressure gradient
FUT	Fan under test
FW-H	Ffowcs Williams-Hawkings
GI	Grazing incidence
HDD	Hard disk drive
IRI	Asymmetric inlet-rotor interaction
IV	Induced vortex
IVTs	Inlet vortex tubes
LBM	Lattice-Boltzmann method
LE	Leading edge
LES	Large eddy simulations
LLT	Lifting-line theory
LONAT	Low-Order Noise Analysis Tool
M	Middle-shortened winglet
MPP	Micro-perforated panel
MPPA	Micro-perforated panel absorber
MRF	Multiple reference frame
MSP	Micro-slit panel
MT	Momentum theory
NH	Normalised helicity
NI	Normal incidence
NRMSE	Normalised root-mean-square error
OASPL	Overall sound pressure level
PS	Pressure side
PSD	Power spectral density
PWM	Pulse-width modulation
R	Rear-shortened winglet
RANS	Reynolds-averaged Navier-Stokes

RMS	Root mean square
ROM	Reduced-order model
RSI	Rotor stator interaction
RSS	Reference sound source
RV	Randeberg and Vigran
SLA	Stereo-lithography
SPIV	Stereoscopic particle image velocimetry
SPL	Sound pressure level
SS	Suction side
TE	Trailing edge
TLF	Tip leakage flow
TLV	Tip leakage vortex
TOASPL	Tonal OASPL
TS	Two sides
TSV	Tip suction vortex
UAV	Unmanned aerial vehicle
URANS	Unsteady Reynolds-averaged Navier-Stokes
VLES	Very large-eddy simulation
VPM	Vortex panel method
VSI	Tip vortex-shroud interaction
W	Winglet
WALE	Wall-adapting local eddy-viscosity
WPS	Wall pressure spectrum
ZPG	Zero pressure gradient

Chapter 1

Introduction

1.1 The importance of axial fans for thermal management challenges

There has been a significant increase in data storage and computation in recent years due to factors such as the growing demand for streaming video and gaming traffic, as well as advancements in digital technologies like machine learning (ML) and artificial intelligence (AI) [1]. This surge in data and network services has led to higher power consumption, heat generation, and noise levels in data centres [2–5].

According to the latest report from the International Energy Agency (IEA), data centres worldwide consumed 460 TWh of electricity in 2022, accounting for approximately 2% of global electricity consumption [6]. Projections indicate that this consumption will increase to between 650 and 1050 TWh by 2026. Data centre power demand is expected to grow by 160% by the end of the decade, according to Goldman Sachs Research [7]. Additionally, carbon dioxide emissions from data centres may more than double between 2022 and 2030 [7]. In the EU, data centre power consumption could increase by 60% by 2030. The impact is particularly significant in Ireland, where data centres are projected to account for 32% of the country's total power consumption by 2026, up from 18% in 2022 [6]. A recent report from IDA Ireland in 2023 [8] highlights that nearly 1,000 companies, including global giants like Apple, Google, Microsoft, and Amazon, have chosen Ireland as their European ICT hub. Ireland's temperate climate makes it a cost-effective location for data centre cooling, offering greater efficiency, reliability, security, and accessibility compared to other European regions. Currently, over 80 data centres operate in the country. However, EirGrid has imposed a moratorium on new data centre connections to the national electricity grid in the Dublin area until 2028 due to their significant power consumption (over 18% of national electricity) and environmental impact [9]. This has spurred interest in developing energy-efficient and sustainable

data centres to meet the rising demands for data storage and computation.

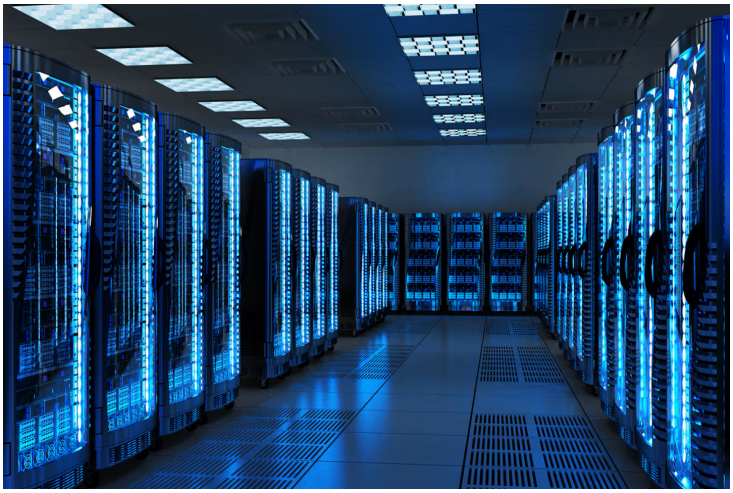

Figure 1.1: Typical data centre server room, sourced from *The Irish Times* [10].

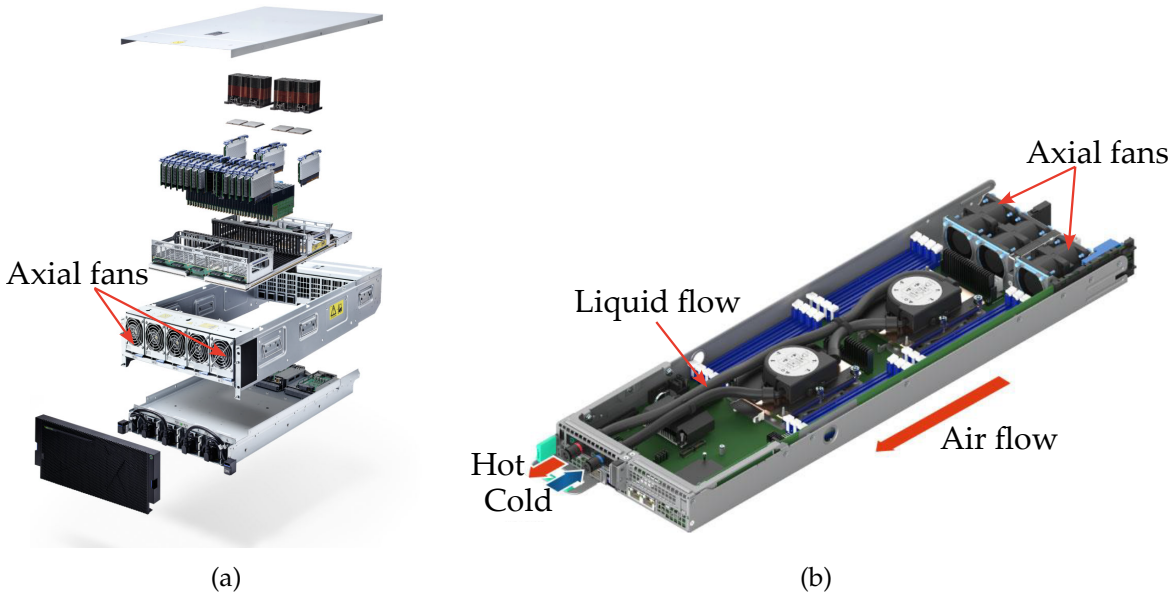

(a) (b)

Figure 1.2: Examples of server cooling systems: (a) Air-cooled IBM E980 5U server with multiple axial fans, adapted from Ref. [11]; (b) Hybrid air/liquid-cooled Intel server board S2600BP with a liquid cooling block and multiple axial fans, adapted from Ref. [12].

Cooling systems in data centres are major energy consumers, with traditional air-cooling methods accounting for approximately 33% of total energy use [2]. While liquid cooling is gaining traction for high-density applications, air cooling remains the dominant solution due to its simplicity and cost-effectiveness [3]. Figure 1.1 shows a typical data centre server room. The rapid advancements in the electronics industry have introduced new challenges in cooling systems, as modern processing chips (CPUs, GPUs) have become more compact and operate at higher speeds, resulting in denser heat generation [4, 5]. Efficient and quiet cooling solutions for data centres are a priority for governments, industries, and academia. In 2023, the U.S. Department of

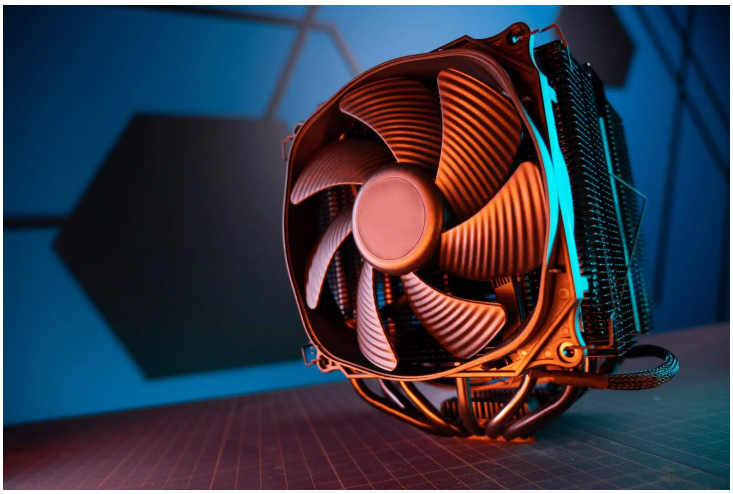

Figure 1.3: Axial fan cooled-heatsink assembly, sourced from *Electronics Cooling* [16].

Energy committed $40 million to advance cooling technology for data centres [13]. Traditional thermal management of data centre servers relies heavily on forced air cooling, typically involving arrays of axial cooling fans that can consume over 20% of the server's total power [14]. In fully air-cooled data centres, bulky heatsinks with high fin densities are required on high flux components (*e.g.*, CPUs, GPUs) [15], creating significant barriers to airflow. Recent hybrid air/liquid-cooled systems have alleviated this issue by freeing up internal space previously occupied by bulky heatsinks, thereby reducing system resistance and achieving a more compact design. Figure 1.2 shows examples of server cooling systems, including an air-cooled IBM E980 5U server [11] and a hybrid air/liquid-cooled Intel server board S2600BP [12]. To meet the increasing demands of compact packaging and high-density thermal management, smaller and higher rotational-speed fans are increasingly being used in these air-cooled systems. A typical axial fan cooled-heatsink assembly is shown in Figure 1.3, sourced from the online version [1] of the published article in *Electronics Cooling* [16].

However, the use of small-sized (40–140 mm), high rotational-speed (5,000–20,000 r/min) axial fans in compact packaging not only consumes substantial energy but also generates excessive aeroacoustic noise, potentially exceeding regulatory workplace noise limits [17–19]. Such noise can compromise worker comfort, affect electronic component reliability, and even lead to data centre failures [20–22]. The noise levels for one signle axial fan in data centres can reach up to 60–80 dB at a distance of 1 meter [20, 23]. With multiple servers equipped with multiple cooling fans, the cumulative noise level in data centres has become a pressing concern, potentially exceeding workplace noise restrictions set by regulatory bodies. The Occupational Safety and Health

[1] W. Zhao, S. Wasala, and T. Persoons, "Rapid and Accurate Analytical Model for Predicting Axial Fan Performance in Electronics Cooling,", *Electronics Cooling*, Oct. 2023. Online: Available at: *Electronics Cooling* Articles.

Table 1.1: Duration (in hours) of allowable exposures based on Occupational Safety and Health Administration (OSHA) [18] and National Institute for Occupational Safety and Health (NIOSH) [19] criteria. PEL = permissible exposure limit; REL = recommended exposure limit.

Noise Level (dBA)	85	88	90	94	95	100	105	110	115
OSHA, PEL	16	-	8	-	4	2	1	0.5	0.25
NIOSH, REL	8	4	-	1	-	0.25	-	-	-

Administration (OSHA) [18] and National Institute for Occupational Safety and Health (NIOSH) [19] criteria on the duration (in hours) of allowable exposures are shown in Table 1.1. Exposure to high noise levels can cause numerous negative health effects for industrial employees, including stress, tinnitus, and hearing loss, as detailed in Figure 1.4. In addition to endangering human health, high noise levels can also compromise the availability and integrity of hard disk drives (HDDs) used in data centres. Several studies and reports have demonstrated that high-frequency tonal noise may damage HDDs [20–22] or even bring down an entire data centre [24]. Therefore, addressing the challenges associated with fan-based air cooling systems is crucial for extending the lifespan of electronic components and achieving efficient and quieter air cooling methods in data centres.

level	Noise source	Health effects
140dB	Jet plane take off, firecracker, gun shot	Sudden damage to hearing
130dB	Pain threshold exceeded	
120dB	Ambulance siren, pneumatic drill, rock concert	
110dB	Night clubs, disco	
100dB	Motor cycle at 50km/h	
90dB	Heavy goods vehicle at 50km/h	
85dB	Hearing protection recommended in industry	Hearing loss, tinnitus
75dB		Cardiovascular effects
70dB		Sleep disturbances
65dB		Stress effects
60dB		Annoyance
55dB	Desirable outdoor level	
50dB	Normal conversation level	
40dB	Quiet suburb	
30dB	Shoft whisper	
20dB	Normal conversation level	

Figure 1.4: Noise effects on human health, adapted from Ref. [25].

Numerous applications of small axial fans in confined spaces, such as high-power gaming consoles, edge computing, office local servers, and 6G base stations, face significant challenges related to aeroacoustic noise. This issue is particularly critical in

environments with many users and staff, where noise sensitivity is higher. Studies have shown that annoyance in offices becomes significant at sound levels above 55 dB [26], a threshold easily surpassed by the high rotational-speed cooling fans commonly found in electronics enclosures. Major industry players, including IBM, Google, Seagate, Intel, and Huawei, recognise the urgent need for innovative design methodologies over the next decade to enhance cooling efficiency while minimising noise in electronics cooling systems [4, 20]. Many of these companies have invested in research and development collaborations with academic institutions to address these challenges. Notable examples include the collaboration between Seagate and Trinity College Dublin (TCD) on aeroacoustic modelling, analysis, and synthesis of data centre systems to enable HDD tracking extendibility [20, 27, 28], as well as the NSF I/UCRC Cooling Technologies Research Center (CTRC) at Purdue University [2] on thermal management and aeroacoustics of air-cooled electronics enclosures (2021–2023) [23, 29–33], funded by a consortium of companies including Seagate, Intel, Google, IBM, and several other leading companies.

Despite the invention of the first axial-flow machine over 200 years ago [34] and the use of fans in electronics for more than 40 years [35], the aerodynamics and aeroacoustics of small electronics cooling fans in confined spaces, such as server chassis and enclosures, remain challenging. Since the introduction of the IBM PC 5150 in 1981 [35], fans have been essential to cooling systems, yet their importance is often underestimated. Axial fans, comprising rotating and stationary blades, are crucial in various applications, including data centres, automotive cooling systems, aerospace, and HVAC systems. Despite their widespread use, research on small-sized, high rotational-speed electronics cooling fans is limited compared to other fields. Several factors contribute to this gap. Firstly, axial fans used in data centres are generally more cost-effective than those in aerospace or automotive applications, leading to smaller research and development budgets. Secondly, for a long time, noise was not the primary concern in many applications where heat transfer performance was paramount. Lastly, the noise generated by axial fans in confined spaces is more complex than in free space due to sound reflection and scattering by nearby enclosure walls, inflow nonuniformity and distortion, and excessive fan back pressure [36, 37].

The lack of understanding of the aerodynamic losses and aeroacoustic noise generation mechanisms in confined geometries has led to poor design practices and suboptimal cooling solutions. For instance, the widespread use of asymmetric inlet bellmouths in electronics cooling fans persists despite early identification of their disadvantages by Huang in 2003 [36]. The detailed flow structures caused by the interaction between the asymmetric inlet shape and the rotor tip remain unexplored, leading to a lack of

[2] Cooling Technologies Research Center, https://engineering.purdue.edu/CTRC/.

awareness in the industry regarding potential noise issues. The presence of stationary obstacles in confined environments significantly increases the backpressure on the fan, resulting in reduced fan flow performance, increased noise generation, and higher thermal resistance [38]. Fans operating under high backpressure conditions are more likely to run closer to or even in stall conditions, causing flow separation, stall, and increased turbulence, which further exacerbates noise levels. Previous studies [39–41] have observed that fan noise becomes more broadband under high load conditions, *i.e.*, high system resistances with high backpressure and low flow rate. However, there is a lack of exploration regarding the underlying mechanisms of noise generation under different operating conditions, including stall. Previous studies and applications [20, 42, 43] have often simplified fans to rotor-stator models, overlooking the effects of small features and backpressure on loss and noise generation. Additionally, due to the small-sized blades of electronic cooling fans, the flow typically falls within the low-Reynolds number regime ($Re \approx 10^4$–3×10^5), where laminar-turbulent transition and flow separation are more likely to occur [44]. The aerodynamic phenomena and noise generation mechanisms in this regime differ from those in the high Reynolds number flows encountered by large rotors. This necessitates a detailed investigation of the flow structures near the flow transition. High-fidelity computational fluid dynamics (CFD) simulations combined with computational aeroacoustics (CAA) techniques are expected to provide detailed insights into turbulent flow structures and noise generation mechanisms [20], this study will unravel the underlying mechanisms of noise generation in confined geometries and develop effective noise mitigation strategies for cooling fans by combining high-fidelity large eddy simulations (LES) with experimental studies.

Another significant challenge in developing quieter and more efficient axial fans is the lack of accurate and efficient tools for initial design and optimisation. Fan manufacturers often rely on simple empirical scaling laws to estimate overall sound levels in free space, which provides limited data for system-level design and optimisation. While high-fidelity CFD simulations combined with CAA techniques can simulate cooling fan noise with great detail, these methods are computationally expensive and difficult to integrate into the design and optimisation processes. A comparsion figure of different modelling approaches is shown in Figure 1.5, highlighting the trade-offs between accuracy and computational cost. Therefore, developing a quick evaluation tool for assessing the aerodynamic and acoustic performance of fans is crucial for effective system assessments and noise control strategies. The present study aims to address these challenges by developing a reduced-order model (ROM) to evaluate the aerodynamic and aeroacoustic performance of electronics cooling fans at low-Reynolds number flows ($Re \approx 10^4$–3×10^5). The insights gained from high-fidelity CFD and CAA simulations

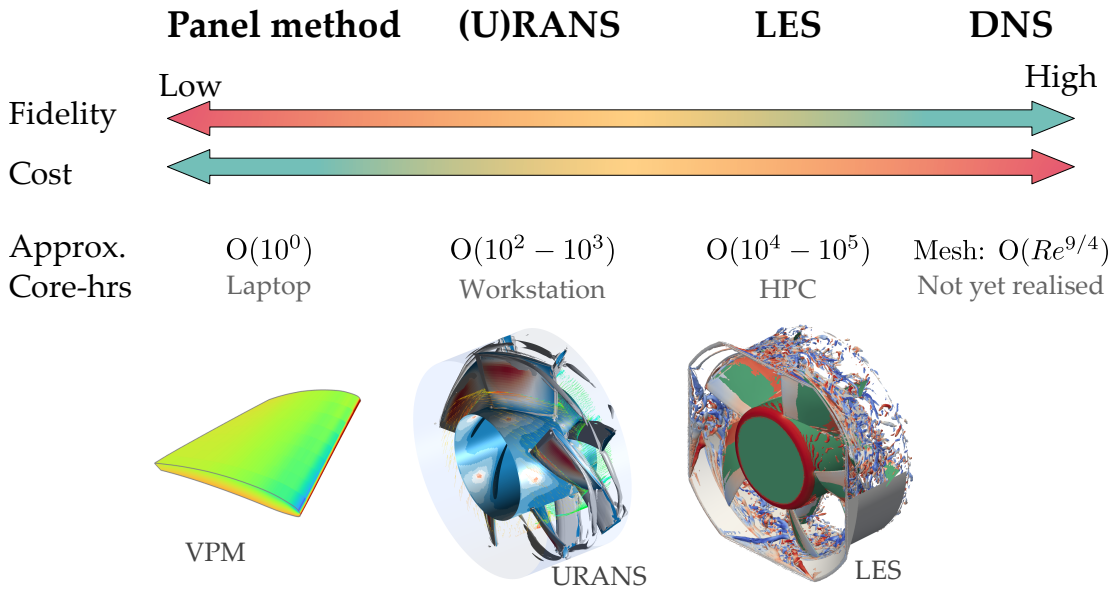

Figure 1.5: Comparison of different modelling approaches for electronics cooling fans, based on the results from this thesis. The trade-offs between accuracy and computational cost are highlighted. (U)RANS: (Unsteady) Reynolds-averaged Navier-Stokes; LES: Large eddy simulation; DNS: Direct numerical simulation; VPM: Vortex panel method.

and experimental studies will be used to develop a fast and reliable ROM that can be integrated into an aeroacoustic design and optimisation tool. This will enable the design of fans with less adverse acoustic emissions at low-Reynolds number flows, thereby contributing to the development of quieter and more efficient air cooling methods in data centres and other applications.

Finally, innovative fan designs and noise control strategies are desired to address the challenges associated with fan-based air cooling systems. Many leading fan manufacturers and data centre operators are investing in research and development of novel fan designs and noise mitigation methods. For example, Noctua [3] has developed a series of low-noise cooling fans with advanced aerodynamic designs and noise reduction features, such as blade serrations and low-noise fan motor. However, their designs are limited to lower rotational speed (less than 5,000 r/min) computer fans. With the insights gained from high-fidelity modelling and reduced-order modelling, this study will explore advanced fan geometric modifications, as well as the latest acoustic liners, aiming to develop innovative fan designs and noise control strategies with reduced noise emissions and improved aerodynamic performance.

This study aims to establish best practice guidelines for high-fidelity modelling, reduced-order modelling, and noise reduction in electronics cooling axial fans. Insights gained from this research, focused on axial fans in data centres, will be applicable across vari-

[3] Noctua.at, https://noctua.at/.

ous industries, including telecommunications (*e.g.*, 6G, edge computing), aerospace, automotive, and urban aerial mobility (UAM). The project seeks to deepen our understanding of flow-induced noise generation mechanisms and develop effective noise mitigation strategies for cooling fans. Achieving these objectives will optimise design practices and lead to quieter data centre cooling systems. Both theoretical and experimental approaches will be employed, contributing to sustainable data centre operations, supporting Ireland's net-zero carbon targets for 2050 [45], and aligning with the United Nations' Sustainable Development Goals [46].

1.2 Goals and objectives of the thesis

The energy consumption and aeroacoustic challenges posed by forced air-cooled data centre systems are well-documented. Accurately predicting the acoustic noise generated by fan-cooled electronics using numerical methods remains difficult, primarily due to high computational costs and a limited understanding of noise generation mechanisms. This research aims to address these challenges by developing quieter air cooling methods for data centres. The primary goals are to investigate the aerodynamic and aeroacoustic performance of axial cooling fans and to explore innovative noise control measures. Specifically, the research objectives are as follows:

1. **LES for high-fidelity modelling of flow physics and noise generation**: Conduct high-fidelity large eddy simulations (LES) combined with the Ffowcs Williams-Hawkings (FW-H) acoustic analogy method to investigate noise generation mechanisms in axial fans under normal operating and stall conditions. This objective aims to provide detailed insights into the flow physics and noise sources of axial fans across various operating conditions. The findings will inform the development of low-fidelity noise prediction models and passive noise control strategies. **Part I** will detail the methodology, validation, and results of the high-fidelity simulations. This work has culminated in a published journal article:

    - **Journal article**: W. Zhao, S. Wasala, T. Persoons, "Large eddy simulation for aeroacoustic prediction and characterization of electronics cooling axial fans under various operating conditions," *Applied Acoustics*, vol. 231, p. 110530, Mar. 2025.

2. **ROM for aerodynamics considering tip flow and cascade effects**: Develop a low-fidelity, meshless prediction model for axial fans to accurately predict aerodynamic performance under normal operating conditions. This reduced-order model (ROM) will use the blade element method and panel method to represent the blade geometry and flow field, respectively. To improve prediction accur-

acy, the model will include the effects of tip clearance. Additionally, a source vortex panel method (SVPM) will be introduced to account for cascade effects in high-solidity fan performance predictions. This objective aims to provide a fast and reliable tool for fan performance assessment, laying the groundwork for subsequent noise prediction studies. This objective will be addressed in Chapter 4 – 6 of **Part II**. This work has resulted in a published journal article, two peer-reviewed conference papers, and one peer-reviewed magazine article:

- **Journal article**: W. Zhao, S. Wasala, T. Persoons, "On the fast prediction of the aerodynamic performance of electronics cooling fans considering the effect of tip clearance," *IEEE Transactions on Components, Packaging and Manufacturing Technology*, vol. 13, no. 8, pp. 1139-1146, Aug. 2023.
- **Conference paper**: Reduced-order model for predicting aerodynamic performance of dual impeller fans in data centre cooling systems," in 2023 29th International Workshop on Thermal Investigations of ICs and Systems (THERMINIC), Budapest, Hungary: IEEE, Sep. 2023, pp. 1-6.
- **Conference paper**: W. Zhao, S. Wasala, T. Persoons, "Development and assessment of an inviscid source vortex panel method for low-Reynolds number airfoil cascades," in AIAA SCITECH 2024 Forum, Orlando, Florida, AIAA 2024-2507, 2024.
- **Magazine article**: W. Zhao, S. Wasala, T. Persoons, "Rapid and accurate analytical model for predicting axial fan performance in electronics cooling," *Electronics Cooling*, pp. 22-26, Jun. 2023.

3. **ROM for aeroacoustics including tonal and broadband noise**: Building on the validated ROM for aerodynamics, develop a low-fidelity noise prediction model for axial fans to accurately predict noise under normal operating conditions. This model will integrate various low-fidelity noise prediction methods to provide a comprehensive prediction of fan tonal and broadband noise. This objective aims to deliver a fast and reliable tool for fan performance assessment, boosting the co-design of flow, heat transfer, and noise solutions in thermal management systems. The findings will also inform the design of passive noise control methods. The ROM for aeroacoustics will be developed and validated in Chapter 7 of **Part II**. This work has resulted in two peer-reviewed conference paper and a journal article currently under review:

   - **Conference paper**: W. Zhao, S. Wasala, T. Persoons, "Reduced-order aeroacoustic modelling of electronics cooling fans," in Proceedings of the International Congress on Sound and Vibration, Society of Acoustics, 2022.

- **Conference paper**: W. Zhao, S. Wasala, T. Persoons, "Towards quieter air-cooling systems: Rotor self-noise prediction for axial cooling fans," in 2022 28th International Workshop on Thermal Investigations of ICs and Systems (THERMINIC), Dublin, Ireland: IEEE, Sep. 2022, pp. 1-4.

- **Journal article**: W. Zhao, S. Wasala, T. Persoons, "Fast prediction of broadband and tonal noise of electronics-cooling axial fans," *Journal of Sound and Vibration*, in Review, JSV-D-25-00091, 2025.

4. **Innovative acoustic liners**: Design and optimise compact acoustic liners aimed at significantly reducing noise without compromising the aerodynamic performance of axial fans in confined spaces. This objective will explore the use of micro-slit panel absorbers (MSPAs) as a novel passive noise control method. The design and optimisation of these acoustic liners will be guided by the insights gained from the high-fidelity simulations and the low-fidelity noise prediction model. The findings will inform the development of innovative passive noise control methods for axial fans that can be integrated into existing systems. This objective will be addressed in Chapter 8 of **Part III**. This work has resulted in a journal article currently under review:

   - **Journal article**: W. Zhao, J. Wang, S. Wasala, J. Kennedy, and T. Persoons, "Compact micro-slit panel absorbers for low-frequency tonal and broadband noise control," *Applied Acoustics*, in Review, APAC-D-25-00510, 2025.

5. **Tip leakage flow investigation using SPIV and noise mitigation with winglets**: Propose a novel passive noise control method using winglets to mitigate tip leakage flow and reduce noise generation in axial fans. This objective will involve a detailed experimental investigation of tip leakage flow structures using stereoscopic particle image velocimetry (SPIV) to gain insights into the underlying flow physics. The findings will inform the development of effective winglet designs aimed at noise reduction. Given the complexity of tip leakage flow in actual fans, a simplified fixed-blade endwall configuration will be employed for initial studies. Chapter 9 will delve into the tip leakage flow structures, while Chapter 10 will focus on the noise reduction mechanisms facilitated by winglets in axial fans. A journal article has been published partially based on this work:

   - **Journal article**: J. Hickey, W. Zhao, T. Persoons, "Experimental and numerical investigation of winglet designs for optimized performance of small axial fans," *Applied Acoustics*, vol. 231, p. 110448, Mar. 2025.

1.3 Outline of the thesis

The outline of the thesis is visualised in Fig. 1.6. Each chapter covers the following topics:

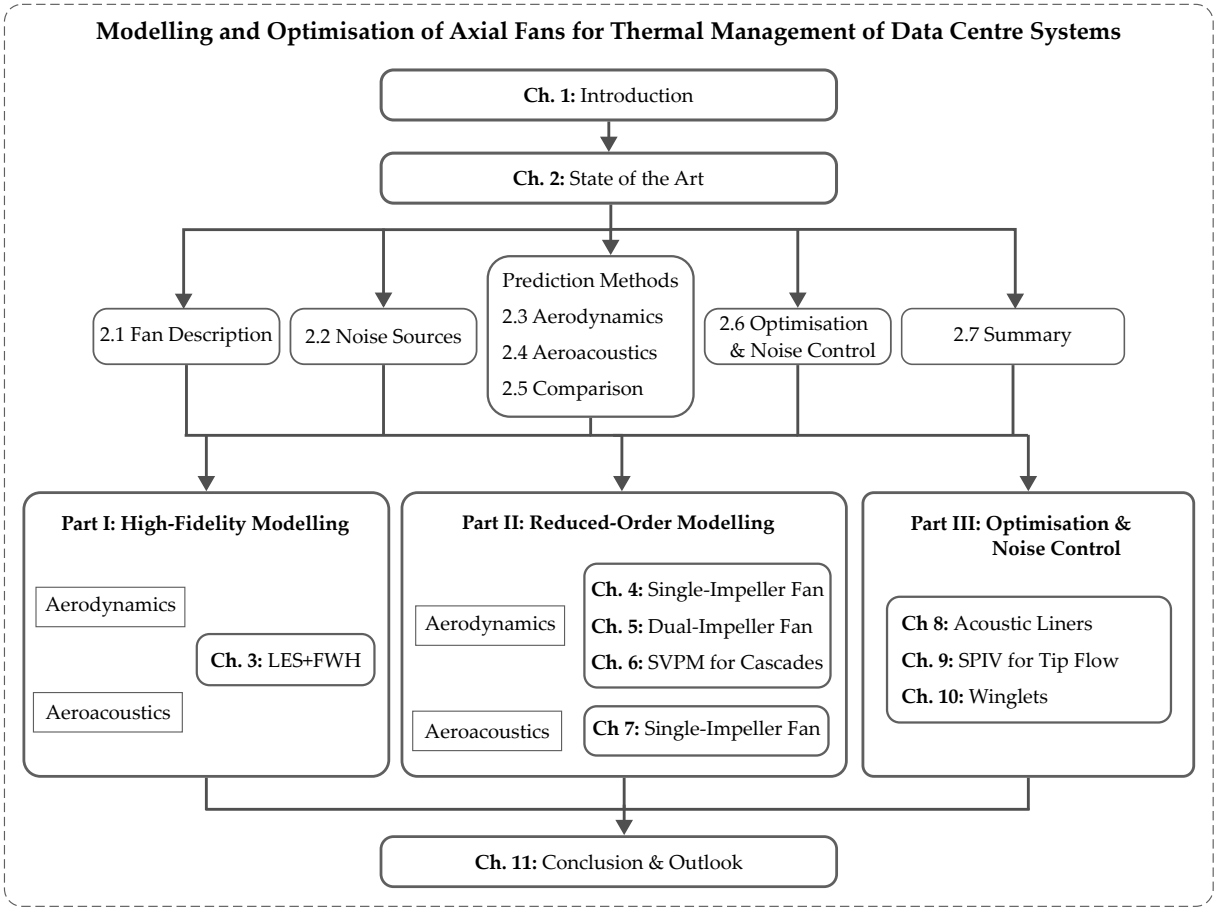

Figure 1.6: Outline of the thesis.

- **Chapter 1** provides an introduction to the research topic and outlines the objectives and structure of the thesis.
- **Chapter 2** reviews the state of the art in the aerodynamic and aeroacoustic performance of axial cooling fans, including noise generation mechanisms, prediction methods, and potential noise control strategies. This chapter also formulates the research questions and specific objectives.
- **Part I: Chapter 3** presents high-fidelity modelling for the flow physics and noise generation of axial fans. This part includes Chapter 3, detailing the methodology, validation, and results of the LES simulations for axial fans.
- **Part II: Chapter 4** details the development and validation of the reduced-order model (ROM) for predicting the aerodynamic performance of a single impeller axial fan, including the impact of tip clearance.

- **Part II: Chapter 5** extends the ROM model for aerodynamics to dual impeller counter-rotating (CR) axial fans, which feature two impellers rotating in opposite directions with a stator in between.
- **Part II: Chapter 6** proposes a source vortex panel method for cascade airfoils to address cascade effects in high-solidity fan performance predictions.
- **Part II: Chapter 7** details the methodology, validation, and results of the ROM for aeroacoustics, including the prediction of tonal and broadband noise of axial fans.
- **Part III: Chapter 8** focuses on the design and optimisation of novel acoustic liners, compact micro-slit panel absorbers (C-MSPAs), for axial fans in confined spaces.
- **Part III: Chapter 9** explores the tip leakage flow structures using stereo particle image velocimetry (SPIV) for a simplified fixed-blade endwall configuration. It provides insights into the flow physics and guides the development of tip flow control strategies.
- **Part III: Chapter 10** further investigates the noise reduction mechanisms of winglets in axial fans, focusing on the design and optimisation of winglet configurations for noise reduction.
- **Chapter 11** summarises the key findings of the study and discusses the implications for future research and industry applications.

Chapter 2

State of the Art

The aim of this chapter is to review the aeroacoustic noise generation mechanisms, aerodynamic and aeroacoustic prediction methods, and potential fan noise control strategies for axial cooling fans. This review will establish the current state of the art in this field. First, a brief overview of fan structures and characteristics is provided to offer a foundational understanding of fans used in the electronics cooling industry, as presented in Section 2.1. The sources of noise in general airfoils, rotating blades, and axial fans, along with their characteristics, are examined in Section 2.2. Widely used analytical, semi-empirical, and numerical models for the aerodynamic and aeroacoustic analysis of fans are discussed in Section 2.3 and Section 2.4, respectively. A comparative analysis of the advantages and disadvantages of these prediction models is provided in Section 2.5. Section 2.6 presents several common methods for mitigating fan noise. Finally, the limitations of existing research and the research gaps that this thesis aims to address are discussed in Section 2.7.

2.1 Small-sized electronics cooling fans

2.1.1 Fan structure

Cooling fans are indispensable for dissipating heat in electronic devices, with axial-flow fans being particularly effective due to their ability to generate a high volume of air parallel to the shaft axis at relatively low pressure differences. As depicted in Fig. 2.1 for a single impeller axial fan, a typical cooling fan consists of rotor blades, stator blades, a hub, and an outer shroud with a short inlet.

- **Rotor blades:** The rotor blades are the primary components responsible for transferring energy from the motor to the fluid. The blade geometry, including the chord length, twist angle, and airfoil shape, significantly influences the aerodynamic performance and noise generation of the fan.

- **Stator blades (struts):** Positioned downstream of the rotor blades, the stator blades guide the airflow, reducing flow swirl and increasing pressure rise. Designed with streamlined shapes, stator blades aim to minimise aerodynamic losses, thereby improving overall fan performance. In small cooling fans, struts are non-streamlined and primarily support the motor assembly and electrical wiring.
- **Hub with motor:** The hub houses a brushless DC motor equipped with built-in driver electronics. Motor speed is precisely controlled using pulse-width modulation (PWM) signals, enabling fine-tuned adjustments to fan speed and performance.
- **Shroud (duct):** The shroud, an outer casing that encloses the rotor and stator blades, prevents radial fluid escape. It also streamlines airflow, reducing aerodynamic losses and contributing to noise reduction.
- **Inlet:** The fan inlet is commonly designed with an incomplete bellmouth shape due to the rectangular fan housing in electronics cooling applications. However, for optimal aerodynamic performance, a bellmouth-shaped inlet is preferred.

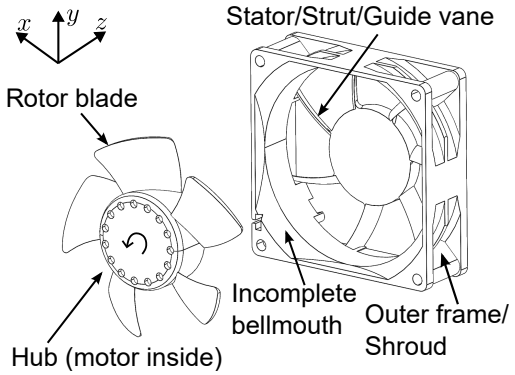

Figure 2.1: Exploded view of a single-impeller axial fan used in electronics cooling applications.

For applications requiring higher pressure rise, counter-rotating (CR) fans, which consist of two rotors rotating in opposite directions, are employed. These fans are commonly used in high-performance cooling systems, such as data centers and high-performance computing (HPC) systems. An exploded view of a counter-rotating (CR) fan typically used in data centers is shown in Fig. 2.2.

The small-sized axial fans used for cooling electroncis in data centre typically have a shroud diameter (D_s) of 40 to 140 mm and a rotational speed (N) of 5,000-20,000 r/min. The total-to-static pressure rise (P) is below 2,000 Pa, with a volumetric flow rate (Q) of below 8 m^3/min. These fans feature:

- **Low Reynolds number:** The Reynolds number (Re) is a dimensionless parameter that characterises the flow regime around the fan blades. Small-sized axial fans

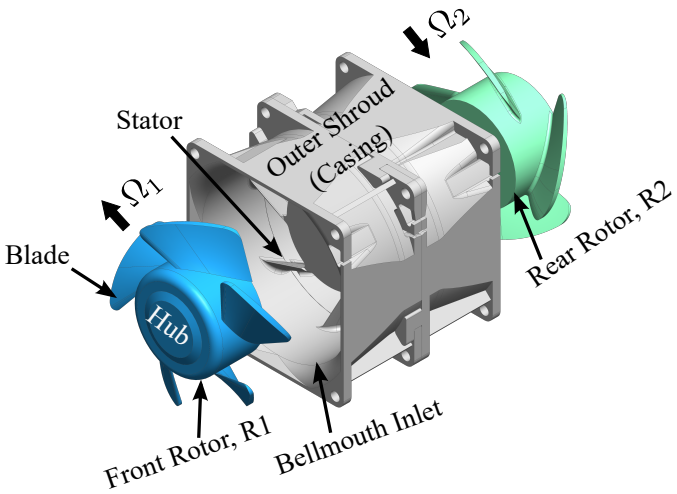

Figure 2.2: Exploded view of a counter-rotating (CR) dual-impeller fan utilised in HDD enclosures within data centers.

operate at low Reynolds numbers, typically ranging from 10^4 to $3{\times}10^5$ based on the blade chord length. This significantly influences their aerodynamic performance and noise characteristics.

- **Low Mach number:** The Mach number (Ma) characterises the flow speed relative to the speed of sound. These fans operate at low Mach numbers, typically less than 0.3. Operating in this subsonic regime ensures that compressibility effects are negligible, simplifying the aerodynamic analysis.
- **Low-to-moderate solidity:** Solidity, defined as the ratio of blade chord length to blade pitch, is crucial for fan performance. Fans with low to moderate solidity (solidity < 1) have fewer blades with larger spacing. In contrast, high solidity fans have more blades with smaller chord lengths. Low-to-moderate solidity fans are typically used in small-sized electronics cooling, where interactions between adjacent blades are less significant.
- **Small blade aspect ratio:** The blade aspect ratio is the ratio of the blade span to the blade chord length. These fans typically have a blade aspect ratio of 0.5–2.0.

2.1.2 Performance characteristics

The aerodynamic performance of a fan is typically characterised by the P-Q curve, also known as the characteristic curve. This curve represents the total-to-static pressure rise P as a function of the volumetric flow rate Q. A schematic of the P-Q curve for a small-sized axial flow fan is shown in Fig. 2.3. The maximum flow rate $Q_{\max}$ is achieved under free flow conditions, where there is zero backpressure, commonly referred to as the **free delivery condition**. Conversely, the maximum pressure rise $P_{\max}$ occurs under fully blocked flow conditions, corresponding to the maximum backpressure.

The **maximum efficiency condition** is identified at the peak of the P-Q curve, representing the point of highest efficiency. Fan efficiency η is defined as the ratio of the mechanical power imparted to the fluid to the total power input to the fan. This peak efficiency is typically found at a flow rate that is 70-80% of the maximum flow rate, making it the preferred operational range for most applications. The operating condition of the fan is determined by the intersection of the system flow resistance curve ($P \propto Q^2$) and the fan's P-Q curve. Ideally, the fan should operate at the maximum efficiency condition.

The **stall condition** occurs when flow separation on the blade surface leads to significant aerodynamic losses and increased noise generation, typically observed at low flow rates.

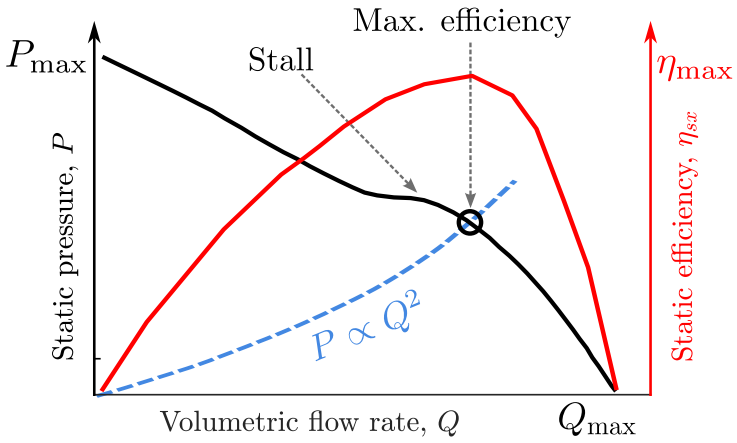

Figure 2.3: Schematic of P-Q curve for a small-sized axial flow fan. Created based on the experimental data from the present thesis.

The aeroacoustic performance of a fan is typically characterised by the overall sound pressure level (OASPL) and the narrowband sound pressure level (SPL) spectrum, as illustrated in Fig. 2.4 (a) and (b), respectively. The SPL is calculated as:

$$L_p = 20 \cdot \log_{10}\left(\frac{p}{p_{\text{ref}}}\right) \text{ dB}, \tag{1}$$

where p represents the sound pressure, and p_{ref} is the reference sound pressure of 2×10^{-5} Pa. The sound power level (SWL) is calculated as:

$$L_W = 10 \cdot \log_{10}\left(\frac{W}{W_{\text{ref}}}\right) \text{ dB}, \tag{2}$$

where W is the sound power and W_{ref} is the reference sound power of 10^{-12} W.

The OASPL is determined by converting the individual SPL values at each frequency from a logarithmic decibel scale to a linear scale, aggregating the sound energies, and

then converting back to a decibel scale using the formula:

$$\text{OASPL} = 10\log_{10}\left(\sum_{i=f_{\min}}^{f_{\max}} 10^{L_{p,i}/10}\right) \tag{3}$$

where $L_{p,i}$ represents the sound pressure level at each frequency, and $f_{\min}$ and $f_{\max}$ denote the minimum and maximum frequencies, respectively.

Ideally, minimising the OASPL at the maximum efficiency condition is desirable for low-noise operation. However, various factors influence the noise level, and the maximum efficiency condition may not always correspond to the lowest noise level. Generally, the noise level at the free delivery condition is higher than at the maximum efficiency condition, while the noise level at the stall condition is the highest.

In a typical noise spectrum under normal operating conditions (see Fig. 2.4 (b)), the noise generated by small-sized axial fans can be classified as tonal and broadband noise. The detailed mechanisms of these noise sources will be discussed in Section 2.2.

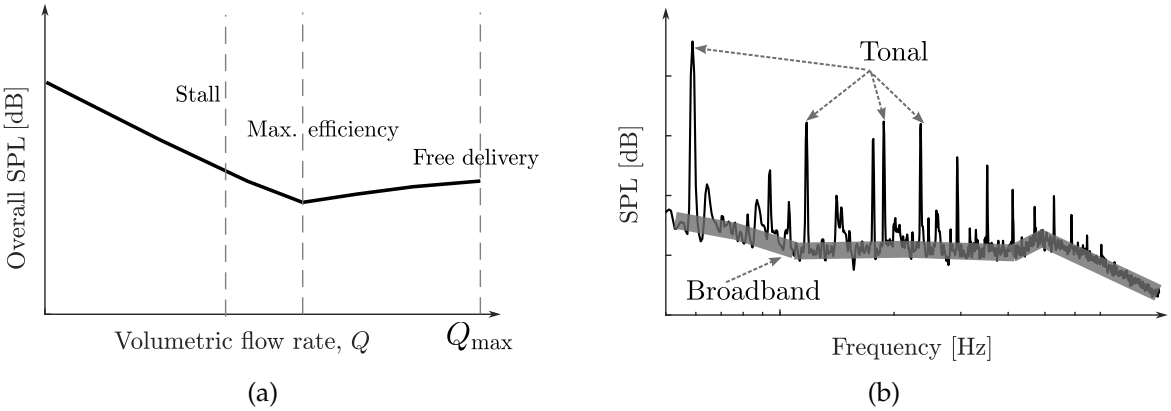

Figure 2.4: Typical noise level curve of a small-sized axial fan under different loading conditions: (a) Overall sound pressure level and (b) Narrowband sound pressure level spectrm at the free delivery condition. Created based on the experimental data from the present thesis.

2.1.3 Scaling laws

As mentioned in Chapter 1, the continuous development of compact packaging and high-power densities in electronic components generates substantial heat flux within small enclosures. This necessitates the use of high-rotational-speed cooling fans to meet stringent performance standards. Fan scaling laws are commonly employed to express the relationships between performance characteristics for dynamically similar fans. The scaling laws for fan flow rate Q, pressure rise P, and acoustic sound power

level L_W are given by [47]:

$$\begin{aligned} Q &\propto ND^3, \\ P &\propto N^2D^2, \\ L_W &\propto 10\log_{10}\left(\underbrace{N^3D^5}_{\text{Fan power}} \times \underbrace{(ND)^a}_{Ma\text{ effect}} \times \underbrace{\left(ND^2\right)^b}_{Re\text{ effect}}\right). \end{aligned} \tag{4}$$

Here, N represents the fan speed in r/min and D the diameter in m. The exponent a varies with different noise sources, with $a = 3$ for a dipole source [47]. The exponent b is typically between -1 and 0 [47]. Assuming representative values of $a = 3$ and $b = -0.5$, L_W can be simplified to:

$$L_W \propto 10\log_{10}\left(N^{5.5}D^7\right). \tag{5}$$

As indicated in Eq. 5, noise levels increase with fan speed. Cooling fans in data centre systems typically operate at high rotational speeds, producing high-frequency tonal noise up to about 10 kHz. Sharp tones within this range are particularly annoying.

Based on the scaling laws, the flow rate and pressure rise can be non-dimensionalised using the following equations [48]:

$$\begin{aligned} \Phi &= \frac{Q}{60\frac{\pi^2}{4}D^3n}, \\ \Psi &= \frac{P}{\frac{\pi^2}{2}\rho D^2n^2}, \end{aligned} \tag{6}$$

where Φ and Ψ represent the non-dimensional flow rate coefficient and pressure coefficient, respectively. Q is the volumetric flow rate in m^3/min, n is the fan speed in (rev)/s ($n = N/60$), P is the total-to-static pressure rise in Pa, and ρ is the air density. The dimensionless P-Q curve eliminates dependencies on small fan speed variations, facilitating the comparison of different fans.

2.2 Fan noise sources

The noise generated by small electronics cooling fans can be classified as aerodynamic, electromagnetic, and mechanical noise [47]. Aerodynamic noise, or flow-induced noise, is caused by the interaction of airflow with the rotors and fixed components. Electromagnetic noise is generated by the electric motor driving the fan, and mechanical noise

comes from the bearings and transmission systems. Aerodynamic noise is typically the dominant source, while electromagnetic and mechanical noise are usually negligible at high rotational speeds. Therefore, this section will focus on aerodynamic noise sources. The noise radiation patterns can be classified as monopole, dipole, and quadrupole sources [49], as shown in Fig. 2.5.

A summary of the noise generation mechanisms in axial fans, including their radiation characteristics, is shown in Table 2.1. The following sections will discuss these noise sources in detail.

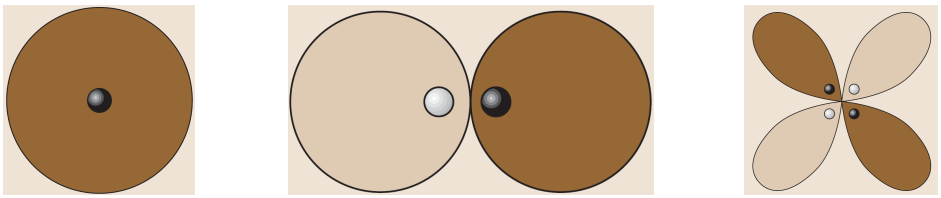

(a) Monopole (b) Dipole (c) Quadrupole

Figure 2.5: Typical radiation patterns for monopole, dipole and quadrupole sources, adapted from Ref. [49].

Table 2.1: Aeroacoustic noise sources and source characteristics ('T' = tonal, 'BB' = broadband).

Noise source		T	BB
Blade self-noise [50–55]	Trailing edge noise		■
	Vortex shedding noise	■	
	Separation and stall noise	■	■
	Tip vortex noise		■
	Steady loading (Gutin) noise	■	
	Thickness noise	■	
Blade interaction noise [36, 39, 42, 56–60]	Rotor-stator interaction	■	
	Non-uniform flow	■	
	Leading edge noise		■

2.2.1 Airfoil self-noise

Airfoil self-noise originates from the interaction between an airfoil blade and its own boundary layer and near wake, which has been widely investigated from 1960 [50, 52, 61]. Brook *et al.* [52] conducted a detailed research on airfoil self-noise and categorised it as the turbulent boundary layer trailing edge noise, laminar boundary layer vortex shedding noise, boundary layer separation noise, blunt trailing edge-vortex shedding noise and tip noise. Each airfoil self-noise source is associated with a typical flow structure. Wang *et al.* [62] comprehensively summarised the flow around the airfoil with increasing angle of attack α in each chord length based Reynolds number Re

regime. Eight different flow structures were identified on the suction side of the airfoil in their study, which is shown in Fig. 2.6.

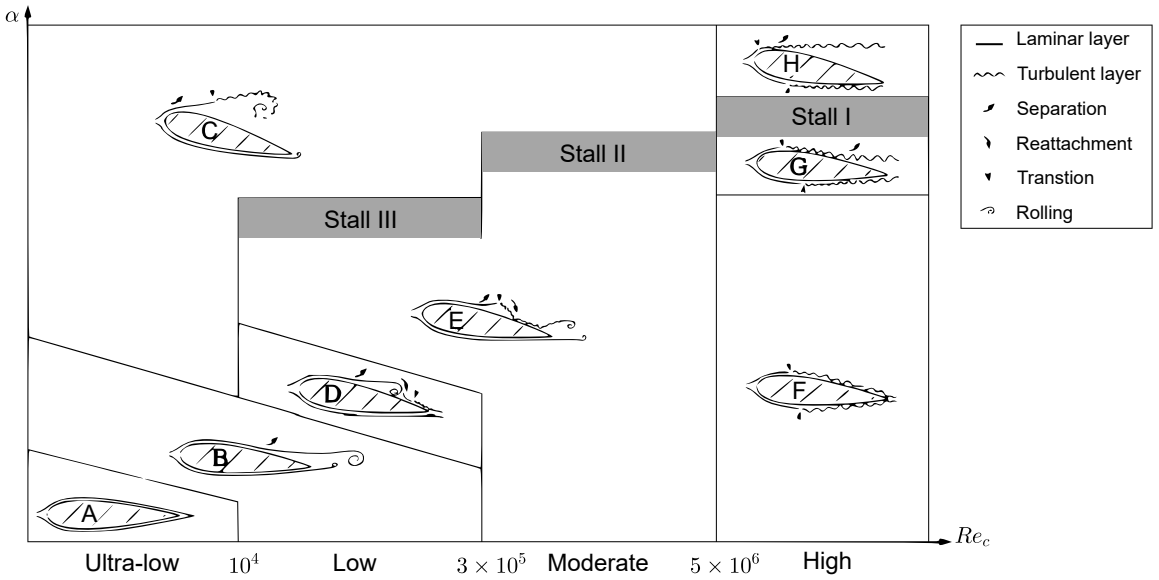

Figure 2.6: Schematic of flow structures around airfoil for each Re regime, adapted from Wang *et al.* [62].

Figure notes: these flow structures are: **A** Fully attached laminar boundary layer; **B** Partially attached laminar boundary layer; **C** Fully separated laminar shear layer near the leading edge with a subsequent transition downstream but without reattachment; **D** Laminar bubble, *i.e.*, laminar flow from separation to reattachment; **E** Partially laminar bubble; **F** Fully attached turbulent boundary layer; **G** Trailing-edge separated turbulent boundary layer; **H** Fully separated turbulent shear layer.

Trailing edge noise

Trailing edge noise arises from energy scattering when a turbulent boundary layer flow passes by a sharp edge of an airfoil (Fig. 2.7). Trailing edge noise is broadband noise and is the dominant noise sources in many cases. Howe [63] presented a review paper about trailing edge noise in 1978, which comprehensively covering the theoretical aspects of trailing edge noise. The review paper written by Doolan and Moreau [64] in 2015 covered a subset of experimental research but only focused on the wind turbine application. Most recently, Lee *et al.* [53] broadly reviewed the state-of-the-art on the turbulent boundary layer trailing edge noise generation in 2021 and summarise recent technical developments in analytical, numerical and experimental area in detail.

Vortex shedding noise

Laminar boundary layer vortex shedding noise is generated when the boundary layer is laminar on at least one side of an airfoil (Fig. 2.8). A pressure wave produced by vortex shedding propagates upstream and interacts with the laminar boundary layer,

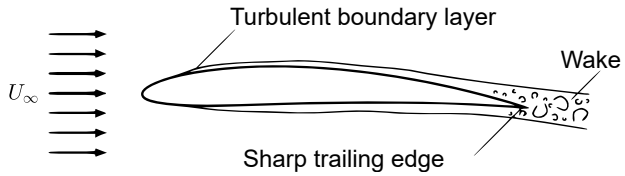

Figure 2.7: Schematic of a turbulent boundary layer which leads to the generation of trailing edge noise [52].

which is called the acoustic feedback loop mechanism [52]. The vortex shedding noise generated due to this mechanism has a tonal nature [52, 61]. Several researchers studied the feedback loop mechanism by direct numerical simulations (Sandberg *et al.* [65], and Jones *et al.* [66]) and found this mechanism is associated with boundary layer instabilities.

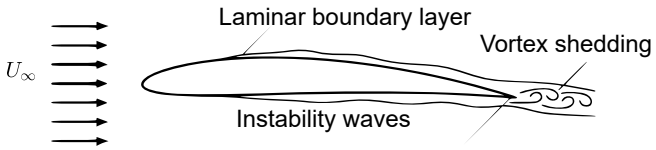

Figure 2.8: Schematic of laminar boundary layer which leads to the generation of vortex shedding noise [52].

Vortex shedding noise also arises from a blunt trailing edge (Fig. 2.9) and could be more important when the trailing edge thickness is large compared to the boundary layer thickness. Vortex shedding similar to the Von Kármán vortex street originates downstream of the blunt aerofoil. This noise has tonal characteristics in nature and is a dipole source [61]. Garcia-Sagrado *et al.* [67] experimentally studied the mechanisms of vortex shedding noise from the instability waves of separated laminar boundary layers and from blunt trailing edges by conducting simultaneous measurements of the unsteady surface-pressure fluctuations and of the velocity field in the boundary layer and wake of a NACA 0012 airfoil. Evidence of unsteady vortex shedding was observed in their study.

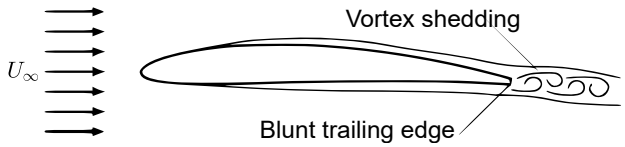

Figure 2.9: Schematic of airfoil bluntness which leads to the generation of vortex shedding noise [52].

Separation and stall noise

When the flow separates on airfoils at a high angle of attack, separation and stall noise arise (Fig. 2.10). This separation causes complex flow instability around the airfoil, creating a significant sound source. The predominant noise is generated along the

entire chord. Stall noise is a major sound source when an airfoil is deeply stalled. Fink and Bailey [68] studied stall noise and trailing edge noise, showing that stall noise is typically about 10 dB higher than trailing edge noise.

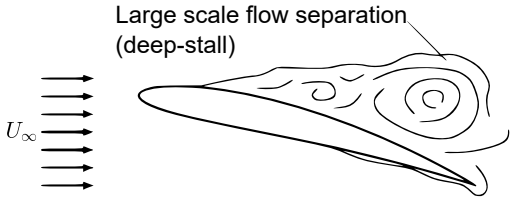

Figure 2.10: Schematic of flow separation which leads to the generation of stall noise [52].

Tip vortex noise

The span of a 2D airfoil is assumed to be infinite when analysing the above self-noise sources. However, for a 3D blade with a free boundary at the tip, a tip vortex originates from the pressure side near the tip and develops downstream. Tip vortex noise, which is similar to trailing edge noise, is generated by the tip vortex interacting with the tip and trailing edge near the tip, as shown in Fig. 2.11. Tip noise has broadband characteristics and is generally less intense than trailing edge noise. However, it can be produced at high frequencies by the separated flow near blade tips [69].

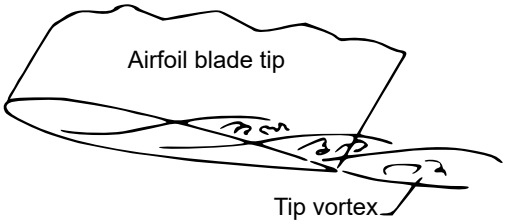

Figure 2.11: Schematic of tip vortex generation which leads to the generation of tip noise [52].

2.2.2 Rotor self-noise

Self-noise is noise produced by airflow over the blades without any unstable inflow [61]. Rotor self-noise includes all the airfoil self-noise sources discussed in Section 2.2.1 and two additional noise mechanisms related to rotation: thickness noise and steady loading noise (Gutin noise [70]). These additional noise sources are directly caused by the fan blade's rotation.

Thickness noise

The blade thickness noise is generated by the displacement of fluid volume. As the rotor rotates, the fluid volume is displaced by the finite blade volume, causing fluctuating pressure in the near field, which creates a periodic noise source. Figure 2.12 presents

a schematic for thickness noise. Thickness noise has tonal characteristics and is a monopole source. This type of noise is severe for high-speed turbomachinery (e.g., gas turbines) [71, 72]. In low-pressure axial fans with low rotational speed, thickness noise is typically considered a weak noise source [36].

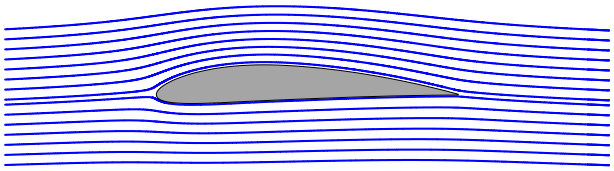

Figure 2.12: Schematic illustrating the solid blade section and the surrounding fluid volume displaced by the blade, which generates thickness noise.

Steady loading noise

Another form of rotor self-noise from rotating blades is steady loading noise, also known as Gutin noise, named after Gutin [70], who first quantified propeller noise induced by steady loading rotation. Steady loading noise is generated by the steady thrust and torque of the rotor blades under uniform inflow conditions. A schematic of the steady loading noise is shown in Fig. 2.13. This noise has tonal characteristics and occurs at multiples of the blade passage frequency (BPF). The BPF is given by:

$$f_{BPF} = B f_r, \tag{7}$$

where f_r is the rotor rotational frequency, and B is the number of blades. The harmonics can be expressed as multiples m of the BPF ($f = m f_{BPF}$). This noise source is generally significant at nearly sonic tip speeds and with a small number of blades [61, 72]. Consequently, it is not identified as the dominant source for cooling fans.

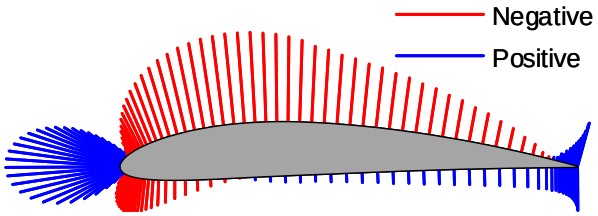

Figure 2.13: Schematic illustrating the steady loading generated by the positive and negative blade forces, which results in steady loading noise.

2.2.3 Rotor interaction noise

Rotor interaction noise arises from unsteady loading when rotating blades encounter time-varying disturbances [61]. Three primary sources contribute to this interaction noise: rotor-stator (or rotor-strut) interaction, non-uniform inlet flow, and turbulence

ingestion-induced unsteady loading. The first two sources are tonal, while the latter is broadband [61]. This subsection introduces these noise sources, and their characteristics and prediction methods will be discussed in Section 2.4.4.

Rotor-stator interaction

The rotating fan can generate a very strong wake, which impinges on the stators (or struts) downstream. This results an unsteady loading generating on the upstream rotor due to the periodic flow blockage by the downstream stators. Consequently, the unsteady loading leads to a tonal sound emission. This kind of noise is at multiples of BPF ($f = mf_{BPF}$), but at a wider range orders compared to the steady loading noise [72].

Non-uniform inflow

Non-uniform inflow at the fan inlet can also produce unsteady forces on the fan blades. This uneven flow can be caused by nearby stationary objects, such as forward grilles, stators, or rotors. Due to the non-uniform inlet flow, a fan blade experiences fluctuating velocities, resulting in changes in the angle of attack α. Consequently, the fan blade is subjected to unsteady loading [73]. This type of noise is tonal as it is caused by unsteady loading.

The incomplete bellmouth inlet can also cause non-uniform inflow, a unique noise source for axial fans in electronics cooling applications. Huang [36] first identified this phenomenon in a computer cooling fan, showing that the incomplete bellmouth inlet generates tonal noise at the blade passing frequency and its harmonics using an analytical method. Subsequent numerical and experimental studies have confirmed these findings [58, 74–76]. However, detailed investigations into the flow structure within the incomplete bellmouth inlet and its impact on fan noise are still lacking. Additionally, the influence of operating conditions, such as backpressure and flow rate, on this interaction mechanism remains unexplored.

Leading edge noise

Leading edge noise, also known as turbulence ingestion noise, arises from the interaction between the leading edge of an airfoil and turbulent inflow [59]. This noise is typically associated with large-scale turbulence structures in the inflow. When these structures interact with the airfoil's leading edge, they cause significant pressure fluctuations on the airfoil surface. Amiet [59] developed an analytical model to investigate leading edge noise using a flat plate as a reference. Additionally, Ffowcs Williams and Hall [77] provided an empirical equation to estimate turbulence ingestion noise, indic-

ating that sound power is proportional to the square of turbulence intensity. Predicting leading edge noise accurately is challenging due to the non-linear nature of turbulent inflow. However, this type of noise is generally more pronounced at low frequencies [61].

2.2.4 Characteristics of noise generation mechanisms

Two schematic noise spectra are presented in this section to illustrate the contributions of different noise sources to axial fan noise. Figure 2.14 shows the schematic noise spectrum of an airfoil, adapted from Blake's research [61]. It shows that leading edge noise dominates the low-frequency range, while trailing edge noise dominates the high-frequency range.

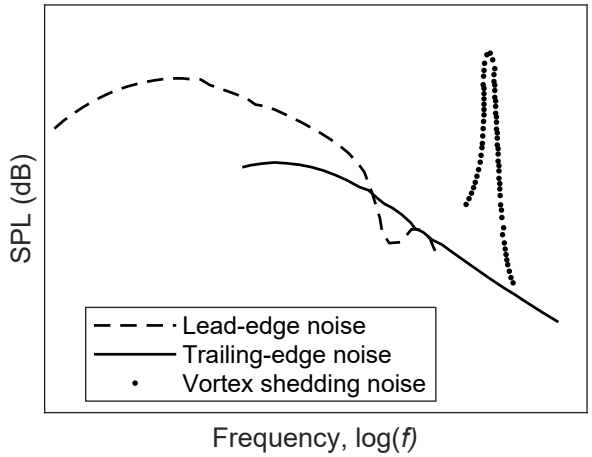

Figure 2.14: Schematic noise spectrum of an airfoil, adapted from Blake [61].

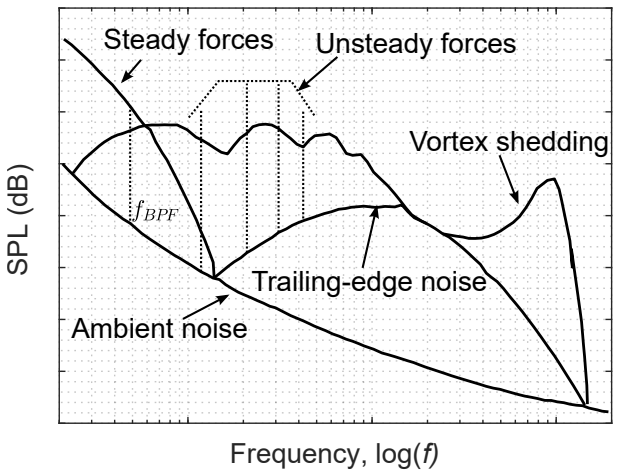

Figure 2.15: Schematic noise spectrum of an axial fan, adapted from Wright [78].

The contributions of different noise sources from axial fans were summarised by Wright [78], as shown in Fig. 2.15. As seen in Fig. 2.15, unsteady loading noise significantly impacts the tonal noise level. Although the effect of leading edge noise is not specifically

marked in Fig. 2.15, it is believed to influence the low-frequency noise range, as illustrated in Fig. 2.14.

2.3 Aerodynamic prediction

Numerous prediction methods [53, 71, 79] have been proposed over the past decades to theoretically and numerically calculate fan noise sources mentioned in Section 2.2. These prediction methods can be broadly classified as follows:

- **Empirical methods** are developed purely based on experience or observation. Rather than relying on theories and conceptions, the empirical approach depends on experimental evidence.
- **Analytical methods** solve governing equations mathematically and can yield exact solutions (symbolic manipulations) for typical flow or acoustic problems.
- **Semi-empirical (semi-analytical) methods** combine empirical and analytical approaches, involving assumptions or approximations to simplify mathematical calculations. These assumptions or approximations are typically proposed or calibrated based on real-world observations.
- **Numerical methods** are approximate algorithms for solving mathematical problems that cannot be solved analytically [80]. Computational fluid dynamics (CFD) methods are well-known numerical techniques. Although fluid dynamics and related phenomena can be described by differential equations such as the Navier-Stokes equations, analytical solutions have only been obtained in special cases. To find an approximate solution numerically, a discretisation method is used to approximate the differential equations, which can then be solved on a computer.

Empirical methods, which predict only the overall fan performance and noise level based on basic machine parameters, are generally not considered feasible for accurate prediction. Theoretical models, such as analytical and semi-empirical models, remain popular for understanding noise mechanisms and designing low-noise shapes, despite their inherent simplifications and limitations [81]. These models, developed based on physical phenomena, offer valuable insights but often lack the precision required for complex geometries and flow conditions. Consequently, they are classified as low-fidelity methods, as they are computationally inexpensive and provide limited flow field information.

In contrast, high-fidelity numerical methods, specifically unsteady scale-resolved CFD methods, provide detailed flow field information and can capture intricate noise generation mechanisms [80]. However, these methods are computationally expensive and

challenging to integrate into optimisation procedures [20]. The primary limitation of high-fidelity methods, such as detached eddy simulation (DES), large eddy simulation (LES), and direct numerical simulation (DNS), is their requirement for extremely fine meshes to resolve small-scale flow structures, demanding significant computational resources.

To address these challenges, reduced-order models (ROMs) have gained popularity. ROMs are low-cost computational approaches that rely on assumptions and simplifications tailored to specific situations. These models strike a balance between computational efficiency and predictive accuracy, making them suitable for integration into optimisation workflows. By leveraging ROMs, researchers can explore a broader design space without the prohibitive computational costs associated with high-fidelity simulations. The following sections will discuss the various prediction methods in detail, and a comparison of these methods will be presented in Section 2.5.

2.3.1 Governing equations for incompressible flow

Given that the flow in axial fans operates well below a Mach number of 0.3, the assumption of incompressible flow is valid. The fundamental equations governing incompressible flow are the incompressible Navier-Stokes (NS) equations. These include the continuity equation (mass conservation) and the momentum equation (Newton's second law). The continuity equation, in tensor notation, is given by [82, 83]:

$$\rho \frac{\partial u_j}{\partial x_j} = 0, \tag{8}$$

The momentum equation is expressed as:

$$\rho \frac{\partial u_i}{\partial t} + \frac{\partial}{\partial x_j}(\rho u_i u_j + p\delta_{ij} - \tau_{ij}) = 0, \tag{9}$$

where ρ denotes the fluid density, and u_i and u_j are the velocity components in the i and j directions, respectively, with $i, j = 1, 2, 3$. Here, t represents time, x_j is the spatial coordinate in the j direction, p is the pressure, δ_{ij} is the Kronecker delta, and τ_{ij} is the viscous stress tensor. This system comprises four equations (three momentum equations and one continuity equation) and four unknowns (three velocity components and pressure). For a Newtonian fluid, the relationship between the viscous stress tensor and the strain rate tensor is linear, given by:

$$\tau_{ij} = \mu \left(\frac{\partial u_i}{\partial x_j} + \frac{\partial u_j}{\partial x_i} \right) - \frac{2}{3}\mu \frac{\partial u_k}{\partial x_k}\delta_{ij}, \tag{10}$$

where μ is the dynamic viscosity.

2.3.2 Turbulence resolving and modelling

The incompressible Navier-Stokes (NS) equations in Section 2.3.1 are non-linear partial differential equations (PDEs) that are difficult to solve analytically. Numerical methods are needed to solve these PDEs, which are discretised in space and time. For the Reynolds number range of the axial fans studied, typically between 10^4 and 3×10^5, both laminar-turbulent transition and turbulent flow are expected. Therefore, modelling turbulence is essential for the CFD simulation of axial fans.

Turbulent eddies are characterised by a wide range of length scales, which need to be resolved or modelled depending on the required fidelity. Three length scales are typically used to characterise turbulent flow [82, 83]:

- **The integral length scale** l_0: This is the largest scale in turbulent flow, representing the distance over which turbulent kinetic energy is transferred from large to small eddies.
- **The Taylor microscale** l_λ: This scale represents the distance over which turbulent kinetic energy is dissipated by viscous forces.
- **The Kolmogorov microscale** l_η: This is the smallest scale in turbulent flow, where viscous forces dominate over inertial forces.

Figure 2.16 shows the energy spectrum of typical isotropic turbulent flow. The spectrum is divided into three regions: the energy-containing range, the inertial subrange, and the dissipation range. The energy-containing range is where energy is injected into the flow, characterised by the range between the integral length scale l_0 and the Taylor microscale l_λ. The inertial subrange is where energy is transferred from large eddies to small eddies, characterised by the range between the Taylor microscale l_λ and the Kolmogorov microscale l_η. In the inertial subrange, the energy spectrum follows a power-law relationship, known as the Kolmogorov -5/3 law ($E \propto k^{-5/3}$) [86]. This law assumes that the energy transfer rate is constant in the inertial subrange, a universal feature of isotropic turbulence. The dissipation range is where energy is dissipated by viscous forces, characterised by the range below the Kolmogorov microscale l_η. The inertial and dissipation ranges are called universal equilibrium ranges, where the flow is statistically universal, and the mean flow can be described by the large structures.

Understanding turbulence characteristics through length scales and energy spectrum regions is crucial for selecting the appropriate modelling method. Each numerical method has its own advantages and limitations, and the choice depends on the required fidelity and computational complexity. As illustrated in Fig. 2.16, direct numerical

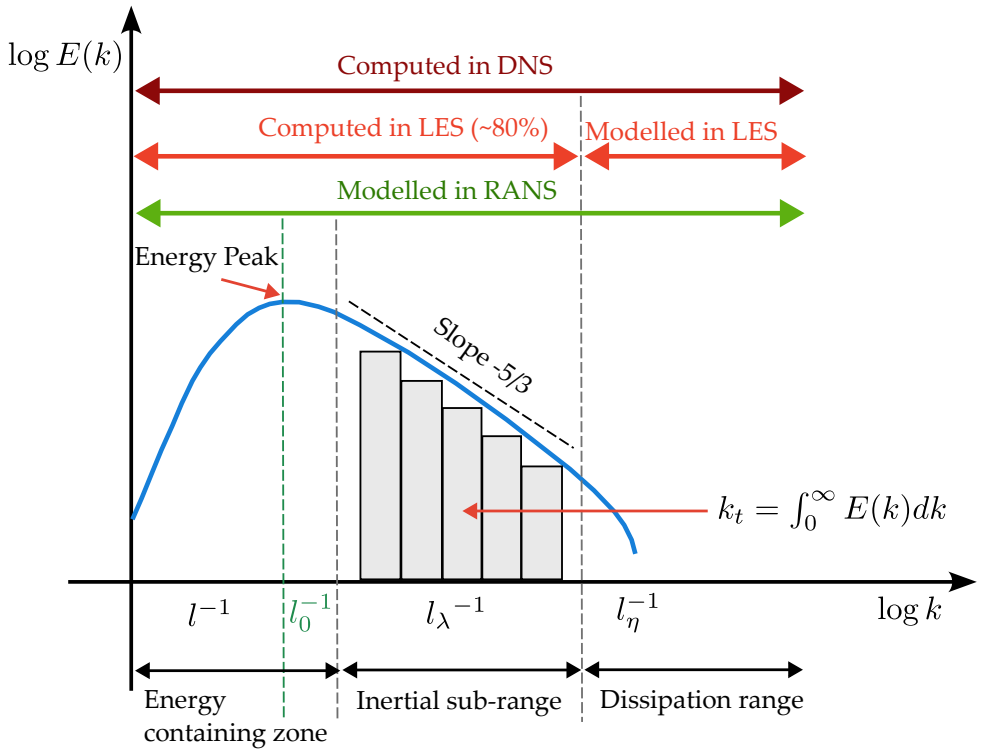

Figure 2.16: Schematic of the energy spectrum of turbulent flow as a function of wavenumber k, adapted from Hirsch [84] and Al-Am [85].

simulation (DNS) is the most accurate method, resolving all turbulent scales without any modelling. However, DNS is computationally very expensive and feasible only for simple geometries and low Reynolds numbers, such as channel flow and airfoil flow at low Reynolds numbers. Typically, the cells required by DNS are at least on the order of the Kolmogorov microscale l_η, and the number of cells is proportional to $Re^{9/4}$ [86]. For turbulent flow over a flat plate, Choi and Moin [87] showed that the number of cells required by DNS is approximately proportional to $Re^{2.65}$, based on the streamwise length of the plate. According to this estimation, for a typical Reynolds number of the investigated axial fans ($Re = 5 \times 10^4$), the mesh required is on the order of 10^{12}, which requires significant computational resources. Therefore, the scale-resolved large eddy simulation (LES) and scale-modelled Reynolds-averaged Navier-Stokes (RANS) models will be introduced and applied in this study.

2.3.3 Large eddy simulation

Large eddy simulation (LES) is a scale-resolved turbulence model that resolves large eddy scales and models small eddy scales. It assumes that large eddy scales contain most of the turbulent kinetic energy (as shown in Fig. 2.16) and transfer energy from large to small eddies. Small eddy scales in the universal equilibrium range can be easily modelled due to their isotropic behaviour, significantly reducing computational cost

compared to direct numerical simulation (DNS). The computational cost of fully wall-resolved LES scales approximately with $Re^{1.86}$ [87], while wall-modelled LES scales more modestly with Re^{1} [87]. For a typical Reynolds number of the investigated axial fans ($Re = 5 \times 10^4$), the mesh required by the wall-resolved LES is on the order of $10^7 - 10^8$ (10–100 million), which is feasible with modern high-performance computing (HPC) systems.

In LES, a spatial filtering operation is applied to the NS equations to separate flow variables into resolved and subgrid scales. A schematic of the filtering operation is shown in Fig. 2.17. A cut-off wavenumber k_c distinguishes resolved scales from subgrid scales in the Fourier space (Fig. 2.17 (b)), expressed as:

$$k_c = \frac{\pi}{\Delta} = \frac{2\pi}{\lambda_c}, \tag{11}$$

where λ_c is the filter wavelength. Δ is the grid characteristic length, determined as:

$$\Delta = (\Delta_x \Delta_y \Delta_z)^{1/3},$$

where Δ_x, Δ_y, and Δ_z are the grid spacings in the x, y, and z directions, respectively.

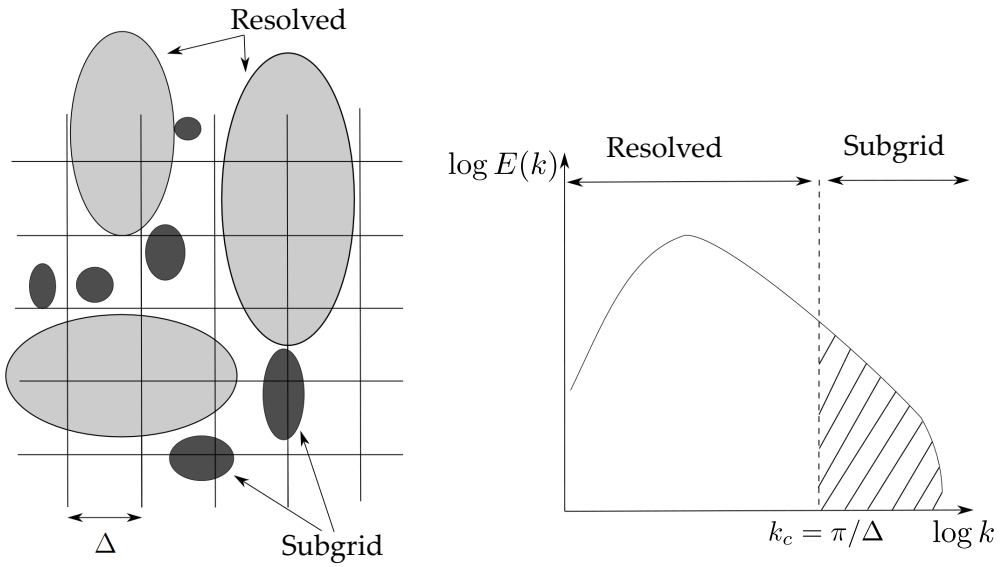

(a) Physical space (b) Fourier space

Figure 2.17: Schematic of the filtering operation in large eddy simulation, showing (a) the spatial filtering operation in physical space and (b) the cut-off wavenumber in Fourier space, adapted from [83].

This step acts as a low-pass filter, modelling any scales smaller than the filter size λ_c as subgrid-scale (SGS) turbulence. An ideal filter in LES should be close to the Taylor

microscale l_λ to accurately resolve large eddy scales, corresponding to resolving at least 80% of the turbulent kinetic energy.

Filtered Navier-Stokes equations

The filtered continuity equation and momentum equation in LES are given by:

$$\begin{aligned} \frac{\partial \overline{u}_i}{\partial x_i} &= 0, \\ \frac{\partial \overline{u}_i}{\partial t} + \overline{u}_j \frac{\partial \overline{u}_i}{\partial x_j} &= -\frac{1}{\rho}\frac{\partial \overline{p}}{\partial x_i} + \nu \frac{\partial^2 \overline{u}_i}{\partial x_j \partial x_j} - \frac{\partial \tau_{ij}^{sgs}}{\partial x_j}, \end{aligned} \tag{12}$$

where $\overline{u}_i$ is the resolved-scale velocity, $\overline{p}$ is the resolved-scale pressure, ν is the kinematic viscosity, and τ_{ij}^{sgs} is the subgrid-scale (SGS) stress tensor.

LES can be classified into two types based on how the SGS is handled: explicit filtering and implicit filtering. Explicit filtering uses a filter operator to separate resolved and subgrid scales. Implicit filtering, on the other hand, relies on the numerical discretisation of the governing equations to naturally filter small scales. In ANSYS Fluent, the finite-volume discretisation inherently performs this filtering, making it computationally efficient while still capturing small-scale turbulence without requiring explicit filtering.

Subgrid scale models

The SGS stress tensor τ_{ij}^{sgs} in LES is explicitly modelled by SGS models. The most widely used SGS model is Smagorinsky's model [88], given by:

$$\tau_{ij}^{sgs} = -2C_s\Delta^2\overline{S}_{ij}\sqrt{2\overline{S}_{ij}\overline{S}_{ij}}, \tag{13}$$

where $\overline{S}_{ij}$ is the resolved-scale strain rate tensor, C_s is the model constant, and Δ is the filter length scale.

Smagorinsky's model [88] is simple and computationally efficient but struggles to capture the anisotropy of subgrid-scale turbulence, especially in wall-bounded flows. It inaccurately produces non-zero turbulent viscosity near walls, leading to incorrect predictions of near-wall flow. To address this, Nicoud and Ducros [89] proposed the Wall-adapting local eddy-viscosity (WALE) model.

The WALE model returns zero eddy viscosity in laminar shear flow regions and finite eddy viscosity in turbulent regions, making it more accurate for laminar-turbulent transition and near-wall flows. The WALE model is given by [89, 90]:

$$\begin{aligned} \tau_{ij}^{sgs} &= -2\mu_t \overline{S}_{ij} + \frac{1}{3}\delta_{ij}k, \\ \mu_t &= \rho L_s^2 \frac{\left(S_{ij}^d S_{ij}^d\right)^{3/2}}{\left(\overline{S}_{ij}\overline{S}_{ij}\right)^{5/2} + \left(S_{ij}^d S_{ij}^d\right)^{5/4}}, \end{aligned} \tag{14}$$

where L_s and S_{ij}^d are the WALE filter length scale and the strain rate tensor, respectively, expressed as:

$$\begin{aligned} L_s &= \min\left(\kappa d, C_w \Delta\right), \\ S_{ij}^d &= \frac{1}{2}\left(\overline{g}_{ij}^2 + \overline{g}_{ji}^2\right) - \frac{1}{3}\delta_{ij}\overline{g}_{kk}^2, \overline{g}_{ij} = \frac{\partial \overline{u}_i}{\partial x_j}, \end{aligned} \tag{15}$$

where $\kappa = 0.41$ is von Kármán's constant, d is the distance to the nearest wall, C_w is the model constant.

2.3.4 Reynolds-averaged Navier-Stokes models

Reynolds-averaged Navier-Stokes (RANS) models use Reynolds decomposition to separate flow variables into mean and fluctuating components. In this study, steady-state RANS models are classified as mid-fidelity aerodynamic prediction methods. They model turbulence by averaging the NS equations over time, resulting in additional terms called Reynolds stresses, which are then modelled by turbulence models. Compared to DNS and LES, RANS models are computationally efficient and widely used in industry. They are accurate enough for predicting mean flow and turbulence statistics in many engineering applications. The number of cells required by RANS models is approximately proportional to Re for a far-field mesh [86, 91], while the near-wall mesh requires a much finer resolution to capture the boundary layer flow. For a typical Reynolds number of the investigated axial fans ($Re = 5 \times 10^4$), the mesh required is on the order of 10^5 – 10^6 (0.1 – 1 million), which is feasible with modern workstation computers. Moreover, the time step required by unsteady RANS models is much larger than that required by LES, making them computationally more efficient. However, RANS models are still computationally expensive at the design and optimisation stage.

RANS models struggle to predict unsteady and separated flows, making them inadequate for predicting noise from axial fans, especially broadband noise. However, a RANS solution can provide sufficient information for mean flow and turbulence statistics, which can predict fan steady-state performance. Additionally, a RANS solution can serve as an initial condition for LES simulations, leading to quicker convergence and saving time. In this study, the shear stress transport (SST) k-ω model will be used for

the aerodynamic simulation of axial fans. The SST k-ω model is an improved version of the k-ω model, solving two transport equations for the turbulent kinetic energy k and the specific rate of dissipation ω. The SST k-ω model is known for its ability to accurately predict near-wall flow and is widely used in industry for predicting flow around complex geometries [91].

Although there are more hybrid RANS-LES models, such as detached eddy simulation (DES) and wall-modelled LES (WMLES), these models are not used in this study. The main reasons are that hybrid RANS-LES models have limitations in predicting laminar-turbulent transition, leading to uncertainties in analysing noise generation mechanisms. Additionally, the computational cost of hybrid RANS-LES models is higher than RANS models when only the mean flow field is of interest. Therefore, RANS models are chosen as the mid-fidelity aerodynamic prediction method, while LES models are selected as the high-fidelity aerodynamic prediction method.

2.3.5 Panel method

The panel method is a low-fidelity aerodynamic prediction technique that models flow around a body using a series of panels. Vortex, source, and doublet panels are commonly used to represent the flow around an airfoil [92]. The panel method is computationally efficient and widely used in industry for predicting the aerodynamic performance of airfoils and wings. In this study, the panel method will be used as a low-fidelity tool for lift and drag calculations of sectional airfoils in axial fans.

Potential flow theory is based on the Laplace equation, which governs inviscid and incompressible flow. The Laplace equation for a 2D flow is given by [82]:

$$\nabla^2 \phi = 0, \tag{16}$$

where ϕ is the velocity potential. The velocity potential is related to the velocity components u and v by the following equations:

$$u = \frac{\partial \phi}{\partial x}, \quad v = \frac{\partial \phi}{\partial y}. \tag{17}$$

The panel method divides the airfoil into linear segments called panels, as shown in Fig. 2.18. Each panel is a flat surface with a velocity distribution, and a source or vortex is placed at the centre of each panel. The velocity potential ϕ is calculated at the control points of each panel. The boundary condition is enforced by satisfying the Kutta condition at the trailing edge, ensuring that the flow leaves the trailing edge smoothly by setting the circulation to zero. The circulation is determined by solving a

linear system of equations, from which the lift coefficient is obtained.

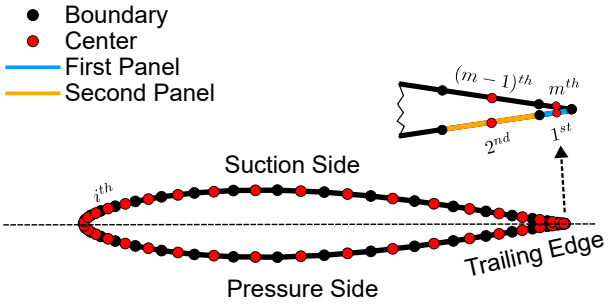

Figure 2.18: Schematic of panel orientation in the panel method, showing the airfoil divided into linear panels.

The panel method is effective for modelling irrotational flows, such as attached, low-speed flows outside the boundary layer. However, it cannot capture boundary layer flows significantly affected by viscosity. To address this, the panel method can be extended by solving the boundary layer equations to include viscous effects. Specifically, the von Kármán integral method can be used to express the mass and momentum conservation equations in the boundary layer [92, 93]. Semi-empirical models, such as Thwaite's method [94] for laminar boundary layers and Head's method [95] for turbulent boundary layers, can then predict the boundary layer flow and integrate it into the panel method.

The boundary layer calculation can be integrated into the panel method with a simple step. First, the inviscid flow is calculated using the panel method, which then initialises the boundary layer calculation. After solving the boundary layer equations, the panel method is run again, changing the flow tangency condition to a no-slip condition. This establishes the viscous-inviscid interaction.

Predicting laminar-turbulent transition, caused by boundary layer instability, is challenging. Although transition is typically predicted as a point, it is actually a region. This region, called the laminar separation bubble (LSB), forms in the boundary layer, characterised by laminar flow surrounded by turbulent flow. The e^N method [96] is a widely used semi-empirical approach that predicts the onset of laminar-turbulent transition in the boundary layer. This method is based on the energy balance between laminar and turbulent boundary layers, where the transition location is determined by the critical value of the energy ratio e^N. The e^N method effectively predicts transition in the boundary layer and has been integrated into many low-fidelity aerodynamic prediction tools.

The most renowned 2D panel method tool is the XFOIL code [1] developed by Drela [97], widely used for predicting the aerodynamic performance of airfoils. XFOIL [97]

[1]XFOIL: https://web.mit.edu/drela/Public/web/xfoil/.

employs a vortex panel method to model flow around an airfoil and calculates the lift and drag coefficients for 2D airfoils. For airfoils in cascade, Drela [98] developed the MISES code [2], which is capable of designing and optimising cascades for turbomachinery applications, especially for high Reynolds-number flows. Recently, Alvarez *et al.* [99] reformulated the vortex particle method as a meshless LES solver for predicting the aerodynamic performance of multi-rotor aircraft. Although vortex particle method does not include viscous effects, it can reasonably predict unsteady flow interactions for 3D rotors with low computational cost and mid-fidelity. The vortex particle method shows promise for predicting the aerodynamic performance of rotors in high Reynolds-number flows ($Re > 10^6$) where viscous effects are negligible. However, for axial fans with low Reynolds numbers ($Re < 10^5$), viscous effects are significant, necessitating careful examination of the applicability of any inviscid panel method.

2.3.6 Blade element theory

The 2D panel method introduced in Section 2.3.5 efficiently predicts aerodynamic quantities like lift and drag coefficients, boundary layer thickness, and pressure distribution for airfoils. However, it is limited to 2D flows and cannot determine the overall performance of 3D rotors. To address this, the blade element theory (BET) is introduced to model the aerodynamic performance of rotating blades in axial fans. BET, or strip theory, models the blade as a series of blade elements, each representing a small section of the blade. These elements are typically defined by the chord length (c), twist angle (β), and airfoil shape.

2D airfoil

Having calculated the lift and drag coefficients using XFOIL [97], the lift force dF_l and drag force dF_d of a 2D airfoil can be expressed as:

$$\begin{aligned} dF_l &= \frac{1}{2}\rho U_\infty^2 c C_l dr, \\ dF_d &= \frac{1}{2}\rho U_\infty^2 c C_d dr, \end{aligned} \tag{18}$$

where c is the chord length and dr is the span length. These forces can be resolved into components parallel (dF_x) and perpendicular (dF_z) to the rotor plane, expressed as:

$$\begin{aligned} dF_x &= dF_l \sin\phi + dF_d \cos\phi, \\ dF_z &= dF_l \cos\phi - dF_d \sin\phi. \end{aligned} \tag{19}$$

[2] MISES: https://web.mit.edu/drela/Public/web/mises/.

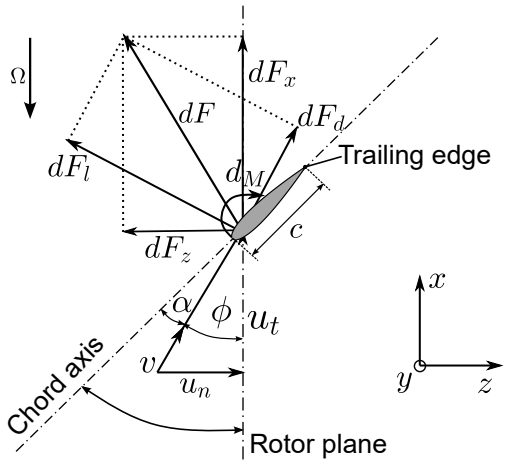

Figure 2.19: Velocity and force triangles of a 2D airfoil.

3D open rotor without a shroud

The performance of a 3D rotor without a shroud can be predicted by integrating the blade element theory (BET) with momentum theory (MT). BET analyses the blade force by dividing the blade into spanwise elements, as shown in Fig. 2.20. The main assumption is that each spanwise element is independent, and the loading of each blade element can be determined without considering interactions between these radial elements. With this assumption, the forces of each spanwise element can be determined using Eq. 19, derived for 2D airfoils (Fig. 2.19). Following the classical BET implementation [100], the thrust dT and torque dM for a circular radial element dr can be given as:

$$dT = B_n dF_z = \frac{1}{2}\rho B v^2 c C_n dr = \frac{1}{2}\rho B \frac{\Omega^2 r^2 (1-a')^2}{\cos^2\phi} c C_n dr \tag{20}$$

$$dM = B_n dF_x r = \frac{1}{2}\rho B v^2 c C_t r dr = \frac{1}{2}\rho B \frac{\Omega^2 r^2 (1-a')^2}{\cos^2\phi} c C_t r dr, \tag{21}$$

where C_n is the force coefficient normal to the rotor plane ($C_n = C_l \cos\phi - C_d \sin\phi$), and C_t is the force coefficient tangential to the rotor plane ($C_t = C_l \sin\phi + C_d \cos\phi$). Here, c is the blade sectional chord, B is the number of blades, and v is the total velocity at each radial element ($v = \sqrt{{u_n}^2 + {u_t}^2}$). u_n and u_t are the axial and tangential velocities, respectively. a' is the tangential velocity induction factor ($u_t = \Omega r\,(1-a')$), and a is the axial velocity induction factor, which can be expressed as a function of inflow wind velocity ($u_n = u_\infty\,(1+a)$). ϕ is the flow induction angle, $\phi = \tan^{-1}(u_n/u_t)$. The sectional angle of attack α can be calculated using the known geometrical twist angle β: $\alpha = \beta - \phi$. The sectional lift and drag coefficients C_l and C_d are calculated by polynomial interpolation from a pre-computed look-up table based on the angle of attack α. For numerical robustness, all the aerodynamic data of the 2D airfoil in the table was calculated by XFOIL [97] in the angle of attack range from −20° to +20°, and

then extended to the entire ±180° angle of attack range using the Viterna method [101]. Figure 2.21 shows a sample C_l and C_d curve for a NACA 0012 profile at $Re = 5 \times 10^4$ as a function of angle of attack α with and without Viterna extrapolation.

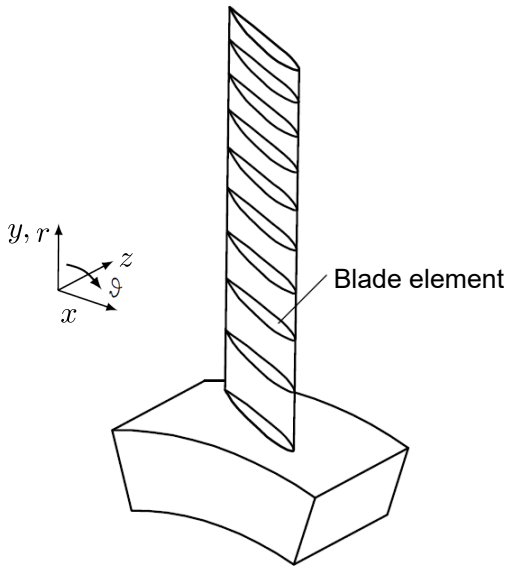

Figure 2.20: Schematic of the blade element method, adapted from Ref. [73].

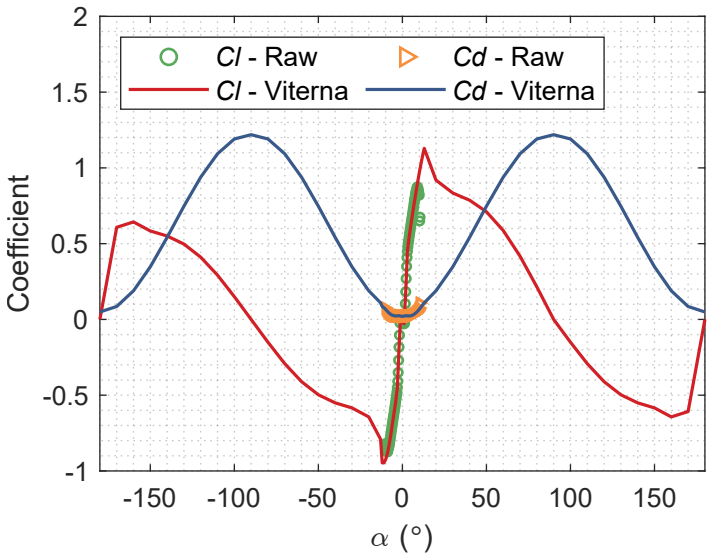

Figure 2.21: Sample C_l and C_d curves as a function of angle of attack α with and without Viterna extrapolation [101] for a NACA 0012 airfoil at $Re = 5 \times 10^4$.

BET alone is insufficient for determining aerodynamic performance. It is usually combined with another theory to determine the flow field. Blade element momentum theory (BEMT), which combines BET and one-dimensional momentum theory, is widely used for calculating rotating blades [100]. From the momentum balance, the thrust and torque for a circular radial element dr can be given as:

$$dT = 4\pi r \rho v_\infty^2 a(1+a)dr \tag{22}$$

$$dM = 4\pi r^3 \rho v_\infty \Omega (1+a) a' dr. \tag{23}$$

By solving Eqs. (20) to (23), the axial and tangential induction factors can be obtained iteratively. The BEMT method is well-defined and validated in the literature for open propeller applications at low Re flows [55]. However, the traditional BEMT is not suitable for a shrouded or ducted rotor with backpressure effects. The shroud changes the flow structure, making momentum equations based on the stream tube assumption invalid [102]. Therefore, in this study, the BEMT method is only used for the 3D rotor without a shroud, while a new method will be developed for the 3D rotor with a shroud.

2.4 Aeroacoustic prediction

2.4.1 Ffowcs Williams and Hawkings (FW-H) acoustic analogy

The earliest approach to aeroacoustic prediction can be traced back to Lighthill's acoustic analogy in 1954 [103]. This foundational work was further extended by Ffowcs Williams and Hawkings in 1969 to account for moving surfaces [104]. The Ffowcs Williams-Hawkings (FW-H) equation represents an exact reformulation of the continuity equation and NS equation into an inhomogeneous wave equation. This equation comprises three distinct terms, known as the monopole, dipole, and quadrupole sources, as illustrated on the right side in Eq. 24.

$$\begin{aligned} \frac{1}{c_o^2}\frac{\partial^2 p'}{\partial t^2} - \nabla^2 p' = & \frac{\partial^2}{\partial x_i \partial x_j}\left\{Q_{ij} H(f)\right\} \\ & - \frac{\partial}{\partial x_i}\left\{\left[P_{ij} n_j + \rho u_i \left(u_n - v_n\right)\right] \delta(f)\right\} \\ & + \frac{\partial}{\partial t}\left\{\left[\rho_0 v_n + \rho \left(u_n - v_n\right)\right] \delta(f)\right\}. \end{aligned} \tag{24}$$

The Lighthill's stress tensor is:

$$Q_{ij} = \rho u_i u_j + P_{ij} - c_0^2 \left(\rho - \rho_0\right) \delta_{ij}, \tag{25}$$

and the compressive stress tensor is:

$$P_{ij} = p' \delta_{ij} \tag{26}$$

where u_i, u_j are the fluid velocity, u_n is the fluid velocity normal to the surface ($f = 0$), v_n is the surface velocity normal to the surface ($f = 0$), $\delta(f)$ is the Dirac delta function, $H(f)$ is the Heaviside function, p' is the acoustic pressure at the far field and f is the

mathematical surface of the moving body.

Farassat [105] developed an integral form of the FW-H equation using the free space Green's function. Farassat Formulation 1A [106], which neglects the quadrupole at subsonic flow, states that the acoustic pressure fluctuation is given by the combination of monopole (thickness) p'_T and dipole (loading) p'_L:

$$4\pi p'_T(\vec{x},t) = \int_{f=0} \left[\frac{\rho_0 \left(\dot{v}_n + v_{\dot{n}}\right)}{r\left(1-Ma_r\right)^2} \right]_{ret} dS + \int_{f=0} \left[\frac{\rho_0 v_n \left(r\dot{M}a_r + c_0\left(Ma_r - Ma^2\right)\right)}{r^2\left(1-Ma_r\right)^3} \right]_{ret} dS \tag{27}$$

$$\begin{aligned} 4\pi p'_L(\vec{x},t) =& \frac{1}{c_0}\int_{f=0} \left[\frac{\dot{l}_r}{r\left(1-Ma_r\right)^2} \right]_{ret} dS + \int_{f=0} \left[\frac{l_r - l_{Ma}}{r^2\left(1-Ma_r\right)^2} \right] dS \\ &+ \frac{1}{c_0}\int_{f=0} \left[\frac{l_r\left(r\dot{M}_{a_r} + c_0\left(Ma_r - Ma^2\right)\right)}{r^2\left(1-Ma_r\right)^3} \right]_{ret} dS \end{aligned} \tag{28}$$

where Ma is the Mach number, v_n is the normal velocity component, r is the distance between the source and observer, ρ_0 is the fluid density, and c_0 is the speed of sound. In each term, the dot above the variables represents a time derivative with respect to the retarded time. The surface loading vector is $l_i = P_i j \hat{n}_j$. The subscripts r and Ma indicate a dot product between the loading vector and the corresponding radiation vector and vectorised Mach number.

The assumption of neglecting quadrupole sources is reasonable for low Mach number flows ($Ma < 0.3$) [107]. This method is computationally efficient compared to the original FW-H calculation. Based on Farassat Formulation 1A, Brentner *et al.* [108, 109] developed a robust noise prediction code called PSU-WOPWOP [3]. Initially designed for predicting the noise of manoeuvring rotorcraft, it is also suitable for other moving bodies [109].

The FW-H method is a popular computational aeroacoustics (CAA) technique, widely used for predicting noise from rotating blades in free-field conditions. It often uses the unsteady flow field obtained from CFD methods but can also work with analytical and semi-empirical models that predict flow information. For tonal noise from periodic interactions, URANS simulations are sufficient to solve the unsteady loading [79, 110]. However, for accurate broadband noise prediction, turbulent eddies must be resolved up to a certain scale using higher-fidelity methods like LES.

[3] PSU-WOPWOP: https://aeroacoustics.psu.edu/software/.

2.4.2 Trailing-edge noise

Brooks, Pope and Marcolini (BPM) model

Several analytical and semi-empirical methods have been developed over the past fifty years for predicting airfoil self-noise. One of the most popular and successful semi-empirical models for trailing-edge noise prediction is the BPM model, developed by Brooks, Pope, and Marcolini in 1989 [52]. This model derives various scaling equations for airfoil self-noise sources, as introduced in Section 2.2.1, and calibrates them using extensive measurement data from NACA 0012 airfoils with different chord lengths and inflow configurations. The BPM model can predict trailing-edge noise, leading-edge noise, vortex-shedding noise, separation-stall noise, and tip noise in third-octave bands. It requires numerous input parameters to obtain the noise spectrum, including airfoil geometry and boundary layer parameters, which can be obtained using flow solvers such as the vortex panel code XFOIL [97] or any CFD methods.

Due to its speed and accuracy, the BPM model has become a reference for estimating trailing-edge noise in many rotating blade applications. Gennaro *et al.* [111] presented two simplified methods for axial fan noise simulation: 2D blade element theory and 3D CFD Reynolds-averaged Navier-Stokes (RANS) flow solution coupled with the BPM model. Their predicted results showed a reasonable match with experimental data from a published ventilation fan case, although there was a tendency to overestimate the noise level. Similarly, Zawodny *et al.* [112] measured unmanned aerial vehicle (UAV) noise with two different propellers and used the BPM model to predict airfoil self-noise. The input parameters required by the BPM model were calculated by an external CFD code. They found that the overall trends of predicted results agreed with the experimental data, but there was a significant underestimation at low-mid frequencies and an overprediction at higher frequencies.

However, the BPM model has its limitations. As an empirical model, it performs well under conditions similar to those of the calibration experiments, but its accuracy decreases significantly under different conditions. For non-symmetric airfoils, the model's predictions deviate from reality. This is because it assumes that differences between the suction and pressure sides are solely due to the angle of attack, ignoring the airfoil's inherent asymmetry.

Amiet's trailing-edge model

For predicting airfoil trailing edge noise, Amiet's model [50] remains a widely accepted approach. Amiet [50] initially employed the Schwarzschild solution to predict scattered noise near the trailing edge of a flat plate with a semi-infinite chord. Based on Amiet's model, the far-field acoustic power spectral density (PSD) S_{pp} for an observer located

in the mid-span plane at position $(x, y = 0, z)$ for a given angular frequency (ω) can be expressed as:

$$S_{pp}(\omega) = \left(\frac{\omega b z}{2\pi c_0 \sigma^2}\right)^2 l_y(\omega) d |\mathcal{L}|^2 \Phi_{pp}(\omega), \tag{29}$$

where b is the semi-chord ($b = c/2$), d is the semi-span, c_0 is the speed of sound, ω is the circular frequency, and the orientation of the blade is defined by the Cartesian coordinate system as x (chordwise), y (spanwise), and z (normal). Here, $\sigma^2 = x^2 + \beta^2 z^2$, $\beta^2 = 1 - Ma^2$, $\Phi_{pp}(\omega)$ is the surface pressure spectrum near the trailing edge, and $l_y(\omega)$ is the spanwise correlation length. The acoustic transfer function $|\mathcal{L}|$ of the airfoil at the (x, y, z) location can be determined as:

$$\begin{aligned} |\mathcal{L}| = & \frac{1}{\Theta} \mid (1+i) \left\{ \sqrt{\frac{1 + Ma + K_x/\mu}{1 + x/\sigma}} E^*[2\mu(1 + x/\sigma)] e^{-i2\Theta} \right. \\ & \left. - E^* \left[2 \left((1 + Ma)\mu + K_x \right) \right] \right\} + 1 - e^{i2\Theta} \mid \end{aligned} \tag{30}$$

where $\Theta = K_x + \mu(Ma - x/\sigma)$, $K_x = \omega/U_c$, $\mu = Ma\omega C/U_\infty \beta$, Ma is the Mach number, and $E^*[]$ is the Fresnel integral [50].

Amiet's model relies on the surface pressure spectrum Φ_{pp} as a crucial input for calculating far-field noise. This surface fluctuating pressure spectrum can be determined either experimentally or numerically. As suggested by Amiet [50], the pressure spectrum should be obtained at the location of 99% chord c on both sides of the airfoil surface, which is slightly upstream of the trailing edge. More details about the wall pressure spectrum model can be found in Section 2.4.2. The convection velocity U_c is typically assumed to be 0.6–0.8 times the free stream velocity U_∞ [50].

The spanwise correlation length $l_y(\omega)$ is determined using Corcos' model [113], expressed as:

$$l_y(\omega) = \frac{b_c U_c}{\omega}, \tag{31}$$

where b_c is a constant. Amiet [50] recommended a value of $b_c = 2.1$ and $U_c = 0.8 U_\infty$ based on empirical data. Alternative constants for both convection velocity and spanwise correlation length have been utilised in other studies [114], demonstrating the flexibility and adaptability of Corcos' model across different experimental conditions.

The aeroacoustic transfer function $|\mathcal{L}|$ given by Amiet is for an infinite plate with no leading edge effect. Roger and Moreau [51, 115] extended Amiet's model to include this effect and improve accuracy at low frequencies. The acoustic transfer function $|\mathcal{L}|$ is then modified as $|\mathcal{L}_\infty| + |\mathcal{L}_\epsilon|$, where $|\mathcal{L}_\infty|$ is the original Amiet transfer function and $|\mathcal{L}_\epsilon|$ is the back-scattering correction term.

Due to its simplicity and flexibility, Amiet's model is widely used for trailing edge noise prediction in many applications [55, 81, 116, 117]. Since Amiet's noise prediction model heavily relies on wall pressure fluctuations near the trailing edge, related research will be introduced later in Section 2.4.2.

Wall pressure spectrum model

Amiet's model uses the wall pressure spectrum (WPS) near the trailing edge as a key input and solves the scattering of the wall pressure fluctuations by a trailing edge. The wall pressure spectrum can be calculated using CFD methods or semi-empirical methods.

In the literature, six different semi-empirical wall pressure spectrum models are available: Goody [118] in 2004, Rozenberg [119] in 2012, Kamruzzaman [120] in 2015, Catlett [121] in 2016, Hu [122] in 2016, and Lee [123] in 2018. All the semi-empirical WPS models can be expressed in the universal form:

$$\frac{\phi_{pp}}{\phi^*} = \frac{a\left(\omega^*\right)^b}{\left[i\left(\omega^*\right)^c + d\right]^e + \left[fR^g\omega^*\right]^h}, \tag{32}$$

where $a - i$ are parameters that depend on the specific model. R_T is the ratio of timescales accounting for the Reynolds number effect ($R_T = (\delta/U_e)/\left(\nu/u_\tau^2\right)$). ϕ^* and ω^* are the spectrum scaling factor and frequency scaling factor, respectively.

Table 2.2 shows the parameters for six different wall pressure models. Goody's model was developed for zero pressure gradient (ZPG) flows in 2004. Hwang *et al.* [124] compared various empirical models published before 2009 and found Goody's model to be the most accurate for ZPG flows. The other WPS models used in this study are based on Goody's model and were extended by the mentioned researchers for adverse pressure gradient (APG) flows.

Küçükosman *et al.* [125] used the semi-empirical wall pressure spectrum models with Amiet's model for a NACA 0012 airfoil at 0° and 4° angles of attack. The boundary layer parameters required by these WPS models were calculated using a 2D RANS model. They found that Lee's model provided the most accurate results for the wall pressure spectrum, while Goody's model performed poorly compared to experimental results.

Table 2.2: Parameters for six semi-empirical wall pressure spectrum models.

	Goody [118]	Rozenberg [119]	Kamruzzaman [120]	Catlett [121]	Hu [122]	Lee [123]
a	3.0	$\left[2.82\Delta^2\left(6.13\Delta^{-0.75}+d\right)^e\right]$ $\times\left[4.2(\Pi/\Delta+1\right]$	$e^{7.98\left(\beta_\Delta Re_\Delta^{0.35}\right)^{0.131}-10.7}+3.0$	$0.45\left[1.75\left(\Pi^2\beta_c^2\right)^m+15\right]$, $m=0.5(H/1.31)^{0.3}$	$(81.004d+2.154)\cdot10^{-7}$	$\max\left(a_{\mathrm{Roz}},\left(0.25\beta_c-0.52\right)a_{\mathrm{Roz}}\right)$
b	2.0	2.0	2.0	2.0	1.0	2.0
c	0.75	0.75	1.637	$0.912+20.9\left(\beta_\delta Re_\delta^{0.05}\right)^{2.76}$	$1.5(1.169\ln(H)+0.642)^{1.6}$	0.75
d	0.5	$4.76(1.4/\Delta)^{0.75}[0.375e-1]$	0.27	$0.397+0.328\left(\beta_5 Re_{\Delta^*}^{0.35}\right)^{0.310}$	0.07	$\max(1.0,1.5d_{\mathrm{Roz}})\left(\beta_c<0.5\right)$ $d_{\mathrm{Roz}}\left(\beta_c>=0.5\right)$
e	3.7	$3.7+1.5\beta_c$	2.47	$3.872-1.93\left(\beta_\delta Re_\delta^{0.05}\right)^{0.628}$	$1.13/(1.169\ln(H)+0.642)^{0.6}$	$3.7+1.5\beta_c$
f	1.1	8.8	$1.15^{-2/7}$	$2.19-2.57\left(\beta_\delta Re_\delta^{0.05}\right)^{0.224}$	7.645	8.8
g	-0.57	-0.57	-2/7	$-0.5424+38.1\left(\beta_\delta H^{-0.5}\right)^{2.11}$	-0.411	-0.57
h	7.0	$\min\left(3.0,19/\sqrt{R_T}\right)+7.0$	7.0	$7.31+0.797\left(\beta_\delta Re_\delta^{0.35}\right)^{0.0724}$	6.0	$\min\left(3.0,\left(0.139+3.1043\beta_c\right)\right)+7.0$
i	1.0	4.76	1.0	1.0	1.0	1.0
ϕ^*	$\tau_w^2\delta/U_e$	$\tau_{\max}^2\delta^*/U_e$	$\tau_w^2\delta^*/U_e$	$\tau_w^2\delta/U_e$	$Q^2\theta/u_\tau$	$\tau_{\max}^2\delta^*/U_e$
ω^*	$\omega\delta/U_e$	$\omega\delta^*/U_e$	$\omega\delta^*/U_e$	$\omega\delta/U_e$	$\omega\theta/U_e$	$\omega\delta^*/U_e$

For predicting rotor trailing-edge noise, Li and Lee [116, 126] combined the blade element momentum method (BEMT), XFOIL [97], Lee's wall pressure spectrum model, and Amiet's model to develop an in-house code, UCD-QuietFly. They found that the predicted trailing-edge noise matched well with measurement data. Similarly, Casalino *et al.* [55] used a BEMT-based model combined with several WPS models and Amiet's model to predict noise from a two-bladed UAV propeller. They found that all WPS models based on Goody's model showed similar trends, but none accurately predicted noise levels for all experimental cases. Sanjosé [117] used Amiet's model with extensions by Roger and Moreau [51], combined with Rozenberg's WPS model, to predict low-speed axial fan noise. The flow parameters in this study were extracted from RANS simulations. They found that the acoustic prediction accurately predicted noise levels and the fan performance curve.

2.4.3 Leading-edge noise

Amiet's leading-edge model

Leading-edge noise, also known as turbulence-interaction noise, is generated when turbulent inflow interacts with the leading edge of an airfoil. Amiet [59] developed a model to predict this type of noise. The model assumes that the turbulence is statistically homogeneous in the streamwise direction and that the airfoil can be approximated as an infinite flat plate in the spanwise direction. This implies that the model does not account for the spanwise wavenumber contributions or the back-scattering effects from the trailing edge. The leading-edge noise is modelled as a distribution of dipoles corresponding to the lift fluctuations induced by the incoming turbulence. The pressure fluctuations due to these lift variations are related to the turbulence spectrum of the inflow. The far-field acoustic power spectral density (PSD) for leading-edge noise can be expressed as [59]:

$$S_{pp} = \left(\frac{\omega \rho b z}{c_0 \sigma^2}\right)^2 \pi U_\infty d |\mathcal{L}|^2 \Phi_{ww}, \tag{33}$$

where Φ_{ww} represents the two-dimensional turbulence spectrum. The aeroacoustic transfer function $|\mathcal{L}|$ accounts for the airfoil's characteristics, while U_∞ represents the relative velocity for the airfoil.

Turbulence spectrum models

The turbulence spectrum is a key part of Amiet's model [59] for predicting leading-edge noise. Homogeneous isotropic turbulence, often assumed in the streamwise direction, is well understood. Theodore von Kármán [127] introduced a semi-empirical

model for the turbulence energy spectrum of homogeneous turbulence in 1948. This model combines Kolmogorov's hypothesis of a universal inertial subrange, where the energy spectrum follows a $k^{-5/3}$ law, with the rate of decay of turbulence at the largest scales, indicating that $E(k) \propto k^4$ at small wavenumbers. An interpolation function was proposed for the energy spectrum based on these theoretical arguments. Liepmann [128] later proposed a different model for the turbulence energy spectrum, known as the Liepmann spectrum. The Liepmann spectrum is similar to the von Kármán spectrum but has a steeper slope at high wavenumbers, implying that $E(k) \propto k^{-2}$ rather than $E(k) \propto k^{-5/3}$.

Both methods are widely used in the literature for modelling inflow turbulence. However, these models do not consider the airfoil geometry, which can lead to inaccuracies when applied directly to axial fan blade noise prediction. Research on using these models specifically for fan noise prediction is limited. Therefore, further investigation into the applicability and accuracy of these turbulence spectrum models for fan noise prediction is necessary.

2.4.4 Rotor interaction noise

The low-fidelity prediction method for the rotor interaction noise introduced in Section 2.2.3 is discussed in this section. The rotor-stator interaction (RSI) noise, caused by the rotor wake interacting with the stator blade, is a major noise source in axial fans. This phenomenon has been well-studied in turbomachinery, resulting in several predictive models. Among these, Lowson's model [129] is one of the most widely used low-fidelity models for predicting RSI noise. This model simplifies the rotor and stator blades as point forces and uses a simplified version of the Ffowcs Williams-Hawkings (FW-H) equation to predict far-field noise.

Lowson derived the sound pressure level for the harmonics of the blade passage frequency (BPF) for both rotor and stator blades [129]. This frequency domain method efficiently predicts tonal noise. However, Lowson's model makes several assumptions: it assumes free-field propagation without reflection or transmission at blade rows or short casing, and it simplifies each blade as a point force rather than using a lifting line or surface approach. The model is designed for acoustically far-field, compact sources and requires unsteady lift and drag data, which can be obtained from other models. Despite its efficiency, it is limited to calculating only the harmonics of the blade passage frequency (BPF).

In the original Lowson's model, only the contributions from the thrust (lift) and torque (drag) forces acting on the rotor blade were considered. Huang [36] further extended Lowson's model to include contributions from the radial force of fan blades, enhancing

its applicability and accuracy in predicting RSI noise. Huang *et al.* [36, 58, 130] also used this model to analyse the noise generated by different rotor and stator blade combinations in a small axial fan for computer cooling, demonstrating the model's effectiveness in analysing noise sources and noise reduction strategies.

This kind of noise is again at multiples of BPF ($f = |m| f_{BPF}$), but at a wider range of orders compared to the steady loading noise [72]. Based on the research of Tyler and Sofrin [131], the mode order ξ can be determined as:

$$\xi = mB - kS, \quad m = 1, 2, 3, \ldots; \quad k = 0, \pm 1, \pm 2, \ldots, \tag{34}$$

where B and S are the number of rotor blades and stator blades, m and k are integers.

The mode order ξ, which is mathematically equivalent to the order of Bessel functions, is the most crucial parameter influencing the radiated intensity of the interaction noise [36]. The Bessel function rapidly vanishes as ξ approaches ∞, implying that the dominating interaction noise occurs when ξ is small, often $|\xi| < 3$ for electric cooling fans. It is worth noting that numerous coincidences occur if the number of rotor blades is an integral multiple of the number of stator vanes or vice versa. This leads to a zero mode order ($\xi = 0$), resulting in a huge increase in the sound emission. The dominating mode orders for small cooling fans used in this study will be further investigated later. The rotor-stator interaction is a dominant tonal noise source of cooling fans [130].

Tian *et al.* [74] showed that non-uniform inflow caused by the incomplete bellmouth inlet increases rotor surface pressure fluctuations, leading to elevated tonal noise. They also provided an expression for the mode of tonal noise emission, based on the work of Tyler and Sofrin [131]. The mode order ξ can be expressed as [74]:

$$\xi = mB + kS + iV, \quad m = 1, 2, 3, \ldots; \quad k, i = 0, \pm 1, \pm 2, \ldots; \quad k \neq 0 \text{ or } i \neq 0, \tag{35}$$

where B is the number of rotor blades, S is the number of downstream stator vanes, and V represents the four sharp edges of the incomplete bellmouth inlet. k and i are integers that define the possible sound radiation modes. When $k = 0$, there is only interaction between the incomplete bellmouth inlet and the rotor. When $i = 0$, it indicates the interaction between the rotor and downstream stator vanes. When both k and i are non-zero, these two interactions work together, leading to more complex interference modes. It should be noted that while all potential interference modes can be calculated, not all of them may be excited during actual fan operation.

The mode order analysis using Eq. 34 and Eq. 35 provides a quick understanding of the interaction noise generation mechanism. Combined with Lowson's model, the tonal noise level emitted by the interactions between the rotor and stationary objects can be predicted.

2.5 Comparison of prediction methods

The common aerodynamic and aeroacoustic prediction methods reviewed in Section 2.3 and Section 2.4 are summarised in Fig. 2.22.

Direct numerical simulation (DNS) and computational aeroacoustics (CAA) at receiver positions are prohibitively expensive and impractical for far-field noise calculations. Consequently, a hybrid approach is often employed, combining near-field aerodynamic simulations with acoustic analogy methods to propagate noise sources from pressure fluctuations to the far field [50, 52, 77]. Large eddy simulation combined with the Ffowcs Williams-Hawkings (LES+FW-H) method is a high-fidelity approach that provides detailed insights into flow physics and noise sources, making it suitable for investigating the noise generation mechanisms of axial fans.

In industrial design and optimisation cycles, the computational cost of noise prediction methods is as crucial as their accuracy. Table 2.3 compares the computational costs of typical low-fidelity and high-fidelity noise modelling methods used in various studies [20, 99, 132–134]. The computational cost is converted to core-hours for comparison, where 1 core-hour equals 1 CPU-core $\times$ 1 hour. This table provides a rough indication of the computational costs required by different numerical methods, acknowledging that not all cases are based on the same computer hardware. For a 2D airfoil, the computational cost of CFD combined with CAA methods is around 10^2 core-hours, while for a 3D case, it is approximately 10^4 core-hours. This highlights the significant computational expense even for an isolated 3D rotor. For instance, on an eight-core processor (*e.g.*, Intel Xeon E5-2660v3), a 3D simulation would take about 1,250 hours (52 days) to complete. Interestingly, the low-fidelity vortex panel method for a 3D rotor requires only about 64 core-hours, compared to 9,216 core-hours for the URANS method, demonstrating a substantial increase in computational efficiency with low-order methods. This suggests that other low-fidelity methods from theoretical or semi-empirical analyses could achieve noise prediction with similarly low computational costs.

Low-fidelity models, such as the BPM model, Amiet's model, and semi-empirical wall pressure spectrum models, have been developed over the past few decades and continue to be used for quick calculations in industrial design and optimisation. How-

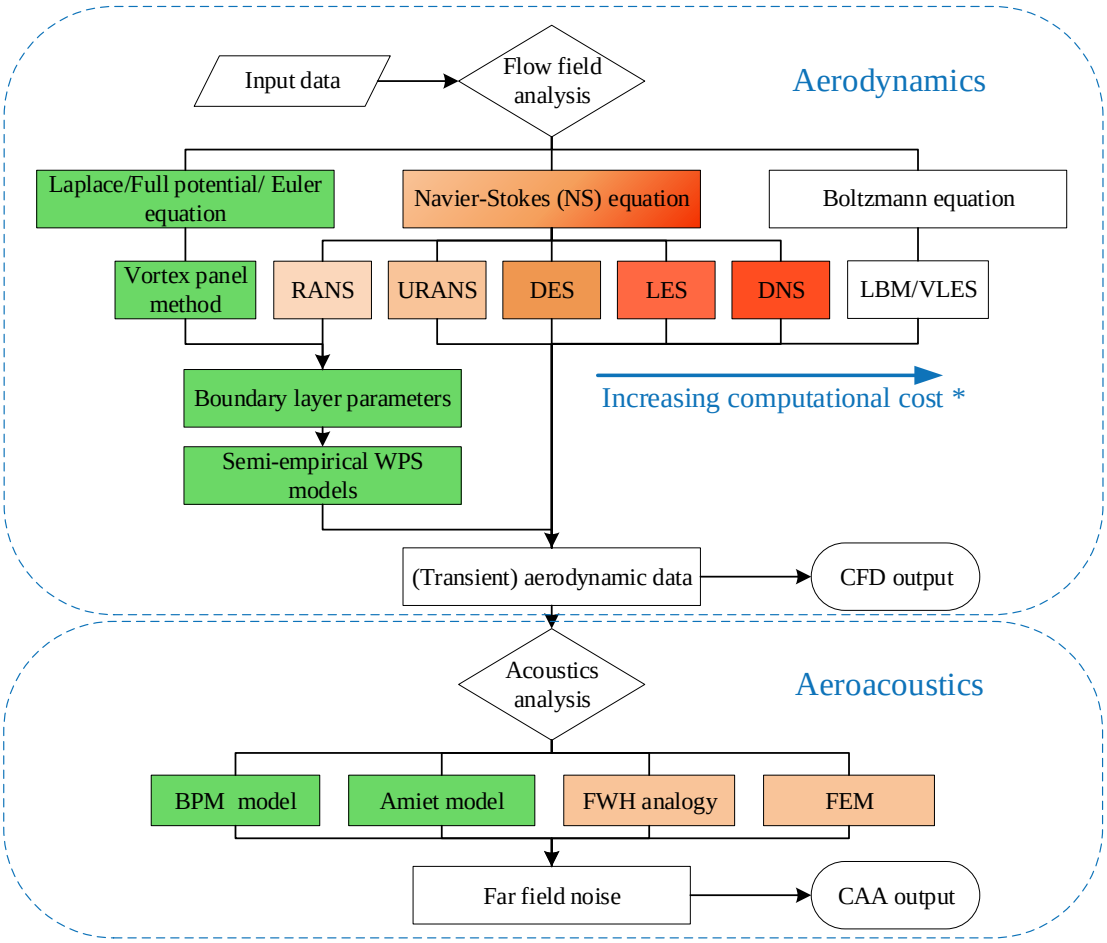

* Note that one exception is the LBM/VLES approach, which is typically thought to be comparable to classical LES method in computational costs.

Figure 2.22: Flow chart of aerodynamic and aeroacoustic prediction methods.

Table 2.3: Comparison of computational time of different modelling methods.

Case geometry	Method	Approx. cost (core-hours) [1]
NACA 0012 airfoil [132]	URANS + FW-H (2D)	45
NACA 0012 airfoil [132]	DES + FW-H (2D)	48
NACA 0012 airfoil [132]	LES + FW-H (2D)	93
UAV rotor-DJI 9443 [99]	VPM + FW-H (3D)	64
UAV rotor-DJI 9443 [99]	URANS + FW-H (3D)	9,216
Low pressure axial fan [133]	DES + FEM (3D)	9,143
Counter-rotating axial fan [20]	LES+ FW-H (3D)	11,000
Automotive axial fan [134]	LBM + FW-H (3D)	16,800
Small axial fan - present study	LES+ FW-H (3D)	24,576
Small axial fan - present study	ROM (3D)	1

[1] Approximate cost listed in the table is used for roughly indicating orders of magnitude of the computational cost required by different numerical methods, as some of these cases are based on different computer hardware.

ever, these models often require parameter tuning, limiting their accuracy to specific parameter ranges. Therefore, further investigation, improvement, and validation of low-fidelity models are necessary for accurate noise prediction in electronics cooling fans. High-fidelity models, such as LES or DNS, offer a deeper understanding of flow physics and complement experimental research by providing high-resolution spatial and temporal data, which may not be available experimentally. These models are expected to elucidate the detailed flow physics behind noise generation mechanisms and guide the development of semi-empirical models. However, the primary challenge with high-fidelity approaches is their high computational cost.

In summary, there is always a trade-off between prediction accuracy and computational time. High-fidelity simulations provide deep insights into flow turbulence physics, while low-fidelity methods allow for the exploration of a wide range of design parameters. In this study, the wall-resolved LES+FW-H method used in this study will be presented in detail in Part I, while the reduced-order model (ROM) will be introduced in Part II.

2.6 Fan optimisation and noise control

This section explores various fan optimisation and noise control strategies aimed at reducing fan noise while maintaining or enhancing aerodynamic performance. Passive control methods are generally favored over active noise control due to their cost-effectiveness and low maintenance requirements. Active noise control techniques, such as active noise cancellation, are more complex and energy-intensive, making them more suitable for specific end-user applications rather than industrial settings. In contrast, passive noise control methods, including geometric modifications and the use of acoustic absorbers, offer practical solutions for fan noise reduction. Therefore, this section focuses on passive noise control methods for axial fans, emphasising geometric modifications and the application of acoustic liners.

Essentially, there is normally a trade-off between aerodynamic performance and noise reduction. Therefore, the challenge is to find the modifications that can achieve a better performance in one factor without significantly compromising the other. Table 2.4 summarises the various fan optimisation and noise control strategies discussed in this section, including their advantages and limitations in aerodynamic performance and noise reduction.

Table 2.4: Fan optimisation and noise control strategies for various axial fan applications.

Strategy	Target sources	Aerodynamics	Aeroacoustics
Winglets [135–139]	Tip, RSI	↑	↑
Serrations [140–145]	TE, LE	↓ (normal) ↑ (stall)	↑
Porous treatments [146–150]	TE, LE	↓	↑
Gurney flaps [151–155]	N/A	↑	↓
Casing treatments [75, 156, 157]	Varied	–	↑
Acoustic liners [157–159]	Varied	–	↑

↑: Increase; ↓: Decrease; –: No significant change; N/A: Not applicable; Varied: Various sources or for general noise reduction. RSI: Rotor-stator interaction; TE: Trailing edge; LE: Leading edge.

2.6.1 Geometric modifications

Geometric modifications have been extensively studied to enhance aerodynamic performance and reduce noise. Typically, there is a trade-off between these two factors, making it challenging to achieve improvements in one without compromising the other. Additionally, some modifications may be more effective in the stall region but decrease performance during normal operation. Given the limited research on electronics cooling fans, this review also includes geometric modifications for general airfoils and turbomachinery. The following sections introduce the most common geometric modifications, including winglets, serrations, and porous treatments, and discuss their effects on aerodynamic performance and noise reduction.

Winglets

Winglet modifications involve adding small fins or winglets to the blade to control the flow and noise. One of the primary factors contributing to efficiency loss [160, 161] and noise propagation [162] in axial fans is the airflow between the fan blade tip and the surrounding shroud, commonly referred to as the tip leakage flow (TLF). Winglets can be added to the blades to control the airflow between the blade tip and the surrounding shroud.

Studies by different reserachers [138, 163–166] demonstrated that well-designed winglets on the pressure side (PS) of industrial fan blades can reduce noise. Additionally, Han *et al.* [139] and Jung *et al.* [167] found that suction side (SS) winglets also enhance performance, particularly in partially shroud-covered axial fans. Zhang *et al.* [136] showed that SS winglets significantly reduce tip leakage vortex (TLV) and noise in diagonal fans.

In the context of small axial fans for electronics cooling, winglets have received less

attention. Yen and Lin [135] found that winglets improve flow stability and efficiency but did not address noise. More recently, Diao *et al.* [137] showed that winglets on both sides, especially the SS, reduce noise and tip leakage flow. However, their study did not explore other winglet parameters like width, location, and shape. These findings suggest a need for comprehensive research on various winglet configurations to optimise the aerodynamic and acoustic performance of small axial fans.

Serrations

Serrations are small, evenly spaced notches or teeth along the leading or trailing edge of the blade, inspired by natural designs. They reduce noise by breaking up large vortices into smaller ones, leading to less pressure fluctuation. Serrations at the trailing edge primarily mitigate noise generated by the trailing edge, while those at the leading edge address noise from the leading edge.

Extensive research has been conducted on using leading and trailing edge serrations to reduce fan noise caused by wake and inflow turbulence. Corsini *et al.* [140] applied leading edge serrations to the outer 20% of an industrial fan blade. They noted a decrease in efficiency below stall conditions and an increase in efficiency post-stall due to the formation of counter-rotating vortices. Biedermann *et al.* [141] found that smaller serration amplitudes improve aerodynamic performance, while larger amplitudes can reduce noise by up to 3.4 dB. Krömer *et al.* [142] showed that sinusoidal leading edge serrations on flat-plate industrial fans enhance both aerodynamic and acoustic performance, achieving noise reductions of up to 30 dB at specific tones. Arina *et al.* [143] used a compressible LES with FW-H acoustic analogy to simulate a NACA 65-1210 airfoil with slightly blunt serration tips and roots at an angle of attack of 5°. They found that noise at low and mid-frequency ranges was primarily reduced due to changes in flow separation at the airfoil trailing edge. Sandberg and Jones [144, 145] studied the effect of trailing-edge serrations on a NACA 0012 at an angle of attack of 5° in a low Reynolds number flow ($Re = 5 \times 10^4$). They found that noise reduction was mainly achieved in the high-frequency ranges and that the flow field on the airfoil was not significantly impacted upstream of the serrations.

Porous treatments

Porous treatments involve adding a porous material to the trailing edge or the entire blade. This approach is inspired by the soft and downy surfaces of owl wings, known for their silent flight. Porous treatments effectively reduce noise but can sometimes lead to aerodynamic performance losses.

Geyer *et al.* [146] investigated fully porous airfoils made from materials like poly-

urethane foams, metal foams, and felts. They found that high-permeability materials significantly reduced noise by absorbing the kinetic energy of incoming turbulent eddies. However, applying porous materials over the entire chord length resulted in notable aerodynamic losses. To mitigate this, partially porous airfoils targeting only the trailing edge were proposed. Geyer and Sarradj [147] applied porous coatings to the last 5% of the chord length, achieving up to an 8 dB noise reduction with minimal lift loss. Rubio Carpio *et al.* [148] extended this approach to the last 20% of the chord, achieving up to an 11 dB noise reduction. Zhang and Chong [150] further reduced the porous coverage to 3.7% of the trailing edge, still observing significant broadband noise reduction. These studies suggest that minimising porous coverage while maintaining high permeability can optimise noise reduction with minimal aerodynamic performance loss. Teruna *et al.* [149] investigated the noise produced by a NACA 0018 airfoil with and without a porous trailing edge at an angle of attack of 0° and Reynolds number flow $Re = 2.8 \times 10^5$. They found that the porous trailing edge can achieve a noise reduction of up to 9 dB. They also observed that flow statistics were barely impacted upstream of the porous trailing edge.

Gurney flaps

Gurney flaps are small, vertical tabs attached to the trailing edge of the blade. Studies have shown that Gurney flaps can effectively increase the lift coefficient of airfoils [151] and the total pressure rise of fans [152]. This enhancement is achieved by increasing the effective back camber and delaying flow separation on the suction surface [151, 153]. However, this improvement comes at the cost of increased drag and aerodynamic noise due to intensified wake blending [168]. Optimal flap heights range from 0.5% to 3% of the chord length [154, 169], with a 2% chord flap increasing the lift coefficient by up to 31.5%, albeit with higher drag.

Chen *et al.* [155] investigated Gurney flaps with heights of 1.25% to 5% chord on axial fan performance. They found that while increasing GF height enhances total pressure rise by accelerating airflow and suppressing separation on the suction surface, it also reduces efficiency. Li *et al.* [152] confirmed that Gurney flaps improve performance but also increase aerodynamic noise levels. To address the noise issue, researchers have proposed combining Gurney flaps with other noise reduction techniques.

Casing treatments

Casing treatments involve modifications to the stationary casing of the fan, such as optimised shrouds [75], porous surface treatments [156], or noise-reducing techniques like acoustic liners [157]. These treatments aim to minimise flow disturbances and absorb noise generated by the fan. Sun *et al.* [75] demonstrated that a short inlet

shroud can effectively reduce noise by controlling the non-uniform inflow and reducing the interaction between the rotor and imcomplete bellmouth inlet. Liu *et al.* [156] demonstrated that porous surface treatments on the casing of a small axial fan can significantly reduce noise while slightly delaying the stall point, thereby enhancing operational stability. These studies show the potential of casing treatments as a practical solution for noise reduction in axial fans.

2.6.2 Acoustic liners

Acoustic liners have emerged as a promising solution for noise mitigation in aerodynamic systems [170–172]. These structured absorptive materials, typically featuring sub-wavelength unit cells in periodic arrangements, exploit visco-thermal dissipation mechanisms to manipulate sound waves beyond the capabilities of conventional materials [173]. By selectively absorbing, reflecting, or transmitting acoustic energy at targeted frequencies, such liners achieve noise suppression without impeding aerodynamic efficiency. Research has identified three dominant absorber categories: (1) Helmholtz resonators (HR) [174, 175], (2) micro-perforated and micro-slit absorbers [157, 176–179], and (3) membrane-based structures [180, 181]. Of these, micro-perforated panel (MPP) and micro-slit panel (MSP) absorbers—comprising perforated surfaces coupled with air cavities—are distinguished by their durability and broadband absorption efficacy [170, 182, 183]. The sub-millimetre perforations in MPPs enhance visco-thermal losses, effectively converting acoustic energy into heat, while their non-porous construction ensures resilience against environmental degradation from dust, moisture, or thermal cycling. This robustness renders them particularly suitable for demanding applications such as electronics cooling fans, where porous alternatives prove inadequate [173]. Recent advances in metamaterial design, including spiral and labyrinthine configurations, have further reduced absorber thickness without compromising performance [184, 185]. However, the manufacturing complexity of these resonant structures often limits their practical implementation.

The efficacy of MPP absorbers in axial fan applications has been validated through diverse implementation strategies, ranging from rotor-adjacent casing treatments [157, 186] to auxiliary duct installations [158]. Early investigations by Allam *et al.* [187] established the potential of MPP splitters in attenuating grazing flow noise, while Lee *et al.* [159] demonstrated substantial blade-passing tone reduction (up to 16 dB) through housing-integrated MPPs in 120 mm axial fans. Subsequent work by Czwielong *et al.* [158] refined these findings, revealing that downstream positioning of MPP absorber ducts optimises both aerodynamic and aeroacoustic performance. Parallel research by Dong *et al.* [157] on counter-rotating (CR) fans demonstrated front rotor treatments yield superior noise reduction (3.5 dBA at design point) versus rear rotor configurations,

with minimal efficiency penalties.

Recent innovations have expanded MPP/MSP functionality through multi-chamber optimisation [176] and hybrid designs. Wang *et al.* [176] achieved ultra-broadband absorption via depth-tuned chambers using a two-point impedance method, while Killeen *et al.* [181] integrated MPPs with decorated membranes in server rack deflectors, achieving 3 dBA reductions at blade-passing frequencies. Wasala *et al.* [28] further adapted these principles through annular fan rings (derived from the EU COST Action DENORMS [188]), achieving 10 dB attenuation at 4.1 kHz in HDD enclosures through retrofittable cavity-filling designs.

Within industrial contexts, micro-slit panel (MSP) absorbers have gained prominence due to their manufacturing simplicity, clog resistance, and structural integrity—attributes particularly advantageous in particulate-laden environments [177]. Though marginally less absorptive than MPP counterparts [189, 190], MSPs offer practical benefits that often outweigh this marginal performance deficit. Their acoustic behaviour is governed by four key parameters: slit width, panel thickness, cavity depth, and porosity, with impedance matching critically dependent on slit-edge effects and cavity resonances [177, 191].

A persistent challenge in conventional MPP/MSP design lies in balancing panel thickness against cavity depth within fixed total thickness constraints. Excessive panel thickness not only diminishes cavity volume—compromising low-frequency absorption—but also increases material costs and system weight. This necessitates innovative geometries that decouple these parameters, enabling thinner panels with deeper cavities. Such optimisation could yield compact, lightweight absorbers without sacrificing acoustic performance, addressing a critical barrier to widespread industrial adoption.

2.7 Summary

The literature review underscores the critical need for a deeper understanding of fan noise generation mechanisms and the advancement of robust prediction and control strategies. Key research gaps include the limited availability of high-fidelity models capable of accurately capturing the complex aeroacoustic phenomena in axial fans, the absence of reduced-order models (ROMs) that balance computational efficiency with predictive accuracy, and the lack of innovative passive noise control methods that effectively mitigate noise without degrading aerodynamic performance.

Addressing these gaps is essential for improving the design and operation of axial fans in electronics cooling applications, where stringent performance and noise require-

ments must be met. High-fidelity modelling can provide detailed insights into the intricate flow physics and noise sources, serving as a foundation for developing more accurate and computationally efficient ROMs. Furthermore, exploring novel passive noise control strategies, such as geometric modifications and acoustic liners, offers the potential to achieve significant noise reduction while maintaining or enhancing aerodynamic efficiency.

Based on the findings of the literature review, the following research questions are formulated to guide this investigation into fan noise generation, prediction, and control methods for electronics cooling applications:

1. **Characterisation of aerodynamic efficiency loss and noise**: *What are the fundamental mechanisms behind aerodynamic loss and noise generation in axial fans under both normal operating and stall conditions, and how do these mechanisms influence the overall noise profile?* This question will be addressed in Part I of the thesis.
2. **Reduced-order modelling**: *Is it possible to develop a low-fidelity meshless prediction model that can accurately predict the aerodynamic performance and noise characteristics of axial fans in electronics cooling applications?* This question will be addressed in Part II: Chapter 4–7 of the thesis.
3. **Optimisation of fan performance and noise reduction**: *How can novel passive noise control methods, such as geometric modifications and acoustic liners, be designed and optimised to achieve significant noise reduction without compromising the aerodynamic performance of axial fans in confined spaces?* This question will be addressed in Part III: Chapter 8–10 of the thesis.

"大音希声，大象无形。"
"The loudest sound cannot be heard;
The greatest form has no shape."

—老子，公元前六世纪，《道德经》
Laozi, 6th-century BC, *Dao De Jing* (Trans. Keith H. Seddon)

Part I

High-Fidelity Modelling

Chapter 3

Large Eddy Simulation for Aerodynamic and Aeroacoustic Characterisation of Electronics Cooling Axial Fans under Various Operating Conditions

This chapter [1] investigates the aerodynamic and aeroacoustic characteristics of a small-sized, high-rotational-speed axial fan used in electronics cooling through experimentally validated high-fidelity numerical methods. The aim is to uncover the mechanisms governing aeroacoustic noise generation in cooling fans.

This chapter is structured as follows: Section 3.1 introduces the research area, followed by the experimental methodology in Section 3.2. The numerical methodology is detailed in Section 3.3, and the validation of the numerical model is presented in Section 3.4. The aerodynamic analysis of the fan flow field is discussed in Section 3.5, while the aeroacoustic analysis of the fan noise is presented in Section 3.6. The chapter concludes with a discussion of the results and their implications for the development of reduced-order models (ROMs) and effective noise reduction strategies.

Abstract

This study provides a comprehensive investigation into the aerodynamic and aeroacoustic characteristics of a small-sized axial fan under various operating conditions, representing different system resistances in electronics cooling applications. A wall-resolved large eddy simulation (LES) approach, combined with the Ffowcs Williams-Hawkings

[1] This chapter is based on the published **journal article**: W. Zhao, S. Wasala, and T. Persoons, "Large eddy simulation for aeroacoustic prediction and characterization of electronics cooling axial fans under various operating conditions", *Applied Acoustics*, vol. 231, p. 110530, Mar. 2025.

(FW-H) acoustic analogy, is used to analyse the flow and noise characteristics for a realistic fan configuration. The numerical simulations are validated through comparison with experimental measurements, showing excellent agreement. The study reveals distinct flow and noise characteristics between normal and stall conditions of the fan. During normal operating conditions, paired inlet vortex tubes are observed due to the asymmetric inlet-rotor interaction. The flow structures near the blade tip, such as the inlet vortex tubes and tip vortices, exhibit higher coherence. However, during stall conditions, these structures become more disorganised. Additionally, laminar-turbulent separation and high leading-edge turbulence are observed during stall conditions, resulting in increased broadband noise level. Aeroacoustic analysis shows that tonal noise is more prominent during normal operating conditions, while broadband noise becomes more significant during stall conditions. The main tonal noise sources during normal conditions are the asymmetric inlet-rotor interaction and the rotor-stator interaction. On the other hand, the tip-gap noise serves as the primary source of broadband noise. During stall conditions, the leading-edge noise and flow separation noise become the main sources of broadband noise. The shroud noise significantly contributes to the tonal noise across all operating conditions. This study identifies the locations and dominant characteristics of the noise sources and analyses the contributions of different noise sources to the overall fan noise.

3.1 Introduction

Axial cooling fans are essential for aerospace [192], automotive [54], and electronics cooling [36] to dissipate heat from electronic components [3, 5]. As compact packaging and high power densities become more common, small-sized axial fans operating at high rotational speeds (*e.g.*, around 10,000 r/min) are increasingly used in electronic devices for cooling. The aeroacoustic noise generated by these fans is a critical concern as it can negatively impact user experience and component performance. Excessive noise levels can be annoying and uncomfortable, especially in noise-sensitive environments. Additionally, aeroacoustic noise can interfere with sensitive electronic components, such as hard disk drives, and degrade system performance [20, 21]. Therefore, understanding the aeroacoustic noise characteristics of cooling fans is crucial for optimising their design and performance.

The noise generated by axial cooling fans originates from multiple sources, including electromagnetic and electromechanical motor noise, mechanical and vibration noise, and aeroacoustic noise [47, 48]. Among these sources, aeroacoustic noise, also known as flow-induced noise, is typically the main contributor to the overall noise level in cooling fans. The aeroacoustic noise sources can be categorized as blade self-noise

and blade interaction noise. Table 2.1 provides an overview of the potential sources of aeroacoustic noise for axial fans, including tonal noise ('T') and broadband noise ('BB').

Previous studies have identified the rotor-stator interaction and the interaction between non-uniform inflow and the rotor as the main sources of tonal noise in fans [39, 56, 57, 193]. Huang *et al.* [36, 58] investigated the tonal noise characteristics of a low-speed axial fan used in computer cooling. They simplified the fan blades as point force sources and used an extended Lowson's model [129] to account for the contributions from thrust, torque, and radial force. They concluded that the rotor-stator interaction was the dominant source of tonal noise, and the irregular inlet shape affected the noise similarly to the stator-rotor interaction. This interaction can generate noise levels comparable to the rotor-stator interaction. Tian *et al.* [74] further confirmed that the non-uniform inflow, caused by the asymmetric inlet shape, can increase rotor surface pressure fluctuation. They demonstrated this through an experimental and numerical unsteady Reynolds-Averaged Navier-Stokes (URANS) study, which in turn increases tonal noise. Correcting the asymmetry of the inlet shape or including a short inlet duct has been confirmed as effective methods for reducing this tonal noise [76, 194, 195].

Broadband noise in axial flow machines is primarily generated by trailing-edge noise, tip vortex noise, leading-edge noise, and flow separation [42, 52, 53, 60]. Trailing-edge noise occurs when a turbulent boundary layer flow passes by the sharp edge of an airfoil, resulting in acoustic scattering. This type of noise is more prominent at high frequencies [51, 52]. Tip vortex noise is caused by the unsteady flow structures that form at the blade tip regions due to the pressure difference between the pressure and suction sides of the blade. These flow structures lead to complex tip vortices, increased aerodynamic losses, and higher noise levels [31, 43]. Previous studies have shown that tip noise is the dominant source of noise for these cooling fans across a wide range of flow rates [54, 196]. Leading-edge noise is generated by the interaction between the incoming turbulent flow and the leading edge of the blade. This type of noise is more noticeable at low frequencies [52, 59]. Moreau and Roger [60] compared the contributions of trailing-edge and leading-edge noise in low-speed automotive fans and found that leading-edge noise is the main source of broadband noise across most frequencies, while trailing-edge noise becomes significant only at high angles of attack. Flow separation noise occurs when the flow separates from the blade surface at high angles of attack, resulting in broadband noise that is more prominent at low frequencies [52]. When a laminar boundary layer separates or a laminar separation bubble (LSB) forms near the trailing edge, coherent perturbations in the separated shear layer are amplified, producing distinct tones when scattered at the trailing edge [52, 197]. This shedding process generates acoustic waves that propagate upstream and interact with

the boundary layer or LSB, forming an acoustic feedback loop.

Previous studies have provided valuable insights into the noise generation mechanisms of axial fans. However, there are still research gaps that need to be addressed. Firstly, there is a lack of understanding regarding the distorted flow structures caused by the asymmetric inlet shape. Despite the early identification of the disadvantages of the asymmetric inlet bellmouth for low-speed computer cooling fans by Huang [36] in 2003, this design is still widely used in modern electronics cooling fans. The detailed flow structures caused interaction between the asymmetric inlet shape and the rotor tip remains unexplored, leading to a lack of awareness in the industry regarding potential noise issues. Additionally, the contribution of shroud noise to the overall fan noise in electronics cooling fans has not been thoroughly investigated. While the shroud is considered insignificant for automotive cooling fans [198], it may play a significant role in electronics cooling fans, where the circumferentially asymmetric bellmouth partially acts as a shroud. Furthermore, axial cooling fans operate under various backpressure conditions, including stall conditions, due to complex system configurations in electronics enclosures. The noise sources of the fan under different operating conditions have not been adequately compared, as most studies have primarily focused on the fan operating at design conditions. Several existing studies [39–41] have observed that fan noise is more broadband at high loaded conditions, *i.e.*, high system resistances with high backpressure and low flow rate. However, there is a lack of exploration regarding the underlying mechanisms of noise generation under different operating conditions, including stall. Therefore, a comprehensive investigation of the aeroacoustic noise characteristics of axial fans under different operating conditions is necessary. Detailed insights into the flow features and noise sources under various operating conditions can provide valuable information for understanding the noise generation mechanisms.

Considerable research efforts have been dedicated to improving the prediction of aeroacoustic noise in axial fans [72, 199, 200]. Moreau and Roger [110, 201] conducted a review of analytical and numerical prediction methods for aeroacoustic noise in turbomachinery. They emphasized the importance of advanced computational techniques, such as large eddy simulation (LES), for studying aeroacoustic noise. While URANS simulations can predict tonal noise, they have limitations in modelling broadband noise generation mechanisms in cooling fans. In contrast, LES provides a more accurate and detailed representation of flow physics, making it well-suited for studying cooling fan noise. Wasala *et al.* [20] used LES to investigate the aeroacoustic noise of a counter-rotating fan used in electronics cooling. They demonstrated that LES, combined with the Ffowcs Williams-Hawkings (FW-H) acoustic analogy [104], can effectively predict the tonal and broadband noise characteristics of the fan. In other related fields, Carolus

et al. [42] employed LES to study broadband noise generation in a low-speed axial fan, while Lewis [202] used it for a turbofan stage. Lu *et al.* [203] evaluated seven turbulence models for noise prediction in a low-speed single-stage axial fan and found that LES provides accurate results, especially for broadband noise. The effect of tip-leakage flow on noise generation has been investigated using high-fidelity CFD methods for various configurations, including a single blade [161, 204], a low-speed axial fan [192], a compressor rotor [205], and a turbofan stage [206]. Al-Am *et al.* [207] employed wall-resolved LES to investigate the noise generated by flow separation for a turbofan stage under different mass-flow conditions. Al-Am [85] also compared wall-modelled and wall-resolved LES, observing some discrepancies in the recirculation region when using wall-modelled LES.

In addition to using LES with the Navier-Stokes (NS) equations for predicting fan noise, significant progress has been made with the Lattice-Boltzmann method (LBM) combined with very large eddy simulation (VLES) for simulating flow-induced noise over the past decade [110]. The LBM models fluid particles using distribution functions, making it inherently unsteady and well-suited for computational aeroacoustics (CAA) [48]. This hybrid LBM/VLES method has shown excellent accuracy in predicting noise for low-Reynolds number, low-tip-Mach-number fans. Although no case has been reported for electronics cooling fans, it has been successfully applied to UAV rotors [55], engine cooling fans [54, 79], and low-speed industrial fans [208]. Moreau *et al.* [54] investigated sub-harmonic humps in the noise spectrum of an engine cooling ring fan using LBM/VLES, revealing that these humps are caused by coherent structures formed in the tip gap. Moreau [79] also showed that LBM/VLES can handle more complex geometries, such as engine cooling modules with upstream obstructions, where RANS-based methods performed poorly. Zhu and Carolus [208] applied LBM to a low-speed industrial fan, focusing on the tip clearance effect on fan noise. They found that coherent structures in the tip region grow with decreasing flow rate, causing distinct far-field noise humps and eventually leading to stall.

These studies have demonstrated the capability of LES in predicting aeroacoustic noise sources for various turbomachinery configurations. However, to the best of our knowledge, a complete wall-resolved LES for a realistic cooling fan configuration in electronics cooling has not yet been reported. A wall-resolved LES study is expected to provide detailed insights into the flow structures and noise sources of cooling fans, which will narrow the existing research gaps and contribute to the development of effective noise reduction strategies.

This study aims to comprehensively investigate the aeroacoustic noise characteristics of a small-sized axial fan used in electronics cooling through numerical and experimental methods. The wall-resolved large eddy simulation (LES) combined with the Ffowcs

Williams-Hawkings (FW-H) acoustic analogy is employed and validated. The objectives of this study are: (1) to investigate the detailed flow structures of the fan under both normal and stall conditions, (2) to quantify the contributions of various noise sources and identify the dominant fan components contributing to noise generation, and (3) to elucidate the physical mechanisms underlying aeroacoustic noise generation across different operating conditions. The findings of this study will contribute to the development of effective noise reduction strategies for cooling fans and enhance the design of low-noise electronic systems.

3.2 Experimental methodology

3.2.1 Selection of the test fan

The selected fan for testing is a small axial fan with an 80 mm rectangular frame, manufactured by Delta Electronics (Model No. FFB0812XHXHC). This fan is commonly used in data center applications, such as servers and hard disk drive enclosures, and has been previously studied in [23, 30, 31, 209]. It has a blade tip radius of 37.35 mm and a hub radius of 18.70 mm. The tip Mach number is approximately 0.1, and the average Reynolds number based on the chord length is around 60,000.

The fan consists of 5 rotor blades, 7 streamlined stator blades, and an outer shroud with an incomplete bellmouth-shaped inlet, as shown in Fig. 2.1. The bellmouth inlet intersects with the square-shaped fan housing, which is designed to fit the fan into a standard 80 mm fan mounting frame. However, the bellmouth inlet is not circumferentially symmetric and comprises four sharp edges and four interrupted sections of a bellmouth-style contraction.

The fan is driven by a brushless direct current (DC) motor, and the rotational speed is controlled using pulse-width modulation (PWM) signal. The parameters of the selected fan are summarised in Table 3.1.

3.2.2 Aerodynamic measurements

Setup for performance curve measurement

To measure the fan performance curve (P-Q), a wind tunnel was constructed. The experimental setup is shown in Fig. 3.1. More details about the experimental aperture, instrumentation, calculations, and uncertainty analysis of this test facility can be found in Appendix A.1. This facility has also been used in the author's published work [31, 32, 209, 210]. It will also be utilised in later chapters, *i.e.*, Chapter 4, 5, 8, and 10.

Table 3.1: Parameters for the selected single impeller fan.

Parameter	Value
Rotor blade number, B [-]	5
Stator blade number, S [-]	7
Shroud radius, R_s [mm]	38.30
Rotor tip radius, R_t [mm]	37.35
Hub radius, R_h [mm]	18.70
Rotor blade chord length, c [mm]	26.00
Rotational speed, N [r/min]	9000
Rotational tip Mach number, Ma [-]	0.1
Chord-based Reynolds number, Re [-]	60,000

The fan speed is determined by recording the feedback generator (FG) signal. The static-to-total pressure rise (P) and the total volume flow rate (Q) are obtained following the standardized procedures outlined in ANSI/AMCA [211]. The uncertainties of the measured parameters are also calculated based on this standard. The P-Q calculation and uncertainty analysis are detailed in Appendix A.1.2 and Appendix A.1.3, respectively.

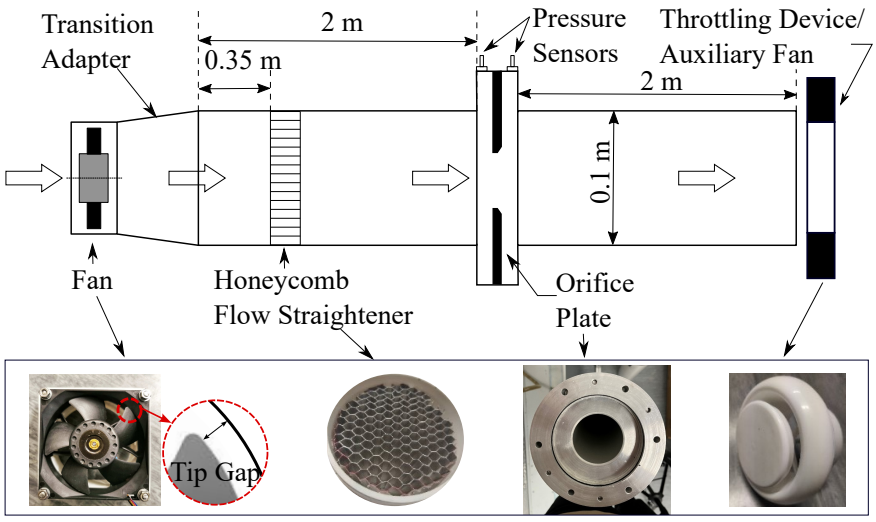

Figure 3.1: Experimental setup for testing the aerodynamic performance of the fan.

Validation of the experimental setup

To verify the accuracy of the experimental setup, a comparison was made with the reference experimental data provided by the manufacturer. As shown in Fig. 3.2, the fan performance curve obtained from the experimental setup agrees well with the reference data. It is important to note that the experimental setup has higher uncertainties at low flow rates ($Q < 0.5$ m^3/min) due to the orifice plate size not being designed for very low flow rates. Additionally, at low flow rates, the fan blades are highly stalled, which leads to less stable pressure measurements. Overall, compared

to the reference data, the fan performance curve obtained from the experimental setup has a normalised root-mean-square error (NRMSE) of less than 3.9% and a correlation coefficient of 0.9767. This indicates that the experimental setup demonstrates a high level of accuracy and repeatability for the pressure below 25 mmH_2O and flow rates above 0.5 m^3/min. The fan performance curve obtained from the experimental setup serves as the reference data for the numerical simulation.

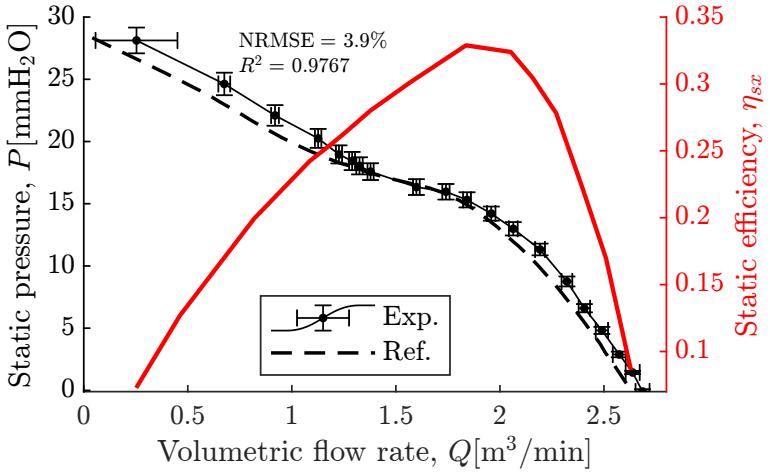

Figure 3.2: Comparison of the fan performance curve with N = 9000 r/min, obtained from the experimental setup and the reference data provided by the manufacturer.

3.2.3 Aeroacoustic measurements

Setup for acoustic noise emission measurements

To measure fan noise, a half-scale test plenum was developed. The test plenum, shown in Fig. 3.3, is designed for acoustic performance measurements of axial and centrifugal fans with adjustable back pressure. More details about the experimental aperture, instrumentation, calculations, and uncertainty analysis of the acoustic test facility can be found in Appendix A.2. This facility has also been used in the author's published work [209, 210]. It will also be ultilised in later chapters, *i.e.*, Chapter 7, 8, and 10.

The noise signal is measured at seven different locations using GRAS 40PH microphones with an uncertainty of ±2 dB in the frequency range of 10 Hz to 20 kHz and a dynamic range that peaks at 135 dB. The sensitivity of each microphone is calibrated using a GRAS 42AG Multifunction Sound Calibrator, set at a sound pressure level of 94 dB and a frequency of 1 kHz.

To account for the non-anechoic nature of the room, background noise correction and environmental correction are applied to the measured data, following ISO 3744 [212] standards. The environmental correction factor K_2 is determined using the VIacoustics AccuLab RSS-101 as the reference sound source (RSS). The background noise correction

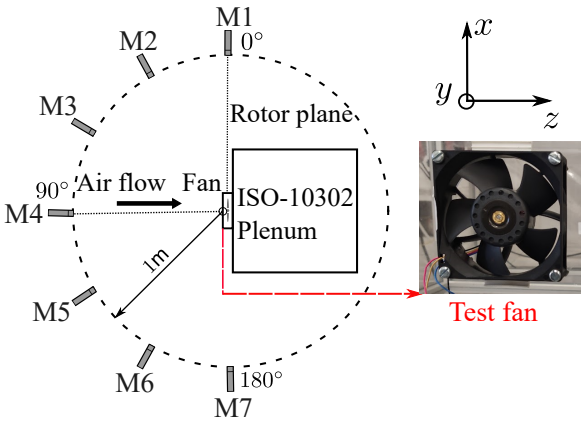

Figure 3.3: The set-up for acoustic noise measurements.

factor K_1 is obtained by repeatedly measuring the background noise and the noise emitted by the test fan. Further details on determining the correction factors can be found in Appendix A.2.2.

The laboratory environment meets the background noise requirements specified in ISO 3744 [212] for frequencies above approximately 250 Hz. To ensure higher accuracy, only noise data above 500 Hz is considered valid, while data below 500 Hz is excluded. The combined uncertainty is within ±3 dB in the valid range, demonstrating compliance with the standards. The uncertainty analysis for the noise measurements is detailed in Appendix A.2.3. An interlaboratory comparison is conducted to validate the accuracy of the noise measurements, and the results are presented in Section 3.2.3.

The measurement surface is located 1 m away from the fan rotor. For each measurement, a sampling frequency of 51.2 kHz and a recording period of 20 s are employed. Acoustic signals are processed using a Hanning window and 50% overlap. The mean time-averaged sound pressure level (SPL) at the reference surface is calculated by averaging the sound pressure levels at the seven microphone locations. It is defined as [212]:

$$\overline{L'_{P(\mathrm{ST})}} = 10 \log_{10} \left[\frac{1}{N_M} \sum_{i=1}^{N_M} 10^{0.1 L_{Pi(\mathrm{ST})}} \right], \tag{36}$$

where $L_{Pi(\mathrm{ST})}$ represents the frequency-band time-averaged sound pressure level measured at the i^{th} microphone position with the fan noise source under test (ST) in operation, in decibels. N_M denotes the total number of microphone positions. The resulting mean time-averaged sound pressure level $\overline{L'_{P(\mathrm{ST})}}$ is expressed in decibels.

The corrected surface time-averaged sound pressure level ($\overline{L_p}$) is calculated by subtracting the background noise correction factor (K_1) and the environmental correction factor (K_2) from the mean time-averaged sound pressure level ($\overline{L'_{P(\mathrm{ST})}}$). This calculation is expressed as [212]:

$$\overline{L_p} = \overline{L'_{P(\mathrm{ST})}} - K_1 - K_2. \tag{37}$$

Potential non-flow-induced noise sources

The discussion has addressed background noise and environmental considerations in measuring fan noise. However, it is important to acknowledge and characterize other potential sources of non-aeroacoustic noise that may impact noise measurements. Two significant sources are fan motor noise and noise resulting from rotor speed fluctuations. Understanding and quantifying these noise sources is crucial for precise and reliable aerodynamic noise measurements.

To investigate motor noise, a measurement was conducted with the fan motor running without blades. The noise level of the fan motor was compared to that of the fan. As shown in Fig. 3.4, the fan motor noise is significantly lower than the fan noise at most frequencies. This is expected as the motor noise is minimised by using a brushless DC motor with low electromagnetic noise. However, three major peaks can be observed in the fan motor noise at around 150 Hz, 1200 Hz, and 1800 Hz. The peak at 150 Hz is likely related to motor imbalance, which has the same frequency as the rotational frequency f_r of the fan. The peaks at 1200 Hz and 1800 Hz are related to electromagnetic forces caused by the 4 poles of the motor, generating noise at frequencies of $8f_r$ and $12f_r$ respectively. Additionally, a small hump in the frequency range of 3000 Hz to 5000 Hz is also observed. Aeroacoustic noise measurements are expected to be affected by the motor noise at these frequencies.

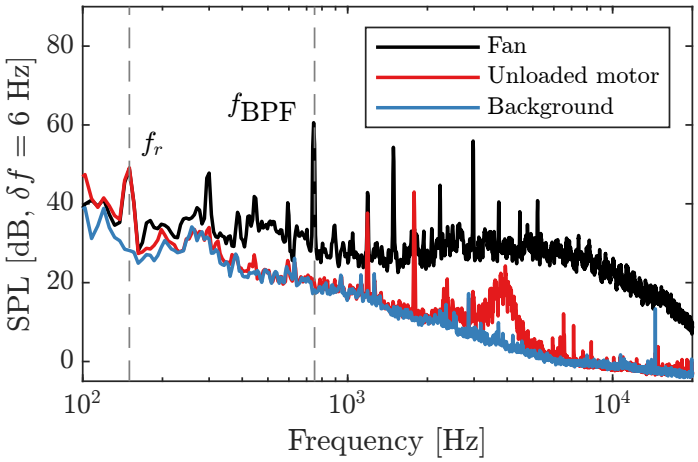

Figure 3.4: Comparison of the noise levels of the fan, the fan operating without blades (unloaded motor noise), and the background noise. The measurements were taken at microphone location M4 (90°) at 0 mmH_2O with a fan speed of 9000 r/min.

The unsteady motion of the rotor due to speed fluctuations can generate noise, as confirmed by recent studies in the field of unmanned aerial vehicles (UAVs) [213, 214].

Zhong *et al.* [213] investigated the noise generated by rotor speed fluctuations of UAV blades and found that even a small fluctuation (less than 1%) in rotor speed can significantly alter the tonal noise and broadband spectrum. However, the discussion of noise generated by rotor speed fluctuations in the context of axial fans is limited. Rotor speed fluctuations in fans can be caused by electromagnetic torque ripple from brushless DC motors and unsteady aerodynamic interactions between fan blades and the flow field, especially during stall conditions. The rotor speed fluctuations, measured from the feedback generator (FG) signal, range from 0.2% to 1.0% of the nominal speed, which is similar to the motor fluctuations (0.4% to 1.4%) reported by McKay *et al.* [214] for UAVs. Investigating the noise generated by rotor speed fluctuations is beyond the scope of this study, but it is worth noting that this unsteady motion is expected to influence the noise spectrum of the fan, particularly for low-frequency tones.

Validation of the experimental setup

To validate the experimental setup at Trinity College Dublin (TCD) for noise measurements, an interlaboratory comparison was conducted. The same fan underwent testing in a hemi-anechoic chamber at Seagate Technology in Longmont, Colorado, USA, following the ISO 10302 standard [215]. The chamber had a low cutoff frequency of 100 Hz and a high cutoff frequency of 20 kHz. Noise measurements were performed under different backpressure conditions to represent various operating conditions of the fan. For brevity, only the results for the free delivery condition (0 mmH_2O) and the stall condition (18 mmH_2O) are presented. As shown in Fig. 3.5, it is important to note that the fan tested at Seagate Technology operated at a slightly higher speed (9120 r/min) compared to the fan tested at TCD (9000 r/min), resulting in a minor shift in the blade passing frequency (f_{BPF}) and its harmonics.

The noise levels of the fan under different backpressure conditions exhibit good agreement between the two laboratories, with only minor discrepancies observed. A noise peak is notably observed at 1800 Hz ($12f_r$), which can be attributed to varying motor noise levels. This observation aligns with the noise measurements of the unloaded motor, as shown in Figure 3.4. Furthermore, the noise levels measured at TCD are slightly higher than those measured at Seagate Technology above 5000 Hz, likely due to differences in background noise levels and environmental conditions.

The interlaboratory comparison supports the reliability and accuracy of the experimental setup at TCD for fan noise measurements. Adhering to ISO 3744 [212] and ISO 10302 [215] standards is effective for small-sized fan noise measurements, even in a non-anechoic room environment.

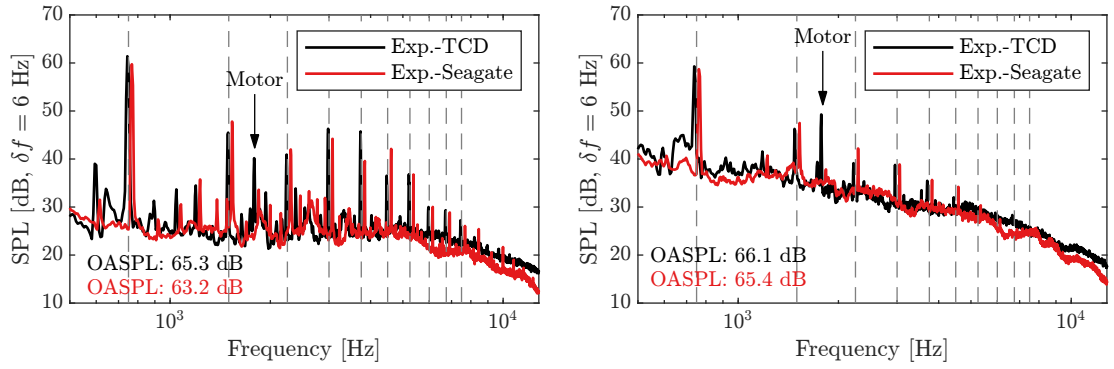

(a) 0 mmH_2O (b) 18 mmH_2O

Figure 3.5: Comparison of sound pressure levels (SPL) $\overline{L_p}$ for the fan noise measurements between TCD and Seagate Technology under different backpressure conditions: (a) free delivery condition of 0 mmH_2O, and (b) stall condition of 18 mmH_2O. The dashed lines represent the first ten harmonics of the blade passing frequency f_{BPF}. The noise levels are measured at a distance of 1 m from the fan rotor (as shown in Fig. 3.3), and the SPL ($\overline{L_p}$) is calculated using Eq. 37.

3.3 Numerical methodology

3.3.1 Computational domain

In this study, an incompressible wall-resolved large eddy simulation (LES) is performed for the axial fan described in Section 3.2. The computational domain, depicted in Fig. 3.6, extends 5 rotor diameters ($5D$) upstream of the fan rotor and 10 rotor diameters ($10D$) downstream of the fan stator. This ensures a fully developed flow at the inlet and outlet of the fan rotor. The computational model accurately represents the fan geometry, including the circumferentially asymmetric inlet bellmouth and the hub. To improve grid quality near the wall, the rotor, and stator trailing edges are slightly rounded. The computational domain does not include some minor geometric features such as small dimples used for balancing and the electrical wires routed along the rear of one of the stator blades, for simplicity.

3.3.2 Numerical scheme and boundary conditions

The wall-resolved large eddy simulation (LES) is performed using the finite volume method to capture the unsteady flow structures and noise sources. The commercial software ANSYS Fluent 2023 R2 is used as the numerical solver. The LES simulations are based on the filtered Navier-Stokes equations, where the large scales are resolved, and the small scales are modelled by the subgrid-scale model. The subgrid model used in the LES simulations is the wall-adapting local eddy-viscosity (WALE) model, known for its ability to capture the anisotropy of the subgrid-scale turbulence and its suitability for wall-bounded flows [89]. The WALE model can capture flow transition and separation

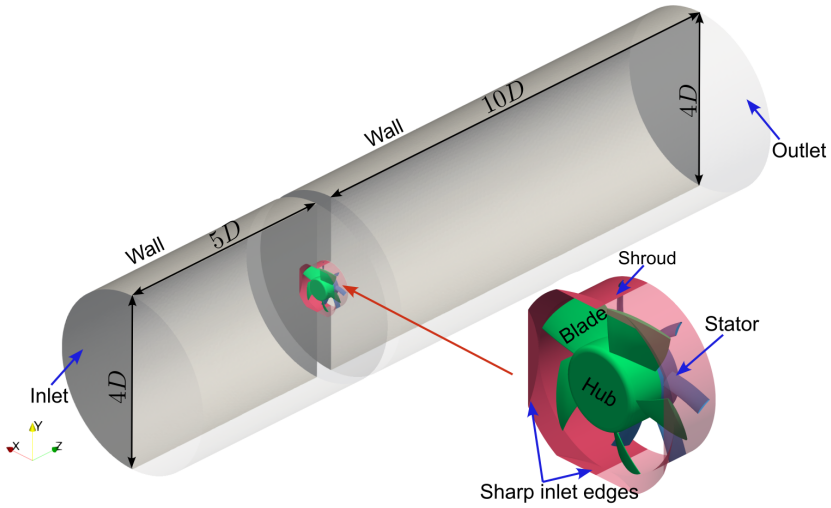

Figure 3.6: Computational domain.

near the wall, which is crucial for simulating fans at stall conditions. This model has previously been applied to study the aeroacoustic noise generation from complex tip flow and flow separation [202, 206]. The constant for the WALE model, C_w, typically ranges from 0.3 to 0.56 [216], based on empirical data. While Nicoud and Ducros [89] initially recommended a value of 0.5, recent studies have shown that a value of 0.325 provides more accurate results across various flow conditions [217]. Consequently, a value of 0.325 was chosen for the WALE model in this study. The LES simulations are performed using the SIMPLEC algorithm. The bounded central difference scheme is used for the convective terms, and the least square cell-based scheme is used for the diffusive terms. A second-order scheme is applied for the time discretization. The simulations are run with a time step of 9.2593×10^{-6} s, corresponding to 0.5° of rotor revolution. The Courant number is kept below one to maintain simulation stability. A smaller time step is not used due to limited computational resources. However, this time step is sufficient to resolve the majority of the flow structures and noise sources. This will be further discussed through experimental validation in Section 3.4.

The LES simulations are initialised with steady-state Reynolds-averaged Navier-Stokes (RANS) simulations, and synthetic turbulence is added at the inlet boundary. A total pressure of 0 mmH_2O is applied at the inlet, while a static pressure ranging from 0 mmH_2O to 18 mmH_2O is applied at the outlet. The inlet condition includes 4.7% turbulence intensity with a turbulence length scale of 0.022 m, estimated from experimental hot-wire anemometry measurements. The walls have a no-slip boundary condition. The fan rotor domain rotates at a constant angular velocity of 9000 r/min. The multiple reference frame (MRF) method is used for the RANS simulations to model the rotating domain, while the sliding mesh method is used for the LES simulations to capture the interactions between the rotating and stationary domains.

The simulations are conducted until the flow reaches a statistically steady state, typically after 5–10 rotor revolutions. Subsequently, the simulations are extended for an additional 15 rotor revolutions to calculate the turbulence statistics and noise sources.

3.3.3 Noise prediction

The far-field noise is calculated using the Ffowcs Williams-Hawkings (FW-H) acoustic analogy [104], assuming free-space propagation of the acoustic waves. This method is widely used in the aeroacoustic community to predict noise from the unsteady motion of rotating blades [54, 55, 202]. The FW-H analogy breaks down noise prediction into two steps: noise source calculation and free-space propagation of the acoustic waves, reducing computational cost. While the cascade effect is included in the flow field calculations, any reflections or transmissions of the sound waves are neglected in the FW-H equation. This method may overpredict noise for fans with long ducts [202], but it is acceptable for axial fans with short ducts [54]. It includes three terms: monopole, dipole, and quadrupole noise sources. In this study, the quadrupole noise source is excluded due to its negligible impact on low-speed blades operating at a Mach number of approximately 0.1. The dipole noise source, caused by the unsteady motion of the fan blades, is typically the dominant noise source for axial fans. Therefore, the FW-H equation is employed to predict the far-field noise by focusing on the noise generated by the fan's solid surfaces. In this study, the FWH surfaces are aligned with the solid surfaces of the fan components, including the rotor, stator, and shroud, facilitating the quantification of noise radiation from each component.

The far-field noise is calculated using the unsteady flow data from each time step of the LES simulations. Microphones are arranged in a circular array 1 m away from the fan rotor plane, following the experimental setup (see Fig. 3.3). The sound pressure level is computed for each microphone location to predict the noise generated by the axial fan accurately. The acoustic compactness is considered due to the use of incompressible LES. With a Mach number of 0.1 and a chord length of 26 mm, the blade remains acoustically compact up to about 13 kHz, which is within the study's frequency range. The noise prediction is validated against measurements from 500 Hz to 12.8 kHz, covering both tonal and broadband noise generated by the fan. Four distinct operating conditions are considered for noise prediction: 0 mmH_2O (free delivery), 6 mmH_2O, 12 mmH_2O (maximum efficiency), and 18 mmH_2O (stall), aligning with the CFD simulations presented in Section 3.3.2. Noise prediction is performed for each condition to explore the noise characteristics of the axial fan under varying backpressure scenarios. The results are validated against experimental data to ensure the accuracy of the numerical model, as discussed in Section 3.4. A comparative analysis of the different operating conditions, including both normal and stall conditions, is presented

in Section 3.6.1.

Each fan component, including the rotor, stator, and shroud, is analysed to determine its individual contribution to the overall noise, as discussed in Section 3.6.2. The noise prediction results are examined to uncover the physical mechanisms behind aeroacoustic noise generation in axial fans. Wall pressure fluctuations are computed for each fan component to identify regions with high fluctuation levels that significantly contribute to noise generation.

Point probes are strategically placed at various spanwise and chordwise locations on the blade to analyse the wall pressure spectrum (WPS). The mid-span location (50% span) represents the average WPS across the blade span, while the tip location (99% span) focuses on the WPS in the tip region. Both leading-edge (2% chord) and trailing-edge (98% chord) locations are considered to provide insights into the generation of leading-edge and trailing-edge noise at different blade sections. This detailed analysis is presented in Section 3.6.3.

3.3.4 Grid development and refinement

The wall-resolved LES requires a high grid resolution to capture detailed turbulence structures. The grid for the LES simulations is generated using ANSYS Fluent Meshing. It combines polyhedral and Cartesian hexcore elements for the main flow region, with prism layers applied for the near-wall region. Figure 3.7 shows the grid system and close-up views of the grid refinements in different regions.

The regions upstream and downstream of the fan are gradually refined to ensure proper resolution of the flow ingestion and wake regions. The fan tip-gap region is refined with approximately 35 layers to capture the complex tip flow. The rotor and stator separation gap is also refined to capture the flow interaction between the blades. The trailing edge (TE) and leading edge (LE) regions are refined to adequately resolve the flow near the boundary layers.

For near-wall resolution of the rotor and stator blades, 18 prism layers are used with a growth rate of 1.08. The first layer is refined near the walls to ensure that the wall-normal grid resolution satisfies $y^+ < 1$. The LES also requires a high grid resolution in the streamwise and spanwise directions. Approximately 130 elements are used in the streamwise direction with a growth ratio of 1.1, while around 60 elements are applied in the spanwise direction along the blades, excluding the tip-gap region.

Figure 3.8 shows the non-dimensional wall-normal distance y^+, streamwise distance x^+, and spanwise distance z^+ for all fan surfaces. The y^+ values are mostly below 1 in the wall regions, while z^+ and x^+ are below 60. Due to resource constraints,

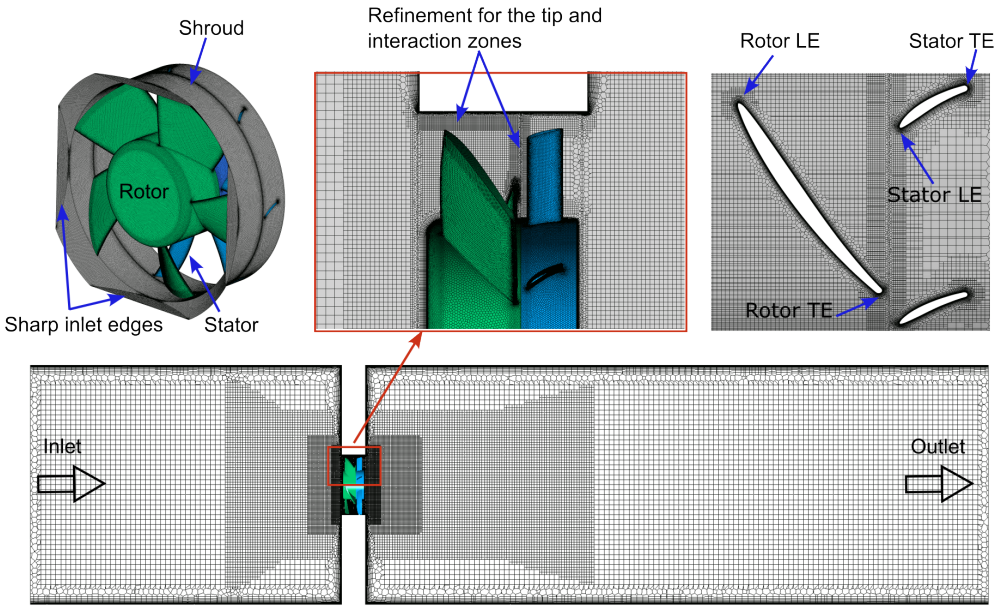

Figure 3.7: Grid system and close-up views of the grid refinements in the upstream and downstream regions of the fan, the blade tip region, and the trailing edge (TE) and leading edge (LE) regions.

achieving low cell aspect ratios near the wall for fully resolved turbulence was not feasible. However, since the boundary layer was predominantly laminar in many cases, a laminar boundary resolution was sufficient.

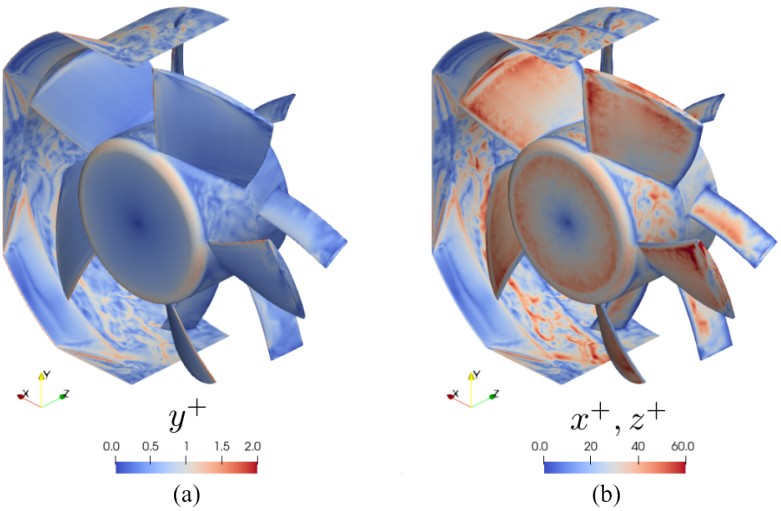

Figure 3.8: The values of y^+ (a), x^+ and z^+ (b) for all fan surfaces.

The LES index of quality, proposed in [218], was used to evaluate the mesh quality of the LES domains. This index ranges from 0 to 1, with higher values indicating higher-quality LES simulations. An acceptable range for the LES index of quality is typically above 0.8, indicating that most of the turbulent energy is resolved. Figure 3.9 shows the LES index of quality calculated for each grid point in the computational

domain. The rotor, stator, and inlet domains have LES index of quality values above 0.85, indicating high-quality grid resolution for resolving turbulent structures. The minimum LES index of quality, slightly below 0.8, occurs in the far downstream of the fan domain, which is not critical for noise prediction. Therefore, the grid resolution is considered adequate for the entire computational domain.

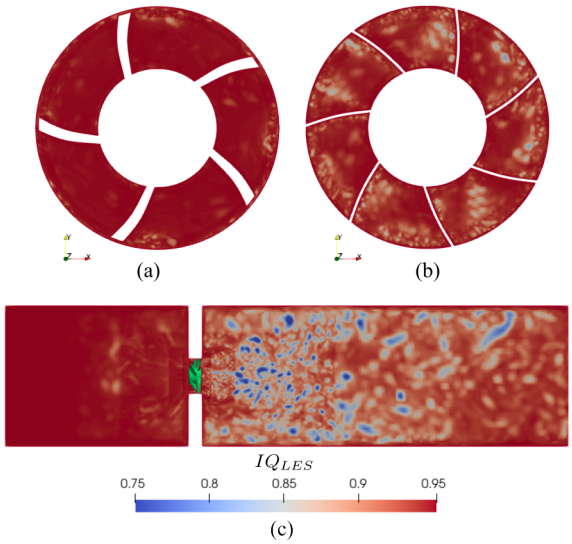

Figure 3.9: LES index of quality for a rotor cut plane (a), a stator cut plane (b), and an axial cut plane (c).

To evaluate numerical accuracy, three mesh sizes were tested: coarse (9.8 million elements), medium (15.1 million elements), and fine (24.5 million elements). The mesh was refined globally by a factor of approximately 1.5. Further refinement was not possible due to computational resource limitations.

Figure 3.10 compares the aerodynamic and acoustic results obtained from the three mesh sizes. Compared to the fine mesh, the coarse mesh underpredicts both the flow rate and OASPL, as shown in Fig. 3.10 (a). Additionally, the coarse mesh significantly underestimates broadband noise levels, particularly at frequencies above 4 kHz, as illustrated in Fig. 3.10 (b). The medium mesh, however, yields results nearly identical to those of the fine mesh, demonstrating its adequacy in accurately capturing both flow quantities and noise levels. The simulations were conducted on a high-performance computing (HPC) cluster with two AMD EPYC 7H12 2.6 GHz processors, totaling 128 cores and 512 GB of memory. The computational time for the coarse, medium, and fine mesh sizes was 16384, 24576, and 38400 core-hours, respectively. The medium mesh was chosen for subsequent aerodynamic and acoustic calculations due to its favorable balance between computational cost and numerical accuracy.

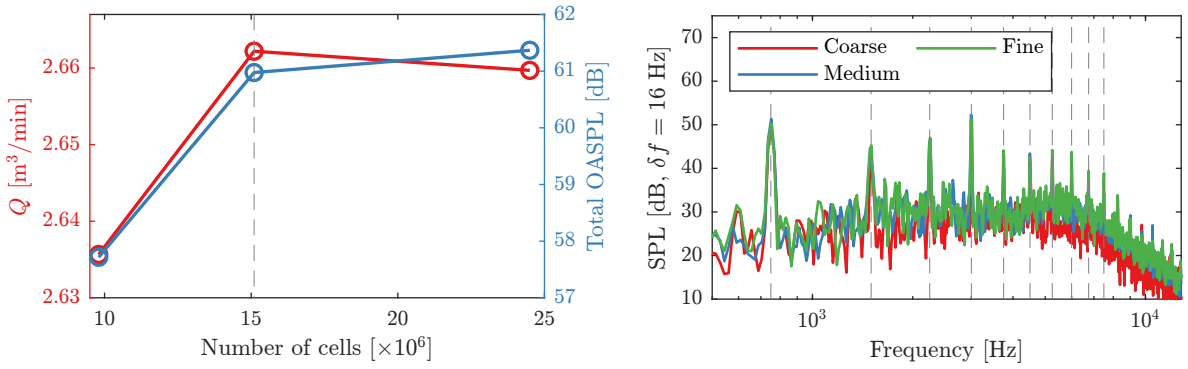

Figure 3.10: Verification of numerical accuracy: (a) Comparison of flow rate Q and OASPL results. (b) SPL spectra comparison. Results are shown for coarse, medium, and fine mesh resolutions. The dashed lines represent the first ten harmonics of the blade passing frequency f_{BPF}. The noise levels are measured at a distance of 1 m from the fan rotor (as shown in Fig. 3.3), and the SPL ($\overline{L_p}$) is calculated using Eq. 37.

3.4 Validation of the numerical model

The numerical model was validated against experimental data obtained from the test facility at TCD, as described in Section 3.2. The validation included assessing the aerodynamic performance and aeroacoustic noise levels of the fan under different backpressure conditions: 0 $\mathrm{mmH_2O}$ (free delivery condition), 6 $\mathrm{mmH_2O}$, 12 $\mathrm{mmH_2O}$ (design point), and 18 $\mathrm{mmH_2O}$ (stall condition). The operating conditions were classified based on the static efficiency curve of the fan (refer to Fig. 3.2). Increasing the backpressure results in a decrease in the fan flow rate and an increase in the angle of attack, as shown in Table 3.2.

The comparison of the fan performance curve is shown in Fig. 3.11. The RANS results exhibit discrepancies with the experimental data, particularly near the stall region. While the RANS model captures the general trend of the fan performance (P-Q) curve, it underpredicts the fan flow rates. Additionally, the RANS model experiences numerical instability at high backpressure cases, leading to simulation divergence at the stall condition. This is expected as the RANS model cannot capture the unsteady flow structures during flow separation at stall conditions. In contrast, the LES results show excellent agreement with the experimental data at all backpressure conditions, indicating its capability to capture the unsteady flow features at stall conditions.

The aeroacoustic results obtained from the LES combined with FW-H method are also in good agreement with the experimental data, as shown in Fig. 3.12. The predicted noise levels under different backpressure conditions are almost identical to the experimental data, with only a few exceptions. Besides the motor noise at the frequency of $8f_r$ discussed in Section 3.2.3, the main difference is observed at low frequencies below 1

Table 3.2: Predicted overall aerodynamic and aeroacoustic results by LES under different backpressure conditions.

Pressure, P [mmH$_2$O]	0	6	12	18
Angle of attack, α [°]	3.22	5.89	8.03	12.30
Flow rate, Q [m^3/min]	2.66	2.43	2.15	1.33
OASPL, [dB]	61.0	60.6	59.5	64.7

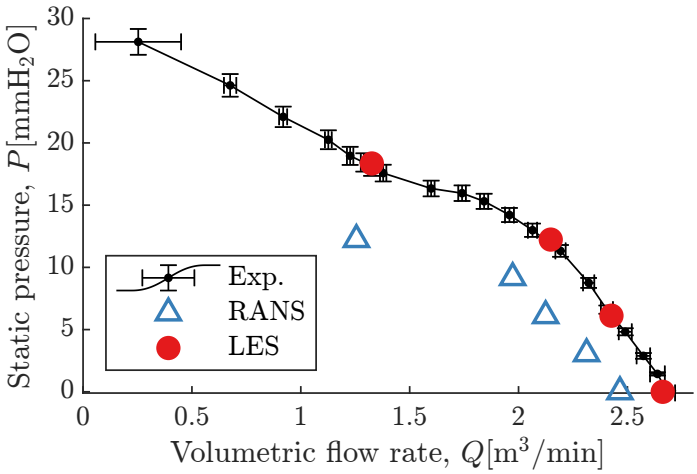

Figure 3.11: Comparison of the fan performance (P-Q) curve under different backpressure conditions with N = 9000 r/min. As the RANS simulations diverged at the stall condition, two extra operating conditions (*i.e.*, 3 mmH$_2$O and 9 mmH$_2$O) are included to show the performance of the RANS model.

kHz, particularly at the first blade passing frequency (f_{BPF}). This difference could be attributed to the unsteady motion of the motor and fan blades, as discussed in Section 3.2.3. The predicted broadband noise level at frequencies above 8 kHz is slightly lower than the experimental data. However, overall, the LES model accurately captures the noise spectrum of the fan under different backpressure conditions.

An interesting observation is that the tonal noise is more noticeable during normal operating conditions compared to the stall condition. This finding has also been reported in [41] for a computer cooling fan. The reasons behind this observation will be further discussed in the aerodynamic analysis (Section 3.5) and aeroacoustic analysis (Section 3.6).

The lowest noise level is observed at the design point of 12 mmH$_2$O, while the noise level at the stall condition of 18 mmH$_2$O is found to be 4.2 dB higher than the design point according to experiments and 5.2 dB higher according to LES simulations.

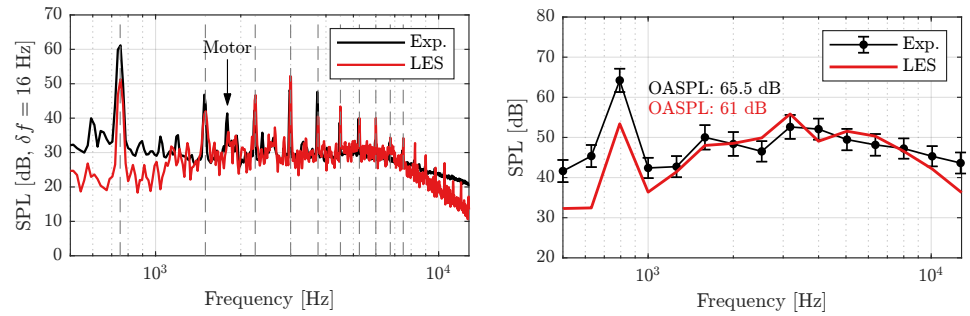

(a) Narrowband SPL, 0 mmH_2O

(b) 1/3 octave band SPL, 0 mmH_2O

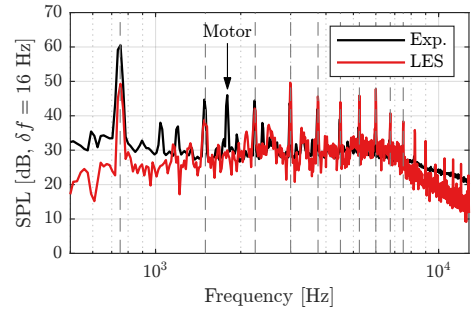

(c) Narrowband SPL, 6 mmH_2O

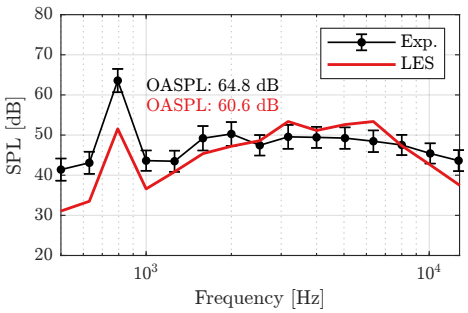

(d) 1/3 octave band SPL, 6 mmH_2O

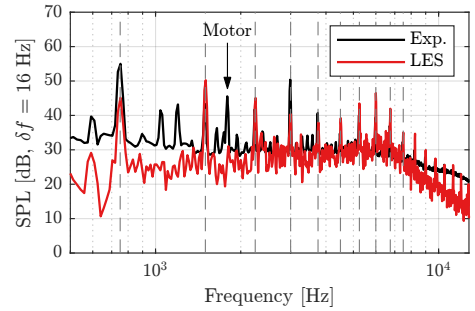

(e) Narrowband SPL, 12 mmH_2O

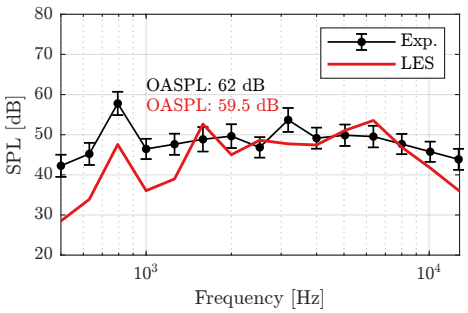

(f) 1/3 octave band SPL, 12 mmH_2O

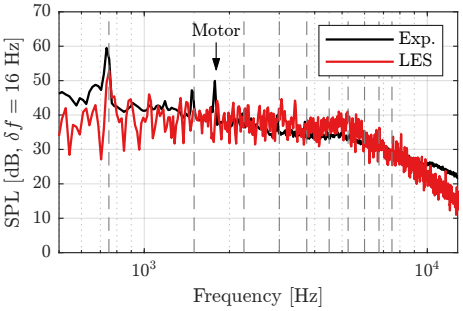

(g) Narrowband SPL, 18 mmH_2O

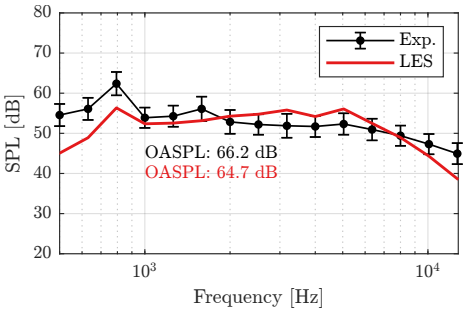

(h) 1/3 octave band SPL, 18 mmH_2O

Figure 3.12: Comparison of fan noise measurements at TCD and LES results under different backpressure conditions with $N = 9000$ r/min. (a) and (b) show the narrowband and 1/3 octave band sound pressure level (SPL) $\overline{L_p}$ at 0 mmH_2O, (c) and (d) show the narrowband and 1/3 octave band SPL at 6 mmH_2O, (e) and (f) show the narrowband and 1/3 octave band SPL at 12 mmH_2O, and (g) and (h) show the narrowband and 1/3 octave band SPL at 18 mmH_2O. The dashed lines represent the blade passing frequency (f_{BPF}) and its harmonics. The noise levels are measured at a distance of 1 m from the fan rotor (as shown in Fig. 3.3), and the SPL ($\overline{L_p}$) is calculated using Eq. 37.

3.5 Aerodynamic analysis

3.5.1 Flow features

Overview of turbulent structures

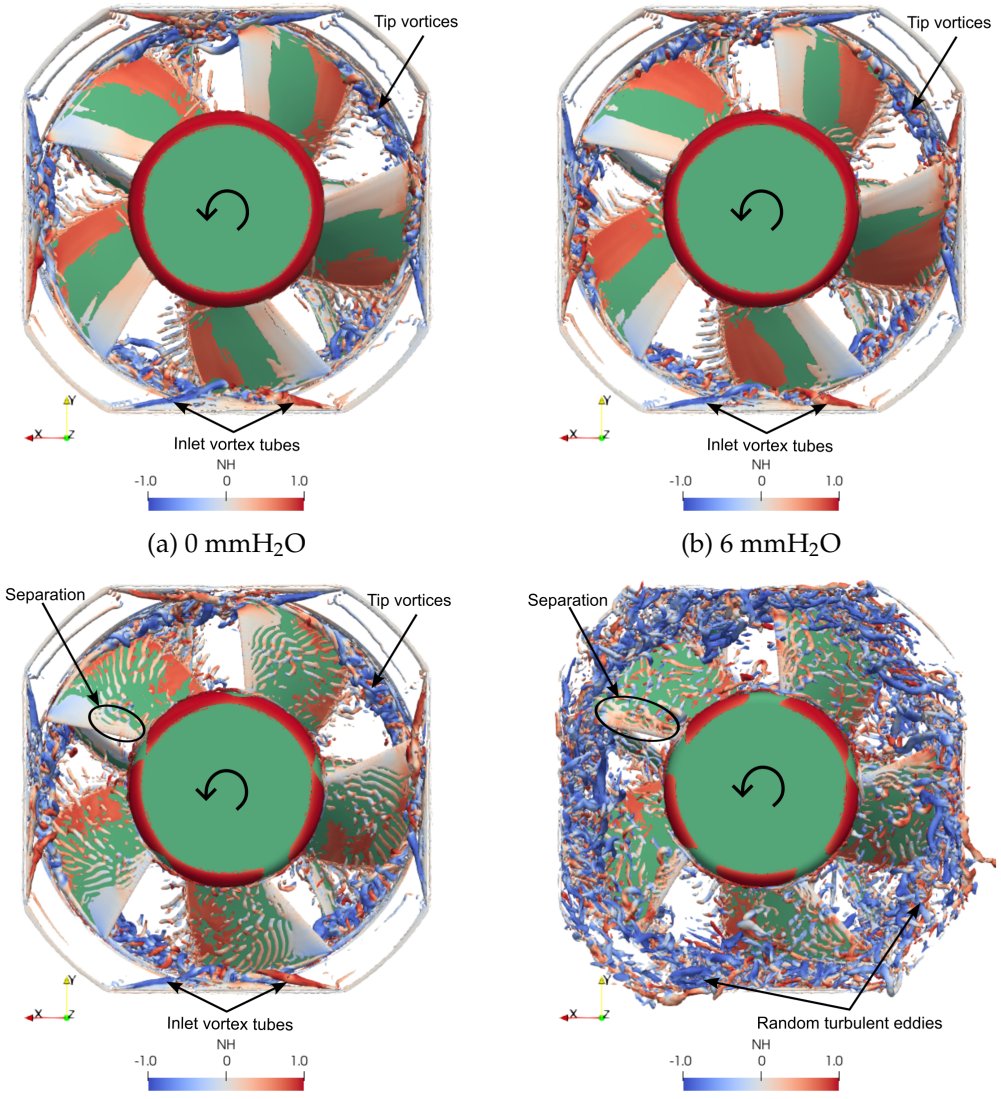

(a) 0 mmH_2O (b) 6 mmH_2O

(c) 12 mmH_2O (d) 18 mmH_2O

Figure 3.13: Instantaneous snapshot of iso-surfaces of the Q-criterion (10^8 s^{-2}) under four different backpressure conditions: 0 mmH_2O (a), 6 mmH_2O (b), 12 mmH_2O (c), and 18 mmH_2O (d). The iso-surfaces are colored based on the normalised helicity (NH). The fan is viewed from the front. An animated sequence is provided as supplementary material, available at Elsevier Storage Repository: Animation 3.13.

The turbulent flow structures of the fan under different backpressure conditions are visualized using the Q-criterion in Fig. 3.13. An animated sequence is provided as supplementary material [2] (Animation 3.13). The iso-surfaces of the Q-criterion at

[2]The animated sequence is available at Elsevier Storage Repository: Animation 3.13.

10^8 s^{-2} represent regions with high vorticity magnitude. These regions are colored based on the normalised helicity (NH), which indicates the swirling direction relative to the flow direction. The NH is calculated as:

$$\mathrm{NH} = \frac{\boldsymbol{\omega} \cdot \mathbf{u}}{|\boldsymbol{\omega}||\mathbf{u}|}, \tag{38}$$

where $\boldsymbol{\omega}$ is the vorticity vector and $\mathbf{u}$ is the velocity vector.

The vortical structures differ when the fan operates under normal conditions (0, 6, 12 mmH_2O) compared to the stall condition (18 mmH_2O). Under normal conditions, the vortex structures are more coherent and concentrated at the asymmetric inlet region and the blade tip region. Two clear inlet vortex tubes (IVTs) appear at each of the sharp inlet edges, indicating a strong circumferentially non-uniform inflow. This discrete vortex structure at the fan inlet has not been previously reported. Additionally, tip vortices can be observed at the blade tip region, which will be further discussed in Section 3.5.1. The flow on the suction side of the rotor blades remains attached to the blade surface at 0 mmH_2O and 6 mmH_2O, while it starts to separate at 12 mmH_2O. A flow separation zone seems to form at the leading edge of the blade from the hub region to around 50% span, which can be attributed to the high angle of attack in this backpressure case. The flow separates at the leading edge and generates stronger vortices compared to the cases of 0 mmH_2O and 6 mmH_2O. The flow separation vortices spiral towards the blade tip region. More discussions on the flow separation and reattachment will be provided in Section 3.5.1.

At the stall condition, the vortex structures become more chaotic and diffused. The previously observed inlet vortex tubes (IVTs) at normal operating conditions are no longer visible. Instead, massive turbulent eddies are generated at the fan inlet and near the blade tip region. This can be attributed to blade stall, which occurs when the flow is partially blocked, especially at the tip region. On the suction side of the blades, the flow separation zone is also clearly visible and appears to span a larger region compared to normal operating conditions.

Inlet vortex structures

The flow topology near the circumferentially asymmetric inlet is visualized using streamlines for one of the fan inlet edges under different backpressure conditions, as shown in Fig. 3.14. Under normal operating conditions, the inlet flow is distorted at the four sharp edges. A pair of inlet vortex tubes (IVTs) is generated at each edge due to the suction of the rotating blades. These vortex tubes have similar magnitudes of tangential velocities but opposite directions. They form at the start and end points of the edge, respectively. The vortex tubes detach from the inlet sharp edge and are

carried downstream by the main flow, periodically interacting with the blade. This interaction between the asymmetric inlet and the rotor (IRI) can cause periodic pressure fluctuations on the blade surface, increasing the tonal noise level. The pressure fluctuations due to the asymmetric inlet influence the circumferential acoustic mode of the radiated noise [74]. The vortex tubes, carried downstream, may also interact with the blade tip vortices, which will be further discussed in Section 3.5.1.

Under stall conditions, the streamlines of the inlet edge flow exhibit more chaotic behavior (see Fig. 3.14 (d)). The flow swirls back around the edge and is carried downstream in a more diffused manner. The absence of coherent inlet vortex tubes reduces the periodic interaction between the edge flow and the blade. As a result, the distorted inflow has a reduced impact on blade pressure fluctuations, leading to a less pronounced tonal noise level at the stall condition compared to normal operating conditions. The unsteady force generated by the distorted flow will be analysed in Section 3.5.3.

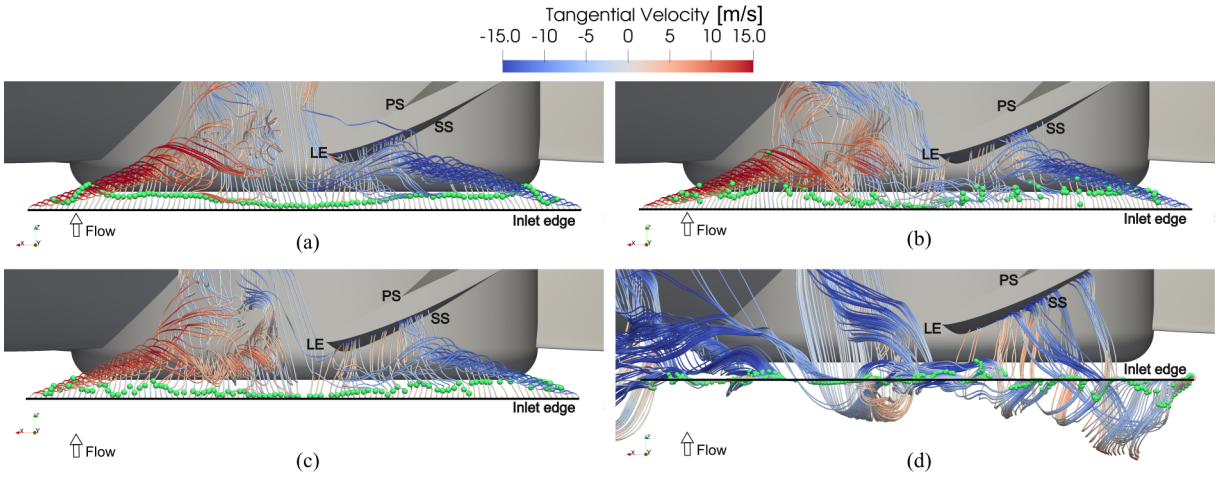

Figure 3.14: Comparison of inlet vortex structures under different backpressure conditions: normal operating conditions of 0 mmH_2O (a), 6 mmH_2O (b), 12 mmH_2O (c), and stall condition of 18 mmH_2O (d). The fan is viewed from the top.

Tip flow topology

The flow structures in the tip-gap region of turbomachinery play a crucial role in determining both aerodynamic performance and noise generation. The presence of a circumferentially asymmetric inlet shape can lead to a more complex flow structure in this region. The tip flow characteristics are visualized using the instantaneous and average Q-criterion at the blade tip region, as shown in Fig. 3.15 (a-b) for the normal operating condition (0 mmH_2O) and Fig. Fig. 3.15 (c-d) for the stall condition (18 mmH_2O).

Under normal operating conditions, conventional coherent flow structures are observed

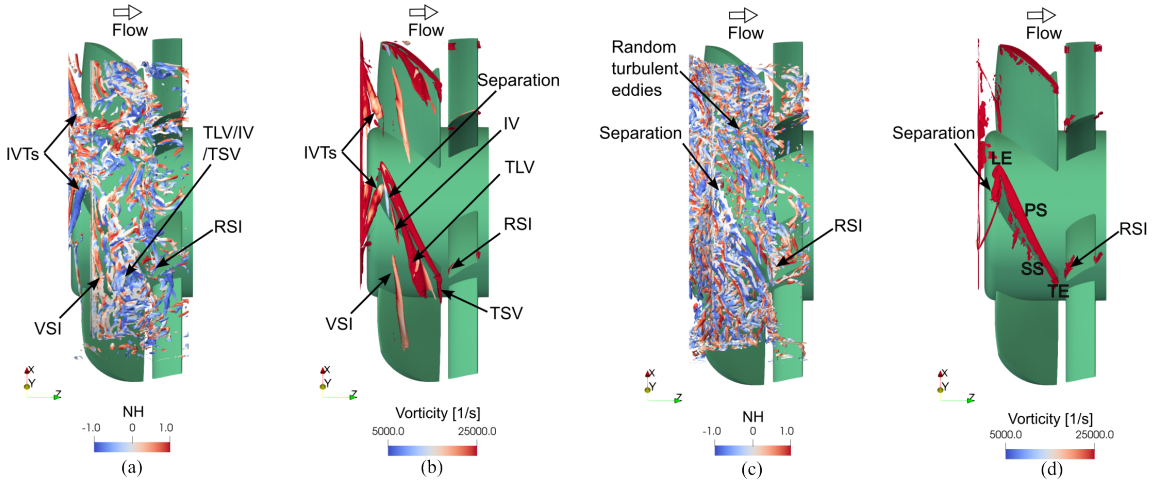

Figure 3.15: Tip flow topology at the blade tip region for the normal operating condition (0 mmH_2O): (a) Instantaneous snapshot of the Q-criterion with 10^8 s^{-2}. (b) Average Q-criterion with 10^8 s^{-2}. And for the stall condition (18 mmH_2O): (c) Instantaneous snapshot of the Q-criterion with 10^8 s^{-2}. (d) Average Q-criterion with 10^8 s^{-2}. The fan is viewed from the top.

in the tip-gap region. The tip-leakage vortex (TLV), which forms from around 30% of the chord c due to the pressure difference between the pressure and suction sides of the blade, is the main contributor to the tip-leakage flow. Adjacent to the TLV, an induced vortex (IV) with the opposite swirling direction is generated. Near the trailing edge, a tip-separation vortex (TSV) forms due to flow separation. These structures, discussed in previous studies [31, 161, 206], are common in typical tip-gap flows. The coherent structures of the tip vortices interact with the leading and trailing edges of the blades, leading to increased broadband noise generation. The tip flow can also interact with the downstream stator blade, resulting in a rotor-stator interaction (RSI), a common occurrence in turbomachinery that primarily leads to tonal and broadband noise generation.

However, unconventional flow structures are also observed near the asymmetric inlet. The inlet vortex tubes (IVTs), previously discussed in Section 3.5.1, are carried downstream and interact with the leading edge of the suction side near the blade tip. This interaction can generate a small leading edge separation vortex near the blade tip, which is then carried to the suction side of the blade tip. In the case of electronics cooling fans, the asymmetric inlet bellmouth also acts as a shroud for a small portion of the blade. This leads to an interaction between the blade tip vortices and the shroud, referred to as "VSI" in this study. The VSI is expected to increase flow unsteadiness and pressure fluctuations on the shroud. It is worth noting that the VSI is a unique flow structure not commonly reported in previous studies on tip-gap flow. These unconventional flow structures in the tip-gap region are expected to have a significant impact on the aerodynamic performance and noise generation. Further discussion on these topics can be found in Section 3.5.2 and Section 3.6.

Under stall conditions, the flow structures in the tip-gap region become less stable, with only a few coherent structures observed, as depicted in Fig. 3.15 (c-d). While the RSI remains, the IVTs, TLV, IV, and TSV become diffused. The primary flow structure is the tip leading edge separation vortex, which forms due to flow separation near the leading edge of the blade tip.

Surface flow separation

Flow separations occur on the suction side of the fan blade under backpressure conditions of 12 mmH_2O and 18 mmH_2O, as discussed in Section 3.5.1. These separations, more prevalent in off-design conditions with higher angles of attack, can negatively impact aerodynamic performance and noise generation. The flow on the blade surface is visualized in Fig. 3.16, which shows the surface streamlines and the distribution of the friction coefficient. The skin friction coefficient (C_f) is defined as:

$$C_f = \frac{\tau_w}{0.5\rho U^2}, \tag{39}$$

where τ_w is the wall shear stress, ρ is the fluid density, and U is the axial flow speed.

The magnitude of the skin friction coefficient ($|C_f|$) indicates flow separation, with values near zero indicating the separation region. While the flow remains attached on the pressure side, several separation regions are observed on the suction side of the blade (see Fig. 3.16). At all backpressure conditions, a small separation zone is seen near the trailing edge of the blade tip on the suction side, caused by the tip-separation vortex (TSV).

An extended separation bubble occurs on the suction side at 12 mmH_2O and 18 mmH_2O, corresponding to high angles of attack of 8.03° and 12.30°, respectively. At 12 mmH_2O, a recirculation zone forms near the blade hub and extends to the mid-span region, covering approximately the first 20% of the chord. In this region, the flow moves towards the blade tip, resulting in a high radial flow component.

Under the stall condition of 18 mmH_2O, the recirculation region expands and almost reaches the blade tip, covering approximately 80% of the span and the first 20% of the chord. Downstream of the separation region, the flow reattaches and remains attached at the trailing edge of the blade. This separation region is caused by the laminar-turbulent transition, resulting in the formation of a laminar separation bubble (LSB) near the leading edge of the suction side. The size of the LSB increases with backpressure, similar to the findings of Al-Am *et al.* [207] in a study on a radial slice of a turbofan configuration, although the Mach number in their study was six times

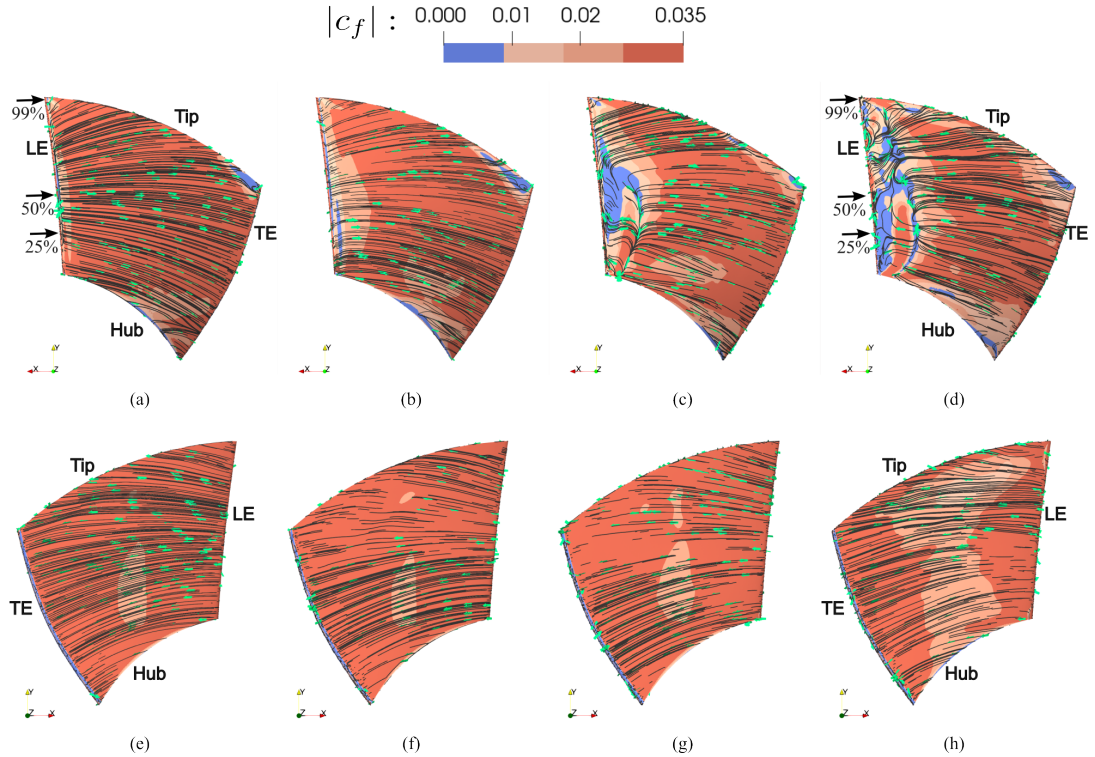

Figure 3.16: Surface streamlines and friction coefficient distribution. The results for the suction side (SS) of blade are shown in (a-d): (a) 0 mmH_2O, (b) 6 mmH_2O, (c) 12 mmH_2O, and (d) 18 mmH_2O. The results for the pressure side (PS) of blade are shown in (e-h): (e) 0 mmH_2O, (f) 6 mmH_2O, (g) 12 mmH_2O, and (h) 18 mmH_2O.

higher than in the present case.

To investigate flow separation, Fig. 3.17 visualizes the flow vectors near the boundary layer at the 25% span slice of the rotor and first 20% of the chord. The visualization is done for the normal operating condition of 0 mmH_2O and the stall condition of 18 mmH_2O. The airfoils are normalised by the chord length, and the boundary layer vectors are calculated using the mean velocity field on the blade surface.

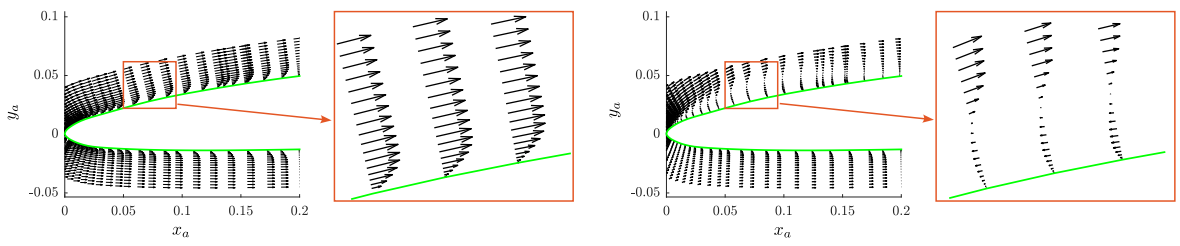

(a) 0 mmH_2O (b) 18 mmH_2O

Figure 3.17: Boundary layer flow vectors at the rotor blade surface of 25% span for a favorable pressure gradient (FPG) at 0 mmH_2O (a) and a large adverse pressure gradient (APG) at 18 mmH_2O (b). x_a and y_a are the local airfoil coordinates. The airfoil is normalised by the chord length c.

For the normal operating condition, the flow remains laminar with a favorable pressure gradient (FPG). However, under stall conditions, the flow experiences separation at the leading edge, resulting in the formation of a laminar separation bubble (LSB) due to the adverse pressure gradient on the suction side of the blade. Within the separation bubble region, the flow recirculates before reattaching downstream. This flow separation phenomenon is consistent with observations made for a controlled diffusion airfoil at an angle of attack of 8° and a Reynolds number of approximately 1.5×10^5 [44, 197]. The presence of the separation bubble can lead to the generation of a high-frequency tone, depending on the flow conditions, such as the Reynolds number and angle of attack [44]. Additionally, the pressure fluctuations resulting from the separation and reattachment can convect downstream and contribute to the generation of broadband noise at the trailing edge [197].

Trailing edge noise generation is closely associated with boundary layer characteristics [53]. The boundary layer shape factor (H) is a key parameter that describes the flow behavior within the boundary layer and is defined as the ratio of the displacement thickness (δ^*) to the momentum thickness (δ_θ) [97]:

$$H = \frac{\delta^*}{\delta_\theta}. \tag{40}$$

The boundary layer shape factor provides insights into the thickness of the boundary layer and the velocity profile. A higher value of the boundary layer shape factor indicates a thicker boundary layer and a more gradual velocity profile. In this study, the boundary layer shape factor is evaluated at 50% span and 99% span on the suction side of the blade under two operating conditions: 0 mmH_2O and 18 mmH_2O, as depicted in Fig. 3.18.

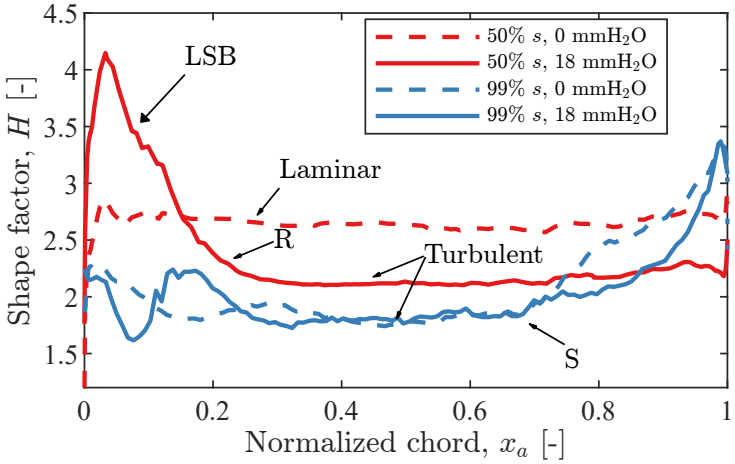

Figure 3.18: Boundary layer shape factor for the suction side of the blade at 50% span and 99% span under 0 mmH_2O and 18 mmH_2O. LSB: laminar separation bubble. S: separation. R: reattachment.

For the free delivery condition (0 mmH_2O), a nearly constant boundary layer shape factor is observed at the 50% span location, indicating the presence of a laminar boundary layer. However, at 99% span, turbulent separation occurs near the trailing edge at approximately 75% of the chord, leading to an increased boundary layer shape factor. This separation phenomenon is attributed to the tip-separation vortex (TSV), as illustrated in Fig. 3.16 (a).

Under stall conditions (18 mmH_2O), a laminar separation bubble (LSB) forms near the leading edge of the blade, resulting in a higher boundary layer shape factor at 50% span. The flow reattaches after 20% of the chord, causing a decrease in the boundary layer shape factor. At 99% span, the boundary layer shape factor exhibits a fluctuating pattern within the first 20% of the chord, strongly influenced by the presence of tip flow separation (see Fig. 3.15). Similar to the free delivery condition, flow separation occurs near the trailing edge at approximately 75% of the chord, leading to an elevated boundary layer shape factor. These distinct boundary layer behaviors are closely linked to variations in wall pressure fluctuations and noise sources, which will be further discussed in Section 3.6.3.

3.5.2 Flow field analysis and statistics

This section aims to provide a comprehensive analysis of the flow field and its statistical characteristics. Understanding the flow behavior and the mechanisms behind noise generation requires a thorough examination of these aspects.

Instantaneous flow field

Figure 3.19 illustrates the vorticity magnitude at the blade tip region, while Fig. 3.20 displays the same for the blade mid-span region. Supplementary material in the form of animated sequences [3] [4] is provided for both figures. The blade tip region is located at 99% span, and the blade mid-span region is at 50% span.

Under normal operating conditions of 0, 6, and 12 mmH_2O, Fig. 3.19 (a), (b), and (c) show the presence of four periodic inlet vortex structures. These structures generate high vorticity magnitudes, leading to the formation and advection of the tip-leakage vortex (TLV) downstream. The TLV interacts with the stator, resulting in another region of high vorticity magnitude near the rotor trailing edge and stator leading edge. The snapshots also reveal the interaction between the inlet vortex structures and the leading edge region of the rotor tip (region “1" in Fig. 3.19 (a), (b), and (c)). The presence of the inlet vortex structures appears to accelerate the shedding of tip leakage vortices,

[3] The animated sequence is available at Elsevier Storage Repository: Animation 3.19.
[4] The animated sequence is available at Elsevier Storage Repository: Animation 3.20.

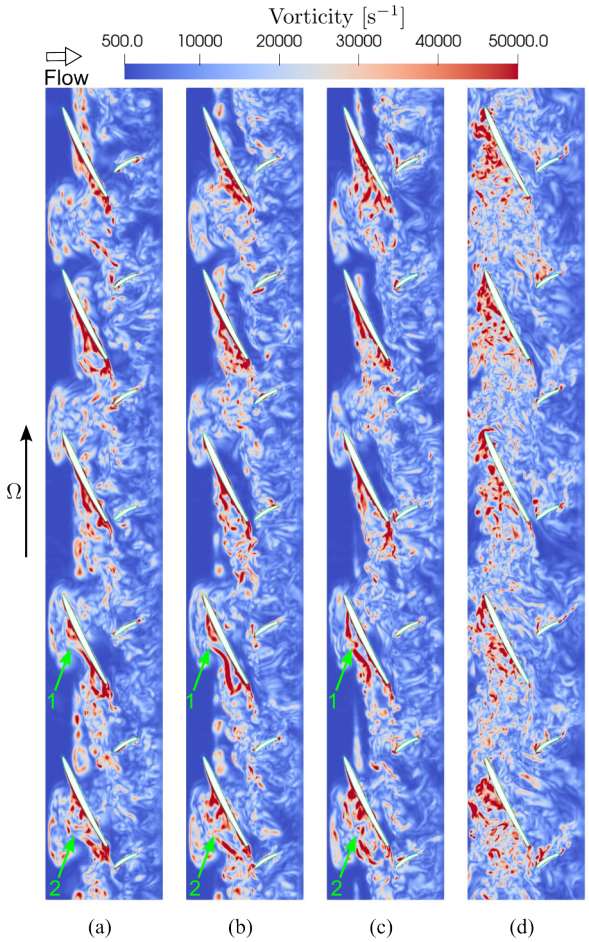

Figure 3.19: Instantaneous blade-to-blade snapshots of the vorticity magnitude at the blade tip region (99% span) under different backpressure conditions: 0 mmH_2O (a), 6 mmH_2O (b), 12 mmH_2O (c), and 18 mmH_2O (d). An animated sequence is provided as supplementary material, available at Elsevier Storage Repository: Animation 3.19.

resulting in the formation of a small vortex at around 20% of the chord and a larger, curved tip-leakage vortex at 50% of the chord. The small vortex at around 20% of the chord corresponds to the small leading edge separation vortex observed in the tip flow topology using the Q-criterion (shown in Fig. 3.15).

When the inlet vortex structures interact with the second half of the blade tip region (region "2" in Fig. 3.19 (a), (b), and (c)), the tip-leakage vortex (TLV) breaks into smaller vortices. This breakdown, induced by the inlet vortex structures, increases flow unsteadiness and is expected to increase pressure fluctuations on the suction side. Thus, the interaction between the inlet vortex structures and the blade tip region can lead to increased broadband noise generation. Previous studies [36, 74] primarily focused on the periodic disturbances on the blade surface caused by distorted inflow, which has also been observed in this study. However, this study also investigates the formation and breakdown of the TLV due to interactions with the inlet vortex structures, suggesting a potential increase in broadband noise generation from flow

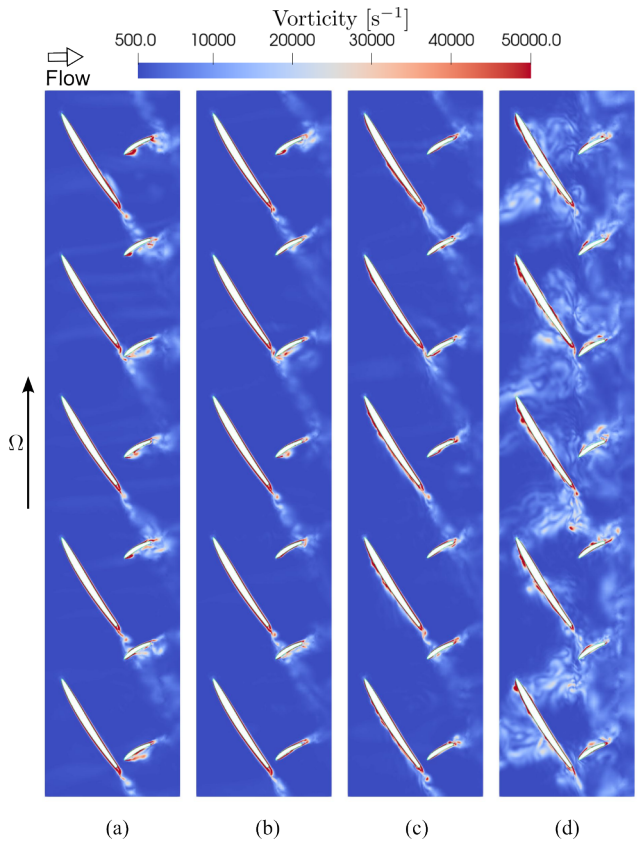

Figure 3.20: Instantaneous blade-to-blade snapshots of the vorticity magnitude at the blade mid-span region (50% span) under different backpressure conditions: 0 mmH_2O (a), 6 mmH_2O (b), 12 mmH_2O (c), and 18 mmH_2O (d). An animated sequence is provided as supplementary material, available at Elsevier Storage Repository: Animation 3.20.

unsteadiness.

Under the stall condition of 18 mmH_2O (Fig. 3.19 (d)), the vorticity field appears diffused and the coherent structures caused by the inlet vortex structures are no longer visible. Numerous small eddies are distributed over the suction side of the blade tip region, resulting from the blade stall and flow passage blockage. Flow separation at the leading edge of the blade tip region is more pronounced, leading to higher vorticity magnitude. The increased vortices can also be observed in Fig. 3.13 (d).

At the blade mid-span slice (Fig. 3.20), the overall vorticity magnitude is lower compared to the blade tip region. The highest vorticity magnitude is found at the rotor wake-stator interaction (RSI) region, which can contribute to tonal noise generation. For the design point of 12 mmH_2O, the downstream stator blade experiences a more optimal incidence angle, resulting in slightly reduced vorticity magnitude on the pressure side of the stator (Fig. 3.20 (c)). This reduction weakens the RSI and can lead to a decrease in tonal noise generation. For the stall condition of 18 mmH_2O, the vorticity magnitude is higher and the flow structures are more chaotic (Fig. 3.20 (d)). Flow separation at the rotor blade leading edge can also be observed at the blade mid-span

region for both the operating conditions of 12 mmH_2O and 18 mmH_2O. Similar to the results in Fig. 3.16 and Fig. 3.18, laminar flow occurs on the rotor pressure side, while a thick, unstable turbulent boundary layer develops on the rotor suction side. The laminar separation bubble generates vortices that shed downstream and eventually feed the wake region.

Mean flow quantities

Figure 3.21 illustrates the turbulent kinetic energy at the rotor leading edge slice and the rotor trailing edge slice, indicating flow unsteadiness. Under normal operating conditions of 0, 6, and 12 mmH_2O, the turbulent kinetic energy slightly increases with backpressure. The energy is higher at the rotor trailing edge slice than at the leading edge slice due to the presence of tip-leakage flow and the wake.

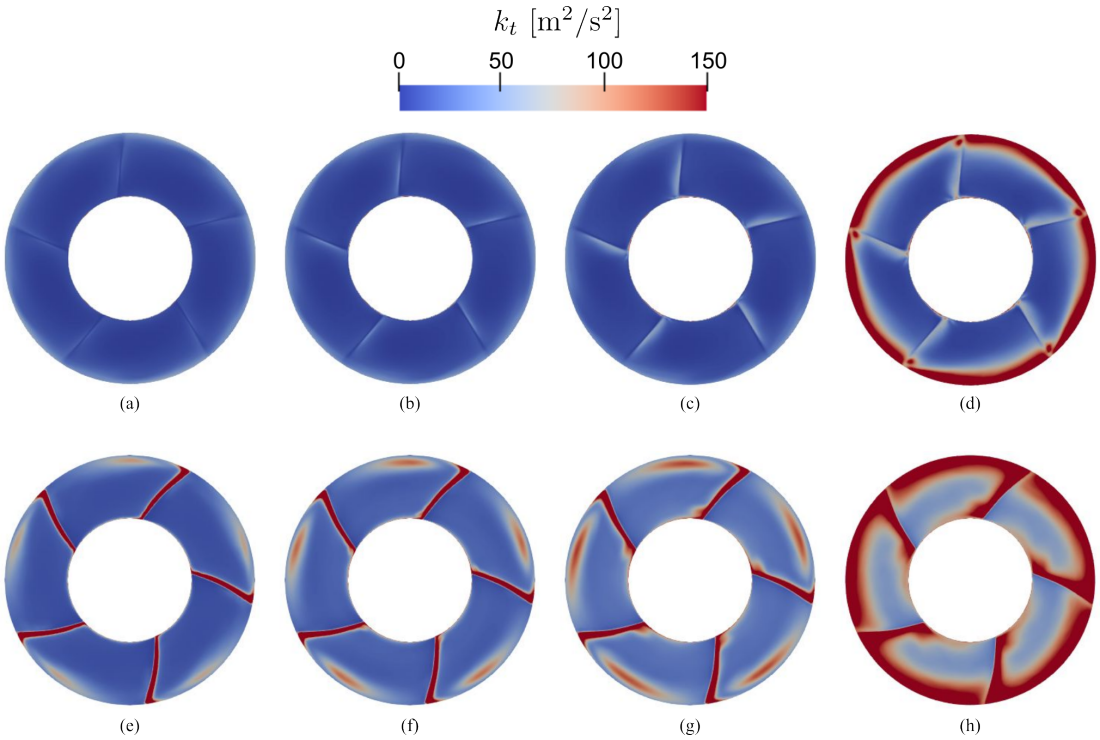

Figure 3.21: Turbulent kinetic energy at the rotor leading edge (LE) slice (a-d) and the rotor trailing edge (TE) slice (e-h) under four different backpressure conditions: 0 mmH_2O (a) and (e), 6 mmH_2O (b) and (f), 12 mmH_2O (c) and (g), and 18 mmH_2O (d) and (h).

At the stall condition of 18 mmH_2O, the turbulent kinetic energy significantly exceeds that of normal operating conditions. This increase is attributed to chaotic flow structures formed in front of the blade tip region and flow separation on the rotor surface. High turbulent kinetic energy is observed from approximately 75% of the rotor span to the blade tip region. Consequently, when the blades are stalled, the turbulent intensity at both the rotor and stator leading edges is expected to increase, leading to increased leading edge noise generation.

The root-mean-square (RMS) of the pressure, which indicates fluctuating pressure related to noise generation, is shown for the blade mid-span region (50% span), the blade tip region (99% span), and the near shroud region (104% span) in Fig. 3.22. Only two rotor blade passages are displayed for clarity, but the results are consistent across all passages.

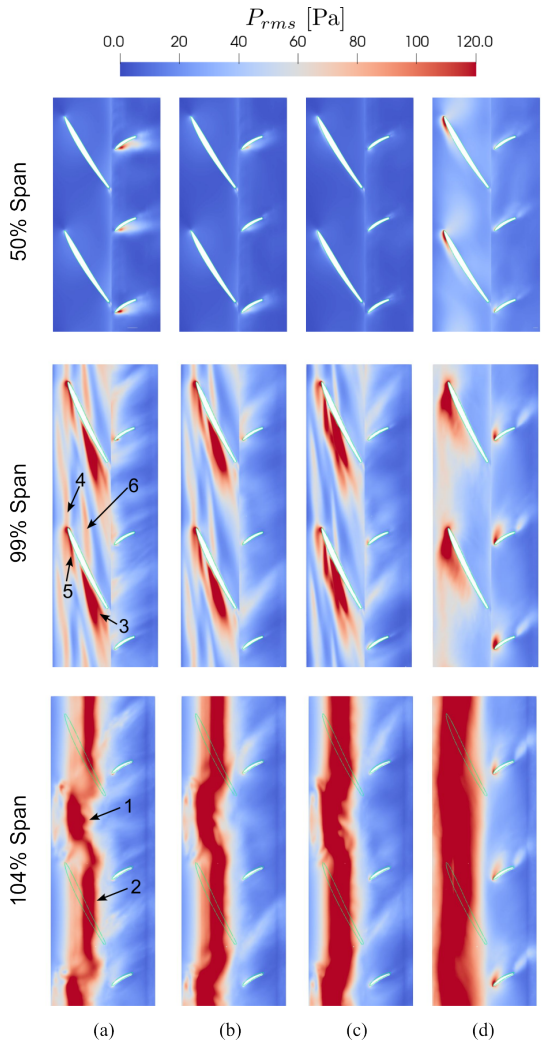

Figure 3.22: Root-mean-square (RMS) of the pressure fluctuation at the blade mid-span region (50% span), the blade tip region (99% span), and the near shroud region (104% span) under four different backpressure conditions: 0 mmH_2O (a), 6 mmH_2O (b), 12 mmH_2O (c), and 18 mmH_2O (d).

The RMS pressure is higher at the near shroud region (104% span) compared to the blade mid-span (50% span) and tip regions (99% span), and it increases with backpressure. Under normal operating conditions of 0, 6, and 12 mmH_2O, the pressure fluctuation near the shroud is primarily caused by the inlet vortex tubes (IVTs, location “1" in Fig. 3.22) and the interaction between the blade tip vortex and the shroud (VSI, location “2" in Fig. 3.22). At the stall condition (Fig. 3.22 (d)), non-coherent vortices generated by the blade stall result in high pressure fluctuation near the shroud.

At the tip region (99% span) under normal operating conditions, the pressure fluctuation is mainly caused by the tip-leakage vortex (TLV), induced vortex (IV), and tip-separation vortex (TSV) (location “3" in Fig. 3.22). The inlet vortex tubes (IVTs) and the separation vortex generated by IVTs-rotor interaction also contribute to the pressure fluctuation at the blade leading edge (locations “4" and “5" in Fig. 3.22). The fluctuation at location “6" is attributed to the vortex-shroud interaction (VSI). At the stall condition of 18 mmH_2O, the pressure fluctuation near the rotor blade tip is primarily caused by the separation of the rotor leading edge due to blade stall.

For the blade mid-span region (50% span), the pressure fluctuation under normal operating conditions of 0, 6, and 12 mmH_2O is mainly due to the rotor-stator interaction (RSI). At the stall condition of 18 mmH_2O, the pressure fluctuation is primarily caused by the separation of the leading edge. The pressure fluctuation at the blade mid-span region is lower compared to the blade tip and near shroud regions, suggesting that the mid-span region contributes less to the generated noise.

3.5.3 Force analysis

Periodic interactions, such as the asymmetric interaction between the inlet and rotor blades and the interaction between the rotor and stator, can generate tonal noise. Analysing the forces is essential for understanding these interaction features. The force components are calculated for one rotor blade and one stator blade under different backpressure conditions. For brevity, only the results of thrust for the normal operating condition of 0 mmH_2O and the stall condition of 18 mmH_2O are presented here, as shown in Fig. 3.23. The torque results have similar frequency components as the thrust but with different magnitudes and are not shown here.

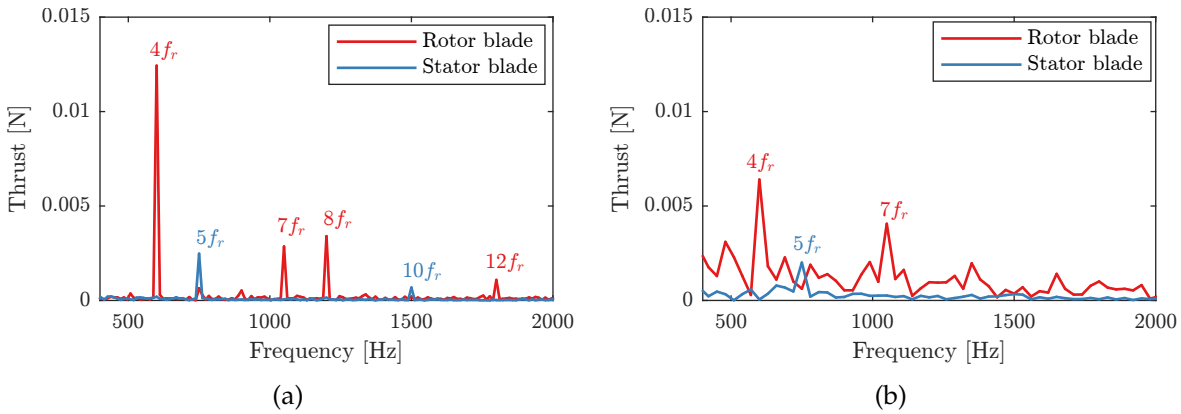

Figure 3.23: Fast Fourier transform (FFT) of the thrust on one rotor and stator blade of the fan under different backpressure conditions: 0 mmH_2O (a) and 18 mmH_2O (b).

The thrust spectra exhibit discrete peaks associated with different interaction mechanisms. These peaks correspond to the rotor blade passing frequency ($f_{\mathrm{BPF}} = 5f_r$), stator

blade passing frequency ($f_{\mathrm{VPF}} = 7f_r$), asymmetric inlet passing frequency ($f_{\mathrm{IPF}} = 4f_r$), and their harmonics. The numbers 5, 7, and 4 are determined by the number of rotor blades B, stator blades S, and inlet sharp edges S_I, respectively.

Under normal operating conditions, the highest magnitudes in the thrust spectra occur at f_{IPF} and its first three harmonics, which result from the interaction between the four inlet sharp edges and the blades. The rotor-stator interaction is also observed on the rotor and stator blades. Due to the potential effect from the stator, the thrust on the rotor blades has frequency components at f_{VPF}, while the thrust on the stator blades has frequency components at f_{BPF} and its first two harmonics. At the stall condition, some frequency components are still present, but their magnitudes are lower due to reduced periodic interactions and increased turbulent flow structures.

The thrust analysis provides valuable insights into the dominant interaction mechanisms. According to Tyler and Sofrin [131], the acoustic mode generated by interaction noise can be described by a Bessel function, given by $\xi = mB - kS$. Here, ξ represents the mode order, with m and k being integers, B representing the number of rotor blades, and S denoting the number of stator blades or inlet sharp edges. The mode order ξ, closely related to the order of Bessel functions, determines the radiated intensity of the interaction noise [36]. As the mode order ξ approaches infinity, the Bessel function rapidly diminishes, indicating that dominant interaction noise occurs when ξ is small.

Although a zero mode order is not present in the current case, a small value of ξ, such as one, can still be expected. For instance, in the case of the first blade passing frequency (BPF), the four periodic disturbances generated by the inlet vortex tubes (IVTs) are in phase, resulting in a low mode order ($\xi = mB - kS_I = 1 \times 5 - 1 \times 4 = 1$) and strong tonal noise emission on the rotor blades. Similarly, for the fourth harmonic, the interaction between the five rotor blade wakes and the seven stator blades leads to a mode order of $\xi = mB - kS = 4 \times 5 - 3 \times 7 = 1$, resulting in another significant tonal noise emission.

The radiated intensity of the interaction noise is affected by the magnitude of the force components. Therefore, the reduced magnitude of the thrust at the stall condition is expected to decrease tonal noise emission. This will be further discussed in Section 3.6.1.

3.6 Aeroacoustic analysis

3.6.1 Overview of far-field noise

The radiated far-field noise is calculated using the FW-H equation [104] at a circular far-field microphone array located 1 m from the fan, representing the experimental test conditions (see Fig. 3.3). Figure 3.24 (a) shows the directivity of the overall sound pressure level (SPL) in the far-field noise under different backpressure conditions. All backpressure conditions exhibit a dipole-like directivity in the far-field noise. The highest SPL is observed at microphone locations perpendicular to the fan axis, while the lowest SPL is found parallel to the fan axis. Downstream of the fan, the SPL is slightly higher than upstream. The far-field noise level is higher at the stall condition (18 mmH_2O) compared to the normal operating conditions (0, 6, 12 mmH_2O). Among the normal operating conditions, the design point of 12 mmH_2O has the lowest far-field noise level. This trend is consistent with the experimental results shown in Fig. 3.12. The lower noise level at the design point of 12 mmH_2O is attributed to the more optimal incidence angle of the stator blade, which reduces the rotor-stator interaction (RSI) and the associated noise generation, as discussed in Section 3.5.2.

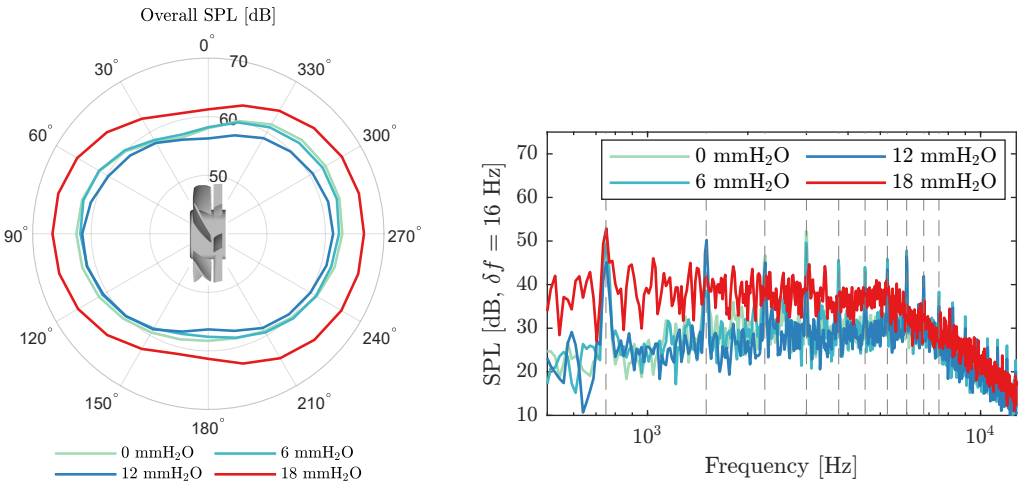

(a) (b)

Figure 3.24: Comparison of far-field noise under different backpressure conditions with N = 9000 r/min: (a) directivity of overall SPL and (b) spectrum of SPL. The dashed lines indicate the blade passing frequency (f_{BPF}) and its harmonics. The noise levels are measured at a distance of 1 m from the fan rotor (as shown in Fig. 3.3), and the SPL ($\overline{L_p}$) is calculated using Eq. 37.

Figure 3.24 (b) compares the spectrum of the far-field noise SPL under different backpressure conditions. Tonal noise is more pronounced at normal operating conditions, while broadband noise is more evident at the stall condition. This observation aligns with previous studies on computer cooling fans [41]. In both cases, the dominant tones occur at the blade passing frequency (f_{BPF}) and its harmonics, as indicated by the dashed lines. Tonal noise is expected to be more pronounced at normal operating

conditions due to the presence of more flow interaction mechanisms, such as the dominant asymmetric inlet-rotor interaction (IRI), rotor-stator interaction (RSI), and blade tip vortex-shroud interaction (VSI). These interaction mechanisms are less pronounced at the stall condition, resulting in less tonal noise.

3.6.2 Contribution of fan components

To facilitate a comprehensive comparison of noise contributions from different fan components, the far-field noise is decomposed into individual contributions from the rotor, stator, and shroud. The noise contribution of each component is computed at the far-field microphone array. Clear similarities have been observed among the three backpressure conditions of 0, 6, and 12 mmH_2O in the normal operating conditions. For clarity, only the results for 0 mmH_2O and 18 mmH_2O are used to represent the normal operating conditions and the stall condition, respectively.

Figure 3.25 compares the noise contributions from the rotor, stator, and shroud at 0 mmH_2O and 18 mmH_2O, alongside the experimental results. The analysis shows that the rotor is the main source of far-field noise, while the stator has a minor contribution. Future work should prioritise the rotor to create a low-cost prediction model (as detailed in Part II) and explore noise reduction strategies (as outlined in Part III).

The shroud and stator noise are more pronounced at microphone locations perpendicular to the fan axis, underscoring their directional nature. This indicates that these noise sources significantly impact the overall far-field noise, particularly at specific microphone locations. Notably, the shroud noise, resulting from the vortex-shroud interaction (VSI), is substantial. The OASPL results in Fig. 3.25 have also been normalised based on the surface area ratio of each component relative to the entire fan to evaluate their relative efficiency in noise generation (not shown here for brevity). The surface area ratios for the rotor, stator, and shroud are 0.3846, 0.2415, and 0.3740, respectively. The normalised OASPL results exhibit a similar trend as Fig. 3.25, with the rotor being the dominant noise source, followed by the shroud and stator. The significant shroud noise in this case is attributed to the strong interaction between the blade tip vortex and the imperfectly designed shroud. This interaction mechanism has been previously discussed in Section 3.5. In a well-designed symmetric shroud, the noise contribution from the shroud would likely be reduced.

Figure 3.26 compares the mean time-averaged sound pressure level (SPL) for different fan components at 0 mmH_2O and 18 mmH_2O. In both normal and stall conditions, the rotor is the primary contributor to both broadband and tonal noise. The stator and shroud also contribute to tonal noise, particularly at the blade passing frequency (f_{BPF}) and its harmonics. While the stator's contribution is relatively minor, the shroud noise

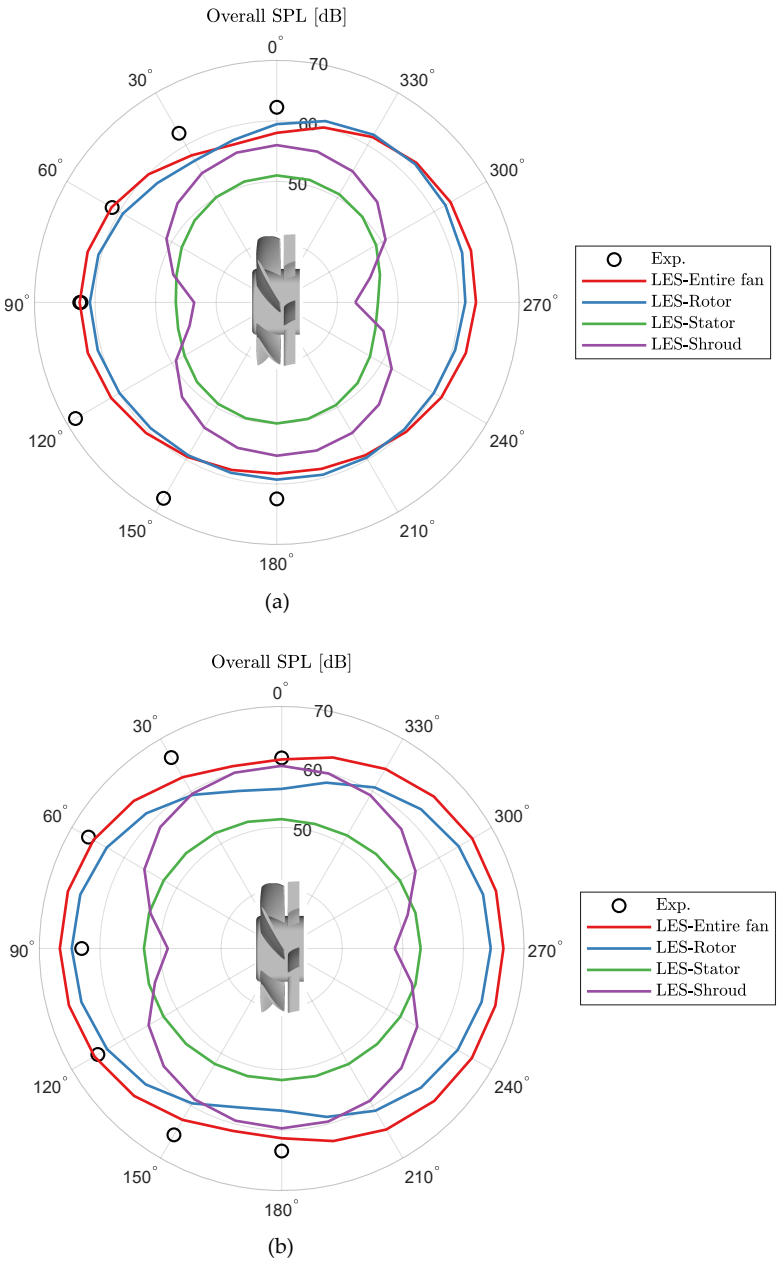

Figure 3.25: Comparison of the overall sound pressure level (OASPL) under two backpressure conditions: 0 mmH_2O (a) and 18 mmH_2O (b).

is more pronounced at the first few harmonics of the blade passing frequency in normal operating conditions. At the stall condition, the shroud noise becomes the dominant noise source at the first blade passing frequency (f_{BPF}). This analysis highlights the directional and tonal nature of the shroud noise, which is important to consider in overall noise prediction.

The incomplete shroud design significantly contributes to noise. However, addressing this issue without a complete redesign is difficult, as the shroud is crucial for the fan's structural assembly. This limitation highlights the need for alternative noise reduction methods that avoid major modifications or compromising the fan's mechanical

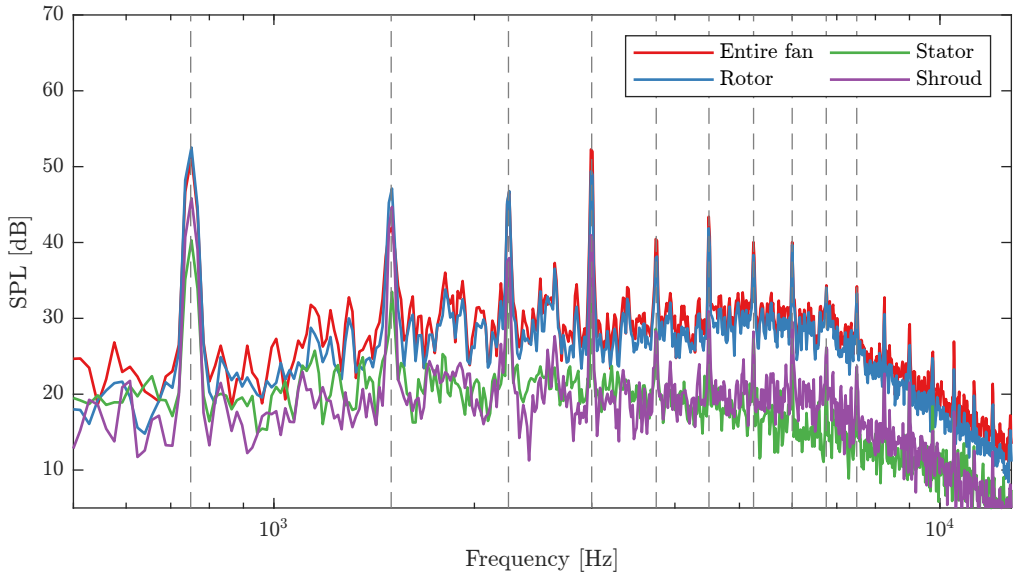

(a)

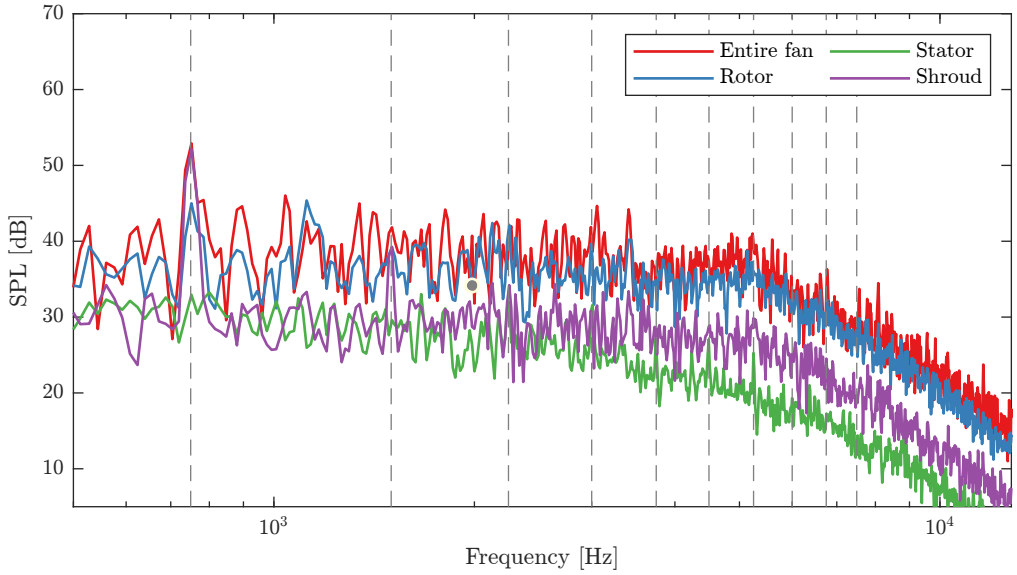

(b)

Figure 3.26: Average sound pressure level (SPL) comparison under two backpressure conditions: 0 mmH_2O and (a) 18 mmH_2O (b). The dashed lines indicate the blade passing frequency (f_{BPF}) and its harmonics. The noise levels are measured at a distance of 1 m from the fan rotor (as shown in Fig. 3.3), and the SPL ($\overline{L_p}$) is calculated using Eq. 37.

integrity.

To address this challenge, two noise reduction strategies will be introduced in Part III. The first involves integrating compact acoustic liners as a passive noise control solution. These liners are designed to target specific frequency ranges, providing a flexible and effective approach to noise reduction. The second focuses on optimising the rotor blade tip design to weaken the tip vortex. Both strategies aim to reduce noise significantly while maintaining the fan's aerodynamic performance and structural integrity, offering practical solutions to the limitations of the shroud design.

3.6.3 Analysis of wall pressure fluctuations

Identifying noise sources is crucial for understanding the mechanisms behind far-field noise generation. Analysing wall pressure fluctuations (WPFs) provides valuable insights into these noise sources and their characteristics, which are directly utilised in the FW-H equation for noise prediction. While surface WPFs alone may not directly indicate the strength of noise sources in the far-field due to varying noise radiation efficiencies of different mechanisms, they offer a practical approach to pinpoint potential noise sources. In this study, the root-mean-square (RMS) value of the wall surface pressure is used to visualize the WPFs across the entire fan, as shown in Fig. 3.27. The results for 0 mmH_2O and 18 mmH_2O are presented.

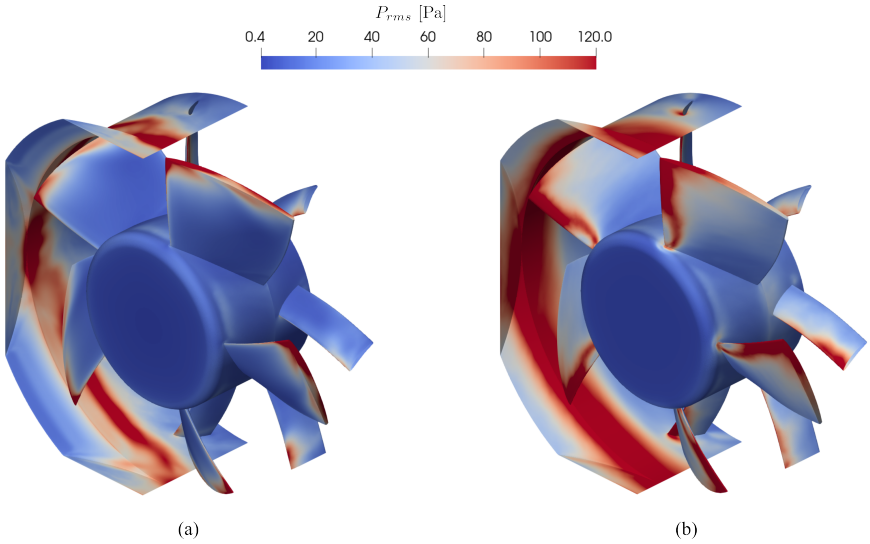

Figure 3.27: Root-mean-square (RMS) value of the wall surface pressure at the fan under two different backpressure conditions, *i.e.*, 0 mmH_2O (a) and 18 mmH_2O (b). The RMS pressure magnitude highlights regions with significant pressure fluctuations on the fan surface, indicating potential noise sources. However, it is important to note that these values do not directly represent the strength of noise radiation in the far-field.

Regarding the fan noise sources at 0 mmH_2O, significant RMS pressure levels are observed at locations where vortices are generated and interact with the blade tip and shroud, as illustrated in Fig. 3.15. Specifically, high RMS pressure regions are predominantly located at 75% span to the tip, aligning with the asymmetric inlet-rotor interaction, tip-leakage vortex (TLV), and the tip-separation vortex (TSV) regions. The influence of the blade tip vortex-shroud interaction (VSI) on the RMS pressure levels is also observed in the near shroud region, consistent with the findings presented in Fig. 3.22. Additionally, a localized high RMS pressure level is observed on the suction side of the stator blade, attributed to the rotor-stator interaction (RSI).

At the stall condition of 18 mmH_2O, the high RMS pressure levels generated by VSI and RSI persist. However, the influence of TLV/TSV becomes less pronounced. Instead,

the high RMS pressure levels are more distributed on the first 20% of the chord on the suction side of the blade. This distribution results from flow separation and high turbulence at the leading edge, as discussed in Section 3.5.1. This analysis indicates that the noise sources at the stall condition primarily arise from flow separation and high turbulence at the leading edge of the blade.

The rotor is identified as the main contributor to far-field noise, as discussed in Section 3.6.2. To analyse the spectral characteristics of wall pressure fluctuation, the wall pressure spectrum (WPS) on the rotor blade surface is calculated and divided into three frequency bands: low frequency (LF) from 500 to 1600 Hz, medium frequency (MF) from 1600 to 5000 Hz, and high frequency (HF) from 5000 to 12800 Hz. Figure 3.28 shows the RMS value of wall pressure fluctuation in these frequency bands at 0 mmH_2O and 18 mmH_2O.

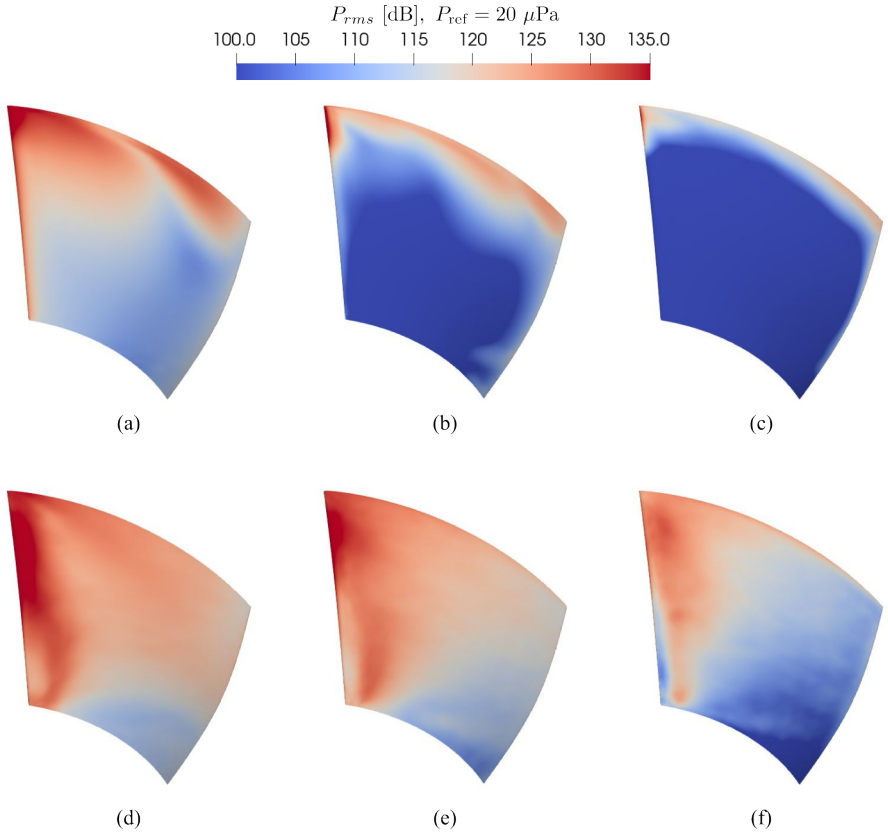

Figure 3.28: Root-mean-square (RMS) value of the wall surface pressure in different frequency bands under two backpressure conditions: (a-c) for 0 mmH_2O — low frequency (LF), medium frequency (MF), and high frequency (HF); (d-f) for 18 mmH_2O — LF, MF, and HF. LF: 500 – 1600 Hz, MF: 1600 – 5000 Hz, HF: 5000 – 12800 Hz. The RMS pressure magnitude in dB highlights regions with significant pressure fluctuations on the blade surface across different frequency bands, indicating potential noise sources. However, it is important to note that these values do not directly represent the strength of noise radiation in the far-field.

Under normal operating conditions, the region near the blade tip exhibits the highest WPS across all frequency bands, resulting from the tip-leakage flow and the asymmetric

inlet-rotor interaction. Additionally, there is an increase in WPS around the leading edge in the LF band, indicating the presence of leading-edge noise caused by turbulence ingestion. For the MF and HF bands, the WPS near the leading edge is less pronounced, while the WPS near the trailing edge is more prominent. This is expected as the leading-edge noise is more dominant in lower frequencies and the trailing-edge noise is more dominant in higher frequencies.

Under the stall condition, the distribution of WPS becomes more widespread on the blade surface, particularly near the leading edge of the suction side. The region near the blade tip still exhibits the high WPS across all frequency bands, while the WPS near the leading edge and flow separation region becomes more pronounced. This confirms that flow separation and high turbulence at the leading edge due to blade stall are the main noise sources across all frequency bands. Importantly, both under normal operating conditions and stall conditions, the WPS is higher in the lower frequency bands, suggesting that the fan noise sources have more energy in the lower frequency range. This observation is consistent with the far-field noise spectrum shown in Fig. 3.24.

The wall pressure spectrum (WPS) is crucial for predicting far-field noise and is widely used in analytical models such as Amiet's trailing-edge noise model [50]. Analysing the WPS at different spanwise locations provides insights into airfoil self-noise sources. In this study, we focus on two spanwise locations: 50% s (mid-span) and 99% s (blade tip), and two chordwise locations: 2% c (leading edge) and 98% c (trailing edge). Figure 3.29 shows the WPS near the leading edge (2% c) and the trailing edge (98% c) for both 0 mmH_2O and 18 mmH_2O conditions.

At the normal operating condition, the WPS near the leading edge (2% c) exhibits distinct tonal peaks due to the interaction between the four asymmetric inlet sharp edges and the rotor (Fig. 3.29 (a) and (b)). This interaction has a base frequency of f_{IPF} and is more pronounced at the tip region (99% s) compared to the mid-span region (50% s). The WPS at the trailing edge location (98% c) for 50% span displays more tonal components generated by the rotor-stator interaction, characterized by a base frequency of f_{VPF}.

A small hump in the frequency range of 4-7 kHz was observed at the trailing edge for the mid-span location (50% s 98% c in Fig. 3.29 (a)). This indicates that the boundary layer is not fully developed at the trailing edge, consistent with the analysis of the boundary layer shape factor in Fig. 3.18. The presence of peaks in the hump suggests the existence of laminar structures in the boundary layer, specifically Tollmien-Schlichting (TS) waves. This observation is expected due to the low effective angle of attack (approximately 3.22°) and the incomplete turbulence in the boundary layer.

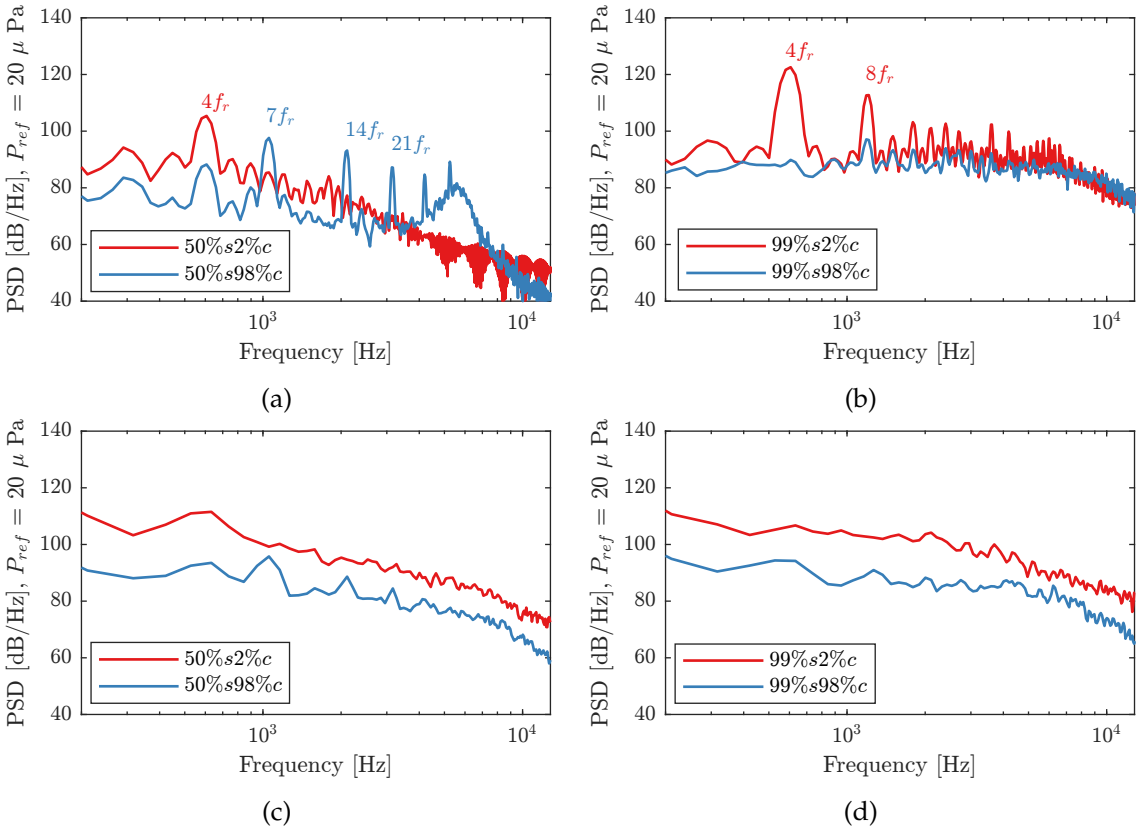

Figure 3.29: Comparison of the power spectral density (PSD) of the wall pressure fluctuation at two spanwise locations for the leading edge (2% c) and trailing edge (98% c) points under the normal operating condition (0 mmH_2O): (a) 50% span and (b) 99% span, and under the stall condition (18 mmH_2O): (c) 50% span and (d) 99% span.

At the 99% span near the tip region, the wall pressure spectrum (WPS) shows significantly higher magnitudes compared to the mid-span region, both near the leading and trailing edges (Fig. 3.29 (b)). This is due to tip leading-edge separation and the tip-separation vortex (TSV), which generate high turbulence levels and interact with the blade (see Fig. 3.15). The complex flow structures near the tip region pose challenges for noise prediction using semi-empirical WPS models [53] and Amiet's model [50, 51], even under normal operating conditions.

At the stall condition, the WPS at all locations becomes more distributed and exhibits fewer tonal components compared to the normal operating condition (Fig. 3.29 (c) and (d)). The magnitudes are significantly higher, particularly for frequencies below 1 kHz. The leading edge WPS becomes more prominent at all frequencies, with less variation between the mid-span and tip regions. This observation is consistent with the high turbulence at the leading edge, as shown in Fig. 3.13 (d) and Fig. 3.21.

These results confirm that the interaction between the circumferentially asymmetric inlet and the rotor (IRI) is the primary tonal noise source on the rotor during normal operation, while the rotor-stator interaction is the secondary tonal noise source. The

tip-gap region, generating high turbulence levels and interacting with the blade, is a critical broadband noise source. At the stall condition, flow separation and high turbulence at the leading edge become the primary noise sources, contributing to elevated broadband noise. The leading-edge noise is more pronounced than the trailing-edge noise. These noise sources establish the rotor as the primary contributor to far-field noise, as discussed in Section 3.6.2. However, it is important to note that shroud noise also plays a significant role in far-field tonal noise, particularly at microphone locations perpendicular to the fan axis, due to vortex-shroud interaction (VSI), as discussed in Section 3.6.2.

The results also indicate that the commonly employed asymmetric bellmouth inlet design for electronics cooling fans can lead to significant asymmetric inlet-rotor interaction (IRI) and vortex-shroud interaction (VSI). These interactions, arising from seemingly inconspicuous features of the fan's geometry, emerge as major contributors to its tonal noise emission.

3.7 Summary

This chapter presents a comprehensive numerical and experimental investigation of the aeroacoustic characteristics of a small-sized axial fan. The fan is operated under different backpressure conditions, representing various system resistances. A wall-resolved large eddy simulation (LES) is performed to simulate the detailed flow field and identify the noise sources. The far-field noise is predicted using the Ffowcs Williams-Hawkings (FW-H) equation. The results from the numerical simulations are validated against experimental data, and the aerodynamic and aeroacoustic characteristics of the fan are analysed.

The LES model accurately captures the flow field and noise sources of the fan. The aerodynamic analysis reveals distinct blade tip-flow structures, flow separation, and turbulence characteristics under different backpressure conditions. At normal operating conditions, the flow structures exhibit greater coherence and periodicity. A strong interaction is observed between the asymmetric bellmouth inlet and the rotor blades, and coherent tip vortices are found at the blade tip region. Paired inlet vortex tubes (IVTs) are generated by the asymmetric inlet-rotor interaction (IRI) and periodically interact with the rotor blades and tip vortices. The tip flow topology is characterized by the presence of tip-leakage vortex (TLV), induced vortex (IV), and tip-separation vortex (TSV). An uncommon flow feature is observed at the tip region, where the tip vortices interact with the shroud, generating a vortex-shroud interaction (VSI). In contrast, the stall condition is characterized by more pronounced flow separation on the blade surfaces and high leading-edge turbulence on the suction side of the blade. The

flow structures at the stall condition are more chaotic and less periodic, with a reduced influence of the asymmetric inlet-rotor interaction (IRI).

The aeroacoustic analysis reveals that the far-field noise of the fan exhibits dipole-like directivity. Tonal noise is more prominent during normal operating conditions, while broadband noise is more noticeable at the stall condition. The dominant tones occur at the blade passing frequency and its harmonics. The rotor is identified as the primary source of far-field noise, with the stator having a lesser impact. Notably, the VSI significantly contributes to the generation of far-field tonal noise, particularly at microphone locations perpendicular to the fan axis.

The analysis of noise sources on rotor blades confirms that the interaction between the asymmetric inlet and the rotor (IRI) is the main source of tonal noise during normal operation. The rotor-stator interaction (RSI) is identified as a secondary source of tonal noise. The tip-gap region is the primary source of broadband noise, generating tip-leakage flows and increasing pressure fluctuations at both the leading edge and trailing edge. At the stall condition, flow separation and high turbulence at the leading edge become the primary sources of noise, contributing to increased broadband noise. The leading-edge noise is more prominent than the trailing-edge noise. These noise sources establish the rotor as the primary contributor to far-field noise.

The findings of this study provide critical insights into the aerodynamics and aeroacoustics of small-sized axial fans, offering a foundation for developing reduced-order models and designing low-noise fans. Figure 3.30 illustrates the logical flow of Part I and its connection to subsequent parts.

The results underscore the rotor as the primary contributor to aerodynamic performance, with tip vortices identified as significant sources of aerodynamic losses. This highlights the importance of accurately modelling tip-clearance effects and blade geometry. Consequently, Part II (Chapters 4–6) will focus on developing reduced-order models (ROMs) for fan aerodynamics, incorporating these critical factors to enhance predictive accuracy.

Furthermore, the study identifies asymmetric inlet-rotor interaction (IRI) and rotor-stator interaction (RSI) as dominant sources of tonal noise, while leading-edge and trailing-edge noise are shown to contribute significantly to broadband noise. These findings will inform the development of reduced-order models for fan aeroacoustics in Part II (Chapter 7), enabling efficient noise prediction and mitigation strategies.

Additionally, the analysis reveals that tip vortices exacerbate trailing-edge noise at the blade tip, motivating the exploration of innovative blade tip treatments. This insight directly inspired the design of the fan winglet, aimed at mitigating tip vortices

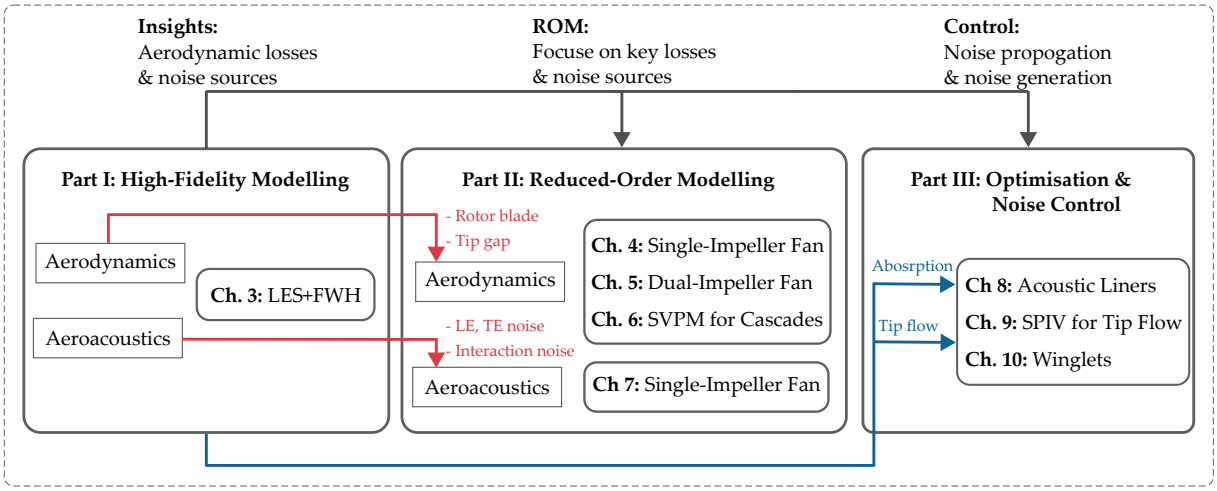

Figure 3.30: Logical flow of Part I and its connection to the subsequent parts. The insights used to inform Part II (Chapters 4–7) are highlighted in red, while the insights used to inform Part III (Chapters 8–10) are highlighted in blue. The chapters in Part I are connected to Part II and Part III through the grey lines.

and reducing noise. The experimental visualisation of tip leakage flow and the fan winglet design are detailed in Part III (Chapter 9 and Chapter 10, respectively). While the incomplete shroud design in this study generates substantial noise, modifying the shroud without a complete redesign is impractical due to its integral role in fan assembly. To address this challenge, compact micro-slit panel absorbers (CMSPAs) are proposed in Part III (Chapter 8). These absorbers can be tailored to specific frequency ranges, offering a flexible and effective solution for noise reduction.

"工欲善其事，必先利其器。"

"A craftsman must sharpen his tools to do good work."

—孔子，公元前551-479年，《论语》
Confucius, 551-479 BC, *The Analects*

Part II

Reduced-Order Modelling

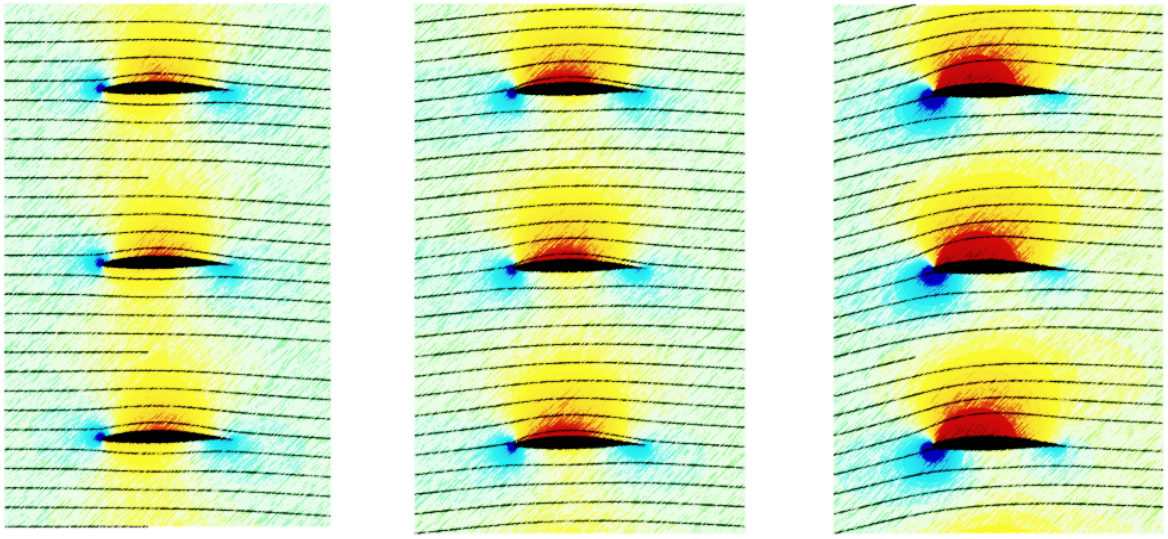

Chapter 4

On the Fast Prediction of the Aerodynamic Performance of Electronics Cooling Fans Considering the Effect of Tip Clearance

This chapter [1] presents the development and validation of a reduced-order model (ROM) for predicting the aerodynamic performance of electronics cooling fans, with a particular emphasis on the impact of tip clearance. This chapter, as the first in the ROM part (*i.e.,* Part II), lays the groundwork for developing a comprehensive ROM for predicting the aerodynamic and aeroacoustic performance of electronics cooling fans, setting the stage for subsequent chapters.

This chapter is structured as follows: Section 4.1 introduces the research context, followed by the proposed analytical method in Section 4.2. The experimental setup is detailed in Section 4.3, and the computational study is outlined in Section 4.4. Section 4.5 validates the analytical method. Finally, Section 4.6 summarises the chapter.

Abstract

This study aims to develop and validate a reduced-order model for the fast prediction of aerodynamic performance (P-Q) curve of electronics cooling fans, taking into account the real fan geometry and the tip clearance effect. The effect of tip clearance on tip vortex generation and fan performance was revealed by an experimentally validated 3D computational fluid dynamics (CFD) method. Six different tip clearance ratios ranging

[1] This chapter is based on the published work in [16, 31]:
Journal article: W. Zhao, S. Wasala, and T. Persoons, "On the fast prediction of the aerodynamic performance of electronics cooling fans considering the effect of tip clearance," IEEE Transactions on Components, Packaging and Manufacturing Technology, vol. 13, pp. 1139–1146, Aug. 2023.
Magazine article: W. Zhao, S. Wasala, T. Persoons, "Rapid and accurate analytical model for predicting axial fan performance in electronics cooling," *Electronics Cooling*, pp. 22-26, Jun. 2023.

from 0% to 12.7% were investigated. The tip clearance was found to have a strong effect on tip vortex generation, which significantly affects the aerodynamic performance of the fan. Fan efficiency increased by up to 7% by reducing the tip clearance ratio by 2.5%. The tip clearance effect was successfully included by the analytical method combined with a correlation equation developed based on the CFD study. The results show that the combined reduced-order model can produce reasonably accurate predictions for fan P-Q curve with errors less than 7.1% compared to CFD results, while having a wide valid range of tip clearance ratio up to 10%. The precision of this model was further validated against experimental results for eight commercial fans. The computational speed of this model is more than three orders of magnitude faster than a steady-state CFD study, making it highly appropriate for fast analysis of fan performance and thermal-flow co-design.

4.1 Introduction

Forced air cooling continues to play an essential role in modern electronics, where high-power density devices and enclosures generate heat that must be dissipated [2]. Electronics cooling fans are widely used in various industrial applications, such as information technology, automotive, and aerospace [219]. However, with the continuing trend towards compact packaging and high-density thermal management, fan energy consumption and acoustic noise emission are becoming a critical concern for these applications [1, 181, 220]. Therefore, improving cooling efficiency and reducing fan noise are crucial to extending the life of air-cooling systems [5].

The aerodynamic characteristics of a fan are crucial information for designing and optimising air-cooling systems. Fan manufacturers typically provide this information based on a standardised testing method, consisting of several fan curves that describe the relationship between static pressure, power demand, speed, and efficiency values as a function of volumetric flow rate [221]. However, when evaluating different fan types and sizes for thermal management, complete information on fan performance may not always be available, which presents a significant hurdle for thermal designs. An efficient and accurate fan performance prediction tool would be highly desirable for industrial design teams.

Modelling fan performance is dependent on numerous factors that must be accurately reflected in the modelling and analysis. The lumped fan (LF) model is a commonly used method for modelling forced convection cooling in electronic enclosures [222]. However, the LF model oversimplifies the fan geometries by using a planar face and assuming uniform flow leaving the fan, making it unable to predict the swirl velocity profile of the flow and leading to errors in thermal-flow designs [223].

Recently, more advanced computational fluid dynamics (CFD) methods have been proposed as alternatives to the LF approach with good results in electronics cooling applications. The large eddy simulation (LES) was combined with the Ffowcs Williams and Hawkings (FW-H) approach to calculate the aerodynamic and aeroacoustic performance of a counter-rotating cooling fan, with excellent agreement with experimental results [20, 27]. Steady/unsteady Reynolds-averaged Navier-Stokes (U/RANS) CFD, combined with the moving reference frame (MRF), have also been found to be reliable for electronics cooling applications [224, 225]. However, the high computational cost of higher-fidelity CFD methods limits their applicability for rapid analysis, design, and optimisation in the industry.

In contrast to numerical methods, analytical methods solve governing equations mathematically and can yield exact solutions for fan performance rapidly. Various analytical techniques have been proposed in the literature [47, 226]. However, these methods tend to overestimate fan performance because they hardly account for the actual geometry of the fan and neglect fan losses. Fan tip clearance has a significant effect on fan tip loss, which has been investigated in several studies [161, 227, 228]. Neglecting this type of loss in analytical models can result in significant errors in predicting fan characteristics.

Fan performance modelling methods face the challenge of balancing computational accuracy and cost. Improving the precision and effectiveness of fan aerodynamic models is crucial. This chapter focuses on developing and validating a reduced-order model (ROM) to predict the aerodynamic performance of electronics cooling fans, considering the effect of tip clearance.

4.2 Proposed analytical method

This section presents the proposed analytical method. The velocity triangles of a typical fan element are depicted in Fig. 4.1. In practical applications, stationary objects such as stators with guide vanes (streamlined) or struts (non-streamlined) are often located downstream of rotor blades. This study assumes an ideal downstream stator with an optimally designed shape that can fully recover the pressure loss equivalent to $\rho {v_u}^2/2$ caused by the rotational velocity component.

The thrust dT and torque dM for a radial element dr can be expressed as:

$$dT = \frac{1}{2}\rho B \frac{\Omega^2 r^2 (1-a')^2}{\cos^2\phi} c(C_l \cos\phi - C_d \sin\phi) dr, \tag{41}$$

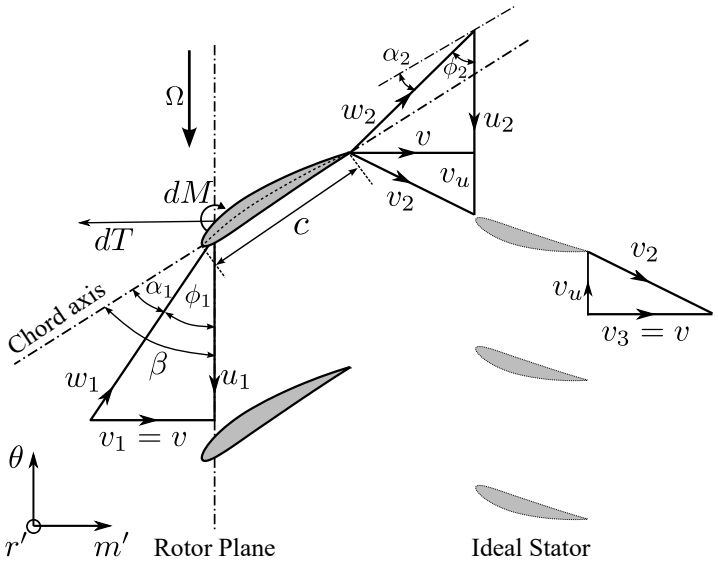

Figure 4.1: Velocity triangles for a typical fan blade element. An imaginary ideal stator is fitted to reduce the pressure loss ($\rho {v_u}^2/2$) due to the rotational velocity component v_u.

$$dM = \frac{1}{2}\rho B \frac{\Omega^2 r^2 (1-a')^2}{\cos^2\phi} c(C_l \sin\phi + C_d \cos\phi) r dr, \tag{42}$$

where C_l, C_d are the lift coefficient and the drag coefficient, respectively. r, Ω, B and c denote the blade radius, rotational speed, number of blades and chord length, respectively. ϕ is the effective inflow angle with respect to the rotor plane, which can be determined as [226]:

$$\cot\phi = \frac{1}{2}(\cot\phi_1 + \cot\phi_2), \tag{43}$$

where ϕ_1 and ϕ_2 are the inflow angle at inlet and outlet, respectively.

a' is the tangential induction velocity factor ($u = \Omega r\,(1 - a')$), which can be expressed as:

$$a' = \frac{w_1}{\Omega r} \sin\phi \tan\alpha_i, \tag{44}$$

where w_1 is the total relative velocity at the blade leading edge ($w_1 = \sqrt{{u_1}^2 + {v_1}^2}$).

The root and tip loss for a finite-span blade can be accounted for by assuming an elliptical lift distribution along the span. Based on the lifting line theory, the induced angle of attack α_i can be determined as [229]:

$$\alpha_i = \alpha_1 - \alpha = \frac{C_l}{\pi A R_{eff}}, \tag{45}$$

where α denotes the effective angle of attack ($\alpha = \beta - \phi$).

The effect of the downwash due to the tip and root vortices is to decrease the slope of the lift coefficient of an infinite-span airfoil. Therefore, the finite airfoil lift coefficient C_l is expressed as:

$$C_l(\alpha) = \frac{C_{l,\infty}(\alpha)}{1 + \frac{m}{\pi AR_{eff}}}, \tag{46}$$

where $C_{l,\infty}$ is the lift coefficient for a 2-D isolated airfoil with infinite span obtained by XFOIL [97], m represents the lift coefficient slope for the infinite span case ($m = dC_{l,\infty}(\alpha)/d\alpha$). It should be noted that XFOIL applies the e^N method to predict the free transition from laminar to turbulent [97]. The parameter, $N_{crit} = 5$, has been used in this study to represent relatively high turbulence inflow conditions.

By substituting Eq. 45 with Eq. 46, and solving iteratively, the effective angle of attack α for each blade element can be obtained. Then the forces and velocities can be obtained by solving Eq. (41) – (44).

The static to total pressure can be determined as:

$$P = \Delta P_t - P_d = \frac{T}{A} - \frac{1}{2}\rho v^2, \tag{47}$$

where, T is the total thrust of the rotor. A is the fan area.

The mechanical efficiency of the fan can be expressed as:

$$\eta = v\frac{T}{Pe}, \tag{48}$$

where Pe is the fan mechanical power ($Pe = \Omega M$).

This method considers the impact of tip clearance on fan performance using the effective aspect ratio AR_{eff}, which incorporates the correction factor M_{AR} with the geometric aspect ratio AR. A shroud can suppress tip vortices and improve blade performance, but its effectiveness decreases with increasing tip clearance. Based on this hypothesis, the tip clearance effect is included by treating the suppression of the tip vortex as an increase in the effective aspect ratio ($M_{AR} > 1$). The hypothesis made for the analytical model will be further discussed and verified by the CFD study in Section 4.4.

Theoretical fan performance based on Euler's work equation can be used for comparison with the proposed method [47]. Assuming flow alignment with the geometrical camber line and ideal stator recovery of downstream pressure loss, the ideal static to total pressure can be expressed as [47]:

$$P_{ideal} = \Delta P_t - P_d = \rho u v_u - \frac{1}{2}\rho v^2, \tag{49}$$

where $v_u = u - v \cot \phi_2$. ϕ_2 can be approximated as the angle between the tangent of the camber line at the trailing edge and rotor plane.

Figure 4.2 compares the predicted performance (P-Q) curves for an 80 mm axial fan using different correction factors ($M_{AR} = 1 \sim \infty$) to the manufacturer's reference data and experimental data, and to the ideal performance curve obtained using Eq. 49. The same fan has been investigated previously, and the geometry can be found in [23, 30]. The experimental data were obtained by a standardised test facility, which will be presented in Section 4.3. Generally, an increasing M_{AR} value leads to higher predicted fan performance. Specifically, $M_{AR} = 1$ indicates a fan with a finite span and large tip clearance, while $M_{AR} \to \infty$ approximates an ideal fan curve for a fan with an infinite span and zero tip clearance. Near and after the stalling dip as shown in Fig. 4.2, the flow will be unstable and be separated, resulting in an increase of radial flow component, *i.e.*, the axial fan would start acting like a mixed-flow fan [221]. The near-stall and post-stall fan performance can be partially predicted by this model based on the viscous solver XFOIL [97]. However, this method is less accurate in the stall region because XFOIL cannot be able to solve the separated flow and the radial flow is not taken into account. Hence, the following sections will only focus on performance discussions of the fan operating at normal conditions. For this test fan, the optimal M_{AR} is between $3 \sim 5$, which gives a decent prediction of the fan performance, as shown in Fig. 4.2.

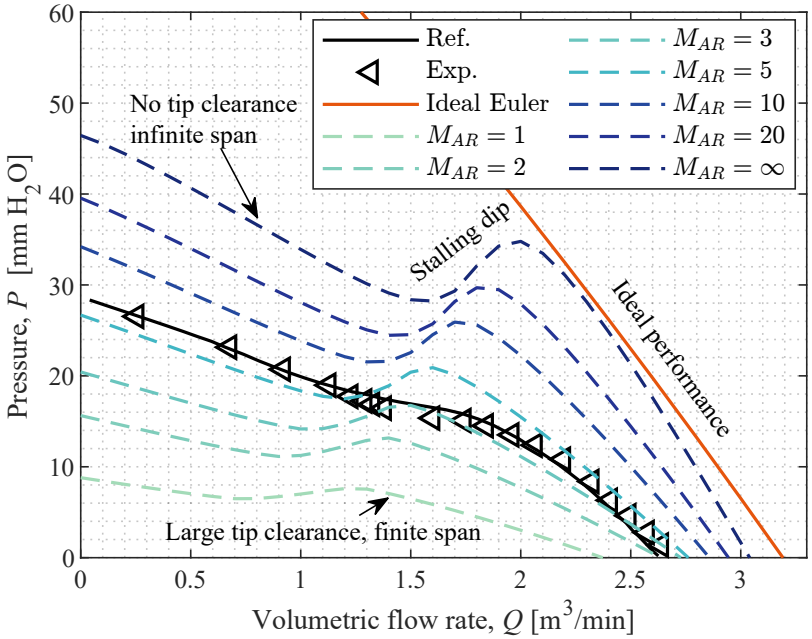

Figure 4.2: Effect of the correction factor M_{AR} on fan performance prediction for an arbitrarily selected 5-bladed fan [23, 30].

The aspect ratio correction factor M_{AR} shows a promising ability to analytically account for the finite span and the effect of tip clearance on fan curve predictions. However, a method for selecting this factor for small electronic cooling fans has not been provided.

To address this, a CFD study is proposed in Section 4.4 to investigate the effect of tip clearance, as well as to guide the selection of the optimal correction factor M_{AR}.

4.3 Experimental setup

The wind tunnel described in Appendix A.1 was employed to evaluate the fan performance curve. The axial fan introduced in Section 3.2.1 was selected as the baseline for these measurements. Figure 4.2 presents a comparison between the experimental results obtained from this facility and the manufacturer's reference data, demonstrating the reliability of the experimental setup in capturing accurate fan performance characteristics.

4.4 Computational study

4.4.1 Computational setup and validation

A three-dimensional RANS CFD simulation was conducted using ANSYS CFX-2022R2 to investigate the aerodynamic performance and internal flow characteristics of the axial fan, considering different tip clearances. The shear stress transport (SST) k-ω model was used as the turbulence model. The computational domain is illustrated in Fig. 4.3 (a). The numerical simulation models one single-blade channel and imposes periodic boundary conditions along the pitch-wise channel boundaries. Some simplifications and approximations were made for the simulation:

- The downstream stator was not modelled since its effect on the tip-leakage flow was considered to be minimal. However, an ideal stator was added mathematically to calculate the fan performance using the method presented in Section 4.2.
- The hub and shroud boundaries were extended to both the inlet and outlet. Hence, the bellmouth feature of the inlet was not modelled.
- The leading edge of the blades was slightly modified and rounded, facilitating the generation of high-quality grids, which can be seen in Fig. 4.3 (b).

The inlet and outlet domains are stationary, while the rotor domain is rotating. The moving reference frame (MRF) method was used at the interfaces. Air at 25 °C was used as the working fluid. Atmospheric pressure was applied to the inlet and mass flow rates were used for the outlet. All walls had no-slip and smooth-wall conditions. A counter-rotating wall was set up in the rotor shroud to counteract the motion of the rotor fluid domain.

The structured grid was constructed by ANSYS Turbogrid using an O-type grid for the rotor impeller and H-type grids for the inlet and outlet domains, as shown in Fig. 4.3 (b). The y^+ values were kept below 1 for all wall regions. To enhance the solution near the blade tip, 40 layers were added in the tip region for all cases, as highlighted in Fig. 4.3 (b). The residual value for achieving the convergence criteria was set below 1×10^{-6}.

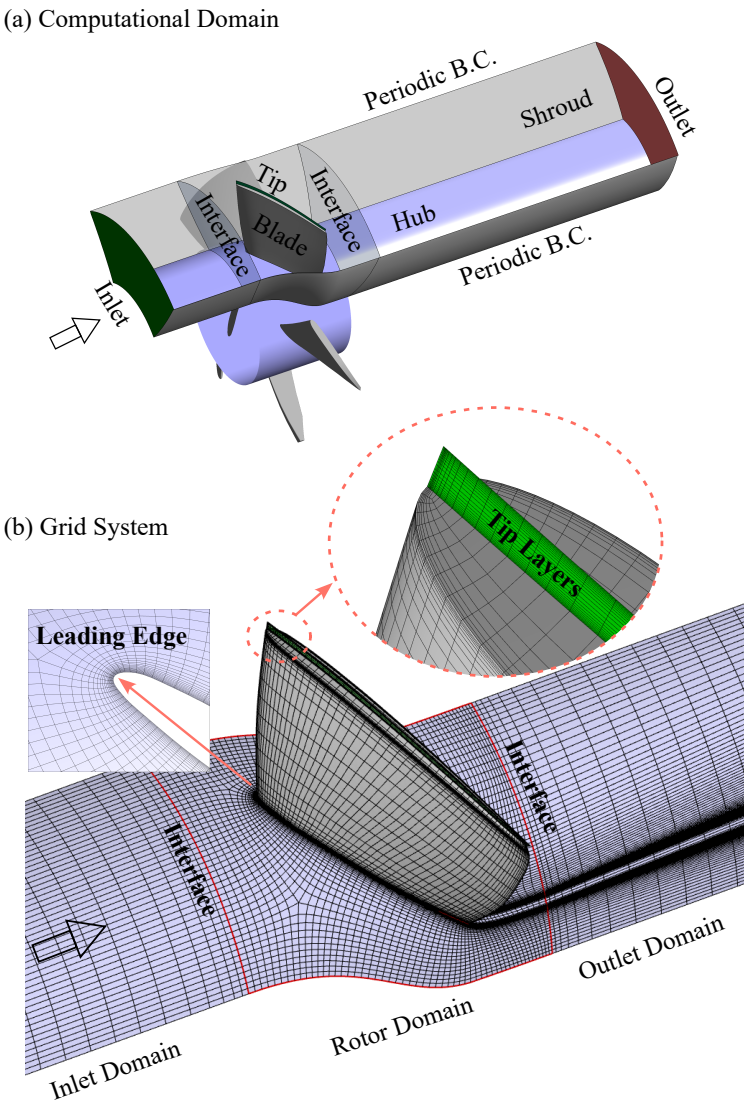

Figure 4.3: Computational domain (a) and grid (b).

A grid independence study was conducted to refine grids ranging from 0.2 to 2.8 million elements at a flow rate of 2.52 m^3/min. The refinement involved homogeneous grid density increase across the domain while adhering to specific criteria: 40 layers at the shroud tip, near wall elements with $y^+ < 1$, and maximum aspect ratio of 800 for the inlet and outlet domains. Convergence of static and total pressures was observed (Fig. 4.4), indicating a grid independent solution. Using approximately 0.9 million elements, the total pressure varied within 0.3%. The optimal grid system consisted of 0.9 million elements with a mean y^+ value of 0.89, striking a balance between accuracy

and computational demands. The total wall clock time for this grid is approximately 18 core-hours.

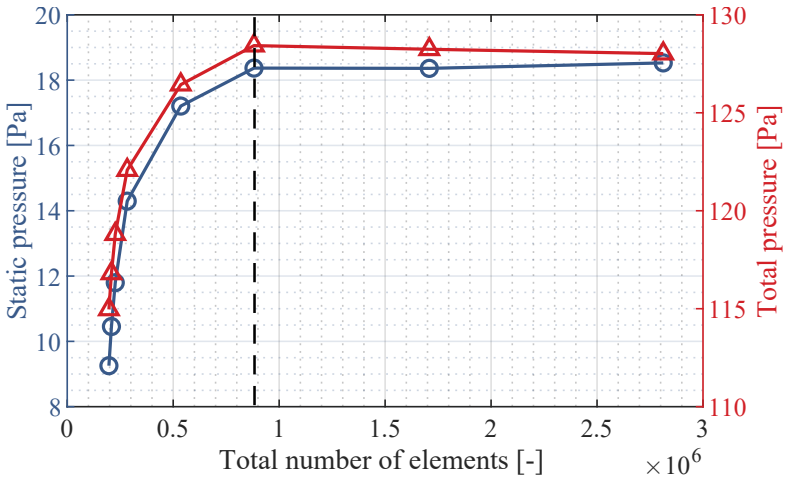

Figure 4.4: Results of grid independence analysis.

The accuracy of this CFD method was validated against experiments. Figure 4.5 shows the fan curve comparison between the CFD results, reference, experiments, and predictions with optimal M_{AR}. The ideal stator effect on the fan curve was calculated based on the theory in Section 4.2. The two CFD-based fan curves represent the performance without and with a stator, which is in line with the experimental data. At the normal working conditions, CFD results agree well with the experimental data. In the stall region ($Q < 1.89$ m^3/min), this RANS-based CFD method encounters convergence issues and a loss of accuracy, since it cannot capture the unsteady dynamics of flow separation and neglects the transition from laminar to turbulent flow. A higher-fidelity model, such as URANS or LES, would be preferable when predicting the performance of the stall region [20].

The prediction results produced by the analytical tool are also illustrated in Fig. 4.5, demonstrating a good match with both simulation data and experimental data. The execution time of this Matlab-based tool is less than 1 min using an Intel Xeon E5-2630v3 CPU (~ 0.1 core-hour). In contrast, obtaining the P-Q curve with eight working conditions using CFD required a total of 160 core hours. Therefore, the computational speed of the analytical tool is over three orders of magnitude faster than the CFD simulation method.

4.4.2 Effect of tip clearance on fan performance

Six different cases were simulated in this study with varying tip clearance ratios: 0%, 1.3%, 2.5%, 5.1%, 7.6%, and 12.7%. The baseline case (B/L) was selected based on the actual fan geometry, which has a tip clearance ratio of 2.5%. A maximum tip clearance

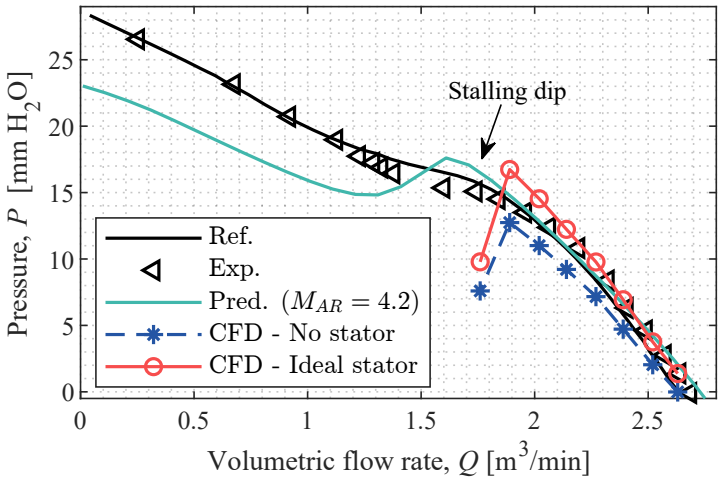

Figure 4.5: Performance comparison between the CFD results with/without an ideal stator, the reference, the experiments, and the prediction with optimal M_{AR}.

ratio of 12.7% was chosen, five times larger than the baseline case, to investigate the behaviour of tip vortical structures with increased tip gap. The tip clearance ratio (T_R) was defined as the distance between the blade tip and shroud (t) divided by the blade radius (R_t), as shown in Fig. 4.6. The tip clearance was modified by changing the shroud radius while maintaining a constant blade radius, which is shown in Fig. 4.6. It is worth noting that a zero-tip clearance ratio is not physically possible. However, simulating such a scenario aided in revealing flow phenomena and fan performance in a hypothetical zero-tip clearance situation.

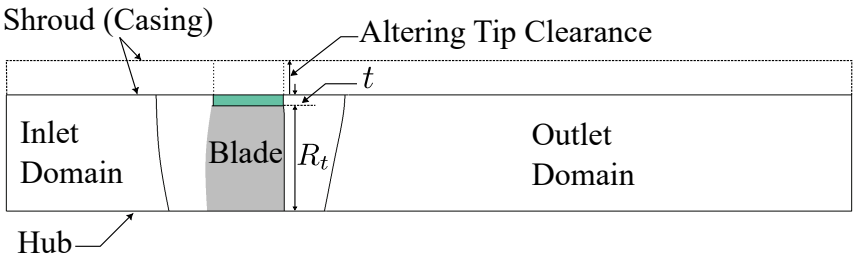

Figure 4.6: A schematic in the meridional view illustrating the procedure for changing tip clearance by altering the shroud radius. Tip clearance ratio (T_R) is defined $T_R = \frac{t}{R_t}$.

Figure 4.7 (a) presents P-Q curves obtained from CFD simulations for different tip clearances at normal operating conditions. The best performance was observed in the zero-tip clearance case, while an increase in tip clearance led to a decrease in fan performance, consistent with the analytical calculation shown in Fig. 4.2. This degradation in fan performance can be treated as a decrease in the effective aspect ratio (M_{AR}) as per the analytical method. Fan efficiency curves under varying tip clearances are shown in Fig. 4.7 (b), revealing that fan efficiency improves as the tip clearance decreases. Reducing the tip clearance from 2.5% to a hypothetical value of zero resulted in approximately 7% improvement in fan efficiency. These findings

indicate that minimizing tip clearance can enhance fan performance and efficiency in fan designs.

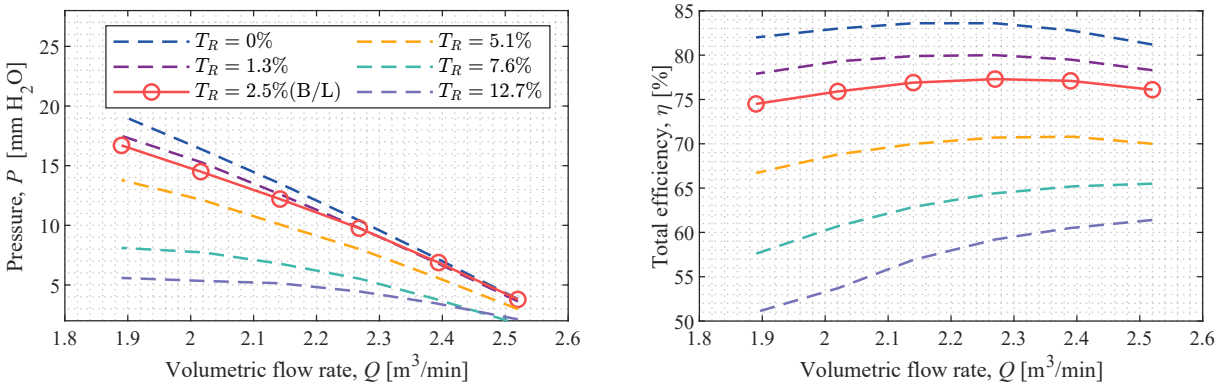

(a) P-Q curves (b) Efficiency curves

Figure 4.7: Fan P-Q curves (a) and Efficiency curves (b) obtained by CFD simulations under different tip clearances at the nominal speed of 9000 r/min. The baseline (B/L) case has a tip clearance ratio of 2.5%.

To gain a better understanding of the flow phenomenon that causes the degradation of fan performance, vortical structures were analysed for various tip clearance cases. Figure 4.8 illustrates a typical structure of tip vortices for the baseline tip clearance ratio at a flow rate of 2.02 m^3/min, approximately 75% of the maximum flow rate. The vortex cores were identified based on swirl strength at 7000 s^{-1} and coloured by the normalised helicity (NH) following the definition presented in [205]. The normalised helicity magnitude aids in determining the direction of vortex cores, with those having the same direction as mainstream assigned a positive one, and those with an opposite direction assigned a negative one. Figure 4.8 illustrates three distinct tip vortex structures, namely the tip leakage vortex (TLV), induced vortex (IV), and tip separation vortex (TSV). Large eddy simulations for a linear cascade in [161] and for an axial fan in [227] have shown similar vortex structures. The most dominant vortex structure is the TLV, which arises due to the tip-leakage jet rolling up from the pressure side (PS) to the suction side (SS). It originates downstream of the leading edge (LE) at a specific location and moves in the mainstream direction. Moreover, the TLV induces the creation of induced vortices, which have an opposite direction to the tip leakage flow. Any flow separated at the blade tip results in the generation of the TSV. In this case, the TSV near the trailing edge (TE) is predominant, as shown in Fig. 4.8.

To visualise and compare the vortical structures in the tip gap at different tip clearance ratios varying from 0% to 12.7%, the vortex cores were extracted from 90% of the blade tip radius to the shroud radius and plotted in a blade-to-blade view, as shown in Fig. 4.9. The volumetric flow rate of 2.02 m^3/min was maintained across all the cases. In the hypothetical zero-tip clearance scenario, no tip vortex is generated, while only minimal

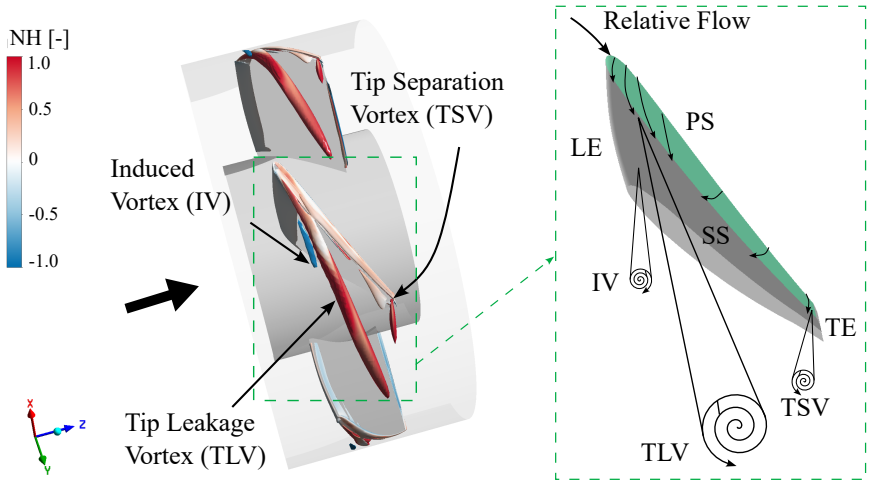

Figure 4.8: Swirl strength contour at 7000 s^{-1} coloured by the normalised helicity (NH) at $Q = 2.02\ m^3/min$ for a tip clearance ratio $T_R = 2.5\%$.

vortices were generated near the shroud. When the tip clearance ratio increased to 1.3%, the three vortex structures — TLV, IV and TSV — were observed prominently. In this case, the onset of a significant tip leakage vortex was approximately 20% of the axial chord downstream from the leading edge. As the tip clearance ratio increased, the shroud's impact on the tip vortices decreased. The TLV's onset propagated in the chordwise direction, and the induced vortex shifted towards the circumferential direction. When the onset of the TLV coincided with the TE location (100% axial chord), the shroud only had a minimal effect on the tip vortices. This coincidence between the onset of TLV and the TE occurred when the tip clearance ratio was within the range of 7.6% to 12.7%, as shown by the dotted line in Fig. 4.9.

Sectional blade efficiency was calculated at 26 different spanwise locations from the blade hub to tip to demonstrate the tip vortex effect on blade efficiency. Results are presented in Fig. 4.10, revealing that the tip vortex has a greater negative impact on the blade's performance in the vicinity of the blade tip. As tip clearance increases, the shroud's suppression effect reduces, and the TLV's onset shifts from the LE towards the TE, causing a decrease in efficiency at each spanwise section.

The CFD studies demonstrate that the proximity of a shroud mitigates tip vortices, leading to an improvement in the fan performance curve and efficiency. The tip clearance width influences the onset of the tip leakage vortex, and the suppression effect weakens with an increase in clearance, reaching a minimum at tip clearance ratios between 7.6% and 12.7%. These findings confirm the hypothesis stated in Section 4.2.

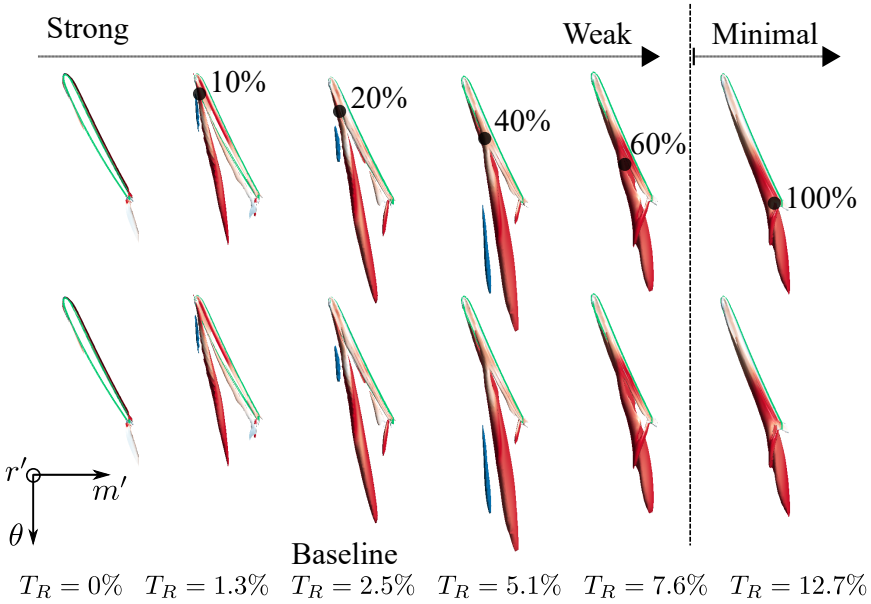

Figure 4.9: Vortical structures in a blade-to-blade view in the tip gap (from 90% of the blade tip radius to the shroud radius) at different tip clearance ratios varying from 0% to 12.7% computed at Q = 2.02 m^3/min. Green polylines denote the airfoil profiles at the blade tip, and black dots indicate the onsets of the main tip leakage vortex.

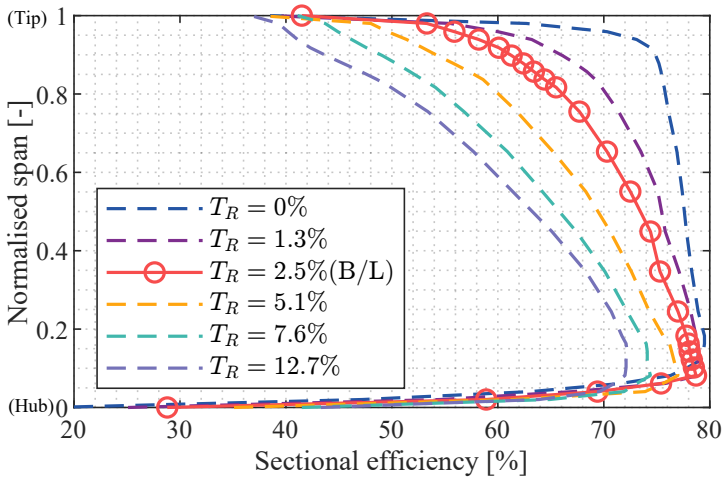

Figure 4.10: Fan sectional blade efficiency curves calculated at 26 different blade spanwise locations from the hub to the tip of the blade. Results were obtained by CFD simulations for Q = 2.02 m^3/min under different tip clearances.

4.5 Validation of the reduced-order model

In this section, a correlation was developed using CFD results from Section 4.4 to select the optimal correction factor M_{AR} of effective aspect ratio. The completed reduced-order model was then validated against additional commercial fan experiments.

4.5.1 Determination of the optimal correction factor

To determine the optimal correction factor M_{AR}, the normalised root-mean-square error (NRMSE) is used to find the best matches between predictions and simulations/experiments. The NRMSE is expressed as:

$$E = \sqrt{\frac{1}{n}\sum_{i=1}^{n}\left|P'_{o,i} - P'_{p,i}\right|^2}, \tag{50}$$

where P'_o is the observed pressure obtained from CFD simulations for given flow rates or from experiments, and P'_p is the predicted pressure obtained from the analytical model. These pressures are normalised by the maximum pressure observed in the experimental fan curve. The optimisation objective is to determine the correction factor M_{AR} with the lowest NRMSE value, which ensures the most accurate fan curve prediction.

4.5.2 Verification and validation of the results

The optimal correction factors for best fan curve predictions compared to CFD results under different tip clearances are shown in table 4.1. The optimal correction factor decreases as the tip clearance ratio increases, consistent with the theory presented in Section 4.2. Analytical predictions have errors within 7.1% except for the case with a tip clearance ratio of 12.7%. This could be due to the minimal vortex suppression effect as the tip clearance becomes large, making the fan act like an open impeller, leading to inaccuracies in the analytical model. However, industrial electronic cooling fans rarely have tip clearance ratios greater than 7.6%, making the valid tip clearance range applicable to most cases. As shown in Fig. 4.11, a linear equation was fitted based on the optimal correction factors and the CFD results, which is:

$$M_{AR} = 1 + \max\left(0, 4.86\left(1 - \frac{T_R}{9.94}\right)\right). \tag{51}$$

The fitted curve has a coefficient of determination of 0.9958, indicating a strong linear correlation between the optimal correction factor and the tip clearance ratio. The

Table 4.1: Optimal correction factors M_{AR} and prediction errors E comparing to CFD results. Tip clearance ratio (T_R) is defined $T_R = t/R_t$.

T_R[%]	M_{AR}[-]	E[%]
0.0	5.9	7.1
1.3	5.1	5.3
2.5	4.7	4.2
5.1	3.4	3.2
7.6	2.1	3.8
12.7	1.2	32.8

optimal correction factor approaches the lower limit of 1 at a tip clearance ratio of approximately 10%, which coincides with the onset of the tip leakage vortex at the trailing edge within the tip clearance ratio range of 7.6% to 12.7%, as confirmed by CFD studies in Section 4.4.2. This range of 10% can be applied as the upper validity limit for the analytical method, completing the P-Q curve prediction for small electronics cooling fans considering tip clearance effects.

Table 4.2: Optimal correction factors M_{AR} and prediction errors E compared to experimental results for eight different commercial fans.

	Index	T_R[%]	Re[-]	M^P_{AR}[-]	M^E_{AR}[-]	E[%]
	1	2.5	60,000	4.6	4.2	1.8
	2	2.1	56,000	4.8	4.8	2.2
Known	3	1.1	73,000	5.3	4.8	0.4
Branded	4	1.3	88,000	5.2	5.1	4.6
	5	3.1	28,000	4.3	4.6	0.4
	6	3.6	20,000	2.8	2.1	2.2
Non	7	2.9	21,000	4.5	2.6	4.0
Branded	8	2.8	23,000	4.5	1.2	2.2

To further validate the reduced-order model for various fan geometries, eight commercial fans were tested in the AMCA standardised test facilities described in Section 4.3. The fans were grouped into two categories: Fans 1-6 were from known brands, while Fans 7-8 were from unknown brands. The optimal correction factor, M^P_{AR}, was calculated using Eq. 51, and M^E_{AR} was determined based on experimental fan performance curves. These factors are shown in Table 4.2 and Fig. 4.11. The NRMSE values calculated using M^E_{AR} were within 5%. For most known branded fans [2], the optimal correction factors aligned well with the fitted curve. Discrepancies were observed for non-branded fans and Fan 6, likely due to poor blade and downstream stator designs,

[2] **Known branded fans** are fans from well-known manufacturers, *i.e.*, Fans 1–2 are from Delta Electronics, Fans 3–4 and 6 are from SanYo Denki, and Fan 5 is from EBM-Papst. **Non-branded fans** are fans from unknown manufacturers.

causing the reduced-order model to overestimate the fan performance curves. Despite this, the method remains useful for fan performance analysis and design optimisation.

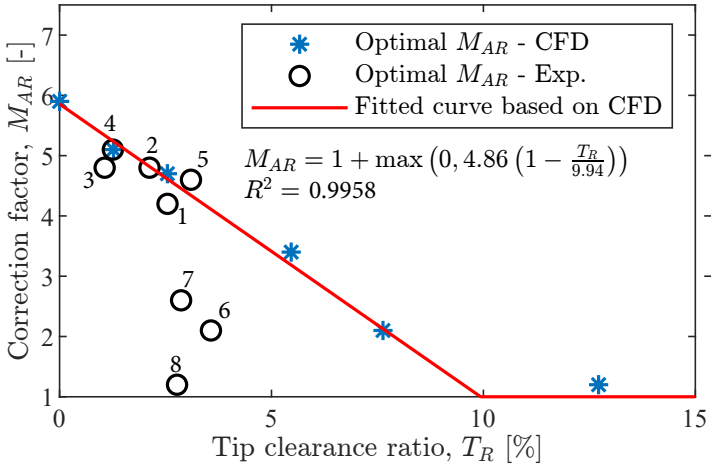

Figure 4.11: Optimal correction factors for CFD cases and for eight different commercial fans as a function of the tip clearance ratio. The correlation equation was fitted based on the CFD cases.

4.6 Summary

In this chapter, an efficient reduced-order model (ROM) was proposed to analyse the aerodynamic performance of electronics cooling fans, accounting for fan geometry and tip clearance effects. The method treats tip vortex suppression in the presence of the shroud as an increase in the blades' lift coefficients, which weakens with increasing clearance. A CFD study verified the effect of tip clearance on fan performance and vortex structures for clearances of 0% to 12.7%. A correlation for the optimal M_{AR} as a function of tip clearance ratio was developed from CFD results, and the validity of the proposed model was verified with experimental tests on eight commercial fans.

The study concludes that:

- Tip clearance significantly affects fan performance. A 2.5% reduction in tip clearance ratio improves efficiency by around 7%.
- Larger tip clearance weakens tip vortex suppression, resulting in delayed onset of tip leakage vortex and degraded fan performance.
- The ROM produces accurate predictions with errors less than 7.1% in fans' normal operating conditions, valid for tip clearance ratios from 0% to 10%, and is computationally efficient, over three orders of magnitude faster than steady-state CFD.

The proposed model can predict fan performance in normal working conditions with acceptable accuracy and low computational cost, making it suitable for rapid analysis, design, and optimisation of electronics cooling fans. It can accelerate the thermal-flow design of fan-cooled electronics systems and facilitate fast aeroacoustic predictions in future. Further work is recommended to validate the accuracy of the model for fans with Reynolds numbers significantly smaller or larger than the range of 20,000 to 88,000 covered in the current validation cases.

This chapter has laid a robust groundwork for developing a rapid and comprehensive tool for predicting the aerodynamic and aeroacoustic performance of fans. The subsequent chapter (*i.e.,* Chapter 5) will build upon this foundation by extending the ROM to encompass counter-rotating (CR) fans, which are prevalent in high-performance electronics cooling systems.

Chapter 5

Reduced-Order Model for Predicting Aerodynamic Performance of Dual Impeller Fans in Data Centre Cooling Systems

As the second chapter of Part II on reduced-order modelling for predicting the aerodynamic performance of electronics cooling fans, this chapter[1] delves into the extension and application of the reduced-order model (ROM) to counter-rotating (CR) dual impeller fans, which are extensively utilised in server cooling systems within data centres.

This chapter is structured as follows: Section 5.1 introduces the research topic and its importance. The experimental setup and fan configuration are detailed in Section 5.2. Section 5.3 outlines the proposed extended analytical method, while the computational study is elaborated in Section 5.4. Section 5.5 presents the results and discussion. Finally, the chapter concludes with key findings in Section 5.6.

Abstract

A reduced-order model (ROM) has been extended and applied to counter-rotating (CR) dual impeller fans commonly employed in cooling electronics enclosures of data centre systems. The model incorporates the actual rotor and stator geometry, and its accuracy was assessed against experimental fan performance (P-Q) curve data, as well as compared with computational fluid dynamics (CFD) results. Additionally, the influences of stator and radial flow were explored through CFD simulations. The limitations of the ROM were further discussed. The ROM's predictions exhibit favourable agreement

[1]This chapter is based on the published **conference paper** [32]: W. Zhao, S. Wasala, and T. Persoons, "Reduced-order model for predicting aerodynamic performance of dual impeller fans in data centre cooling systems," in 2023 23rd International Workshop on Thermal Investigations of ICs and Systems (THERMINIC), 2023.

with experimental and numerical findings, with normalised root-mean-square errors of 4.6% in the normal working region and 13.2% in the stall region. Notably, the ROM offers significant computational savings compared to CFD simulations, rendering it a valuable cost-effective tool for preliminary design, analysis, and optimisation of CR fans.

5.1 Introduction

In line with the ongoing trend towards compact electronics enclosures within data centre systems, the demand for more efficient and less noisy air movement devices is increasingly critical [5]. High-rotational-speed counter-rotating (CR) axial fans, featuring opposing impeller rotations, hold significant potential in terms of efficiency and compactness for cooling and propulsion applications [230–232]. Particularly noteworthy in the data centre industry, these fans mitigate swirl in the wake flow and deliver substantial pressure rise, aligning well with the requirements of enclosures with high system impedance.

Ensuring the optimal aerodynamic performance of CR fans is paramount when designing and optimising cooling systems within data centres. However, modelling fan performance presents challenges, necessitating accurate consideration of various factors such as blade geometry, tip clearance, and more. For small-sized axial fans used in electronics cooling within data centres, typical parameters include a casing diameter of less than 120 mm and speeds below 20,000 r/min. These fans exhibit a distinct profile characterised by a high hub-to-shroud ratio (approximately 0.5), moderate solidity (ranging from 0.7 to 1), and a low Reynolds number (below 3×10^5) [30]. Despite being situated within the realm of low-pressure fan applications governed by incompressible flow principles, these fans are challenged by their geometry and flow features, including the influence of end walls (*i.e.* hub and shroud), interactions with adjacent blades, and elevated drag losses.

The utilisation of computational fluid dynamics (CFD) methods always involves a trade-off between computational accuracy and cost. While high fidelity 3D CFD have demonstrated reliability in modelling CR fan performance [20], their extensive computational requirements restrict their applicability in fast industrial design and optimisation processes. The lumped fan model necessitates fan performance (P-Q) curves as input and oversimplifies fan geometries as planar, limiting prediction of swirl velocity profiles and fan performance. Consequently, this simplification introduces some level of error in thermal-flow designs [223].

In the realm of computationally cheap approaches, several analytical design methods

can serve as inverse analysis tools [34, 47, 48, 226]. The isolated airfoil method (blade element/strip theory) and cascade method find extensive use in fan design [233], yet they are confined to specific ranges: the isolated airfoil method suits low solidity (< 0.7), while the cascade method accommodates high solidity rotors (> 1). However, for moderate solidity rotors ($0.7 - 1$), prevalent among electronics cooling fans, these methods are inapplicable, necessitating the adoption of novel techniques [233].

Previously in Chapter 4, a reduced-order model (ROM) for single impeller axial fans was introduced and validated. This chapter extends the ROM to predict the performance of counter-rotating (CR) dual impeller fans. The extended ROM accounts for the effects of the stator and the second CR rotor. Additionally, a CFD study is conducted to analyse flow behaviour and validate the ROM's predictions.

5.2 Fan configuration and experimental setup

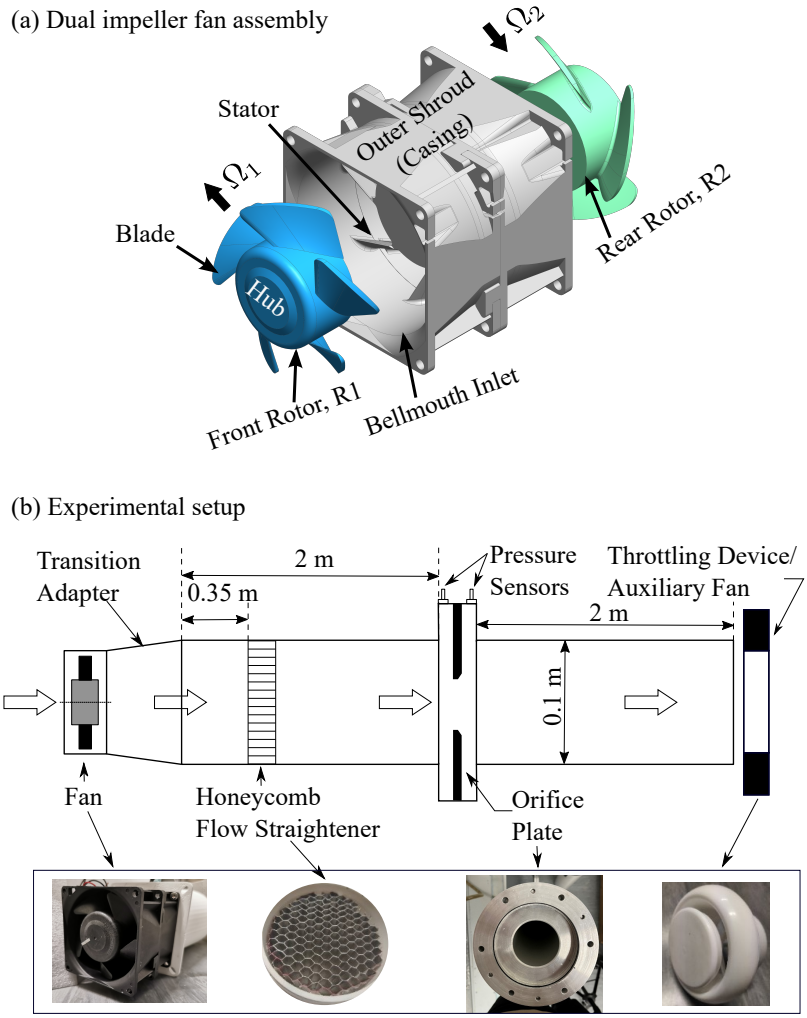

Figure 5.1: (a) Test dual impeller fan and (b) experimental setup according to ANSI / AMCA 210-16 [211] and ISO 5167-2:2003 [234].

The test case involves a commercially available counter-rotating (CR) fan enclosed within a $80 \times 80 \times 80$ mm^3 casing. This fan, utilised in a multiple hard disk drive enclosure, comprises two rotors with opposing rotation directions and an intermediate stator. A previous study has also investigated this fan [20]. It consists of 5 front rotor blades, 7 stator blades, and 4 rear rotor blades, with the front rotor operating at a nominal speed of $N_1 = 14200$ r/min and the rear rotor at $N_2 = 15000$ r/min. The averaged blade chord lengths for the front rotor and rear rotor are 28.5 mm and 39.6 mm, respectively. The corresponding averaged chord-based tip Reynolds numbers are 100,000 and 160,000. The hub to shroud ratio is 0.57, and the blade solidities for the front rotor and rear rotor are 0.77 and 0.86, respectively. The geometric configuration of this dual impeller fan is illustrated in Fig. 5.1 (a).

The fan performance curve was determined using the wind tunnel detailed in Appendix A.1. This wind tunnel, previously employed in Chapter 3 and Chapter 4 to test single impeller fans, is depicted in Fig 5.1 (b). The experimental setup involved testing the fan P-Q curves at 100% pulse width modulation (PWM) conditions, with the rotating speeds set to $N_1 = 13200$ r/min and $N_2 = 13950$ r/min. These speeds are slightly lower than the manufacturer's nominal values. To ensure comparability of P-Q curves at the same speed, the tested P-Q curve was scaled using fan laws [47].

5.3 Extension of reduced-order model

The previously established reduced-order model (ROM) designed for predicting the aerodynamic performance of single impeller axial fans has been showcased and validated in Chapter 3. The computational tool XFOIL [97], utilising a viscous vortex panel method, was harnessed to determine isolated airfoil aerodynamic coefficients. These coefficients were subsequently adjusted to consider blade aspect ratio and tip clearance effects [31]. The ROM efficiently encompasses crucial rotor blade geometry considerations and accommodates tip clearance effects. The current study advances the ROM's capabilities by extending its application to counter-rotating (CR) dual impeller fans.

Figure 5.2 illustrates the velocity triangles at a representative radial section of a typical CR fan. For the development of the ROM, the following assumptions have been taken into consideration:

1. The flow is purely axial, lacking any radial component along the span. This permits treating a fan blade as a sequence of 2-D radial elements. The justification for this assumption is elaborated in Section 5.5.3.

2. The influence of the downstream component on the upstream component's flow

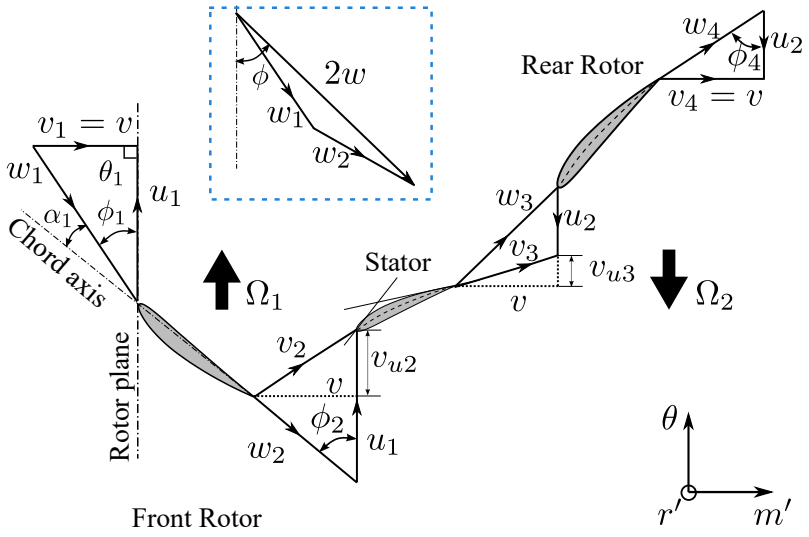

Figure 5.2: Velocity triangles for a typical CR fan blade section. The diagram in the blue dashed box illustrates the definition of w as the vectorial mean of w_1 and w_2.

is neglected, simplifying the fan flow as a unidirectional chain from the initial component to the final one.

3. The flow direction upon exiting the stator is approximated as aligning with the geometric blade camber line near the trailing edge.

Based on the assumption 1 and 2, the front rotor (R1) can be treated as an isolated rotor and its performance can be calculated using the same method in [30, 31]. The impact of tip clearance can be incorporated by employing Equation (11) from [31]. All pertinent parameters (*i.e.* velocity, pressure, and force) can be derived through this approach. For comprehensive method details, readers are referred to [30, 31], which are not reiterated in this study due to brevity.

Regarding the calculation of the swirl component (v_{u2}), two methods are available. The method I relies on Euler's turbomachinery equation [48, 226]. For a given blade section i, the total pressure rise is expressed as:

$$\Delta P_{t,i} = \rho u_1 (v_{u2} - v_{u1}). \tag{52}$$

For the front fan, $v_{u1} = 0$ m/s. The pressure rise can be calculated based on the thrust ($\Delta P_{t,i} = dT/dA$).

The method II employs relative velocity triangles, as depicted in the dashed box in Fig. 5.2. The effective flow angle with respect to rotor plane ϕ is acquired using the approach outlined in [31]. Consequently, the exit swirl component can be formulated as:

$$v_{u2} = u_1 - v\cot\phi_2 = u_1 - v((2\cot\phi - \cot\phi_1)). \tag{53}$$

Both methods are viable for computing exit flow angles and swirl components of rotating blades. However, the method I is not applicable to stationary guide vanes due to the absence of tangential velocity ($u = 0$ m/s). Regarding the stator, with the assumption of a known exit flow angle θ_3 (assumption 3), and by calculating velocity triangles in a stationary frame, the method II remains applicable to determine effective flow angles and effective angles of attack. Forces can then be derived using XFOIL [97] based on the effective angle of attack [31]. Consequently, the second method was employed in this study for both rotors and the stator.

The rear rotor, rotating in the opposite direction to the front rotor, can recover the kinetic energy in the swirl component (v_{u3}) of the wake generated by the front rotor and the stator, as indicated by the velocity triangles in Fig. 5.2. Consequently, the relative inflow velocity experienced by the rear rotor requires modification as follows:

$$w_3 = \left(v^2 + (u_2 + v_{u3})^2\right)^{1/2}. \tag{54}$$

Subsequently, the flow and forces for the rear rotor can be computed using the approach outlined in [31]. Finally, the total-to-static pressure can be determined by summing the pressures exerted by all rotor blades and stator blades and subtracting the dynamic pressure term P_d, which is represented by the equation:

$$P_{t-s} = \Delta P_{t,R1} + \Delta P_{t,S1} + \Delta P_{t,R2} - P_d. \tag{55}$$

The mechanical efficiency of the fan can be computed using Equation 48.

The presented model was implemented in MATLAB and seamlessly integrated with XFOIL. For solving a fan performance curve, an estimated computational time of 0.1 core-hours is needed by this code.

5.4 Computational study

A 3D Reynolds-averaged Navier-Stokes (RANS) computational fluid dynamics (CFD) simulation was performed using ANSYS CFX-2022R2 to analyse the aerodynamic performance and internal flow characteristics of the CR fan. The chosen turbulence model is the shear stress transport (SST) k-ω model, without incorporating transition effects. The simulation focuses on a multi-stage channel, employing periodic boundary condi-

tions along the pitch-wise channel boundaries. The computational domain is depicted in Fig. 5.3 (a). The simulation incorporated several simplifications:

- The hub and shroud boundaries were extended to both the inlet and outlet, thus excluding the modelling of the inlet's bellmouth feature.
- The leading and trailing edges of the blades were given slight rounding, which aided in generating high-quality grids. This can be observed in Fig. 5.3 (b).

(a) Computational domain

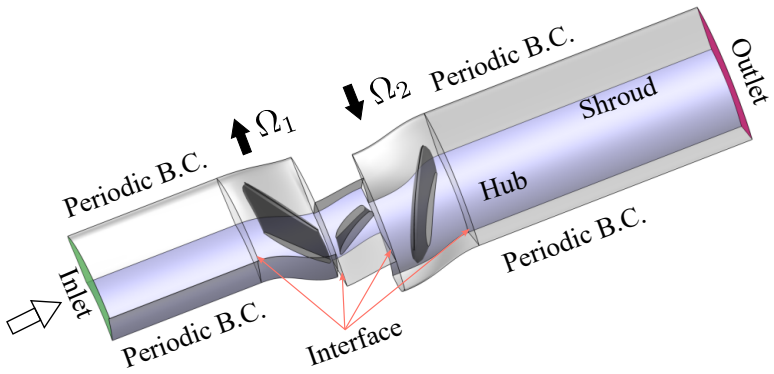

(b) Grid system

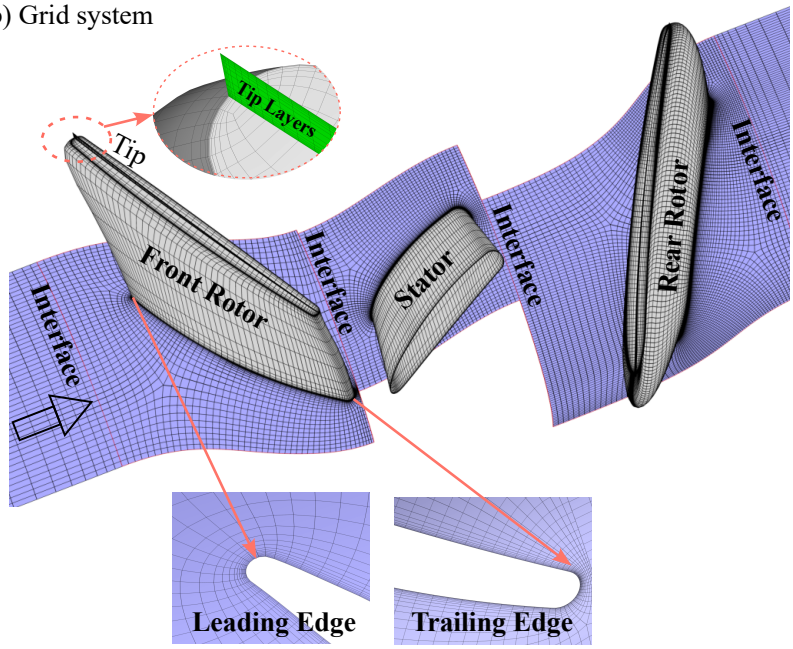

Figure 5.3: Computational domain (a) and grid system(b).

The moving reference frame (MRF) technique was applied in this CFD study. The stationary domains encompass the inlet, outlet, and the stator, whereas the front and rear rotor domains exhibit counter rotating motions at speeds of N_1 = 14200 r/min and N_2 = 15000 r/min, respectively. Air at a temperature of 25 °C was designated as the working fluid. Inlet conditions adhered to atmospheric pressure, while static

pressure conditions governed the outlet. Walls were assigned no-slip and smooth-wall attributes. To counteract rotor fluid domain motion, counter-rotating walls were introduced in the rotor shrouds.

ANSYS Turbogrid was utilised to construct a structured multi-block mesh. The O-type grids were employed for the rotor impellers and the stator guide vanes, while H-type grids were applied for the inlet and outlet regions, as depicted in Fig. 5.3 (b). A grid convergence study based on the grid convergence index (GCI) method was executed. A range of five globally refined grids spanning 0.4 to 5.2 million elements with a refinement factor of 2 were employed to assess convergence. As illustrated in Fig. 5.4, convergence of flow rate was achieved using a grid system comprising 2.6 million elements. An averaged y^+ value of 0.51 was obtained across all blade regions, with roughly 40 layers positioned around the blade tip regions of both the front and rear rotors. The total wall clock time for this grid approximated 80 core-hours. Solving the P-Q curve for five distinct operating conditions necessitated approximately 400 core-hours.

To assess the stator's impact on the P-Q curve, an additional case without the stator was investigated. Domain comparisons with and without the stator are presented in Fig. 5.5.

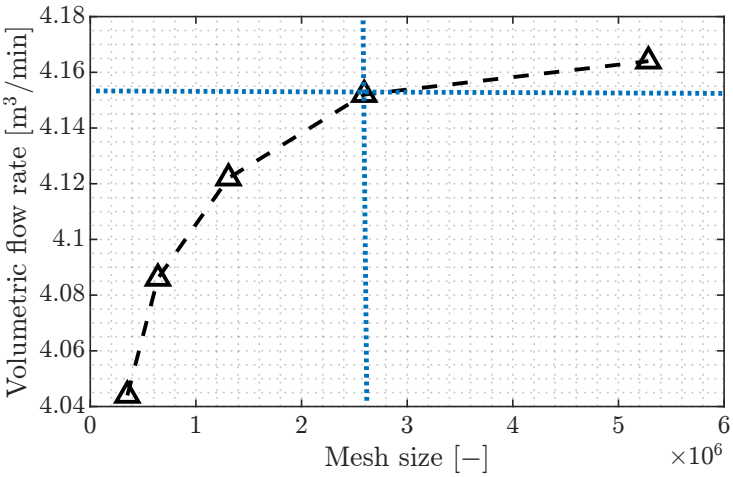

Figure 5.4: Results of the grid independence analysis.

5.5 Results and discussion

5.5.1 Model validation

The ROM's predictions were compared with CFD simulations and experimental data. Figure 5.6 (a) presents a comparison of the fan P-Q curve among experiments, manufacturer-provided reference data, CFD results using large eddy simulations (LES) from [20], CFD

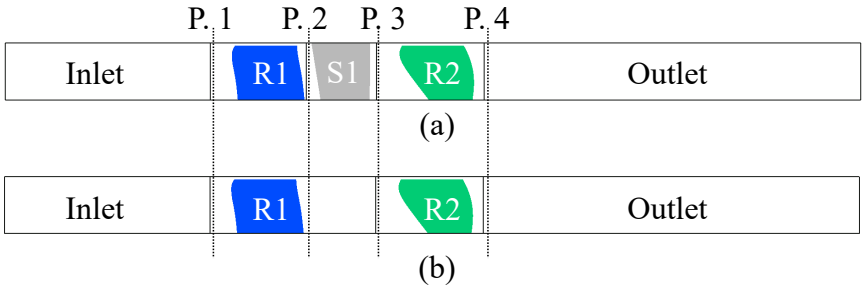

Figure 5.5: Meridional view of the computational domain (a) with stator and (b) without stator. P. 1 – P. 4 indicate the analysed planes, slightly offset from the interface planes.

RANS results, and ROM predictions. The CFD RANS results exhibit good agreement with experimental data under normal working conditions ($P \lesssim 120$ Pa). However, in the stall region ($P > 120$ Pa), where highly unsteady flows occur, the RANS-based CFD method encounters convergence issues. The high-fidelity LES model is capable of predicting transient features in the stall region [20]. Similar to the validation results conducted for single impeller fans in [31], the proposed ROM provides reasonably accurate predictions of the P-Q curve under normal working conditions, but its accuracy diminishes when predicting the stall region. Compared to the reference data, the root-mean-square error of ROM predictions, normalised with respect to the maximum pressure (NRMSE), for the normal working region and stall region are 4.6% and 13.2%, respectively.

The comparison of fan efficiency curves between CFD and ROM results is shown in Fig. 5.6 (b), demonstrating that the ROM captures the efficiency trend reasonably.

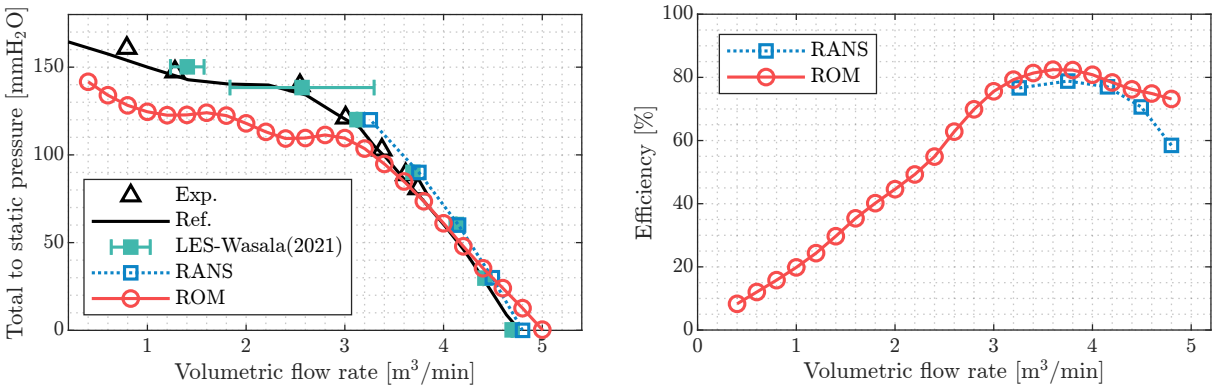

Figure 5.6: The result comparisons of (a) fan P-Q curve and (b) efficiency curve obtained from different sources at the speed of $N_1 = 14200$ r/min and $N_2 = 15000$ r/min.

5.5.2 Effect of stator

Figure 5.7 (a) illustrates a comparison of the P-Q curves with and without the stator, as predicted by RANS and ROM, respectively. According to the RANS results, the overall

effect of the stator on this test fan is found to be insignificant. The P-Q curves exhibit a near-identical behaviour at pressures below 60 mmH_2O. In the pressure range of 60–120 mmH_2O, the case without the stator exhibits slightly higher flow rates. The ROM predictions also follow a similar trend under normal working conditions. However, interestingly, the ROM predictions indicate that the case with the stator performs better in the stall region. This observation needs further investigation, as the current RANS-based CFD model has not successfully predicted fan stall phenomena.

In Fig. 5.7 (b), a comparison of the averaged swirl velocity upstream of the rear rotor is presented for cases with and without the stator. Notably, the presence of the stator induces alterations in the swirl velocity across most conditions. This type of stator exhibits more pronounced effects on swirl flow at low flow rate (high backpressure) conditions. The ROM effectively captures the averaged swirl velocity both in the presence and absence of the stator, as shown in Fig. 5.7 (b). In the scenario with the stator, while some deviations become more pronounced at lower flow rates, it appears that the ROM developed for the stator, based on assumption 3, effectively captures the declining trend of the averaged swirl velocity. However, considering the potential influence of wall effects from the hub and shroud on flow distribution, there is a suspicion that the ROM may not fully capture the radial distribution of the swirl velocity.

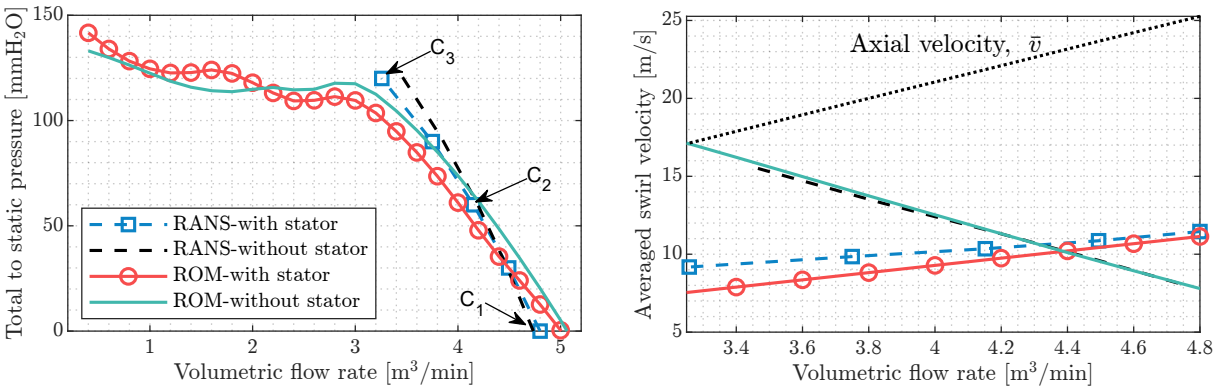

Figure 5.7: The result comparisons of (a) fan P-Q curves and (b) swirl velocity distributions in P. 3, in the presence and absence of stator at the speed of N_1 = 14200 r/min and N_2 = 15000 r/min. $C_1 - C_3$ indicate three typical working conditions in (a) and the averaged axial velocity $\bar{v}$ (·····) was shown in (b).

5.5.3 Effect of radial flow

The key assumption of this ROM is that the influence of 3D radial flow effects is negligible. To assess the validity of this assumption across different normal working conditions, the radial velocity distribution was analysed. Contours depicting the circumferentially averaged radial velocity in meridional view were generated for three

distinct backpressure cases (P = 0, 60, 120 mmH$_2$O), as illustrated in Fig 5.8. The analysis clearly reveals the presence of radial velocity components in all three pressure cases.

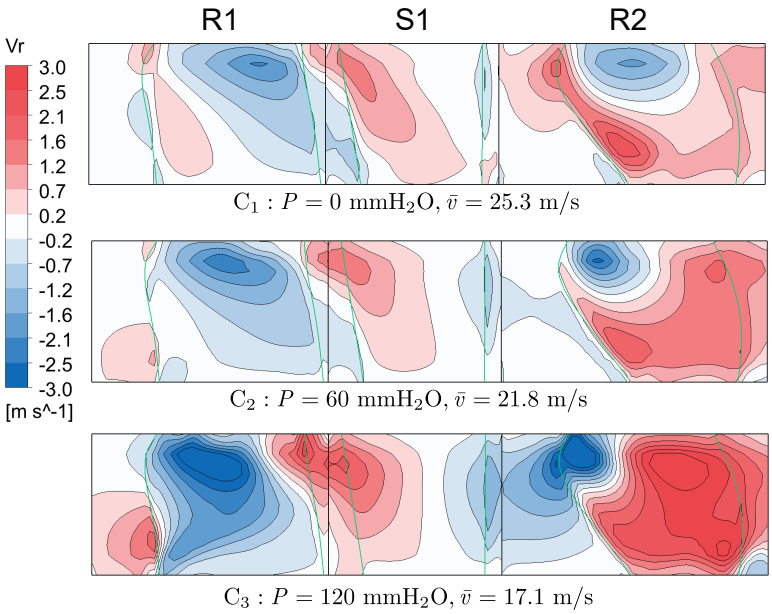

Figure 5.8: The contour of radial velocity distribution of R1, S1 and R2 domain in meridional view. Positive radial velocity is defined as pointing from the hub to the shroud, and vice versa. The blade profiles are represented by the green curves.

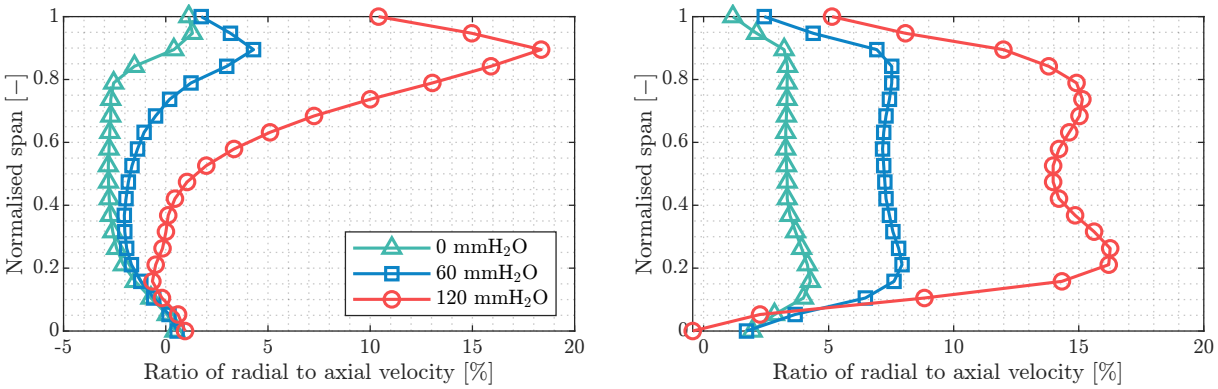

Figure 5.9: The radial velocity distribution from hub to shroud of (a) P. 2 near R1 (b) P. 4 near R2 at three different pressures. Span was normalised based on $(r - r_{hub})/(r_{shroud} - r_{hub})$ and ratio of radial to axial velocity was obtained by $v_r/\bar{v}$.

The radial velocity distributions downstream of the front rotor (P. 2) and rear rotor (P. 4) relative to their axial components $\bar{v}$ are plotted in Fig. 5.9 at three different pressure conditions (P = 0, 60, 120 mmH$_2$O). The averaged ratios of radial components relative to their axial components $\bar{v}$ were calculated. For the front rotor, these ratios are -1.6%, -0.2%, and 5.1%, respectively, while for the rear rotor, they are 3.2%, 6.5%, and 12.1%, respectively. Generally, the impact of radial velocity becomes more prominent with

increasing backpressure, and the rear rotor exhibits a higher radial velocity effect. To account for the influence of radial flow in the ROM predictions, the ratios of the rear fan (*i.e.* 3.2%, 6.5%, and 12.1%) were applied as a confidence range to correct the P-Q in the normal working conditions. Since radial flow information in the stall region is absent in the current CFD study, an arbitrary range of 20% was adopted. For the sake of simplicity, the confidence range percentages were interpolated based on flow rate, and then were incorporated into the uncertainties of the pressure predictions. The ROM's confidence range is illustrated in Fig. 5.10.

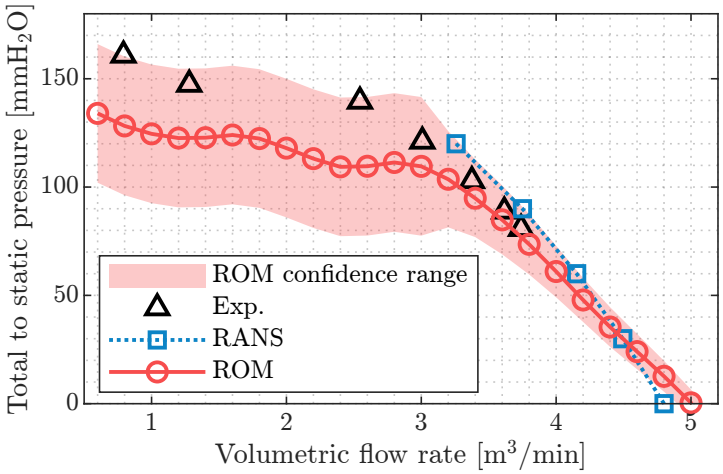

Figure 5.10: ROM prediction with confidence range incorporating uncertainties stemming from the radial flow effect, at the speed of N_1 = 14200 r/min and N_2 = 15000 r/min.

5.5.4 Limitations

The main focus of this study revolves around small-sized electronics cooling fans characterised by moderate solidity (0.7 – 1) and Reynolds numbers below 3×10^5. As highlighted earlier, the developed ROM does not account for complex 3D flow phenomena like radial flow and wall effects. Moreover, its predictive abilities are limited when it comes to the stall region. The current investigation also does not incorporate blade sweep effects. Additionally, it is important to note that the precision of the numerical airfoil analysis code XFOIL depends on high-quality airfoil coordinates. The present study does not account for fan blade transition effects. Nevertheless, it is worth noting that the XFOIL software has the capability to predict the natural and forced transition of airfoils using the e^N method [97]. This aspect could be considered for further exploration in future investigations.

5.6 Summary

This study extended and validated a reduced-order model (ROM) for the efficient analysis of the aerodynamic performance of dual impeller counter-rotating (CR) fans commonly employed in data centre systems. Based on the analysis conducted for a representative CR fan, the following conclusions can be drawn:

- The ROM predictions exhibit an error of 4.6% in the normal working region and 13.2% in the stall region.
- The presence of the stator has negligible impact on the P-Q curve prediction in the normal working conditions for this test fan.
- The presence of significant 3D radial flows can diminish the accuracy of this ROM.

Overall, the extended ROM demonstrated the capability to reasonably predict fan aerodynamic characteristics, all while demanding minimal computational resources.

The work in this chapter shows the potential of the ROM approach for efficiently analysing CR fans, building on the ROM for single impeller fans discussed in Chapter 4. However, this study also highlights the ROM's limitations, particularly in handling 3D radial flows and predicting performance in the stall region. Additionally, the ROM is limited to low-to-moderate solidity fans with Reynolds numbers below 3×10^5, due to the assumptions of the integrated vortex panel method solver XFOIL [97], which overlooks cascade effects. Consequently, the next chapter (*i.e.*, Chapter 6) will focus on developing a more advanced panel method solver to address these limitations.

Chapter 6

Development and Assessment of an Inviscid Source Vortex Panel Method for Low-Reynolds Number Airfoil Cascades

As the third chapter of Part II on reduced-order modelling for predicting the aerodynamic performance of electronics cooling fans, this chapter [1] presents the development and assessment of an inviscid source vortex panel method (SVPM) for low-Reynolds number airfoil cascades. In chapter 4 and chapter 5, the vortex panel method XFOIL was used as the 2D airfoil solver, assuming low solidity. This assumption holds for most axial fan cases investigated. However, for high solidity cases where the solidity exceeds unity, the XFOIL solver may lack accuracy. Consequently, the SVPM is developed based on potential flow theory, providing a computationally efficient framework for analysing the interaction between multiple blades. The accuracy and limitations of the proposed methodology are thoroughly assessed through comprehensive validation against available experimental data. This chapter extends the ROM for aerodynamic performance prediction of axial fans, offering a more robust and accurate method for high solidity cases.

This chapter is structured as follows: Section 6.1 provides an overview of the research topic, followed by the proposed analytical method in Section 6.2. The results and discussion are presented in Section 6.3, and conclusions are drawn in Section 6.4. This chapter finalises the ROM development for the aerodynamics of axial fans, laying the groundwork for the subsequent chapter on the ROM for aeroacoustic performance prediction of axial fans.

[1] This chapter is based on the published **conference paper** [33]: W. Zhao, S. Wasala, and T. Persoons, "Development and assessment of an inviscid source vortex panel method for low-Reynolds number airfoil cascades," in AIAA SCITECH 2024 Forum, Orlando, Florida, AIAA 2024-2507, 2024.

Abstract

In this study, a source vortex panel method (SVPM) is developed for 2-D airfoil flows in cascade based on the potential flow theory. The accuracy and limitations of the proposed methodology are assessed through comprehensive validation against available experimental data. Interference factors due to the cascade effect are derived using this inviscid approach, and employed to adjust the force information obtained from isolated airfoils. The SVPM demonstrates good predictions for the lift and pressure coefficients of 2-D cascades with Reynolds numbers exceeding 1.84×10^5, turbulence levels over around 2.5%, and low-to-moderate angles of attack. The interference factors also effectively modify lift coefficients from isolated airfoils for low angle of attack cases. The results provide insights into applying a potential flow method to low-Reynolds number airfoil cascades, facilitating the design and optimisation of small-scaled axial fans.

6.1 Introduction

Small-scaled axial flow fans have attracted considerable attention for their widespread use in electronics cooling systems [5] and their growing application in small unmanned aerial vehicles (UAVs) [235]. Small axial cooling fans are preferred in electronics applications due to its reliability and cost-effectiveness for heat dissipation. Similarly, in the realm of UAVs, electric ducted fans offer advantages such as increased efficiency, enhanced safety, and reduced noise [236]. Designing and optimising fan blades is a complex and computationally demanding process [48]. Therefore, utilising a 2-D airfoil flow in a linear cascade provides a simplified representation for fundamental aerodynamic analysis in fan studies. This approach aids in predicting blade performance and optimising design.

Low-Reynolds number flows in small axial fans present significant challenges for accurate performance prediction. The small axial fans typically feature multiple blades operating at chord Reynolds numbers of $1 \times 10^4 < Re < 3 \times 10^5$ [32]. Such low-Reynolds number flows, characterised by reduced fluid velocities and increased viscous effects, present significant challenges in accurately predicting the aerodynamic behavior [62, 237]. At these low Reynolds numbers, laminar to turbulent transition phenomena play a crucial role, further complicating flow characteristics. The effect of Reynolds number on linear cascade flow has been experimentally investigated in several early studies [238, 239]. The transition from laminar to turbulent flow depends on various factors, including inflow turbulence level, surface roughness, pressure gradients, and boundary layer characteristics, making it challenging to capture the flow physics accurately [240]. Additionally, the interaction between viscous and inviscid

flow regions becomes intricate, necessitating the consideration of both viscous and inviscid effects for accurate predictions.

The development and assessment of efficient computational methods for the complexities of low-Reynolds number flow are crucial for designing and optimising airfoil cascades. High-fidelity computational fluid dynamics (CFD) methods, such as large eddy simulation (LES), relying on solving the Navier-Stokes equations, are considered viable for capturing laminar-to-turbulent transition and resolving near-wall viscous flow structures [241]. However, the high computational cost associated with resolving fine viscous flow details limits the practicality of CFD for extensive parametric studies and design optimisation [20, 31]. The panel method based on potential flow theory offers an alternative for the fast analysis of airfoil cascades flow, albeit with limitations in fully capturing three-dimensional flow phenomena. This method, utilising a distribution of source and vortex singularities and discretizing the airfoil surface into panels, provides a computationally efficient framework. Within the context of cascade airfoils, Howell [242] employed a conformal transformation technique to map a linear cascade onto an S-shaped closed contour, and subsequently utilised two or more Joukowski transformations to further deform the S-shaped contour into an irregular circle. Building upon Howell's work, Thwaites [243] employed the same mapping function to investigate the flow characteristics of cascades. In a related development, Lewis [244] introduced the vortex element method, discretizing the blade surface into a series of infinitesimal singularities forming an infinite array. Bhimarasetty *et al.* [245] presented a combined approach that integrated Howell's conformal mapping with the vortex panel method developed by Kuethe and Chow [246]. Recently, Baddoo *et al.* [247, 248] developed an analytical solution to describe the potential flow through a cascade composed of thin airfoils.

While there have been numerical and analytical studies on solving the potential flow of airfoil cascades, there is limited documentation on the application of the more robust source vortex panel method (SVPM) in addressing these issues. Additionally, there is a lack of comprehensive analysis and conclusive findings regarding the limitations associated with applying potential flow theory to analyse complex flow under low-Reynolds number conditions.

This study aims to develop an SVPM for 2-D linear airfoils cascade and assess its suitability for low-Reynolds number flows. The paper presents the formulation and implementation details of this inviscid SVPM. The performance of the inviscid solver is assessed by comparing its predictions with extensive experimental data from the literature. Furthermore, the study analyses the interaction effects induced by the cascade using the inviscid method, and interference factors are employed to modify the lift coefficients obtained from isolated airfoils. The investigation highlights both the

strengths and limitations of the inviscid solver. While the inherent inviscid nature of the panel method restricts its applicability in cases dominated by viscous effects, making it challenging to precisely capture laminar-to-turbulent transition phenomena, it serves as a fundamental tool for initial design exploration and assessment. By emphasizing the inviscid solver in this paper, the objective is to establish a foundation for future inquiries that incorporate viscous effects, thereby enhancing the accuracy of predictions for low-Reynolds number cascade flows. The outcomes of this study provide valuable insights into the aerodynamic behavior of low-Reynolds number cascade flows, aiding in the design and optimisation of small fans for electronics cooling systems and UAV applications.

6.2 Methodology

The methodology in this study combines Howell's conformal mapping [242] technique with the source vortex panel method (SVPM) to analyse airfoil cascade flows. Howell's conformal mapping is utilised to transform the complex cascade configuration into a simplified single airfoil representation, while the SVPM discretizes the airfoil geometry and solves the potential flow equations. The transformed results are then converted back to the original cascade plane. By leveraging the computational efficiency of the panel method and considering the complex flow interaction between multiple blades, this methodology enables the prediction of flow properties such as pressure distribution and lift coefficients.

6.2.1 Conformal mapping

Howell's conformal mapping technique is a potent mathematical tool employed to simplify the complex cascade configuration. The conformal mapping function can be expressed as:

$$z_2 = \tanh \frac{\pi z_1}{h}, \tag{56}$$

where, h is the non-dimensional spacing ($h = s/c$). Figure 6.1 shows the schematic of this conformal mapping applied to an infinite linear cascade. This mathematical approach simplifies the periodic geometry of cascade configurations by transforming them into a single airfoil representation while preserving important flow characteristics.

Thwaites [243] and Bhimarasetty [245] demonstrated that upstream in the z_1-plane, the flow maps to $(-1, 0)$ in the z_2-plane, and downstream it maps to $(1, 0)$. Consequently, the incoming z_1-plane flow is represented in the z_2-plane by an upstream

point source ($Q_{\text{up}} = V_\infty h \cos\beta_1$) and an upstream point vortex ($\Gamma_{\text{up}} = V_\infty h \sin\beta_1$) at $(-1, 0)$. Exit conditions in the z_1-plane are modelled in the z_2-plane by a downstream sink ($Q_{\text{down}} = -V_\infty h \cos\beta_1$) and a vortex at $(+1, 0)$ with an unknown strength ($\Gamma_{\text{down}} = V_e h \sin\beta_2$).

This transformation is a fundamental step that enables subsequent analysis using the SVPM, effectively reducing the computational complexity associated with cascade geometry.

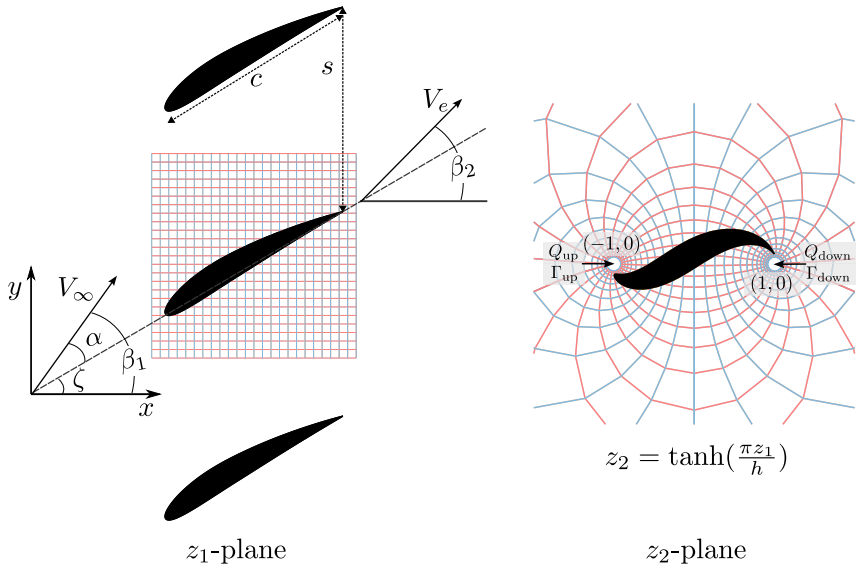

Figure 6.1: Schematic illustrating the concept of Howell's [242] conformal mapping technique.

6.2.2 Potential flow system equation

After applying Howell's conformal mapping, the transformed single airfoil geometry is discretized into a series of panels (m panels). Each panel (i) is assigned a source ($\phi_{s,i}$) and constant vortex term ($\phi_{v,i}$) to accurately represent the flow behavior around the airfoil. The SVPM can be then used to solve the potential flow equations within the transformed domain.

For incompressible potential flow, Laplace's equation is given by:

$$\nabla^2 \phi = 0. \tag{57}$$

For the mapped airfoil in z_2-plane, based on the principle of superposition, the scalar potential is expressed as:

$$\begin{aligned}\phi &= \underbrace{\phi_{s,\text{up}} + \phi_{v,\text{up}} + \phi_{s,\text{down}} + \phi_{v,\text{down}}}_{\text{flow}} + \underbrace{\sum_{i=1}^{m} \phi_{s,i} + \sum_{i=1}^{m} \phi_{v,i}}_{\text{panel}} \\ &= \phi_{\text{flow}} + \phi_{\text{panel}}.\end{aligned} \tag{58}$$

Here, the potential flow is classified into two terms: ϕ_{flow} and ϕ_{panel}. $\sum_{i=1}^{m} \phi_{s,i}$ and $\sum_{i=1}^{m} \phi_{v,i}$ from the panel term represent the summation of point sources and vortices for m panels in the z_2-plane. $\phi_{s,i}$ has a varied strength σ_i, and $\phi_{v,i}$ has a constant strength of γ. The strengths of the point sources ($\phi_{s,\text{up}}$, $\phi_{s,\text{down}}$) and vortices ($\phi_{v,\text{up}}$, $\phi_{v,\text{down}}$) for the flow term ϕ_{flow}, are given by:

$$\begin{aligned}Q_{\text{up}} &= V_\infty h \cos\beta_1, \\ \Gamma_{\text{up}} &= V_\infty h \sin\beta_1, \\ Q_{\text{down}} &= -V_\infty h \cos\beta_1, \\ \Gamma_{\text{down}} &= V_e h \sin\beta_2.\end{aligned}$$

As the strength of the downstream vortex Γ_{down} is unknown, an additional equation must be introduced to solve for its strength. Utilising the periodicity in airfoil cascades, the formulation for the strength of this unknown vortex was provided in [245], expressed as:

$$\Gamma_{\text{down}} = \Gamma - \Gamma_{\text{up}}. \tag{59}$$

Here, Γ represents the total circulation around one of the airfoils. It can be determined by summing the circulation of the vortex terms along the panels ($\Gamma = \sum_{i=1}^{m} \gamma l_i$).

With the potential flow equation in place, the SVPM can be developed to solve the flow. A typical panel distribution is illustrated in Fig. 6.2 and the definitions for a single i^{th} panel geometry are shown in Fig. 6.3. The transformed airfoil consists of m panels, starting from the point near the trailing edge at the pressure side and pointing to the leading edge. In total, the potential flow equation involves $m + 2$ unknowns, including m source strengths (σ_i), one constant vortex strength (γ), and one unknown downstream vortex strength (Γ_{down}). Since the term Γ_{down} can be obtained from Eq. 59, the remaining unknown quantities are $m + 1$.

The velocity potential for a single i^{th} panel is given by:

$$\phi\left(x_{c_i}, y_{c_i}\right) = \phi_{\text{flow}}\left(x_{c_i}, y_{c_i}\right) + \phi_{\text{panel}}\left(x_{c_i}, y_{c_i}\right). \tag{60}$$

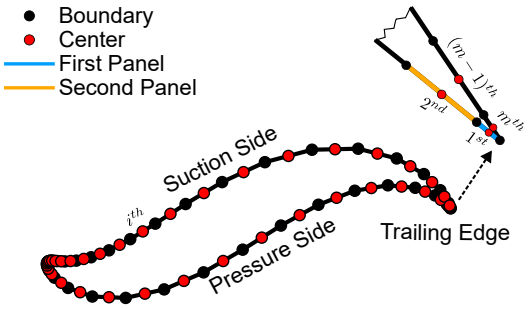

Figure 6.2: Panel distribution around a transformed airfoil.

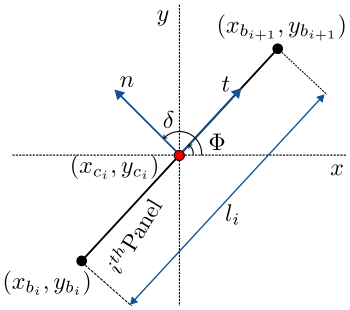

Figure 6.3: Geometry definitions of the i^{th} panel.

The potential flow is subject to the flow tangency boundary condition, enforced at the center of each panel, and expressed as:

$$0 = \mathbf{V} \cdot \mathbf{n} = \frac{\partial}{\partial n_i} \left\{ \phi \left(x_{c_i}, y_{c_i} \right) \right\}. \tag{61}$$

Here, $\mathbf{V}$ is the velocity vector, $\mathbf{n}$ is the unit normal vector at the center of panel i, and ϕ represents the potential function.

By substituting Eq. 60 into Eq. 61, the following expression can be formulated as:

$$\sum_{j=1, j\neq i}^{m} A_{p,ij}^{\ n} \sigma_j + \frac{\sigma_i}{2} - \sum_{j=1, j\neq i}^{m} B_{p,ij}^{\ n} \gamma + B_{s,i}^{\ n} \gamma = V k_{x,i} \sin \Phi_i - V k_{y,i} \cos \Phi_i. \tag{62}$$

The detailed derivations of Eq. 62 can be found in Appendix E.2. Equation 62 provides m linear equations, and an additional equation can be obtained by applying the Kutta condition. To satisfy the Kutta condition at the trailing edge, the pressure coefficient on the first panel (on the pressure surface, near the trailing edge) must equal that on the last panel (on the suction surface, near the trailing edge). This condition is expressed as:

$$V_{t_1} = -V_{t_m}. \tag{63}$$

Here, V_{t_i} is the tangential velocity, which is given by:

$$V_{t_i} = \frac{\partial}{\partial t_i} \left(\phi \left(x_{c_i}, y_{c_i} \right) \right)$$

Appendix E provides a detailed derivation that applies Kutta's condition. By incorporating the flow tangency boundary condition (Eq. 61) and the Kutta condition (Eq. 63), a linear system of equations is derived, detailed in Appendix E. The final linear equations can be expressed as:

$$\mathbf{A}\begin{bmatrix}\boldsymbol{\sigma}\\ \gamma\end{bmatrix} = \mathbf{b}. \tag{64}$$

The matrix $\mathbf{A}$, with dimensions $(m+1)\times(m+1)$, consists of three blocks: a $(m+1)\times m$ source matrix, a $m\times 1$ vortex array γ for each panel, and a $1\times(m+1)$ Kutta array representing the Kutta condition. $\boldsymbol{\sigma}$ is a $m\times 1$ source array, and γ is a 1×1 constant vortex. Complete formulations for the matrices $\mathbf{A}$ and $\mathbf{b}$ can be found in the appendix E.

6.2.3 Velocity and pressure transformation

Once the potential flow solutions are obtained in the transformed domain, they are converted back to the original cascade plane using the inverse of Howell's conformal mapping. The inverse mapping ensures that the computed results are transformed back to their original coordinates, providing accurate predictions for the cascade system.

The velocity transformation is given by:

$$\begin{aligned} u_1 - iv_1 &= (u_2 - iv_2)\frac{dz_2}{dz_1} \\ &= (u_2 - iv_2)\frac{\pi}{h}\frac{1}{\cosh^2(\text{arctanh}z_2)}. \end{aligned} \tag{65}$$

The pressure coefficient at the center of i^{th} panel is formulated as:

$$C_{p_i} = 1 - \left(\frac{V_{t_i}}{V_\infty}\right)^2. \tag{66}$$

Finally, the lift coefficient can be written as:

$$C_l = \frac{\Gamma}{\frac{1}{2}V_\infty c} \tag{67}$$

Here, the lift is given by the Kutta-Joukowski theorem:

$$L = \rho\Gamma V_\infty \tag{68}$$

6.3 Results

In this section, results computed by the source vortex panel method (SVPM) are compared with experimental data acquired from relevant low-Reynolds number and low-Mach number flow conditions outlined in [239, 249–251]. Quantitative evaluations are conducted to assess errors and discrepancies between predicted flow properties and experimental measurements.

The accuracy of the SVPM is first evaluated by comparing it to the exact solution of the potential flow in a derived cascade, as outlined by Gostelow in [252]. Figure 6.4 illustrates the airfoil profile and the corresponding theoretical pressure distribution of this cascade. The SVPM exhibits excellent agreement with the theoretical calculations for this specific cascade, showing only a slight discrepancy of 0.39° in the outlet flow angle. This emphasizes the method's effectiveness, demonstrating its ability to provide high accuracy with minimal computational effort, approximately 10 seconds per computation.

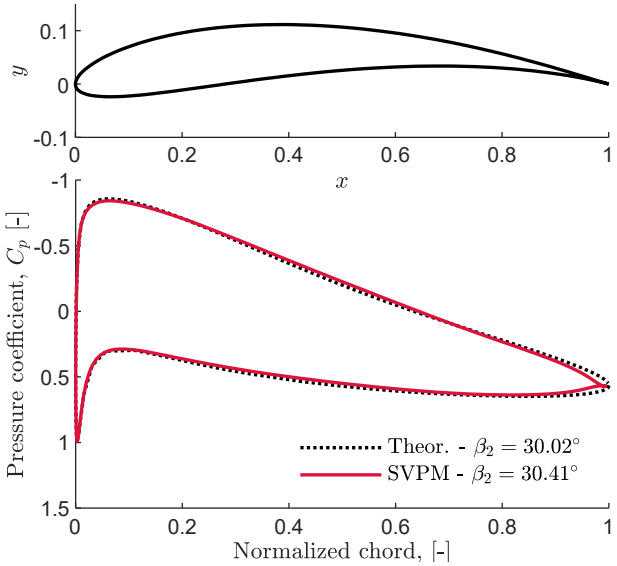

Figure 6.4: Validation of SVPM pressure coefficients against theoretical results in [252]. The airfoil profile and pressure distribution of a theoretical cascade are characterised by $\alpha = 16°$, $\beta_1 = 53.5°$, and $\sigma_c = 1.01$.

A summary of selected experimental validation cases for low-Reynolds number cascades is tabulated in Table 6.1. This selection covers various airfoil profiles with solidity ranging of 0.5 to 1.0 at a Mach number below 0.3, representative of small axial fans for electronics cooling applications. Validations are performed at Reynolds numbers within the range $0.5\times10^5 \leq Re \leq 3\times10^5$ due to the limited availability of experimental data for cascade flows. The chosen angles of attack range from 0° to 16.5°. The airfoil profiles selected are from the National Advisory Committee for Aeronautics (NACA) 65 series and the National Gas Turbine Establishment (NGTE) C4 series. Airfoil co-

Table 6.1: Test cases for low-Reynolds number cascade experiments.

Case	Airfoil	Shape	σ_c [-]	Re [-]	α[°]	β_1[°]	Ma [-]	I [%]	Data source
1	NACA 0010	Symmetric	1.00	3×10^5	10	10	0.25	-	Ref. [249]
2	NACA 65-410	Asymmetric	0.75	2.45×10^5	0	45	0.08	-	Ref. [250]
3	NACA 65-410	Asymmetric	0.75	2.45×10^5	6.3	45	0.08	-	Ref. [250]
4	NACA 65-410	Asymmetric	0.75	2.45×10^5	14	45	0.08	-	Ref. [250]
5	NACA 65-410	Asymmetric	0.50	2.45×10^5	5.8	45	0.08	-	Ref. [250]
6	NACA 65-410	Asymmetric	1.00	2.45×10^5	7	45	0.08	-	Ref. [250]
7	NACA 65-(12)10	Asymmetric	1.00	2.8×10^5	13.1	30	≈ 0.10	0.4	Ref. [251]
8	NGTE 10C4/30C50	Asymmetric	1.00	1.84×10^5	16.5	52.5	≈ 0.06	0.28	Ref. [239]
9	NGTE 10C4/30C50	Asymmetric	1.00	0.82×10^5	16.5	52.5	≈ 0.06	0.28	Ref. [239]
10	NGTE 10C4/30C50	Asymmetric	1.00	2×10^5	15.0	51	≈ 0.06	2.68	Ref. [239]
11	NGTE 10C4/30C50	Asymmetric	1.00	0.5×10^5	15.0	51	≈ 0.06	2.68	Ref. [239]

ordinates for NACA 65-(12)10 and NGTE 10C4/30C50 were sourced from [251], while coordinates for NACA 0010 and NACA 65-410 were obtained from [253].

The coefficient of pressure predicted by the SVPM is validated against experimental data. To align with the distinct pressure coefficient definition of the NACA reports [250, 251], computed results were adjusted to conform to this definition, namely $1 - C_p$ for cases 2–7. Figure 6.5 illustrates comparison plots of the pressure coefficient for these cases. In Fig. 6.5 (a) and (i), the y-axis direction is reversed to enhance differentiation between the airfoil's pressure and suction sides. Consequently, for all sub-figures, results for the suction side are depicted by the upper curves, and vice versa.

In general, predicted pressure distributions align well with experimental data for cases with Reynolds numbers above 1.84×10^5, with a more accurate match observed for cases at low-to-moderate angles of attack. At low Reynolds numbers and with low turbulence intensity, airfoils in cascade are more susceptible to viscous effects and prone to laminar flow separation. This phenomenon has been experimentally investigated in several early studies [238, 239]. Research on compressor cascades as documented in [238, 254, 255], suggests that the critical chord Reynolds number is around 1×10^5 to 2×10^5, and the critical turbulence intensity is approximately 2.5%. These studies indicate that separation bubbles occur when both the Reynolds number and turbulence intensity fall below these critical values, resulting in reduced cascade performance.

A comparison of pressure distributions across a range of Reynolds numbers at various turbulence levels for a NGTE 10C4/30C50 profile is depicted in Fig. 6.5 (h) and (i). At relatively high Reynolds numbers (1.84×10^5 and 2.0×10^5), no separation bubble is evident, and the predicted pressure coefficients align well with experiments. However, at a Reynolds number of 0.82×10^5 with a turbulence level of 0.28%, a distinct laminar separation bubble is observed on the suction side at around 50% to 75% chord of the airfoil, as shown in Fig. 6.5 (h). Conversely, with a higher turbulence level of 2.68%

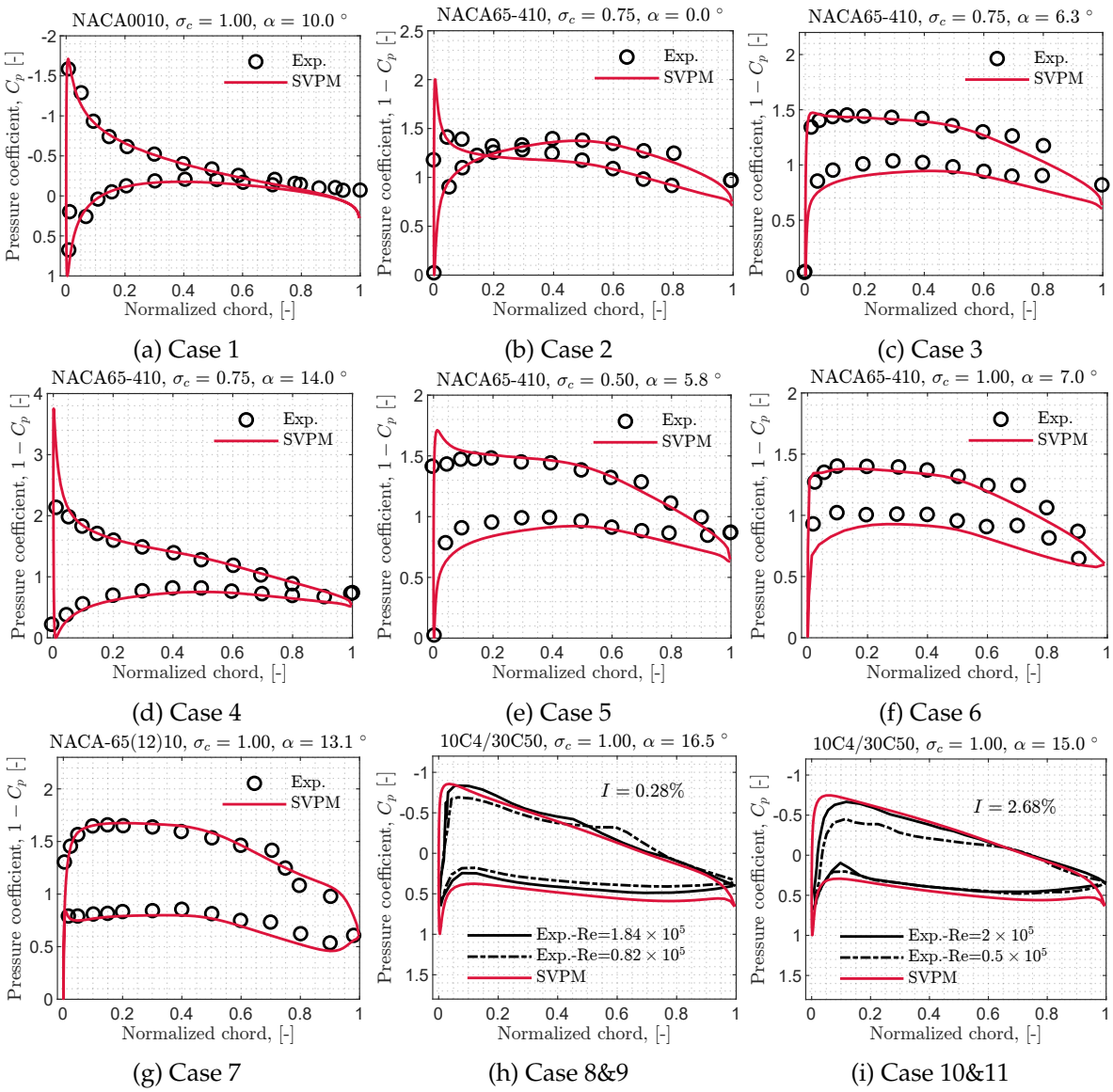

(a) Case 1 (b) Case 2 (c) Case 3

(d) Case 4 (e) Case 5 (f) Case 6

(g) Case 7 (h) Case 8&9 (i) Case 10&11

Figure 6.5: Comparison of the pressure coefficients between experimental data [239, 249–251] and SVPM predictions for eleven different cascade cases as outlined in Table 6.1.

at a Reynolds number of 0.5×10^5, no significant separation bubble is observed, and once again, the predicted pressure coefficients hold for this case. The critical Reynolds number and turbulence intensity serve as a reference for the applicable range of the developed inviscid solver. Beyond this range, more accurate methods are required to solve the boundary layer flow.

Figure 6.6 presents a comparison of the lift coefficients (C_l) from experimental data in [250] and SVPM predictions at three different solidities for a NACA 65-410 profile. The normalised root-mean-square error (NRMSE) is used to assess the errors between

predictions and experiments. The NRMSE is defined as:

$$E = \sqrt{\frac{1}{n}\sum_{i=1}^{n} |C_{l'_{o,i}} - C_{l'_{p,i}}|^2}, \tag{69}$$

where $C_{l'_o}$ is the observed lift coefficient obtained from experiments, and $C_{l'_p}$ is the predicted data obtained from the SVPM model. These lift coefficients are normalised by the maximum lift coefficient, defined as $C_l = 1.5$.

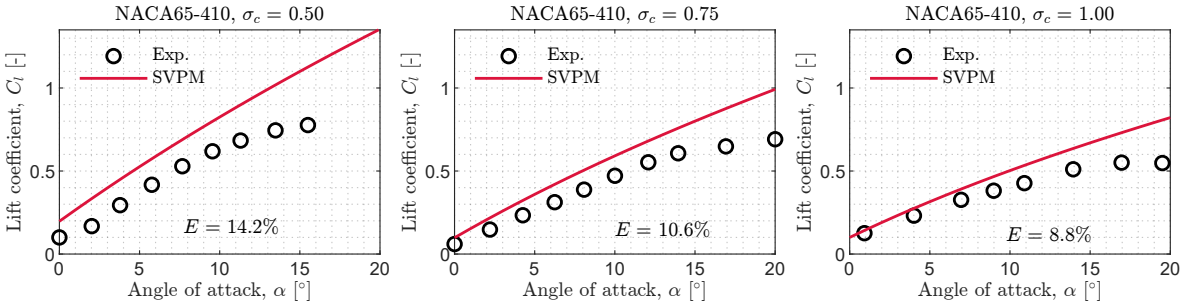

(a) $\sigma_c = 0.5$ (b) $\sigma_c = 0.75$ (c) $\sigma_c = 1$

Figure 6.6: Comparison of the lift coefficients between experimental data [250] and SVPM predictions at three different solidities ($\sigma_c = 0.5, 0.75$ and 1) with $Re = 2.45 \times 10^5$ and $\beta_1 = 45°$ for the NACA 65-410.

The SVPM method overpredicts the lift coefficients, which is expected as it does not account for viscous effects, as shown in Fig. 6.6. Despite this, it captures the trend well compared to experimental data at various solidities, particularly at angles of attack below 14° and high solidity cases. However, at higher angles of attack, where flow separation is prone to occur, and viscous effects lead to increased losses, the inviscid solver significantly overpredicts lift coefficients. The overall NRMSE for all cases remains below 14.2%, indicating an acceptable margin of error for preliminary designs.

To illustrate the effect due to the cascade nature, lift coefficients were compared between cascaded airfoils ($C_{l,casc}(\sigma_c, \alpha)$) and isolated airfoils ($C_{l,iosl}(\alpha)$), as shown in Fig. 6.7. Isolated airfoil lift coefficients were determined using XFOIL [97], employing both inviscid and viscous modes at the same Reynolds number. For a low solidity of 0.01, the inviscid SVPM method aligns well with XFOIL's inviscid prediction, as the cascade effect is minimal. As solidity increases, lift coefficients decrease. The interference factor (IF) is commonly used to quantify the effect due to adjacent airfoils. In terms of the lift coefficient, the interference factor k can be expressed as:

$$k(\sigma_c, \alpha) = \frac{C_{l,casc}(\sigma_c, \alpha)}{C_{l,iosl}(\alpha)}, \tag{70}$$

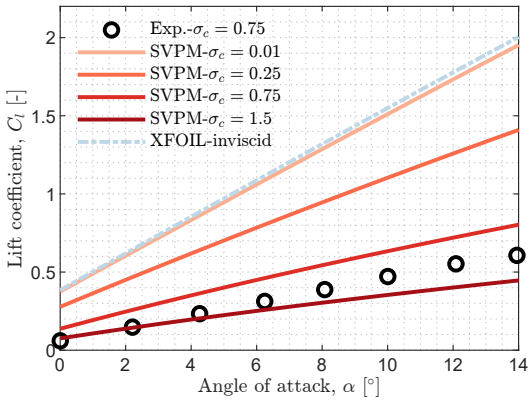

Figure 6.7: Effect of the solidity on lift coefficients for the NACA 65-410.

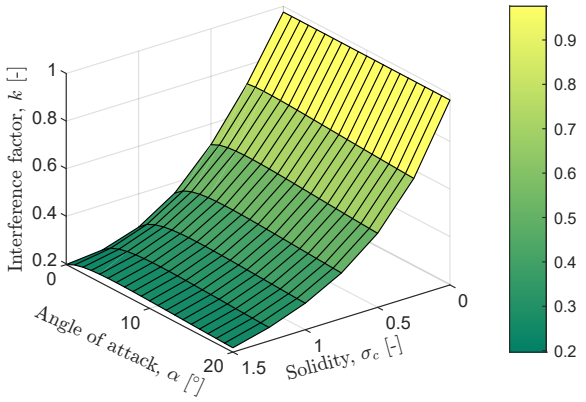

Figure 6.8: Interference factor for lift coefficients obtained using the inviscid method for the NACA 65-410.

where $C_{l,iosl}(\alpha)$ is computed by the XFOIL inviscid solver. The results of the interference factors calculated from the inviscid solver are presented in Fig. 6.8.

The interference factors derived from the inviscid solver were used to adjust isolated lift coefficients obtained by the XFOIL viscous solver. As presented in Fig. 6.9, the modified curve, in contrast to the original, shows a more pronounced agreement up to angles of attack of 10°. Using these modified lift coefficients, XFOIL was reapplied to determine corresponding pressure coefficients. Figure 6.10 compares pressure coefficients using the modification procedures for a NACA 65-410 airfoil with a solidity of 0.75 and an angle of attack of 6.3°. The presence of the cascade induces a reduction in the lift coefficient, akin to a decrease in the angle of attack for an isolated airfoil. With the modified lift coefficient, a pre-generated lookup table for isolated airfoil lift coefficients helps establish the effective angle of attack. Subsequently, XFOIL generated the modified pressure coefficient based on this effective angle of attack. As shown in Fig. 6.10, the modified pressure coefficients align more favorably compared to those predicted for the isolated airfoil. This analysis suggests that modifying isolated 2-D lift coefficients using interference factors from inviscid flow theory is acceptable for cascades at low angles of attack.

Figures 6.11 and 6.12 present contour plots illustrating the pressure coefficient along with streamlines obtained through the SVPM for a NACA 65-410 airfoil at different angles of attack. These plots showcase the cascade's behavior at varying angles of attack, with a constant stagger angle in Fig. 6.11 and a constant inlet flow angle in Fig. 6.12. The visual representation emphasizes the method's effectiveness in resolving internal flow fields across diverse inflow conditions.

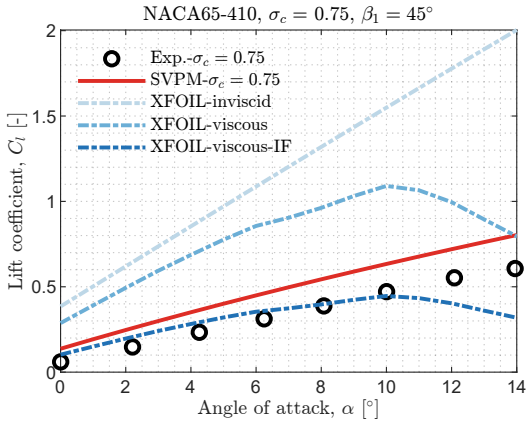

Figure 6.9: Comparison of lift coefficients for the NACA 65-410 airfoil involves the isolated airfoil with XFOIL, modified results using IF, a cascade with SVPM, and experimental data.

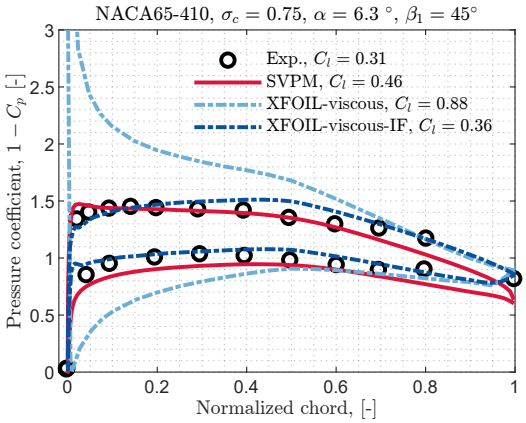

Figure 6.10: Comparison of pressure coefficients for the NACA 65-410 airfoil involves the isolated airfoil with XFOIL, modified results using IF, a cascade with SVPM, and experimental data.

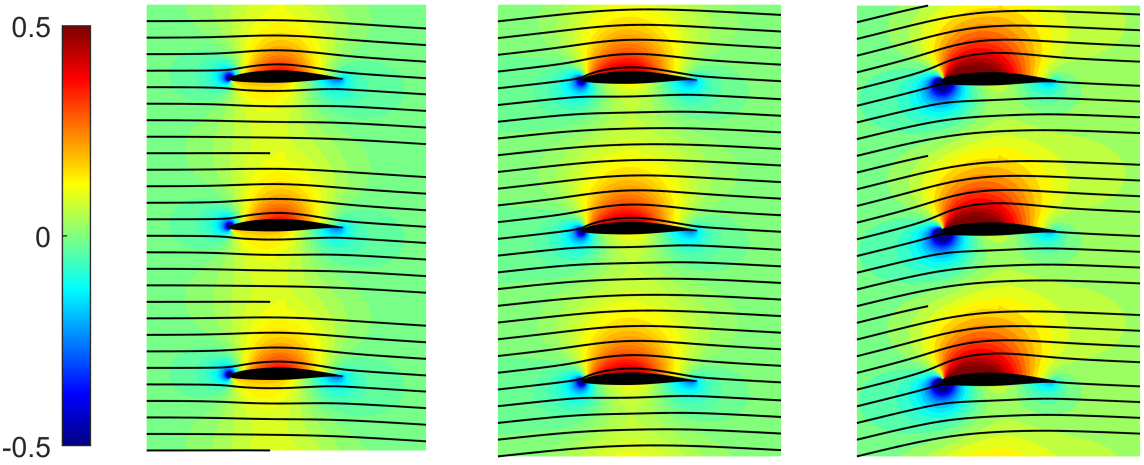

(a) $\alpha = 0°, \beta_1 = 0°$ (b) $\alpha = 6.3°, \beta_1 = 6.3°$ (c) $\alpha = 14°, \beta_1 = 14°$

Figure 6.11: Contour plots of the pressure coefficient C_p with streamlines for a NACA 65-410 airfoil at three different angles of attack ($\alpha = 0°, 6.3°$ and $14°$) with $\sigma_c = 0.75$, $Re = 2.45 \times 10^5$ and a constant stagger angle of $\zeta = 0°$.

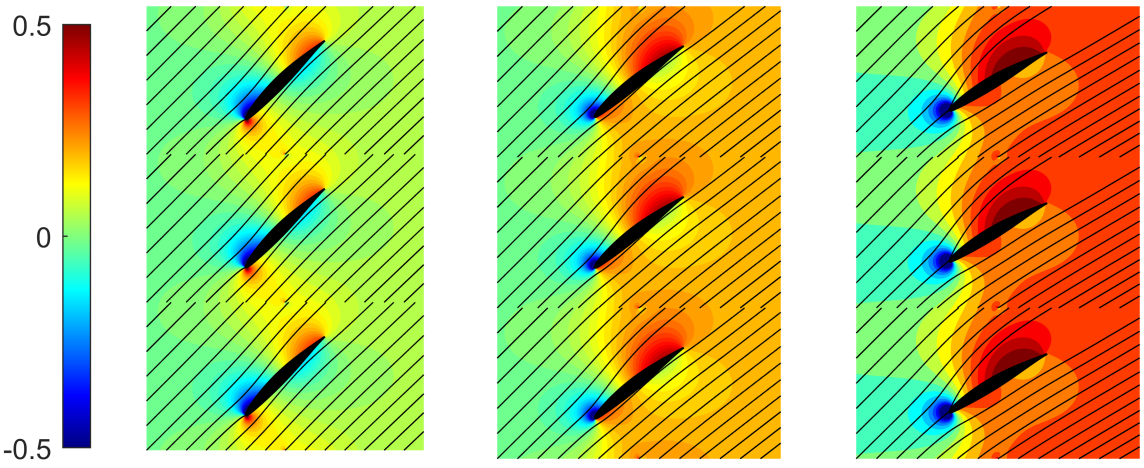

(a) $\alpha = 0°, \beta_1 = 45°$ (b) $\alpha = 6.3°, \beta_1 = 45°$ (c) $\alpha = 14°, \beta_1 = 45°$

Figure 6.12: Contour plots of the pressure coefficient C_p with streamlines for a NACA 65-410 airfoil at three different angles of attack ($\alpha = 0°, 6.3°$ and $14°$) with $\sigma_c = 0.75$, $Re = 2.45 \times 10^5$ and a constant inlet flow angle of $\beta_1 = 45°$.

6.4 Summary

In this study, a numerical methodology that combines Howell's conformal mapping [242] with the source vortex panel method (SVPM) was formulated for analysing potential flow in airfoil cascades. The reliability of the methodology was confirmed through validation against available experimental data, and the applicable range of this method was thoroughly assessed. The inviscid method was utilised to derive interference factors, which were then applied to modify the lift coefficients obtained from isolated airfoils. The following conclusions can be drawn:

- The SVPM demonstrates the ability to predict lift and pressure coefficients with engineering precision for cascade cases featuring Reynolds numbers above 1.84×10^5, turbulence levels exceeding 2.5%, and low-to-moderate angles of attack.
- The modified isolated 2-D lift coefficients, employing interference factors derived from the inviscid method, are considered suitable for low-to-moderate angles of attack in cascade configurations.

Overall, the developed SVPM efficiently resolved potential flow, capturing essential flow characteristics. The established applicable range for low-Reynolds number flows serves as a guideline for using this method. The methodology offers insights for the design and optimisation of cascade flows in electronics cooling systems and unmanned aerial vehicle (UAV) applications. Future work should concentrate on incorporating viscous effects and addressing laminar-to-turbulent transition for a more comprehensive analysis.

This chapter, along with Chapters 4 and 5 in Part II, comprehensively develops the

reduced-order modelling methodology for fan flows, addressing the effects of tip clearance, dual rotors, and cascades. Building on the aerodynamic ROM, the subsequent chapter will introduce the aeroacoustic ROM for predicting fan noise, encompassing both tonal and broadband noise components.

Chapter 7

Fast Prediction Methods for Broadband and Tonal Noise of Electronics-Cooling Axial Fans

As the final chapter of Part II on reduced-order modelling for predicting the aerodynamic performance of electronics cooling fans, this chapter [1] presents a cost-effective and efficient method for predicting the broadband and tonal noise generated by axial fans used in electronics cooling. Based on insights and data from large-eddy simulation (LES), experiments, and analytical methods, the reduced-order model (ROM) for fan noise prediction is developed.

This chapter is structured as follows: Section 7.1 introduces the topic of fan noise and its importance in engineering applications, highlighting the challenges in predicting fan noise and the need for accurate and efficient methods. Section 7.2 – 7.4 describes the methodology for predicting the broadband and tonal noise of axial fans, combining the blade element theory (BET) with Amiet's theory for broadband noise and Lowson's theory for tonal noise. The accuracy of various turbulence spectrum models and wall pressure spectrum (WPS) models is evaluated by comparing them with the LES data. Section 7.5 presents the results of the ROM for fan noise prediction, including validation against experimental data and LES data for a small-sized cooling fan. The predicted aerodynamic quantities and overall noise levels are compared with the experimental data and LES data, demonstrating the high accuracy and efficiency of the proposed method. Section 7.6 concludes the study and discusses the implications of the ROM for designing quieter and more efficient fan systems.

[1] This chapter is based on the **journal article** in review: W. Zhao, S. Wasala, T. Persoons, "Fast prediction of broadband and tonal noise of electronics-cooling axial fans," *Journal of Sound and Vibration*, in Review, JSV-D-25-00091, 2025.

Abstract

Axial fan noise is a critical issue in various cooling systems due to its impact on human health, the reliability of electronic components, and compliance with regulations. This study presents a cost-effective and efficient method for predicting the broadband and tonal noise generated by axial fans used in electronics cooling. The method combines the blade element theory (BET) with Amiet's theory for broadband noise and Lowson's theory for tonal noise. The accuracy of various turbulence spectrum models and wall pressure spectrum (WPS) models is evaluated by comparing them with large eddy simulation (LES) data. The predicted far-field noise is validated against experimental data and LES data for a small-sized cooling fan. Among the tested WPS models, all underestimated the wall pressure spectrum and far-field noise level when combined with Amiet's trailing-edge model. A modified version of Lee's WPS model was proposed, which showed the closest agreement with the LES data. The predicted aerodynamic quantities and overall noise levels exhibited good agreement with the experimental data, with deviations of 6.5% and 2.8 dB, respectively, demonstrating the high accuracy and efficiency of the proposed method. This comprehensive and efficient approach for predicting fan noise enables the design and optimisation of quieter and more efficient fan systems.

7.1 Introduction

Fan noise is a significant concern in various engineering applications, particularly in the aerospace [192], automotive [54], and electronics industries [36]. It not only affects the comfort and well-being of individuals but also has environmental and regulatory implications. In fan-cooled electronics, such as computers, servers, and data centers, fan noise poses a critical challenge due to the high rotational speeds and compact packaging of cooling fans. The noise generated by axial fans can impact human health, electronic component reliability, and regulatory compliance [20, 21]. Therefore, there is a growing need for effective methods to predict and mitigate fan noise in electronics cooling systems [5].

Predicting fan noise is complex and challenging due to the aerodynamic and aeroacoustic interactions in fan systems. Flow-induced noise, also known as aeroacoustic noise, is the primary source of fan noise. It can be categorized into two types: broadband noise and tonal noise. The noise characteristics of axial fans are highly dependent on fan geometry, operating conditions, and flow characteristics [47, 48]. A recent study on a single impeller fan [210] found that broadband noise of the fan is more pronounced during stall conditions, while tonal noise is dominant under normal operating conditions.

Under different operating conditions, the fan noise can vary significantly, emphasizing the importance of predicting both broadband and tonal noise for designing quieter and more efficient fan systems.

Various methods have been developed to predict fan noise in engineering applications, ranging from empirical models to coupled computational fluid dynamics (CFD)-computational aeroacoustics (CAA) simulations. Different noise prediction models require varying levels of flow field information. Moreau and Roger [79, 110, 201] reviewed state-of-the-art methods for predicting turbomachinery noise, highlighting their challenges and limitations. Lee *et al.* [53] presented a comprehensive review of trailing-edge noise prediction methods for airfoils. Empirical models are simple and easy to use but may have limited accuracy and applicability. One successful method is the BPM model proposed by Brooks, Pope, and Marcolini [52] for broadband noise prediction. The BPM model, based on measurements on the NACA 0012 airfoil, predicts airfoil noise using spectral scaling of various self-noise mechanisms. It has been widely used in the industry for initial noise estimations of airfoils, wings, and wind turbines [53]. For high-fidelity methods, direct numerical simulation (DNS) resolves all turbulence scales and calculates sound wave propagation but is limited to low-Reynolds number airfoil cases due to computational costs. Therefore, two viable pathways are commonly found for fan noise prediction: high-fidelity hybrid numerical simulations and low-cost analytical methods.

High-fidelity numerical simulations provide detailed flow features of the noise generation mechanisms but are computationally expensive. Compared to DNS, large eddy simulation (LES) is a more practical approach for predicting fan noise as it resolves large-scale turbulent structures and models small-scale turbulence. LES, coupled with the Ffowcs Williams-Hawkings (FW-H) acoustic analogy for free-field [104], has successfully predicted both broadband and tonal noise of axial fans [20, 42, 210]. LES can also be coupled with the infinite duct Goldstein's analogy for ducted fan noise prediction [256], which is more relevant to turbofan engine noise prediction [202]. However, albeit less so than DNS, LES is still computationally expensive and time-consuming. The typical simulation cost of electronics cooling fans can be at least $O(10^4)$ CPU core hours [20, 210], which may only be affordable for the final design step. They require detailed geometric models, high-quality meshes, and extensive computational resources, making them impractical for rapid design iterations and optimisation studies.

Analytical methods provide a cost-effective and efficient approach for predicting fan noise compared to high-fidelity numerical simulations. They also offer valuable insights by separately evaluating different noise sources, which can be challenging to isolate in numerical simulations. Amiet's theory, widely used for leading-edge noise [59] and trailing-edge noise [50], remains popular due to its simplicity and flexibility. It has been

applied to predict broadband noise in wind turbines [257], unmanned aerial vehicle (UAV) propellers [55], and cooling fans [114, 258]. The original Amiet's theory has been extended and modified to improve its accuracy and applicability. Roger and Moreau [51] extended Amiet's trailing-edge noise model [50] by considering the back-scattering effect, improving its accuracy for low-frequency noise. Grasso *et al.* [259] accounted for swept airfoils and further developed an analytical extension based on Amiet's method [50]. Lyu and Azarpeyvand [260] extended Amiet's leading-edge model [59] to include serrated leading edges.

To predict the broadband noise of rotating blades, Li and Lee [261] developed the in-house code UCD-QuietFly. They combined the blade element momentum method (BEMT), XFOIL [97], Lee's wall pressure spectrum (WPS) model [123], and Amiet's trailing-edge model [50]. The code accurately captured the trailing-edge noise against the measurement data. Alvarez *et al.* [262] developed a meshless Lagrangian solver based on the vortex particle method and incorporated the PSU-WOPWOP solver [107] to predict noise from a DJI9443 UAV rotor. The vortex particle method simulation was 140 times faster than Unsteady RANS while maintaining equivalent noise prediction performance. Casalino *et al.* [55] utilised a BEMT-based model along with multiple WPS models and Amiet's model to predict the noise of an UAV propeller (300 mm diameter). They found that all the WPS models, developed based on Goody's model, exhibited a similar trend. However, none of them accurately predicted the noise level for all experimental cases.

In the field of axial fans, Rozenberg *et al.* [114] conducted experiments on a low-speed axial fan (800 mm diameter) without a shroud. They used the measured WPS data as input for Amiet's model. By applying the strip theory with the measurement data, they found good agreement between the predicted and measured noise levels, especially for observer locations close to the rotor plane. Sanjosé *et al.* [117] extracted flow information for an automotive fan (380 mm diameter) from Reynolds-averaged Navier-Stokes (RANS) simulations. They combined this information with Rozenberg's WPS model [119] to calculate the wall pressure data. Zarri *et al.* [258] used a similar approach to predict the trailing-edge noise of a low-speed axial fan (380 mm) based on the RANS input. Zhao *et al.* [23] employed the blade element theory (BET) coupled with lifting-line theory, XFOIL [97], and six WPS models to predict the trailing-edge noise of a high-rotational-speed axial fan (80 mm diameter). The predicted noise showed a decent trend compared to the experimental data, although all WPS models combined with Amiet's model underestimated the noise level. A similar observation was made in [55] for the low-Reynolds number UAV propeller noise prediction.

The primary sources of tonal noise in axial fans are the asymmetric inlet-rotor interaction (IRI) and rotor-stator interaction (RSI). Zhao *et al.* [210] conducted a comprehensive

LES study on fans under various operating conditions and concluded that IRI and RSI contribute to unsteady forces on blades, resulting in tonal noise generation. Kemp and Sears' theory [263] can estimate the unsteady force due to rotor-stator interaction, but accurately modelling the combined IRI and RSI interactions requires high-fidelity CFD methods such as unsteady RANS and LES. Once the unsteady force is known, tonal noise can be predicted using the time domain FW-H solver or the frequency domain Lowson's model [129], which simplifies the rotating blade as a fluctuating point force in the FW-H equation. Huang [36] extended Lowson's model to account for contributions from thrust, torque, and radial force. The irregular inlet-rotor interaction, similar to the stator-rotor interaction, affects the noise. Tian *et al.* [74] confirmed that non-uniform inflow caused by the asymmetric inlet shape increases rotor surface pressure fluctuation and leads to increased tonal noise.

Lowson's model [129] makes several assumptions to simplify the analysis while maintaining reasonable accuracy. Firstly, it assumes sound propagation in a free field, neglecting any reflection or transmission at the blade rows or short casing. Secondly, a simplified point force model is employed to represent the forces acting on each blade, disregarding the effects of lifting line or surface. Lastly, the analysis concentrates on the acoustically far-field region, where sound waves can be treated as compact sources. These assumptions strike a balance between computational efficiency and capturing the essential physics of tonal noise generation. Despite its simplifications and assumptions, Lowson's model [129] remains a valuable tool for predicting tonal noise in axial fans.

While these analytical methods have been successfully applied to various fan systems, they have limitations when applied to smaller axial fans with higher solidity and lower Reynolds numbers. The existing models are often based on simplified assumptions and empirical correlations for larger wings and rotors, which may not accurately capture low-Reynolds number flows. Additionally, past studies have investigated broadband and tonal sources separately, lacking unified prediction methods that accurately predict both broadband and tonal noise in axial fans. Therefore, further investigation is needed to assess the validity and accuracy of these analytical methods for predicting broadband noise in smaller axial fans.

This work aims to develop and validate a fast and accurate method for predicting the broadband and tonal noise of axial fans used in electronics cooling. The method utilises a comprehensive analytical and semi-empirical approach, serving as a unified reduced-order model (ROM) for predicting both aerodynamic and aeroacoustic performance. The ROM incorporates a recently developed aerodynamic model [23, 31, 32], which combines the blade element theory, lifting line theory, and XFOIL [97], and accounts for the tip clearance effect. This model will be applied in the ROM for steady-state

prediction. To predict the noise radiation from the fan, the ROM will utilise Amiet's theory [50, 59] for broadband noise and Lowson's theory [129] for tonal noise. The accuracy of different turbulence spectrum models and wall pressure spectrum models will be checked by comparing with LES data [210]. Furthermore, the predicted far-field noise will be compared to experimental data and LES data to validate the acoustic method. Overall, this fully validated ROM will provide a cost-effective and efficient approach for predicting the broadband and tonal noise of axial fans, enabling the design and optimisation of quieter and more efficient fan systems.

7.2 Blade element theory for fan aerodynamics

This section uses a reduced-order method combining blade element theory (BET) with lifting-line theory, as detailed in Chapter 4. This approach provides a reliable framework for analysing the aerodynamic performance of axial fans. Figure 7.1 shows the BET, where each spanwise element of the fan blade is treated as a two-dimensional airfoil. The inflow schematic for a fan blade element is shown in Fig. 7.2, illustrating the velocity and force components essential for the analysis.

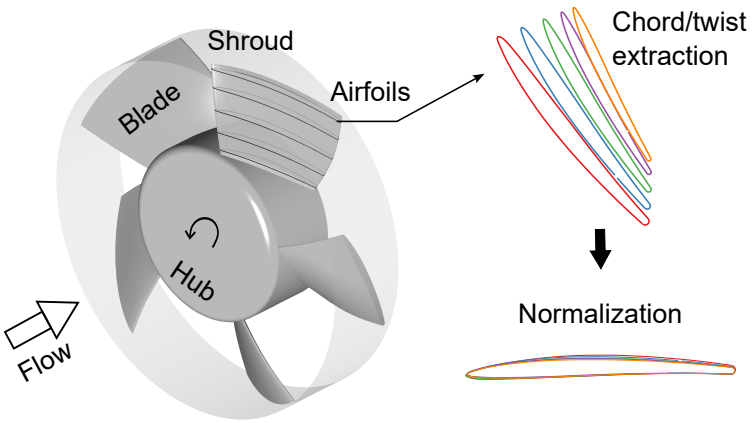

Figure 7.1: Schematic of the blade element theory for a fan blade, where each spanwise element is treated as a two-dimensional airfoil.

XFOIL [97], a widely-used vortex panel solver with viscous corrections, offers the capability to predict flow transition by employing the e^N method. The critical N_{crit} value plays a pivotal role in determining the lift coefficient and boundary layer properties, as it governs the transition from laminar to turbulent flow. However, Mack's correlation [264], which is commonly used to estimate N_{crit}, exhibits nonphysical behavior by yielding negative N_{crit} values for turbulence intensities exceeding 2.98%. To address this issue, Drela [98] proposed a modified e^N method that rectifies the correlation and establishes a robust relationship between the turbulence intensity I and the critical

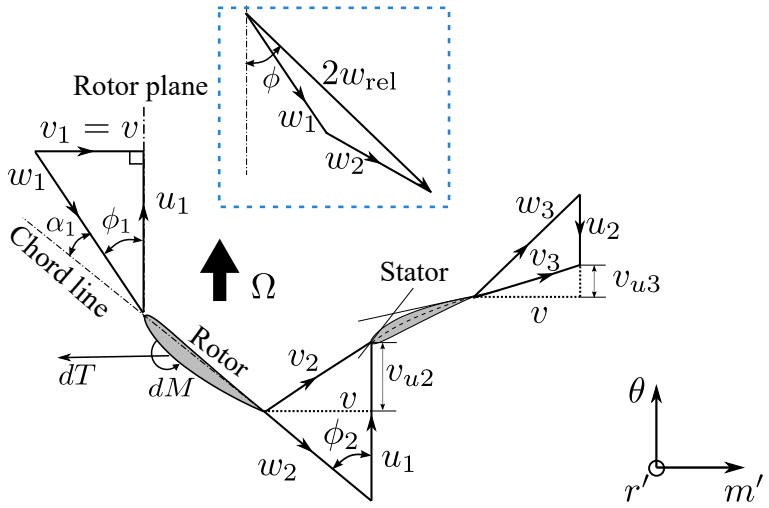

Figure 7.2: Velocity and force triangles for each blade element in a fan system. The coordinate system is defined in the airfoil frame, where m' and r' are normalized by the sectional radius r.

N_{crit}. The modified correlation adopted in this study is expressed as [98]:

$$\begin{aligned} I' &= 2.7 \tanh(I/2.7), \\ N_{crit}(I) &= -8.43 - 2.4 \ln\left(\frac{I'}{100}\right). \end{aligned} \tag{71}$$

Here, I represents the turbulence intensity in percentage. I' is the modified turbulence intensity. This modified value closely aligns with I when I is less than or equal to 2.7%, and is capped at 2.7% for turbulence intensities exceeding this threshold. By incorporating this modified e^N method, the analysis accounts for a wide range of flow conditions, enhancing the robustness and reliability of aerodynamic predictions.

7.3 Broadband noise prediction

The fan broadband noise is calculated using blade element theory (BET) combined with Amiet's theory for leading-edge noise [59] and trailing-edge noise [50]. This study only focuses on the broadband noise emitted by rotor blades, as rotor noise is more pronounced than stator noise in the fan system [210]. The leading-edge and trailing-edge noise are significant sources of broadband noise in the rotor blade, which will be modelled in the following sections. However, the broadband noise due to tip vortices and flow separation will not be modelled in this study due to the complexity of the flow field and limitations of the XFOIL solver.

Amiet's theory [50, 59] is widely used for predicting broadband noise in various applications, particularly for large span airfoils like wind turbine blades [257] and ring fans [117]. It has shown accuracy and reliability in these contexts. To enhance its

applicability, Roger and Moreau [51] proposed a back-scattering correction term for predicting trailing-edge noise, which significantly improves the model's accuracy for low-frequency noise from smaller blades. This corrected model has been extensively validated against experimental data for industrial ring fans [79, 117]. However, when considering electronics cooling axial fans, it is important to note that the blade aspect ratio is typically much smaller, around one, which is significantly lower than that of helicopter rotors and wind turbine blades. Although the correction made by Roger and Moreau [51] is taken into account in this study, the accuracy of Amiet's model for electronics cooling axial fans remains a subject of investigation. Therefore, it is crucial to thoroughly examine the applicability of Amiet's model in this specific context to ensure accurate and reliable predictions of broadband noise.

7.3.1 Coordinates transformation and Doppler effect

In order to predict the broadband noise using Amiet's theory [50, 59], it is essential to transform the observer locations from the global fan frame $\vec{x} = [x, y, z]^{\mathrm{T}}$ to the airfoil frame $\vec{x_a} = [x_a, y_a, z_a]^{\mathrm{T}}$ for each blade segment. A schematic of the observer location transformation is illustrated in Fig. 7.3. The airfoil frame has its origin at the leading edge of the airfoil, with the x_a, y_a, and z_a axes aligned with the chord line, span, and normal direction of the airfoil, respectively. The observer location in the airfoil frame can be expressed as:

$$\vec{x_a} = \mathbf{M}_\beta \mathbf{M}_\theta \left[\vec{x} + \mathbf{M_r}\right], \tag{72}$$

where $\mathbf{M}_\beta$, $\mathbf{M}_\theta$, and $\mathbf{M_r}$ are the transformation matrices for the twist angle β, azimuth angle of the observer θ, and radial distance r, respectively. These matrices are defined as:

$$\mathbf{M}_\beta = \begin{bmatrix} -\cos\beta & 0 & \sin\beta \\ 0 & 1 & 0 \\ -\sin\beta & 0 & -\cos\beta \end{bmatrix},$$

$$\mathbf{M}_\theta = \begin{bmatrix} \cos\theta & -\sin\theta & 0 \\ \sin\theta & \cos\theta & 0 \\ 0 & 0 & 1 \end{bmatrix}, \quad \mathbf{M_r} = \begin{bmatrix} -r\cos\theta \\ -r\sin\theta \\ 0 \end{bmatrix}.$$

Furthermore, it is crucial to consider the Doppler effect, which accounts for the change in frequency of a wave due to the relative motion between the observer and the sound source. The Doppler shift can be expressed as [265]:

$$\frac{\omega}{\omega_e} = 1 + \frac{\vec{M}_{a,\mathrm{SO}} \cdot \widehat{\mathbf{CO}}}{1 + (\vec{M}_{a,\mathrm{FO}} - \vec{M}_{a,\mathrm{SO}}) \cdot \widehat{\mathbf{CO}}}, \tag{73}$$

where ω is the frequency of the observer sound wave, ω_e is the emission frequency of the source sound wave, $M_{a,\mathrm{SO}}$ is the source Mach number, and $M_{a,\mathrm{FO}}$ is the freestream Mach number. For axial fans in a relatively large expansion space, the freestream velocity can be considered negligible [114], leading to a simplified expression of the Doppler factor:

$$\frac{\omega_e}{\omega} = 1 - \vec{M}_{a,\mathrm{SO}} \cdot \widehat{\mathbf{CO}}. \tag{74}$$

In Eq. 73, $\widehat{\mathbf{CO}}$ represents the unit vector from the convected noise source to the observer, given by:

$$\widehat{\mathbf{CO}} = \frac{\vec{x}_c - \vec{x}}{|\vec{x}_c - \vec{x}|}. \tag{75}$$

Here, $\vec{x}_c$ represents the coordinates of the convected noise source in the global frame, and $\vec{x}$ denotes the observer location in the global frame. In this study, we approximate the convected noise source as the center of each blade element ($\vec{x}_c = r[\cos\theta, \sin\theta, 0]^{\mathrm{T}}$) when the freestream Mach number is close to zero.

These transformations and considerations are applicable to any far-field observer location. For observers located in the plane normal to the rotor plane, a simplified version of the Doppler effect, as proposed by Rozenberg *et al.* [114], can be employed.

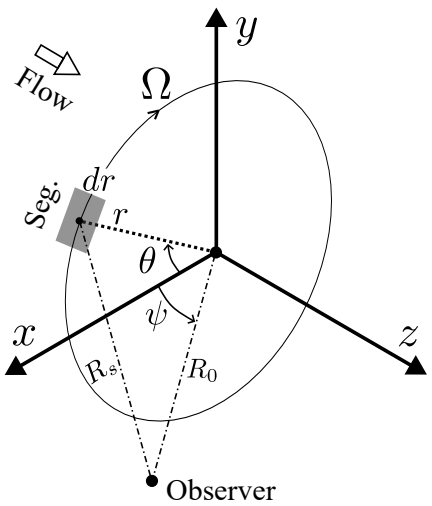

Figure 7.3: Coordinates transformation of the observer locations from the global frame to the airfoil frame.

7.3.2 Leading-edge noise prediction

Amiet's leading-edge model

The generation of leading-edge (LE) noise is attributed to the interaction between the turbulent inflow and the airfoil's leading edge. To predict the leading-edge noise,

Amiet's theory [59] is employed. The far-field acoustic power spectral density (PSD) emitted at mid-span is given by:

$$S_{pp,i}^{\mathrm{LE}}(\omega_e) = \left(\frac{\omega \rho c z_a}{2c_0\sigma^2}\right)^2 \pi w_{\mathrm{rel}} \frac{s}{2} |\mathcal{L}|^2 \Phi_{ww}(k_x, k_y), \tag{76}$$

where $\omega = 2\pi f$, c represents the chord length, c_0 is the speed of sound, s denotes the span length, $\sigma^2 = x_a^2 + \beta^2(y_a^2 + z_a^2)$, $\beta^2 = 1 - Ma^2$, and Ma represents the Mach number. The aeroacoustic transfer function $|\mathcal{L}|$ accounts for the airfoil's characteristics, while w_{rel} represents the relative velocity for the airfoil. The hydrodynamics wavenumbers in the chordwise and spanwise directions are denoted as k_x and k_y, respectively. $\Phi_{ww}(k_x, k_y)$ represents the two-dimensional turbulence spectrum, which will be discussed in Section 7.3.2. The origin of the coordinate system for Amiet's leading-edge model [59] is at the mid-chord of the airfoil, so that an offset of $-c/2$ is added to chordwise direction of the transformed observer location $\vec{x_a}$. The single-sided PSD can be computed by integrating the double-sided PSD over the positive frequency range, such as $G_{pp,i}^{\mathrm{LE}} = 2S_{pp,i}^{\mathrm{LE}}$.

Turbulence Spectrum Models

The turbulence spectrum plays a crucial role in Amiet's model [59] for leading-edge noise prediction. In this study, two types of turbulence spectra are considered: the von Kármán spectrum [127] and the Liepmann spectrum [128]. The two-dimensional von Kármán spectrum is defined as [127]:

$$\Phi_{uu}(k_x, k_y) = \frac{1}{\sqrt{\pi}} \frac{\Gamma(5/6)}{\Gamma(1/3)} \frac{u_{\mathrm{rms}}^2}{k_e} \frac{1}{\left[1 + (k_x/k_e)^2 + \left(k_y/k_e\right)^2\right]^{5/6}}, \tag{77}$$

where u_{rms} denotes the root-mean-square velocity ($u_{\mathrm{rms}} = Iw_{rel}$), and k_e is the characteristic wavenumber representing the scale of the largest turbulent eddies. The value of k_e can be calculated as:

$$k_e = \frac{\sqrt{\pi}}{L_f} \frac{\Gamma(5/6)}{\Gamma(1/3)}, \tag{78}$$

where L_f represents the integral length scale of the turbulence. The two-dimensional Liepmann spectrum is given by [128]:

$$\Phi_{uu}(k_x, k_y) = \frac{u_{\mathrm{rms}}^2 L_f^2}{4\pi} \frac{1 + \left(k_x L_f\right)^2 + 4\left(k_y L_f\right)^2}{\left[1 + \left(k_x L_f\right)^2 + \left(k_y L_f\right)^2\right]^{5/2}}. \tag{79}$$

For ease of comparison with the simulated data, one-dimensional wavenumber spectra

are of particular interest. In this context, the one-dimensional von Kármán spectrum and Liepmann spectrum are also considered. The one-dimensional von Kármán spectrum is expressed as [266]:

$$\Phi_{uu}(k_x) = \frac{1}{\sqrt{\pi}} \frac{\Gamma(5/6)}{\Gamma(1/3)} \frac{u_{\text{rms}}^2}{k_e} \frac{1}{\left[1 + (k_x/k_e)^2\right]^{5/6}}, \tag{80}$$

while the one-dimensional Liepmann spectrum takes the form of [266]:

$$\Phi_{uu}(k_x) = \frac{u_{\text{rms}}^2 L_f}{\pi} \frac{1}{1 + \left(k_x L_f\right)^2}. \tag{81}$$

It is worth noting that the von Kármán spectrum and Liepmann spectrum exhibit slightly different characteristics for high frequencies in the dissipation range. The von Kármán spectrum has a slope of -5/3, while the Liepmann spectrum has a slope of -2.

7.3.3 Trailing-edge noise prediction

Amiet's trailing-edge model

In this study, trailing-edge (TE) noise is calculated using Amiet's model [50], which has been widely accepted for its accuracy in predicting TE noise. To compute the far-field acoustic power spectral density (PSD), we employ the formula derived by Roger and Moreau [51], which is given by:

$$S_{pp,i}^{\text{TE}}(\omega_e) = \left(\frac{\omega_e c z_a}{2\pi c_0 \sigma^2}\right)^2 l_y(\omega_e) \frac{s}{2} |\mathcal{L}|^2 \Phi_{pp}(\omega_e), \tag{82}$$

here, the aeroacoustic transfer function $|\mathcal{L}|$ includes the back-scattering correction proposed by Roger and Moreau [51], which improves the accuracy of the model ($|\mathcal{L}| = |\mathcal{L}_\infty| + |\mathcal{L}_\epsilon|$). The surface pressure spectrum near the trailing edge, denoted as $\Phi_{pp}(\omega)$, is derived from Amiet's model [50]. The origin of the coordinate system for the original Amiet's trailing-edge model [50] is at the trailing edge of the airfoil, so an offset of $-c$ is added to the chordwise direction of the transformed observer location $\vec{x_a}$.

To account for the spanwise correlation length, the approach developed by Corcos [267] was utilised. The spanwise correlation length is approximated as $l_y(\omega) = b_c U_c/\omega$, where U_c represents the convection velocity ($U_c = 0.75 w_{\text{rel}}$). The constant b_c is assumed to be $b_c = 1.56$ based on empirical data [114].

It is worth noting that the formula in Eq. 82, derived by Roger and Moreau [51],

includes the back-scattering correction term $|\mathcal{L}_\epsilon|$ and an additional factor of 4. This factor accounts for the scattering effect from the opposite side of the airfoil [53], and its validity has been confirmed through comparisons with experimental data for airfoils [51, 114].

To compute the single-sided power spectral density (PSD), the contributions from the suction side (SS) and pressure side (PS) of the airfoil are combined. This is expressed as $G_{pp,i}^{\mathrm{TE}} = S_{pp,i}^{\mathrm{TE,SS}} + S_{pp,i}^{\mathrm{TE,PS}}$.

Wall pressure spectrum models

The selection of wall pressure spectrum (WPS) models for predicting trailing-edge noise lacks consensus in the research community. In this study, we investigate six semi-empirical WPS models: Goody (2004) [118], Rozenberg (2012) [119], Kamruzzaman (2015) [120], Catlett (2016) [121], Hu (2016) [122], and Lee (2018) [123]. These models are expressed in a universal form, as shown in Eq. 32 in Section 2.4.2.

The boundary layer parameters required by these WPS models were extracted at 98% of the chord using the viscous panel XFOIL solver [97] for each blade segment. The boundary layer thickness δ is not provided by XFOIL [97], so it is determined based on an empirical equation [268]:

$$\delta = \delta_\theta(3.15 + \frac{1.72}{H-1}) + \delta^*, \tag{83}$$

where δ_θ and δ^* are the boundary layer momentum thickness and displacement thickness, respectively, and H is the shape factor ($H = \delta^*/\delta_\theta$).

The semi-empirical WPS models are often calibrated based on empirical data at moderate to high-Reynolds numbers, resulting in a lack of validation cases at low-Reynolds number flows. The calibrated Reynolds number ranges based on the boundary layer momentum thickness for each WPS model are summarised in Table 7.1. Except for Goody's model [118] which is only calibrated for zero pressure gradient (ZPG) flows, the other models are applicable to adverse pressure gradient (APG) flows. However, due to the different empirical data used for calibration, the Reynolds number ranges for each model vary significantly. Typical small axial fans for electronics cooling applications operate at low-Reynolds numbers in a range of $Re_\theta = \mathrm{O}(10^2 - 10^3)$, which may fall outside the calibrated range of these models. Therefore, it is essential to investigate the performance of these WPS models at low-Reynolds number flows to ensure accurate and reliable predictions of trailing-edge noise.

Table 7.1: Calibrated momentum thickness Reynolds number (Re_θ) range for wall pressure spectrum (WPS) models. APG: adverse pressure gradient; ZPG: zero pressure gradient; FPG: favorable pressure gradient.

Model	$Re_\theta \times 10^{-3}$
Goody (2004) [118]	ZPG: 1.40 – 23.40
Rozenberg (2012) [119]	APG: 0.56 – 17.60
Kamruzzaman (2015) [120]	ZPG: 3.39 – 23.40 APG: 0.76 – 19.57
Catlett (2016) [121]	APG: 6.75 – 22.72*
Hu (2016) [122]	ZPG: 3.52 – 8.69 APG: 5.37 – 11.05 FPG: 2.04 – 3.26
Lee (2018) [123]	ZPG: 1.40 – 23.40 APG: 0.50 – 16.50

* Re_θ is not provided in [121], and the range is estimated based on the boundary layer momentum thickness.

7.3.4 Overall broadband noise

The overall broadband noise emitted by a single blade at each azimuth angle θ can be computed by summing the contributions from all blade segments, which can be expressed as:

$$G_{pp,\text{blade}}(\omega, \theta) = \sum_{i=1}^{N_s} G_{pp,i}(\omega_e, \theta) \left(\frac{\omega_e}{\omega}\right)^2. \tag{84}$$

Here, N_s represents the number of blade segments. The term $G_{pp,i}(\omega_e)$ denotes the total broadband noise emitted by the i^{th} blade segment, which encompasses contributions from both the leading-edge noise and trailing-edge noise ($G_{pp,i} = G^{\text{LE}}_{pp,i} + G^{\text{TE}}_{pp,i}$). To obtain the total broadband noise emitted by the rotor, the contributions from all the blades are integrated and averaged over all azimuth angles:

$$G_{pp,\text{rotor}}(\omega) = \frac{B}{2\pi} \int_0^{2\pi} G_{pp,\text{blade}}(\omega, \theta) \mathrm{d}\theta. \tag{85}$$

As highlighted by Sinayoko *et al.* [265], there exists conflicting usage of the exponent (-2, 1, or 2) in the Doppler factor (ω_e/ω) in the literature for Eq. 84. In this study, we adopt the exponent of 2 in the Doppler factor $(\omega_e/\omega)^2$, which has been validated as the correct value in [265].

Finally, the far-field sound pressure level (SPL) for the broadband contributions at the

observer location $\vec{x}$ can be calculated using the following equation:

$$L_p^{\mathrm{BB}}(f) = 10 \log_{10} \left[\frac{2\pi G_{pp,\mathrm{rotor}}(\omega) \delta f}{P_{\mathrm{ref}}^2} \right]. \tag{86}$$

Here, $P_{\mathrm{ref}} = 2 \times 10^{-5}$ Pa represents the reference sound pressure and δf denotes the spectral resolution.

7.4 Tonal noise prediction

In this study, the prediction of tonal noise emitted by the fan system is accomplished using Lowson's model [129], a well-established and widely used approach in the field. The model considers the major tonal noise sources, including the asymmetric inlet-rotor interaction (IRI) noise, the rotor-stator interaction (RSI) noise on the rotor blade, and the RSI noise on the stator blade. These noise sources have been identified as the dominant contributors to the overall fan system noise [210].

To obtain the necessary unsteady loading data for Lowson's model [129], LES results are utilised [210]. This ensures that the model is based on reliable and validated data, enhancing the credibility of the tonal noise predictions. It is important to note that the model focuses specifically on the harmonics of the blade passage frequencies (BPFs), which are known to be the primary tonal components of fan noise.

The asymmetric inlet-rotor interaction (IRI) noise arises from the interaction between the incoming non-uniform flow and the rotor blade. The periodic flow blockage by the downstream stator blades leads to unsteady loading on the rotor blade, resulting in tonal sound emission. Similarly, the rotor-stator interaction (RSI) noise is generated by the interaction between the rotor blade and the stator blade.

The forces acting on each blade can be decomposed into thrust, drag, and radial force components, represented by $\vec{F} = (-T, -D \sin\theta, -D \cos\theta)^{\mathrm{T}}$, where T denotes the thrust of one blade, D represents the drag ($D = M/r$), and θ is the azimuth angle. It is worth noting that for stator blades, the azimuth angle remains constant.

The unsteady loading on both the rotor and stator blades is expressed as Fourier expansions using a complex Fourier series:

$$\vec{F} = \sum_{\lambda=-\infty}^{+\infty} \vec{F}_\lambda e^{-i\lambda\Omega t}. \tag{87}$$

Here, Ω denotes the rotational speed of the rotor, and λ represents the order of the

harmonic. The sound pressure of the m^{th} harmonics of the blade passage frequency (BPF) for the rotor, due to S periodic pulses, is given by:

$$\begin{aligned} c_{m,\text{rotor}} =& \frac{imB^2\Omega}{2\pi c_0 R_0} \sum_{k=-\infty}^{+\infty} (-i)^{mB-kS} \\ & \times \left(-\frac{zT_k}{R_0} - \frac{mB-kS}{mBM_r} D_k \right) J_{mB-kS}\left(\frac{mBM_r x}{R_0} \right). \end{aligned} \tag{88}$$

Here, R_0 represents the distance from the blade to the observer, which is approximated as the distance from the blade mid-span to the observer. J_{mB-kS} denotes the Bessel function of the first kind. The positive integer m ranges from 1 to $+\infty$, while k ranges from $-\infty$ to $+\infty$. M_r corresponds to the Mach number, calculated as $M_r = \Omega r/c_0$. x and z represent the observer's coordinates in the global frame.

For stationary blades (stator), the source Mach number M_r is zero. Consequently, the sound pressure of the m^{th} harmonics of the BPF for the stator, due to B periodic pulses, can be expressed as:

$$\begin{aligned} c_{m,\text{stator}} =& \sum_{k=-\infty}^{+\infty} \frac{-imBS\Omega}{2\pi c_0 R_0} \left[-\frac{zT_m}{R_0} - \frac{(mB-kS)}{mBM_r} D_m \right] \\ & \times i^{mB-kS} J_{mB-kS}\left(\frac{mBM_r x}{R_0} \right). \end{aligned} \tag{89}$$

The asymmetric inlet-rotor interaction noise is generated by the interaction between the non-uniform flow and the rotor blade. The presence of four sharp edges in the asymmetric inlet creates strong vortex tubes that interact with the rotor blades [210]. To predict this noise source, Eq. 88 is applied by setting four periodic disturbances $S = 4$. It has been observed that the asymmetric inlet-rotor interaction significantly affects approximately 25% of the rotor blades near the blade tip, acting as a prominent noise source [210]. Although approximating the unsteady force due to this effect as a fluctuating point force acting on the rotor blade may introduce certain inaccuracies, it is a reasonable assumption for simplifying the analysis as the fan blades remain acoustically compact sources below 10 kHz under the far-field assumption.

The rotating fan generates a powerful wake that impinges on the downstream stator, resulting in unsteady loading on the stator blade due to the periodic flow impingement by the wake. The unsteady loading on the stator blade can be predicted using Eq. 89, taking into account the number of rotor blades B and stator blades S.

Furthermore, the presence of downstream stator blades induces unsteady loading on the upstream rotor blade due to the periodic flow blockage by the stator. As demon-

strated by LES results in [210], the presence of downstream stator blades generates a periodic force on the rotor blades, with the same frequency as the stator blade passing frequency. The unsteady loading on the rotor blade can be predicted using Eq. 88, considering the number of rotor blades B and periodic disturbances S equal to the number of stator blades.

Finally, the total tonal noise emitted by the fan system can be obtained by integrating the contributions from noise sources on the rotor and stator blades. The magnitude of the total tonal noise at the BPFs can be expressed as:

$$L_p^{\mathrm{T}}(mf_{\mathrm{BPF}}) = 20\log_{10}\left(\frac{c_{m,\mathrm{fan}}}{P_{\mathrm{ref}}}\right), \tag{90}$$

where $c_{m,\mathrm{fan}}$ represents the total tonal noise emitted by the rotor and stator blades at the BPFs, which is $c_{m,\mathrm{fan}} = (c_{m,\mathrm{rotor}}^2 + c_{m,\mathrm{stator}}^2)^{0.5}$.

The mode order ξ can be expressed as $\xi = mB - kS$, which is mathematically equivalent to the Tyler-Sofrin mode [131]. This mode order, closely related to the order of Bessel functions, plays a crucial role in determining the radiated intensity of the interaction noise [36]. As ξ approaches ∞, the Bessel function rapidly diminishes, indicating that the dominant interaction noise occurs when ξ is small. Therefore, only the low order modes ($|\xi| \leq 5$) are considered in the tonal noise prediction in this study. It is worth noting that numerous coincidences arise if the number of rotor blades is an integral multiple of the number of stator vanes, or *vice versa*. These coincidences result in a zero mode order, leading to a significant increase in sound emission. Therefore, fan designs always avoid such coincidences to minimise the interaction noise [194].

7.5 Validation and discussion

7.5.1 Test case description

The fan considered in this study is the same axial flow fan as described in Chapter 3 and Chapter 4. The turbulence intensity and integral length scale of the incoming flow near the leading edge were obtained from the previous LES study, as detailed in Chapter 3. The averaged turbulence intensity at the fan inlet, denoted as $\bar{I}$, was found to be 3.23%, while the averaged integral length scale, denoted as $\overline{L_f}$, was measured to be 35.2 mm (approximately 1.4 times the chord length, c). The far-field observers are located at a distance of 1 m from the fan system, which are identical to those described in the experimental measurements and numerical study [209, 210]. The averaged sound pressure level (SPL) is computed at over all observer locations, following the same procedure as the experimental measurements [209, 210].

The convergence study of the reduced-order model has been conducted by varying the number of blade segments N_s and number of azimuth angles N_θ. The results of far-field noise show that the prediction method is converged when $N_s = 10$ and $N_\theta = 24$, which are used in the following analysis. The computational cost of the prediction method is remarkably small (4–5 orders of magnitude smaller than high-fidelity numerical simulations [20, 210]), which is around 1 core hour for one observer location. The prediction method is implemented in Matlab, and the computation is performed on a workstation with two Intel Xeon E5-2667v3 CPUs.

7.5.2 Comparison of aerodynamic prediction

The aerodynamic model presented in Section 7.2 has been validated against experimental and LES data of the fan system. The reduced-order model (ROM) uses the flow rate as input to efficiently predict the aerodynamic performance. The ROM predicts a static pressure of 115 Pa, deviating by only 4.2% from the experimental and LES data of 120 Pa [210]. The effective angle of attack is predicted to be 6°, which is within 2° of the LES data of 8°. The slight difference in angle of attack prediction can be attributed to the exclusion of tip leakage flow in the ROM, which affects axial flow velocities near the blade tip and is not captured by the blade element model.

Table 7.2 presents a comprehensive comparison between the ROM predictions and LES data for mean relative velocity ($\overline{w_{\text{rel}}}$), thrust ($T$), torque ($M$), and total efficiency (η). The relative differences between the ROM predictions and LES data are calculated for each aerodynamic quantity. The ROM demonstrates excellent agreement with the LES data, with relative differences of 4.5%, 3.1%, 6.5%, and 2.2% for mean relative velocity, thrust, torque, and total efficiency, respectively.

However, some discrepancies are observed in the comparisons for sectional thrust, torque, and efficiency, as depicted in Fig. 7.4. The ROM predicts a relatively smooth distribution of these quantities, while the LES data exhibits significant variation near the blade tip region. This discrepancy is attributed to the exclusion of tip leakage flow in the ROM, which significantly affects the flow behavior near the blade tip region. The blade element theory used in the ROM assumes a uniform axial velocity profile, which may not accurately capture the non-uniform flow near the blade tip region.

Nevertheless, the ROM provides a reasonable estimation of the overall aerodynamic performance of the fan system, with good agreement for mean aerodynamic quantities. The computational cost of the ROM is significantly low, making it a practical and efficient tool for further noise analysis.

Table 7.2: Comparison of the averaged aerodynamic quantities between prediction and LES [210].

Quantities	ROM	LES	Difference [%]
$\overline{w_{rel}}$ [m/s]	25.1	24.9	4.5
$T \times 10^{-1}$ [N]	1.16	1.20	3.1
$M \times 10^{-3}$ [Nm]	1.84	1.97	6.5
η [%]	74.7	72.1	2.2

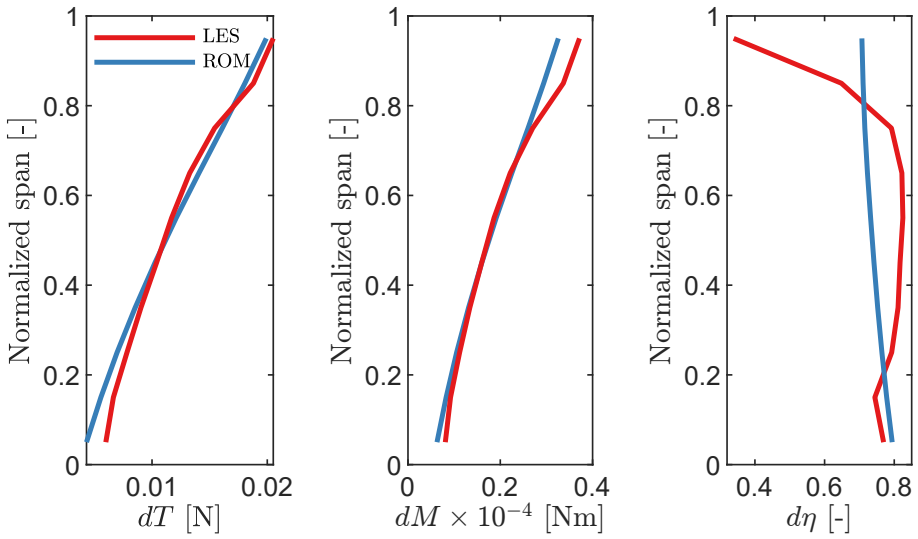

Figure 7.4: Comparison of sectional thrust (a), torque (b), and efficiency (c) between prediction and LES [210].

7.5.3 Results of broadband noise prediction

The broadband noise prediction is conducted using the reduced-order model (ROM) based on the aerodynamic quantities obtained in Section 7.5.2. The broadband noise prediction includes the leading-edge noise, trailing-edge noise, and total broadband noise emitted by the fan system. The prediction of the broadband noise is compared against the LES data and experimental measurements [210], which serve as the reference solutions. The comparison of the turbulence spectrum models, wall pressure spectrum models, and far-field noise prediction is presented in the following sections.

Selection of turbulence spectrum models

The reduced-order model (ROM) incorporates two turbulence spectrum models, namely the von Kármán spectrum [127] and the Liepmann spectrum [128], to simulate turbulence inflow conditions. The turbulence intensity and integral length scale are obtained from a previous LES study [210], with values of $\bar{I} = 3.23\%$ and $\overline{L_f} = 35.2$ mm ($\sim 1.4c$), respectively. These values are averaged over five spanwise locations from the hub to the tip. For each spanwise location, the turbulence intensity and integral length scale

are calculated based on measurements from point probes at distances of -0.01, -2, -4, -6, and -8 leading-edge radii (R_{LE}) from the leading edge. The -2R_{LE} distance is recommended as the optimal location based on experimental airfoil studies presented by Dos Santos *et al.* [269]. The variations across the five probe locations are considered as uncertainties.

The turbulence intensity and integral length scale vary significantly across the spanwise locations from the hub to the tip. The turbulence intensity ranges from 0.77% to 6.54%, while the integral length scale ranges from 41.2 mm to 10.2 mm. Therefore, the uncertainties in turbulence intensity and integral length scale are considered in the far-field noise predictions, with standard deviations of 1.93% and 18.8 mm, respectively.

To validate the accuracy of the turbulence spectrum models, a comparison with LES data was conducted at the 50% span location. Figure 7.5 shows the results, indicating that both the von Kármán and Liepmann spectra closely capture the turbulence characteristics within the frequency range of approximately 700–3000 Hz. However, the peaks observed in the LES data, attributed to the asymmetric inlet-rotor interaction, are not captured by the turbulence spectrum models, which are primarily designed for predicting homogeneous isotropic turbulence. Both models tend to overestimate turbulence intensity at low frequencies (< 700 Hz) and high frequencies (> 3000 Hz). Nevertheless, the Liepmann spectrum exhibits better agreement with the LES data in the high-frequency range due to its steeper slope of -2 used for the dissipation range.

The leading-edge noise results predicted by the ROM using the von Kármán spectrum and Liepmann spectrum are shown in Fig. 7.6, along with experimental data, LES data [210], and predicted trailing-edge noise data for reference. The trailing-edge noise prediction will be discussed in the Section 7.5.3. The noise spectra from experiments and LES data include both tonal and broadband noise, while the ROM predictions only consider the leading-edge noise. The uncertainties in turbulence intensity and integral length scale are considered in the ROM predictions combined with Liepmann spectrum.

The results indicate that the predicted leading-edge noise levels are in reasonable agreement with the experimental data and LES data, particularly at frequencies below 1000 Hz. The ROM predictions using both turbulence spectrum models exhibit similar trends, with the Liepmann spectrum showing slightly higher noise levels at low frequencies and lower noise levels at high frequencies. The leading-edge noise is more pronounced at frequencies below 1500 Hz compared to the predicted trailing-edge noise data. The Liepmann spectrum is selected for subsequent noise prediction due to its better agreement with the LES data in the high-frequency range.

The uncertainties in turbulence intensity and integral length scale are found to have a significant impact on the leading-edge noise predictions. In particular, the turbulence intensity uncertainties lead to variations in the noise levels at all frequencies. This effect will be further discussed in Section 7.5.6. Therefore, the uncertainties in turbulence intensity and integral length scale should be considered in the noise predictions to provide a more accurate representation of the noise levels.

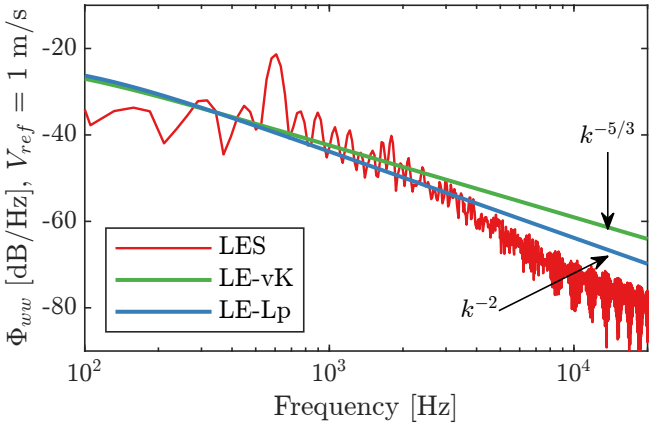

Figure 7.5: Comparison of turbulence spectrum models against LES data [210] for 50% span location. The turbulence spectrum models used in ROM include the von Kármán spectrum ('vK') and Liepmann spectrum ('Lp').

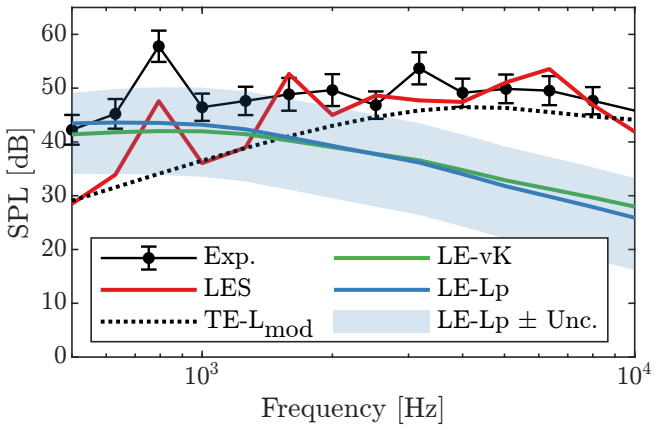

Figure 7.6: Comparison of far-field leading-edge noise prediction against experimental data and LES data [210] in one-third octave bands.

Selection of wall pressure spectrum models

The reduced-order model (ROM) incorporates six wall pressure spectrum (WPS) models from literature and one modified model to predict wall pressure fluctuations. These models include Goody's model ('G') [118], Rozenberg's model ('R') [119], Kamruzzaman's model ('K') [120], Catlett's model ('C') [121], Hu's model ('H') [122], Lee's model ('L') [123], and a modified Lee's model proposed in this study ('L_{mod}'). To evaluate their performance at low-Reynolds number flows, we classify the WPS models

into two groups: models calibrated for low-Reynolds number flows (Rozenberg [119], Kamruzzaman [120], Lee [123], $Re_\theta \leq 1000$) and models calibrated for high-Reynolds number flows (Goody [118], Catlett [121], Hu [122], $Re_\theta > 1000$). The calibrated Reynolds number ranges (Re_θ) for each model are summarised in Table 7.1. We evaluate their performance by comparing the predicted WPS near the trailing edge with the LES data from Zhao *et al.* [210] for an axial fan blade. The WPS is predicted at five spanwise locations along the blade span: 5%, 25%, 50%, 75%, and 95%. The Reynolds numbers based on momentum thickness Re_θ range from approximately 600 to 1600, with an angle of attack of 8° on the suction side of all segments.

The comparison of the predicted WPS at 98% chord on the suction side using six original WPS models against the LES data conducted at the 50% span location is shown in Fig. 7.7 (a). The results indicate that all the original WPS models underestimate the wall pressure fluctuations near the trailing edge. Among the original models, Lee's, Rozenberg's, and Kamruzzaman's models exhibit better agreement with the LES data, while Goody's, Kamruzzaman's, and Catlett's models show significant discrepancies. This underestimation has also been observed in the unmanned aerial vehicle (UAV) case [55], which shares similar low-Reynolds number flow conditions. This underestimation can be attributed to the fact that the original WPS models, primarily developed for higher Reynolds number flows, lack the capability to accurately predict the wall pressure fluctuations at low-Reynolds numbers. Lee's, Rozenberg's, and Hu's models seem to correctly predict the major trend of the WPS as they contain the several low-Reynolds number data points. However, they still underestimate the magnitude of the wall pressure fluctuations.

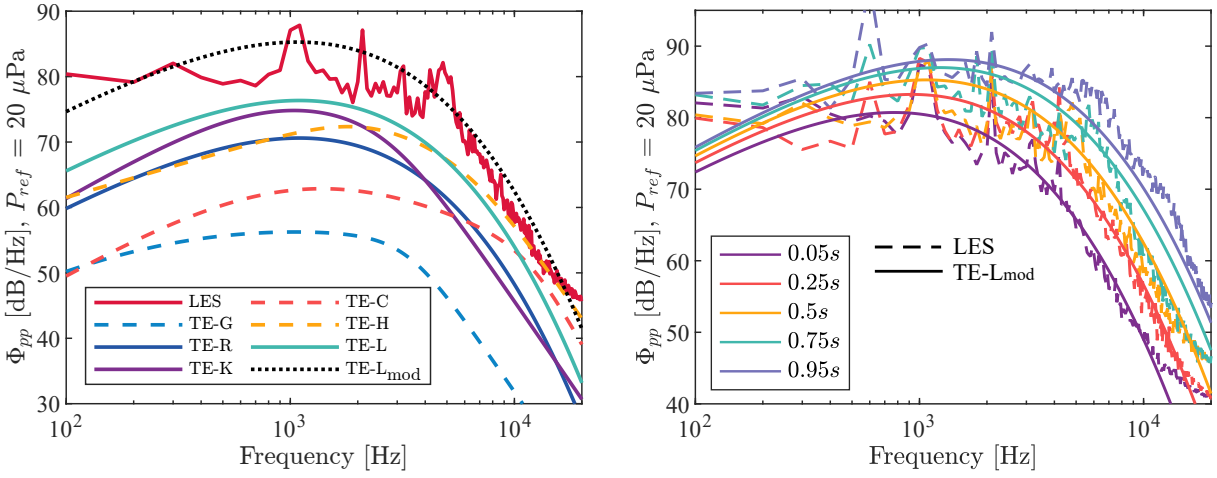

Figure 7.7: Comparison of PSD of wall pressure fluctuations (Φ_{pp}) at 98% of the chord on suction side between prediction and LES [210] for 50% span location (a) and five different span locations (b). The WPS models used in the ROM include Goody ('G'), Rozenberg ('R'), Kamruzzaman ('K'), Catlett ('C'), Hu ('H'), Lee ('L'), and modified Lee ('L$_{mod}$').

Among these models, Lee's model shows better agreement with the LES data and has the lowest Reynolds number range. To further improve the prediction accuracy, a modified Lee model ('L_{mod}') is proposed. It incorporates a scaling factor of 8.3 for the model parameter a in Eq. 32. This factor is determined by fitting the predicted WPS to the LES data for all spanwise locations using the least squares method. Figure 7.7 (b) shows that the modified Lee model ('L_{mod}') agrees well with the LES data, especially at lower span locations below 50% span. However, some discrepancy is observed at higher span locations. The modified model still underestimates the WPS near the blade tip due to the strong tip leakage flow increasing the wall pressure fluctuations. This indicates that using a single factor for all spanwise locations may not be optimal, as the flow conditions vary along the blade span. Combining this factor with a spanwise-dependent scaling factor could further improve the prediction accuracy. Nevertheless, the modified Lee model ('L_{mod}') with a scaling factor of 8.3 provides a reasonable prediction of the wall pressure fluctuations at low-Reynolds number flows, making it suitable for noise prediction in this study.

Figure 7.8 shows the comparison of trailing-edge noise prediction against experimental data and LES data [210]. Similar to the WPS comparison, the trailing-edge noise prediction using the original WPS models underestimates the noise levels near the trailing edge, while the Lee's, Rozenberg's, and Kamruzzaman's models exhibit slightly better agreement with the LES data. The modified Lee model ('L_{mod}') provides the best prediction of the trailing-edge noise, with good agreement with the experimental data and LES data. The trailing-edge noise is more pronounced at higher frequencies, with the modified Lee model ('L_{mod}') providing a better match with the experimental data and LES data. The trailing-edge noise is a significant contributor to the total broadband noise, and the improved prediction of the trailing-edge noise enhances the overall noise prediction accuracy. The modified Lee model ('L_{mod}') is selected for subsequent noise prediction due to its better agreement with the LES data and experimental measurements.

Broadband noise characteristics

The broadband noise prediction using the Liepmann spectrum for turbulence inflow and the modified Lee model for wall pressure fluctuations is presented in Figure 7.9. The contour plots depict the leading-edge noise, trailing-edge noise, and total broadband noise in one-third octave bands along the blade. At frequencies below approximately 1500 Hz, the leading-edge noise dominates, while at frequencies above 1500 Hz, the trailing-edge noise takes over. The total broadband noise is a combination of the leading-edge and trailing-edge noise, with varying noise levels along the blade span. Spanwise variations of broadband noise are observed, with higher noise levels at the

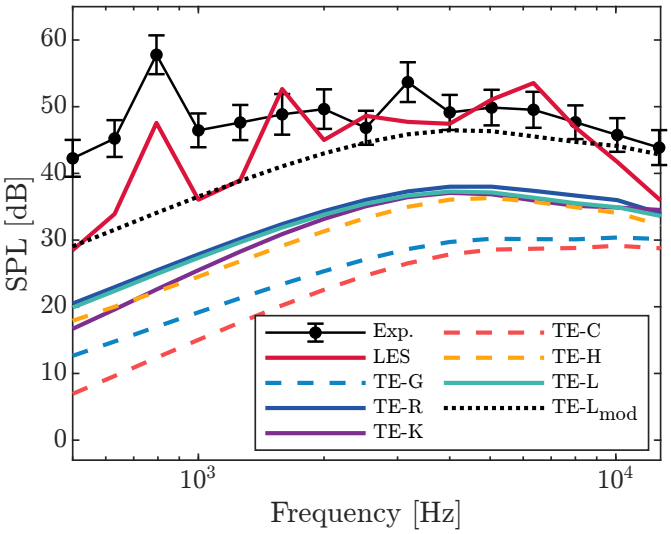

Figure 7.8: Comparison of trailing-edge noise prediction against experimental data and LES data [210]. The WPS models used in the ROM include Goody ('G'), Rozenberg ('R'), Kamruzzaman ('K'), Catlett ('C'), Hu ('H'), Lee ('L'), and modified Lee ('L_{mod}').

60%-80% span locations. It is worth noting that this study does not consider tip noise, as the focus is on the broadband noise generated by the leading-edge and trailing-edge noise sources. The contour plots provide valuable insights into the noise sources of the fan system, emphasizing the significance of the leading-edge and trailing-edge noise in determining the total broadband noise levels.

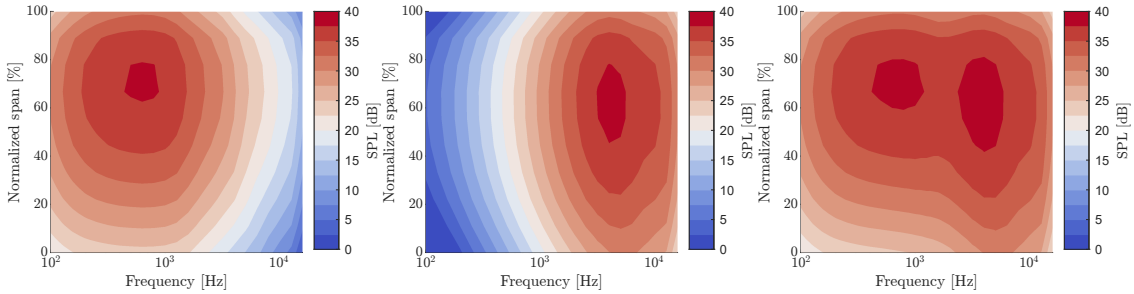

(a) (b) (c)

Figure 7.9: Contour plots of (a) leading-edge noise, (b) trailing-edge noise, and (c) total broadband noise in one-third octave contours along the blade.

7.5.4 Results of tonal noise prediction

The tonal noise prediction is conducted using Lowson's model [129], which considers the noise sources of asymmetric inlet-rotor interaction noise (IRI) and rotor-stator interaction noise (RSI). Figure 7.10 compares the tonal noise prediction with experimental data and LES data for the first five harmonics of the blade passing frequency (BPF). The results show good agreement between the tonal noise prediction and the experimental and LES data, with a discrepancy of less than 6 dB. Lowson's model accurately captures

the tonal noise levels based on the LES input data, demonstrating its effectiveness in predicting the tonal noise characteristics of the fan system.

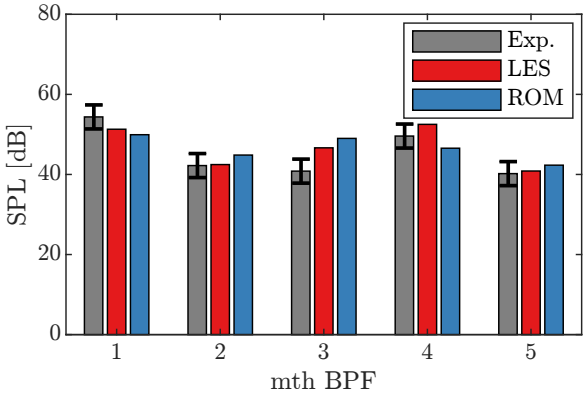

Figure 7.10: Comparison of tonal noise prediction against experimental data and LES data [210] for the first five harmonics of the blade passing frequency (BPF).

Figure 7.11 compares the contributions of different noise sources, including IRI and RSI on the rotor blade and stator, to the tonal noise for the first five harmonics. The results indicate that both IRI and RSI on the rotor blade and stator significantly contribute to the tonal noise, with slightly higher overall contribution from the IRI noise source. The IRI noise source dominates at the first BPF, while the RSI noise source becomes more prominent at the fourth harmonic. This can be explained by analysing the Tyler-Sofrin's mode order [131]. For the first BPF, the four periodic disturbances generated by the IRI noise source are in phase, resulting in a low mode order ($\xi = mB - kS = 1 \times 5 - 1 \times 4 = 1$) and a strong tonal noise emission on rotor blades. Similarly, for the fourth harmonic, the five rotor blade wakes interact with the seven stator blades, and the mode order is $\xi = mB - kS = 4 \times 5 - 3 \times 7 = 1$, leading to another strong tonal noise emission. These results highlight the importance of considering both the noise sources and their contributions to accurately capture the tonal noise characteristics of the fan system.

These findings also suggest that controlling IRI and RSI noise sources is an effective strategy for reducing tonal noise in fan systems. As shown in the LES study in Part I, IRI arises from asymmetric inlet flow. Addressing this non-uniformity could significantly reduce tonal noise. However, modifying the shroud to correct the inlet flow is impractical without a complete redesign, as it is integral to the fan assembly.

To address this, the focus will shift to optimising the rotor blades to reduce tonal noise. Tip vortices, identified in the LES study in Part I as major contributors to flow losses and noise, will be targeted. The potential of incorporating winglets will be explored. Winglets are expected to weaken tip vortex strength, reduce tip flow structures, and minimise pressure fluctuations on the blade tip, thereby lowering rotor-stator interaction noise.

Additionally, since the asymmetric inlet is close to the blade tip, winglets may also help reduce asymmetric inlet-rotor interaction noise. This dual benefit makes winglet integration a promising approach for noise reduction. The effectiveness of this strategy will be further investigated in Part III.

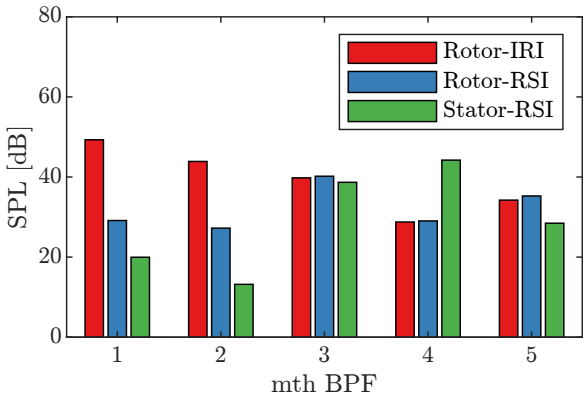

Figure 7.11: Comparison of different noise source contributions to the tonal noise for the first five harmonics of the blade passing frequency (BPF). The investigated noise sources include the asymmetric inlet-rotor interaction noise (IRI), rotor-stator interaction noise (RSI) on rotor blade and stator.

7.5.5 Comparison of total noise prediction

The comparison of the combined far-field noise prediction against experimental data and LES data [210] is presented in Fig. 7.12. The turbulence inflow is characterized using the Liepmann spectrum, and the wall pressure fluctuations are modelled by the modified Lee's model. The reduced-order model (ROM) demonstrates reasonable accuracy in predicting both the broadband noise trend and tonal noise characteristics, as depicted in Figure 7.12 (a). The uncertainties in turbulence intensity and length scale are considered in the ROM predictions, resulting in a more realistic representation of the noise characteristics. The ROM predictions closely align with the experimental and LES data, exhibiting an overall sound pressure level (OASPL) of 59.2 ± 2.5 dB, compared to 62±3 dB for the experimental data and 59.5 dB for the LES data (Fig. 7.12 (b)). Compared to the experimental data, the ROM predictions show a discrepancy of approximately 2.8 dB, while the LES data exhibit a difference of 0.7 dB. The ROM predictions provide a reliable and robust estimation of the total noise levels, capturing the noise sources and propagation mechanisms of the fan system. These results underscore the effectiveness of the ROM in predicting the total noise levels and highlight its potential for fast exploration of different design parameters and inflow conditions.

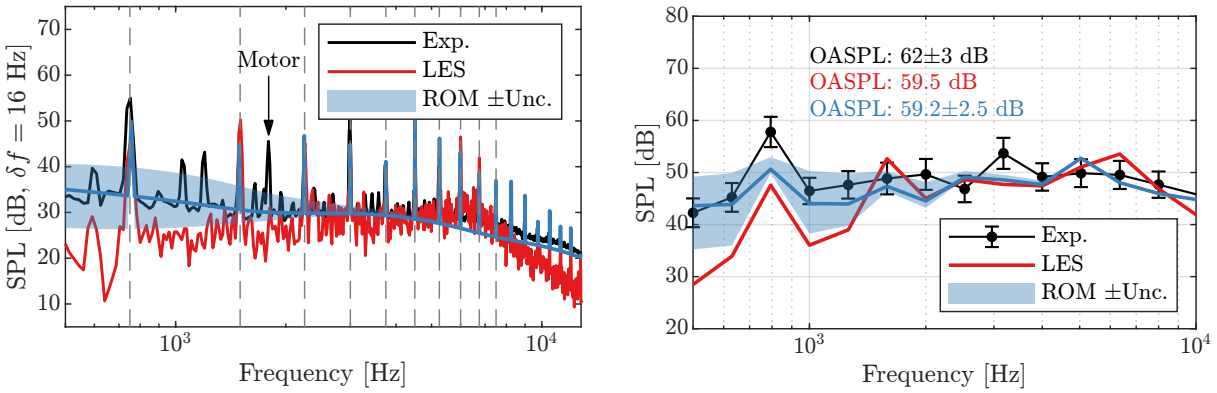

Figure 7.12: Comparison of total far-field noise prediction against experimental data and LES data [210] in narrowband (a), and one-third octave bands (b). The uncertainties in turbulence intensity ±1.93% and length scale ±18.8 mm are considered in the ROM. The gray dashed lines in (a) represent the harmonics of the blade passing frequency (BPF).

7.5.6 Effect of turbulence inflow on broadband noise

The effect of turbulence inflow on broadband noise is investigated by varying the turbulence intensity and turbulence length scale. The turbulence intensity is varied from 0.01% to 16%, while the turbulence length scale is varied from $0.01c$ to $4c$ with $c = 26$ mm. The turbulence intensity significantly influences broadband noise level, as shown in Fig. 7.13. Higher turbulence intensity leads to increased noise levels, with the leading-edge noise being more sensitive to turbulence intensity than the trailing-edge noise (Fig. 7.13 (a)). Increasing turbulence intensity from 0.01% to 16% results in a 64 dB increase in leading-edge noise. The trailing-edge noise is not significantly affected by turbulence intensity for this case (Fig. 7.13 (b)), as the angle of attack is relatively high (8°), leading to a fully turbulent boundary layer at the trailing edge even with low turbulence intensity. It is expected that the trailing-edge noise would be more sensitive to turbulence intensity at lower angles of attack.

The turbulence length scale also plays a crucial role in determining the leading-edge noise characteristics. The effect of varying turbulence length scale on leading-edge noise is shown in Fig. 7.14. Smaller length scales result in a shift of the noise peak towards higher frequencies. This is expected as smaller length scales lead to higher turbulence frequencies, which in turn impact the broadband noise characteristics. The largest noise level is observed for a turbulence length scale of $0.2c$, with an overall sound pressure level (OASPL) of 57.4 dB. The noise level decreases with increasing or decreasing length scales, with a noise reduction of 12 dB for a length scale of $0.01c$ and 9.2 dB for a length scale of $4c$. This finding suggests that a critical length scale exists for leading-edge noise generation, with the noise level being most sensitive to length scales around $0.2c$. The results highlight the importance of accurately characterizing

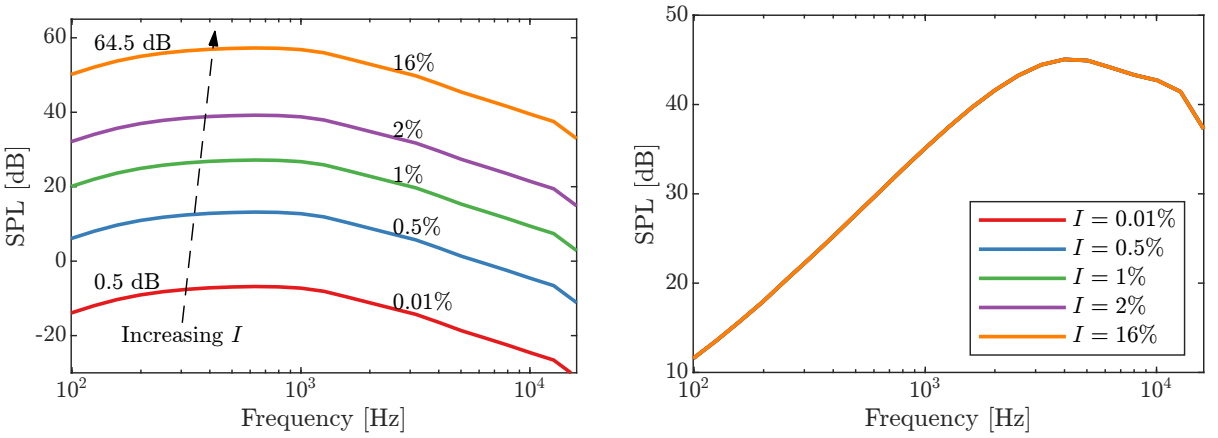

(a) (b)

Figure 7.13: Effect of turbulence intensity I on leading-edge noise (a) and trailing-edge noise (b) in one-third octave bands.

the turbulence inflow conditions for noise prediction, as turbulence intensity and length scale significantly influence the broadband noise levels. These findings can also provide valuable insights into the selection of optimal turbulence inflow conditions for noise reduction strategies.

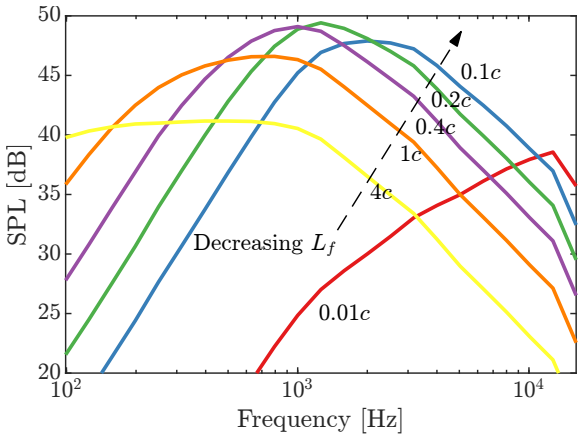

Figure 7.14: Effect of turbulence length scale on leading-edge noise in one-third octave bands. The length scale L_f is normalized by the chord length $c = 26$ mm.

7.6 Summary

This study presents a comprehensive investigation of noise prediction for a small-sized axial flow fan using a reduced-order model (ROM). The ROM incorporates aerodynamic prediction, broadband noise prediction, and tonal noise prediction to accurately capture the noise characteristics of the fan system. The aerodynamic prediction is conducted using blade element theory, and the ROM shows good agreement with large eddy simulation (LES) data.

Broadband noise prediction is performed using the ROM based on aerodynamic quantities obtained from the aerodynamic prediction. Liepmann's spectrum [128] provides better agreement with LES data in the high-frequency range and is selected for subsequent noise prediction. Wall pressure spectrum (WPS) models are evaluated against LES data. Among the six original WPS models, all of them underestimate the wall pressure fluctuations near the trailing edge, since our study uses a fan typically found in electronics cooling application with a low chord Reynolds number ($10^4 - 10^5$). However, Lee's model [123] shows better agreement with the LES data. To improve the prediction accuracy, a modified Lee model ('L_{mod}') is proposed, which captures wall pressure fluctuations more accurately. The ROM demonstrates reasonable accuracy in predicting broadband noise levels compared to experimental and LES data. It provides valuable insights into noise sources and spanwise variations of the fan system, facilitating the development of noise reduction strategies.

Tonal noise prediction is conducted using Lowson's model [129], which considers noise sources of asymmetric inlet-rotor interaction noise (IRI) and rotor-stator interaction noise (RSI). The ROM consistently predicts tonal noise levels with a discrepancy of less than 6 dB compared to experimental and LES data. By using Lowson's model, the ROM decouples noise sources and provides valuable insights into noise characteristics from each interaction mechanism. It is worth noting that Lowson's model requires accurate input data of unsteady force to predict tonal noise characteristics effectively.

Overall, the ROM demonstrates satisfactory precision in predicting total noise levels, with an overall sound ressure level (OASPL) difference of 2.8 dB compared to experimental data and LES data. It provides valuable insights into noise sources and propagation mechanisms of the fan system, facilitating the development of noise reduction strategies. The ROM is a reliable and robust tool for predicting total noise levels of the fan system, offering significant benefits for the design and optimisation of fan systems.

This chapter concludes Part II, which has focused on the development and application of a reduced-order model (ROM) for the rapid prediction of aerodynamic and aeroacoustic performance in axial flow fans. The ROM has demonstrated its capability to accurately capture the flow and noise characteristics of axial flow fans while maintaining minimal computational cost. It operates three orders of magnitude faster than Reynolds-averaged Navier-Stokes (RANS) simulations (discussed in Part II) and at least four to five orders of magnitude faster than large eddy simulations (LES) (presented in Part I). This efficiency makes the ROM an invaluable tool for exploring design parameters and inflow conditions, enabling the development of effective noise reduction strategies. By significantly reducing computational demands, the ROM facilitates the design and optimisation of axial flow fans, contributing to the advancement of

low-noise fan systems for diverse thermal management applications.

Figure 7.15 illustrates the logical flow of Part II and its integration with subsequent parts of this thesis. The contributions and sensitivity analyses presented in Part II will directly inform the design and optimisation strategies in Part III, which focuses on achieving low-noise axial fan designs. The insights gained from this ROM framework provide a solid foundation for addressing the challenges of noise reduction while maintaining aerodynamic efficiency.

Building on the findings from high-fidelity modelling in Part I and the reduced-order modelling in Part II, the next section (Part III) will delve into the optimisation of low-noise axial fans. This will involve exploring both acoustic liner designs and geometric modifications to achieve noise reduction without compromising aerodynamic performance. These strategies, informed by the comprehensive analyses in the preceding parts, will establish a robust framework for designing and optimising low-noise axial fans tailored for electronics cooling applications.

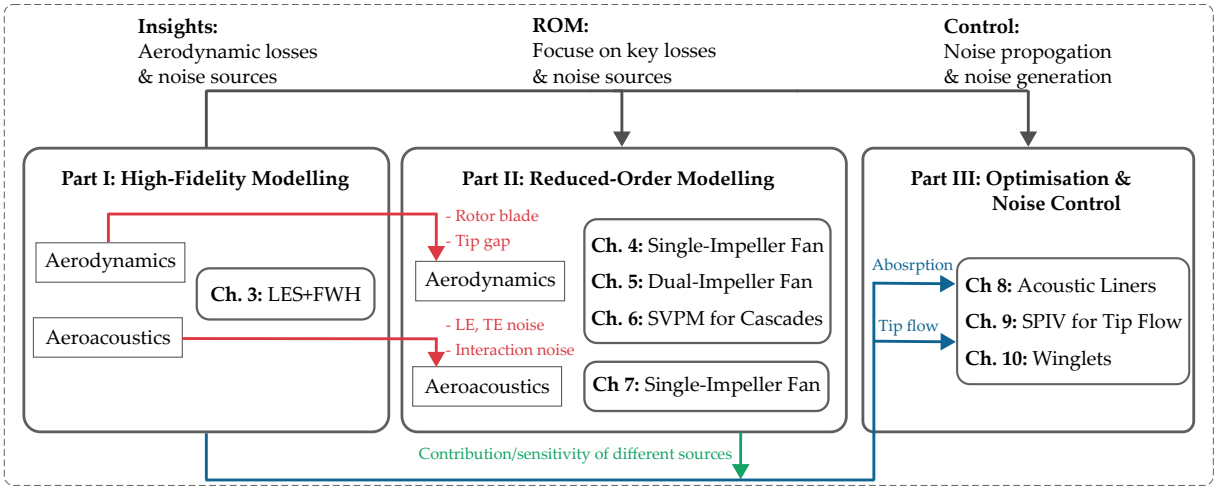

Figure 7.15: Logical flow of Part II and its connection to the subsequent parts. Insights from Part II that inform Part III are highlighted in green, while contributions from Part I are emphasized using a similar style as in Fig. 3.30. This visualisation underscores the integration of findings across parts, demonstrating a cohesive framework for advancing low-noise fan design.

"削繁就简三秋树，领异标新二月花。"

"Prune complexity to reveal simplicity like autumn trees;
Pioneer uniqueness like blossoms in early spring."

—郑板桥，1693-1766年，《赠君谋父子》

Banqiao Zheng, 1693-1766, *Poems for Junmou and His Son*

Part III

Optimisation and Noise Control

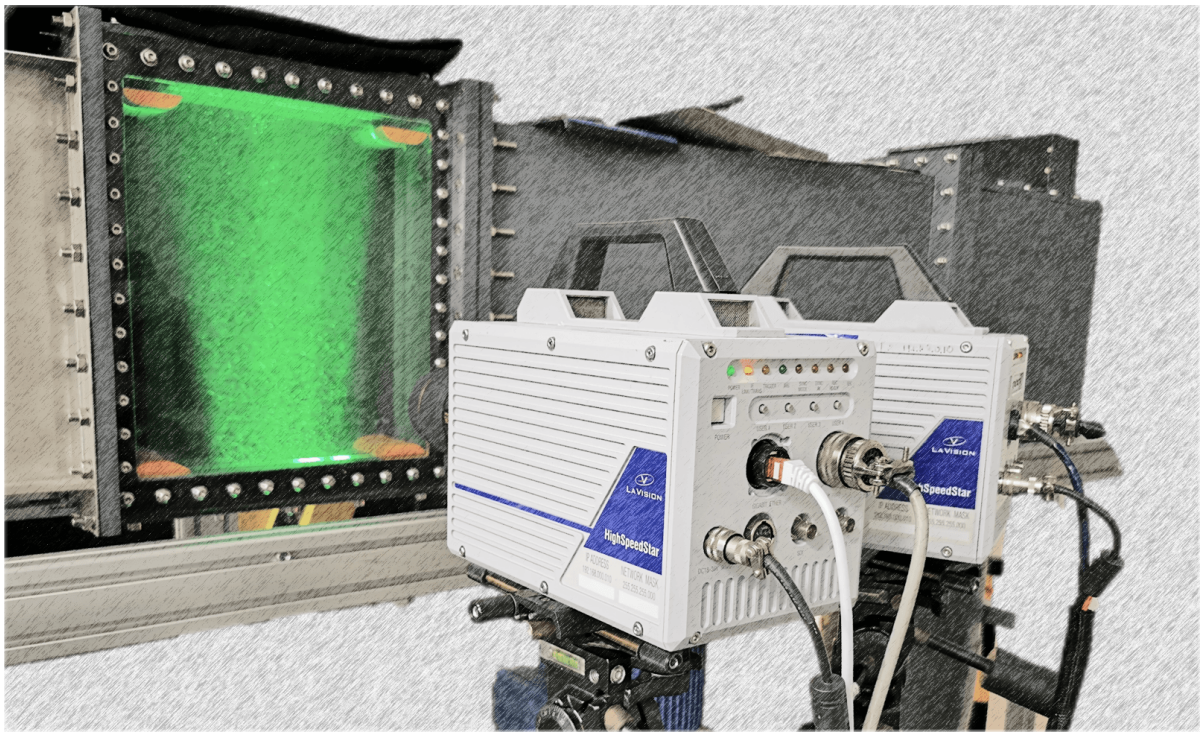

Chapter 8

Compact Micro-Slit Panel Absorbers for Enhanced Low-Frequency Noise Control

The first chapter of Part III focuses on reducing fan noise using novel acoustic liners. This chapter [1] details the design, analytical prediction, optimisation, and validation of compact micro-slit panel absorbers (C-MSPAs) for low-frequency, broadband noise reduction in electronics cooling applications. These innovative acoustic liners are engineered to mitigate noise generated by high-rotational-speed counter-rotating (CR) axial fans without compromising aerodynamic performance.

This chapter is structured as follows: Section 8.1 reviews the current challenges posed by CR fan noise in electronics cooling systems and explores the potential of C-MSPAs as effective noise control solutions. The concept and design improvements of C-MSPAs over standard micro-slit panel absorbers (MSPAs) are introduced in Section 8.2. Section 8.3 validates the C-MSPA designs through numerical simulations and experimental measurements in an impedance tube. The validation is extended to grazing incidence sound waves in Section 8.4. Finally, Section 8.5 presents the experimental testing of optimised C-MSPA designs on a CR fan. The chapter concludes with a summary of findings and suggestions for future work in Section 8.6.

Abstract

Counter-rotating (CR) dual impeller axial fans are essential in electronics cooling systems for their compact design and high efficiency, but their noise can impair user experience and system performance. This study proposes a novel compact micro-slit panel absorber (C-MSPA) designed to improve low-frequency noise absorption while

[1] This chapter is based on the **journal article** under review: W. Zhao, J. Wang, S. Wasala, J. Kennedy, and T. Persoons, "Compact micro-slit panel absorbers for low-frequency tonal and broadband noise control," *Applied Acoustics*, in Review, APAC-D-25-00510, 2025.

conserving material and space. The C-MSPA utilises optimised slit and air cavity geometry, achieving reduced panel thickness and greater cavity depth for enhanced acoustic performance. Analytical models are developed to predict C-MSPA performance and validated via numerical simulations and impedance tube measurements. Three analytical impedance models are compared to refine the sound absorption predictions, and parametric studies assess the influence of slit width, panel thickness, and air cavity depth. Optimisation techniques integrating analytical models are applied to maximize C-MSPA performance. Additionally, 3D finite element analysis (FEA) simulations examine sound absorption under normal and grazing incidence sound waves, corroborated by experimental data in an impedance tube. Testing with an 80 mm counter-rotating (CR) fan (nominal speed of 12000/11300 RPM, max axial-flow Mach number of 0.047), commonly found in data center servers, shows that C-MSPAs achieve superior noise reduction compared to hardwall and industrial acoustic foam setups, with over 6 dB reduction in sound pressure level (SPL) at target frequencies of 600 Hz, 1200 Hz, and 900–1800 Hz versus a hardwall, and more than 1.5 dB versus standard industrial acoustic foam. C-MSPAs minimally impact aerodynamic performance, with only a 0.5% deviation from the baseline P-Q curve. These results highlight C-MSPAs as effective noise control solutions for CR fans in compact electronics cooling applications, providing significant noise reduction without compromising airflow performance.

8.1 Introduction

Turbomachinery noise from axial fans is a common issue in aerospace engines, heat ventilation and air conditioning (HVAC) systems, and electronics cooling [5, 201]. It can negatively impact user experience and lead to health problems such as stress, tinnitus, and hearing loss [18, 19]. In the electronics cooling industry, counter-rotating (CR) dual impeller axial fans are widely used due to their compact design and high efficiency [20, 28]. Their opposing impeller rotations improve performance and compactness, making them ideal for high-impedance systems [231, 232]. However, in confined spaces like data centers and offices, CR fans generate significant noise, adversely affecting user comfort and system performance [5, 41, 222]. Noise levels from a single server fan can reach 60–80 dB at 1 meter [20, 23], and with numerous fans operating simultaneously, cumulative noise often exceeds workplace limits set by regulations such as the European Commission directive 2003/10/EC [17], OSHA [18], and NIOSH [19]. Office environments exacerbate the issue, as studies show annoyance at sound levels above 55 dB [26]. Therefore, effective noise control solutions for CR fans are critical to enhancing user experience and ensuring regulatory compliance.

Mitigating noise from CR axial fans in confined electronics enclosures presents significant challenges. It necessitates reducing noise levels within a limited space while preserving the fan's aerodynamic performance. This requires compact noise control solutions that effectively attenuate noise without inducing flow disturbances or pressure drops. The interaction between the rotor-stator and the two rotors generates numerous tones within a narrow bandwidth, resulting in a high noise level "quasi-broadband" spectrum, along with regular broadband noise [28, 157, 270]. Additionally, varying cooling conditions in servers cause fan speeds to fluctuate with system cooling requirements, leading to shifting tonal frequencies. Therefore, an effective noise control solution must attenuate noise across a broad frequency range, particularly at low frequencies, where noise is most prominent and challenging to mitigate.

The development of acoustic liners has opened up new possibilities for low-frequency sound absorption [171, 172, 271]. Unlike traditional porous sound-absorbing materials, such as glass fibers and resin foams [272], whose performance is heavily dependent on thickness, metamaterial-based structures offer flexibility in tuning acoustic impedance and constructing artificial boundaries. This innovation provides solutions for low-frequency sound absorption [178], which has traditionally been a challenge due to the weak interaction between sound waves and absorbing materials at these frequencies. Three primary categories of absorption materials have emerged from research: (1) Helmholtz resonators (HR) [174, 175], (2) micro-perforated and micro-slit absorbers [157, 176–179], and (3) membrane structures [180, 181].

Recent studies have shown that MPP absorbers can significantly reduce fan noise without compromising efficiency [157, 158, 176, 181, 187]. Allam *et al.* [187] investigated the sound absorption performance of an MPP splitter silencer under grazing flow for axial fans. Czwielong *et al.* [158] applied an MPP near an axial fan and found it significantly reduced sound pressure levels by up to 16 dB without compromising efficiency. Similarly, Dong *et al.* [157] studied single-layer MPP casing treatments for a small CR fan. They found that submillimeter pore diameters effectively absorb sound in the 1-2 kHz range. Placing the MPP over the front rotor reduced noise by up to 3.5 dBA around the design point without significantly affecting fan performance.

In typical MPP or MSP absorber designs, noise absorption performance may not always be optimal due to a trade-off between panel thickness and air cavity depth when the total thickness of the absorbers is fixed. Sound absorption performance may be compromised when excessive panel thickness limits air cavity depth. Moreover, excessive solid material in the panel can increase the weight and cost of MPP absorbers. To address these limitations and enhance the sound absorption performance of MSP absorbers, a novel type called compact micro-slit panel absorber (C-MSPA) is proposed in this study. C-MSPA optimises the geometry of the slits and air cavity, featuring reduced

panel thickness and increased air cavity depth. These design improvements make C-MSPAs compact, lightweight, and cost-effective, making them highly suitable for noise control applications in electronics cooling systems, HVAC systems, and various industrial settings.

The objective of this study is to develop and validate compact micro-slit panel absorbers (C-MSPAs) for low-frequency, broadband noise reduction under normal and grazing incidence sound waves for axial electronics cooling fans. Analytical methods are created to predict the sound absorption performance of C-MSPAs, validated through numerical simulations and experimental measurements using an impedance tube. The validated C-MSPA designs are then additively manufactured and applied to server-cooling counter-rotating (CR) axial fans to evaluate their noise reduction performance. This study aims to provide analytical predictions, numerical simulations, and experimental validations of the proposed C-MSPAs. It seeks to offer insights into the design and optimisation of C-MSPAs for noise control applications in confined spaces, particularly for reducing CR fan noise in electronics enclosures.

8.2 Concept, analytical prediction and optimisation

8.2.1 Concept of C-MSPAs

Micro-slit panel (MSP) absorbers, a variation of micro-perforated panel (MPP) absorbers, are widely used in noise control applications, especially in industrial settings. These absorbers consist of a panel with micro-slits backed by an air cavity, as shown in Fig. 8.1 (a). To enhance structural integrity during manufacturing, internal segments were introduced in this study, as depicted in Fig. 8.1 (a) and (b). The sound absorption performance of MSP absorbers is influenced by several factors, including the impedance of the slits (Z_s) due to thermal-viscous losses, the impedance of edge effects (Z_e) caused by flow distortion at the slit edges, the impedance of cavity effects (Z_D) associated with the resonant air cavity, and the impedance (Z_{vib}) resulting from the structural vibrations of the panel interacting with the incident sound wave. For an impervious panel, where Z_{vib} approaches infinity, the total impedance simplifies to [177, 191]:

$$Z_1 = Z_s + Z_e + Z_D. \tag{91}$$

The impedance of the slits depends on four geometrical parameters, which are panel thickness (t), slit width (d), air cavity depth (D), and panel porosity (ϕ). However, a practical limitation of MSP absorbers is their panel thickness, which can increase

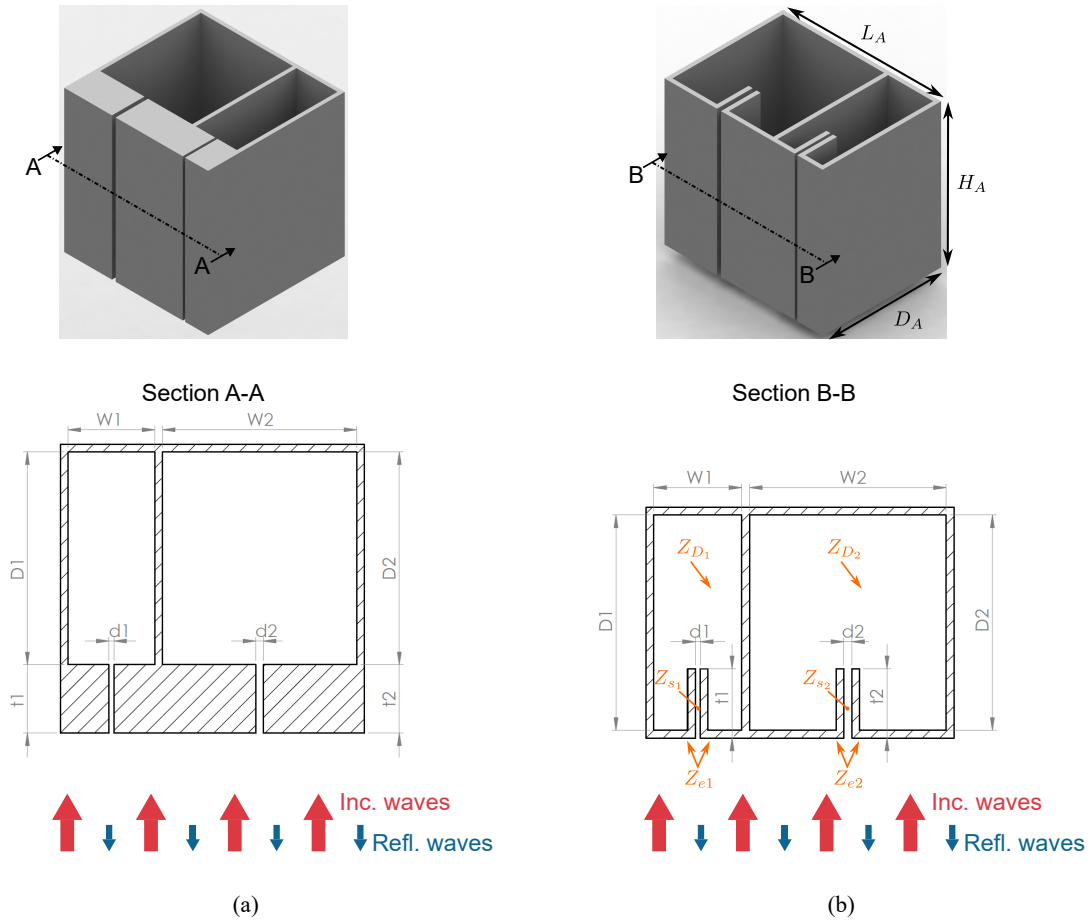

(a) (b)

Figure 8.1: Schematic of the concept of the compact micro-slit absorbers. The comparison is made for a single-layer, dual-cell between (a) A standard micro-slit panel absorber (SD-MSPA), (b) A compact micro-slit panel absorber (C-MSPA). For normal incidence sound waves, the figure indicates incident (inc.) and reflected (refl.) waves.

weight, cost, and restrict the air cavity depth, potentially compromising the sound absorption performance.

To overcome these limitations and further enhance the sound absorption performance, we propose the development of compact micro-slit panel absorbers (C-MSPAs). The concept of a single-layer, dual-cell C-MSPA is illustrated in Fig. 8.1 (b). C-MSPAs optimise the panel geometry by removing excess solid material, maintaining a small yet sufficient panel thickness, and increasing the air cavity depth. These design improvements offer advantages such as material and space savings, as well as enhanced sound absorption performance, making C-MSPAs highly suitable for noise control applications in confined spaces. Due to the structural simplicity of using micro-slits, C-MSPAs are easy to be manufactured and fabricated. No additional supports or only minimal supports are required to maintain the structural integrity of the panel. Similar to standard MSP absorbers (SD-MSPAs), the total impedance of single-layer C-MSPAs can be expressed as Eq. 91.

8.2.2 Analytical methods

Several impedance models have been developed in the literature to predict the impedance of micro-perforated panel (MPP) and micro-slit panel (MSP) absorbers. In this study, we employ and modify three impedance models to accurately predict the impedance of compact micro-slit panel absorbers (C-MSPAs): the Maa model [170, 182, 183], the equivalent fluid (EF) model [273, 274], and the Randeberg and Vigran (RV) model [275, 276].

Maa [170, 182, 183] first proposed the concept of MPP absorbers and later extended it to MSP absorbers [189]. His work established the theoretical basis and design guidelines that have been widely adopted in the literature. To improve the prediction accuracy of the Maa model under grazing flow conditions, some researchers have made efforts to enhance its performance for MPP absorbers [277–279]. The equivalent fluid (EF) model, developed by Atalla and Sgard [273], is based on the concept of replacing the porous material with an equivalent fluid possessing complex density and complex speed of sound. This model incorporates the Biot theory and the Johnson-Champoux-Allard model [274], providing a comprehensive approach to calculate the impedance of micro-holes or micro-slits. The Randeberg and Vigran (RV) model [275, 276] is specifically tailored for MSP absorbers.

Recent comparative analyses conducted by Cobo *et al.* [177, 191] have shown that the EF and Maa models outperform the RV model in predicting the sound absorption performance of micro-slit absorbers. They conducted their analysis by comparing the predictions of the impedance models with experimental measurements obtained from a normal incidence impedance tube. Despite some discrepancies between the predictions and measurements, both the EF and Maa models demonstrate promising performance, while the RV model underperforms in accurately predicting the sound absorption performance of MSP absorbers under normal incidence sound waves.

Built upon the work of Cobo *et al.* [177, 191], we employ and modify the EF, Maa, and RV models to predict the impedance of C-MSPAs. The slit impedance (Z_s), edge impedance (Z_e), and cavity impedance (Z_D) for the EF, Maa, and RV models are summarised in Table 8.1. Detailed derivations of these impedance models can be found in the original works by Maa [170, 182, 183], Atalla and Sgard [273, 274], Randeberg and Vigran [275, 276], and in the comparative analysis conducted by Cobo *et al.* [177, 191].

The final forms of the impedance of a single-layer, single-cell C-MSPAs for the EF, Maa, and RV models are given by [177, 191]

Table 8.1: Impedance models for micro-slit panel absorbers (C-MSPAs).

Model	Slit impedance Z_s	Edge impedance Z_e	Cavity impedance Z_D
EF [273, 274]	$Z_s + Z_e = i\frac{\omega\rho_0 t\alpha_\infty}{\phi}\left[1+\frac{\sigma\phi G_J(\omega)}{i\omega\rho_0\alpha_\infty}\right]$*		$-iZ_0\cot(kD_e)$
Maa [170, 182, 183]	$i\frac{\omega\rho_0 t}{\phi}\left[1-\frac{2}{s\sqrt{-i}}\frac{J_1(s\sqrt{-i})}{J_0(s\sqrt{-i})}\right]^{-1}$	$\frac{\sqrt{2}\mu s}{\phi d}+i\frac{\omega\rho_0 0.85d}{\phi}$	$-iZ_0\cot(kD_e)$
RV [275, 276]	$i\frac{\omega\rho_0 t}{\phi}\left[1-\frac{\tanh(s\sqrt{i})}{s\sqrt{i}}\right]^{-1}$	$\frac{2\sqrt{2}\mu s}{\phi d}-i\frac{2}{\pi}\frac{\rho_0\omega d}{\phi}\ln\left[\sin\left(\frac{\phi\pi}{2}\right)\right]$	$-iZ_0\cot(kD_e)$

* $G_J(\omega)=\left(1+i\frac{4\omega\rho_0\alpha_\infty^2\mu}{\sigma^2\phi^2r^2}\right)^{1/2}$.

$$Z_{1,\mathrm{EF}} = i\frac{\omega\rho_0\alpha_\infty t}{\phi}\left[1+\frac{\sigma\phi}{i\rho_0\omega\alpha_\infty}\left(1+i\frac{4\omega\rho_0\alpha_\infty^2\mu}{\sigma^2\phi^2r^2}\right)^{1/2}\right]-iZ_0\cot(kD_e) \tag{92}$$

$$Z_{1,\mathrm{Maa}} = \frac{\sqrt{2}\mu s}{\phi d_h}+i\frac{\omega\rho_0}{\phi}\left\{0.85dF_1(\epsilon)+t\left[1-\frac{2}{s\sqrt{-i}}\frac{J_1\left(s\sqrt{-i}\right)}{J_0\left(s\sqrt{-i}\right)}\right]^{-1}\right\}-iZ_0\cot(kD_e) \tag{93}$$

$$Z_{1,\mathrm{RV}} = \frac{2\sqrt{2}\mu s}{\phi d_h}+i\frac{\omega\rho_0}{\phi}\left\{t\left[1-\frac{\tanh\left(s\sqrt{i}\right)}{s\sqrt{i}}\right]^{-1}-0.636dF_2\left(\sqrt{\phi}\right)\ln\left[\sin\left(\frac{\phi\pi}{2}\right)\right]\right\} \tag{94}$$
$$-iZ_0\cot(kD_e)$$

Equations 92 to 94 represent the impedance equations for standard MSP absorbers as presented in [177]. The only distinction is the consideration of the effective air cavity depth D_e for C-MSPAs. To calculate D_e, we divide the effective air cavity by the width of the panel cell: $D_e = (WD-(d+2h)t)/W$. Here, h is the thickness of the panel at the neck of the slit.

The remaining parameters in Eqs. 92 to 94 are defined as follows: ω is the angular frequency, ρ_0 is the air density, t is the panel thickness, D is the air cavity depth, Z_0 is the characteristic impedance of air ($Z_0=\rho_0 c_0$), c_0 is the speed of sound in air, k is the wavenumber ($k=\omega/c_0$), α_∞ is the geometrical tortuosity [273], σ is the flow resistivity, $s=d_h\sqrt{\rho_0\omega/(4\mu)}$, d_h is the hydraulic diameter, μ is the dynamic viscosity of air, and $i=\sqrt{-1}$.

The porosity ϕ is defined as the ratio of the open area to the total area of the panel. In this study, the realistic geometry of the C-MSPA is considered. For the j^{th} cell of the C-MSPA shown in Fig. 8.1 (b), ϕ_j is calculated as $\phi_j \backsimeq d_j / (W_j + h)$, where h is the wall thickness of the panel, and n is the number of cells in the panel. For an annular C-MSPA with inner radius R_{in} and outer radius R_{out}, the porosity is calculated as $\phi_j \simeq d_j R_{in} / \left((W_j + h) \cdot (R_{in} + R_{out})/2\right)$.

For different types of perforations, such as rectangular slits, circles, and squares, we calculate the hydraulic diameter d_h as follows: for a rectangular slit, $d_h = 2dL_s/(d + L_s) \approx 2d$, where d is the width of the slit and L_s is the length of the slit; for a circular hole, $d_h = d$, where d is the diameter of the hole; for a square hole, $d_h = d$, where d is the side length of the square.

Let r_h be the hydraulic radius of the hole, defined as $r_h = d_h/2$. The flow resistivity σ for slits is given by [274] as $\sigma = 12\mu/\left(\phi r_h^2\right)$, for circular holes, $\sigma = 8\mu/\left(\phi r_h^2\right)$, and for square holes, $\sigma = 7\mu/\left(\phi r_h^2\right)$.

To account for the overperforation effect when the perforation ratio is high, we introduce the Fok function $F_1(\epsilon)$ [280]. This correction term considers the significant interactions between the holes or slits. The Fok function is given by:

$$F_1(\epsilon) = 1 - 1.4092\epsilon + 0.33818\epsilon^3 + 0.06793\epsilon^5 - 0.02287\epsilon^6 + 0.03015\epsilon^7 - 0.01641\epsilon^8, \quad (95)$$

where $\epsilon = \sqrt{\phi}$. In the RV model, Vigran [276] introduced a correction term $F_2(\epsilon)$ to account for the overperforation effect, given by:

$$F_2(\epsilon) = 1 - 1.25\epsilon. \quad (96)$$

The above equations (Eqs. 92 to 94) are sufficient to calculate the impedance for single-layer, single-cell C-MSPAs. For single-layer, multi-cell C-MSPAs, the total impedance of the parallel cells can be calculated by the equivalent circuit method. The total impedance of the parallel cells is given by:

$$Z_t = \left(\sum_{j=1}^{n} \frac{1}{Z_{1,j}} \frac{A_j}{A_t} \right)^{-1}, \quad (97)$$

where n is the number of cells in parallel, $Z_{1,j}$ is the impedance of the j^{th} cell, A_j is the area of the j^{th} cell, and A_t is the total area of the C-MSPAs.

Finally, the sound absorption coefficient α_0 under normal incidence is calculated by

$$\alpha_0 = 1 - |R|^2 , \tag{98}$$

where R is the reflection coefficient, given by

$$R = \frac{Z_t - Z_0}{Z_t + Z_0}.$$

For C-MSPAs under grazing incidence, the transmission loss is calculated to evaluate their sound insulation performance. It is defined as the ratio of the incident sound power to the transmitted sound power, given by:

$$TL = 10 \log_{10} \left(\frac{L_{W,in}}{L_{W,ts}} \right), \tag{99}$$

where,

$$L_{W,in} = \frac{|p_{in}|^2}{2\rho_0 c_0} S_{in},$$

and,

$$L_{W,ts} = \int_{S_{ts}} \frac{|p_{ts}|^2}{2\rho_0 c_0} dS,$$

represent the incident sound power and transmitted sound power, respectively. S_{in} and S_{ts} are the areas of the incident and transmitted surfaces, respectively, and p_{in} and p_{ts} are the incident and transmitted sound pressures.

8.2.3 Optimisation of C-MSPAs

The optimisation of C-MSPAs is crucial for enhancing their sound absorption performance. In this study, we base the optimisation process on the impedance models of C-MSPAs introduced in Section 8.2.2. These models provide a theoretical foundation for the optimisation process. The optimised C-MSPAs are validated through numerical simulations and experimental measurements, as described in the following sections.

To optimise acoustic liners for tonal and broadband noise absorption, various strategies can be employed. McKay *et al.* [281] proposed a method to optimise the sound absorption performance of membrane-based acoustic liners, by varying the geometrical parameters of the membrane. However, this method is only suitable for broadband white noise and does not consider the weight function for different frequency com-

ponents, limiting its applicability to arbitrary target spectra. Typical noise sources, such as electronics cooling fans, generate noise with a mixture of tones and broadband components, requiring the optimisation of sound absorption performance at specific frequencies. Killeen *et al.* [181] and Wang *et al.* [176] addressed this challenge by adopting an overall absorption coefficient weighted by the auto-spectral density of the noise spectrum. By assigning different weights to the absorption coefficient at different frequencies based on the spectrum density, the optimisation process can be tailored to the targeted noise sources, providing more flexibility for optimising mixed tonal and broadband noise absorption. In this study, we adopt a similar optimisation strategy to enhance the sound absorption performance of C-MSPAs at targeted frequencies.

The analytical methods presented in Section 8.2.2 were implemented in MATLAB and combined with optimisation algorithms to optimise the geometrical parameters of the C-MSPAs. The optimisation of C-MSPAs can be formulated as an objective optimisation problem, where the objective aims to maximize sound absorption at targeted frequencies. Considering a C-MSPA with an absorption spectrum $\alpha_0(f)$, the objective function is defined as follows:

$$F_N(d_i, t_i, D_i, \phi_i) = \min\left(1 - \sum_{f_1}^{f_2} \alpha_0(f) G(f)\right). \tag{100}$$

Here, the weight function $G(f)$ accounts for the importance of different frequency components in the optimisation process. It is calculated as:

$$G(f) = \frac{\Phi_{pp}(f)}{\sum_{f_1}^{f_2} \Phi_{pp}(f)}, \tag{101}$$

where $\Phi_{pp}(f)$ represents the power spectral density of the noise source at the targeted frequency f, reflecting the strength of the noise source at these frequencies. If the noise source needs to be reduced at all interested frequencies, the weight function $G(f)$ can be set to unity.

The objective function is formulated as a minimisation problem to maximize sound absorption at target frequencies. The optimisation process uses the gradient-based method, sequential quadratic programming (SQP) [282], available in MATLAB's Optimisation Toolbox. Specifically, the **`fmincon`** function is used to minimise the objective function with constrained nonlinear multiple variables.

The design variables for the C-MSPAs include the slit width d_i, panel thickness t_i, air cavity depth D_i, and porosity ϕ_i. Therefore, the air cavity width W_i can replace the porosity ϕ_i as a design variable. Constraints are set to ensure that the geometrical parameters remain within a feasible range, preventing unrealistic configurations. The

walls of the panels, necks, and internal segments between the air cavities have a fixed thickness of $h = 1$ mm in this study to ensure structural integrity. This thickness can be adjusted based on manufacturing requirements.

For a given C-MSPA with a depth of D_A and width of W_A, as shown in Fig. 8.1 (b), the constraints are defined as follows: $d_i \in [d_{\min}, d_{\max}]$, $t_i < D_A - h$, $D_i \leq D_A - 2h$, $W_i > t_i + 2h$, and $\sum W_i \leq L_A$. These constraints are based on practical considerations of the manufacturing process and sound absorption performance.

The minimum slit width of $d_{\min} = 0.3$ mm is chosen to ensure successful production of numerous slits using a desktop 3D printer, comparable to the smallest drill bit size used in computer numerical control (CNC) milling machines for thin panels [176]. A maximum slit width of $d_{\max} = 1$ mm is selected to keep the slits within the sub-millimeter range, ensuring significant viscous and thermal losses for sound absorption performance.

The bounds of the design variables are selected to ensure physically realizable optimised geometrical parameters that achieve the desired sound absorption performance. The optimisation process is performed iteratively, starting with randomly selected initial geometrical parameters within the feasible range. The process terminates when the objective function converges to a local minimum, indicating the optimal geometrical parameters of the C-MSPAs.

Similarly, for the optimisation of C-MSPAs under grazing incidence, the same weight function of Eq. 101 can be used. The transmission loss is calculated using Eq. 99 based on the hybrid method, which will be detailed in Section 8.4. The objective function can be formulated as:

$$F_T(d_i, t_i, D_i, \phi_i) = \min\left(-\sum_{f_1}^{f_2} TL(f)G(f)\right). \tag{102}$$

The optimised C-MSPAs are then validated through numerical simulations and experimental measurements. Further details regarding the optimisation of annular ring designs of the C-MSPAs will be presented and discussed in Section 8.4.

8.3 Sound absorption of C-MSPAs under normal incidence

8.3.1 Experimental and numerical setup

To validate the sound absorption performance of the compact micro-slit panel absorbers (C-MSPAs) under normal incidence, a comprehensive approach combining numerical modelling and experimental setups was employed. The experimental facilities were developed based on the impedance tube method, following the ISO 10534-2 standard [283]. This widely recognized method is specifically designed for measuring the sound absorption coefficient of sound absorbers under normal incidence. The two-microphone technique calculates the sound absorption coefficient based on the transfer function between incident and reflected sound waves. The experimental setup, depicted in Fig. 8.2 (a), has been successfully utilised in previous studies [176, 284], demonstrating its reliability and effectiveness.

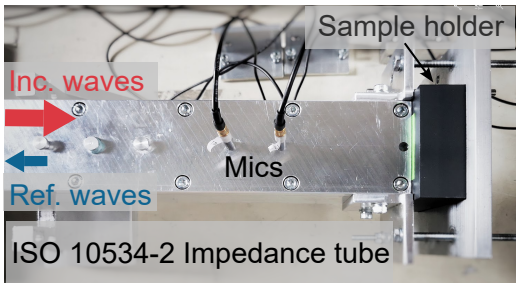

(a) Experimental setup

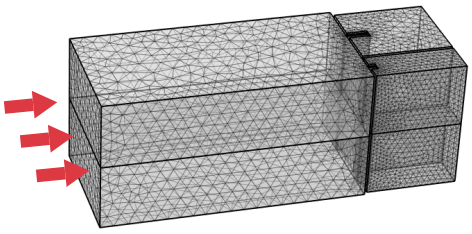

(b) Numerical model for normal incidence

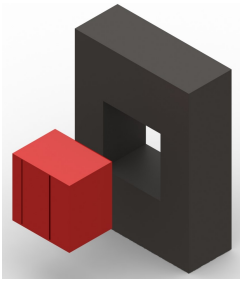

(c) Test sample holder

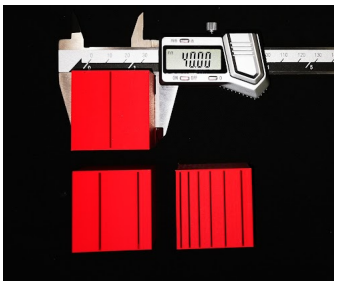

(d) 3D-printed test samples

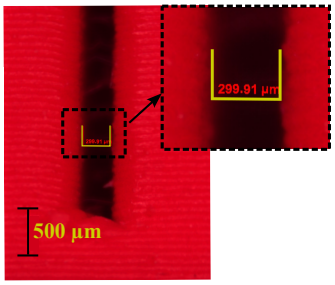

(e) Optical microscope inspection

Figure 8.2: Experimental setup of the impedance tube method [283] and numerical model based on the 3D FEM method.

To ensure accurate measurement of the noise signal, GRAS 40PH microphones were employed. Within the frequency range of 50 Hz to 5 kHz these microphones have an uncertainty of ±1.5 dB and a dynamic range topping at around 135 dB. Prior to the experiments, the sensitivity of each microphone was calibrated using a GRAS 42AG Multifunction Sound Calibrator. The calibrator was set at a sound pressure level of 94 dB and a frequency of 1 kHz, ensuring precise and consistent measurements.

On the numerical modelling side, a thermoviscous solver employing a 3D finite element method (FEM) in COMSOL Multiphysics 6.1 was utilised. A planar sound wave was employed as the incident sound wave. To accurately capture the thermal-viscous effects of the narrow slits, the viscous and thermal boundary layers thickness were used as a meshing control parameter at the boundaries, which were calculated as follows:

$$\begin{aligned} \delta_{visc} &= \sqrt{\frac{2\mu}{\omega\rho_0}}, \\ \delta_{therm} &= \sqrt{\frac{2k_a}{\omega\rho_0 C_P}}, \end{aligned} \tag{103}$$

where μ is the dynamic viscosity of air, k_a is the thermal conductivity of air, C_P is the specific heat capacity of air at constant pressure. The maximum element size was carefully calculated based on the wavelength of the incident sound wave at the highest frequency of interest. A meticulous mesh independence study was conducted to ensure the accuracy of the numerical model, resulting in a final mesh containing an optimal number of elements. A total of 12 cell layers near walls of the slits and air cavities, ensuring accurate capture of the thermal-viscous effects. The numerical model is depicted in Fig. 8.2 (b). The frequency range of interest spanned from 300 to 3000 Hz, effectively covering the low-frequency broadband noise absorption range of the C-MSPAs.

To validate the sound absorption performance of the C-MSPAs under normal incidence (NI), three different frequency ranges were targeted:

- NI-1: a single frequency at 600 Hz,
- NI-2: dual frequencies at 600 and 1200 Hz,
- NI-3: broadband noise ranging from 1000 to 2000 Hz.

These three cases represent typical noise sources encountered in axial fans, considering low-frequency tonal noise and broadband noise. The optimisation of the C-MSPAs under normal incidence was conducted using the EF model [273], which has comparable accuracy to the Maa model and superior accuracy compared to the RV model, as reported by Cobo *et al.* [177, 191]. The optimisation process involved varying the geometrical parameters of the C-MSPAs, as described in Section 8.2.3. The thickness of all walls, including the panel, slits, and air cavities, was set to 1 mm for manufacturability. The test samples were securely mounted in the impedance tube using a sample holder with sealing gaskets to ensure airtightness, as shown in Fig. 8.2 (c). For all three optimisation cases, the weight function $G(f)$ was set to unity for simplicity, as the noise sources were assumed to be equally important at all targeted frequencies.

The geometrical parameters of the optimised C-MSPAs can be found in Table F.1 in the Appendix.

The test samples were additively manufactured using fused deposition modelling (FDM) with a Bambu P1S printer, featuring a layer height of 0.08 mm and a nozzle diameter of 0.4 mm, as shown in Fig. 8.2 (c). Ciochon *et al.* [285] carefully examined the effect of surface roughness on sound absorbers by using four layer heights of 0.1 mm, 0.15 mm, 0.2 mm, and 0.25 mm on an FDM 3D printer and found that a rougher surface with a larger layer height increased the sound absorption, which is one of the reasons for the discrepancy between experiments and simulations. To minimise the effect of surface roughness, the 0.08 mm layer height was selected for the test samples. The ironing smooth feature was enabled for all layers in the slicing software to further reduce the surface roughness, although the printing time was significantly increased. In addition, a small dimension correction was necessary based on electron microscopy inspection, as the actual slit width was smaller (approximately 0.03 mm) than the designed width due to the material deposition process. This issue is commonly encountered in additive manufacturing [176, 286] and was addressed through meticulous trial and error to determine the optimal dimension corrections. The sizes of the slits were carefully verified using electron microscopy, as shown in Fig. 8.2 (d). It should be noted that the edges of the slits fabricated by the FDM process are not perfectly sharp due to the layer-by-layer deposition process, which slightly affects the impedance from the edges of the slits. However, this effect is negligible compared to the impedance from the slits and air cavities, as confirmed by analytical analysis. Initially, the stereolithography (SLA) process was considered for fabricating the C-MSPAs with sharper edges, but it was found unsuitable for thin-walled structures due to deformation issues. Increasing the wall thickness to prevent deformation would decrease the air cavity volume, which is undesirable for sound absorption performance. Therefore, the FDM process was selected for this research.

8.3.2 Results

Results comparison among experimental, numerical, and analytical methods

Figure 8.3 shows the experimental, numerical, and analytical results of the sound absorption coefficient of the C-MSPAs under normal incidence. The results are presented for different frequency ranges: (a) 600 Hz, (b) 600 and 1200 Hz, and (c) 1000–2000 Hz. The schematics of the C-MSPAs are also shown in the insets of Fig. 8.3. Several key findings can be observed. Firstly, the optimised C-MSPAs exhibit a remarkably high sound absorption coefficient in the targeted frequency ranges for single tone, dual tones, and broadband spectra, confirming their exceptional effectiveness. Furthermore,

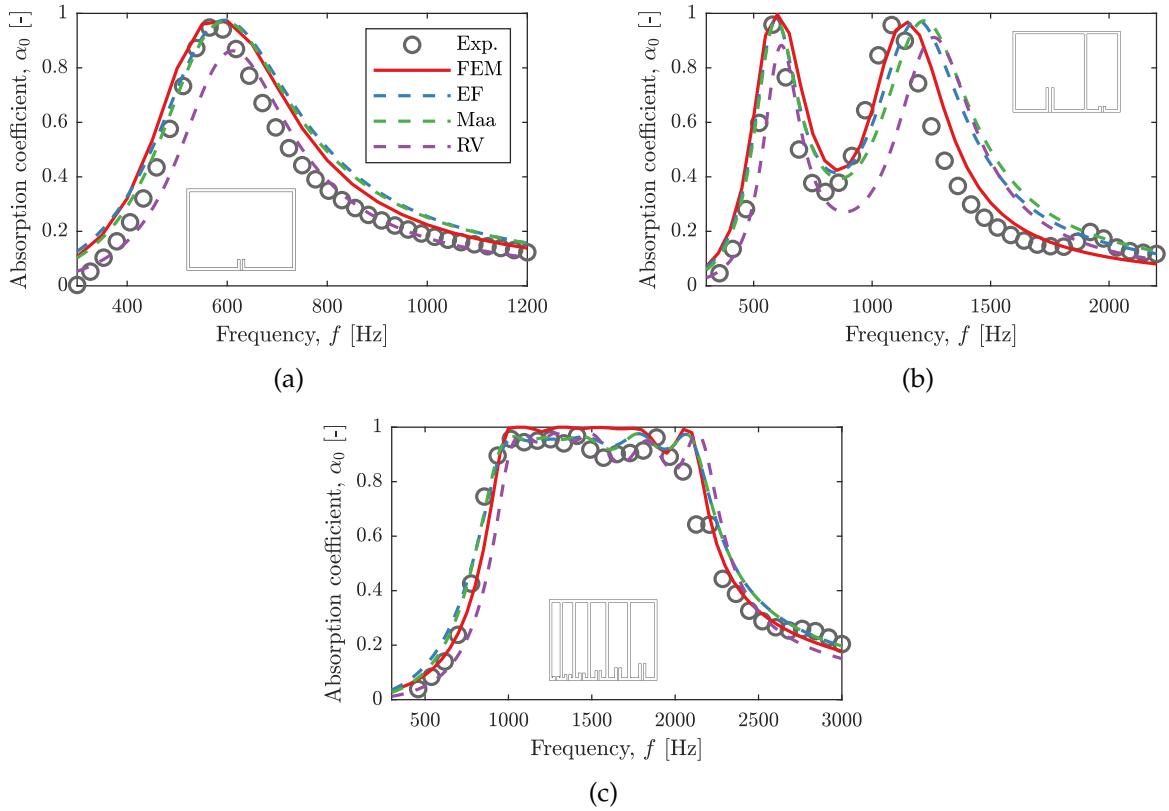

Figure 8.3: Experimental, numerical and analytical results of the sound absorption coefficient of the compact micro-slit absorbers under normal incidence targeting different frequency ranges: (a) NI-1: 600 Hz, (b) NI-2: 600 and 1200 Hz, and (c) NI-3: 1000–2000 Hz. Three analytical models used for impedance prediction are compared: the equivalent fluid (EF) model [273, 274], the Maa model [170, 182, 183], and the Randeberg and Vigran (RV) model.

the results also demonstrate excellent agreement between the numerical model and the experimental setup, validating the accuracy of the numerical model in predicting the sound absorption performance of the C-MSPAs. Lastly, the three analytical models (EF, Maa, and RV) were used to predict and optimise the sound absorption performance of the C-MSPAs. The results indicate that the EF model achieves comparable accuracy to the Maa model, while the RV model exhibits slightly lower accuracy. These findings align with those reported by Cobo *et al.* [177, 191] for standard micro-slit resonator designs. These results highlight the effectiveness of the optimisation process and the sound absorption performance of the C-MSPAs, showcasing their potential for noise control applications under normal incidence.

Results comparison with SD-CMSPA

To further evaluate the benefits of using compact micro-slit panel absorbers (C-MSPAs), a comparison was made with the standard micro-slit panel absorber (SD-MSPA) under normal incidence. Both absorbers were optimised using the analytical models presented in Section 8.2.2 to achieve the highest sound absorption coefficient at the targeted

frequency (i.e., NI-1: 600 Hz) while maintaining a thinner absorber thickness.

The results, depicted in Fig. 8.4, show that the C-MSPA exhibits similar sound absorption performance to the SD-MSPA at 600 Hz. However, the C-MSPA is much thinner and lighter, achieving a 36% thickness reduction and 75% weight reduction. This demonstrates the superior performance of the C-MSPA in terms of weight and thickness, making it a promising alternative for noise control applications where these factors are critical.

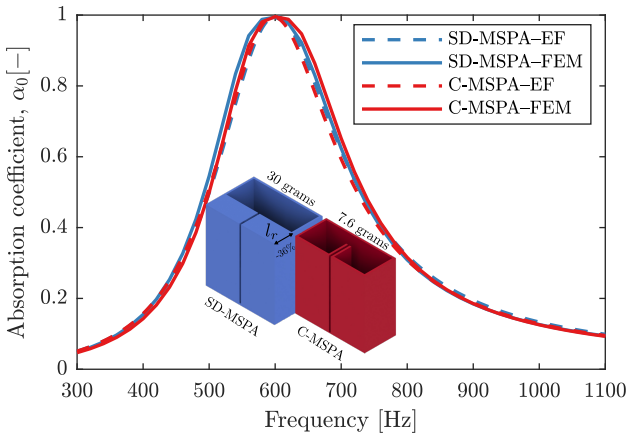

Figure 8.4: Comparison of the sound absorption coefficient between the standard micro-slit panel absorber (SD-MSPA) and the compact micro-slit panel absorber (C-MSPA) under normal incidence. For SD-MSPA, the geometrical parameters are $d = 1.00$ mm, $t = 10.91$ mm, $D = 16.00$ mm, $W = 38.00$ mm, while for C-MSPA, these are $d = 1.00$ mm, $t = 10.95$ mm, $D = 16.00$ mm, $W = 38.00$ mm, respectively.

Results comparison with commercial acoustic foams

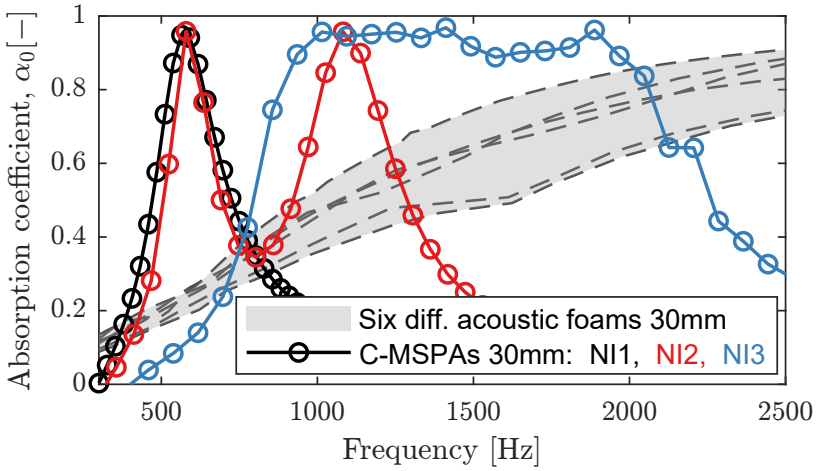

Figure 8.5: Comparison of the sound absorption coefficient between the three C-MSPAs (*i.e.* NI-1, NI-2, NI-3) and six commercially available acoustic foams made of porous materials (*e.g.*, melamine foam and polyurethane foam).

To further evaluate the sound absorption performance of the C-MSPAs, a comparison

was made with six commercially available acoustic foams made of porous materials, such as melamine foam and polyurethane foam. The foams from BASF (*i.e.*, Basotect UL, Basotect UF, Basotect G, and Basotect G+) and Advanced Acoustics were selected for comparison due to their widespread use in various noise control applications. The sound absorption coefficients for the same thickness (*i.e.*, 30 mm) of the acoustic foams were provided by the manufacturers and obtained based on the same standardized method [283].

The results, depicted in Fig. 8.5, show that the C-MSPAs have better sound absorption performance than commercial acoustic foams at the designed frequencies. While porous materials can achieve high sound absorption coefficients up to 0.8 above 2000 Hz, their performance drops significantly at lower frequencies. In contrast, the C-MSPAs maintain a high sound absorption coefficient at the designed frequencies of 600 Hz, 1200 Hz, and 1000–2000 Hz. This demonstrates their exceptional performance for low-frequency, broadband noise absorption. Additionally, the C-MSPAs are resistant to dust, moisture, and other environmental factors, making them a promising alternative to traditional porous materials for noise control, especially in the low-frequency range.

Results comparison with other compact broadband MPP-Type absorbers reported in the literature

Figure 8.6 compares the sound absorption bandwidth (sound absorption coefficient > 0.8) of the C-MSPAs with other compact broadband MPP-type absorbers reported in the literature. The red bars represent the C-MSPAs under NI-I, NI-II, and NI-III conditions, with experimental data derived from Fig. 8.3. The green bar corresponds to the hybrid absorber proposed by [287], which integrates an MPP with coiled-up Fabry–Pérot channels. The yellow bar denotes an MPP absorber with partitions incorporating a Helmholtz resonator, as investigated in [288]. The magenta and cyan bars represent the single-layer and double-layer MPP absorbers with partitions, respectively, from [288]. The orange bar indicates a single-layer absorber with multiple parallel-arranged inhomogeneous microperforations, as studied in [289]. All data in this comparison are based on experimental results. The C-MSPAs demonstrate enhanced sound absorption characteristics, achieving a wide absorption bandwidth with compact thickness, making them highly promising for compact noise control applications.

8.3.3 Sensitivity analysis

To investigate the sensitivity of the sound absorption coefficient of the compact micro-slit absorbers (C-MSPAs) to various geometrical parameters, a comprehensive sensitiv-

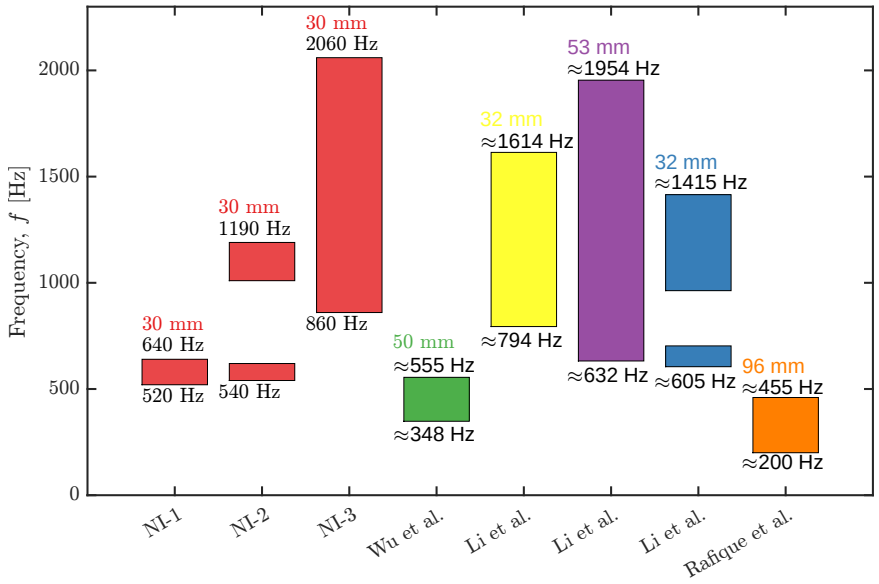

Figure 8.6: Comparison of the sound absorption bandwidth (sound absorption coefficient > 0.8) of C-MSPAs and other compact broadband MPP-type absorbers.

ity analysis was conducted. This analysis focused on four key parameters: slit width (d), panel thickness (t), air cavity depth (D), and porosity (ϕ). By utilising the equivalent fluid (EF) model [273], the sound absorption performance of the C-MSPAs was accurately predicted. For the sake of simplicity and clarity, the sensitivity analysis was performed for a single frequency of 600 Hz under normal incidence, *i.e.*, the NI-1 case.

The results, depicted in Fig. 8.7, show the significant impact of these geometrical parameters on the sound absorption coefficient. Several key findings emerge from the sensitivity analysis. Firstly, increasing the slit width (d) from 0.3 mm to 1 mm shifts the frequencies of the sound absorption peaks, as shown in Fig. 8.7 (a). This is because the impedance is approximately inversely proportional to the slit width [189]. This indicates an optimal slit width that maximizes the sound absorption coefficient. Similarly, increasing the porosity (ϕ) from 0.5% to 20% shows a similar trend, as depicted in Fig. 8.7 (d). Conversely, increasing the panel thickness (t) from 0.5 mm to 15 mm shows an opposite trend, as shown in Fig. 8.7 (b). This is because the impedance is approximately proportional to the thickness [189]. The sound absorption coefficient decreases with increasing thickness due to the rise in the impedance of the slits. Thus, an optimal solution exists for varying the panel thickness. Lastly, the depth of the air cavity (D) significantly impacts the frequencies of the sound absorption peaks, while the magnitudes of the sound absorption coefficient are less sensitive to the air cavity depth, as demonstrated in Fig. 8.7 (c). These results provide valuable insights into the design and optimisation of the C-MSPAs for sound absorption applications, which can also contribute to the development of tunable sound absorbers in future research.

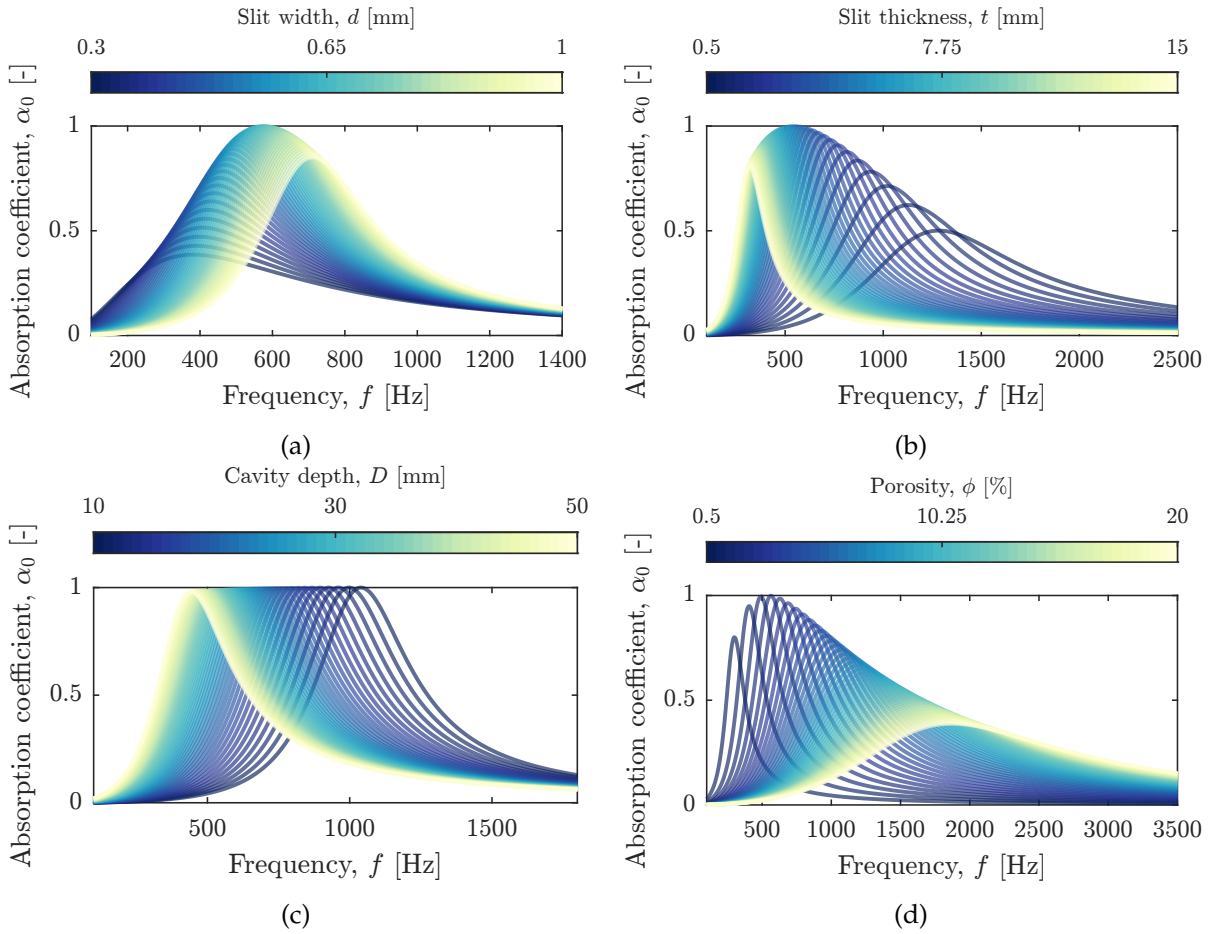

Figure 8.7: Sensitivity analysis of the NI-1 C-MSPA for the sound absorption coefficient under normal incidence. The analysis examines four geometrical parameters: (a) slit width d, (b) thickness t, (c) air cavity depth D, and (d) porosity ϕ using the EF model. The baseline values for NI-1 case are $d = 0.73$ mm, $t = 4.06$ mm, $D = 28.00$ mm, and $\phi = 1.85\%$ (*i.e.*, $W = 38$ mm) as shown in Table F.1. Each parameter is varied with a constant step size while keeping the others constant.

8.4 Transmission loss of C-MSPAs under grazing incidence

8.4.1 Methodology

Annular designs of acoustic liners have gained special attention for various duct applications, including aircraft engines, HVAC systems, and automotive exhaust systems. The proposed compact micro-slit panel absorbers (C-MSPAs) can be a promising candidate for these applications due to their lightweight nature and exceptional sound absorption performance for low-frequency, broadband noise. The design and optimisation of the annular rings of C-MSPAs will be introduced in this section, focusing on the sound absorption performance under grazing incidence. The hybrid method, combining analytical impedance models with a 3D numerical impedance tube, will

be employed to optimise the annular rings of C-MSPAs under grazing incidence. The optimised C-MSPAs will be validated through 3D numerical simulations.

The numerical model was developed using a 3D finite element method (FEM) thermoviscous solver. To reduce computational costs, only a quarter of the C-MSPAs was modelled, with symmetry boundary conditions applied. Perfectly matched layers (PMLs) were implemented at the boundaries to absorb outgoing waves, as shown in Fig. 8.8. The numerical model featured a circular cross-section impedance tube with a diameter of 77 mm, representing a typical internal diameter for server fans with an 80 mm frame. The annular rings of C-MSPAs had a length of 60 mm and a thickness of 30 mm, which can be adjusted based on the available space in the duct system or electronics enclosures. A planar sound wave was generated in the background acoustic field. The transmission loss was calculated using Eq. 99, comparing the incident sound power at PL1 to the transmitted sound power at PL2. This 3D numerical model simulates the detailed geometry of the annular rings of C-MSPAs, providing accurate predictions of the sound absorption performance under grazing incidence.

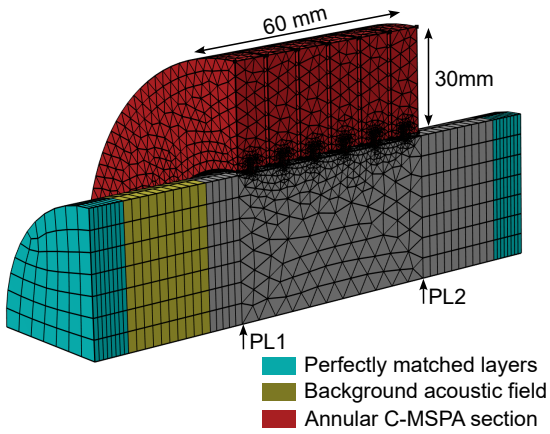

Figure 8.8: Numerical model of the compact micro-slit absorbers under grazing incidence. The 3D finite element method (FEM) thermoviscous solver was employed to simulate the detailed geometry of the annular rings of C-MSPAs in COMSOL Multiphysics 6.1.

However, the 3D FEM models proved to be computationally expensive for simulating and optimising the annular rings of C-MSPAs under grazing incidence, as the detailed geometry of the C-MSPAs significantly increased the computational time. Therefore, we developed a hybrid method that combines analytical impedance models (EF, Maa, and RV) with the 3D numerical impedance tube. In this hybrid method, we simplified the detailed geometry of the annular rings of C-MSPAs as impedance boundary conditions, and calculated the impedance using the analytical models. Subsequently, we applied the impedance of the C-MSPAs to the 3D numerical impedance tube to calculate the transmission loss. This hybrid method significantly accelerated the optimisation process of the annular rings of C-MSPAs under grazing incidence by avoiding the need

to simulate the detailed geometry in the 3D FEM model. The optimisation procedures for the annular rings of C-MSPAs can be found in Section 8.2.3. For the optimisation, we utilised the EF model to calculate the impedance of the C-MSPAs.

To verify the sound absorption performance of C-MSPAs under grazing incidence (GI), we considered three test cases:

- GI-1: a single frequency at 600 Hz,
- GI-2: a single frequency at 1200 Hz,
- GI-3: broadband noise ranging from 900 to 1800 Hz.

The dual frequency case was omitted due to its similarity to the broadband noise case regarding the optimisation process. The optimisation process aimed to maximize the transmission loss of the C-MSPAs at the targeted frequencies. The weight function $G(f)$ was set to unity for simplicity, as the noise sources were assumed to be equally important at all targeted frequencies. The optimised geometrical parameters of the annular rings of C-MSPAs under grazing incidence were validated through 3D numerical simulations.

8.4.2 Results

The results of the transmission loss of C-MSPAs under grazing incidence are shown in Fig. 8.9. We compared the transmission loss for different frequency ranges: (a) GI-1: 600 Hz, (b) GI-2: 1200 Hz, and (c) GI-3: 900–1800 Hz. The hybrid methods exhibit slight mismatches compared to the numerical model, primarily due to the simplification of the C-MSPAs' geometry. Among the three analytical models—EF, Maa, and RV—all provide similar results, with the RV model showing slightly better agreement with the numerical model. The computational time of the hybrid methods is significantly less than that required by the 3D FEM model, demonstrating the efficiency of the hybrid method for the initial design of the annular rings of C-MSPAs under grazing incidence.

Ultimately, the results from the 3D FEM model were used for the final design of the annular rings of C-MSPAs under grazing incidence. Although the hybrid method sacrifices some accuracy compared to the 3D FEM model due to the simplification of the C-MSPAs' geometry, it remains a suitable choice for the initial optimisation of the annular rings of C-MSPAs under grazing incidence. However, the 3D FEM model is essential for the final validation of the optimised C-MSPAs, ensuring accurate predictions of the sound absorption performance under grazing incidence. The final optimised geometrical parameters of the annular rings of C-MSPAs under grazing

incidence can be found in Table F.2 in the Appendix. These optimised C-MSPAs will be further applied to CR fan noise reduction in Section 8.5.

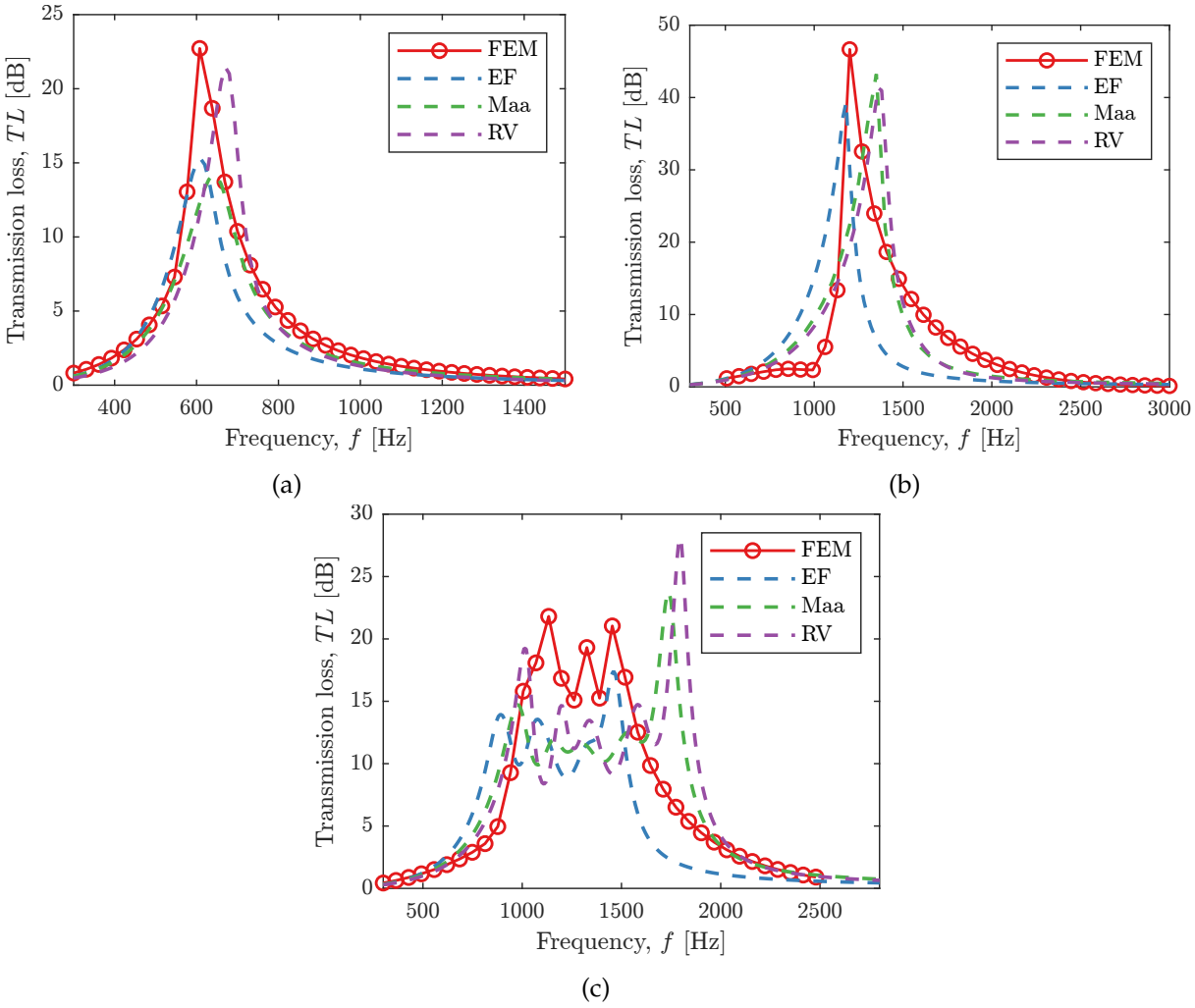

Figure 8.9: Numerical and analytical results of the transmission loss of the compact micro-slit absorbers under grazing incidence targeting different frequency ranges: (a) GI-1: 600 Hz, (b) GI-2: 1200 Hz, and (c) GI-3: 900–1800 Hz.

8.5 Experimental investigation of C-MSPAs for counter-rotating fan noise reduction

8.5.1 Experimental setup and test conditions

The annular ring designs of the C-MSPAs discussed in Section 8.4 were fabricated and subjected to rigorous testing to evaluate their effectiveness in reducing counter-rotating (CR) fan noise. The fabrication process involved the use of additive manufacturing techniques, and the dimensions of the C-MSPAs were meticulously examined using microscopy, as previously discussed in Section 8.3.1.

To assess the noise reduction performance of the C-MSPAs, an experimental setup was used as depicted in Fig. 8.10. The acoustic test facilities have been detailed in Appendix A.2. The fan was operated at various speeds to generate noise, which was then measured at seven distinct locations using GRAS 40PH microphones. The effectiveness of the C-MSPAs in reducing noise levels was evaluated by comparing the measurements obtained with and without the presence of the C-MSPAs. This evaluation was conducted for three different scenarios: a single frequency at 600 Hz (GI-1), a single frequency at 1200 Hz (GI-2), and broadband noise ranging from 900 to 1800 Hz (GI-3).

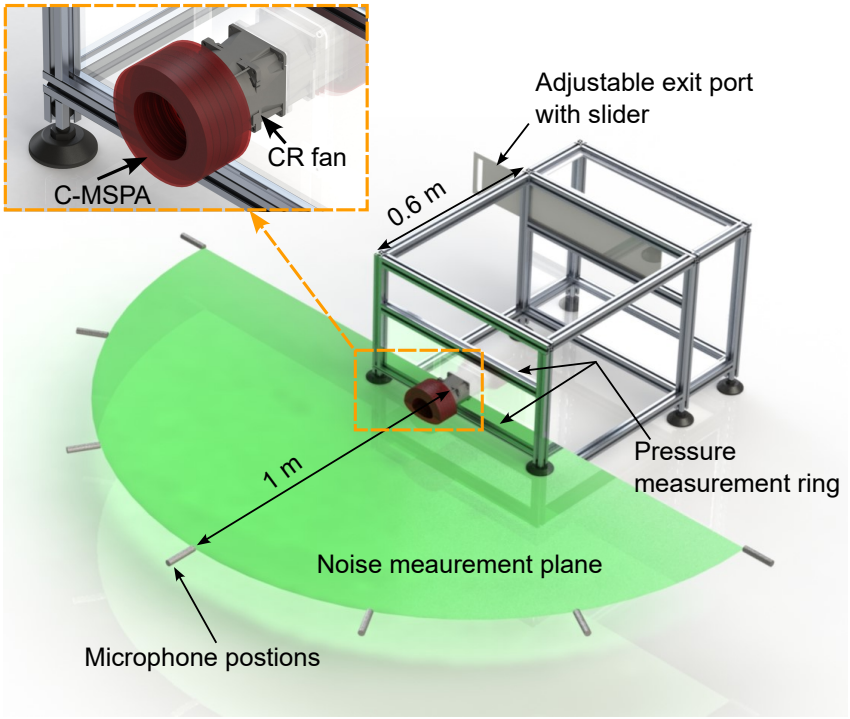

Figure 8.10: Experimental setup of the compact micro-slit absorbers for the counter-rotating fan noise reduction.

The test fan used in the experiments was the SanYo Denki 9CRA0812P8G001, a CR fan equipped with two rotors. The fan speed was controlled using pulse width modulation (PWM) signals. The inlet fan and outlet fan have the nominal speeds of 12000 RPM and 11300 RPM, respectively. The maximum Mach number based on the axial velocity of the fan is around 0.047, which is considered low-speed flow.

The CR fan is expected to generate high tonal and broadband noise due to the complex interactions within the fan system. The tonal noise is generated by the interactions between the turbulent flow and the front rotor, front rotor-stator/stator-rear rotor, and front rotor-rear rotor. The broadband noise is mainly caused by pressure fluctuations in the turbulent flow, particularly at the leading and trailing edges. The tonal noise is primarily caused by the interaction frequency f_m and the circumferential mode order

m of the prominent tones, which can be determined as [157, 270]:

$$f_m = \frac{1}{60}|m_1 B_1 \Omega_1 + m_2 B_2 \Omega_2| \quad \text{and} \quad m = m_2 B_2 - m_1 B_1, \tag{104}$$

where m, m_1, and m_2 are integers, f_m is the interaction frequency, $B_1 = 5$ and $B_2 = 4$ are the number of blades of the front and rear rotors, and Ω_1 and Ω_2 are the rotational speeds of the front and rear rotors in RPM. To generate the desired frequencies of 600 Hz, 1200 Hz, and 900–1800 Hz, the fan speeds were adjusted accordingly.

In addition to the noise generated by the CR fan, which exhibits complex tonal and broadband noise components, a supplementary investigation was conducted using loudspeaker white noise to assess the noise reduction performance of the C-MSPAs under flow-free conditions. The noise generated by the Visaton FR8 speaker was amplified by the IMG Stageline STA500 amplifier and emitted at a frequency range of 300–3000 Hz. This supplementary investigation aimed to establish a flow-free case for comparison with the CR fan noise reduction performance.

To establish a benchmark, an industrial standard acoustic foam (Advanced Acoustics Acousti-Slab Acoustic Foam) was used as a reference sound absorber, while a solid panel served as the baseline case. Each measurement was repeated three times to ensure reliability and consistency.

During each acoustic measurement, a sampling frequency of 51.2 kHz and a recording period of 20 s were utilised. The acquired acoustic signals were processed using a Hanning window with 50% overlap. The mean time-averaged sound pressure level (SPL) at the reference surface was calculated by averaging the sound pressure levels recorded at the seven microphone locations. The noise reduction performance of the C-MSPAs and the acoustic foam was evaluated by comparing the sound pressure levels in one-third octave bands with and without the sound absorbers. Furthermore, the directivity of the sound absorbers was investigated by plotting the sound pressure levels at different angles within the specified frequency ranges.

The results of the noise reduction performance of the C-MSPAs under CR fan noise and loudspeaker white noise conditions will be presented in Section 8.5.2 and Section 8.5.2, respectively.

To comprehensively assess the impact of the sound absorbers on fan performance, the fan performance curves were measured in an AMCA 210-16 wind tunnel [211], which has been detailed in Section 3.2.2. The baseline case, the acoustic foam, and the C-MSPAs were tested, and their respective fan performance curves were compared to evaluate the influence of the sound absorbers on fan performance. These findings will be presented in Section 8.5.2.

8.5.2 Results

Noise reduction performance of C-MSPAs without flow

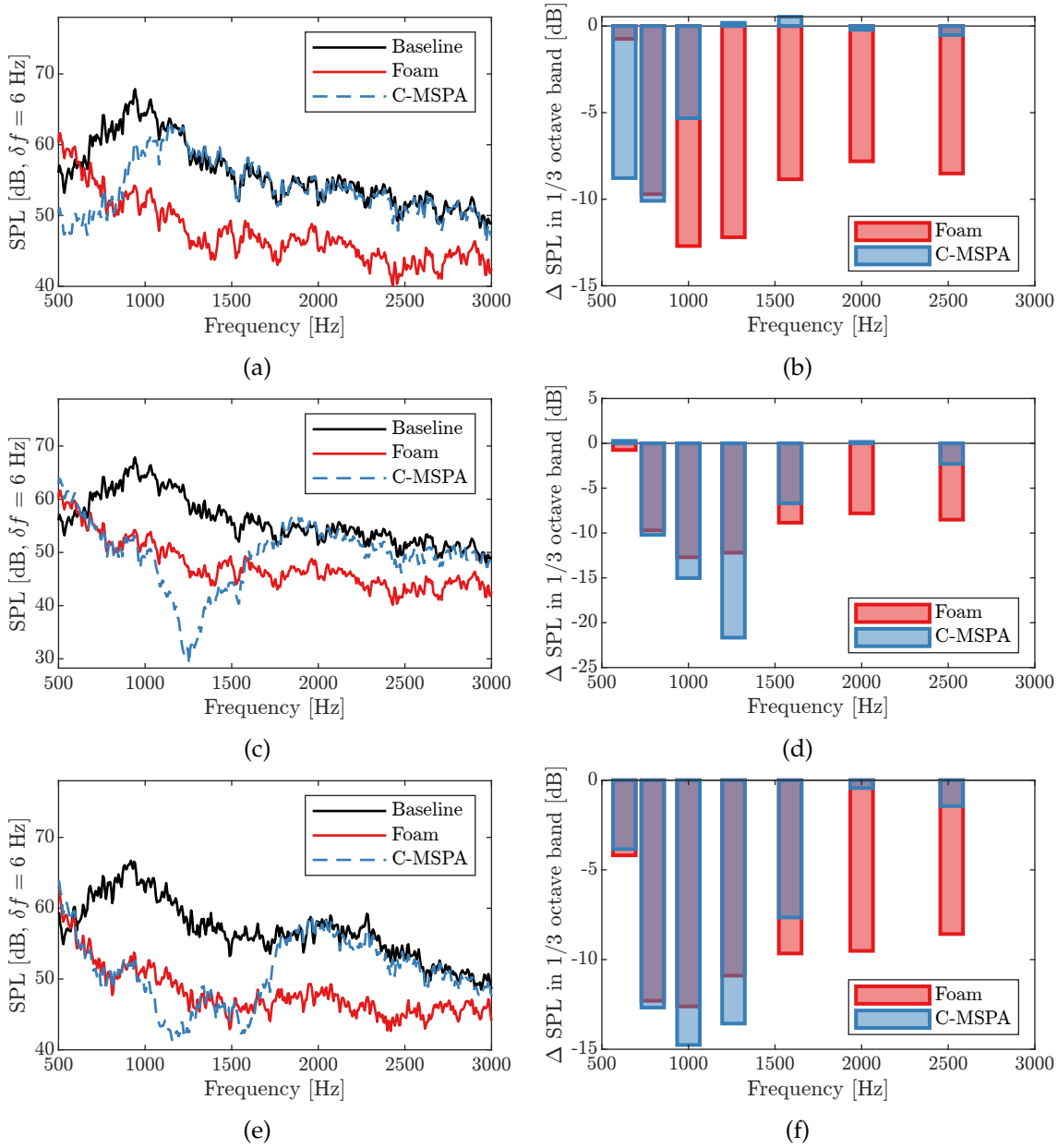

Figure 8.11: Experimental results of the sound pressure level (SPL) and noise reduction performance (ΔSPL) of the compact micro-slit absorbers for loudspeaker white noise without flow. The acoustic spectra comparisons among the baseline, the acoustic foam, and the C-MSPAs are shown for three distinct cases: (a) GI-1: 600 Hz, (c) GI-2: 1200 Hz, and (e) GI-3: 900–1800 Hz. The noise reduction in one-third octave bands with respect to the baseline is presented for the same cases: (b) GI-1, (d) GI-2, and (f) GI-3.

Figure 8.11 presents the experimental results of the sound pressure level (SPL) (Fig. 8.11 (a), (c), (e)) and the corresponding noise reduction performance in one-third octave band of the C-MSPAs (Fig. 8.11 (b), (d), (f)) for loudspeaker white noise without flow. These results are obtained for three different cases: GI-1: a single frequency at 600 Hz,

GI-2: a single frequency at 1200 Hz, and GI-3: broadband noise ranging from 900 to 1800 Hz. The acoustic spectra comparisons among the baseline, the acoustic foam, and the C-MSPAs are shown in Fig. 8.11 (a), (c), (e), while the noise reduction in one-third octave bands with respect to the baseline is presented for the same cases in Fig. 8.11 (b), (d), (f).

The findings show that the C-MSPAs effectively reduce noise at the targeted frequencies, validating the design and optimisation approach used in Section 8.4.1. For consistency, the C-MSPAs were compared with the baseline and the acoustic foam, and the noise reduction performance was evaluated in the center frequencies of the one-third octave bands with respect to the baseline. Overall, the C-MSPAs demonstrate excellent noise reduction performance over baseline case, with noise reduction levels of around 9 dB for GI-1, 22 dB for GI-2, and averaged 12 dB for GI-3.

Notably, the C-MSPAs outperform the industrial standard acoustic foam, especially at the specified frequencies. For the GI-1 case, the C-MSPAs achieve more than 8 dB noise reduction at 630 Hz compared to the acoustic foam, as shown in Fig. 8.11 (b). Similarly, for the GI-2 case, the C-MSPAs achieve more than 10 dB noise reduction at 1250 Hz compared to the acoustic foam, as depicted in Fig. 8.11 (d). Although it is challenging to surpass the noise reduction performance of the acoustic foam in the broadband noise case, the C-MSPAs demonstrate remarkable noise reduction capabilities for broadband noise (900–1800 Hz). The C-MSPAs show an averaged noise reduction of more than 2 dB over 900–1800 Hz compared to the acoustic foam, as shown in Fig. 8.11 (f). These results confirm the effectiveness of C-MSPAs for noise reduction without flow.

Noise reduction performance of C-MSPAs for CR fan with flow

To further investigate the noise reduction performance of the C-MSPAs for CR fan noise under real flow conditions, comprehensive measurements of sound pressure level and noise reduction performance were conducted. As the Mach number of the fan flow is relatively low (around 0.035 with 76% PWM), the convection effect on the sound absorption performance of the C-MSPAs is negligible.

The experimental results of the noise reduction performance of the C-MSPAs for CR fan noise are presented in Fig. 8.12. The C-MSPAs were tested with flow for three distinct cases: CR1: a single frequency at 600 Hz, CR2: a single frequency at 1200 Hz, and CR3: broadband noise ranging from 900 to 1800 Hz. The acoustic spectra comparisons among the baseline, the acoustic foam, and the C-MSPAs are shown in Fig. 8.12 (a), (c), (e), while the noise reduction in one-third octave bands with respect to the baseline is presented for the same cases in Fig. 8.12 (b), (d), (f).

The C-MSPAs consistently exhibit exceptional noise reduction performance at the tar-

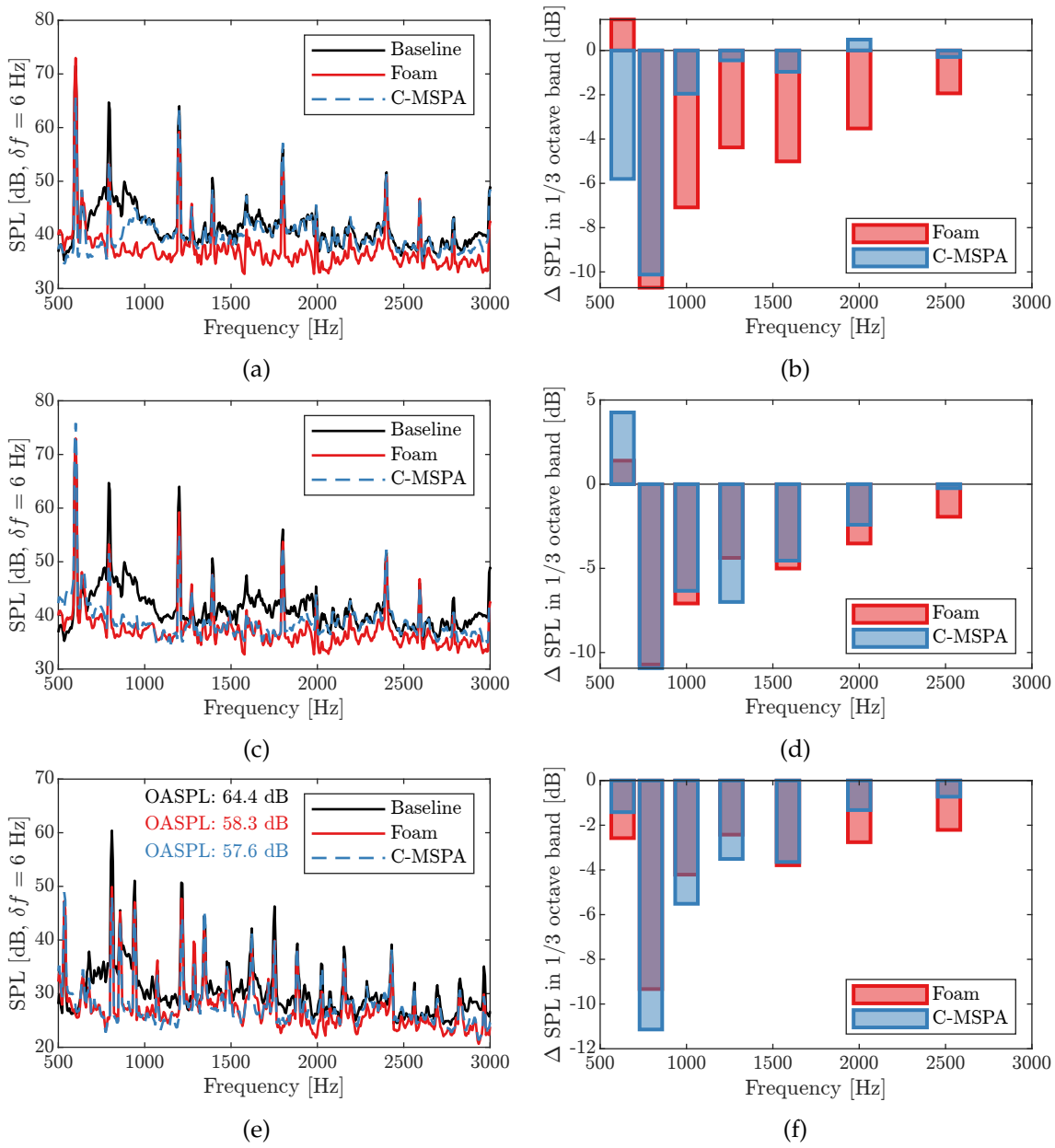

Figure 8.12: Experimental results of the sound pressure level (SPL) and noise reduction performance (ΔSPL) of the C-MSPAs for CR fan noise with flow. The acoustic spectra comparisons among the baseline, the acoustic foam, and the C-MSPAs are shown for three distinct cases: (a) GI-1: 600 Hz, (c) GI-2: 1200 Hz, and (e) GI-3: 900–1800 Hz. The noise reduction in one-third octave bands with respect to the baseline is presented for the same cases: (b) GI-1, (d) GI-2, and (f) GI-3. For GI-1 and GI-2, the fan speed is set to 76% PWM, while for GI-3, the fan speed is set to 46% PWM.

geted frequencies, surpassing the performance of industrial standard acoustic foam. In the CR1 case, C-MSPAs achieve around 6 dB noise reduction at the target frequency compared to the baseline case (Fig. 8.12 (b)). Similarly, in the CR2 case, C-MSPAs achieve around 7 dB noise reduction at 1250 Hz compared to the baseline case, which is more pronounced than the acoustic foam (around 4.5 dB) (Fig. 8.12 (d)). For broadband noise, C-MSPAs effectively reduce noise over the frequency range of 900–1800 Hz,

achieving an average noise reduction of around 6 dB compared to the baseline case, which is more effective than the acoustic foam (around 1.5 dB) (Fig. 8.12 (f)). That can also be seen in the narrowband spectral comparison in Fig. 8.12 (e), where the C-MSPAs exhibit lower sound pressure levels than the baseline and the acoustic foam, exhibiting an overall sound pressure level (OASPL) of 57.6 dB, outperforming solid panels (64.4 dB) and acoustic foam (58.3 dB) within the frequency range of 500 Hz to 3000 Hz. These results confirm the remarkable effectiveness of C-MSPAs in noise control applications with flow, particularly for CR fan noise.

However, both the C-MSPAs and the acoustic foam influence the noise generation of the CR fan. Their presence alters the blade passage frequency (BPF) of the inlet rotor and reduces the BPF of the outlet rotor. This is particularly evident in Fig. 8.12 (c), (d), where the tone at 600 Hz (first BPF of the inlet fan) is increased by the C-MSPAs and the acoustic foam, while the tone at around 800 Hz (first BPF of the outlet fan) is reduced. This phenomenon can be attributed to the surface roughness of the C-MSPAs and the acoustic foam, as well as the annular imperfections resulting from the 3D printing process. These factors may induce higher turbulence and impact the noise generation of the CR fan. Czwielong *et al.* [158] also reported similar findings, where the presence of a micro-perforated duct absorber altered the noise generation of the axial fan by changing the inflow conditions. Dong *et al.* [157, 186] investigated the position of the micro-perforated duct absorber in the fan system and its impact on fan performance, as well as the flow interaction between the fan blades and the micro-perforated duct absorber. This phenomenon should be considered in future studies to optimise the design of the C-MSPAs and minimise their impact on the noise generation of the CR fan.

Comparing the noise reduction performance of C-MSPAs for loudspeaker white noise and CR fan noise, C-MSPAs consistently demonstrate noise reduction capabilities across different noise sources and conditions. However, the noise reduction performance of C-MSPAs is slightly more pronounced for the loudspeaker white noise case than for the CR fan noise case. For example, in the GI-1 case, the noise reduction of C-MSPAs for the loudspeaker white noise case is around 2–3 dB higher than that for the CR fan noise case. It should be noted that directly comparing the noise reduction performance of C-MSPAs for loudspeaker white noise and CR fan noise is unfair due to the different noise sources and conditions. This discrepancy cannot be simply attributed to the flow effect on the sound absorption performance of C-MSPAs, as the Mach number of the fan flow is relatively low. Instead, the complex noise generation mechanism of the CR fan, involving intricate interactions between the front and rear rotors, the stator, and the turbulent flow, may contribute to the discrepancy. While the noise emission of the loudspeaker white noise is relatively simple and uniform, the noise generated by the CR

fan is more complex and contains monopole, dipole, and quadrupole components. A detailed flow-acoustic coupled simulation is outside the scope of this study but is worth considering in future investigations. Despite this, C-MSPAs still exhibit satisfactory noise reduction performance for CR fan noise, highlighting their robust engineering potential for noise reduction applications.

Directivity of C-MSPA noise reduction

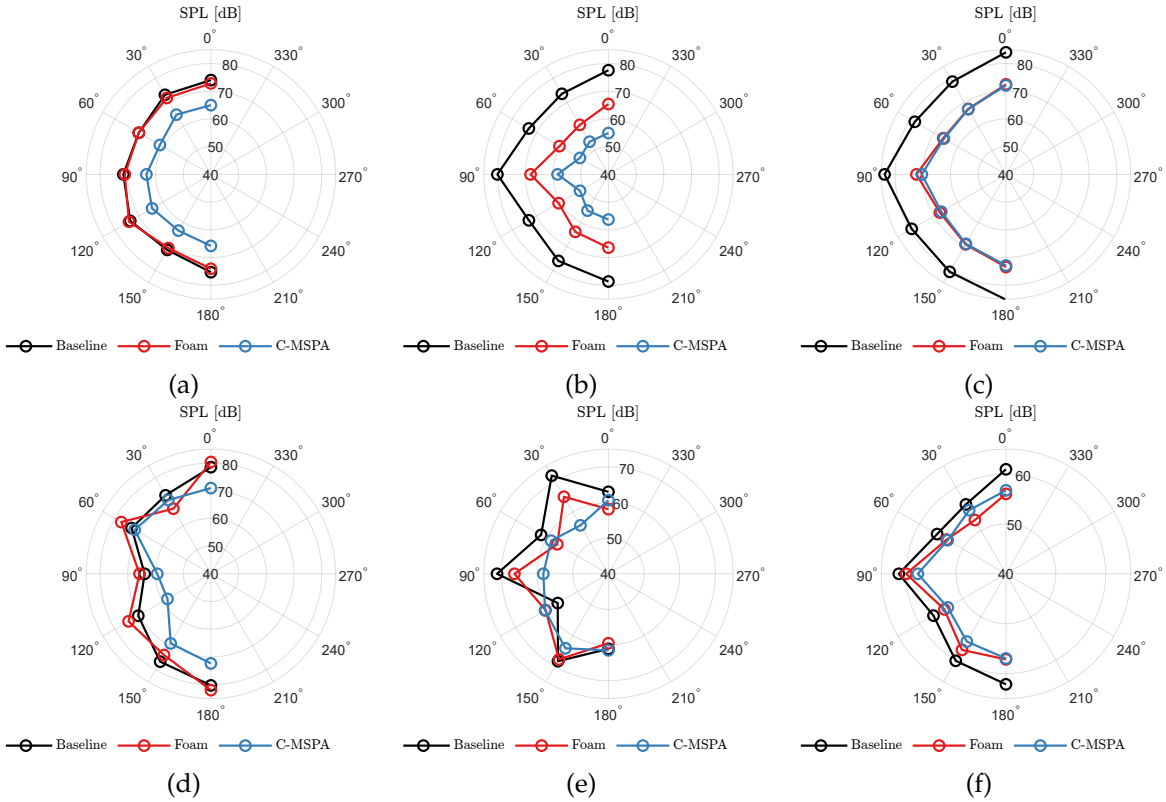

Figure 8.13: Experimental results of the sound directivity of the C-MSPAs for the loudspeaker and counter-rotating fan noise. The sound pressure levels at different angles are measured and plotted in limited 1/3 octave bandwidth for three distinct cases: (a), (d) GI-1: 561–707 Hz (centered at 603 Hz), (b), (e) GI-2: 1122–1414 Hz (centered at 1250 Hz), and (c), (f) GI-3: 890–1781 Hz. The first row (a), (b), (c) is for the loudspeaker noise, while the second row (d), (e), (f) is for the counter-rotating fan noise.

To investigate the directivity of the sound reduction performance of the compact micro-slit absorbers, we measured the overall sound pressure level for the targeted frequencies at various angles around the absorbers for both the loudspeaker and CR fan noise.

Figure 8.13 (a)–(c) present the sound directivity of the C-MSPAs for the loudspeaker noise at three distinct cases: GI-1: 561–707 Hz (centered at 603 Hz), GI-2: 1122–1414 Hz (centered at 1250 Hz), and GI-3: 890–1781 Hz. The results demonstrate that the C-MSPAs effectively reduce noise at all tested angles, showcasing their consistent noise reduction performance regardless of the sound direction. No significant deviations

in noise reduction performance are observed across different angles, indicating the robustness of the C-MSPAs in mitigating noise from various directions. The C-MSPAs outperform the baseline hard wall and acoustic foam at most angles, confirming their superior noise reduction capabilities without major directivity dependence.

Figure 8.13 (d)–(f) present the sound directivity of the C-MSPAs for the CR fan noise at the same three cases. The results exhibit a slightly more complex pattern, which can be attributed to the intricate noise generation mechanism and the complex mixture of noise sources of the CR fan. Nevertheless, the C-MSPAs still exhibit satisfactory noise reduction performance across most of the tested angles. This further reinforces the effectiveness of the C-MSPAs in mitigating noise, even in challenging scenarios.

Effect of C-MSPA on the fan aerodynamic performance

One of the main concerns when using sound absorbers for fan noise reduction is their potential impact on fan aerodynamic performance. It is important to ensure that sound absorbers do not compromise the fan's efficiency.

To evaluate the fan performance (P-Q) curve, we used a wind tunnel that complies with the ANSI/AMCA 210-16 standard. Detailed information about this test facility can be found in [23, 31]. The fan speed is determined by recording the feedback generator (FG) signal. The static-to-total pressure rise (P) and the total volume flow rate (Q) are obtained following the standardized procedures outlined in ANSI/AMCA [211]. We also calculate the uncertainties of the measured parameters based on this standard.

The P-Q curve is measured for three cases: the baseline case, the acoustic foam case, and the C-MSPA case. Fig. 8.14 shows the pressure-flow rate (P-Q) curves of the CR fan under these cases. For simplicity, only one representative curve of the C-MSPA cases is shown (*i.e.* GI-3), as the results are consistent across multiple measurements. The results indicate that the implementation of compact micro-slit absorbers has a negligible effect on the fan's aerodynamic performance. The normalized root-mean-square error (NRMSE) of the C-MSPA case compared to the baseline case is only 0.5%, providing strong evidence for the effectiveness of C-MSPAs in reducing fan noise without compromising the fan's aerodynamic performance.

8.6 Summary

In this study, a comprehensive investigation was conducted into the sound absorption performance of compact micro-slit panel absorbers (C-MSPAs) under both normal and grazing incidence. Analytical, numerical, and experimental methods were used

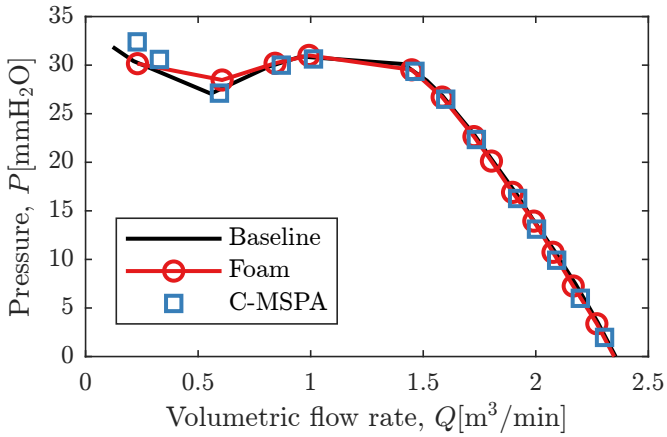

Figure 8.14: Pressure-flow rate (P-Q) curves of the counter-rotating fan under the baseline case, acoustic foam and C-MSPA case.

to evaluate the noise reduction capabilities of the C-MSPAs. These absorbers were designed and optimised for high performance in low-frequency, broadband noise reduction applications. The final designs were tested with loudspeaker white noise and counter-rotating (CR) fan noise to assess their performance under both flow-free and flow conditions.

Three analytical impedance models were employed: the Maa model, the equivalent fluid (EF) model, and the Randeberg-Vigran (RV) model. These models were validated against experimental and numerical results for three test cases: NI-1: 600 Hz, NI-2: 600 & 1200 Hz, and NI-3: 1000–2000 Hz. The EF model showed similar performance to the Maa model and outperformed the RV model under normal incidence. While 3D FEM simulations provided more accurate results, the EF and Maa models were reliable and efficient alternatives for predicting the sound absorption performance of the C-MSPAs. These models were used in the optimisation process to determine the optimal geometrical parameters for different frequency ranges. A sensitivity analysis revealed the significant influence of geometrical parameters on the sound absorption coefficient, providing valuable insights for design and optimisation.

To optimise the annular rings of the C-MSPAs under grazing incidence, a hybrid method combining analytical impedance models with 3D numerical impedance tubes was employed. This model was verified against 3D FEM simulations for the detailed geometry of the C-MSPAs. The hybrid method showed excellent computational efficiency, though some discrepancies were observed compared to the 3D FEM simulations. Among the three analytical impedance models, the EF model showed the best agreement with the 3D FEM simulations.

In the experimental investigation of CR fan noise, the performance of the C-MSPAs was evaluated in reducing noise from both loudspeakers and CR fans with flow for three test

cases: GI-1: 600 Hz, GI-2: 1200 Hz, and GI-3: 900–1800 Hz. The results confirmed the high noise reduction performance of the C-MSPAs across a wide range of frequencies and angles. The C-MSPAs exhibited superior noise reduction performance compared to industrial standard acoustic foam at all designed frequencies, highlighting their versatility and effectiveness.

The impact of the C-MSPAs on fan aerodynamic performance was also assessed, as this is a critical consideration when implementing sound absorbers. The findings demonstrated that the C-MSPAs had a negligible effect on the fan's aerodynamic performance, underscoring their effectiveness in reducing fan noise without compromising aerodynamic performance.

Overall, this study provides compelling evidence for the remarkable potential of C-MSPAs in noise reduction applications. Analytical predictions, optimisation, numerical simulations, and experimental validations of the C-MSPAs offer a comprehensive understanding of their noise reduction capabilities. The C-MSPAs demonstrate high performance for low-frequency broadband noise from both loudspeakers and CR fans, with minimal impact on fan aerodynamics. These findings contribute to the knowledge on noise reduction techniques and provide practical insights for designing and implementing effective noise control strategies.

Future work will focus on assessing the performance of the C-MSPAs in a flow impedance tube and investigating the flow effect on their sound absorption performance. Additionally, optimal positioning of the C-MSPAs in real engineering applications will be explored to maximize noise reduction while minimising impact on aerodynamic performance. This study provides a foundation for further research on the development of advanced multi-layered C-MSPAs and their applications in aerospace, automotive, and HVAC systems.

This chapter in Part II presents an innovative approach to designing and optimising compact micro-slit panel absorbers (C-MSPAs) for noise reduction applications, addressing research question 3 outlined in Section 2.7. The primary advantages of C-MSPAs are summarised as follows: they are compact and suitable for confined spaces, have a negligible impact on aerodynamic performance, achieve low-frequency tonal and broadband noise reduction, target noise absorption rather than specific noise sources, and can be easily integrated into existing systems. While highlighting the benefits of C-MSPAs, the subsequent chapters (*i.e.*, Chapter 9 and 10) will focus on fan geometric modifications, particularly tip leakage flow control, to further enhance fan noise reduction performance.

Chapter 9

Investigation of Tip Leakage Flow via Stereoscopic Particle Image Velocimetry (SPIV) in a Fixed Blade-Endwall Configuration

As the second chapter of Part III, this chapter delves into the investigation of tip leakage flow in a simplified fixed blade-endwall configuration using stereoscopic particle image velocimetry (SPIV). This study aims to deepen our understanding of tip leakage flow and verify computational fluid dynamics (CFD) results for low-Reynolds number flows below 10^5, thereby facilitating the development of effective tip-flow control devices. This study can reveal the flow structure and the effects of Reynolds number, angle of attack, and tip gap size on the tip leakage flow. The findings will guide the design of novel winglets.

The chapter is structured as follows: Section 9.1 introduces the concept of tip leakage flow, emphasising its significance in low-Reynolds number turbomachinery blades and the complexities involved in comprehending its flow structure. Section 9.2 details the experimental setup and methodology, covering the test section, blade design, and the SPIV system. Section 9.3 presents the findings and discusses the impacts of Reynolds number, angle of attack, and tip gap size on the tip leakage flow. Finally, Section 9.4 summarises the chapter's conclusions.

Abstract

The stereoscopic particle image velocimetry (SPIV) is used to investigate the tip leakage flow in a fixed blade-endwall configuration, focusing on low-Reynolds number flows below 10^5. A high-transparency 3D printed NACA 0012 blade is employed to study the effects of Reynolds number ($0.25–1\times10^5$), angle of attack (0–16°), and tip gap size (0–0.2 chord) on the tip leakage flow. The results enhance our understanding of the tip leakage

flow and validate computational fluid dynamics (CFD) results for low-Reynolds number flows, such as those encountered in small axial fans for cooling electronics. The SPIV measurements reveal that the tip leakage flow exhibits a complex 3D structure with pronounced unsteadiness near the blade tip. The flow structures at the tip are minimally influenced by Reynolds number. However, the tip gap size significantly affects the flow structure, with larger gaps resulting in stronger tip leakage vortices. Furthermore, the angle of attack noticeably impacts the flow structure, causing the tip leakage vortex to move upstream as the angle of attack increases. These findings provide a benchmark dataset for numerical simulations and contribute to the development of data-driven models for predicting the structure of tip leakage flow.

9.1 Introduction

Tip leakage flow occurs through the gap between the blade tip and the casing in turbomachinery. This flow is important because it impacts flow separation [161], cavitation [290], loss generation [31], and noise generation [79, 201]. It is a complex 3D flow with strong interactions between the blade and the tip leakage flow, driven by the pressure difference between the pressure and suction sides of the blade. This interaction leads to intricate flow structures near the casing wall.

Due to the complexity of rotating blades in turbine machinery, tip gap flow is often studied in simplified configurations. Table 9.1 provides a review of previous studies on tip leakage flow. You *et al.* [161] investigated the flow structures in the tip flow of a linear cascade (chord-based Reynolds number of $Re = 4\times10^5$) with a moving wall using large eddy simulations (LES). Experimental measurements were conducted by Wang *et al.* [291]. They identified dominant tip vortical structures, including the tip leakage vortex (TLV), the induced vortex (IV), and the tip suction vortex (TSV) [161]. Recently, Koch *et al.* [292] used wall-resolved LES combined with acoustic analogy to investigate the noise generation for the same linear cascade configuration and employed dynamic mode decomposition to identify the main noise sources. They found that the TLV and TSV are the primary tip noise sources, with a frequency of 5–6 kHz and located at around 75% chord.

Grilliat and Jacob *et al.* [293–295] conducted experiments on a cambered NACA 5510 airfoil ($Re = 2.7$–12×10^5) with a stationary wall, focusing on the generation mechanisms of tip leakage noise. They identified two main noise sources due to the tip leakage flow by correlating near-field flow and pressure measurements with far-field noise measurements. A low-frequency hump in pressure spectra was likely caused by flow separation at the pressure side (PS) edge. The size of the separation bubble varies with gap size, reattaching for smaller gaps but not for larger ones. Additionally, a high-

Table 9.1: Review of studies for blade tip flow.

Reference	Profile	Method	AOA [°]	t/c * [%]	Re [$\times 10^5$]
Wang [291]	Circular-arc cascade	Exp.	8.2 **	0.8–3.3	3.88
You *et al.* [161]	Circular-arc cascade	Num.	8.2 **	3	4
Koch *et al.* [292]	Circular-arc cascade	Num.	8.2 **	1.6	3.88
Grilliat *et al.* [293–295]	NACA 5510 airfoil	Exp.	0–18	0–12.5	2.7–12
Saraceno *et al.* [296–299]	NACA 5510 airfoil	Exp.+Num.	0–30	0–10	5.6–8.4
Koch *et al.* [204, 300]	NACA 5510 airfoil	Num.	15	5	9.6
Dreyer *et al.* [290, 301]	NACA 0009 hydrofoil	Exp.+Num.	3–12	0–20	5–20
Present study	**NACA 0012 hydrofoil**	**Exp.**	**0–16**	**0–20**	**0.25–1**

* t/c is the tip gap size as a percentage of the chord length.
** Effective angle of attack is calculated based on the cascade geometry.

frequency noise source linked to small turbulent eddies from the suction side edge was detected.

Koch *et al.* [204] used LES to investigate the tip leakage noise based on the same experimental configuration. They found that tip noise is dominant in the high-frequency range, generated when turbulent structures scrape the suction side tip around the mid-chord. The tip leakage flow generates coherent vortices that break up when interacting with the aerofoil wake. Recently, Saraceno *et al.* [296–299] used a similar experimental setup for the same NACA 5510 airfoil to investigate tip leakage noise at $Re = 5.6$–8.4×10^5. They identified two humps in the far-field noise spectra, corresponding to two different noise sources: one linked to tip leakage flow instabilities and the other to vortex shedding. They concluded that while vortex shedding occurs only when the tip gap is large enough for extended separation, instabilities due to the rolling up are always present.

In addition to cambered airfoils, the tip leakage flow in symmetrical NACA 0009 foils has been studied for hydro applications. Dreyer *et al.* [290] used stereoscopic particle image velocimetry (SPIV) to investigate the effect of tip clearance on the vortical structures of a NACA 0009 hydrofoil at $Re = 5$–20×10^5, focusing on cavitation inception. They found there is a specific tip clearance where the vortex strength is maximized, leading to the highest cavitation inception. Decaix *et al.* [301] used LES to investigate flow topology for the same hydrofoil configuration at $Re = 1 \times 10^6$. They found that a large gap size leads to flow separation at the pressure side edge, generating a tip separation vortex that merges with the TLV near the trailing edge. For smaller gaps, the separation vortex is less developed, and the TLV moves upward along the suction side.

Past studies have focused on high Reynolds number flows, but there is a recent need for low-Reynolds number studies. The small axial fans for electronic cooling in data centers and other similar applications operate at low Reynolds numbers [20, 23, 31], where the

tip flow causes significant loss and noise. Additionally, recent interests in ducted propellers in the area of urban air mobility (UAM) have led to a need for low-Reynolds number studies [235]. These flows typically operate at Reynolds numbers of 10^4–10^5, which have not been extensively studied. Although a few studies [290, 293, 294] show the tip flow structures are not significantly different at the Reynolds numbers (10^5–10^6) they investigated, to the best of the authors' knowledge, no data is available for Reynolds numbers below 10^5. This limits the understanding of the tip leakage flow at low Reynolds numbers and presents a lack of experimental data for benchmarking numerical simulations.

The objectives of this study are to investigate the flow structure at the tip and the effects of Reynolds number, angle of attack, and tip gap size for a fixed NACA 0012 blade-end wall configuration in low-Reynolds number flow using stereoscopic particle image velocimetry (SPIV). By focusing on a non-rotating airfoil, we exclude the interaction of tip gap flow with upstream disturbances and downstream stator vanes. Additionally, the cascade effect is not considered due to the relatively low solidity of the blade, which further simplifies the flow. The results will enhance understanding of tip leakage flow and validate computational fluid dynamics (CFD) results previously presented in [31]. The novelty of this study lies in using SPIV and a highly transparent NACA 0012 blade to investigate tip leakage flow at low Reynolds numbers. The findings will provide a benchmarking dataset for numerical simulations and guide the design of passive flow control devices like winglets. Additionally, the experimental data will help develop data-driven models to predict tip leakage flow structure.

9.2 Experimental methodology

9.2.1 Experimental setup

The experiment is conducted in a low-speed closed-loop water tunnel at Trinity College Dublin (TCD), as illustrated in Fig. 9.1. The water tunnel features a test section with a cross-sectional area of 400 mm × 400 mm and a length of 120 mm. The top and bottom of the test section are equipped with glass windows, while the front window is made of polymethyl methacrylate (PMMA), ensuring excellent optical access for flow visualisation and particle image velocimetry (PIV) measurements. An axial flow pump drives the water flow, achieving a maximum flow rate of 0.17 m^3/s, which corresponds to a maximum freestream velocity of 3.564 m/s in the test section.

The schematic of the experimental setup for stereoscopic particle image velocimetry (SPIV) measurements in the fixed blade-endwall configuration is shown in Fig. 9.2. A photo of the implemented SPIV test facilities at TCD is shown in Fig. 9.3. The

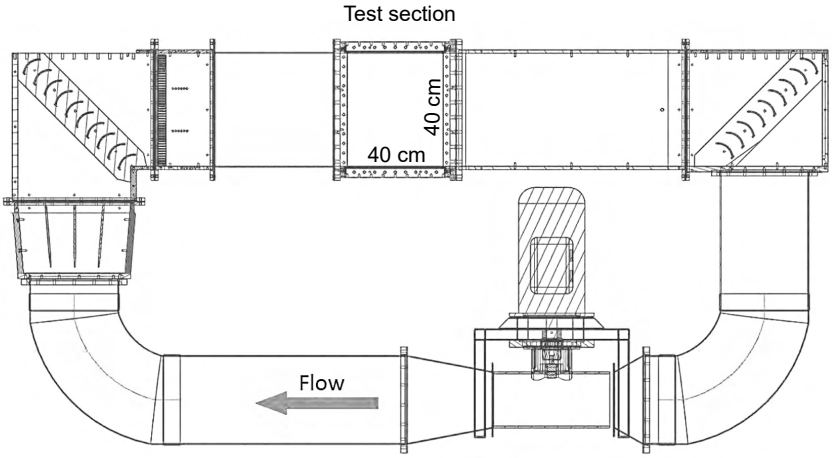

Figure 9.1: Sectional view of the low-speed close-loop water tunnel at Trinity College Dublin (TCD) adopted from Jackson [302], showing the location of the test section.

particles are illuminated by a double-pulsed neodymium-doped yttrium lithium fluoride (Nd:YLF) laser (Quantronix DarwinDuo 527-40) with a wavelength of 527 nm and a maximum power of 45W (maximum energy of 15 mJ per pulse at 3000 pulses/second). The laser sheet is generated by a LaVision sheet optic and a cylindrical divergent lens ($f = -20$ mm), directed underneath the blade tip as shown in Fig. 9.2. The time delay dt between two laser pulses ranges from 100 to 800 μs, depending on the flow conditions.

Two high-speed complementary metal-oxide-semiconductor (CMOS) Photron Fastcam SA 1.1 cameras with a resolution of 1024 × 1024 pixels and a frame rate of 0.25–2 kHz capture the tip gap flow. The cameras are equipped with Sigma 105 mm f/2.8 lenses and Scheimpflug adapters to capture the flow field in a 75×75 mm^2 area near the blade tip. Positioned at an angle of approximately 31°, they provide stereoscopic images for two-dimensional three-components (2D3C) SPIV measurements. Both cameras and laser pulses are synchronized using a LaVision Programmable Timing Unit. Adjustable transverse systems mount the cameras and laser lens, facilitating easy alignment. An additional planar (2D2C) PIV configuration captures the upstream flow field without the blade, while a stereoscopic PIV configuration captures the tip leakage flow.

The test section features a high-transparency blade with a chord length of 50 mm and a span of 70 mm (aspect ratio of 1.4). The blade is 3D printed using stereo-lithography (SLA) on an Elegoo Saturn 3 printer. The printer has a 10-inch LCD screen with a resolution of 12k (11520×5120 pixels), providing an XY resolution of 19×24 μm^2, and a construction volume of 218.88 mm × 122.88 mm × 250 mm. A layer thickness of 25 μm is used to print the blade in the Z direction. Since the Z resolution is finer than the XY resolution in an SLA printer, the minimum resolution of printed objects is determined by the XY resolution of 24 μm. This printer ensures high accuracy and resolution for

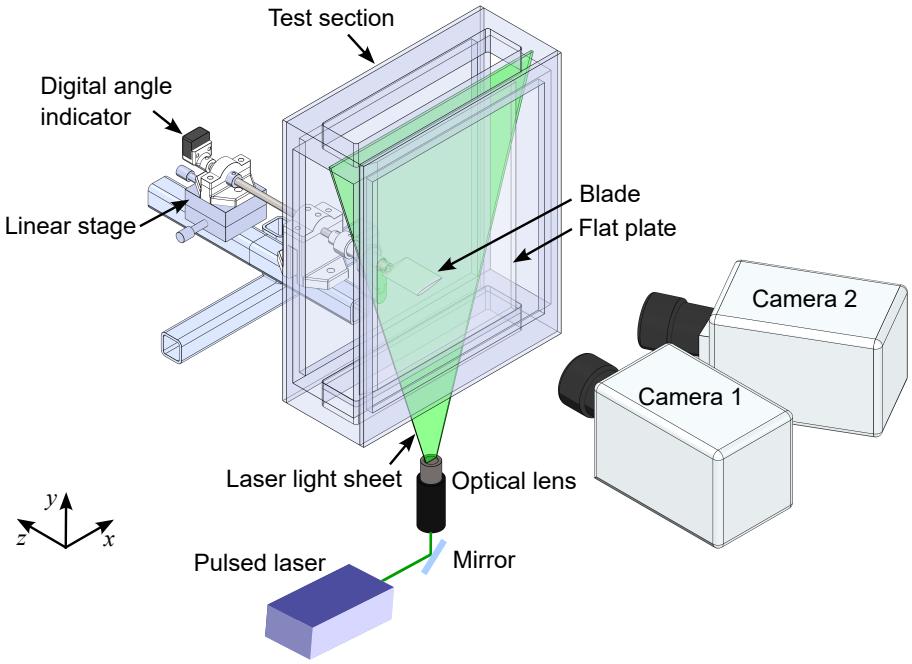

Figure 9.2: Experimental setup for stereoscopic particle image velocimetry (SPIV) measurements in the fixed blade-endwall configuration. Streamline-shaped holders (not shown here, only shown in Fig. 9.3) are used to mount the flat-plate endwall.

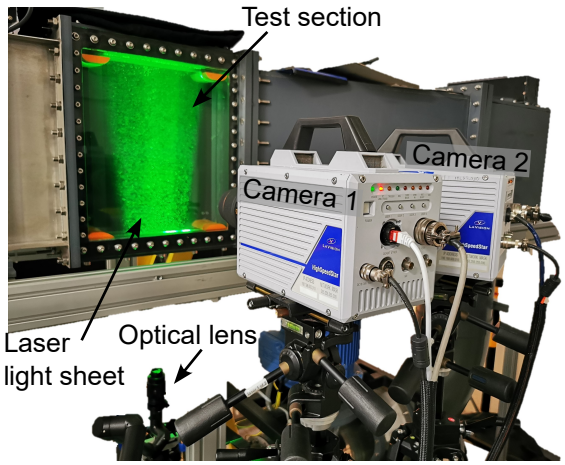

Figure 9.3: Photo of the SPIV experimental setup in the water tunnel at TCD.

printing the blade geometry.

One novelty of this study is exploring the use of high-transparency 3D printed blades for SPIV measurements. High-transparency additive manufacturing offers a cost-effective solution for producing complex geometries with optical access. However, practical challenges such as yellowing, oxidation, and shrinkage have limited its application in the PIV community. In this study, we demonstrate good practices for using high-transparency resin in SPIV measurements.

To ensure optical access and minimise light reflection and refraction, we used a high-

transparency resin from Anycubic. This UV-curable resin has a high refractive index and excellent resistance to yellowing. According to the manufacturer, objects printed with this resin have a refractive index of approximately 1.50 in the visible light wavelength range of 400–800 nm. Our initial printed blades did not yellow even after several weeks of light exposure. However, their transparency was not optimal due to surface roughness, despite a fine resolution of approximately 24 μm.

Initially, we applied a thin resin coating to improve transparency, as recommended by the supplier. However, this coating did not achieve the desired transparency due to thickness variations and dust accumulation, which caused light scattering. To resolve this, we polished the blade surface using an extra fine polishing compound (1.2 μm) and a polishing cloth wheel, resulting in a glass-like finish. After polishing, the blade was cleaned with isopropyl alcohol and dried with compressed air.

The blade dimensions are verified, and the tip airfoil profile is extracted from the PIV images. A comparison between the extracted profile and the original NACA 0012 profile shows a deviation within 5 pixels, approximately 37 μm, which is about 1.5 times the printer's minimum resolution.

Fig. 9.4 shows the transparency of the printed blade when illuminated by the laser sheet. The light intensity in the tip gap region is uniformly distributed (Fig. 9.4 (a)). When the laser sheet hits a spanwise section of the blade, the light intensity remains uniform except for two shielded areas near the leading and trailing edges (Fig. 9.4 (b)). Further polishing could improve these shielded areas, but since this study does not focus on the flow around the leading and trailing edges in the spanwise sections, no additional polishing was done. This printing method provided satisfactory results in terms of blade geometry and transparency.

The blade is mounted on a 10 mm shaft using a rigid coupling and clamped by a rigid bearing system. The shaft is connected to a high-precision linear stage for controlling the tip gap size. The angle of attack of the blade is adjusted using a digital angle indicator (QLUUE) with an accuracy of $\pm 0.2^\circ$.

To generate a stable boundary layer flow and minimise uncertainty, a flat plate with a sharp leading edge and a thickness of 10 mm is used as an endwall. The plate is mounted using 3D printed holders designed to ensure a stable flow field.

Blockage can significantly affect flow velocity and pressure recovery in the test section. The blockage ratio is the ratio of the frontal area of all solid objects to the cross-sectional area of the test section. The 10 mm flat plate with mounting holders has a blockage ratio of 8.3%. Additionally, for an angle of attack (AOA) of 16° and a tip clearance of 0 mm, the blade has a blockage ratio of 2.0%. While the extra flat plate and holders increase

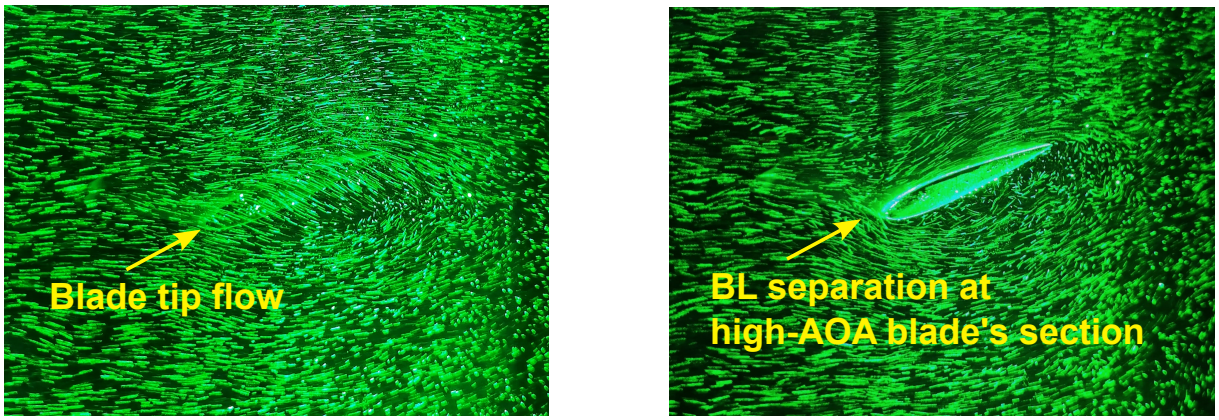

(a) (b)

Figure 9.4: Transparency of the high-transparency SLA-printed NACA 0012 blade: (a) Illuminated by the laser sheet in the tip gap region, showing uniform light intensity around the tip gap flow field. (b) Illuminated by the laser sheet in a spanwise section, showing uniform light intensity except for two shielded areas above pressure side due to the leading and trailing edges.

the blockage ratio, they minimise flow disturbances and ensure a stable boundary layer. A 10 mm thickness is chosen to minimise deformation under flow and maintain a sharp leading edge. Due to time constraints, no further optimisation of the blockage ratio was performed. Future studies could optimise the blockage ratio by reducing the thickness of the flat plate and holders.

9.2.2 Test conditions

The tip leakage flow is investigated at different tip gap sizes (0–10 mm), angles of attack (0°–16°), and Reynolds numbers (2.5×10^4–1×10^5). Four tip gap sizes are considered: 0 mm, 2.5 mm, 5 mm, and 10 mm. The tip gap size t is defined as the distance between the blade tip and the flat-plate endwall (see Fig. 9.5). The coordinate system is defined with the x-axis along the stream-wise direction of the freestream flow, the y-axis along the normal direction, and the z-axis along the span-wise direction.

The angle of attack ranges from 0° to 16° with an interval of 4°. It is defined as the angle between the blade chord line and the freestream velocity vector. The angle of attack is the same on both the suction and pressure sides because the NACA 0012 profile is symmetric. Positive angles indicate clockwise rotation when the blade is illuminated by the laser sheet from the suction side to the pressure side. The rotational axis is at the 30% chord of the blade ($x = 0.3c$, $y = 0$), which corresponds to the location of maximum thickness (see Fig. 9.5).

The Reynolds number is defined as $Re = U_\infty c/\nu$, where U_∞ is the freestream velocity, c is the blade chord length, and ν is the kinematic viscosity of water (0.96×10^{-6} m^2/s at 22°C). Four Reynolds numbers are obtained by adjusting the freestream velocity U_∞

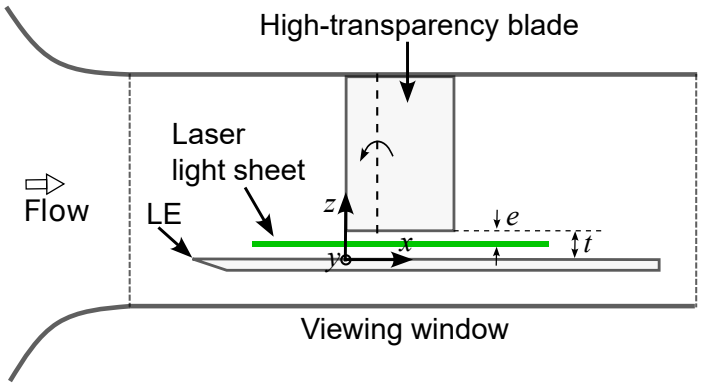

Figure 9.5: Schematic of the tip gap between the high-transparency SLA-printed NACA 0012 blade and the flat-plate endwall. t is the tip gap size, e is the distance between the blade tip and the laser sheet t_{sheet} ($e = t - z_{\text{sheet}}$), x is the stream-wise direction, y is the normal direction, and z is the span-wise direction. The rotational axis is at the 30% chord of the blade ($x = 0.3c,\ y = 0$).

in the water tunnel: 2.5×10^4, 5×10^4, 7.5×10^4, and 1×10^5. The Reynolds number is varied by adjusting the freestream velocity while keeping the blade chord length and the kinematic viscosity constant.

The laser sheet is positioned $e = 1$ mm away from the blade tip to capture the tip leakage flow, as shown in Fig. 9.5. The laser sheet position is optimised by adjusting it from $e = -2$ mm to $e = 2$ mm. This ensures the laser sheet is not too close to the blade tip edges, which could cause strong reflection and refraction, while still being close enough to capture the tip flow and downstream leakage vortex.

The flow is seeded with 50 μm polyamide particles, chosen for their balance between high scattering intensity and low response time in water [303]. The particles are mixed in alcohol and injected into the flow. Seeding homogeneity is ensured by multiple water tunnel cycles. Dissolved gas bubbles stuck to surfaces within the field of view are eliminated by injecting water using a syringe with a flexible tube, and a soft sponge stick is used to remove any remaining bubbles before measurements. However, some bubbles are still present during measurements, especially near the tip gap at high angles of attack. The background noise in the SPIV images caused by bubbles is mitigated conducting pre-processing of PIV images, discussed in Section 9.2.3.

The SPIV system is calibrated using a LaVision 3D calibration plate with two surfaces at different depths in the z direction (spaced 2 mm apart). The calibration plate is positioned at the same location as the blade tip and filled with water to ensure a consistent optical path. The calibration process is repeated before each measurement when there are changes in the tip gap sizes to ensure accurate velocity measurements.

9.2.3 PIV processing and data analysis

The PIV images are processed using LaVision DaVis 10.0.5.53613 software. Pre-processing removes background noise and enhances the signal-to-noise ratio [304]. A high-pass filter eliminates noise from bubbles in the water tunnel while preserving flow structures. The images are then processed using a cross-correlation algorithm to obtain the velocity field. Measurements are taken at a frame rate of 500 Hz for 0.5 seconds, resulting in 250 image pairs. For certain conditions, measurements are repeated at different frame rates up to 2 kHz or for longer durations to provide a more refined frequency resolution. Unless otherwise specified, results are presented using the 500 Hz frame rate and 0.5-second duration.

The interrogation window size is optimised to balance spatial resolution and signal-to-noise ratio. A 32 × 32 pixel interrogation window, corresponding to a 2.3 mm × 2.3 mm area in the image, is used. This resolution avoids significant peak-locking effects and ensures a well-resolved velocity field. The combined uncertainty in velocity measurements is around $\delta_U/U = \pm(2.8 - 7.7\%)$.

Three velocity components (u, v, and w) are obtained from the SPIV measurements. The velocity magnitude U is calculated as:

$$U = \sqrt{u^2 + v^2 + w^2}. \tag{105}$$

The velocity fluctuations σ_u, σ_v, and σ_w are calculated as the standard deviation of the velocity components. The turbulence intensity is defined as σ_U/U_∞. Since the flow is 2D3C which lacks the information of dz, the gradients of the velocity components u and v are normalised and calculated as $d(u/U_\infty)/d(x/c)$ and $d(v/U_\infty)/d(y/c)$.

The normalised 2D divergence of the flow field is expressed as:

$$\mathrm{div}(u, v) = \left(\frac{du}{dx} + \frac{dv}{dy}\right)\frac{c}{U_\infty}. \tag{106}$$

For an ideal incompressible flow, the 3D divergence should be zero. For a 2D flow, the 2D divergence should be zero. Therefore, the 2D divergence is a good indicator of 3D motions in the tip flow field due to the presence of flow separation and tip leakage vortex.

9.3 Results and discussion

9.3.1 Upstream flow conditions

The flow field upstream of the blade is measured to provide a reference for the tip flow. Velocity measurements are taken around 10% of the chord length upstream of the blade leading edge ($x/c = -0.1$) and at the blade centerline ($y/c = 0$) without the blade in place. A planar (2D2C) PIV configuration is used with an image rate of 250 Hz for 1 second. The freestream velocity is approximately 1 m/s ($Re = 5 \times 10^4$). The velocity profile and turbulence intensity are shown in Fig. 9.6 (a) and (b), respectively. Velocity is normalised by the freestream velocity U_∞, and the distance from the endwall is normalised by the boundary layer thickness. The velocity profile reveals a boundary layer thickness of about 19 mm, extracted from the velocity profile at 99% of the freestream velocity, corresponding to approximately $0.38c$. The turbulence intensity (σ_U/U_∞) is around 2.5% outside the boundary layer and increases to around 30% near the endwall ($t = 1$ mm). This indicates the presence of a turbulent boundary layer near the endwall, expected for a fan blade tip flow near the casing. Saraceno *et al.* [297] have shown that the casing boundary layer thickness has an insignificant effect on the tip flow structure, as demonstrated by comparing two different casing boundary layer thicknesses of 5 mm and 20 mm. Therefore, the endwall boundary layer thickness is considered representative for investigating the tip leakage flow in this study.

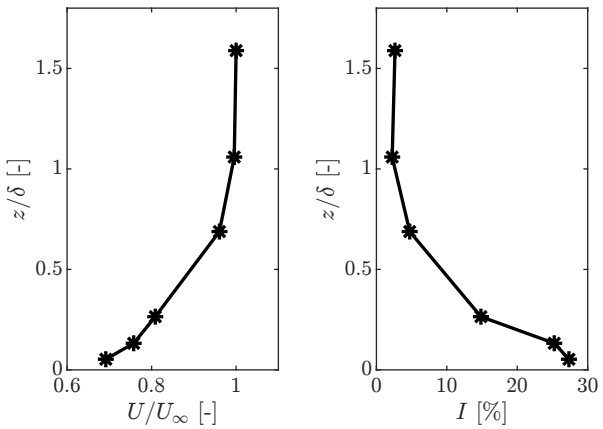

Figure 9.6: Upstream flow field near the sharp flat-plate endwall: (a) Velocity profile, (b) Turbulence intensity. The data is taken near the blade leading edge ($x/c = -0.1$ and $y/c = 0$) but without the blade in place. The velocity is normalised by the freestream velocity U_∞, and the distance from the endwall is normalised by the boundary layer thickness $\delta \approx 19$ mm (about $0.38c$), extracted from the velocity profile at 99% of the freestream velocity.

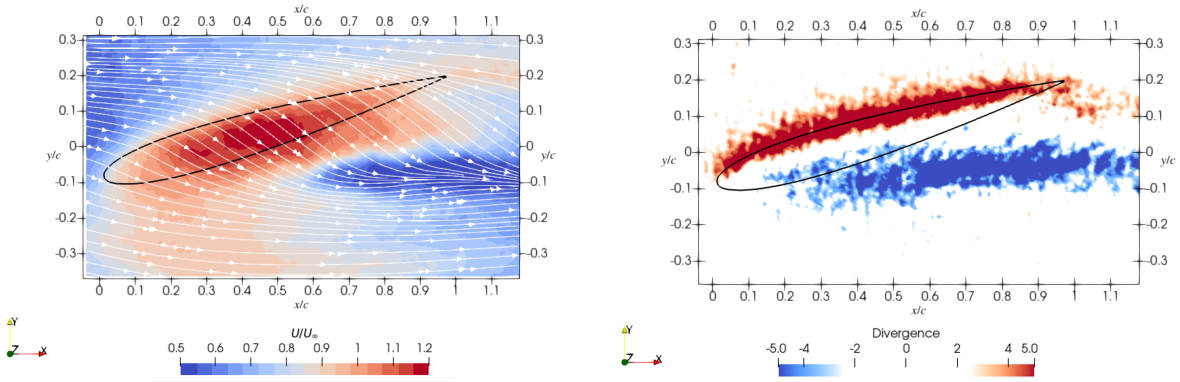

Figure 9.7: Tip leakage flow at a tip clearance size of 5 mm (t/c = 10%), an angle of attack of 16° and a freestream velocity of around 1 m/s ($Re = 5 \times 10^4$). (a) Normalised velocity magnitude (U/U_∞), (b) Normalised 2D divergence div(u, v).

9.3.2 Topology of the tip leakage flow

Figure 9.7 illustrates a typical tip leakage flow at a tip gap of $t = 5$ mm for an angle of attack of 16° and a freestream velocity of approximately 1 m/s ($Re = 5 \times 10^4$). All velocity components are normalised by the freestream velocity U_∞. The normalised velocity magnitude (U/U_∞) and normalised 2D divergence div(u, v) are shown in (a) and (b), respectively.

The tip leakage flow exhibits a high-velocity region near the blade tip and a low-velocity region downstream. The velocity magnitude plot (Fig. 9.7 (a)) clearly shows the jet-like structure of the tip leakage flow, consistent with previous studies [31, 295]. The maximum velocity, occurring around 0.4–0.6c at the blade tip, exceeds 1.2 times the freestream velocity. As the tip flow convects downstream, it mixes with the freestream flow at around 0.6c, resulting in a distinct low-velocity region downstream of the suction side of the blade. This low-velocity region is associated with the tip leakage vortex (TLV), a key feature of the tip leakage flow.

The TLV is fed by the jet-like flow of the tip, which pushes fluid from the pressure side to the suction side. The reduced stream-wise velocity u and normal-wise velocity v in the low-velocity region compared to the blade tip are shown in Fig. 9.8 (a) and (c), respectively.

The 2D divergence plot (Fig. 9.7 (b)) shows the gradient of the velocity field div(u, v), indicating the presence of high-shear regions. Two high-shear regions are observed: one near the pressure side of the blade tip and the other on the suction side, moving downstream parallel to the stream-wise (x) direction. The former is generated as the main flow accelerates around the tip gap and separates from the blade tip plane. The span-wise flow is then pushed towards the endwall, as shown in Fig. 9.8 (c). Near the

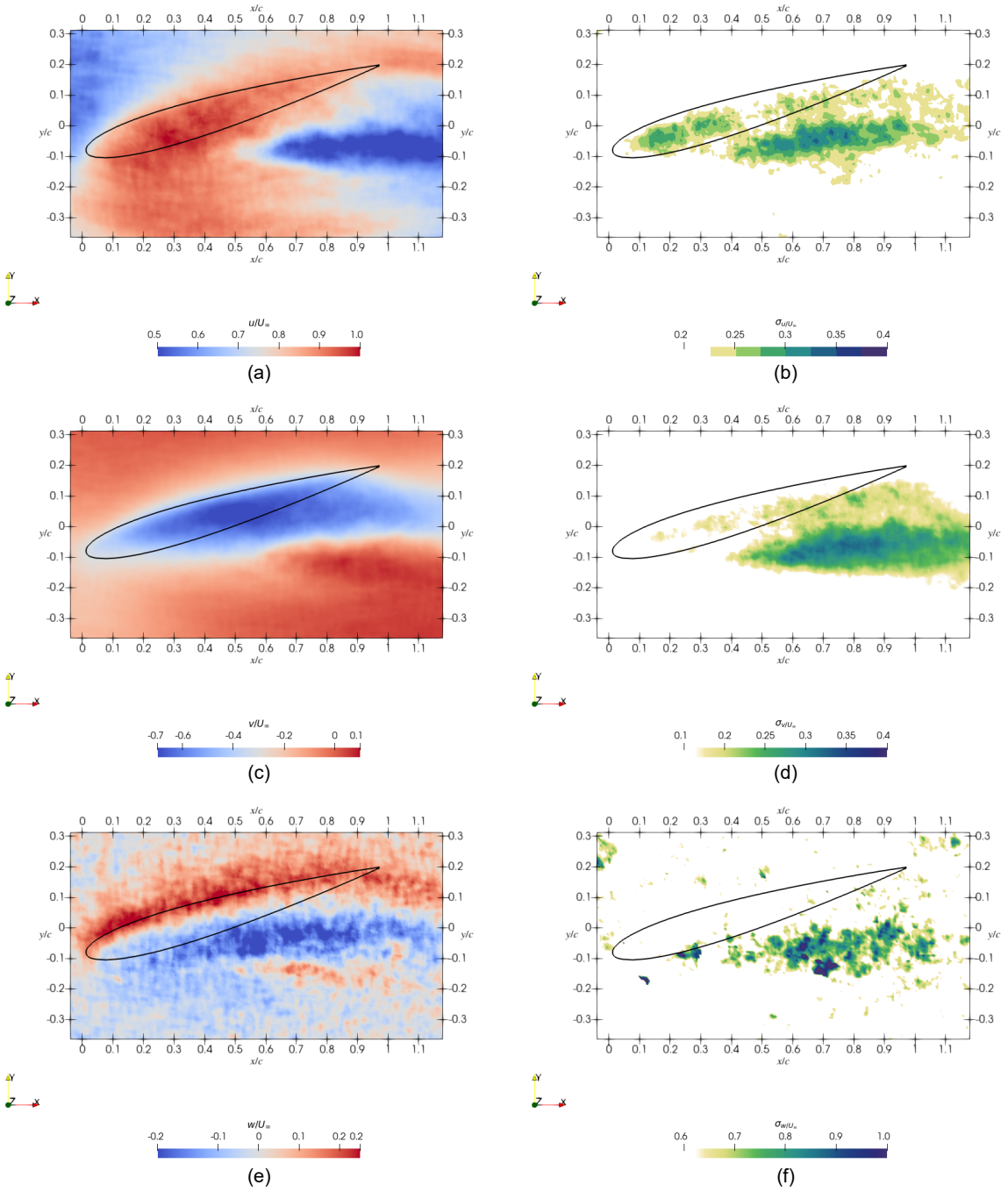

Figure 9.8: Tip leakage flow at a tip clearance size of 5 mm (t/c = 10%), an angle of attack of 16° and a freestream velocity of 1 m/s ($Re = 5 \times 10^4$): (a) averaged velocity u/U_∞, (b) velocity fluctuations σ_u/U_∞, (c) averaged velocity v/U_∞, (d) velocity fluctuations σ_v/U_∞, (e) averaged velocity w/U_∞, (f) velocity fluctuations σ_w/U_∞.

trailing edge, the sign of tip separation vortex (TSV) can also be observed based on the high velocity gradient (see Fig. 9.7 (b)), consistent with previous studies [31, 161]. This region near the blade tip features a relatively high turbulence intensity in the x and y directions, as shown in Fig. 9.8 (b) and (d).

The second high-shear region forms at around 0.15c on the suction side of the blade tip,

covering the trace of the TLV in the downstream region (Fig. 9.7 (b)). Although only a 2D plane (e = 1 mm) is measured, the trajectory of the TLV is clearly visible as the plane cuts through the tip vortex. This high-shear region is associated with the motion of the TLV. As the jet-like flow leaves the gap, roughly at 0.15c shown by the trajectory in Fig. 9.7 (b), it rolls up into the TLV and interacts with the incoming flow and. It can be identified by a high turbulence region created by the vortical motion of the vortex, as seen in the velocity fluctuations of σ_u/U_∞ (Fig. 9.8 (b)), σ_v/U_∞ (Fig. 9.8 (d)), and especially σ_w/U_∞ (Fig. 9.8 (f)). The unsteady nature of the TLV is evident in the high velocity fluctuations, which result in aerodynamic losses and noise generation.

9.3.3 Effect of angle of attack

The effect of angle of attack (AOA) on the tip leakage flow is investigated at t = 5 mm for freestream velocities of 1 m/s ($Re = 5 \times 10^4$). The normalised velocity magnitude and normalised 2D divergence of the tip leakage flow are shown in Fig. 9.9 for AOAs of 4°, 8°, and 12°. The velocity magnitude plot (Fig. 9.9 (a), (c), (e)) shows that the tip leakage flow is significantly affected by the AOA.

At 4° AOA, the tip leakage flow is relatively stream-wise, with a relatively high-velocity region near the blade tip and a low-velocity region downstream. The mixing of the tip flow with the freestream flow is less pronounced, resulting in a delayed mixing location (roughly at 0.9c at this measurement plane) and a less distinct TLV. The velocity gradient near the blade tip is relatively low, as shown in the 2D divergence plot (Fig. 9.9 (b)), indicating a less turbulent and more stable flow. The trajectory shown in (Fig. 9.9 (b)) indicates the TLV exits the blade tip at around 0.5 c.

As the AOA increases to 8°, 12°, and 16° (Fig. 9.7), the high-velocity region near the blade tip becomes more pronounced, and the low-velocity region downstream becomes more distinct. The mixing of the tip flow with the freestream flow occurs closer to the blade leading edge. The velocity gradient near the blade tip becomes higher, as shown in the 2D divergence plot (Fig. 9.9 (d), (f) and Fig. 9.7 (b)). The exit location of the TLV also moves towards leading edge, with a more distinct separation point at the blade tip. The TLV exits the blade tip at around 0.3 c for 8° AOA, 0.2 c for 12° AOA.

9.3.4 Effect of tip clearance size

Tip clearance size is an important parameter that affects the tip leakage flow. We investigate the effect of tip clearance size on the tip leakage flow at an angle of attack of 16° and a freestream velocity of 1 m/s ($Re = 5 \times 10^4$). In addition to the case at t = 5 mm shown in Fig. 9.7, we vary the tip clearance size to 2.5 mm and 10 mm, as depicted in Fig. 9.10.

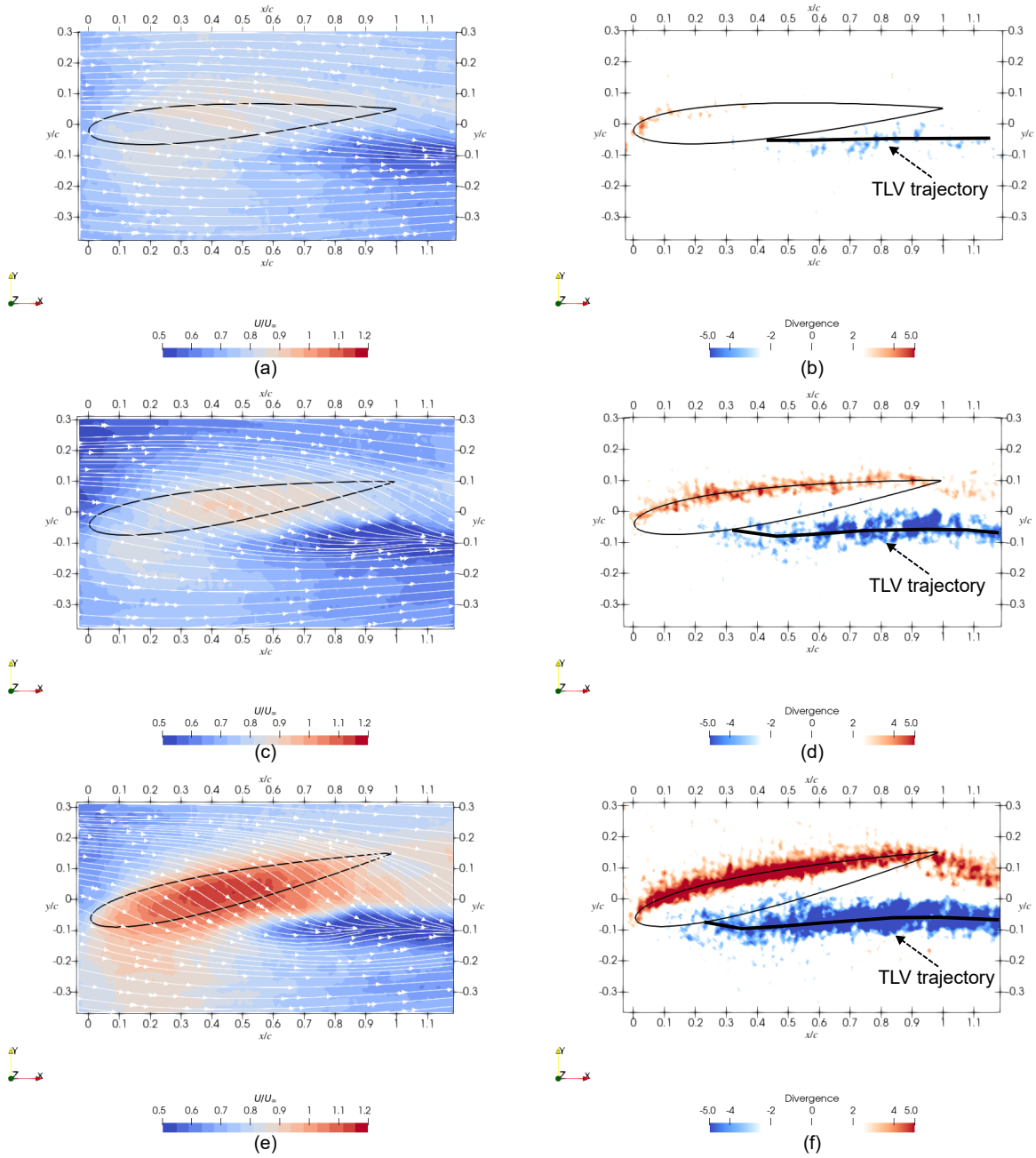

Figure 9.9: Effect of angle of attack on the tip leakage flow at a tip clearance size of 5 mm (t/c = 10%) and a freestream velocity of 1 m/s ($Re = 5 \times 10^4$). (a), (c), (e) are the velocity magnitude (U/U_∞), (b), (d), (f) are the 2D divergence div(u, v) of the tip leakage flow for angles of attack of 4° (top), 8° (middle), 12° (bottom), respectively.

Both the mixing location and the TLV separation point are influenced by the tip clearance size. As the tip clearance size increases from 2.5 mm to 10 mm, the mixing location and TLV separation point move closer to the blade trailing edge. This observation is consistent with previous studies on single-impeller axial fans and fixed blade-endwall configurations. The delayed mixing location and TLV separation point can be attributed to the weaker suppression effect of the tip leakage flow by the endwall or casing. When the blade tip moves away from the endwall, the tip leakage vortex is less affected

by the endwall, resulting in a more distinct TLV. Similar to the scenario of a 3D wingtip with a large tip gap, a larger TLV generated freely from the blade tip can eventually shed downstream, forming a clear vortex shedding pattern. Recent studies have shown that although the roll-up of the TLV will occur regardless of the tip gap size, the vortex shedding pattern is only observed when the tip gap is large. Besides the tip gap size, other parameters such as blade shape, inflow velocity, and tip shear layer thickness can also impact the vortex shedding pattern. While a quantitative comparison is beyond the scope of this study, our qualitative observation is consistent with previous studies.

Although the averaged velocity changes in different cases due to the presence of the endwall boundary layer, the velocity magnitude plot (Fig. 9.10 (a), (c) and Fig. 9.7 (a)) shows that the high-velocity region near the blade tip remains relatively consistent, typically around $0.4c$–$0.6c$. The TLV trajectory also remains consistent, running nearly parallel to the stream-wise direction.

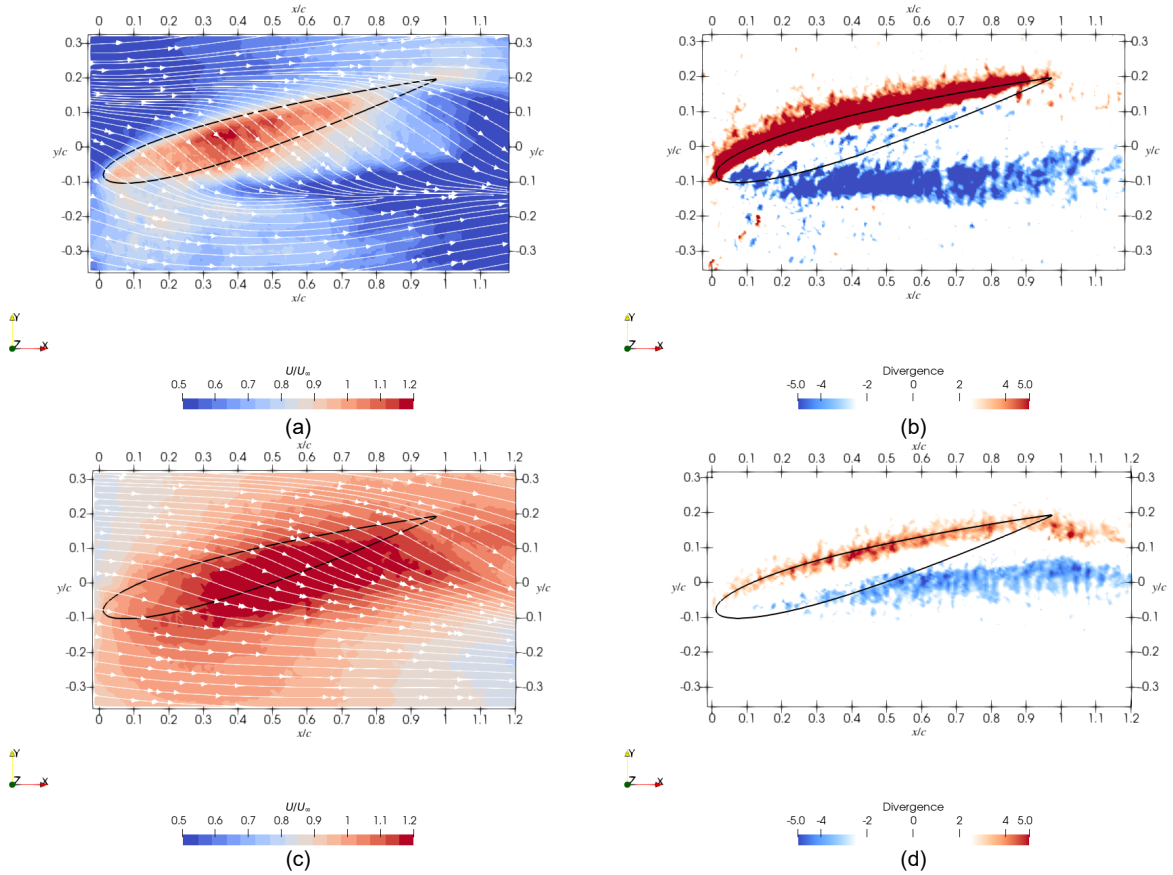

Figure 9.10: Effect of tip clearance size on the tip leakage flow at an angle of attack of 16° and a freestream velocity of 1 m/s ($Re = 5 \times 10^4$). (a), (c) are the velocity magnitude (U/U_∞), (b), (d) are the 2D divergence div(u, v) of the tip leakage flow for tip clearance sizes of 2.5 mm ($t/c = 5\%$) and 10 mm ($t/c = 20\%$), respectively.

9.3.5 Effect of velocity

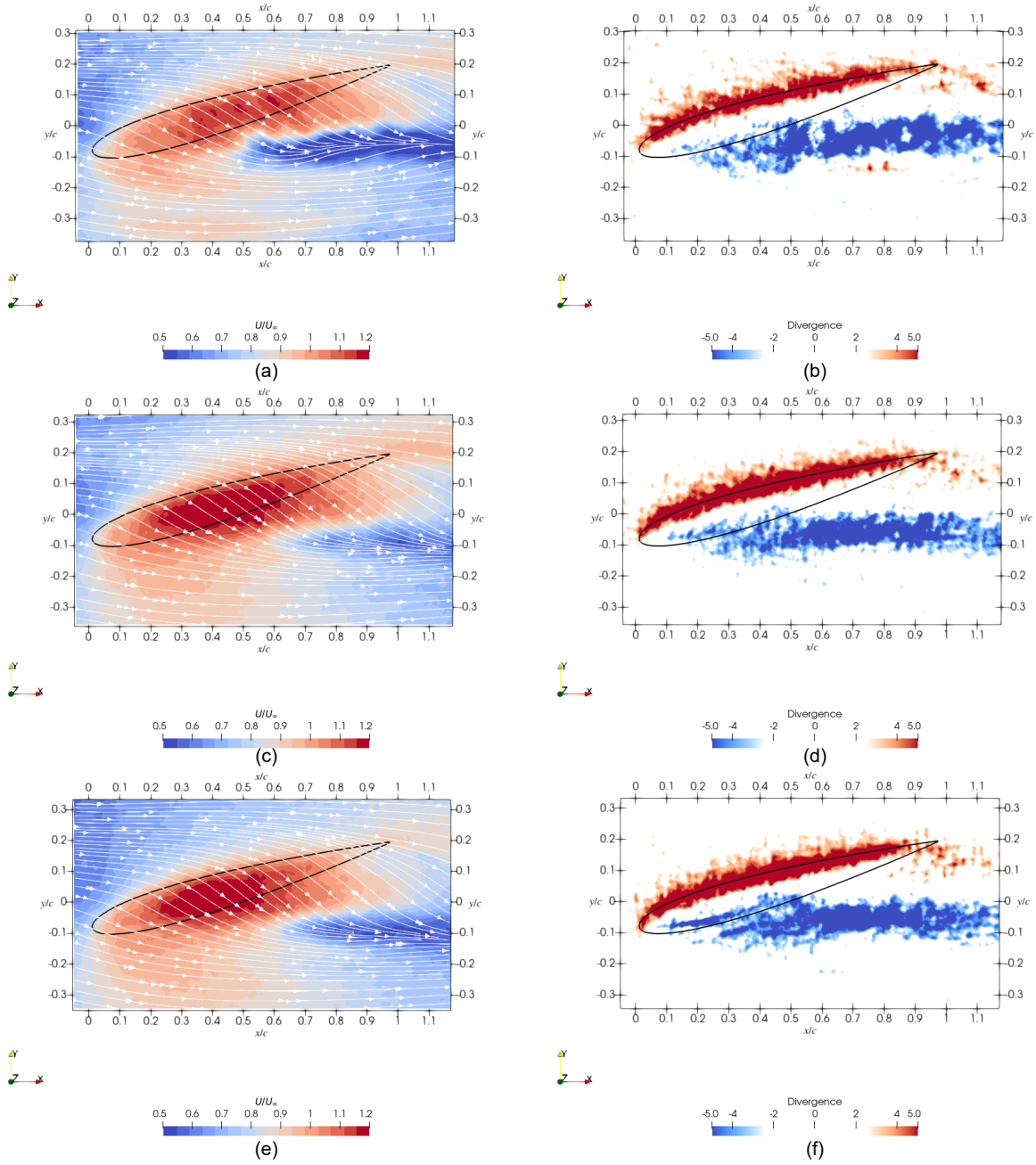

Figure 9.11: Effect of Reynolds number on the tip leakage flow at a tip clearance size of 5 mm (t/c = 10%) and an angle of attack of 16°. (a), (c), (e) are the velocity magnitude (U/U_∞), (b), (d), (f) are the 2D divergence div(u, v) of the tip leakage flow for Reynolds numbers of 2.5×10^4 (top), 7.5×10^4 (middle), 1×10^5 (bottom), respectively.

The effect of freestream velocity on the tip leakage flow is investigated at a tip clearance size of t = 5 mm and an angle of attack of 16°. The freestream velocity is varied from 0.5 m/s (Re = 25,000) to 2 m/s (Re = 100,000). The velocity magnitude and 2D divergence of the tip leakage flow are shown in Fig. 9.11 for freestream velocities of 0.5 m/s, 1.5 m/s, and 2 m/s, and are previously shown in Fig. 9.7 for a freestream velocity of 1

m/s.

The tip leakage flow scales with the freestream velocity. Both the velocity magnitude and the 2D divergence are consistent across different freestream velocities. This indicates that the flow physics of the tip leakage flow are independent of the velocity or Reynolds number ($Re = 0.25 - 1 \times 10^5$) considered in this study. This independence is commonly agreed upon in the literature, as demonstrated by Jacob *et al.* [294] for a wide range of higher Reynolds numbers ($Re = 0.27 - 1.2 \times 10^6$).

This independence justifies the use of low-speed water tunnel experiments to study the tip leakage flow. The flow physics are not significantly affected by the Reynolds number. Conducting measurements in a low-speed water tunnel offers advantages, such as higher spatial and temporal resolution of SPIV, which is essential for capturing the complex flow structures of the tip leakage flow. The improved resolution of SPIV enables accurate measurement of the tip leakage flow, facilitating better understanding of the flow physics.

9.3.6 Comparison with CFD

Directly comparing experimental results of a stationary blade with CFD simulations of rotating fan blades presents challenges due to differing flow conditions and geometries. Nevertheless, a qualitative comparison between the tip leakage flow of a NACA 0012 blade and CFD results of a fan blade tip flow can provide valuable insights into the flow physics. A previous study [31] conducted CFD simulations of a fan tip flow with various tip gap sizes at a mid-span Reynolds number of approximately 5×10^4, with a tip radius of 37.35 mm and an effective angle of attack of around 8°, as introduced in Chapter 4. These conditions are comparable to the tip clearance sizes examined in this study. Table 9.2 outlines the comparison cases between the CFD simulations of the fan blade tip flow and the SPIV measurements of the NACA 0012 blade tip flow. The tip gap sizes are normalised by the blade chord length c to facilitate a meaningful comparison.

Table 9.2: Comparison cases between CFD simulations of fan blade tip flow (c = 26mm, See Chapter 4) and SPIV measurements of NACA 0012 blade tip flow (c = 50mm). Both blades have a mid-span Reynolds number of around 5×10^4 and an effective angle of attack of around 8°.

CFD	t [mm]	0.95	1.9	2.85	4.75
	t/c [%]	3.65	7.31	10.96	18.27
SPIV	t [mm]	0	2.5	5	10
	t/c [%]	0	5	10	20

The 2D divergence, defined in Eq. 106, is calculated from the CFD results of the fan

blade tip flow in [31], as shown in Fig. 9.12. When compared to the SPIV results in Fig. 9.10, the CFD results exhibit a similar topology of the tip leakage flow. High-shear regions are evident near the blade tip and the TLV. The TSV is also distinctly observed near the trailing edge, aligning with the SPIV findings. Unlike the SPIV measurements, the CFD results reveal a pronounced positive velocity gradient near the suction side of the tip, likely due to the detailed capture of the TLV's rolling-up feature in the CFD simulations.

The TLV trajectory was extracted from the 2D divergence plots of both the CFD and SPIV results, as shown in Fig. 9.13. For better comparison, the figures were rotated to align the streamwise direction with the horizontal axis. As the tip clearance size decreases, the TLV trajectory moves closer to the blade leading edge, as observed in both the CFD and SPIV results. However, while the TLV trajectory in the SPIV results for the isolated blade aligns consistently with the streamwise direction for all tip clearance sizes, the CFD results for a rotating blade show a clear variation in the TLV trajectory with tip clearance size. This discrepancy may be attributed to the different geometries between the two cases. Additionally, the isolated blade in the SPIV measurements lacks the rotational effects, which may influence the TLV trajectory. Nevertheless, the qualitative comparison between the CFD and SPIV results highlights both the similarities and differences in the tip leakage flow of a NACA 0012 blade and a fan blade tip flow.

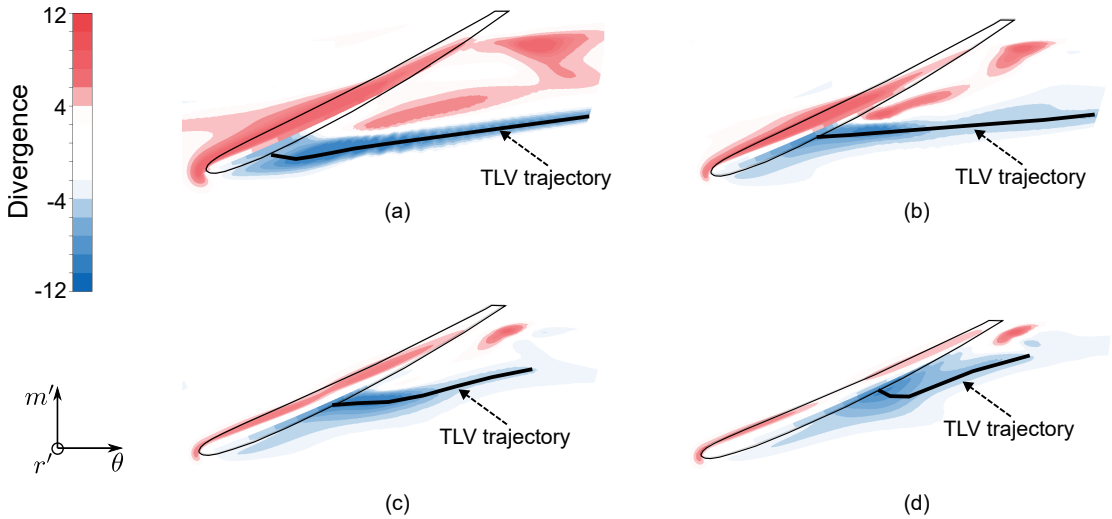

Figure 9.12: The 2D divergence $\mathrm{div}(m', \theta)$ for a fan blade tip flow based on CFD simulation results from Zhao *et al.* [31] (See Chapter 4). Four tip gap sizes are considered: (a) $t/c = 3.65\%$, (b) $t/c = 7.31\%$, (c) $t/c = 10.96\%$, (d) $t/c = 18.27\%$. The fan operates at a mid-span Reynolds number of around 5×10^4, with a tip radius of 37.35 mm and an effective angle of attack of around 8°. Only one blade out of five is shown for clarity. m' is the normalised axial coordinate, and θ is the normalised circumferential coordinate.

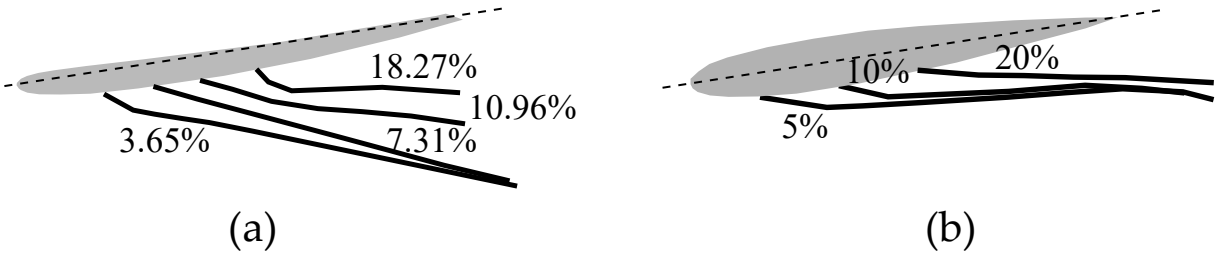

Figure 9.13: Comparison of the TLV trajectory between CFD (Fig. 9.12) and SPIV results (an example is shown in Fig. 9.9 (d)) at an angle of attack of 8° and a Reynolds number of around 5×10^4. The TLV trajectory is extracted from the 2D divergence plot of the CFD results of the fan blade tip flow and the SPIV results of the NACA 0012 blade tip flow. The figures are rotated to align the streamwise direction with the horizontal axis.

9.4 Summary

In this study, we investigate the tip leakage flow of a NACA 0012 blade in a low-speed water tunnel using 2D3C stereoscopic particle image velocimetry (SPIV). The blade is fabricated with high-transparency resin to ensure optical access and minimise light reflection and refraction. We analyse the topology of the tip leakage flow and examine the effects of different tip gap sizes (0–10 mm), angles of attack (0°–16°), and Reynolds numbers (25,000–100,000). The findings are as follows:

- The jet-like tip leakage flow features a high-velocity region near the blade tip and a low-velocity region downstream. This flow separates from the pressure side, rolls up into the tip leakage vortex (TLV), exits the suction side, and convects downstream parallel to the stream-wise direction, mixing with the mainstream.
- The tip leakage flow scales with the freestream velocity, and the flow physics are independent of the Reynolds number considered in this study.
- The angle of attack significantly influences the tip leakage flow. A higher angle of attack results in a more pronounced high-velocity region near the blade tip and a more distinct TLV. The onset of the TLV exiting the suction side moves closer to the blade leading edge as the angle of attack increases.
- The tip clearance size affects the mixing location and TLV separation point. A larger tip clearance size results in a delayed mixing location and TLV separation point closer to the blade trailing edge.

The findings of this study provide insights into the tip leakage flow of a NACA 0012 blade and demonstrate the capabilities of 2D3C SPIV for investigating complex flow structures. The results can be used to validate CFD simulations, guide the design of passive flow control devices, and train data-driven models to predict the flow structure at the tip. Future studies can explore the reduction of blockage in the water tunnel,

investigate the circulation of the tip leakage vortex and its characteristics, and develop a data-driven model to predict the tip leakage flow.

This chapter explored the tip leakage flow in a simplified configuration, compared to the rotating fan blade tip flow discussed in Part I–II. This approach helps to better understand the flow physics of an isolated blade tip. The findings highlighted the tip leakage vortex (TLV) and its trajectory under various conditions, providing valuable insights into the flow dynamics. Combined with the high-fidelity simulations in Part I, these experimental results can guide the design of novel passive flow control devices, *i.e.*, winglets, to reduce noise and improve fan performance. This topic will be further explored in Chapter 10.

Chapter 10

Winglet Designs for Optimised Performance of Small Axial Fans

The final chapter of Part III presents a comprehensive experimental and numerical investigation of winglet designs for small axial fans. This chapter [1] aims to enhance the aerodynamic and acoustic performance of these fans by incorporating winglets at the blade tips. This chapter is based on our published work [209], where J. Hickey, co-supervised by W. Zhao and T. Persoons, conducted the experimental investigation and prepared the experimental part of the manuscript. W. Zhao developed the experimental facilities, performed the numerical simulations, and conducted the analysis, manuscript writing, and revision. For brevity, the complete experimental results conducted by J. Hickey are not included in this chapter; only the key information and findings are presented. Readers interested in the full experimental results can refer to the original publication [209].

The chapter is organised as follows: Section 10.1 provides an overview of the study, emphasising the importance of axial fans in various industries and summarising existing research on winglet designs. Section 10.2 details the experimental methodology and key findings by J. Hickey, highlighting significant results. Section 10.3 describes the numerical methodology used to simulate the flow physics of the selected winglet configurations. Section 10.4 presents the numerical simulation results, offering insights into the flow physics and noise generation mechanisms of the optimised winglet configurations. Finally, Section 10.6 summarises the key findings and discusses their implications for optimising axial fan designs.

[1] This chapter is based on the published **journal article** [209]: J. Hickey, W. Zhao, and T. Persoons, "Experimental and numerical investigation of winglet designs for optimized performance of small axial fans," *Applied Acoustics*, p. 110448, Mar. 2025.

Abstract

This study investigates the impact of winglets on the aerodynamic and acoustic performance of small axial fans. An extensive experimental investigation tested 20 winglet configurations on a reference fan. The winglets varied in width, side, location, and shape. The aerodynamic performance was evaluated using a wind tunnel, while the acoustic performance was assessed using a standardized plenum setup. Among the tested configurations, suction-side winglets with a moderate-smooth profile were the most effective in enhancing efficiency and reducing noise simultaneously. The full-length suction-side winglet demonstrated the greatest reduction in noise, while placing the winglet only in the front-shortened position proved to be the most effective in improving efficiency. The optimised winglet designs increased efficiency by up to 1.8% and reduced the overall sound pressure level by up to 3.6 dB. Numerical simulations provided deeper insights into the flow physics and noise generation mechanisms of the optimised winglet configurations. The simulations revealed that the optimised winglets effectively control tip-gap flow, reducing aerodynamic losses and noise levels. Tonal noise was reduced by up to 15.9 dB at the first blade passing frequency, and trailing-edge noise at high frequencies (5.5 – 10 kHz) was reduced by up to 2.5 dB. These findings offer valuable insights for optimising winglet designs for axial fans to enhance efficiency and reduce noise levels in various applications.

10.1 Introduction

Axial fans are widely used in various industries, including automotive, aviation, and refrigeration, to facilitate air movement. They play a crucial role in cooling electronic components in data centers, which are experiencing rapid growth [5]. However, the increasing demand for compact storage enclosures has led to higher strain on cooling fans, resulting in elevated noise levels that approach workplace exposure limits [181]. This poses significant health risks and compliance challenges. Furthermore, there is often a trade-off between noise reduction and operational efficiency, as attempts to reduce noise can decrease fan efficiency, thereby impacting energy costs. Considering that cooling accounts for up to 40% of total energy consumption in data centers, any reduction in fan efficiency can lead to substantial increases in energy costs. Globally, data centers consume over 2% of the total energy, underscoring the urgent need to improve axial fan efficiency [305]. Given the substantial energy consumption of data centers and the approaching workplace exposure limits for noise, it is crucial to enhance axial fan efficiency while simultaneously reducing noise levels.

One of the primary factors contributing to efficiency loss and noise propagation in axial

fans is the airflow between the fan blade tip and the surrounding shroud, commonly referred to as the tip leakage flow (TLF). Early experimental studies conducted by Longhouse [162] focused on investigating the aerodynamic performance and noise characteristics of industrial axial fans. Their findings revealed significant improvements in aerodynamic efficiency and reductions in broadband noise when the tip gap was reduced. Subsequent research by You *et al.* [160, 161] utilised large eddy simulations (LES) to identify various flow structures responsible for these effects, including the tip leakage vortex (TLV), tip separation vortex (TSV), and other induced vortices. These flow interactions result in substantial tonal and broadband noise as well as aerodynamic losses. Similar acoustic effects were also observed by Zhu *et al.* [208, 306]. Furthermore, Zhao *et al.* [31] reported that reducing the tip clearance can significantly enhance the aerodynamic efficiency of axial fans, with a 2.5% decrease in tip clearance ratio resulting in a 7% improvement in efficiency. These collective findings underscore the critical role of tip gap management in optimising axial fan performance.

In some cases, reducing the tip gap in axial fans may not be possible due to mechanical limitations. As an alternative, winglets can be added to the blades to control the airflow between the blade tip and the surrounding shroud. Winglets have been used in turbomachinery to improve aerodynamic performance and reduce noise levels. Previous studies by Corsini *et al.* [163–166] have conducted comprehensive numerical and experimental investigations on the implementation of winglets on the pressure side (PS) of industrial fan blades. Their findings indicate that well-designed winglets can improve both tonal and broadband noise characteristics while increasing the peak fan efficiency. Similarly, Akturk *et al.* [138] performed an experimental study on an industrial fan, examining the length and chord-wise location of various PS winglets. They observed similar enhancements in overall efficiency and increased downstream airflow for specific PS winglet configurations. Furthermore, Han *et al.* [139] conducted an experimental study on a compressor cascade, comparing the effects of suction side (SS) and PS winglets. Their results demonstrated that SS winglets notably reduced total pressure loss and improved aerodynamic performance at various incidence angles. Moreover, the study by Jung *et al.* [167] investigated the effects of winglets on the aerodynamic performance of axial fans used in air conditioning systems. Their findings revealed that SS winglets increase the efficiency of partially shroud-covered axial fans, while decreasing the efficiency of fully shroud-covered axial fans. Additionally, Zhang *et al.* [136] investigated the effects of different blended winglet designs on the aerodynamic and acoustic performance of diagonal fans. Their findings revealed that the implementation of winglets, particularly on the SS, significantly reduced the tip leakage vortex (TLV) and noise levels while enhancing overall efficiency. Although there is no consensus on the optimal winglet location, these studies demonstrate the potential of

winglets to enhance turbomachinery performance in terms of both aerodynamics and acoustics.

In the realm of small axial fans for electronics cooling, the integration of winglets has received relatively less attention. Yen and Lin [135] conducted a study using particle image velocimetry (PIV) and wind tunnel tests to explore the influence of winglets on axial flow fans. They found that winglets enhance flow stability and fan efficiency while increasing lift and reducing drag. Fans equipped with winglets demonstrated higher efficiency and more stable flow fields than those without winglets. However, this study only examined a single type of winglet and did not address the impact of winglets on fan noise. More recently, Diao *et al.* [137] investigated the effects of different blade tip winglet side positions on axial flow fans, with a focus on noise reduction. Their research showed that winglet blades positioned on both sides, the SS, and the PS effectively reduced tip leakage flow and noise levels. The suction-side winglet blade exhibited the most substantial noise reduction. However, this study did not consider other winglet parameters such as width, location, and shape, and there were limited experimental aerodynamic comparisons between the different winglet configurations. These findings highlight the need for a comprehensive investigation to thoroughly examine the effects of various winglet parameters and their combinations on the aerodynamic and acoustic performance of small axial fans.

The objective of this study is to optimise the aerodynamic and acoustic performance of small axial fans by adding winglets to the blade tips. Through a systematic variation of winglet parameters such as width, side, location, and shape, this research aims to identify configurations that enhance both efficiency and noise reduction. The study employs a combination of experimental and numerical methods to investigate the effects of winglets on axial fan performance. A comprehensive experimental study is conducted to evaluate the aerodynamic and acoustic performance of various winglet configurations, with the goal of identifying optimised designs. Subsequently, numerical simulations are performed to provide detailed insights into the flow physics and noise generation mechanisms associated with the most promising winglet configurations. This integrated approach enables a thorough evaluation of the impact of winglets on axial fan performance. The findings of this study will contribute valuable insights for optimising axial fan designs and reducing noise in various applications.

10.2 Experimental methodology and key findings

This section outlines various fan configurations tested in the experimental study, the experimental setup, and the key findings of the experimental investigation. The detailed experimental results are published in [209].

10.2.1 Designing winglets for axial fans

The reference fan used as the baseline for all modifications in this study is same as the one shown in Section 3.2.1 (see Fig. 2.1). The fan operates at a speed of 7050 r/min, resulting in an average chord-based Reynolds number of 46,000 at the blade tip. More details on the reference fan can be found in the work by Zhao *et al.* [23, 31].

This study proposes 20 winglet configurations for the fan blades, each of which was experimentally tested. The modified fan blades were manufactured using stereolithography (SLA) 3D printing and mounted onto the hub assembly of the reference fan. An identical version of the reference fan was also 3D printed to serve as a baseline for comparison.

To eliminate the effect of tip clearance, all winglet configurations were designed to maintain a constant tip clearance ratio of 2.5% of the blade tip radius, consistent with the reference fan. The winglet parameters of the fan blades are determined by fixed and variable elements. The height of the winglet, defined as the spanwise dimension, is set at 1 mm (2.7% of the tip radius) as a fixed parameter to ensure mechanical integrity.

Figure 10.1 illustrates the different winglet types tested in this study, labeled with their unique identifiers. The initial letter denotes the type of modification, with 'W' representing a winglet design. The subsequent letters depend on the combination of variable winglet parameters. These parameters include:

- **Side of the winglets**: Specifies the placement of the winglet on the airfoil, which can be on the suction side (SS), the pressure side (PS), or two sides (TS).

- **Chord-wise location of the winglets**: Determines the winglet's position along the chord of the fan blade. The tested locations are front-shortened (F), middle-shortened (M), rear-shortened (R), and full-length (leave as blank).

- **Width of the winglets**: Refers to the maximum dimension of the winglet perpendicular to the chord line. The width of the winglet is based on the maximum thickness of the original airfoil (1.6 mm). Two widths are investigated: double the thickness (3.2 mm) and triple the thickness (4.8 mm).

- **Smoothness of the winglets**: Refers to the smoothness at the front and rear edges of the winglet. This includes sharp profile (01), moderate-smooth profile (02), and smooth profile (03).

For clarity, three examples for the identifiers are given below:

- Figure 10.1 (d) W.SS.3.2mm.02: Suction-side winglet, full-length, 3.2 mm width, moderate-smooth profile.

- Figure 10.1 (g) W.PS.M.4.8mm.03: Pressure-side winglet, middle-shortened, 4.8 mm width, smooth profile.
- Figure 10.1 (i) W.TS.4.8mm.01: Two-sides winglet, full-length, 4.8 mm width, sharp profile.

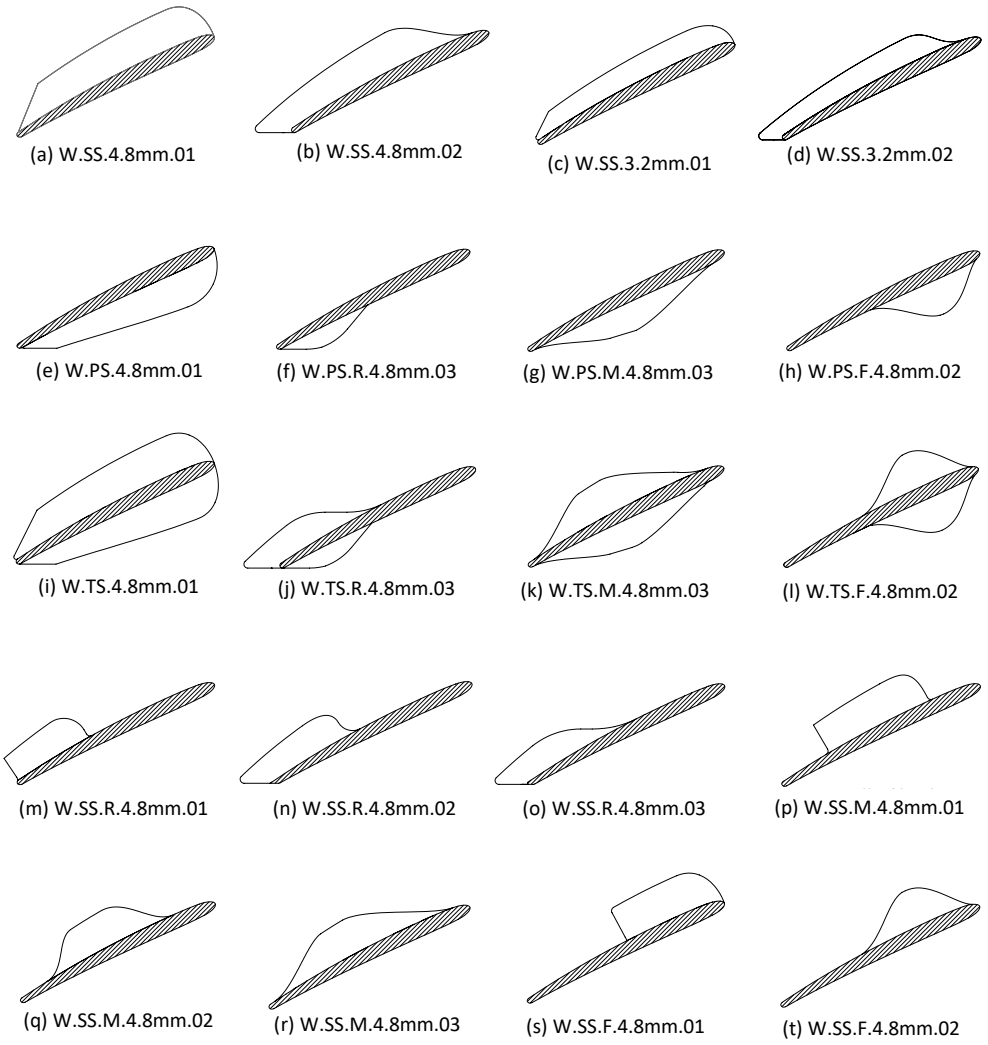

Figure 10.1: Winglet parameters tested. Hatching shows the original airfoil shape at the blade tip. 'W' denotes winglet. 'SS', 'PS', and 'TS' denote suction side, pressure side, and two sides, respectively. 'F', 'M', and 'R' denote front, middle, and rear winglets, respectively. '01', '02', and '03' represent sharp, moderate smooth, and smooth-edged winglets, respectively. Figure credit: J. Hickey [209].

10.2.2 Key findings from the experimental investigation

The aerodynamic and acoustic measurements were conducted for all 20 winglet configurations, as well as the reference fan. The aerodynamic performance was evaluated using the wind tunnel as described in Appendix A.1, while the acoustic performance was assessed using a standardized plenum setup as described in Appendix A.2. The

aerodynamic and acoustic metrics were used to evaluate the performance of each winglet configuration and identify the most effective designs for enhancing efficiency and reducing noise levels.

The key findings of the experimental investigation of winglet shape effects are summarised below [209]:

- **Impact of winglet width:** Smaller winglets (3.2 mm) show a slight reduction in overall sound pressure level (OASPL) compared to larger winglets (4.8 mm), but their aerodynamic performance is slightly lower as well.
- **Impact of winglet smoothness:** Smoother winglets generally improve aeroacoustic performance compared to sharper winglets. However, the aerodynamic performance of smoother winglets is slightly reduced compared to sharper winglets for full-length winglets. On the other hand, moderate-smooth winglets exhibit the best aerodynamic performance than other winglets for front, middle, and rear winglets.
- **Optimal winglet shape:** The optimal smoothness of the winglet shape may vary depending on the winglet position. However, moderate-smooth, suction-side winglets with a width of 4.8 mm offer increased aerodynamic performance and reduced noise levels for all winglet configurations.

These findings highlight the potential for optimising winglet shape to achieve a balance between aerodynamic and acoustic performance. The results suggest that moderate-smooth, suction-side winglets with a width of 4.8 mm offer the best balance for all winglet configurations. These findings provide valuable insights for designing optimised winglet configurations that enhance both aerodynamic and acoustic performance. The next section outlines the numerical methodology used to simulate the flow physics of the selected winglet configurations.

10.3 Numerical methodology

10.3.1 Computational domain and boundary conditions

The numerical simulations utilise steady-state Reynolds-averaged Navier-Stokes (RANS) equations and the k-ω shear stress transport (SST) turbulence model. This model has been validated against experimental data for various flow conditions and has demonstrated accurate predictions of axial fan flow fields. The simulations are conducted using the commercial software ANSYS Fluent 2023 R2, employing a coupled pressure-based solver to solve the governing equations.

The computational domain extends 5 rotor diameters upstream of the fan rotor and 10 rotor diameters downstream of the fan stator, as shown in Fig. 10.2. This configuration ensures fully developed flow at the inlet and outlet of the fan rotor. The computational model accurately represents the realistic fan geometry, including the circumferentially asymmetric inlet bellmouth and the hub. To improve grid quality near the wall, the trailing edges of the rotor and stator are slightly rounded.

At the inlet, a total pressure is applied, while the outlet is subjected to a static pressure. The walls are assigned a no-slip boundary condition. The fan rotor domain rotates at a constant angular velocity of 7050 r/min. The multiple reference frame (MRF) method is employed for the RANS simulations to model the rotating domain.

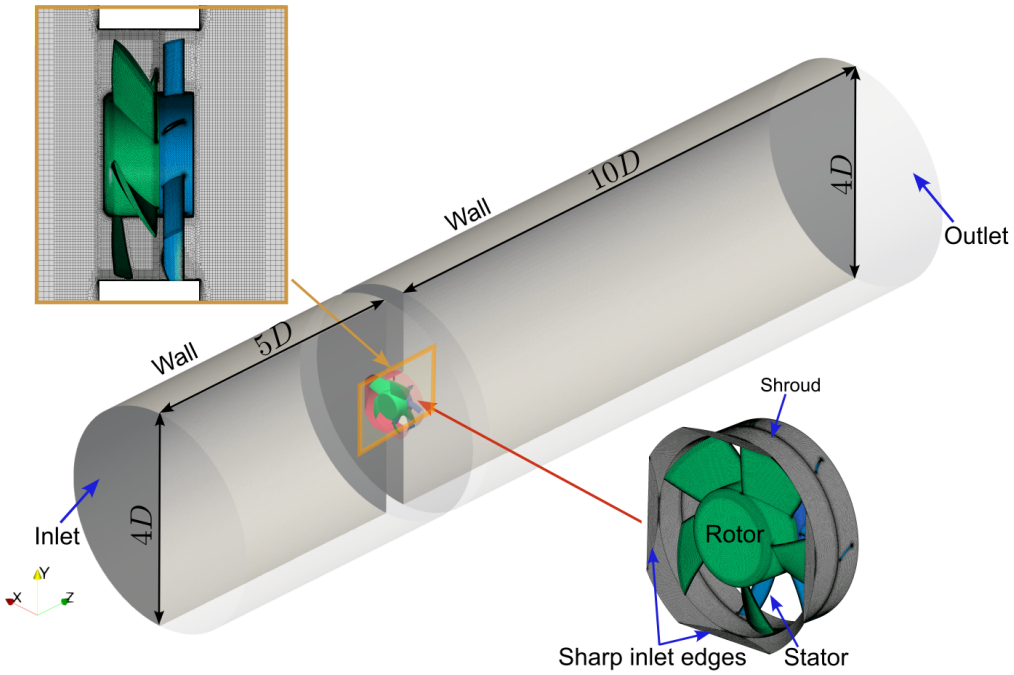

Figure 10.2: Computational domain and grid system.

10.3.2 Grid independence study

The computational grid was generated using ANSYS Fluent Meshing, employing a combination of polyhedral and Cartesian hexcore elements for the main flow region, as depicted in Fig. 10.2. To accurately capture the complex flow near the fan tip-gap region, approximately 35 layers were added. Additionally, the rotor and stator separation gap were refined. For precise resolution of the rotor and stator blades, 18 prism layers were employed with a growth rate of 1.15. The first layer was specifically refined near the walls to ensure that the wall-normal grid resolution satisfied the condition $y^+ < 1$.

To evaluate the numerical accuracy, five different mesh sizes were tested, ranging from 3 million to 23.5 million elements. The mesh was globally refined with a factor of

approximately 1.5. Figure 10.3 illustrates the comparison of flow rates obtained using the five mesh sizes for the zero total-to-static pressure rise case. The results demonstrate that the flow rate converges as the mesh size increases, indicating grid independence. Notably, the mesh with approximately 10 million elements yielded nearly identical results to the finest mesh, affirming the independence of this medium mesh size. This mesh, which required 576 core-hours of computational time for each simulation, was selected for subsequent aerodynamic analysis due to its favorable balance between computational cost and numerical accuracy.

Furthermore, the numerical method was validated against experimental data for the baseline fan. A comparison was made between the aerodynamic performance of the fan obtained from the numerical simulations and the corresponding experimental data, which will be presented in Section 10.4.

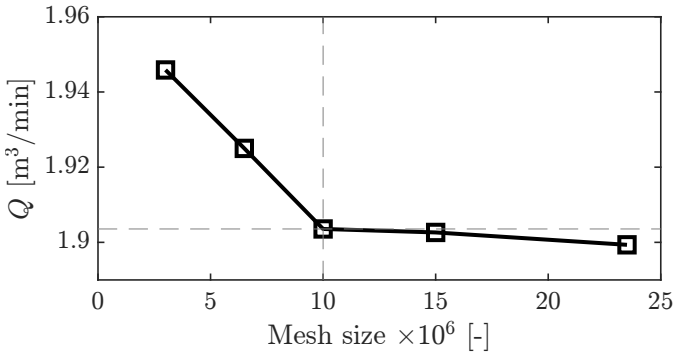

Figure 10.3: Grid independence verification for the zero pressure rise case.

10.4 Discussion: Flow enhancement and noise reduction mechanisms in winglet designs

This discussion investigates the underlying mechanisms that drive the observed performance improvements in the SS winglet designs. The focus is on the SS configurations with a moderate-smooth profile, as they consistently demonstrate superior performance. To comprehensively analyse the performance of winglet designs, a detailed computational fluid dynamics (CFD) analysis is conducted, comparing the designs of full-length, front, middle, and rear winglets to the baseline fan. The analysis centers around the flow field surrounding the fan blades, with particular attention given to the tip leakage flow (TLF) at the tip gap. By examining these key flow features, the aim is to uncover the fundamental mechanisms that enhance flow and reduce noise in winglet designs.

10.4.1 Aerodynamic performance curve comparison

The performance curves of the baseline fan and the optimised winglet designs (SS winglet with a moderate-smooth profile) are compared to illustrate the aerodynamic enhancements achieved through the winglet design. Figure 10.4 presents the performance curves obtained from experiments and CFD simulations for both the baseline fan and the optimised winglet design. Four fan pressure coefficients (Ψ) were selected for comparison: 0 (free-delivery point), 0.065, 0.130, and 0.163 (approximately maximum-efficiency point). Fan operated at stall conditions are excluded for the simulations, due to the limitations of the CFD solver in capturing stall characteristics. These selected pressure coefficients represent the normal operating conditions of the fan.

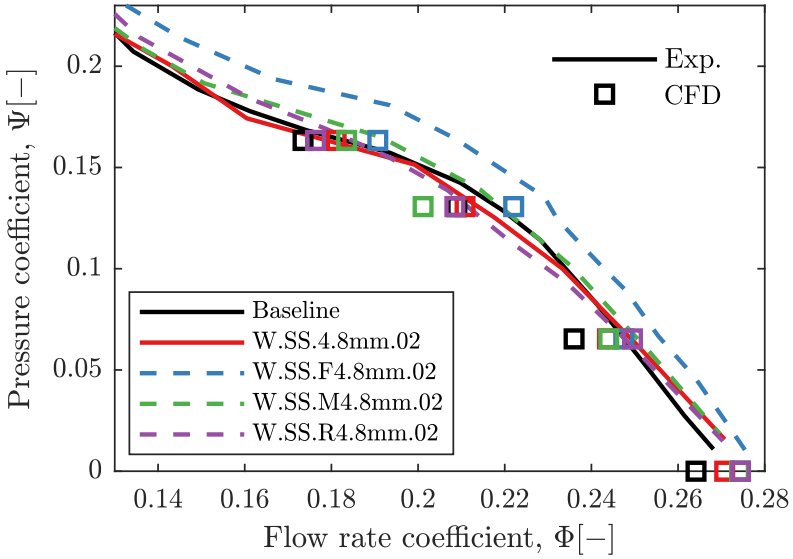

Figure 10.4: Comparison of performance curves between the baseline fan and four suction side winglet designs.

Overall, the CFD results show satisfactory agreement with the experimental data for the baseline fan and the optimised winglet designs. However, certain discrepancies are observed between the CFD and experimental results. The CFD simulations slightly underestimate the flow rate for certain configurations. Additionally, the CFD simulations do not fully capture the relative flow rate increase achieved by different winglet configurations at high pressure coefficients (*e.g.*, $\Psi = 0.130$). These discrepancies may be attributed to the limitations of the steady-state solver used in this study. The solver may not fully capture the unsteady nature of the flow, especially at high loading conditions, resulting in differences between the CFD and experimental results.

At low flow rates, the CFD results show better agreement with the experimental data, particularly near the free-delivery point. Despite these discrepancies, both the experimental and CFD results consistently demonstrate that the selected winglet designs outperform the baseline fan across most pressure coefficients, highlighting the per-

formance improvements achieved through the optimised winglet design.

It should be noted that using a steady-state solver has limitations in capturing the dynamic behavior of vortices. Steady-state RANS simulations do not fully capture the transient interaction between the rotating blades and the downstream stator vanes. To obtain more detailed information on the dynamic behavior of vortices, unsteady simulations such as detached eddy simulations (DES) or large eddy simulations (LES) are required. However, these simulations are computationally expensive and complex. For example, a full LES for a single operating condition of a small axial fan can require around 10,000 core-hours using high-performance computing facilities [20]. Simulating detailed wall-bounded flows for acoustic analogies with complex geometries, like the axial fan with a shroud and winglets, demands substantial computational resources. Given the large number of winglet configurations tested in this study, conducting unsteady simulations for each case would be computationally prohibitive. Therefore, steady-state RANS simulations were chosen as a cost-effective approach to provide insights into the overall flow characteristics influenced by the winglets. Despite the limitations of the numerical model, the CFD results can offer valuable insights into the flow physics and performance improvements achieved through the optimised winglet design.

10.4.2 Flow field analysis

To analyse the flow enhancement and noise reduction mechanisms in the optimised winglet design, computational fluid dynamics (CFD) is used to examine the flow field around the fan blades. The analysis focuses on the free-delivery fan operating at zero total-to-static pressure rise. This choice is motivated by the fact that the acoustic measurements were conducted at this operating condition, and the CFD results were found to be in better agreement with the experimental data at this point. Specifically, the analysis investigates the tip vortices and flow separation patterns on the blade surfaces to identify the key flow features contributing to the improved aerodynamic performance in the winglet designs.

Tip-gap flow structures

The Q-criterion is utilised to visualize the tip-gap flow structures. Figure 10.5 displays the iso-surfaces of the Q-criterion at 10^8 for the baseline fan, with the vorticity magnitude indicated by color. The flow field exhibits distinct tip vortex structures. Paired inlet vortex tubes (IVTs) are observed near the sharp asymmetric inlet edges of the incomplete bellmouth. The tip leakage vortex (TLV) is visible, extending from the blade tip to the downstream region. Additionally, the induced vortex (IV) forms near

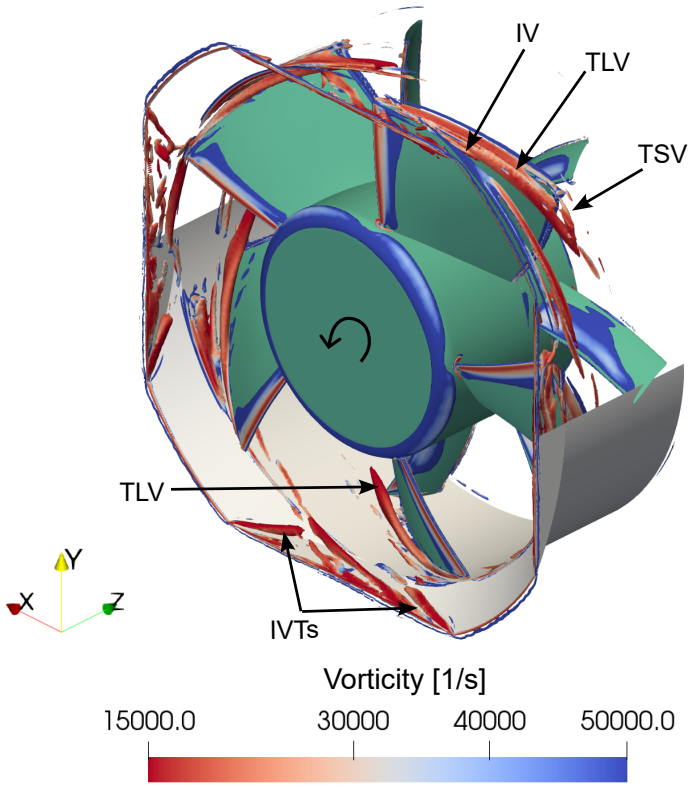

Figure 10.5: Iso-surfaces of the Q-criterion at 10^8 s^{-2} for the baseline fan under $P = 0$ Pa and $N = 7050$ r/min, colored by the vorticity magnitude.

the TLV, while the tip separation vortex (TSV) is observed near the trailing edge at the blade tip. These structures, namely the TLV, IV, and TSV, are the primary contributors to aerodynamic losses and noise generation. Previous studies on rotor-only fan stages have identified these structures [31]. The interaction between the IVTs and the blade leading edge is expected to generate tonal noise, as investigated in other axial cooling fans [36, 74, 76, 195].

Figure 10.6 compares the iso-surfaces of the Q-criterion at 10^8 for the optimised winglet design (SS winglet with a moderate-smooth profile) and the baseline fan. Only the tip region ranging from 75% span to the blade shroud is shown, as this region is critical for the tip flow structures. The iso-surfaces are projected to a blade-to-blade view to facilitate a clear comparison between the baseline fan and the winglet design, with only one blade shown for clarity.

The SS winglet designs effectively suppress the TLV, with the full-length winglet design (W.SS.4.8mm.02) with a moderate-smooth profile exhibiting the most significant suppression (Fig. 10.6 (b)). The front winglet design (W.SS.F.4.8mm.02) with a moderate-smooth profile also shows a slight TLV suppression, accompanied by a notable change in the TLV direction compared to the baseline fan. This change is expected to reduce

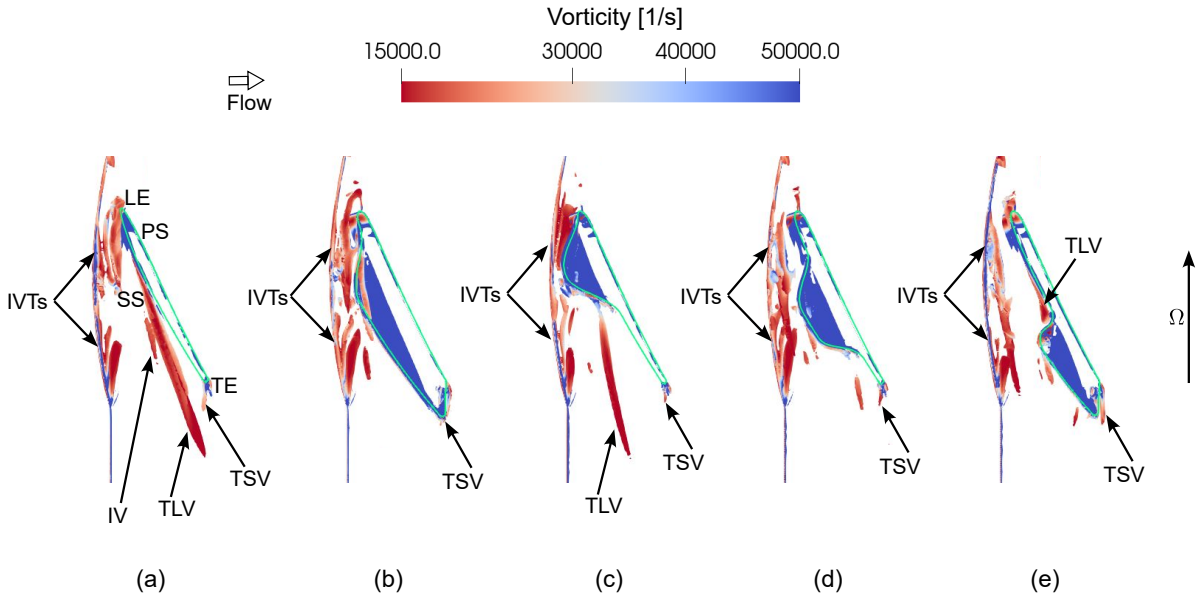

Figure 10.6: Comparison of the iso-surfaces of the Q-criterion at 10^8 s^{-2} for the baseline fan and the optimised winglet designs under $P = 0$ Pa and $N = 7050$ r/min: (a) baseline fan, (b) full-length winglet design (W.SS.4.8mm.02), (c) front winglet design (W.SS.F.4.8mm.02), (d) middle winglet design (W.SS.M.4.8mm.02), and (e) rear winglet design (W.SS.R.4.8mm.02). The iso-surfaces are projected to a blade-to-blade view, with only one blade shown for clarity.

the interaction between the TLV and adjacent blades and downstream stator, resulting in reduced tonal noise (Fig. 10.6 (c)). The middle winglet design (W.SS.M.4.8mm.02) exhibits significant TLV suppression (Fig. 10.6 (d)), while the rear winglet design (W.SS.R.4.8mm.02) shows moderate TLV suppression, particularly in the second half of the blade chord (Fig. 10.6 (e)).

The winglet designs do not exhibit the induced vortex (IV), and the tip separation vortex (TSV) is also reduced, especially in the full-length winglet design (W.SS.4.8mm.02) and the front winglet design (W.SS.F.4.8mm.02) with a moderate-smooth profile (Fig. 10.6 (b) and (c)). These winglets interfere with the generation of the inlet vortex tubes (IVTs), leading to their suppression. The reduction of the TLV, IV, TSV, and IVTs is expected to decrease aerodynamic losses and noise generation.

Surface flow patterns

The surface flow patterns on the blade surfaces are analysed to identify flow separation and the impact of the winglets on the flow behavior. Figure 10.7 displays the distribution of the skin friction coefficient and the surface streamlines on the blade surfaces for both the baseline fan and the optimised winglet design (SS winglet with a moderate-smooth profile). The skin friction coefficient is calculated based on the wall shear stress distribution on the blade surfaces, given by:

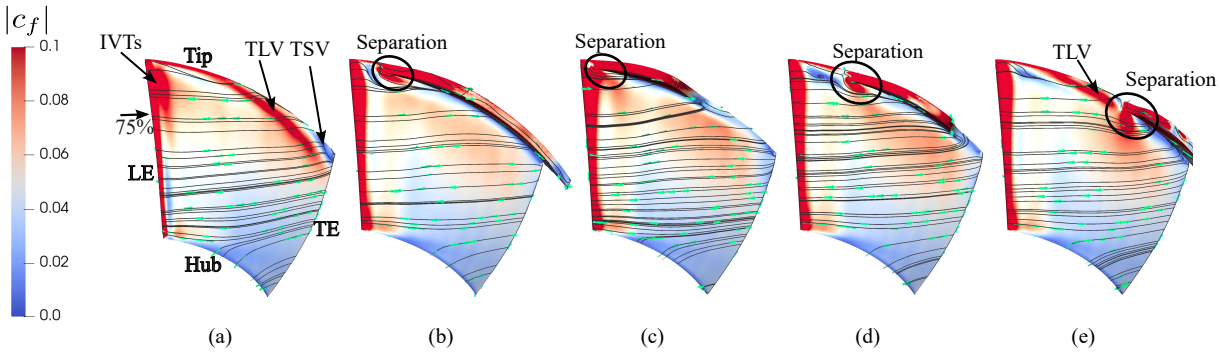

Figure 10.7: Comparison of the skin friction coefficient distribution and surface streamlines on the suction side of blade surfaces for the baseline fan and the optimised winglet designs under $P = 0$ Pa and $N = 7050$ r/min: (a) baseline fan, (b) full-length winglet design (W.SS.4.8mm.02), (c) front winglet design (W.SS.F.4.8mm.02), (d) middle winglet design (W.SS.M.4.8mm.02), and (e) rear winglet design (W.SS.R.4.8mm.02).

$$C_f = \frac{\tau_w}{0.5\rho U^2}, \tag{107}$$

where τ_w represents the wall shear stress, ρ is the air density, and U is the inlet axial velocity.

The distribution of the skin friction coefficient reveals flow patterns on the blade surfaces. The baseline fan exhibits significant flow separation near the blade tip, influenced by the tip separation vortex (TSV) (shown in Fig. 10.7 (a)). High skin friction zones are observed at the blade tip due to the effects from the tip leakage vortex (TLV) and inlet vortex tubes (IVTs), indicating high aerodynamic losses.

In contrast, the optimised winglet design (SS winglet with a moderate-smooth profile) shows reduced effects from the TLV, TSV, and IVTs, resulting in lower skin friction near the blade tip (Fig. 10.7 (b-e)). The impact of tip vortices is significantly reduced in the winglet design, indicating a more stable and efficient flow behavior. However, a high skin friction zone is observed on the blade surface below the front end of the winglet, marked by the circle in Fig. 10.7 (b-e). This indicates that tip flow still slightly separates beneath the winglet, even with a moderate-smooth profile. Further optimisation of the winglet shape may be required to suppress this flow separation and reduce aerodynamic losses.

10.4.3 Mean flow quantities

The flow quantities, such as the sectional blade efficiency, surface pressure distribution, and boundary layer displacement thickness distribution, are also compared between the baseline fan and the optimised winglet design (SS winglet with a moderate-smooth profile). Figure 10.8 shows the comparison of sectional blade efficiency for the baseline

fan and the four optimised winglet designs. The sectional blade efficiency is calculated as:

$$d\eta = \frac{dTU_a}{dQ\,\Omega}, \tag{108}$$

where dT represents sectional blade thrust, U_a is the axial velocity, dQ is the sectional blade torque, and Ω is the rotational speed.

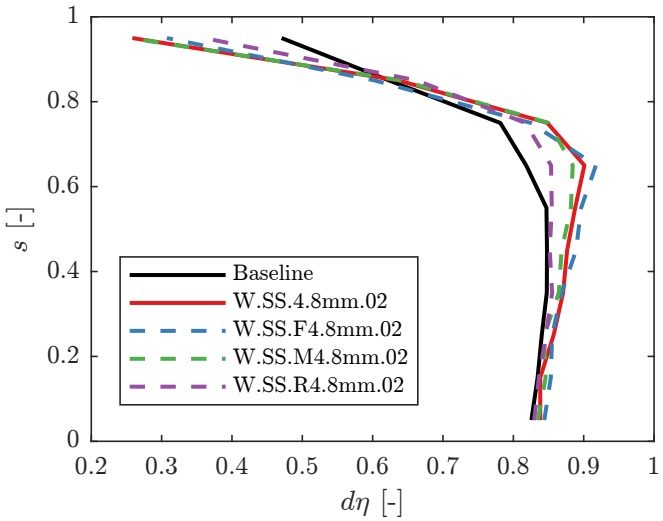

Figure 10.8: Spanwise distribution of sectional blade efficiency for the baseline fan and optimised winglet designs under $P = 0$ Pa and $N = 7050$ r/min, highlighting the sectional performance improvement achieved by the winglet designs. s represents the normalised spanwise location of the blade, with 0 and 1 indicating the hub and blade tip, respectively.

The sectional blade efficiency distribution reveals that all SS winglet designs with a moderate-smooth profile achieve an improvement in the sectional blade efficiency for the blade sections from the hub to around 90% of the span, particularly in the range of 50% to 80% span (See Fig. 10.8). The front winglet design (W.SS.F.4.8mm.02) and full-length winglet design (W.SS.4.8mm.02) with a moderate-smooth profile show the most significant improvement in the sectional blade efficiency, indicating the effectiveness of the winglet design in enhancing blade performance. However, for the 90% to 100% span, the sectional blade efficiency is slightly reduced in the winglet design, which can be attributed to the axial flow blockage by the winglet at the blade tip, resulting in a reduction in the axial velocity.

The surface pressure coefficient C_p and the boundary layer displacement thickness δ^* are also compared between the baseline fan and the four optimised winglet designs at 75% span, as shown in Fig. 10.9 (a) and (b), respectively. The surface pressure coefficient is calculated based on the wall pressure distribution using the equation:

$$C_p = \frac{p - p_\infty}{0.5\rho U^2}, \tag{109}$$

where p represents the wall pressure, p_∞ is the free stream pressure (set to 0 Pa), ρ is the air density, and U is the inlet total velocity.

The boundary layer displacement thickness is calculated using the equation:

$$\delta^* = \int_0^\delta (1 - \frac{u}{U_e})dy, \tag{110}$$

where u is the velocity parallel to the surface, U_e is the edge velocity (99% of the maximum main flow velocity), δ is the boundary layer thickness, and y is the distance from the surface.

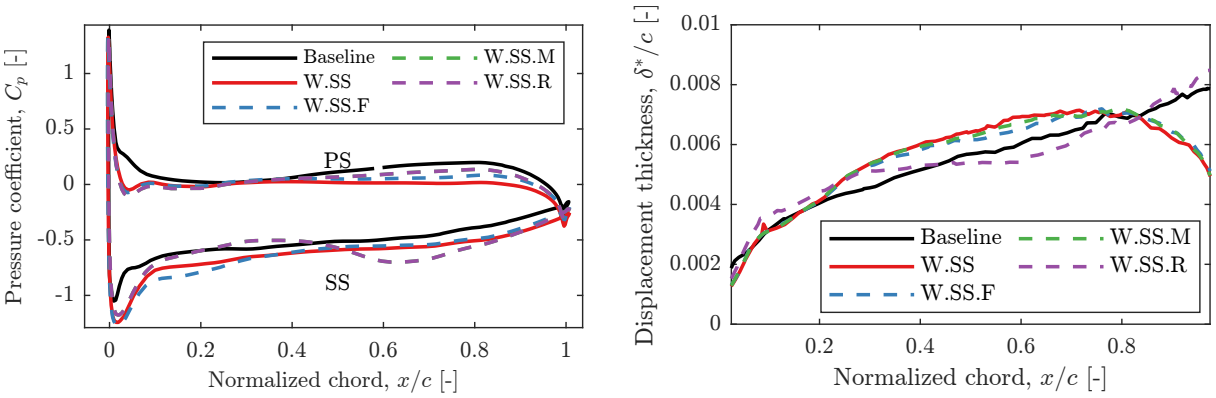

(a) (b)

Figure 10.9: Comparison of the surface pressure coefficient (a) and boundary layer displacement thickness distribution on the suction side (b) between the baseline fan and the optimised winglet design at 75% span under $P = 0$ Pa and $N = 7050$ r/min.

The surface pressure coefficient distribution reveals a higher pressure difference between the blade PS and SS in all optimised winglet designs, indicating a more efficient pressure recovery (See Fig. 10.9 (a)). For the rear winglet design (W.SS.R.4.8mm.02) with a moderate-smooth profile, a hump is observed in the SS C_p distribution, which is attributed to the flow separation induced by the winglet, as observed in the surface flow patterns analysis (Fig. 10.7 (e)).

The boundary layer statistics are closely related to wall pressure fluctuations and the generation of trailing-edge noise. Figure 10.9 (b) displays the distribution of boundary layer displacement thickness for the baseline fan and the four optimised winglet designs at 75% span. Significant differences are observed in the displacement thickness distribution near the trailing edge, particularly in the range of 85% to 100% of the blade chord.

The full-length, front, and middle winglet designs exhibit thinner boundary layers

near the trailing edge, indicating more stable boundary layer behavior with potentially smaller turbulent structures. These differences can be attributed to the suppression of the tip leakage vortex in the winglet designs, as observed in the analysis of tip-gap flow structures (Fig. 10.6) and surface flow patterns (Fig. 10.7 (e)).

However, the rear winglet design exhibits a thicker boundary layer in this region, similar to the baseline fan. This thicker boundary layer at the trailing edge of the rear winglet design (W.SS.R.4.8mm.02) may be caused by the flow separation near the blade tip induced by the winglet (as shown in Fig. Fig. 10.7 (e)). It can affect the boundary layer development near the trailing edge at the 75% spanwise location. These variations are expected to impact the generation of broadband noise, which will be further discussed in the comparison of noise spectra (Section 10.4.4).

10.4.4 Noise spectrum comparison

The noise spectra of the baseline fan and the four optimised winglet designs were compared to evaluate the noise reduction achieved through the winglet design. To assess the noise reduction mechanisms in the winglet designs, the mean-time averaged sound pressure level was calculated over six microphone measurements between the baseline fan and the optimised suction-side winglet designs based on the ISO 3744 standard [212]. The noise spectra comparison is presented in Fig. 10.10.

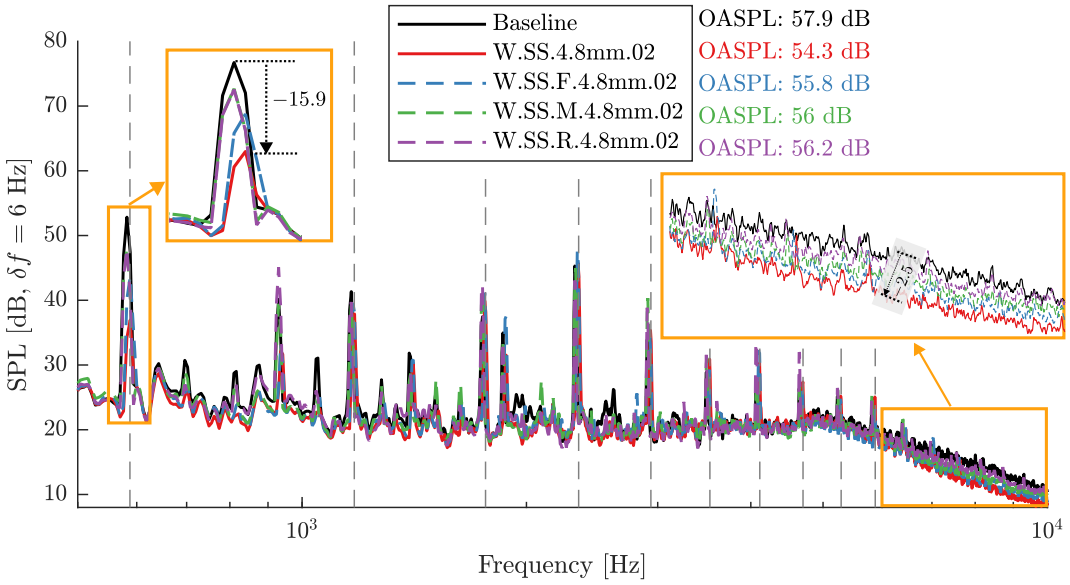

Figure 10.10: Experimental noise spectrum comparison between the baseline fan and the four optimised winglet designs under $P = 0$ Pa and $N = 7050$ r/min. The dashed lines represent first ten harmonics of the blade passing frequency. Figure plotted by W. Zhao based on the experimental data obtained by J. Hickey [209].

The comparison of noise spectra revealed two significant noise reduction mechanisms in the optimised designs featuring the SS winglet: suppression of tonal noise in the first

blade passing frequency (BPF) and reduction of high-frequency broadband noise.

Firstly, the full-length winglet design (W.SS.4.8mm.02) with a moderate-smooth profile exhibited the most substantial reduction in the first BPF compared to the baseline fan, achieving a reduction of 15.9 dB. The front winglet design (W.SS.F.4.8mm.02) with a similar profile also demonstrated a notable reduction in the BPF, with a reduction of 9.2 dB. The middle winglet design (W.SS.M.4.8mm.02) and the rear winglet design (W.SS.R.4.8mm.02), both with moderate-smooth profiles, exhibited the same reduction in the BPF, with a reduction of 4.8 dB.

The noise generation mechanism for the first BPF is primarily associated with the interaction between the rotor blade wakes/tip leakage vortices (TLV) and the stator vanes, as well as the interaction between the incomplete bellmouth and the rotor blades. The mode order of the tonal noise emission is determined by the Tyler-Sofrin's mode order [131], as given in Eq. 35. The rotor-stator interaction alone generates tonal noise due to the interaction between the rotor blade wakes/TLV and the stator vanes, resulting in a mode order of $\xi = mB + kS = -2$ ($m = 1, k = -1, i = 0$) for this interaction. The interaction between the incomplete bellmouth and the rotor blades generates tonal noise due to the interaction between the inlet vortex tubes (IVTs) and the leading edge of the rotor blades, resulting in a mode order of $\xi = mB + iV = 1$ ($m = 1, k = 0, i = -1$). Both mechanisms, working in isolation, are expected to contribute to strong tonal noise emission on the rotor blades at the first BPF, given the low mode order. Additionally, there could be more potential interference modes when the two interactions work together, such as $\xi = 0$ when $m = 1, k = 1$ and $i = -3$, leading to a stronger tonal noise emission at the first BPF.

The optimised winglet designs effectively suppress the tip vortices, including the TLV, IV, and TSV, as evident in the Q-criterion iso-surfaces (Fig. 10.6), surface flow patterns (Fig. 10.7), and boundary layer displacement thickness distribution (Fig. 10.9). These results confirm the successful control of tip flow and the subsequent reduction in tonal noise associated with the rotor-stator interaction. Notably, the full-length, front, and middle winglet designs interfere with the generation of IVTs (Fig. 10.6 (b-d)), while the rear winglet design does not exhibit clear interference (Fig. 10.6 (e)). This interference is expected to suppress the tonal noise emission at the first BPF, resulting from the interaction between IVTs and the leading edge of the rotor blades. This observation explains the more significant reduction in the first BPF observed in the full-length, front, and middle winglet designs compared to the rear winglet design. However, it is still unclear which interaction mechanism contributes more to the tonal noise reduction. In real-fan operation, the two mechanisms may work together, and it is challenging to separate their relative importance. Therefore, high-fidelity transient simulations are recommended in further work to gain a deeper understanding of the noise generation

mechanisms and the impact of the winglets on tonal noise emission. By simulating the two interaction mechanisms in a controlled numerical environment, their relative importance can be better clarified. For a fan with a well-designed bellmouth, it is plausible that winglets may not achieve such significant noise reduction at the BPF.

Secondly, the winglet designs also achieved reductions in high-frequency broadband noise levels in the frequency range from 5.5 kHz to 10 kHz (Fig. 10.10). The full-length winglet design with a moderate-smooth profile exhibited the most substantial reduction in high-frequency broadband noise, followed by the front winglet design, the middle winglet design, and the rear winglet design. The thinner boundary layers near the trailing edge in these designs, as indicated by the analysis of the boundary layer displacement thickness distribution (Fig. 10.9 (b)), contribute to reduced turbulence and wall pressure fluctuations, resulting in effective reduction of broadband trailing-edge noise. Surprisingly, the rear winglet design, despite having a slightly thicker boundary layer at the trailing edge, also exhibited a reduction in broadband noise levels. This reduction may be attributed to the combined effect of tip leakage flow control and vortex suppression. To provide a more detailed explanation of the mechanisms behind the reduction in broadband noise, further investigation using high-fidelity simulations is required.

In summary, the optimised winglet designs featuring the SS winglet demonstrate significant noise reduction in both tonal and broadband noise components. The suppression of tonal noise in the first BPF, achieved through the interference with IVTs and the suppression of the TLV-stator interaction, highlights the effectiveness of the winglet design in controlling tip flow and reducing noise generation. Additionally, the reductions in high-frequency broadband noise levels, attributed to the thinner boundary layers and the combined effect of tip leakage flow control and vortex suppression, further emphasise the noise reduction capabilities of the winglet designs. These findings underscore the potential of winglet technology in improving the aerodynamic performance and noise characteristics of fan systems.

10.5 High-fidelity simulations

To gain deeper insights into the tip vortex structures and noise sources in the optimised winglet designs, high-fidelity large eddy simulations (LES) were conducted. Due to the computational cost of LES and time constraints, the front winglet design (W.SS.F.4.8mm.02) with a moderate-smooth profile was chosen for detailed analysis. The LES simulations followed the methodology outlined in Chapter 3 to ensure consistency. These simulations were performed under the same operating conditions as the RANS simulations, with a rotational speed of 7050 r/min and a total-to-static pressure

rise of 0 Pa.

Figure 10.11 compares the noise spectra from the LES simulations for the baseline fan and the optimised winglet design. The LES results support the experimental findings, showing significant noise reductions. Specifically, the LES simulations revealed a 2.1 dB reduction in the overall sound pressure level (OASPL) for the front winglet design, compared to the 3.6 dB reduction observed experimentally. While the reduction in the first blade passing frequency (BPF) was smaller in the LES results (3.2 dB) than in the experimental data (15.9 dB), the trend remains consistent, highlighting the winglet's effectiveness in reducing tonal noise.

Interestingly, the LES results also showed a 3.2 dB reduction in the fourth harmonic of the BPF, which was similarly observed in the experimental data. This harmonic, attributed to rotor-stator interactions, aligns with predictions from the reduced-order model discussed in Chapter 7 (see Fig. 7.11). Overall, the LES results strongly support the experimental findings.

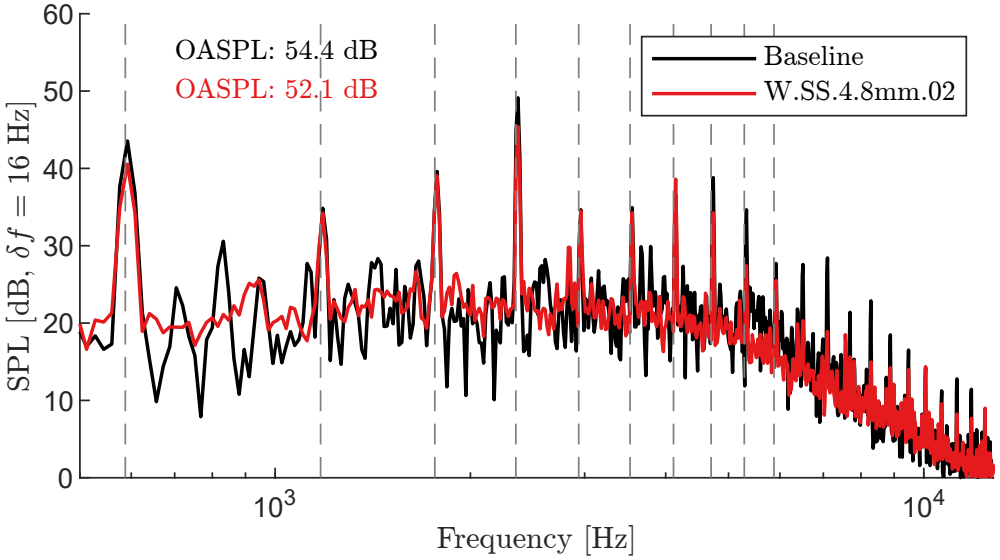

Figure 10.11: LES noise spectrum comparison between the baseline fan and the four optimised winglet designs under $P = 0$ Pa and $N = 7050$ r/min. The dashed lines represent first ten harmonics of the blade passing frequency.

Figure 10.12 compares the tip vortex structures between the baseline fan and the optimised front winglet design (W.SS.F.4.8mm.02) using the Q-criterion. The iso-surfaces of the Q-criterion at 10^8 are shown, with vorticity magnitude indicated by colour. The LES results reveal that the front winglet design primarily changes the trajectory and separation point of the TLV, rather than significantly reducing its strength. This aligns with the RANS results, which also showed minor reduction in TLV strength. However, the altered TLV trajectory and separation point help reduce tonal noise by lessening interactions between the TLV and other flow structures.

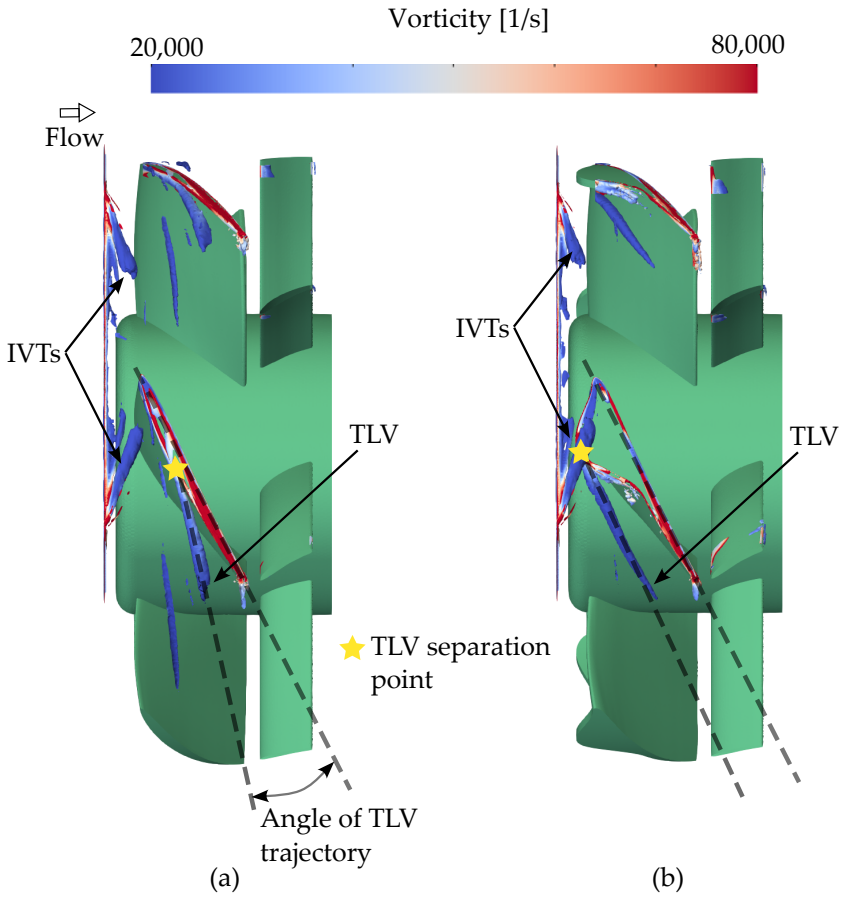

Figure 10.12: LES tip vortex structures comparison between the baseline fan and the optimised winglet design under $P = 0$ Pa and $N = 7050$ r/min: (a) baseline fan, (b) front winglet design (W.SS.F.4.8mm.02).

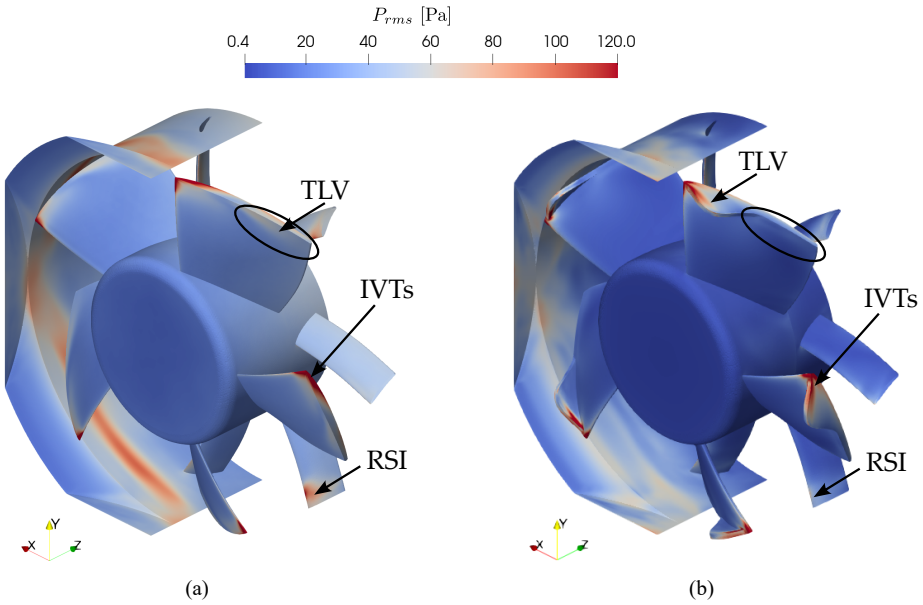

Figure 10.13: LES surface pressure fluctuation comparison between the baseline fan and the optimised winglet design under $P = 0$ Pa and $N = 7050$ r/min: (a) baseline fan, (b) front winglet design (W.SS.F.4.8mm.02).

Figure 10.13 shows the surface pressure fluctuations for both the baseline fan and the front winglet design. The optimised winglet design clearly reduces surface pressure fluctuations, especially in the blade tip region and the stator area where rotor-stator interactions occur. By altering the TLV trajectory, the winglet reduces its interaction with the blade tip, lowering surface pressure fluctuations in this critical region. This reduction is closely linked to decreased broadband noise. Additionally, the modified TLV trajectory reduces its interaction with the downstream stator, significantly lowering tonal noise, including the fourth harmonic of the BPF observed in the experimental results.

Interestingly, the LES results do not conclusively show that the front winglet design significantly suppresses the asymmetric inlet vortex tubes (IVTs), which contribute to tonal noise at the first BPF. While the IVTs remain present in the optimised design, their strength appears slightly reduced compared to the baseline fan. This subtle reduction may still help mitigate tonal noise, but its exact impact remains unclear.

Future studies should explore the dynamics of IVTs and their interactions with the rotor blades in more detail. Conducting force analyses on the IVTs could provide valuable insights into how the winglet design affects their behaviour. High-resolution simulations or experimental techniques could also quantify the extent of IVT suppression and its role in noise reduction. These investigations would clarify how the winglet design contributes to the observed noise reduction, particularly at the first BPF.

Overall, the LES results offer a deeper understanding of the flow physics and noise reduction mechanisms in the optimised front winglet design. The findings support the experimental observations, showing the winglet's effectiveness in improving aerodynamic performance and reducing noise. These results highlight the potential of the proposed winglet configuration as a practical solution for enhancing axial cooling fan performance.

10.6 Summary

This study investigates the effects of winglet position and shape on the aerodynamic and acoustic performance of an axial cooling fan. The analysis focuses on the impact of winglet design on flow enhancement and noise reduction mechanisms. Experimental tests were conducted on twenty winglet configurations, including full-length, front, middle, and rear winglets with varying shapes and positions. The performance of the winglet designs was evaluated based on flow rate, pressure rise, efficiency, and noise generation. The optimised winglet designs were identified based on superior performance achieved in the experimental tests.

Suction side (SS) winglet designs with a moderate-smooth profile consistently demonstrated superior performance across all configurations. Full-length, front, middle, and rear SS winglets with a moderate-smooth profile achieved significant improvements in flow rate, pressure rise, and efficiency compared to the baseline fan, as well as reductions in noise. These four configurations were selected as the optimised winglet designs for further numerical analysis.

Computational fluid dynamics (CFD) simulations were conducted to analyse the flow field around the fan blades and identify the key flow features that contribute to the improved performance of the optimised winglet designs. The CFD model was validated against experimental data for both the baseline fan and the four optimised winglet configurations, demonstrating good agreement.

The front winglet design with a moderate-smooth profile achieved the highest aerodynamic performance, with a slight improvement in efficiency of 1.8%. The analysis of the flow field revealed reduced aerodynamic losses and noise generation in the optimised winglet designs by suppressing tip leakage vortices (TLVs), induced vortices (IVs), tip separation vortex, and inlet vortex tubes (IVTs). The surface flow patterns on the blade surfaces indicated more stable and efficient flow behavior in the optimised winglet designs, with reduced skin friction near the blade tip. Comparing flow quantities, such as sectional blade efficiency, surface pressure distribution, and boundary layer displacement thickness, further confirmed the enhanced performance of the optimised winglet designs.

The noise spectrum comparison revealed effective noise reduction mechanisms in the optimised winglet designs. These designs achieved significant reductions in tonal noise peaks and broadband noise levels. Among the designs, the full-length winglet with a moderate-smooth profile demonstrated the most substantial noise reduction. It achieved an overall sound pressure level (OASPL) reduction of 3.6 dB and a 15.9 dB reduction in the first blade passing frequency (BPF). The front winglet with a similar profile also showed a notable noise reduction, with an OASPL reduction of 2.2 dB. The tonal noise reduction in the optimised winglet designs was attributed to the suppression of tip leakage vortices, induced vortices, and tip separation vortices, as well as the interference with inlet vortex tubes. The reduction in broadband noise levels was closely linked to the reduction of trailing-edge noise, which was achieved through thinner boundary layers near the trailing edge.

These results demonstrate the superior noise reduction capabilities of the optimised suction side winglet designs, particularly the full-length and front winglet designs. This highlights their potential for reducing noise in axial cooling fans. The study provides valuable insights into the flow enhancement and noise reduction mechanisms in winglet

designs, contributing to the development of more efficient and noise-reducing cooling fan designs in the future.

This chapter highlights the significant potential of winglet technology in enhancing the aerodynamic performance and noise characteristics of axial cooling fans. The optimised winglet designs have demonstrated effective control of tip leakage flow, leading to substantial noise reduction. Unlike the acoustic liners discussed in Chapter 8, winglets are particularly adept at targeting noise sources, improving aerodynamic efficiency, and facilitating the development of new blade designs or retrofits. This chapter concludes the discussion on noise reduction technologies for axial cooling fans in Part III, providing a viable solution for future research and development in fan noise control.

Chapter 11

Conclusions and Outlook

This thesis provides a thorough analytical, numerical, and experimental investigation into the aerodynamic and aeroacoustic characteristics of small-sized axial fans used in electronics cooling systems, alongside innovative passive noise control methods. The primary aim is to enhance our understanding of flow-induced noise generation mechanisms and to develop effective noise mitigation strategies for cooling fans, thereby contributing to more sustainable data centre operations and quieter electronics cooling systems. The research objectives are accomplished through three main parts: high-fidelity modelling of flow physics and noise generation in axial fans, reduced-order modelling for rapid prediction of aerodynamics and aeroacoustics, and the development of novel passive noise control methods. This chapter summarises the key findings and contributions of the study and provides an outlook on future research directions.

11.1 Conclusions

11.1.1 High-fidelity modelling for flow physics and noise generation of axial fans

The first part (Part I) of this study focuses on high-fidelity modelling to understand the flow physics and noise generation of axial fans. Utilising large eddy simulations (LES) and Ffowcs Williams-Hawkings (FW-H) acoustic analogy method, the research investigates the fan's flow field and noise sources under both normal and stall conditions.

Aerodynamic analysis shows that, during normal operation, the flow structures are more coherent and periodic, with significant interaction between the asymmetric bell-mouth inlet and the rotor blades. The tip flow topology includes tip-leakage vortex

(TLV), induced vortex (IV), and tip-separation vortex (TSV). An unusual feature at the tip region is the vortex-shroud interaction (VSI). In contrast, the stall condition is characterized by pronounced flow separation on the blade surfaces and high leading-edge turbulence, resulting in more chaotic and less periodic flow structures with reduced influence from the asymmetric inlet-rotor interaction (IRI).

Aeroacoustic analysis indicates that the fan's far-field noise has a dipole-like directivity, with tonal noise being more prominent during normal operation and broadband noise more noticeable during stall conditions. The dominant tones occur at the blade passing frequency and its harmonics, with the rotor being the primary source of far-field noise. The VSI notably contributes to far-field tonal noise, especially at microphone locations perpendicular to the fan axis.

The analysis of noise sources on rotor blades identifies the asymmetric inlet-rotor interaction (IRI) as the main source of tonal noise during normal operation, while the tip-gap region is the primary source of broadband noise. During stall conditions, flow separation and high turbulence at the leading edge become the main noise sources, increasing broadband noise. These findings confirm the rotor as the primary contributor to far-field noise.

Part I including Chapter 3 achieves the first objective of the study by providing crucial insights into the aerodynamics and aeroacoustics of small-sized axial fans. These insights are instrumental in developing low-fidelity noise prediction models and passive noise control methods, leading to quieter and more efficient fan designs.

11.1.2 Reduced-order modelling for fast prediction of aerodynamics and aeroacoustics of axial fans

The second part (Part II) of this study focuses on developing reduced-order models (ROMs) for the rapid prediction of the aerodynamics and aeroacoustics of axial fans. These ROMs are designed to deliver accurate and efficient predictions of fan performance under normal operating conditions, facilitating the co-design of flow, heat transfer, and noise solutions in thermal management systems.

Building on insights from high-fidelity modelling (Chapter 3), it is clear that the aerodynamic and aeroacoustic performance of axial fans is significantly influenced by tip leakage flow. Consequently, the ROMs incorporate realistic fan geometry and tip clearance effects, which are crucial for precise performance predictions, as detailed in Chapter 4. The aerodynamic ROM, based on blade element theory combined with the vortex panel solver XFOIL [97], quantifies the impact of tip clearance on fan performance through CFD Reynolds-averaged Navier-Stokes (RANS) simulations. The

ROM demonstrates that reducing the tip clearance ratio by 2.5% can enhance efficiency by approximately 7%. Validated against experimental data for eight commercial fans, the ROM demonstrates prediction errors of less than 7.1%. Additionally, it is highly computationally efficient, being over three orders of magnitude faster than steady-state CFD, making it ideal for the rapid analysis, design, and optimisation of electronics cooling fans.

Chapter 5 extends the aerodynamic ROM to counter-rotating (CR) dual-impeller axial fans. These fans, featuring two impellers rotating in opposite directions with a stator in between, present complex flow fields and noise generation mechanisms. The ROM's predictions, validated against CFD simulations and experimental data, show errors of 4.6% in the normal operating region and 13.2% in the stall region. This extended ROM effectively predicts the aerodynamic characteristics of CR fans with minimal computational resources, proving to be a valuable tool for efficient analysis of P-Q curves in CR fans.

For low-solidity fans (solidity less than unity), where the interaction between adjacent blades is minimal, the vortex panel method solver XFOIL provides reasonable predictions for lift and drag coefficients. However, for high-solidity fans, the cascade effect between adjacent blades becomes significant, rendering XFOIL unsuitable for accurate predictions. Chapter 6 introduces a source vortex panel method specifically designed for cascade airfoils to address these cascade effects in high-solidity fan performance predictions. This method efficiently resolves potential flow, capturing essential flow characteristics and providing reliable lift and pressure coefficient predictions for cascade cases with Reynolds numbers above 1.84×10^5, turbulence levels exceeding 2.5%, and low-to-moderate angles of attack. The methodology can modify isolated 2D lift coefficients for low-to-moderate angles of attack in cascade configurations, further extending the applicability of the ROM to a broader range of fan designs.

Chapter 7 presents a detailed analysis of noise prediction for small axial flow fans using a ROM. This ROM integrates aerodynamic, broadband noise, and tonal noise predictions to accurately capture the fan system's noise characteristics. The model shows strong agreement with large eddy simulation (LES) data. For broadband noise prediction, Amiet's theory combined with Liepmann's spectrum [128] for turbulence inflow and a modified Lee model [123] for wall pressure fluctuations are used, yielding results that closely match LES data. Tonal noise prediction utilises Lowson's model [129], achieving noise level predictions with discrepancies of less than 6 dB. Overall, the ROM demonstrates high precision in predicting total noise levels, with an overall sound pressure level (OASPL) difference of just 2.8 dB compared to experimental and LES data. This model also investigates broadband noise sources and spanwise variations of the fan system, providing valuable insights into the impact of turbulence intensity and

length scale on noise generation. The ROM is a reliable and robust tool for predicting total noise levels of the fan system, offering significant benefits for the design and optimisation of fan systems.

This part of the thesis, including Chapters 4, 5, 6, and 7, successfully addresses the second research question by developing a series of ROMs for predicting the aerodynamic and aeroacoustic performance of axial fans. The combination of these ROMs provides a comprehensive toolset for the rapid analysis, design, and optimisation of axial fans, facilitating the development of quieter and more efficient fan systems.

11.1.3 Novel passive noise control methods for axial fans

The third part (Part III) of this study focuses on the development of novel passive noise control methods for axial fans. By designing and optimising innovative noise control strategies, this research aims to achieve significant noise reduction without compromising the aerodynamic performance of axial fans in confined spaces.

Chapter 8 details the design and optimisation of a novel compact micro-slit panel absorber for axial fans. This absorber, known as the C-MSPA, is designed to improve low-frequency noise absorption while conserving material and space. The C-MSPA utilises optimised slit and air cavity geometry to achieve reduced panel thickness and greater cavity depth for enhanced acoustic performance. Analytical models, numerical simulations, and impedance tube measurements validate the C-MSPA's performance. The C-MSPA was applied to an 80 mm counter-rotating (CR) fan, commonly found in data centre servers, and demonstrated superior noise reduction compared to hardwall and industrial acoustic foam setups. The C-MSPA achieved over 6 dB reduction in sound pressure level (SPL) at target frequencies of 600 Hz, 1200 Hz, and 900–1800 Hz compared to a hardwall, and more than 1.5 dB versus standard industrial acoustic foam. The C-MSPA minimally impacted aerodynamic performance, with only a 0.5% deviation from the baseline P-Q curve. These results highlight the C-MSPA as an effective noise control solution for CR fans in compact electronics cooling applications, providing significant noise reduction without compromising airflow performance.

In addition to absorbing fan noise, directly mitigating noise sources by modifying fan geometry is another effective approach. Since tip leakage flow (TLF) has been identified as one of the main sources of aerodynamic loss and aeroacoustic noise in axial fans in the high-fidelity modelling part (Part I), Chapter 9 investigates the tip leakage flow structures using stereo particle image velocimetry (SPIV) for a simplified fixed-blade endwall configuration. This study aims to provide insights into the flow physics of tip leakage flow. The jet-like tip leakage flow features a high-velocity region near the blade tip and a low-velocity region downstream. The flow scales with the free-stream

velocity, and the flow physics are independent of the Reynolds number considered in this study. The angle of attack significantly influences the tip leakage flow, with a higher angle of attack resulting in a more pronounced high-velocity region near the blade tip and a more distinct tip leakage vortex (TLV). The tip clearance size affects the mixing location and TLV separation point, with a larger tip clearance size resulting in a delayed mixing location and TLV separation point closer to the blade trailing edge. These findings demonstrate the capabilities of SPIV for investigating complex flow structures and provide valuable insights into the tip leakage flow of axial fans, guiding the development of effective tip flow control strategies.

Chapter 10 explores the noise reduction mechanisms of winglets in axial fans, focusing on the design and optimisation of winglet configurations for noise mitigation. This study investigates the effects of winglet position and shape on the aerodynamic and acoustic performance of an axial cooling fan. Experimental tests were conducted on twenty winglet configurations, including full-length, front, middle, and rear winglets with varying shapes and positions.

The results reveal that suction-side (SS) winglet designs with a moderate-smooth profile consistently exhibit superior performance across all configurations. The full-length winglet with a moderate-smooth profile demonstrates the most substantial noise reduction, achieving an overall sound pressure level (OASPL) reduction of 3.6 dB and a 15.9 dB reduction in the first blade passing frequency (BPF). The front winglet with a similar profile also shows a notable noise reduction, with an OASPL reduction of 2.2 dB.

The flow field analysis reveals reduced aerodynamic losses and noise generation in the optimised winglet designs by suppressing tip leakage vortices (TLVs), induced vortices (IVs), tip separation vortex, and inlet vortex tubes (IVTs). Overall, the optimised winglet designs increased efficiency by up to 1.8% and reduced the overall sound pressure level by up to 3.6 dB. These findings underscore the superior noise reduction capabilities of the optimised suction-side winglet designs, particularly the full-length and front winglet designs, highlighting their potential for reducing noise in axial cooling fans.

This part of the thesis, including Chapters 8, 9, and 10, successfully addresses the third research question by developing novel passive noise control methods for axial fans. The two noise control strategies have the following features:

- **Acoustic liners: C-MSPAs** target noise reduction for specific frequency ranges, has negligible impact on aerodynamic performance, achieves low-frequency tonal and broadband noise reduction, is compact and suitable for confined spaces, and can be easily integrated into existing systems.

- **Blade tip modifications: Winglets** target noise reduction for tonal (blade passing frequency) and broadband noise (high-frequency trailing-edge noise), has the potential to improve aerodynamic performance, and is suitable for new fan designs or retrofits.

In summary, Part I to Part III of this study successfully address the research objectives by providing a comprehensive understanding of the aerodynamic and aeroacoustic performance of axial fans and developing innovative noise control methods. The findings contribute to the development of quieter and more efficient fan systems, offering valuable insights for future research and industry applications.

11.2 Outlook

The research conducted in this study lays a robust foundation for future investigations into the aerodynamic and aeroacoustic performance of axial fans and the development of noise control methods. Several promising research directions are outlined below:

- **High-fidelity modelling**: Future research should delve deeper into the unsteady tip flow phenomena and noise generation mechanisms in axial fans with varying tip clearances. Employing data-driven models, such as proper orthogonal decomposition (POD) and dynamic mode decomposition (DMD), can help decouple the flow structures and noise sources under different operating conditions. These models will provide valuable insights into the correlation between flow physics and noise generation, guiding the development of advanced noise prediction models and control strategies.
- **Reduced-order modelling**: The ROMs developed in this study can be extended to predict the aeroacoustic noise of dual impeller CR fans and other configurations by incorporating additional noise sources, such as stator and interaction noise. Additionally, exploring machine learning techniques, such as artificial neural networks (ANNs), convolutional neural networks (CNNs), and physics-informed neural networks (PINNs), can enhance the prediction accuracy and efficiency of the ROMs. Training these models on extensive datasets will improve their predictive capabilities for various fan designs and operating conditions.
- **Passive noise control methods**: The novel noise control methods developed, such as the C-MSPA and winglets, offer effective solutions for noise reduction in axial fans. Future research should explore their application in real-world engineering systems and assess their performance under different conditions. Additionally, developing new noise control methods and innovative fan designs will further

enhance noise reduction capabilities and improve performance. For instance, optimising the incomplete bellmouth design can reduce noise emissions and improve efficiency, while replacing the fan casing with the C-MSPA can create a more compact and quieter system.

- **Multi-objective optimisation**: Developing multi-objective optimisation techniques to simultaneously improve aerodynamic performance and reduce noise emissions is crucial. Integrating the ROMs with optimisation algorithms, such as genetic algorithms (GAs) and particle swarm optimisation (PSO), will help identify optimal fan designs that balance efficiency, noise reduction, and other performance metrics.
- **Tip flow visualisation**: Investigating the tip leakage flow structures for a rotating blade in a realistic fan configuration can provide valuable insights into the flow physics and noise generation mechanisms. The present study has demonstrated the capabilities of SPIV for investigating complex flow structures of a 3D printed transparent blade. Future research should extend this study to explore the tip flow characteristics of realistic axial fans. It will help capture the complex flow structures and turbulence characteristics near the blade tip. These studies will enhance our understanding of tip flow control strategies and their impact on fan performance.
- **Real-world applications**: The noise control methods and prediction models developed have significant potential for application in various real-world scenarios, such as server chassis in data centres, electronics cooling devices, and HVAC systems. Future research should focus on implementing these methods in practical engineering systems and evaluating their performance in real-world operating conditions.

Overall, building on the findings and contributions of this study, future research should aim to advance the field of thermal management and fan noise control in electronics cooling systems. Addressing these research directions will enhance our understanding of fan noise generation mechanisms and lead to effective noise control strategies for a wide range of applications, contributing to quieter and more sustainable cooling systems.

References

[1] A. Isazadeh, D. Ziviani, and D. E. Claridge, "Global trends, performance metrics, and energy reduction measures in datacom facilities," *Renewable and Sustainable Energy Reviews*, vol. 174, p. 113149, Mar. 2023. DOI: 10.1016/j.rser.2023.113149.

[2] S. V. Garimella, L.-T. Yeh, and T. Persoons, "Thermal management challenges in telecommunication systems and data centers," *IEEE Transactions on Components, Packaging and Manufacturing Technology*, vol. 2, no. 8, pp. 1307–1316, Aug. 2012. DOI: 10.1109/TCPMT.2012.2185797.

[3] A. C. Kheirabadi and D. Groulx, "Cooling of server electronics: A design review of existing technology," *Applied Thermal Engineering*, vol. 105, pp. 622–638, Jul. 2016. DOI: 10.1016/j.applthermaleng.2016.03.056.

[4] S. V. Garimella, T. Persoons, J. Weibel, and L.-T. Yeh, "Technological drivers in data centers and telecom systems: Multiscale thermal, electrical, and energy management," *Applied Energy*, vol. 107, pp. 66–80, Jul. 2013. DOI: 10.1016/j.apenergy.2013.02.047.

[5] S. V. Garimella, T. Persoons, J. A. Weibel, and V. Gektin, "Electronics thermal management in information and communications technologies: Challenges and future directions," *IEEE Transactions on Components, Packaging and Manufacturing Technology*, vol. 7, no. 8, pp. 1191–1205, Aug. 2017. DOI: 10.1109/TCPMT.2016.2603600.

[6] International Energy Agency - IEA, "Electricity 2024 - Analysis and Forecast to 2026," pp. 1–170, 2024. https://www.iea.org/reports/electricity-2024, (Accessed 2024-12-01).

[7] Goldman Sachs Research, "GS SUSTAIN: Generational Growth — AI/data centers' global power surge and the sustainability impact," Apr. 2024. https://www.goldmansachs.com/insights/goldman-sachs-research/gs-sustain-generational-growth-ai-data-centers-global-power, (Accessed 2024-10-05).

[8] Industrial Development Agency (IDA) Ireland, "Annual report & accounts 2023," Jul. 2024. https://www.epa.ie/publications/corporate/governance/epa-annual-report--accounts-2023.php, (Accessed 2024-10-04).

[9] EirGrid, "Ireland capacity outlook 2022-2031," p. 82, 2022. https://cms.eirgrid.ie/sites/default/files/publications/EirGrid_SONI_Ireland_Capacity_Outlook_2022-2031.pdf, (Accessed 2023-11-09).

[10] G. Deegan, "Plan for Ennis data centre gets green light," Apr. 2024. https://www.irishtimes.com/business/2024/04/09/ennis-data-centre-plan-given-go-ahead/, (Accessed 2024-12-04).

[11] J. Cruickshank, L. V. Yongsheng, A. Röll, and V. Haug, *IBM power system E980: Technical overview and introduction*, Sep. 2018. https://www.redbooks.ibm.com/abstracts/redp5510.html, (Accessed 2024-12-04).

[12] Intel, *Intel® server board S2600BP and intel® compute module HNS2600BP product family technical product specification*, Jul. 2022. https://www.intel.com/content/www/us/en/support/articles/000024315/server-products.html, (Accessed 2024-12-04).

[13] The U.S. Department of Energy, "DOE announces $40 million for more efficient cooling for data centers," May 2023. https://www.energy.gov/articles/doe-announces-40-million-more-efficient-cooling-data-centers, (Accessed 2024-10-05).

[14] W. Huang and Y. Wang, "An optimal speed control scheme supported by media servers for low-power multimedia applications," *Multimedia Systems*, vol. 15, no. 2, pp. 113–124, 2009. DOI: 10.1007/s00530-009-0153-5.

[15] M. Iyengar, M. David, P. Parida, V. Kamath, B. Kochuparambil, D. Graybill, M. Schultz, M. Gaynes, R. Simons, R. Schmidt, and T. Chainer, "Server liquid cooling with chiller-less data center design to enable significant energy savings," *Annual IEEE Semiconductor Thermal Measurement and Management Symposium*, vol. 1, pp. 212–223, 2012. DOI: 10.1109/STHERM.2012.6188851.

[16] W. Zhao, S. Wasala, and T. Persoons, "Rapid and accurate analytical model for predicting axial fan performance in electronics cooling," *Electronics Cooling*, Jun. 2023. https://learn.electronics-cooling.com/electronics-cooling-summer-2023/.

[17] The European Parliament and The Council, Directive 2003/10/EC, "On the minimum health and safety requirements regarding the exposure of workers to the risks arising from physical agents (noise)," Online, Feb. 2003. https://eur-lex.europa.eu/legal-content/EN/TXT/?uri=CELEX:02003L0010-20190726.

[18] Occupational Safety and Health Administration (OSHA), "Occupational noise exposure," Online, 1983. https://www.osha.gov/laws-regs/regulations/standardnumber/1910/1910.95, (Accessed 2023-11-27).

[19] National Institute for Occupational Safety and Health (NIOSH), "Criteria for a recommended standard: Occupational noise exposure," Online, p. 2397, 2002. DOI: 10.1121/1.4778162. https://www.cdc.gov/niosh/docs/98-126/pdfs/98-126.pdf.

[20] S. Wasala, Y. Xue, T. Wiegandt, L. Stevens, and T. Persoons, "Aeroacoustic noise prediction from a contra-rotating cooling fan used in data center cooling systems," in *AIAA Paper 2021-2313*. VIRTUAL EVENT: American Institute of Aeronautics and Astronautics, Aug. 2021, pp. AIAA 2021–2313. DOI: 10.2514/6.2021-2313.

[21] C. Bolton, S. Rampazzi, C. Li, A. Kwong, W. Xu, and K. Fu, "Blue Note: How intentional acoustic interference damages availability and integrity in hard disk drives and operating systems," in *2018 IEEE Symposium on Security and Privacy (SP)*. IEEE, may 2018, pp. 1048–1062. DOI: 10.1109/SP.2018.00050.

[22] M. Shahrad, A. Mosenia, L. Song, M. Chiang, D. Wentzlaff, and P. Mittal, "Acoustic denial of service attacks on hard disk drives," *Proceedings of the ACM Conference on Computer and Communications Security*, pp. 34–39, 2018. DOI: 10.1145/3266444.3266448.

[23] W. Zhao, S. Wasala, and T. Persoons, "Towards quieter air-cooling systems: Rotor self-noise prediction for axial cooling fans," in *2022 28th International Workshop on Thermal Investigations of ICs and Systems (THERMINIC)*. Dublin, Ireland: IEEE, Sep. 2022, pp. 1–4. DOI: 10.1109/THERMINIC57263.2022.9950669.

[24] A. Fiscutean, "A loud sound just shut down a bank's data center for 10 hours," 2016. https://www.vice.com/en/article/8q8dqg/a-loud-sound-just-shut-down-a-banks-data-center-for-10-hours, (Accessed 2024-08-30).

[25] P. P. Elke Schneider, "Noise in figures," Online, pp. 1–116, 2005. https://osha.europa.eu/en/publications/report-noise-figures, (Accessed 2022-09-01).

[26] W. Passchier-Vermeer and W. F. Passchier, "Noise exposure and public health." *Environmental Health Perspectives*, vol. 108, no. suppl 1, pp. 123–131, Mar. 2000. DOI: 10.1289/ehp.00108s1123.

[27] S. Wasala, Y. Xue, L. Stevens, T. Wiegandt, and T. Persoons, "Numerical simulations of flow induced noise from a dual rotor cooling fan used in electronic cooling systems," *INTER-NOISE and NOISE-CON Congress and Conference Proceedings*, vol. 263, no. 5, pp. 1308–1319, Aug. 2021. DOI: 10.3397/IN-2021-1809.

[28] S. Wasala, W. Zhao, O. Ogun, L. Stevens, R. Sosseh, J. Kennedy, and T. Persoons, "Acoustic metamaterials for electronics cooling fan noise reduction," *INTER-NOISE and NOISE-CON Congress and Conference Proceedings*, vol. 268, no. 5, pp. 3145–3153, Nov. 2023. DOI: 10.3397/IN_2023_0454.

[29] W. Zhao, S. Wasala, S. Spence, and T. Persoons, "Poster: Thermal management and aeroacoustics of air-cooled electronics enclosures," in *24th Sir Bernard Crossland Symposium*, Dublin, Ireland, Sept. 22–23 2021.

[30] W. Zhao, S. Wasala, and T. Persoons, "Reduced-order aeroacoustic modeling of electronics cooling fans," in *Proceedings of the International Congress on Sound and Vibration*. Society of Acoustics, 2022, pp. 1–8. https://www.proceedings.com/67680.html, (Accessed 2023-09-30).

[31] W. Zhao, S. Wasala, and T. Persoons, "On the fast prediction of the aerodynamic performance of electronics cooling fans considering the effect of tip clearance," *IEEE Transactions on Components, Packaging and Manufacturing Technology*, vol. 13, no. 8, pp. 1139–1146, Aug. 2023. DOI: 10.1109/TCPMT.2023.3293003.

[32] W. Zhao, S. Wasala, and T. Persoons, "Reduced-order model for predicting aerodynamic performance of dual impeller fans in data centre cooling systems," in *2023 29th International Workshop on Thermal Investigations of ICs and Systems (THERMINIC)*. Budapest, Hungary: IEEE, Sep. 2023, pp. 1–6. DOI: 10.1109/THERMINIC60375.2023.10325888.

[33] W. Zhao, S. Wasala, and T. Persoons, "Development and assessment of an inviscid source vortex panel method for low-Reynolds number airfoil cascades," in *AIAA SCITECH 2024 Forum*. Orlando, Florida: American Institute of Aeronautics and Astronautics, 2024. DOI: 10.2514/6.2024-2507.

[34] S. Castegnaro, "Aerodynamic design of low-speed axial-flow fans: A historical overview," *Designs*, vol. 2, no. 3, p. 20, Jun. 2018. DOI: 10.3390/designs2030020.

[35] IBM, "The IBM PC." https://www.ibm.com/history/personal-computer, (Accessed 2024-10-05).

[36] L. Huang, "Characterizing computer cooling fan noise," *The Journal of the Acoustical Society of America*, vol. 114, no. 6, pp. 3189–3200, Dec. 2003. DOI: 10.1121/1.1624074.

[37] S. J. Majumdar and N. Peake, "Noise generation by the interaction between ingested turbulence and a rotating fan," *Journal of Fluid Mechanics*, vol. 359, pp. 181–216, Mar. 1998. DOI: 10.1017/S0022112097008318.

[38] S.-C. Lin and C.-A. Chou, "Blockage effect of axial-flow fans applied on heat sink assembly," *Applied Thermal Engineering*, vol. 24, no. 16, pp. 2375–2389, Nov. 2004. DOI: 10.1016/j.applthermaleng.2004.03.009.

[39] R. E. Longhouse, "Noise mechanism separation and design considerations for low tip-speed, axial-flow fans," *Journal of Sound and Vibration*, vol. 48, no. 4, pp. 461–474, Oct. 1976. DOI: 10.1016/0022-460X(76)90550-2.

[40] J. M. Fitzgerald and G. C. Lauchle, "Reduction of discrete frequency noise in small, subsonic axial-flow fans," *The Journal of the Acoustical Society of America*, vol. 76, no. 1, pp. 158–166, Jul. 1984. DOI: 10.1121/1.391112.

[41] M. Hodgson and I. Li, "Experimental study of the noise emission of personal computer cooling fans," *Applied Acoustics*, vol. 67, no. 9, pp. 849–863, Sep. 2006. DOI: 10.1016/j.apacoust.2005.12.007.

[42] T. Carolus, M. Schneider, and H. Reese, "Axial flow fan broad-band noise and prediction," *Journal of Sound and Vibration*, vol. 300, no. 1, pp. 50–70, Feb. 2007. DOI: 10.1016/j.jsv.2006.07.025.

[43] T. Zhu and T. H. Carolus, "Experimental and unsteady numerical investigation of the tip clearance noise of an axial fan," in *ASME 2013 Turbine Blade Tip Symposium*. Hamburg, Germany: American Society of Mechanical Engineers, Sep. 2013, p. V001T04A001. DOI: 10.1115/TBTS2013-2034.

[44] M. Deuse and R. D. Sandberg, "Different noise generation mechanisms of a controlled diffusion aerofoil and their dependence on mach number," *Journal of Sound and Vibration*, vol. 476, p. 115317, Jun. 2020. DOI: 10.1016/j.jsv.2020.115317.

[45] Department of the Environment, Climate and Communications, "Climate action plan 2024," Dec. 2023. https://www.gov.ie/en/publication/79659-climate-action-plan-2024/, (Accessed 2024-12-04).

[46] United Nations, "The 17 goals | Sustainable development," 2024. https://sdgs.un.org/goals, (Accessed 2024-12-04).

[47] W. T. W. Cory, *Fans & Ventilation: A Practical Guide*. Amsterdam ; Boston: Elsevier in association with Roles & Assoc, 2005.

[48] T. Carolus, *Fans: Aerodynamic design - noise reduction - optimization*. Wiesbaden: Springer Fachmedien Wiesbaden, 2022. DOI: 10.1007/978-3-658-37959-9.

[49] T. D. Rossing, *Springer handbook of acoustics*. New York: Springer, 2014. DOI: 10.1007/978-1-4939-0755-7.

[50] R. Amiet, "Noise due to turbulent flow past a trailing edge," *Journal of Sound and Vibration*, vol. 47, no. 3, pp. 387–393, Aug. 1976. DOI: 10.1016/0022-460X(76)90948-2.

[51] M. Roger and S. Moreau, "Back-scattering correction and further extensions of Amiet's trailing-edge noise model. Part 1: Theory," *Journal of Sound and Vibration*, vol. 286, no. 3, pp. 477–506, Sep. 2005. DOI: 10.1016/j.jsv.2004.10.054.

[52] T. F. Brooks, D. S. Pope, and M. A. Marcolini, "Airfoil self-noise and prediction," Online, NASA Langley Research Center, VA, United States, Tech. Rep. NASA-RP-1218, 1989. https://ntrs.nasa.gov/citations/19890016302.

[53] S. Lee, L. Ayton, F. Bertagnolio, S. Moreau, T. P. Chong, and P. Joseph, "Turbulent boundary layer trailing-edge noise: Theory, computation, experiment, and application," *Progress in Aerospace Sciences*, vol. 126, no. May, p. 100737, October 2021. DOI: 10.1016/j.paerosci.2021.100737.

[54] S. Moreau and M. Sanjose, "Sub-harmonic broadband humps and tip noise in low-speed ring fans," *The Journal of the Acoustical Society of America*, vol. 139, no. 1, pp. 118–127, Jan. 2016. DOI: 10.1121/1.4939493.

[55] D. Casalino, E. Grande, G. Romani, D. Ragni, and F. Avallone, "Definition of a benchmark for low Reynolds number propeller aeroacoustics," *Aerospace Science and Technology*, vol. 113, p. 106707, Jun. 2021. DOI: 10.1016/j.ast.2021.106707.

[56] C. L. Morfey, "Rotating blades and aerodynamic sound," *Journal of Sound and Vibration*, vol. 28, no. 3, pp. 587–617, Jun. 1973. DOI: 10.1016/S0022-460X(73)80041-0.

[57] B. D. Mugridge, "Axial flow fan noise caused by inlet flow distortion," *Journal of Sound and Vibration*, vol. 40, no. 4, pp. 497–512, Jun. 1975. DOI: 10.1016/S0022-460X(75)80059-9.

[58] L. Huang and J. Wang, "Acoustic analysis of a computer cooling fan," *The Journal of the Acoustical Society of America*, vol. 118, no. 4, pp. 2190–2200, Oct. 2005. DOI: 10.1121/1.2010367.

[59] R. Amiet, "Acoustic radiation from an airfoil in a turbulent stream," *Journal of Sound and Vibration*, vol. 41, no. 4, pp. 407–420, Aug. 1975. DOI: 10.1016/S0022-460X(75)80105-2.

[60] S. Moreau and M. Roger, "Competing broadband noise mechanisms in low-speed axial fans," *AIAA Journal*, vol. 45, no. 1, pp. 48–57, Jan. 2007. DOI: 10.2514/1.14583.

[61] W. K. Blake, "Noise from rotating machinery," in *Mechanics of Flow-Induced Sound and Vibration, Volume 2*. Elsevier, 2017, pp. 505–658. DOI: 10.1016/B978-0-12-809274-3.00006-4.

[62] S. Wang, Y. Zhou, M. M. Alam, and H. Yang, "Turbulent intensity and Reynolds number effects on an airfoil at low Reynolds numbers," *Physics of Fluids*, vol. 26, no. 11, p. 115107, Nov. 2014. DOI: 10.1063/1.4901969.

[63] M. Howe, "A review of the theory of trailing edge noise," *Journal of Sound and Vibration*, vol. 61, no. 3, pp. 437–465, Dec. 1978. DOI: 10.1016/0022-460X(78)90391-7.

[64] C. J. Doolan and D. J. Moreau, "A review of airfoil trailing ddge noise with some implications for wind turbines," *International Journal of Aeroacoustics*, vol. 14, no. 5-6, pp. 811–832, Oct. 2015. DOI: 10.1260/1475-472X.14.5-6.811.

[65] R. D. Sandberg, L. E. Jones, N. D. Sandham, and P. F. Joseph, "Direct numerical simulations of tonal noise generated by laminar flow past airfoils," *Journal of Sound and Vibration*, vol. 320, no. 4-5, pp. 838–858, 2009. DOI: 10.1016/j.jsv.2008.09.003.

[66] L. E. Jones and R. D. Sandberg, "Numerical analysis of tonal airfoil self-noise and acoustic feedback-loops," *Journal of Sound and Vibration*, vol. 330, no. 25, pp. 6137–6152, 2011. DOI: 10.1016/j.jsv.2011.07.009.

[67] A. Garcia-Sagrado and T. Hynes, "Wall-pressure sources near an airfoil trailing ddge under separated laminar boundary layers," *AIAA Journal*, vol. 49, no. 9, pp. 1841–1856, Sep. 2011. DOI: 10.2514/1.J050477.

[68] M. R. Fink and D. A. Bailey, "Airframe noise reduction studies, wheat beer and clean-airframe noise investigation," Langley Research Center, Tech. Rep. NASA-CR-159311, Apr. 1980. https://ntrs.nasa.gov/citations/19800024667.

[69] A. R. George, F. E. Najjar, and Y. N. Kim, "Noise due to tip vortex formation on lifting rotors," in *AIAA Paper*, 1980. DOI: 10.2514/6.1980-1010.

[70] L. Gutin, "On the sound field of a rotating propeller," Online, National Advisory Committee for Aeronautics, VA, USA, Tech. Rep. NACA-TM-1195, 1936. https://ntrs.nasa.gov/citations/20030068996.

[71] S. Moreau and M. Roger, "Advanced noise modeling for future propulsion systems," *International Journal of Aeroacoustics*, vol. 17, no. 6-8, pp. 576–599, 2018. DOI: 10.1177/1475472X18789005.

[72] N. Peake and A. B. Parry, "Modern challenges facing turbomachinery aeroacoustics," *Annual Review of Fluid Mechanics*, vol. 44, no. 1, pp. 227–248, Jan. 2012. DOI: 10.1146/annurev-fluid-120710-101231.

[73] F. J. Krömer, "Sound emission of low-pressure axial fans under distorted inflow conditions," Ph.D. dissertation, University of Erlangen-Nuremberg, Bavaria, Germany, 2018. DOI: 10.25593/978-3-96147-089-1. https://open.fau.de/handle/openfau/9601.

[74] J. Tian, Z. Sun, P. Chai, and H. Ouyang, "Study on the influence of inlet asymmetry on aerodynamic noise of cooling fan," *Journal of Engineering for Gas Turbines and Power*, vol. 142, no. 12, p. 121014, Dec. 2020. DOI: 10.1115/1.4048449.

[75] Z. Sun, J. Tian, G. Liśkiewicz, Z. Du, and H. Ouyang, "Noise reduction analysis of electronic device cooling fan with duct and its application under variable working conditions," *Journal of Engineering for Gas Turbines and Power*, vol. 144, no. 2, pp. 1–9, 2022. DOI: 10.1115/1.4052429.

[76] Z. Sun, J. Tian, Y. Zheng, X. Zhu, Z. Du, and H. Ouyang, "Design of sinusoidal-shaped inlet duct for acoustic mode modulation noise reduction of cooling fan," *Applied Acoustics*, vol. 216, p. 109741, Jan. 2024. DOI: 10.1016/j.apacoust.2023.109741.

[77] J. E. Ffowcs Williams and L. H. Hall, "Aerodynamic sound generation by turbulent flow in the vicinity of a scattering half plane," *Journal of Fluid Mechanics*, vol. 40, no. 4, pp. 657–670, 1970. DOI: 10.1017/S0022112070000368.

[78] S. E. Wright, "The acoustic spectrum of axial flow machines," *Journal of Sound and Vibration*, vol. 45, no. 2, pp. 165–223, 1976. DOI: 10.1016/0022-460X(76)90596-4.

[79] S. Moreau, "Turbomachinery noise predictions: Present and future," *Acoustics*, vol. 1, no. 1, pp. 92–116, Mar. 2019. DOI: 10.3390/acoustics1010008.

[80] J. H. Ferziger, M. Perić, and R. L. Street, *Computational methods for fluid dynamics*. Cham: Springer International Publishing, 2020, vol. 5. DOI: 10.1007/978-3-319-99693-6.

[81] A. Zarri, J. Christophe, S. Moreau, and C. Schram, "Influence of swept blades on low-order acoustic prediction for axial fans," *Acoustics*, vol. 2, no. 4, pp. 812–832, 2020. DOI: 10.3390/acoustics2040046.

[82] F. M. White, *Fluid mechanics*, 8th ed. New York, NY: McGraw-Hill Education, 2016.

[83] P. Sagaut, Ed., *Large eddy simulation for incompressible flows: An introduction*, 3rd ed., ser. Scientific Computation. Berlin: Springer, 2006. DOI: 10.1007/b137536.

[84] C. Hirsch, *Numerical computation of internal and external flows: fundamentals of computational fluid dynamics*, 2nd ed. Oxford ; Burlington, MA: Elsevier/Butterworth-Heinemann, 2007.

[85] J. Al-Am, "Broadband noise predictions of a fan stage using large eddy simulations," Ph.D. dissertation, Ecole Centrale de Lyon, Dec. 2022. https://theses.hal.science/tel-03986348.

[86] S. B. Pope, *Turbulent flows*, 1st ed. Cambridge: Cambridge Univ. Press, 2015.

[87] H. Choi and P. Moin, "Grid-point requirements for large eddy simulation: Chapman's estimates revisited," *Physics of Fluids*, vol. 24, no. 1, p. 011702, Jan. 2012. DOI: 10.1063/1.3676783.

[88] J. Smagorinsky, "General circulation experiments with the primitive equations: I. the basic experiment*," *Monthly Weather Review*, vol. 91, no. 3, pp. 99–164, Mar. 1963. DOI: 10.1175/1520-0493(1963)091<0099:GCEWTP>2.3.CO;2.

[89] F. Nicoud and F. Ducros, "Subgrid-scale stress modelling based on the square of the velocity gradient tensor," *Flow, Turbulence and Combustion*, vol. 62, no. 3, pp. 183–200, Sep. 1999. DOI: 10.1023/A:1009995426001.

[90] ANSYS, Inc, "Ansys Fluent theory guide," 2024. https://www.ansys.com/products/fluids/ansys-fluent.

[91] J. H. Ferziger, M. Perić, and R. L. Street, *Computational methods for fluid dynamics*. Cham: Springer International Publishing, 2020. DOI: 10.1007/978-3-319-99693-6.

[92] J. Katz and A. Plotkin, *Low speed aerodynamics*, 2nd ed., ser. Cambridge aerospace series. Cambridge, UK; New York: Cambridge University Press, 2001, no. 13.

[93] J. D. Anderson, *Fundamentals of aerodynamics*, 5th ed., ser. Anderson series. New York: McGraw-Hill, 2011.

[94] B. Thwaites, "Approximate calculation of the laminar boundary layer," *Aeronautical Quarterly*, vol. 1, no. 3, pp. 245–280, Nov. 1949. DOI: 10.1017/S0001925900000184.

[95] M. R. Head, "Entrainment in the turbulent boundary layer," Aeronautical Research Council, Tech. Rep., 1958. https://web.stanford.edu/~cantwell/AA200_Course_Material/AA200_References/Head_R&M_3152.pdf.

[96] J. van Ingen, "The en method for transition prediction. historical review of work at tu delft," in *38th Fluid Dynamics Conference and Exhibit*. Seattle, Washington: American Institute of Aeronautics and Astronautics, Jun. 2008. DOI: 10.2514/6.2008-3830.

[97] M. Drela, "XFOIL: An analysis and design system for low Reynolds number airfoils," in *Low reynolds number aerodynamics*, T. J. Mueller, Ed., vol. 54, no. 54. Berlin, Heidelberg: Springer Berlin Heidelberg, 1989, pp. 1–12. DOI: 10.1007/978-3-642-84010-4_1.

[98] M. Drela, *MISES implementation of modified Abu-Ghannam/Shaw transition criterion*, 1995. https://web.mit.edu/drela/Public/web/mises/.

[99] E. J. Alvarez, A. Schenk, T. Critchfield, and A. Ning, "Rotor-on-rotor aeroacoustic interactions of multirotor in hover," *Vertical Flight Society's 76th Annual Forum and Technology Display*, 2020.

[100] J. G. Leishman, *Principles of helicopter aerodynamics*, 2nd ed. Cambridge University Press, 2016.

[101] R. D. Viterna, L. A., Corrigan, "Fixed pitch rotor performance of large horizontal axis wind turbines," in *NASA Lewis Research Center: Energy Production and Conversion Workshop*. NASA Lewis Research Center Cleveland, OH, United States, 1982.

[102] S. Allsop, C. Peyrard, P. R. Thies, E. Boulougouris, and G. P. Harrison, "Hydrodynamic analysis of a ducted, open centre tidal stream turbine using blade element momentum theory," *Ocean Engineering*, vol. 141, no. 6, pp. 531–542, 2017. DOI: 10.1016/j.oceaneng.2017.06.040.

[103] M. J. Lighthill, "On sound generated aerodynamically II. Turbulence as a source of sound," *Proceedings of the Royal Society of London. Series A. Mathematical and Physical Sciences*, vol. 222, no. 1148, pp. 1–32, Feb. 1954. DOI: 10.1098/rspa.1954.0049.

[104] J. E. Ffowcs Williams and D. L. Hawkings, "Sound generation by turbulence and surfaces in arbitrary motion," *Philosophical Transactions of the Royal Society of London. Series A, Mathematical and Physical Sciences*, vol. 264, no. 1151, pp. 321–342, May 1969. DOI: 10.1098/rsta.1969.0031.

[105] F. Farassat, "Linear acoustic formulas for calculation of rotating blade noise," *AIAA Journal*, vol. 19, no. 9, pp. 1122–1130, 1981. DOI: 10.2514/3.60051.

[106] F. Farassat, "Derivation of Formulations 1 and 1A of Farassat," Online, NASA Langley Research Center Hampton, VA, United States, Tech. Rep., Mar. 2007. https://ntrs.nasa.gov/citations/20070010579.

[107] K. S. Brentner and F. Farassat, "Modeling aerodynamically generated sound of helicopter rotors," *Progress in Aerospace Sciences*, vol. 39, no. 2-3, pp. 83–120, 2003. DOI: 10.1016/S0376-0421(02)00068-4.

[108] B. A. Goldman, "Modifications to PSU-WOPWOP for enhanced noise prediction capabilities," Master's thesis, Penn State University, 2013. https://etda.libraries.psu.edu/catalog/16434.

[109] C. C. Hennes, L. V. Lopes, J. Shirey, R. Cheng, J. Erwin, S. Lee, B. A. Goldman, M. Botre, D. R. Zachos, Z. Feng, T. Gan, R. Rau, E. Greenwood, and K. S. Brentner, *PSU-WOPWOP 3.4.4 User's Guide*, 2021. https://aeroacoustics.psu.edu/software/, (Accessed 2023-08-30).

[110] S. Moreau, "The third golden age of aeroacoustics," *Physics of Fluids*, vol. 34, no. 3, p. 031301, Mar. 2022. DOI: 10.1063/5.0084060.

[111] M. D. E. Gennaro and H. Kuehnelt, "Broadband noise modelling and prediction for axial fans," in *Fan 2012*, no. Apr. 2012, 2012, pp. 18–20.

[112] N. S. Zawodny, "Acoustic characterization and prediction of representative, small-scale rotary-wing unmanned aircraft system components," in *American Helicopter Society (AHS) Annual Forum*, vol. 2016000905. NASA Langley Research Center, 2016.

[113] G. M. Corcos, "The structure of the turbulent pressure field in boundary-layer flows," *Journal of Fluid Mechanics*, vol. 18, no. 03, p. 353, Mar 1964. DOI: 10.1017/S002211206400026X.

[114] Y. Rozenberg, M. Roger, and S. Moreau, "Rotating blade trailing-edge noise: Experimental validation of analytical model," *AIAA Journal*, vol. 48, no. 5, pp. 951–962, 2010. DOI: 10.2514/1.43840.

[115] S. Moreau and M. Roger, "Back-scattering correction and further extensions of Amiet's trailing-edge noise model. Part II: Application," *Journal of Sound and Vibration*, vol. 323, no. 1-2, pp. 397–425, 2009. DOI: 10.1016/j.jsv.2008.11.051.

[116] S. Li and S. Lee, "UCD-QuietFly: A new program to predict multi-rotor eVTOL broadband noise," in *International Powered Lift Conference 2020, IPLC 2020, Held at Transformative Vertical Flight 2020*, no. Jan., 2020, pp. 12–23.

[117] M. Sanjosé and S. Moreau, "Fast and accurate analytical modeling of broadband noise for a low-speed fan," *The Journal of the Acoustical Society of America*, vol. 143, no. 5, pp. 3103–3113, 2018. DOI: 10.1121/1.5038265.

[118] M. Goody, "Empirical spectral model of surface pressure fluctuations," *AIAA Journal*, vol. 42, no. 9, pp. 1788–1794, September 2004. DOI: 10.2514/1.9433.

[119] Y. Rozenberg, G. Robert, and S. Moreau, "Wall-pressure spectral model including the adverse pressure gradient effects," *AIAA Journal*, vol. 50, no. 10, pp. 2168–2179, 2012. DOI: 10.2514/1.J051500.

[120] M. Kamruzzaman, D. Bekiropoulos, T. Lutz, W. Würz, and E. Krämer, "A semi-empirical surface pressure spectrum model for airfoil trailing-edge noise prediction," *International Journal of Aeroacoustics*, vol. 14, no. 5-6, pp. 833–882, October 2015. DOI: 10.1260/1475-472X.14.5-6.833.

[121] R. M. Catlett, J. M. Anderson, J. B. Forest, and D. O. Stewart, "Empirical modeling of pressure spectra in adverse pressure gradient turbulent boundary layers," *AIAA Journal*, vol. 54, no. 2, pp. 569–587, 2016. DOI: 10.2514/1.J054375.

[122] N. Hu and M. Herr, "Characteristics of wall pressure fluctuations for a flat plate turbulent boundary layer with pressure gradients," in *22nd AIAA/CEAS Aeroacoustics Conference*. Reston, Virginia: AIAA Paper 2016-2749, May 2016, p. 2749. DOI: 10.2514/6.2016-2749.

[123] S. Lee, "Empirical wall-pressure spectral modeling for zero and adverse pressure gradient flows," *AIAA Journal*, vol. 56, no. 5, pp. 1818–1829, Sep. 2018. DOI: 10.2514/1.J056528.

[124] Y. F. Hwang, W. K. Bonness, and S. A. Hambric, "Comparison of semi-empirical models for turbulent boundary layer wall pressure spectra," *Journal of Sound and Vibration*, vol. 319, no. 1-2, pp. 199–217, 2009. DOI: 10.1016/j.jsv.2008.06.002.

[125] Y. C. Küçükosman, J. Christophe, and C. Schram, "Trailing edge noise prediction based on wall pressure spectrum models for NACA0012 airfoil," *Journal of Wind Engineering and Industrial Aerodynamics*, vol. 175, pp. 305–316, Apr 2018. DOI: 10.1016/j.jweia.2018.01.030.

[126] S. Li and S. Lee, "Prediction of rotorcraft broadband trailing-edge noise and parameter sensitivity study," *The Vertical Flight Society - Forum 75: The Future of Vertical Flight - Proceedings of the 75th Annual Forum and Technology Display*, 2019. DOI: 10.4050/jahs.65.042006.

[127] T. von Kármán, "Progress in the statistical theory of turbulence*," *Proceedings of the National Academy of Sciences*, vol. 34, no. 11, pp. 530–539, Nov. 1948. DOI: 10.1073/pnas.34.11.530.

[128] H. W. Liepmann, J. Laufer, and K. Liepmann, "On the spectrum of isotropic turbulence," California Institute of Technology, Tech. Rep. NACA-TN-2473, Nov. 1951. https://ntrs.nasa.gov/citations/19930083180.

[129] M. V. Lowson, "Theoretical analysis of compressor noise," *The Journal of the Acoustical Society of America*, vol. 47, no. 1B, pp. 371–385, Jan. 1970. DOI: 10.1121/1.1911508.

[130] J. Wang, L. Huang, and L. Cheng, "A study of active tonal noise control for a small axial flow fan," *The Journal of the Acoustical Society of America*, vol. 117, no. 2, pp. 734–743, Feb. 2005. DOI: 10.1121/1.1848072.

[131] J. M. Tyler and T. G. Sofrin, "Axial flow compressor noise studies," in *Pre-1964 SAE Technical Papers*, vol. 70, Jan. 1962, p. 620532. DOI: 10.4271/620532.

[132] R. O'Mara, "Characterising flow induced noise from high speed fans in data centres," Master's thesis, Trinity College Dublin, 2021.

[133] S. Schoder, C. Junger, and M. Kaltenbacher, "Computational aeroacoustics of the EAA benchmark case of an axial fan," *Acta Acustica*, vol. 4, no. 5, p. 22, 2020. DOI: 10.1051/aacus/2020021.

[134] F. Pérot, M. S. Kim, S. Moreau, M. Henner, and D. Neal, "Direct aeroacoustics prediction of a low speed axial fan," *16th AIAA/CEAS Aeroacoustics Conference (31st AIAA Aeroacoustics Conference)*, pp. 1–15, 2010. DOI: 10.2514/6.2010-3887.

[135] S. C. Yen and F. K. T. Lin, "Exit flow field and performance of axial flow fans," *Journal of Fluids Engineering*, vol. 128, no. 2, pp. 332–340, Mar. 2006. DOI: 10.1115/1.2169809.

[136] C. Zhang, L. Ji, L. Zhou, and S. Sun, "Effect of blended blade tip and winglet on aerodynamic and aeroacoustic performances of a diagonal fan," *Aerospace Science and Technology*, vol. 98, p. 105688, Mar. 2020. DOI: 10.1016/j.ast.2020.105688.

[137] L. Diao, F. Ge, Y. Liu, L. Yang, Y. Liu, and Q. Huang, "Effect of tip winglet position on tip flow and noise of axial flow fan," *Heliyon*, vol. 9, no. 8, p. e18483, Aug. 2023. DOI: 10.1016/j.heliyon.2023.e18483.

[138] A. Aktürk and C. Camci, "Axial flow fan tip leakage flow control using tip platform extensions," *Journal of Fluids Engineering*, vol. 132, no. 5, p. 051109, May 2010. DOI: 10.1115/1.4001540.

[139] S. Han, J. Zhong, H. Lu, X. Kan, and L. Yang, "Effect of winglet geometry arrangement and incidence on tip clearance control in a compressor cascade," *Journal of Thermal Science*, vol. 23, no. 4, pp. 381–390, Aug. 2014. DOI: 10.1007/s11630-014-0721-7.

[140] A. Corsini, G. Delibra, and A. G. Sheard, "The application of sinusoidal blade-leading edges in a fan-design methodology to improve stall resistance," *Proceedings of the Institution of Mechanical Engineers, Part A: Journal of Power and Energy*, vol. 228, no. 3, pp. 255–271, May 2014. DOI: 10.1177/0957650913514229.

[141] T. M. Biedermann, T. P. Chong, F. Kameier, and C. O. Paschereit, "Statistical–empirical modeling of airfoil noise subjected to leading-edge serrations," *AIAA Journal*, vol. 55, no. 9, pp. 3128–3142, Sep. 2017. DOI: 10.2514/1.J055633.

[142] F. Krömer and S. Becker, "Experimental investigation of the sound reduction by leading edge serrations on a flat-plate axial fan," in *2018 AIAA/CEAS Aeroacoustics Conference*. Atlanta, Georgia: American Institute of Aeronautics and Astronautics, Jun. 2018. DOI: 10.2514/6.2018-2955.

[143] R. Arina, R. Della Ratta Rinaldi, A. Iob, and D. Torzo, "Numerical study of self-noise produced by an airfoil with trailing-edge serrations," in *18th AIAA/CEAS Aeroacoustics Conference (33rd AIAA Aeroacoustics Conference)*, no. June. Reston, Virigina: American Institute of Aeronautics and Astronautics, June 2012, pp. 4–6. DOI: 10.2514/6.2012-2184.

[144] R. D. Sandberg and L. E. Jones, "Direct numerical simulations of low Reynolds number flow over airfoils with trailing-edge serrations," *Journal of Sound and Vibration*, vol. 330, no. 16, pp. 3818–3831, 2011. DOI: 10.1016/j.jsv.2011.02.005.

[145] L. E. Jones and R. D. Sandberg, "Acoustic and hydrodynamic analysis of the flow around an aerofoil with trailing-edge serrations," *Journal of Fluid Mechanics*, vol. 706, pp. 295–322, 2012. DOI: 10.1017/jfm.2012.254.

[146] T. Geyer, E. Sarradj, J. Giesler, and M. Hobracht, "Experimental assessment of the noise generated at the leading edge of porous airfoils using microphone array techniques," in *17th AIAA/CEAS Aeroacoustics Conference (32nd AIAA Aeroacoustics Conference)*. Portland, Oregon: American Institute of Aeronautics and Astronautics, Jun. 2011. DOI: 10.2514/6.2011-2713.

[147] T. F. Geyer and E. Sarradj, "Trailing edge noise of partially porous airfoils," in *20th AIAA/CEAS Aeroacoustics Conference*. Atlanta, GA: American Institute of Aeronautics and Astronautics, Jun. 2014. DOI: 10.2514/6.2014-3039.

[148] A. Rubio Carpio, R. Merino Martínez, F. Avallone, D. Ragni, M. Snellen, and S. Van Der Zwaag, "Experimental characterization of the turbulent boundary layer over a porous trailing edge for noise abatement," *Journal of Sound and Vibration*, vol. 443, pp. 537–558, Mar. 2019. DOI: 10.1016/j.jsv.2018.12.010.

[149] C. Teruna, F. Manegar, F. Avallone, D. Ragni, D. Casalino, and T. Carolus, "Noise reduction mechanisms of an open-cell metal-foam trailing edge," *Journal of Fluid Mechanics*, vol. 898, 2020. DOI: 10.1017/jfm.2020.363.

[150] M. Zhang and T. P. Chong, "Experimental investigation of the impact of porous parameters on trailing-edge noise," *Journal of Sound and Vibration*, vol. 489, p. 115694, Dec. 2020. DOI: 10.1016/j.jsv.2020.115694.

[151] R. H. Liebeck, "Design of subsonic airfoils for high lift," *Journal of Aircraft*, vol. 15, no. 9, pp. 547–561, Sep. 1978. DOI: 10.2514/3.58406.

[152] C. X. Li, C. Zhang, R. X. Zhang, and X. M. Ye, "Effect of gurney flap on performance and aeroacoustics of variable-pitch axial fans," *AIAA Journal*, vol. 58, no. 6, pp. 2546–2559, Jun. 2020. DOI: 10.2514/1.J059192.

[153] M. D. Maughmer and G. Bramesfeld, "Experimental investigation of gurney flaps," *Journal of Aircraft*, vol. 45, no. 6, pp. 2062–2067, Nov. 2008. DOI: 10.2514/1.37050.

[154] A. Bianchini, F. Balduzzi, D. Di Rosa, and G. Ferrara, "On the use of gurney flaps for the aerodynamic performance augmentation of darrieus wind turbines," *Energy Conversion and Management*, vol. 184, pp. 402–415, Mar. 2019. DOI: 10.1016/j.enconman.2019.01.068.

[155] L. Chen, H. Xie, J. Xu, R. Dai, and J. Chen, "Experimental and numerical study on the performance of an axial fan with a gurney flap," *Advances in Mechanical Engineering*, vol. 10, no. 10, p. 1687814018803804, Oct. 2018. DOI: 10.1177/1687814018803804.

[156] N. Liu, C. Jiang, L. Huang, and C. Wang, "Effect of porous casing on small axial-flow fan noise," *Applied Acoustics*, vol. 175, p. 107808, Apr. 2021. DOI: 10.1016/j.apacoust.2020.107808.

[157] B. Dong, D. Xie, F. He, and L. Huang, "Noise attenuation and performance study of a small-sized contra-rotating fan with microperforated casing treatments," *Mechanical Systems and Signal Processing*, vol. 147, no. 6, p. 107086, jan 2021. DOI: 10.1016/j.ymssp.2020.107086.

[158] F. Czwielong, S. Floss, M. Kaltenbacher, and S. Becker, "Influence of a micro-perforated duct absorber on sound emission and performance of axial fans," *Applied Acoustics*, vol. 174, p. 107746, Mar. 2021. DOI: 10.1016/j.apacoust.2020.107746.

[159] S. Lee, "Application of microperforated elements in axial fan noise control and silencer design," Ph.D. dissertation, Purdue University, 2015. https://docs.lib.purdue.edu/open_access_dissertations/1308.

[160] D. You, M. Wang, P. Moin, and R. Mittal, "Effects of tip-gap size on the tip-leakage flow in a turbomachinery cascade," *Physics of Fluids*, vol. 18, no. 10, p. 105102, Oct. 2006. DOI: 10.1063/1.2354544.

[161] D. You, M. Wang, P. Moin, and R. Mittal, "Large-eddy simulation analysis of mechanisms for viscous losses in a turbomachinery tip-clearance flow," *Journal of Fluid Mechanics*, vol. 586, pp. 177–204, Sep. 2007. DOI: 10.1017/S0022112007006842.

[162] R. Longhouse, "Control of tip-vortex noise of axial flow fans by rotating shrouds," *Journal of Sound and Vibration*, vol. 58, no. 2, pp. 201–214, May 1978. DOI: 10.1016/S0022-460X(78)80075-3.

[163] A. Corsini, B. Perugini, F. Rispoli, A. G. Sheard, and I. R. Kinghorn, "Investigation on improved blade tip concept for axial flow fan," in *Volume 6: Turbomachinery, Parts A and B*. Barcelona, Spain: ASMEDC, Jan. 2006, pp. 313–325. DOI: 10.1115/GT2006-90592.

[164] A. Corsini, F. Rispoli, and A. G. Sheard, "Development of improved blade tip endplate concepts for low-noise operation in industrial fans," *Proceedings of the Institution of Mechanical Engineers, Part A: Journal of Power and Energy*, vol. 221, no. 5, pp. 669–681, Jan. 2007. DOI: 10.1243/09576509JPE386.

[165] A. Corsini, F. Rispoli, and A. G. Sheard, "Aerodynamic performance of blade tip end-plates designed for low-noise operation in axial flow fans," *Journal of Fluids Engineering*, vol. 131, no. 8, p. 081101, Aug. 2009. DOI: 10.1115/1.3026723.

[166] S. Bianchi, A. Corsini, and A. Sheard, "A critical review of passive noise control techniques in industrial fans," *Journal of Engineering for Gas Turbines and Power*, vol. 136, no. 4, p. 044001, Apr. 2014. DOI: 10.1115/1.4025837.

[167] J. H. Jung and W.-G. Joo, "Effect of tip clearance, winglets, and shroud height on the tip leakage in axial flow fans," *International Journal of Refrigeration*, vol. 93, pp. 195–204, Sep. 2018. DOI: 10.1016/j.ijrefrig.2018.07.010.

[168] Y. Li, J. Wang, and J. Hua, "Experimental investigations on the effects of divergent trailing edge and gurney flaps on a supercritical airfoil," *Aerospace Science and Technology*, vol. 11, no. 2-3, pp. 91–99, Mar. 2007. DOI: 10.1016/j.ast.2006.01.006.

[169] B. L. Storms and C. S. Jang, "Lift enhancement of an airfoil using a gurney flap and vortex generators," *Journal of Aircraft*, vol. 31, no. 3, pp. 542–547, May 1994. DOI: 10.2514/3.46528.

[170] D. Y. Maa, "Theory and design of microperforated panel sound-absorbing constructions," *Scientia Sinica*, 1975. DOI: 10.1360/YA1975-18-1-55.

[171] S. A. Cummer, J. Christensen, and A. Alù, "Controlling sound with acoustic metamaterials," *Nature Reviews Materials*, vol. 1, no. 16001, pp. 1–13, Feb. 2016. DOI: 10.1038/natrevmats.2016.1.

[172] T. G. Zieliński, K. C. Opiela, P. Pawłowski, N. Dauchez, T. Boutin, J. Kennedy, D. Trimble, H. Rice, B. Van Damme, G. Hannema, R. Wróbel, S. Kim, S. Ghaffari Mosanenzadeh, N. X. Fang, J. Yang, B. Briere De La Hosseraye, M. C. Hornikx, E. Salze, M.-A. Galland, R. Boonen, A. Carvalho De Sousa, E. Deckers, M. Gaborit, and J.-P. Groby, "Reproducibility of sound-absorbing periodic porous materials using additive manufacturing technologies: Round robin study," *Additive Manufacturing*, vol. 36, p. 101564, Dec. 2020. DOI: 10.1016/j.addma.2020.101564.

[173] H. J. Rice, J. Kennedy, P. Göransson, L. Dowling, and D. Trimble, "Design of a Kelvin cell acoustic metamaterial," *Journal of Sound and Vibration*, vol. 472, p. 115167, 2020. DOI: 10.1016/j.jsv.2019.115167.

[174] H. Duan, X. Shen, E. Wang, F. Yang, X. Zhang, and Q. Yin, "Acoustic multilayer helmholtz resonance metamaterials with multiple adjustable absorption peaks," *Applied Physics Letters*, vol. 118, no. 24, p. 241904, Jun. 2021. DOI: 10.1063/5.0054562.

[175] E. Choi and W. Jeon, "Near-perfect sound absorption using hybrid resonance between subwavelength helmholtz resonators with non-uniformly partitioned cavities," *Scientific Reports*, vol. 14, no. 1, p. 3174, Feb. 2024. DOI: 10.1038/s41598-024-53595-y.

[176] J. Wang and G. J. Bennett, "Multi-chamber micro-perforated panel absorbers optimised for high amplitude broadband absorption using a two-point impedance method," *Journal of Sound and Vibration*, vol. 547, p. 117527, Mar. 2023. DOI: 10.1016/j.jsv.2022.117527.

[177] P. Cobo, C. De La Colina, and F. Simón, "On the modelling of microslit panel absorbers," *Applied Acoustics*, vol. 159, p. 107118, Feb. 2020. DOI: 10.1016/j.apacoust.2019.107118.

[178] J. Wang, G. Bennett, T. Humbert, Y. Aurégan, M. Abom, and H. Bodén, "Low-frequency broadband noise absorption of multi-chamber micro-perforated pane absorbers in normal and grazing acoustic incidence," Jun. 2023. DOI: 10.2514/6.2023-3829.

[179] Y. Li and Y. S. Choy, "Broadband and low-frequency sound absorption of compact meta-liner under grazing flow," *Applied Acoustics*, vol. 224, p. 110146, Sep. 2024. DOI: 10.1016/j.apacoust.2024.110146.

[180] F. Bucciarelli and M. Meo, "Broadening sound absorption coefficient with hybrid resonances," *Applied Acoustics*, vol. 160, p. 107136, Mar. 2020. DOI: 10.1016/j.apacoust.2019.107136.

[181] J. Killeen, I. Davis, J. Wang, and G. J. Bennett, "Fan-noise reduction of data centre telecommunications' server racks, with an acoustic metamaterial broadband, low-frequency sound-absorbing liner," *Applied Acoustics*, vol. 203, p. 109229, Feb. 2023. DOI: 10.1016/j.apacoust.2023.109229.

[182] D. Y. Maa, "Microperforated-panel wideband absorbers," *Noise Control Engineering Journal*, vol. 29, no. 3, pp. 77–84, Nov. 1987. DOI: 10.3397/1.2827694.

[183] D. Y. Maa, "Potential of microperforated panel absorber," *The Journal of the Acoustical Society of America*, vol. 104, no. 5, pp. 2861–2866, Nov. 1998. DOI: 10.1121/1.423870.

[184] Q. Li, R. Dong, D. Mao, X. Wang, and Y. Li, "A compact broadband absorber based on helical metasurfaces," *International Journal of Mechanical Sciences*, vol. 254, p. 108425, 2023. DOI: 10.1016/j.ijmecsci.2023.108425.

[185] J. Guo, X. Zhang, Y. Fang, and R. Qu, "An extremely-thin acoustic metasurface for low-frequency sound attenuation with a tunable absorption bandwidth," *International Journal of Mechanical Sciences*, vol. 213, p. 106872, Jan. 2022. DOI: 10.1016/j.ijmecsci.2021.106872.

[186] B. Dong, Y. Zhao, T. Tang, and F. He, "Flow effects of microperforated-panel casing treatments in a contra-rotating fan," *International Journal of Mechanical Sciences*, vol. 239, p. 107879, Feb. 2023. DOI: 10.1016/j.ijmecsci.2022.107879.

[187] S. Allam and M. Åbom, "Fan noise control using microperforated splitter silencers," *Journal of Vibration and Acoustics*, vol. 136, no. 3, p. 031017, Jun. 2014. DOI: 10.1115/1.4027245.

[188] J. Kennedy, L. Flanagan, L. Dowling, G. J. Bennett, H. Rice, and D. Trimble, "The influence of additive manufacturing processes on the performance of a periodic acoustic metamaterial," *International Journal of Polymer Science*, vol. 2019, pp. 1–11, Jul. 2019. DOI: 10.1155/2019/7029143.

[189] D. Y. Maa, "Theory of microslit absorbers," *Acta Acustica*, vol. 25, no. 6, pp. 481–485, 2000. DOI: 10.15949/j.cnki.0371-0025.2000.06.001.

[190] F. Bucciarelli, G. Malfense Fierro, and M. Meo, "A multilayer microperforated panel prototype for broadband sound absorption at low frequencies," *Applied Acoustics*, vol. 146, pp. 134–144, Mar. 2019. DOI: 10.1016/j.apacoust.2018.11.014.

[191] P. Cobo, "Modelling of microperforated panel absorbers with circular and slit hole geometries," *Acoustics*, vol. 3, no. 4, pp. 665–678, Dec. 2021. DOI: 10.3390/acoustics3040042.

[192] B. Luo, W. Chu, and H. Zhang, "Tip leakage flow and aeroacoustics analysis of a low-speed axial fan," *Aerospace Science and Technology*, vol. 98, p. 105700, Mar. 2020. DOI: 10.1016/j.ast.2020.105700.

[193] H. Kobayashi and J. F. Groeneweg, "Effects of inflow distortion profiles on fan tone noise," *AIAA Journal*, vol. 18, no. 8, pp. 899–906, Aug. 1980. DOI: 10.2514/3.50832.

[194] J. Wang and L. Huang, "Quantification and control of noise sources in a small axial-flow fan," *Noise Control Engineering Journal*, vol. 54, no. 1, pp. 27–32, Jan. 2006. DOI: 10.3397/1.2888776.

[195] Z. Sun, J. Tian, T. Zhang, Z. Du, and H. Ouyang, "Cooling fan aerodynamic noise reduction with short inlet duct and its applicability," *International Journal of Refrigeration*, vol. 148, p. S0140700723000142, Jan. 2023. DOI: 10.1016/j.ijrefrig.2023.01.013.

[196] S. M. Alavi Moghadam, S. Loosen, M. Meinke, and W. Schröder, "Reduced-order analysis of the acoustic near field of a ducted axial fan," *International Journal of Heat and Fluid Flow*, vol. 85, p. 108657, Oct. 2020. DOI: 10.1016/j.ijheatfluidflow.2020.108657.

[197] H. Wu, S. Moreau, and R. D. Sandberg, "On the noise generated by a controlled-diffusion aerofoil at $Re_c = 1.5 \times 10^5$," *Journal of Sound and Vibration*, vol. 487, p. 115620, Nov. 2020. DOI: 10.1016/j.jsv.2020.115620.

[198] M. Sanjose, D. Lallier-Daniels, and S. Moreau, "Aeroacoustic analysis of a low-subsonic axial fan," in *ASME Turbo Expo 2015: Turbine Technical Conference and Exposition*. American Society of Mechanical Engineers Digital Collection, Aug. 2015, p. V001T09A015. DOI: 10.1115/GT2015-43737.

[199] P. Tucker, "Computation of unsteady turbomachinery flows: Part 2—LES and hybrids," *Progress in Aerospace Sciences*, vol. 47, no. 7, pp. 546–569, Oct. 2011. DOI: 10.1016/j.paerosci.2011.07.002.

[200] J. Tyacke, N. Vadlamani, W. Trojak, R. Watson, Y. Ma, and P. Tucker, "Turbomachinery simulation challenges and the future," *Progress in Aerospace Sciences*, vol. 110, p. 100554, Oct. 2019. DOI: 10.1016/j.paerosci.2019.100554.

[201] S. Moreau and M. Roger, "Turbomachinery noise review," *International Journal of Turbomachinery, Propulsion and Power*, vol. 9, no. 1, p. 11, Mar. 2024. DOI: 10.3390/ijtpp9010011.

[202] D. Lewis, S. Moreau, M. C. Jacob, and M. Sanjosé, "Large eddy simulation of the ACAT1 fan stage for broadband noise prediction," *Journal of Sound and Vibration*, vol. 565, p. 117888, Oct. 2023. DOI: 10.1016/j.jsv.2023.117888.

[203] H. Lu, Y. Xiao, Z. Liu, Y. Yuan, P. Zhou, and G. Yang, "Investigation on accuracy of numerical simulation of aerodynamic noise of single-stage axial fan," *Physics of Fluids*, vol. 35, no. 11, p. 115136, Nov. 2023. DOI: 10.1063/5.0174731.

[204] R. Koch, M. Sanjosé, and S. Moreau, "Large-eddy simulation of a single airfoil tip-leakage flow," *AIAA Journal*, vol. 59, Jan. 2021. DOI: 10.2514/1.J060057.

[205] K. Yamada, K. Funazaki, and M. Furukawa, "The behavior of tip clearance flow at near-stall condition in a transonic axial compressor rotor," in *Volume 6: Turbo Expo 2007, Parts A and B*. Montreal, Canada: ASMEDC, Jan. 2007, pp. 295–306. DOI: 10.1115/GT2007-27725.

[206] J. Al-Am, V. Clair, A. Giauque, J. Boudet, and F. Gea-Aguilera, "Aeroacoustic analysis of the tip-leakage flow of an ultrahigh bypass ratio fan stage," *Physics of Fluids*, vol. 35, no. 4, p. 047104, Apr. 2023. DOI: 10.1063/5.0146143.

[207] J. Al-Am, V. Clair, A. Giauque, J. Boudet, and F. Gea-Aguilera, "On the effects of a separation bubble on fan noise," *Journal of Sound and Vibration*, vol. 537, Jul. 2022. DOI: 10.1016/j.jsv.2022.117180.

[208] T. Zhu and T. H. Carolus, "Axial fan tip clearance noise: Experiments, Lattice–Boltzmann simulation, and mitigation measures," *Interna-*

tional Journal of Aeroacoustics, vol. 17, no. 1-2, pp. 159–183, Mar. 2018. DOI: 10.1177/1475472X17743627.

[209] J. Hickey, W. Zhao, and T. Persoons, "Experimental and numerical investigation of winglet designs for optimized performance of small axial fans," *Applied Acoustics*, vol. 231, p. 110448, Mar. 2025. DOI: 10.1016/j.apacoust.2024.110448.

[210] W. Zhao, S. Wasala, and T. Persoons, "Large eddy simulation for aerodynamic and aeroacoustic characterization of electronics cooling axial fans under various operating conditions," *Applied Acoustics*, 2024, in Review.

[211] AMCA, "ANSI/AMCA Standard 210-16/ ASHRAE Standard 51-16 - laboratory methods of testing fans for certified aerodynamic performance rating," Aug. 2016.

[212] International Organization for Standardization, "ISO 3744:2010 acoustics determination of sound power levels and sound energy levels of noise sources using sound pressure," Oct. 2010.

[213] S. Zhong, P. Zhou, W. Chen, H. Jiang, H. Wu, and X. Zhang, "An investigation of rotor aeroacoustics with unsteady motions and uncertainty factors," *Journal of Fluid Mechanics*, vol. 956, p. A16, Feb. 2023. DOI: 10.1017/jfm.2022.1097.

[214] R. McKay and M. J. Kingan, "Multirotor unmanned aerial system propeller noise caused by unsteady blade motion," in *25th AIAA/CEAS Aeroacoustics Conference*. Delft, The Netherlands: American Institute of Aeronautics and Astronautics, May 2019, p. 2499. DOI: 10.2514/6.2019-2499.

[215] International Organization for Standardization, "ISO 10302-1:2011 acoustics – measurement of airborne noise emitted and structure - borne vibration induced by small air - moving devices – Part 1 : Airborne noise measurement," 2011.

[216] W. A. McMullan, S. Gao, and C. M. Coats, "Organised large structure in the post-transition mixing layer. Part 2. large-eddy simulation," *Journal of Fluid Mechanics*, vol. 762, pp. 302–343, Jan. 2015. DOI: 10.1017/jfm.2014.660, (Accessed 2024-12-10).

[217] K. J. Forster, S. Diasinos, G. Doig, and T. J. Barber, "Large eddy simulation of transient upstream/downstream vortex interactions," *Journal of Fluid Mechanics*, vol. 862, pp. 227–260, Mar. 2019. DOI: 10.1017/jfm.2018.949, (Accessed 2024-12-10).

[218] I. B. Celik, Z. N. Cehreli, and I. Yavuz, "Index of resolution quality for large eddy simulations," *Journal of Fluids Engineering*, vol. 127, no. 5, pp. 949–958, Sep. 2005. DOI: 10.1115/1.1990201.

[219] M. Piwowarski and D. Jakowski, "Areas of fan research—a review of the literature in terms of improving operating efficiency and reducing noise emissions," *Energies*, vol. 16, no. 3, p. 1042, Jan. 2023. DOI: 10.3390/en16031042.

[220] S. Wasala, W. Zhao, O. Ogun, and L. Stevens, "Fan noise reduction using acoustic metamaterials towards efficient data centers," in *OCP Future Technologies Symposium - Open Compute Project Global Summit*, San Jose CA, USA, Oct. 2022.

[221] F. P. Bleier, *Fan handbook: Selection, application, and design*. New York: McGraw-Hill, 1998.

[222] H. A. Alissa, K. Nemati, U. L. Puvvadi, B. G. Sammakia, K. Schneebeli, M. Seymour, and T. Gregory, "Analysis of airflow imbalances in an open compute high density storage data center," *Applied Thermal Engineering*, vol. 108, pp. 937–950, Sep. 2016. DOI: 10.1016/j.applthermaleng.2016.07.186.

[223] G. V. Shankaran and M. B. Dogruoz, "Validation of an advanced fan model with multiple reference frame approach," in *2010 12th IEEE Intersociety Conference on Thermal and Thermomechanical Phenomena in Electronic Systems (ITherm)*. Las Vegas, NV, USA: IEEE, Jun. 2010, pp. 1–9. DOI: 10.1109/ITHERM.2010.5501404.

[224] J. Stafford and C. Xu, "Cooling in poor air quality environments—Impact of fan operation on particle deposition," *IEEE Transactions on Components, Packaging and Manufacturing Technology*, vol. 11, no. 8, pp. 1206–1213, Aug. 2021. DOI: 10.1109/TCPMT.2021.3084047.

[225] Y. Manaserh, M. Tradat, C. H. Hoang, B. G. Sammakia, A. Ortega, K. Nemati, and M. J. Seymour, "Degradation of fan performance in cooling electronics: Experimental investigation and evaluating numerical techniques," *International Journal of Heat and Mass Transfer*, vol. 174, p. 121291, 2021. DOI: https://doi.org/10.1016/j.ijheatmasstransfer.2021.121291.

[226] S. L. Dixon and C. A. Hall, *Fluid Mechanics and Thermodynamics of Turbomachinery*, 7th ed. Amsterdam ; Boston: Elsevier/Butterworth-Heinemann, 2014.

[227] S. M. Alavi Moghadam, M. Meinke, and W. Schröder, "Analysis of tip-gap size on tip-leakage flow in an axial fan at design and off-design operating conditions," in *13th European Conference on Turbomachinery Fluid dynamics and Thermodynamics*, Lausanne, Switzerland, 2019. DOI: 10.29008/ETC2019-306.

[228] Y.-I. Kim, H.-M. Yang, K.-Y. Lee, and Y.-S. Choi, "Numerical investigation on functional limitations of the anti-stall fin for an axial fan: One-factor analyses," *Sci. Rep.*, vol. 12, no. 1, p. 15240, Sep. 2022. DOI: 10.1038/s41598-022-19530-9.

[229] L. Prandtl, "Applications of modern hydrodynamics to aeronautics," Online, Goettingen University Germany, Tech. Rep. NACA-TR-116, Jan. 1923. DOI: 10.1016/S0016-0032(22)90719-7. https://ntrs.nasa.gov/citations/19930091180.

[230] T. Shigemitsu, J. Fukutomi, and Y. Okabe, "Performance and flow condition of small-sized axial fan and adoption of contra-rotating rotors," *Journal of Thermal Science*, vol. 19, no. 1, pp. 1–6, Feb. 2010. DOI: 10.1007/s11630-010-0001-0.

[231] P. Schimming, "Counter rotating fans — an aircraft propulsion for the future?" *Journal of Thermal Science*, vol. 12, no. 2, pp. 97–103, May 2003. DOI: 10.1007/s11630-003-0049-1.

[232] J. Lewis, A. J. Lofthouse, and A. Bagai, "CFD study of a counter-rotating propeller evtol concept," in *AIAA SCITECH 2023 Forum*. National Harbor, MD & Online: American Institute of Aeronautics and Astronautics, Jan. 2023. DOI: 10.2514/6.2023-0421.

[233] S. Castegnaro, "Fan blade design methods: cascade versus isolated airfoil approach — experimental and numerical comparison," in *Volume 1: Aircraft Engine; Fans and Blowers; Marine*. Seoul, South Korea: American Society of Mechanical Engineers, Jun. 2016, p. V001T09A007. DOI: 10.1115/GT2016-56994.

[234] International Organization for Standardization, "ISO 5167-2:2003 Measurement of fluid flow by means of pressure differential devices inserted in circular cross-section conduits running full — Part 2: Orifice plates," 2003.

[235] T. Zhang and G. N. Barakos, "Review on ducted fans for compound rotorcraft," *The Aeronautical Journal*, vol. 124, no. 1277, pp. 941–974, Jul. 2020. DOI: 10.1017/aer.2019.164.

[236] S. Deng, S. Wang, and Z. Zhang, "Aerodynamic performance assessment of a ducted fan uav for vtol applications," *Aerospace Science and Technology*, vol. 103, p. 105895, Aug. 2020. DOI: 10.1016/j.ast.2020.105895.

[237] J. Winslow, H. Otsuka, B. Govindarajan, and I. Chopra, "Basic understanding of airfoil characteristics at low Reynolds numbers (10^4–10^5)," *Journal of Aircraft*, vol. 55, no. 3, pp. 1050–1061, May 2018. DOI: 10.2514/1.C034415.

[238] H. G. Rhoden, "Effects of Reynolds number on the flow of air through a cascade of compressor blades," Aeronautical Research Council, Tech. Rep. R. & M. No. 2919, 1952. https://reports.aerade.cranfield.ac.uk/handle/1826.2/3481.

[239] D. Pollard and J. P. Gostelow, "Some experiments at low speed on compressor cascades," *Journal of Engineering for Power*, vol. 89, no. 3, pp. 427–436, Jul. 1967. DOI: 10.1115/1.3616709.

[240] T. J. Mueller and J. D. DeLaurier, "Aerodynamics of small vehicles," *Annual Review of Fluid Mechanics*, vol. 35, no. 1, pp. 89–111, Jan. 2003. DOI: 10.1146/annurev.fluid.35.101101.161102.

[241] X. Wang and Z. Xiao, "Transition-based constrained large-eddy simulation method with application to an ultrahigh-lift low-pressure turbine cascade flow," *Journal of Fluid Mechanics*, vol. 941, p. A22, Jun. 2022. DOI: 10.1017/jfm.2022.286.

[242] A. Howell, "Cix. a theory of arbitrary aerofoils in cascade," *The London, Edinburgh, and Dublin Philosophical Magazine and Journal of Science*, vol. 39, no. 299, pp. 913–927, Dec. 1948. DOI: 10.1080/14786444808521701.

[243] B. Thwaites, *Incompressible aerodynamics: An account of the theory and observation of the steady flow of incompressible fluid past aerofoils, wings, and other bodies*. New York: Dover Publications, 1987.

[244] R. I. Lewis, *Vortex element methods for fluid dynamic analysis of engineering systems*, 1st ed. Cambridge University Press, Mar. 1991. DOI: 10.1017/CBO9780511529542.

[245] A. Bhimarasetty and R. N. Govardhan, "A simple method for potential flow simulation of cascades," *Sadhana*, vol. 35, no. 6, pp. 649–657, Dec. 2010. DOI: 10.1007/s12046-010-0046-5.

[246] A. M. Kuethe and C.-Y. Chow, *Foundations of aerodynamics: Bases of aerodynamic design*, 5th ed. New York: J. Wiley, 1998.

[247] P. J. Baddoo and L. J. Ayton, "Potential flow through a cascade of aerofoils: Direct and inverse problems," *Proceedings of the Royal Society A: Mathematical, Physical and Engineering Sciences*, vol. 474, no. 2217, p. 20180065, Sep. 2018. DOI: 10.1098/rspa.2018.0065.

[248] P. J. Baddoo, "Analytic solutions for flows through cascades," Ph.D. dissertation, University of Cambridge, Feb. 2020. DOI: 10.17863/CAM.46697. https://www.repository.cam.ac.uk/handle/1810/299624.

[249] H. Schlichting, "Cascade flow problems," The Advisory Group for Aerospace Research and Development (AGARD), Tech. Rep. 93, Feb. 1957. https://web.iitd.ac.in/~pmvs/courses/mcl822/Schlischting-cascade.pdf.

[250] L. J. Herrig, J. C. Emery, and J. R. Erwin, "Systematic two-dimensional cascade tests of naca 65-series compressor blades at low speeds," Langley Aeronautical Lab, National Advisory Committee for Aeronautics, Langley Field, VA, US, Tech. Rep. NACA-TN-3916, Feb. 1957. https://ntrs.nasa.gov/citations/19930084843.

[251] A. R. Felix and J. C. Emery, "A comparison of typical national gas turbine establishment and naca axial-flow compressor blade sections in cascade at low speed," Langley Aeronautical Laboratory, Tech. Rep. NACA-RM-L53B26a, May 1953. https://ntrs.nasa.gov/citations/19930087847.

[252] J. P. Gostelow, *Cascade aerodynamics*, 1st ed. Oxford; New York: Pergamon Press, 1984.

[253] M. Selig, "UIUC airfoil coordinates database," Online. https://m-selig.ae.illinois.edu/ads/coord_database.html, (Accessed 2023-11-27).

[254] H. Schlichting and A. Das, "Recent research on cascade-flow problems," *Journal of Basic Engineering*, vol. 88, no. 1, pp. 221–228, Mar. 1966. DOI: 10.1115/1.3645808.

[255] N. A. Cumpsty, *Compressor aerodynamics*. Malabar, Florida: Krieger Publishing, 2004.

[256] M. E. Goldstein, *Aeroacoustics*. New York: McGraw-Hill International Book Co, 1976.

[257] L. Botero-Bolívar, O. A. Marino, C. H. Venner, L. D. de Santana, and E. Ferrer, "Low-cost wind turbine aeroacoustic predictions using actuator lines," *Renewable Energy*, vol. 227, p. 120476, Jun. 2024. DOI: 10.1016/j.renene.2024.120476.

[258] A. Zarri, J. Christophe, and C. F. Schram, "Low-order aeroacoustic prediction of low-speed axial fan noise," in *25th AIAA/CEAS Aeroacoustics Conference*. Delft, The Netherlands: American Institute of Aeronautics and Astronautics, May 2019, p. 2760. DOI: 10.2514/6.2019-2760.

[259] G. Grasso, M. Roger, and S. Moreau, "Analytical model of the source and radiation of sound from the trailing edge of a swept airfoil," *Journal of Sound and Vibration*, vol. 493, p. 115838, Feb. 2021. DOI: 10.1016/j.jsv.2020.115838.

[260] B. Lyu and M. Azarpeyvand, "On the noise prediction for serrated leading edges," *Journal of Fluid Mechanics*, vol. 826, pp. 205–234, Sep. 2017. DOI: 10.1017/jfm.2017.429.

[261] S. (Kevin) Li and S. Lee, "Prediction of urban air mobility multirotor vtol broadband noise using ucd-quietfly," *Journal of the American Helicopter Society*, vol. 66, no. 3, pp. 1–13, Jul. 2021. DOI: 10.4050/JAHS.66.032004.

[262] E. J. Alvarez, "Reformulated vortex particle method and meshless large eddy simulation of multirotor aircraft," Ph.D. dissertation, Brigham Young University, Utah, United States, 2022. http://hdl.lib.byu.edu/1877/etd12420.

[263] N. H. Kemp and W. R. Sears, "The unsteady forces due to viscous wakes in turbomachines," *Journal of the Aeronautical Sciences*, vol. 22, no. 7, pp. 478–483, Jul. 1955. DOI: 10.2514/8.3376.

[264] L. M. Mack, "Transition prediction and linear stability theory," *In AGARD Laminar-Turbulent Transition 22 p (SEE N78-14316 05-34*, 1977.

[265] S. Sinayoko, M. Kingan, and A. Agarwal, "Trailing edge noise theory for rotating blades in uniform flow," *Proceedings of the Royal Society A: Mathematical, Physical and Engineering Sciences*, vol. 469, no. 2157, p. 20130065, Sep. 2013. DOI: 10.1098/rspa.2013.0065.

[266] S. Glegg and W. Devenport, *Aeroacoustics of Low Mach Number Flows: Fundamentals, Analysis, and Measurement*. London: Academic Press, 2017.

[267] G. M. Corcos, "Resolution of pressure in turbulence," *The Journal of the Acoustical Society of America*, vol. 35, no. 2, pp. 192–199, Feb. 1963. DOI: 10.1121/1.1918431.

[268] M. Drela and M. B. Giles, "Viscous-inviscid analysis of transonic and low Reynolds number airfoils," *AIAA Journal*, vol. 25, no. 10, pp. 1347–1355, 1987. DOI: 10.2514/3.9789.

[269] F. L. Dos Santos, L. Botero-Bolívar, C. H. Venner, and L. D. De Santana, "Inflow turbulence distortion for airfoil leading-edge noise prediction for large turbulence length scales for zero-mean loading," *The Journal of the Acoustical Society of America*, vol. 153, no. 3, pp. 1811–1822, Mar. 2023. DOI: 10.1121/10.0017458.

[270] B. Dong, C. Jiang, X. Liu, Y. Deng, and L. Huang, "Theoretical characterization and modal directivity investigation of the interaction noise for a small contra-rotating fan," *Mechanical Systems and Signal Processing*, vol. 135, p. 106362, Jan. 2020. DOI: 10.1016/j.ymssp.2019.106362.

[271] G. Ma and P. Sheng, "Acoustic metamaterials: From local resonances to broad horizons," *Science Advances*, vol. 2, no. 2, p. e1501595, Feb. 2016. DOI: 10.1126/sciadv.1501595.

[272] L. Cao, Q. Fu, Y. Si, B. Ding, and J. Yu, "Porous materials for sound absorption," *Composites Communications*, vol. 10, pp. 25–35, Dec. 2018. DOI: 10.1016/j.coco.2018.05.001.

[273] N. Atalla and F. Sgard, "Modeling of perforated plates and screens using rigid frame porous models," *Journal of Sound and Vibration*, vol. 303, no. 1-2, pp. 195–208, Jun. 2007. DOI: 10.1016/j.jsv.2007.01.012.

[274] J. F. Allard and N. Atalla, *Propagation of sound in porous media: Modelling sound absorbing materials*, 1st ed. Wiley, Oct. 2009. DOI: 10.1002/9780470747339.

[275] R. T. Randeberg, "Adjustable slitted panel absorber," *Acta Acustica*, vol. 88, no. 4, pp. 507–512, Jul. 2002. https://www.ingentaconnect.com/content/dav/aaua/2002/00000088/00000004/art00006?crawler=true.

[276] T. E. Vigran, "The acoustic properties of panels with rectangular apertures," *The Journal of the Acoustical Society of America*, vol. 135, no. 5, pp. 2777–2784, May 2014. DOI: 10.1121/1.4871363.

[277] S. Allam and M. Åbom, "A new type of muffler based on microperforated tubes," *Journal of Vibration and Acoustics*, vol. 133, no. 3, p. 031005, Jun. 2011. DOI: 10.1115/1.4002956.

[278] X. Zhang and L. Cheng, "Acoustic silencing in a flow duct with micro-perforated panel liners," *Applied Acoustics*, vol. 167, p. 107382, Oct. 2020. DOI: 10.1016/j.apacoust.2020.107382.

[279] Y. Li and Y. S. Choy, "Acoustic behaviour of micro-perforated panel backed by shallow cavity under fully developed grazing flow," *Journal of Sound and Vibration*, vol. 569, p. 117985, Jan. 2024. DOI: 10.1016/j.jsv.2023.117985.

[280] T. Melling, "The acoustic impendance of perforates at medium and high sound pressure levels," *Journal of Sound and Vibration*, vol. 29, no. 1, pp. 1–65, Jul. 1973. DOI: 10.1016/S0022-460X(73)80125-7.

[281] A. McKay, I. Davis, J. Killeen, and G. J. Bennett, "SeMSA: a compact super absorber optimised for broadband, low-frequency noise attenuation," *Scientific Reports*, vol. 10, no. 1, p. 17967, Oct. 2020. DOI: 10.1038/s41598-020-73933-0.

[282] J. Nocedal and S. J. Wright, *Numerical optimization*, 2nd ed., ser. Springer series in operations research. New York: Springer, 2006.

[283] International Organization for Standardization, "ISO 10534-2:2023 acoustics – determination of acoustic properties in impedance tubes: Two-microphone technique for normal sound absorption coefficient and normal surface impedance," 2023. DOI: 10.3403/30427271.

[284] J. Wang and G. J. Bennett, "Ultra-broadband sound absorption in a compact multi-chamber micro-perforated panel absorber with varying depths," *AIP Advances*, vol. 14, no. 1, p. 015009, Jan. 2024. DOI: 10.1063/5.0187328.

[285] A. Ciochon, J. Kennedy, R. Leiba, L. Flanagan, and M. Culleton, "The impact of surface roughness on an additively manufactured acoustic material: An experimental and numerical investigation," *Journal of Sound and Vibration*, vol. 546, p. 117434, Mar. 2023. DOI: 10.1016/j.jsv.2022.117434.

[286] A. Ciochon and J. Kennedy, "Practical guidance on the additive manufacturing of acoustic materials," *INTER-NOISE and NOISE-CON Congress and Conference Proceedings*, vol. 268, no. 8, pp. 194–205, Nov. 2023. DOI: 10.3397/IN_2023_0046.

[287] F. Wu, Y. Xiao, D. Yu, H. Zhao, Y. Wang, and J. Wen, "Low-frequency sound absorption of hybrid absorber based on micro-perforated panel and coiled-up channels," *Applied Physics Letters*, vol. null, p. null, 2019. DOI: 10.1063/1.5090355.

[288] H. Li, J. Wu, S. Yan, and Q. Mao, "Design and study of broadband sound absorbers with partition based on micro-perforated panel and helmholtz resonator," *Applied Acoustics*, vol. 205, p. 109262, 2023. DOI: 10.1016/j.apacoust.2023.109262.

[289] F. Rafique, J. H. Wu, S. M. A. Naqvi, and F. Ma, "Enhanced wideband low-frequency sound absorption of a single-layer multiple parallel-arranged inhomogeneous microperforated panel absorber," *Acoustics Australia*, vol. 50, no. 1, pp. 49–69, 2022. DOI: 10.1007/s40857-021-00252-3. https://doi.org/10.1007/s40857-021-00252-3.

[290] M. Dreyer, J. Decaix, C. Münch-Alligné, and M. Farhat, "Mind the gap: A new insight into the tip leakage vortex using stereo-piv," *Experiments in Fluids*, vol. 55, no. 11, p. 1849, Nov. 2014. DOI: 10.1007/s00348-014-1849-7.

[291] Y. Wang and W. J. Devenport, "Wake of a compressor cascade with tip gap, Part 2: Effects of endwall motion," *AIAA Journal*, vol. 42, no. 11, pp. 2332–2340, Nov. 2004. DOI: 10.2514/1.5272.

[292] R. Koch, M. Sanjosé, and S. Moreau, "Numerical aeroacoustic analysis of a linear compressor cascade with tip gap," *AIAA Journal*, vol. 60, no. 8, pp. 4840–4854, Aug. 2022. DOI: 10.2514/1.J061380.

[293] J. Grilliat, M. Jacob, R. Camussi, and G. Caputi-Gennaro, "Tip leakage experiment - Part one: Aerodynamic and acoustic measurements," in *13th AIAA/CEAS Aeroacoustics Conference (28th AIAA Aeroacoustics Conference)*, ser. Aeroacoustics Conferences. American Institute of Aeronautics and Astronautics, May 2007. DOI: 10.2514/6.2007-3684.

[294] M. C. Jacob, J. Grilliat, R. Camussi, and G. C. Gennaro, "Aeroacoustic investigation of a single airfoil tip leakage flow," *International Journal of Aeroacoustics*, vol. 9, no. 3, pp. 253–272, May 2010. DOI: 10.1260/1475-472X.9.3.253.

[295] M. C. Jacob, E. Jondeau, and B. Li, "Time-resolved PIV measurements of a tip leakage flow," *International Journal of Aeroacoustics*, vol. 15, no. 6-7, pp. 662–685, Oct. 2016. DOI: 10.1177/1475472X16659384.

[296] I. Saraceno, S. Palleja-Cabre, P. Jaiswal, C. C. Paruchuri, and B. Ganapathisubramani, "On the tip leakage noise generating mechanisms of single-fixed aerofoil," in *28th AIAA/CEAS Aeroacoustics 2022 Conference*. Southampton, UK: American Institute of Aeronautics and Astronautics, Jun. 2022. DOI: 10.2514/6.2022-2881.

[297] I. Saraceno, S. Palleja Cabre, C. C. Paruchuri, and B. Ganapathisubramani, "Influence of non-dimensional parameters on the tip leakage noise," in *AIAA AVIATION 2023 Forum*. San Diego, CA and Online: American Institute of Aeronautics and Astronautics, Jun. 2023. DOI: 10.2514/6.2023-3838.

[298] I. Saraceno, C. Paruchuri, B. Ganapathisubramani, A. Alguacil, S. Moreau, and M. Sanjose, "On the numerical investigation of the tip leakage noise sources of a stationary aerofoil," in *30th AIAA/CEAS Aeroacoustics Conference (2024)*. Rome, Italy: American Institute of Aeronautics and Astronautics, Jun. 2024. DOI: 10.2514/6.2024-3116, (Accessed 2024-12-06).

[299] I. Saraceno, C. Paruchuri, P. Jaiswal, S. Palleja-Cabre, L. Wu, and B. Ganapathisubramani, "On the tip leakage noise mechanisms of a stationary aerofoil," Rochester, NY, Sep. 2024. DOI: 10.2139/ssrn.4956547.

[300] R. Koch, M. Sanjose, and S. Moreau, "Numerical investigation of noise sources in a single airfoil tip-leakage flow," in *25th AIAA/CEAS Aeroacoustics Conference*. Delft, The Netherlands: American Institute of Aeronautics and Astronautics, May 2019. DOI: 10.2514/6.2019-2625.

[301] J. Decaix, G. Balarac, M. Dreyer, M. Farhat, and C. Münch, "RANS and LES computations of the tip-leakage vortex for different gap widths," *Journal of Turbulence*, vol. 16, no. 4, pp. 309–341, Apr. 2015. DOI: 10.1080/14685248.2014.984068.

[302] D. Jackson, "Active fluidic control of a cylinder in a cross-flow using synthetic jet actuation," Ph.D. dissertation, Trinity College Dublin, Dublin, Ireland, 2016. http://www.tara.tcd.ie/handle/2262/82914.

[303] T. Persoons, "Measuring flow velocity and turbulence fields in thermal sciences using particle image velocimetry: A best practice guide," in *Advances in Heat Transfer*. Elsevier, 2022, vol. 54, pp. 37–87. DOI: 10.1016/bs.aiht.2022.07.001.

[304] M. Raffel, C. E. Willert, F. Scarano, C. J. Kähler, S. T. Wereley, and J. Kompenhans, *Particle image velocimetry: A practical guide*. Cham: Springer International Publishing, 2018. DOI: 10.1007/978-3-319-68852-7.

[305] Z. Song, X. Zhang, and C. Eriksson, "Data center energy and cost saving evaluation," *Energy Procedia*, vol. 75, pp. 1255–1260, Aug. 2015. DOI: 10.1016/j.egypro.2015.07.178.

[306] L. Zhu, Y. Jin, Y. Li, Y. Jin, Y. Wang, and L. Zhang, "Numerical and experimental study on aerodynamic performance of small axial flow fan with splitter blades," *Journal of Thermal Science*, vol. 22, no. 4, pp. 333–339, Aug. 2013. DOI: 10.1007/s11630-013-0632-z.

[307] International Organization for Standardization, "ISO 5167-2:2003 measurement of fluid flow by means of pressure differential devices inserted in circular cross-section conduits running full Part 2: Orifice plates," Mar. 2003.

[308] G. Ananda, "UIUC Propeller Database - Vol 1," 2015. https://m-selig.ae.illinois.edu/props/propDB.html, (Accessed 2024-07-28).

[309] M. Herr, R. Ewert, C. Rautmann, M. Kamruzzaman, D. Bekiropoulos, R. Arina, A. Iob, P. Batten, S. Chakravarthy, and F. Bertagnolio, "Broadband trailing-edge noise predictions—Overview of BANC-III results," in *21st AIAA/CEAS Aeroacoustics Conference*, no. June. Reston, Virginia: American Institute of Aeronautics and Astronautics, June 2015, pp. 1–31. DOI: 10.2514/6.2015-2847.

[310] L. Barba and O. Mesnard, "Aero Python: Classical aerodynamics of potential flow using Python," *Journal of Open Source Education*, vol. 2, no. 15, p. 45, May 2019. DOI: 10.21105/jose.00045.

"致广大而尽精微。"
"Reach the broadest horizons while exhausting the subtlest details."

—大约公元前475-221年,《中庸》
Around 475-221 BC, *Doctrine of the Mean*

Appendices

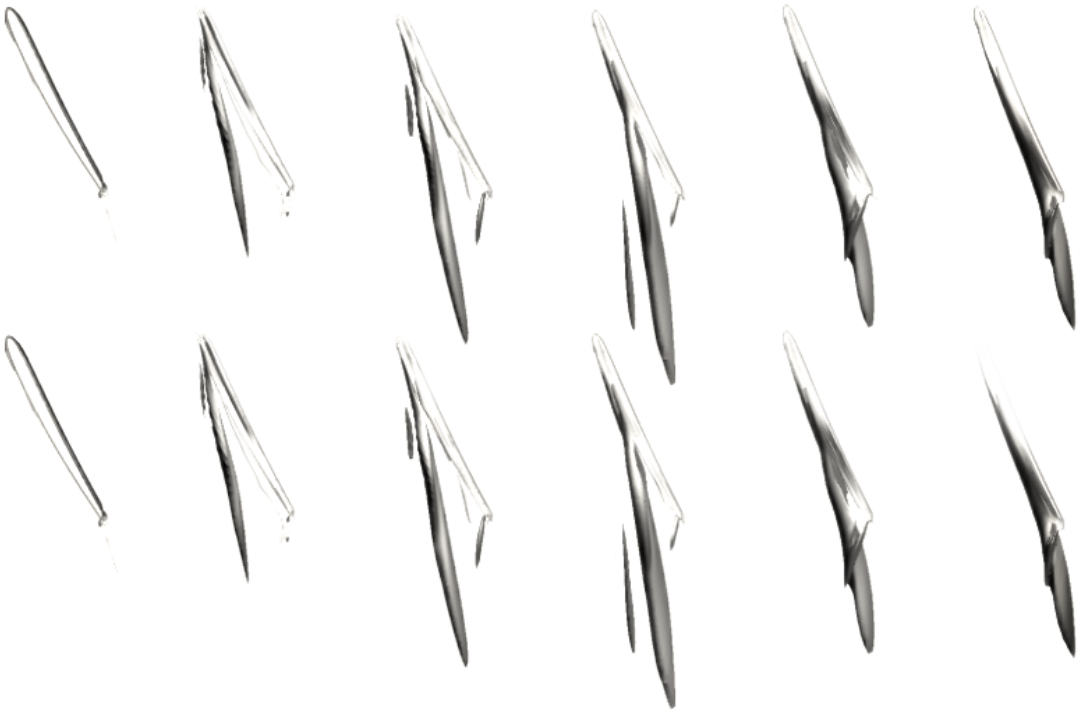

Appendix A

Experimental Measurements and Uncertainty Analysis

A.1 Experimental methodology for aerodynamics

This section describes the experimental aperture, instrumentation, calculations, and uncertainty analysis used to evaluate the performance of electronics cooling axial fans. As discussed in Chapter 2.1, fan performance is measured using pressure-flow rate (P-Q) curves, which require specialized equipment to measure pressure and airflow simultaneously. Uncertainty analysis ensures the accuracy and reliability of the experimental results.

A.1.1 Experimental configurations

The experimental setup includes a wind tunnel facility designed based on two international standards:

- **ANSI/AMCA 210-16 [211]**: This standard outlines laboratory testing methods for aerodynamic performance certification. Configuration 7A, as detailed in the standard, was chosen for the wind tunnel's structural design.

- **ISO 5167-2:2003 [307]**: This standard specifies the use of orifice plates for fluid flow measurement in circular ducts. It was selected for its simplicity compared to the pitot tube methods in Configuration 7A of ANSI/AMCA 210-16 [211]. The orifice plate has a diameter ratio $\beta = D_O/D_{WT} = 0.499$, where D_O is the orifice diameter and D_{WT} is the tunnel's internal diameter.

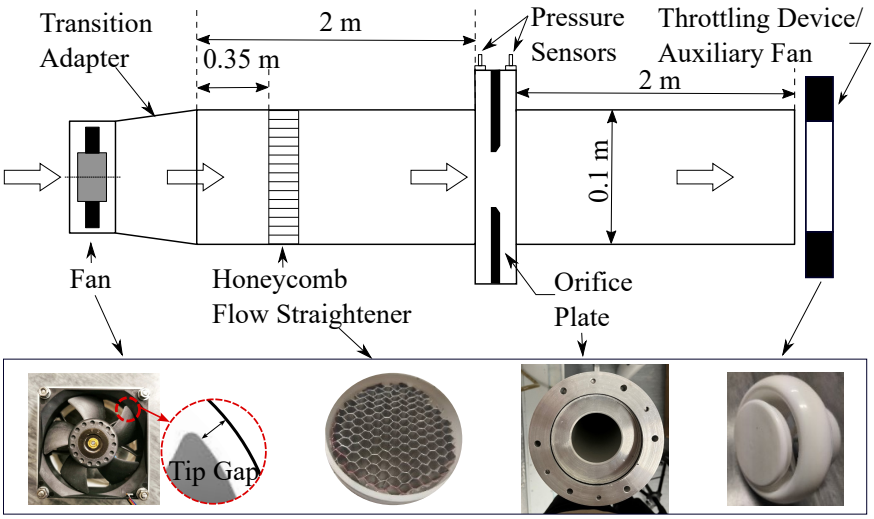

Figure A.1: Experimental setup for testing the aerodynamic performance of the fan according to ANSI/AMCA 210-16 [211] and ISO 5167-2:2003 [307].

Wind tunnel components

Figure A.1 shows the experimental setup, which includes the following key components:

- **Fan under test (FUT)**: A fan positioned at the tunnel inlet with sufficient upstream clearance to ensure uniform airflow.
- **Transition adapter**: A tapered adapter designed to meet the ANSI/AMCA 210-16 standard [211]. It minimises flow separation during the transition from an 80 mm to a 100 mm diameter.
- **Flow conditioning elements**: Two honeycomb flow straighteners located downstream of the FUT and upstream of the auxiliary fans. These eliminate swirl and align the airflow with the duct axis.
- **Measurement section**: Includes a $\beta = 0.499$ orifice plate with pressure taps 25.4 mm from the plate centreline, as specified by ISO 5167-2:2003 [307]. Differential pressure measurements calculate airflow, while static pressure is measured at the upstream tap.
- **Flow control system**: Two counter-rotating auxiliary fans at the tunnel outlet, controlled by PWM signals, adjust operational points from choked (zero-flow rate) to free-delivery (zero-pressure) conditions. A throttling device can also be used to provide additional backpressure control.

Instrumentation

The measurement system includes:

- **Pressure Transducers**:
  - Halstrup Walcher P26 sensor: Measures static pressure (upstream tap to ambient).
  - Halstrup Walcher P92 sensor: Measures differential pressure across the orifice plate.

  Both transducers were calibrated prior to testing.
- **Thermal Monitoring**: Envisense environmental sensor to determine air properties for flow rate calculations.
- **Data Acquisition**: NI cDAQ-9178 chassis with:
  - NI-9205 (x1): Acquires pressure signals.
  - NI-9401 (x2): Generates PWM signals (for FUT and auxiliary fan control) and captures tachometer feedback.
  - LabVIEW 2021 interface: Provides system control and real-time monitoring.
- **Power Management**:
  - Elektro-Automatik EA-PS 2042-10: Supplies power to the FUT with integrated current and voltage monitoring.
  - Elektro-Automatik PS 8360: Powers the auxiliary fan.

Measurement procedure

The automated measurement sequence follows these steps:

1. Start the axial fan at the target speed by adjusting the PWM duty cycle.
2. Activate the auxiliary fan to create a zero-flow condition.
3. Record 20-second averaged measurements at a 1 Hz sampling rate.
4. Gradually tune the auxiliary fan speed to lower backpressure.
5. Allow 30 seconds for stabilisation between measurement points.
6. Repeat for approximately 20 operational points, covering choked flow to free delivery.

Post-processing uses the 20-sample averages from each operational point to generate a P-Q curve and calculate fan efficiency. The next section explains the computational methods for data reduction and uncertainty analysis.

A.1.2 Performance curve calculation

The fan performance curve is determined by measuring the static pressure rise and total volume flow rate for each operating condition. The total electric efficiency of the fan is calculated using the total pressure rise, volume flow rate, and electric power input. This efficiency is a key parameter for assessing the fan's ability to convert electrical power into mechanical power. For clarity, the definitions of each parameter are provided below. The fan static pressure is defined as,

$$P = P_{s2} - P_{t1}, \tag{111}$$

where P_{s2} is the static pressure at the fan outlet and P_{t1} is the total pressure at the fan inlet. In this setup, P_{t1} equals 0 Pa. The total pressure rise is defined as,

$$P_t = P_{t2} - P_{t1}, \tag{112}$$

where P_{t2} is the total pressure at the fan outlet.

The dynamic pressure is defined as,

$$\begin{aligned} P_v &= P_t - P \\ &= \frac{1}{2}\rho V^2, \end{aligned} \tag{113}$$

where ρ is the air density, and V is the axial velocity over the fan.

The volume flow rate is defined as,

$$Q = A_1 V_1 = A_2 V_2, \tag{114}$$

where A_1 and A_2 are the cross-sectional areas at the fan inlet and outlet, respectively, and V_1 and V_2 are the axial velocities at the fan inlet and outlet, respectively.

$$\eta_e = \frac{P_t Q}{Pe}, \tag{115}$$

where Pe is the electric power input to the fan.

The volumetric flow rate measured by the orifice plate is calculated as,

$$Q = CAe\left(\frac{2\Delta P}{\rho}\right)^{1/2}, \tag{116}$$

where C is the orifice discharge coefficient, g is the acceleration due to gravity, ρ is the air density, A is the orifice area, e is the expansibility factor, and ΔP is the pressure drop over the orifice.

The total pressure at fan outlet is calculated as,

$$P_t = P_{t2} = P_{s3} + P_{v3} + f(\frac{L_{2,3}}{D_{h3}} + \frac{L_e}{D_{h3}})P_{v3}, \tag{117}$$

where P_{s3} is the static pressure at the measurement plane, P_{v3} is the velocity pressure at the measurement plane, $L_{2,3}$ is the length of the straight duct from the fan outlet to the measurement plane, D_{h3} is the hydraulic diameter, L_e is the equivalent length of the flow straightener, and f is the friction factor. Then the static pressure takes the form of $P = P_t - P_v$.

A.1.3 Uncertainty analysis for flow measurements

The uncertainties of the measured parameters are calculated based on the ANSI / AMCA 210-16 standard [211] and ISO 5167-2:2003 [307]. The combined uncertainty of the flow rate and pressure measurements are calculated as,

$$\begin{aligned} \sigma_Q &= (\sigma_{Q,std}^2 + \sigma_{Q,sys}^2)^{1/2}, \\ \sigma_P &= (\sigma_{P,std}^2 + \sigma_{P,sys}^2)^{1/2}. \end{aligned} \tag{118}$$

Where $\sigma_{Q,std}$ and $\sigma_{P,std}$ are the standard uncertainties. $\sigma_{Q,sys}$ and $\sigma_{P,sys}$ are the systematic uncertainty. The standard uncertainty is calculated based on 20 repeated measurements, and the systematic uncertainty for pressure measurements is calculated based on the AMCA standard [211], which is expressed as,

$$\sigma_{P,sys} = (\sigma_g^2 + \sigma_\rho^2 + 2\sigma_N^2)^{1/2}, \tag{119}$$

where σ_g is the uncertainty of the pressure measurement instruments, σ_ρ is the uncertainty of the air density, and σ_N is the uncertainty of the fan rotational speed. The values of σ_g, σ_ρ, and σ_N are determined based on the AMCA standard [211] and instrument specifications.

The systematic uncertainty for flow rate measurements is expressed as,

$$\sigma_{Q,sys} = (\sigma_{Q,of}^2 + \sigma_N^2)^{1/2}, \tag{120}$$

where $\sigma_{Q,of}$ is the uncertainty of the orifice flow rate measurement. The uncertainty of the orifice flow rate measurement is calculated based on the ISO standard [307], which is expressed:

$$\sigma_{Q,of} = ({\sigma_C}^2 + \sigma_e^2 + \left(\frac{2b^4}{1-b^4}\right)^2 + \sigma_D^2 + \left(\frac{2}{1-b^4}\right)^2 \sigma_d^2 + \frac{1}{4}\sigma_{\Delta_P}^2 + {\sigma_\rho}^2)^{1/2}, \tag{121}$$

where σ_C is the uncertainty of the orifice discharge coefficient, σ_e is the uncertainty of the expansibility coefficient, σ_D is the uncertainty of the pipe diameter, σ_d is the uncertainty of the orifice diameter, σ_{Δ_P} is the uncertainty of the pressure drop over orifice, b is the diameter ratio ($b = d/D$). The values of σ_C, σ_e, σ_D, σ_d, σ_{Δ_P}, and σ_ρ are determined based on the ISO standard [307] and instrument specifications. The typical values of the combined uncertainties for the pressure and flow rate measurements are summarised in Table A.1.

Table A.1: Uncertainty analysis of the measured parameters.

Parameter	Condition	Relatively uncertainty, %
σ_Q	$Q \geqq 0.5$ m^3/min	1.0 – 4.0
σ_Q	$Q < 0.5$ m^3/min	$\geqq 4.0$
σ_P	$Q \geqq 0.5$ m^3/min	1.5 – 5.0
σ_P	$Q < 0.5$ m^3/min	5.0 – 8.0

A.2 Experimental methodology for aeroacoustics

This section describes the experimental setup, instrumentation, calculations, and uncertainty analysis used to study noise emissions from small electronics cooling axial fans. The methodology is inspired by the ISO 10302 standard [215] and ISO 3744 standard [212], which provide guidelines for measuring and evaluating small fan acoustics in controlled environments. The setup ensures accurate measurements while minimising background noise and environmental interference.

A.2.1 Experimental configurations

The experimental plenum chamber was designed following the ISO 10302 standard [215] for small fan acoustics. It uses a 1:2 scale model derived from full-scale specifications. Figure A.2 shows the design, featuring a fan mounted in a plenum chamber with an adjustable rear aperture slider to control backpressure. The facility, built at

Trinity College Dublin (TCD), allows for acoustic measurements in a controlled laboratory environment, as shown in Figure A.3. This setup enables systematic evaluation of aeroacoustic properties under various operating conditions.

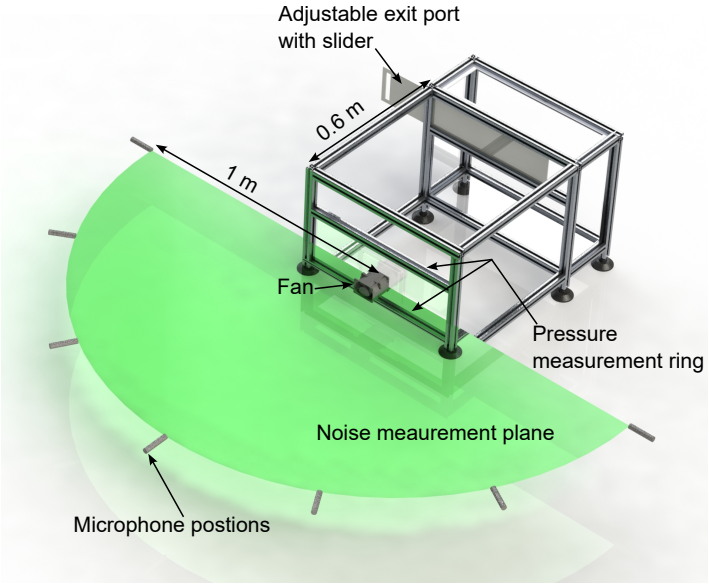

Figure A.2: Schematic of a 1:2 scaled ISO standardised test facility. The fan is mounted in the plenum chamber, with the microphone array positioned at a distance of 1 m from the fan. The backpressure is controlled by an adjustable rear aperture slider.

Sound measurement geometry

Figure A.2 shows the acoustic measurement setup, which uses a semicircular microphone array on the intake side of the fan. The array is designed to capture sound emissions while minimising interference from the plenum chamber walls. Seven measurement stations are spaced at 30° intervals, ranging from 0° (axial alignment) to 150°, with all microphones positioned 1 m from the fan's rotational axis.

Although the array does not fully comply with the ISO 3744 standard [212] for hemispherical sound field sampling, as it does not cover a complete hemisphere, it is optimised for the dipole nature of the fan's sound emissions. This design balances accurate acoustic characterisation with practical constraints. The microphones are placed at the same height as the fan's rotational plane, avoiding obstruction from the plenum walls or other components. This arrangement enables effective directional noise profiling and a thorough analysis of the fan's acoustic performance under controlled conditions.

Instrumentation

The acoustic assessment system included:

- **Transducers**: Two GRAS 40PH-10 free-field microphones (IEPE-powered) with a

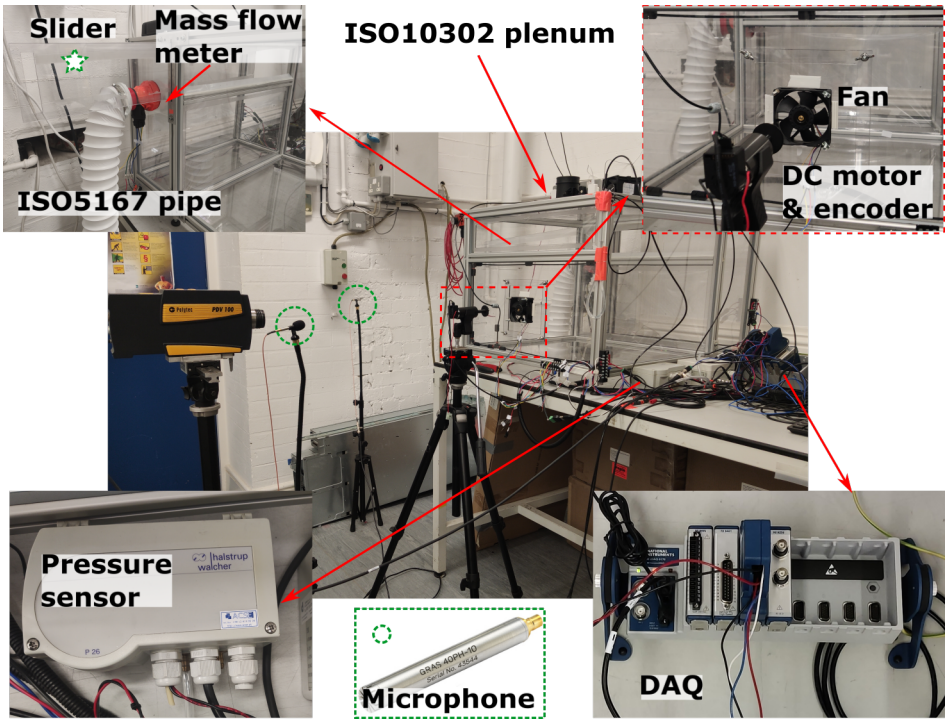

Figure A.3: A 1:2 scaled ISO standardised test facility developed at Trinity College Dublin.

±2 dB frequency response from 10 Hz to 20 000 Hz and a dynamic range of up to 135 dB.

- **Signal Acquisition**: An NI-9250 analogue input module with 102.4 kHz simultaneous dual-channel sampling. It was integrated with the centralised DAQ chassis described in Appendix A.1.1.
- **Calibration**: Each microphone was calibrated using a GRAS 42AG Multifunction Sound Calibrator at a sound pressure level of 94 dB and a frequency of 1 kHz.

Measurement Procedure

The measurement sequence included:

1. Record baseline ambient noise before each test session.
2. Operate the fan at a fixed rotational speed and adjust the rear aperture slider to achieve the target backpressure.
3. Calculate the background noise correction factor K_1 as per ISO 3744 [212]. Details are provided in Appendix A.2.2.
4. Determine the environmental correction factor K_2 following ISO 3744 [212]. Details are in Appendix A.2.2.
5. Sample continuously for 20 s at 51.2 kHz at each measurement location.

6. Process the data to compute the mean sound pressure level (SPL) at each microphone position. A.2.2.

All experiments were conducted in a controlled laboratory environment at Trinity College Dublin, ensuring minimal ambient noise interference. The measurement accuracy and reliability were validated through an interlaboratory comparison with the semi-anechoic chamber at Seagate Technology, Colorado, USA. This rigorous cross-validation process confirmed the consistency and robustness of the results. Detailed results have been previously published in [210] and included in 3.5.

A.2.2 Experimental calculations and corrections

This section outlines the experimental calculations and corrections for noise measurements. The mean sound pressure level at the reference surface, corrected for meteorological conditions and uncertainties, is calculated as [212, 215]:

$$\begin{aligned}\overline{L_p} = L_W - 10\log_{10}\frac{S}{S_0} = \overline{L_{p(\mathrm{FUT})}} - K_1 - K_2 + C + \delta_{\mathrm{angle}} \\ + \delta_{\mathrm{slm}} + \delta_{\mathrm{mount}} + \delta_{\mathrm{oc}} + \delta_{\mathrm{mic}} + \delta_{\mathrm{meth}},\end{aligned} \tag{122}$$

where L_W is the sound power level, S is the measurement surface area, S_0 is the reference surface area (1 m^2), $\overline{L_{p(\mathrm{FUT})}}$ is the uncorrected mean time-averaged sound pressure level of the fan under test (FUT) in decibels, K_1 is the background noise correction factor, K_2 is the environmental correction factor, and C is a meteorological and radiation impedance correction to account for different reference quantities in sound pressure level and sound power level and for changes in sound power level with ambient temperature and pressure, in decibels. δ_{angle} is the uncertainty for the angle difference between the sound emission and measurement, in decibels, δ_{slm} is the uncertainty for the sound pressure measuring instrumentation, in decibels, δ_{mount} is the uncertainty for the influence of mounting, in decibels, δ_{oc} is the uncertainty for the deviation from the operating conditions, in decibels, δ_{mic} is the uncertainty due to the finite number of microphone positions, in decibels, and δ_{meth} is the uncertainty for the influence of the method, in decibels.

Background noise correction factor

The background noise was measured by positioning the microphone at the same location as the noise measurement, but with the fan turned off. The background noise correction factor K_1 was calculated using the following equation:

$$K_1 = -10\log_{10}(1 - 10^{-0.1\Delta L_p}). \tag{123}$$

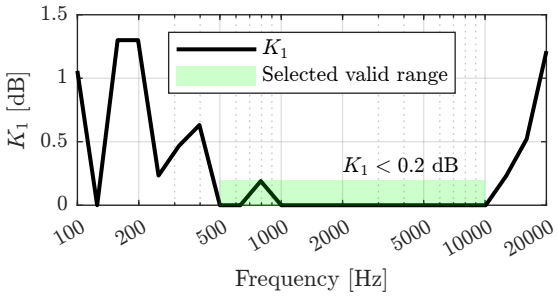

Figure A.4: Background noise correction factor K_1 for the baseline fan in ISO 10302 plenum box [215]. The selected valid frequency range [500 Hz, 10 kHz] are highlighted in green with a correction factor $K_1 < 0.2$ dB.

Here, ΔL_p represents the difference between the measured noise from the test fan and the background noise ($\Delta L_p = \overline{L_{p(\mathrm{FUT})}} - \overline{L_{p(\mathrm{B})}}$). $\overline{L_{p(\mathrm{FUT})}}$ denotes the mean time-averaged sound pressure level of the fan under test (FUT) in decibels, and $\overline{L_{p(\mathrm{B})}}$ represents the mean time-averaged sound pressure level of the background noise. The mean time-averaged sound pressure levels of the FUT and the background noise are determined as follows:

$$\overline{L_{p(\mathrm{FUT})}} = 10 \log_{10} \left[\frac{1}{N_M} \sum_{i=1}^{N_M} 10^{0.1 L_{Pi(\mathrm{FUT})}} \right], \tag{124}$$

$$\overline{L_{p(\mathrm{B})}} = 10 \log_{10} \left[\frac{1}{N_M} \sum_{i=1}^{N_M} 10^{0.1 L_{Pi(\mathrm{B})}} \right], \tag{125}$$

where N_M denotes the total number of microphone positions.

In Eq. 123, the correction factor K_1 is applied when ΔL_p falls within the range of 6 dB to 15 dB. If ΔL_p exceeds 15 dB, no correction is necessary. Conversely, if ΔL_p is less than 6 dB for any frequency band, the measurement is deemed invalid, and the correction factor K_1 is set to 1.3 dB to account for the upper limit of measurement uncertainty.

Figure A.4 presents the results of the noise difference ΔL_p and the background noise correction factors K_1 for the fan in the ISO 10302 plenum box [215] under zero total-to-static pressure rise and a rotational speed of 7050 r/min. This case has been published in [209] and is used as an example here and in following sections.

Figure A.4 confirms that the measurement environment meets the background noise requirements specified in ISO 3744 [212] for frequencies above 500 Hz. This compliance ensures the reliability and accuracy of the acoustic measurements conducted in this study. However, for lower-speed fans like those used in computers, more careful examination of the acoustic measurement quality, is crucial to ensure the reliability of the results. This ensures that even minor noise contributions are accurately accounted

for, maintaining the integrity of the measurements.

Environmental correction factor

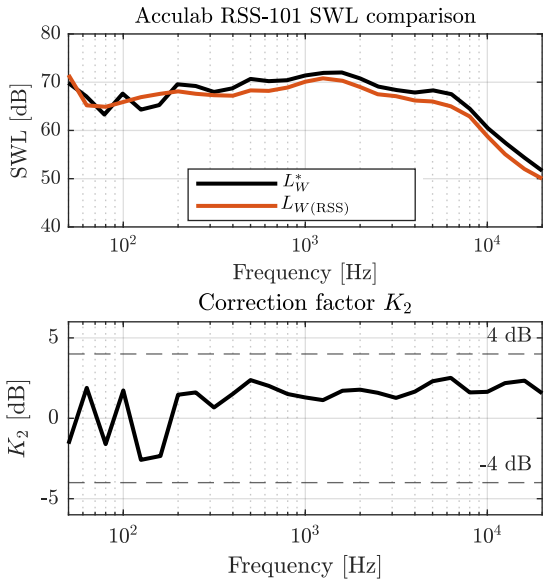

Figure A.5: Sound power level comparison (top) and the environmental correction factor K_2 (bottom) for the laboratory environment. The valid limit of ±4 dB is highlighted in gray dashed lines.

The environmental correction factor K_2 is determined by comparing the measured noise with a calibrated reference sound source (RSS). In this study, we use the AccuLab RSS-101, manufactured by VIacoustics, as the reference sound source. The RSS is positioned at a hemispherical surface with a radius of 1 m, and the noise is recorded. The environmental correction factor K_2 is then calculated as the difference between the environmentally uncorrected sound power level of the RSS, denoted as L_W^*, and the sound power level of the calibrated reference sound source, denoted as $L_{W(\mathrm{RSS})}$, which is expressed as:

$$K_2 = L_W^* - L_{W(\mathrm{RSS})}. \tag{126}$$

Since $\overline{L_p} = L_W - 10\log_{10}(S/S_0)$, the environmental correction factor K_2 can also be calculated as the difference between the mean time-averaged sound pressure level of the RSS, denoted as $\overline{L_p^*}$, and the mean time-averaged sound pressure level of the calibrated reference sound source, denoted as $\overline{L_{p(\mathrm{RSS})}}$, which is $K_2 = \overline{L_P^*} - \overline{L_{P(\mathrm{RSS})}}$.

Figure A.5 shows the environmental correction factor K_2 for the laboratory environment. The calculated K_2 values fall within the valid range of ±4 dB for the frequency range of 50 Hz to 20 kHz, indicating the acceptability of these factors for accurate noise measurements.

Corrected sound pressure level

Figure A.6 illustrates the raw and corrected sound pressure level (SPL) for the reference fan operating at zero total-to-static pressure rise and a rotational speed of 7050 r/min. The SPL is presented in both narrowband and one-third octave bands, providing a comprehensive view of the fan's acoustic performance. These results, previously published in [209], are included here for completeness and to contextualise the correction methodology.

The narrowband SPL of the reference fan, shown in Figure A.6 (a), highlights the detailed frequency content of the noise emissions, capturing both tonal and broadband components. Figure A.6 (b) presents the SPL in one-third octave bands, comparing the raw measurement, background noise, and corrected data. It is clear that the background noise significantly lower than the fan noise, with a correction factor K_1 of 0.2 dB, as previously shown in Figure A.4. The environmental correction factor K_2 is also applied, as shown in Figure A.5, which further refines the SPL measurements.

The corrections, applied following the procedures outlined in Appendix A.2.2, ensure that the reported SPL accurately reflects the fan's noise emissions, free from environmental and background noise interference. The uncertainty analysis for the noise measurements is detailed in Appendix A.2.3.

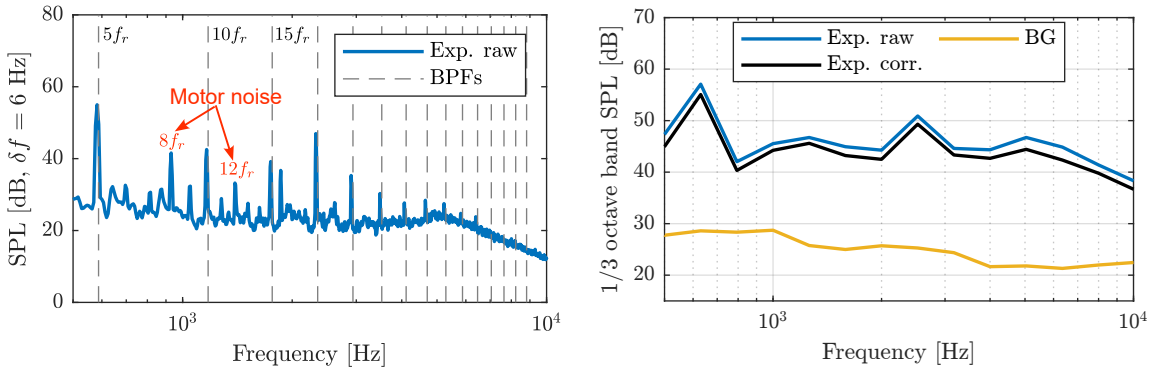

(a) (b)

Figure A.6: Sound pressure level (SPL) in (a) narrowband and (b) one-third octave band of the raw measurement (Exp. raw), background noise (BG), and corrected measurement (Exp. corr.) for the reference fan under P = 0 Pa and N = 7050 r/min.

The correction factors K_1 and K_2 are calculated in 1/3-octave bands. To convert these factors to narrowband, which can be applied for the correction of narrowband SPL, an energy-based method is used. This method converts 1/3-octave band sound pressure levels (SPL) to a narrowband spectrum with adjustable resolution through the following steps:

For each 1/3-octave band with center frequency f_c:

1. Calculate band edges:

$$f_{\text{low}} = f_c \cdot 2^{-1/6}, \quad f_{\text{high}} = f_c \cdot 2^{1/6} \tag{127}$$

2. Determine narrowband centers within $[f_{\text{low}}, f_{\text{high}}]$:

$$f_{n,k} = \delta f \cdot \left\lceil \frac{f_{\text{low}}}{\delta f} \right\rceil + (k-1)\delta f, \quad k \in \mathbb{N} \text{ where } f_{n,k} \leq f_{\text{high}} \tag{128}$$

   where δf is the target narrowband resolution.

3. Calculate total acoustic energy in the 1/3-octave band:

$$E_{1/3} = p_0^2 \cdot 10^{L_{1/3}/10} \cdot (f_{\text{high}} - f_{\text{low}}) \tag{129}$$

   where $p_0 = 20$ μPa is the reference sound pressure, and $L_{1/3}$ is the SPL in the 1/3-octave band.

4. Distribute energy equally to contained narrowbands:

$$E_{n,k} = \frac{E_{1/3}}{N}, \quad N = \text{number of narrowbands in the interval} \tag{130}$$

For all narrowband frequencies f_j in the complete spectrum:

$$E_{\text{total}}(f_j) = \sum_i E_{n,k}^{(i)} \quad \text{where } f_j = f_{n,k}^{(i)} \tag{131}$$

Finally, convert aggregated energy to narrowband SPL:

$$L_{\text{narrow}}(f_j) = 10 \cdot \log_{10}\left(\frac{E_{\text{total}}(f_j)}{p_0^2 \cdot \delta f}\right) \tag{132}$$

The conversion process involves redistributing the acoustic energy from each 1/3-octave band into its corresponding narrowband components. This approach ensures that the correction is consistent across the entire frequency spectrum while maintaining the integrity of the narrowband resolution. After applying this method, the narrowband correction factors $K_{1,\text{narrow}}$ and $K_{2,\text{narrow}}$ are obtained, which can be applied to the narrowband SPL data. The corrected narrowband SPL is then calculated as:

$$\overline{L_{p,\text{corr}}} = \overline{L_{p,\text{raw}}} - K_{1,\text{narrow}} - K_{2,\text{narrow}}. \tag{133}$$

Figure A.7 shows the narrowband SPL of the reference fan, including the raw measurement (Exp. raw) and the corrected measurement (Exp. corr.) calculated based on Eq. 133.

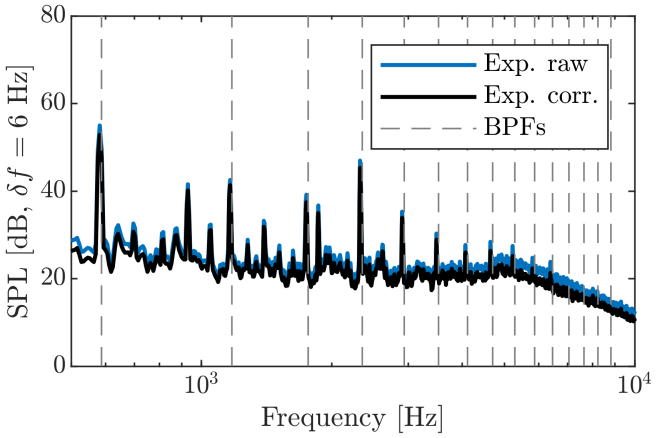

Figure A.7: Sound pressure level (SPL) in narrowband of the raw measurement (Exp. raw) and the corrected measurement (Exp. corr.) for the reference fan under $P = 0$ Pa and $N = 7050$ r/min.

A.2.3 Uncertainty analysis for noise measurements

The combined uncertainty of the noise measurements for the mean sound power level $\overline{L_p}$ is calculated using the following equation

$$\sigma_{\overline{L_p}} = k\sqrt{\left(\sigma_{omc}^2 + \sigma_{R0}^2\right)}, \tag{134}$$

here, k is the coverage factor. For a normal distribution, $k = 2$ is used to achieve a 95% confidence level. σ_{omc} is the standard deviation, describing the uncertainty due to the instability of the noise source under test. It was determined by repeated measurements using the same instrumentation and setup. σ_{R0} is the systematic uncertainty, including all uncertainties from the measurement system and environment as per the ISO 10302 standard [215]. The systematic uncertainty is calculated as

$$\sigma_{R0} = \sqrt{\sum_{i=1}^{n}(u_i c_i)^2}, \tag{135}$$

where u_i is the uncertainty of the i^{th} quantity, and c_i is the sensitivity coefficient of the i^{th} quantity. An uncertainty budget with valid quantities and their uncertainties of the noise measurements is presented in Table A.2. Here, the entire band of frequencies [500 Hz, 10 kHz] is considered to calculate the overall sound pressure level.

Table A.2: Uncertainty budget for determinations of σ_{R0} for the noise measurements. The entire band of frequencies [500 Hz, 10 kHz] is considered to calculate the combined uncertainty.

Quantity	Estimate, [dB]	Standard uncertainty, u [dB]	Probability distribution	Sensitivity coefficient, c	Uncertainty contribution uc [dB]
$\overline{L_p}$	$\overline{L_{P,\text{est}}}$	u_{L_P}	Normal	$1 + \left(10^{0.14\Delta L_p - 1}\right)^{-1}$	0.459
K_1	$K_{1,\text{est}}$	u_{K_1}	Normal	$\left(10^{0.14\Delta L_p - 1}\right)^{-1}$	0.500
S	S_{est}	$\Delta r/\sqrt{3}$	Rectangular	$8.7/r$	0.502
K_2	$K_{2,\text{est}}$	u_{K_2}	Normal	1	0.290
C	C_{est}	u_C	Normal	1	0.500
δangle	0.25	$u_{\delta\text{angle}}$	Normal	1	0.192
δslm	0	$u_{\delta\text{slm}}$	Normal	1	0.700
δmount	0	$u_{\delta\text{mount}}$	Normal	1	0.192
δoc	0	$u_{\delta\text{oc}}$	Normal	1	0.116
δmic	0	$u_{\delta\text{mic}}$	Normal	1	0.100
δmeth	0	$u_{\delta\text{meth}}$	Normal	1	0.400

Table A.3: Combined uncertainty for noise measurements.

k (95% confidence level)	σ_{omc} [dB]	σ_{R0} [dB]	$\sigma_{\overline{L_p}}$ [dB]
2	0.842	1.326	3.141

The combined uncertainty of the noise measurements calculated using the above quantities is shown in Table A.3. The combined uncertainty of the noise measurements is 3.141 dB for the overall frequency range, which is within the typical range suggested by the ISO standards [212, 215].

Appendix B

Development of the ROM code LONAT

B.1 Work flow of the reduced-order model

To implement a reduced-order analysis program, MATLAB was used to apply the equations and methods presented in Part II. The in-house MATLAB code, Low-Order Noise Analysis Tool (LONAT), was developed in this study. Figure B.1 shows the flow chart of LONAT, which consists of four main modules: pre-processing, flow solver, noise solver, and post-processing. The pre-processing module prepares the input data, including airfoil geometry, blade design parameters, aerodynamic coefficients, and boundary layer parameters. The flow solver module calculates the aerodynamic performance of the rotor/fan, including thrust, torque, and surface pressure distribution. The noise solver module predicts the tonal and broadband noise of the rotor/fan. The post-processing module visualises the results, including the rotor/fan performance curve, surface pressure distribution, and noise spectrum. Detailed descriptions of each module are provided in the following sections of this Appendix.

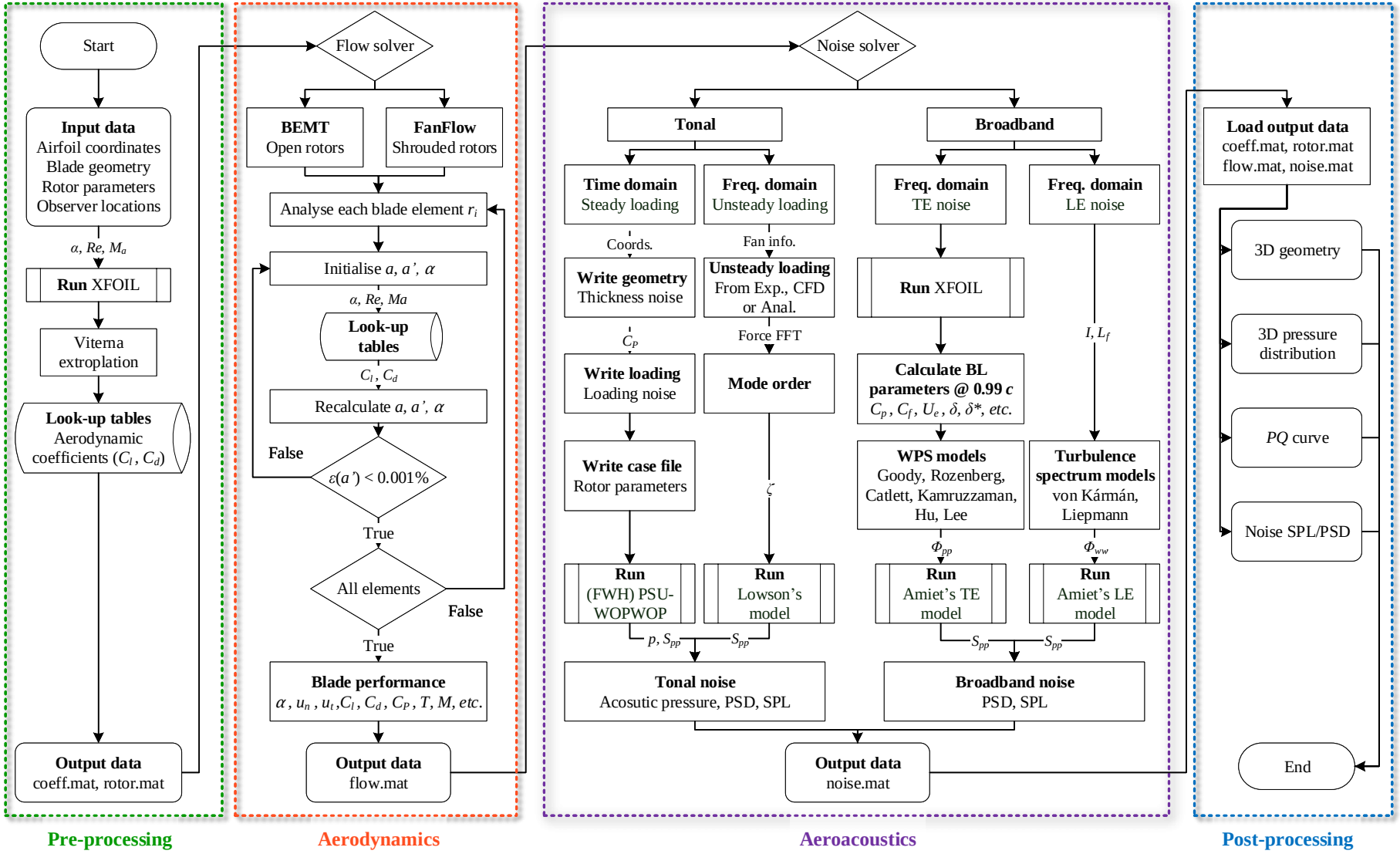

Figure B.1: Flow chart of the Low-Order Noise Analysis Tool (LONAT).

B.1.1 Pre-processing

In the pre-processing stage, the tool requires necessary input information. In terms of the 3D rotor calculation, the input parameters are different from these of 2D airfoil as mentioned in 2.3.6. In addition to the 2D airfoil coordinates, the sectional chord and twist distributions are also required, which can be seen in Fig. B.1. This distribution file is typically assembled by the values of the chord c and twist angle β as a function of several blade radial locations r. The method for parametrically defining the blades is same as the way used in the University of Illinois at Urbana-Champaign (UIUC) propeller database [308]. The rotor design parameters such as tip radius, hub radius, rotational speed and the number of rotor blades are also required by this tool. As mentioned in Section 2.3.6, for the sake of numerical robustness, all the aerodynamic coefficients of the 2D airfoil are pre-calculated by XFOIL [97] in the angle of attack range from $-20°$ to $+20°$, and then extended to the entire $\pm 180°$ angle of attack range using the Viterna method [101]. Finally, all the aerodynamic data is used to generate a look-up table based on the angle of attack α.

B.1.2 Flow solver

Two flow solvers have been developed based on the blade element momentum theory (BEMT) and lifting-line theory (LLT) as detailed in Section 2.3.6 and Part II. The flow chart of these solvers is illustrated in Fig. B.1. The BEMT solver evaluates the aerodynamic performance of an open rotor, whereas the FanFlow solver (discussed in Chapters 4–5) is tailored for shrouded fan scenarios. Both solvers address steady-state flow conditions. The flow solver, in conjunction with XFOIL [97] and wall pressure fluctuation models [118, 119, 123], generates the rotor/fan performance curve, surface pressure distribution, thrust, and torque data. This comprehensive dataset is crucial for subsequent noise calculations. Figure B.2 depicts the predicted pressure coefficient distribution on a single blade at maximum flow rate.

B.1.3 Noise solver

In accordance with the noise prediction methodologies outlined in Section 2.4 and Chapter 7, LONAT incorporates two noise calculation procedures: tonal noise and broadband noise. For tonal noise, two solvers have been empolyed: the PSU-WOPWOP code [109], which utilises the Ffowcs Williams-Hawking (FW-H) equation [105] for time-domain blade self-noise calculation, and Lowson's method [129], based on the simplified FW-H equation, for blade interaction noise calculation. The broadband noise calculation employs Amiet's method [50] for predicting turbulent boundary layer-trailing edge (TBL-TE) noise and leading-edge (LE) noise. The flow chart of these noise

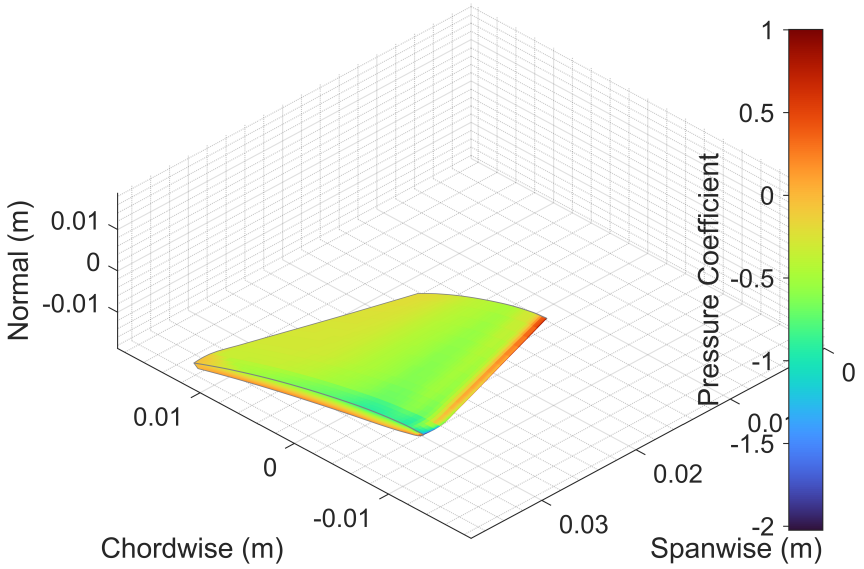

Figure B.2: Surface pressure of a fan blade, predicted by LONAT.

solvers is illustrated in Fig. B.1. The noise solver, in conjunction with the fan geometry, aerodynamic data, wall pressure spectrum models, and turbulence spectrum models, calculates the tonal and broadband noise of the rotor/fan. A sample of the predicted noise spectrum is shown in Fig. 7.12 in Chapter 7.

B.1.4 Post-processing

The post-processing procedure primarily focuses on saving and visualising the results. The 3D rotor geometry, 3D surface pressure, P-Q curve, and the acoustic spectrum can be visualised using the post-processing scripts, as illustrated in Fig. B.1. This programme also provides the commonly used 1/3 octave band noise spectrum and overall SPL. The centre frequencies used in the 1/3 octave band can be expressed as:

$$f_c(i) = 1000[2^{(i-18)/3}], \quad i = 1, 2, 3, \ldots, \tag{136}$$

Additionally, the broadband noise sources (i.e., TBL-TE noise and LE noise) can be visualised separately in a contour plot (as shown in Fig. 7.9) to identify the dominant noise sources on the rotor/fan blade.

Appendix C

ROM Code Validation for 2D Airfoil Trailing Edge Noise Prediction

As mentioned in Section 2.2, turbulent boundary trailing-edge noise is the most dominant noise source in airfoil self-noise. Hence, in this Appendix [1], the 2D model developed for airfoil trailing edge noise prediction is validated against several published benchmark cases with available experimental data.

C.1 Validation against BANC experiments

Benchmark Problems for Airframe Noise Computations (BANC) [309] results are first used to validate the aerodynamic and aeroacoustic models for 2D airfoils. Trailing edge noise is a key topic in the BANC workshop presented by the American Institute of Aeronautics and Astronautics (AIAA), with numerous experimental results provided by the BANC-III workshop [309].

In this study, two different airfoil profiles with various Reynolds numbers and angles of attack were used to validate the prediction tool. It should be noted that the benchmark cases from BANC-III are all moderate/high Reynolds number flow cases ($Re > 1\times10^6$). However, to the best of the author's knowledge, there are no benchmark cases reported at low Re with experimental wall pressure spectrum data. As a result, the BANC-III cases were chosen as the fundamental cases to validate the reduced-order model because they offered more complete experimental data, such as the pressure coefficient, wall pressure spectrum at the trailing edge, and far-field acoustic noise.

The setup of BANC-III experiments is shown in Fig. C.1. The observer is located orthogonal to the chord line above the trailing edge of the airfoil at a distance of 1 m

[1] This Appendix is based on the work presented in Ref. [29]: W. Zhao, S. Wasala, S. Spence, and T. Persoons, "Poster: Thermal management and aeroacoustics of air-cooled electronics enclosures," in 24th Sir Bernard Crossland Symposium, Dublin, Ireland, Sept. 22–23, 2021.

for the acoustic measurement. A summary of the selected BANC-III validation cases is tabulated in Tab. C.1. For cases 1–3, a NACA 0012 airfoil was chosen, while a DU96-W-180 airfoil was chosen for case 4. The boundary layer was tripped near the leading edge on both the pressure side (PS) and suction side (SS) for all cases to enforce fully turbulent flows. Details about the tripping methods used in the measurements can be found in Ref. [309]. The same trip transition position was applied in the numerical calculation for each case.

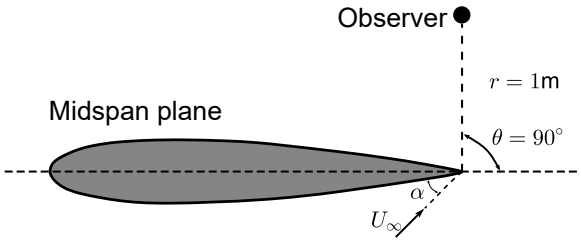

Figure C.1: The set-up of BANC-III measurements.

Table C.1: Test conditions for BANC-III experiments.

Case	Airfoil	Chord length, m	U_∞, m/s	Re	α,°	Trans. pos. (x/c)
1	NACA 0012	0.4	56	1.5×10^6	0	SS: 0.065 PS: 0.065
2	NACA 0012	0.4	54.8	1.5×10^6	4	SS: 0.065 PS: 0.065
3	NACA 0012	0.4	53	1.5×10^6	6	SS: 0.060 PS: 0.070
4	DU96-W-180	0.3	60	1.13×10^6	4	SS: 0.120 PS: 0.150

C.1.1 Aerodynamic validation

The coefficient of pressure of the airfoil was calculated using XFOIL and validated against experimental data. Figure C.2 shows plots of the pressure coefficient for the BANC-III cases. The predicted pressure distribution agrees very well with the experimental data for all cases.

Figure C.3 shows comparisons of wall pressure spectrum between the measurement data and six WPS model predictions. Goody's model and Catlett's model are not suitable for all cases, as they consistently show significant underpredictions or overpredictions for the wall pressure spectrum. Hu's model shows large discrepancies for

all cases, especially at high frequencies. Kamruzzaman's model shows notable discrepancies at low frequencies and slight discrepancies at high frequencies for all cases. Lee's model yields similar results to Rozenberg's model for cases 1–3, as it was derived from Rozenberg's model with corrections for high Clauser's parameter (β_c) cases [123]. As shown in Tab. 2.2, the amplitude parameter a in Rozenberg's model was replaced by a new parameter a^* in Lee's model for high β_c cases. In case 4, a relatively high value of β_c was observed, which is 21.7867. Lee's model provides better predictions than Rozenberg's model, especially on the pressure side in this case.

Overall, for the wall pressure spectrum prediction, Lee's model shows better agreement with the experimental data for all BANC-III cases.

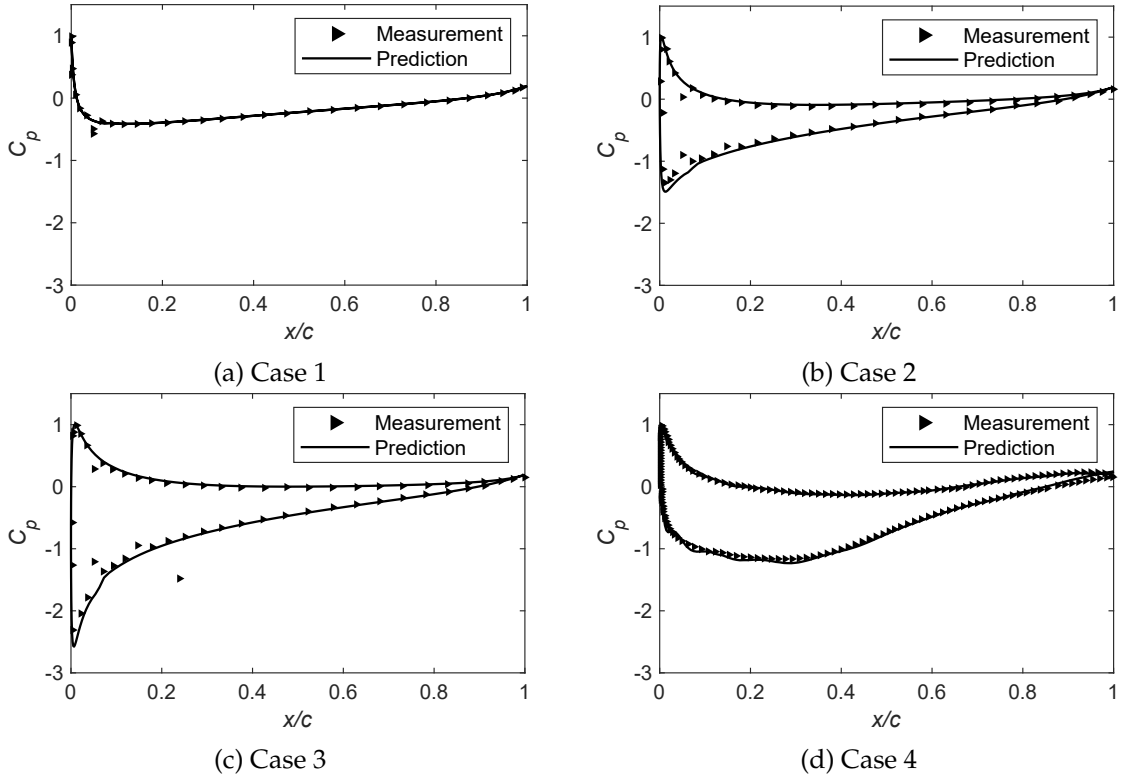

(a) Case 1 (b) Case 2

(c) Case 3 (d) Case 4

Figure C.2: Pressure coefficient validation against BANC-III results.

C.1.2 Aeroacoustic validation

For acoustic validation, the observer is 1 m from the trailing edge, and the airfoil span is 1 m for all cases. The observer angle from the trailing edge is 90° for all cases. Figure C.4 shows comparisons of the trailing-edge noise predictions for the six wall-pressure spectrum models and measurement data for all cases. The measurement data includes uncertainty bars of ±3 dB, as recommended by Herr *et al.* [309]. Depending on the wind-tunnel facility and equipment, measured noise levels for the same airfoil tested under the same conditions could differ by ±3 dB.

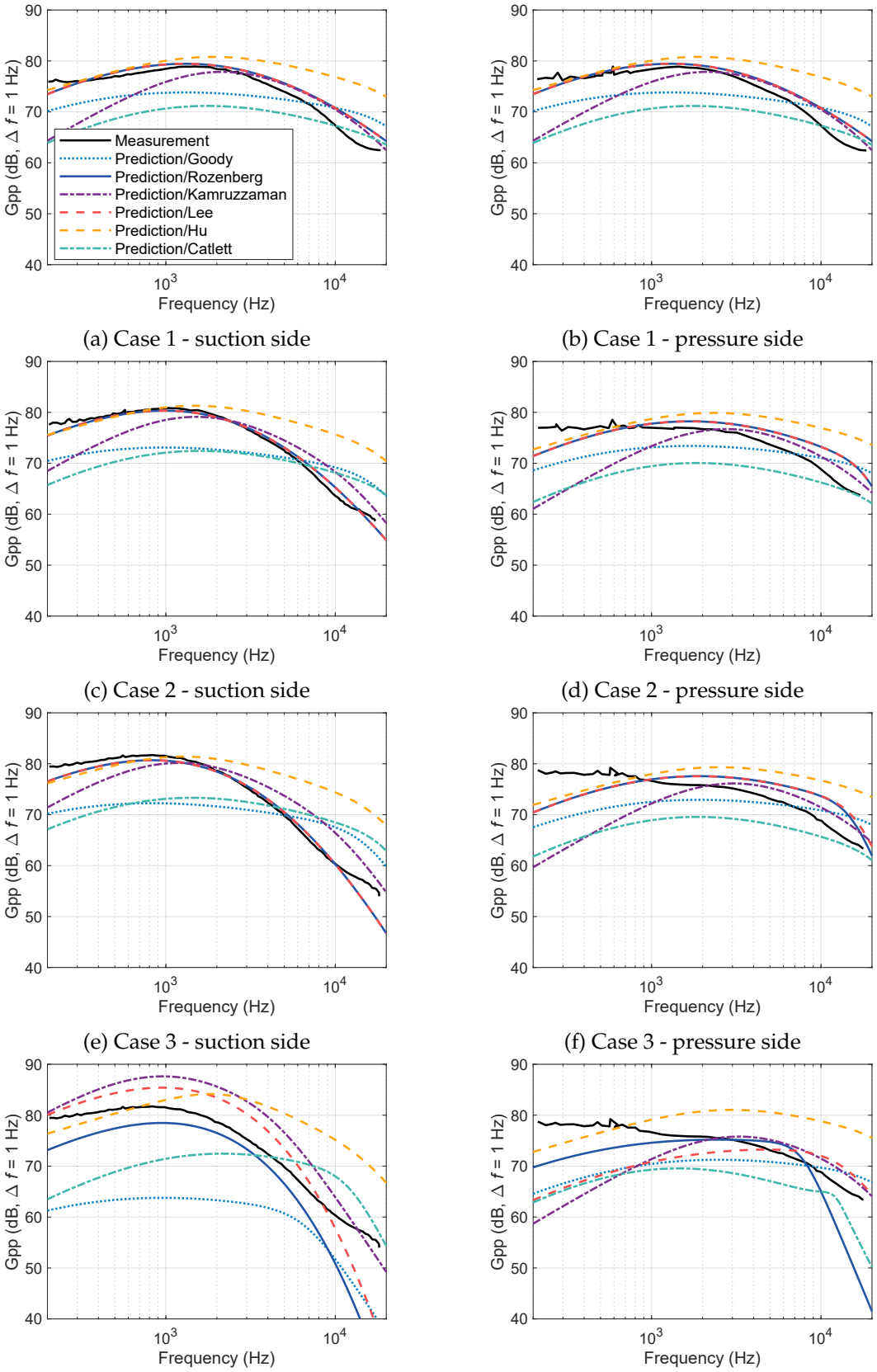

(a) Case 1 - suction side

(b) Case 1 - pressure side

(c) Case 2 - suction side

(d) Case 2 - pressure side

(e) Case 3 - suction side

(f) Case 3 - pressure side

(g) Case 4 - suction side

(h) Case 4 - pressure side

Figure C.3: Comparison between experimental data [309] and six WPS models for the wall pressure spectrum predictions.

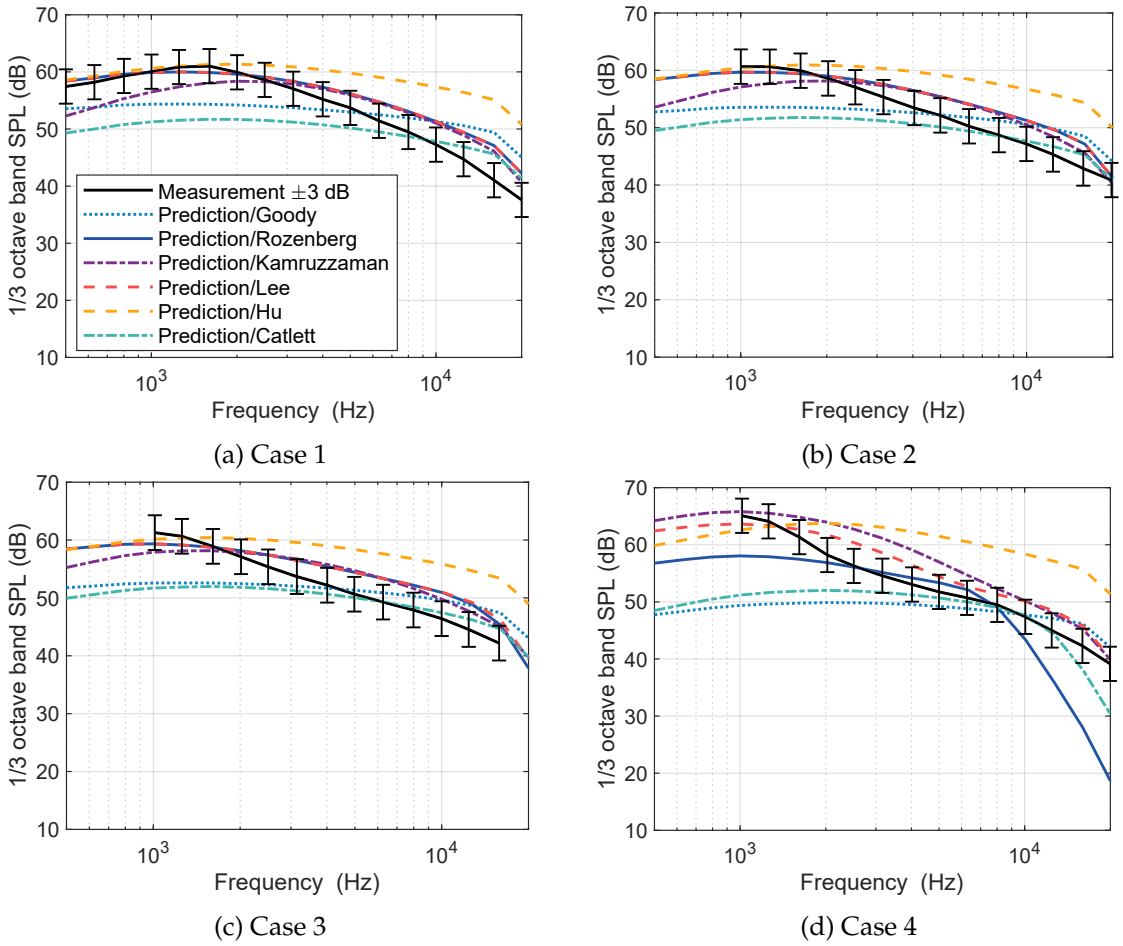

(a) Case 1

(b) Case 2

(c) Case 3

(d) Case 4

Figure C.4: Comparison between experimental data [309] and six WPS models for the far-field noise predictions in 1/3 octave band.

Similar to the wall pressure spectrum results, Goody's model and Catlett's model significantly underpredict the noise levels at low frequencies for all cases. Hu's model overpredicts the noise levels by more than 5 dB at high frequencies for all cases. Kamruzzaman's model matches the data well for cases 1–3 but underpredicts the noise levels by about 3 dB for case 4 at moderate frequencies. The results from Rozenberg's model are identical to Lee's model for cases 1–3, both showing good agreement with the experimental data. However, Lee's model matches case 4 best, while Rozenberg's model shows a large discrepancy at high frequencies, underpredicting the noise levels by more than 20 dB.

In conclusion, Lee's model performs better for noise prediction in terms of both magnitude and shape for the BANC-III cases.

C.1.3 Directivity of trailing edge noise emission

In this section, the directivity of trailing edge noise emission is investigated using Lee's WPS model and Amiet's acoustic analogy. The setup for calculating trailing edge noise

directivity is shown in Fig. C.5. The far-field noise levels were calculated at 26 observer locations around the airfoil at 15° intervals and a distance of 1 m. Due to a singularity in the numerical method at 0° and 270°, these locations were replaced by 1°, 269°, 271°, and 359°, as shown in Fig. C.5.

Figure C.6 presents the noise directivity results from the trailing edge. Figure C.5 (a) shows the sound pressure level (dB) at 500 Hz, 1 kHz, 2 kHz, and 4 kHz, while Fig. C.5 (b) shows the overall SPL results. Theoretically, the noise directivity from the airfoil trailing edge is a dipole source, as introduced in Section 2.2. According to Lee's model predictions, the directivity agrees well with the ideal dipole acoustic source.

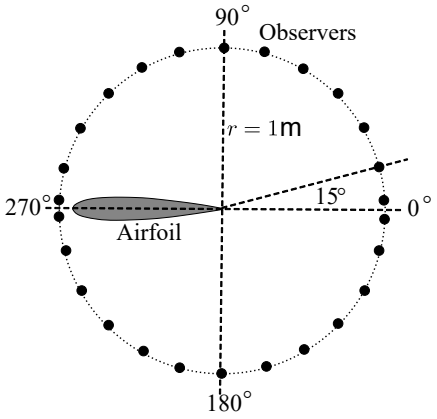

Figure C.5: Setup for calculating trailing edge noise directivity.

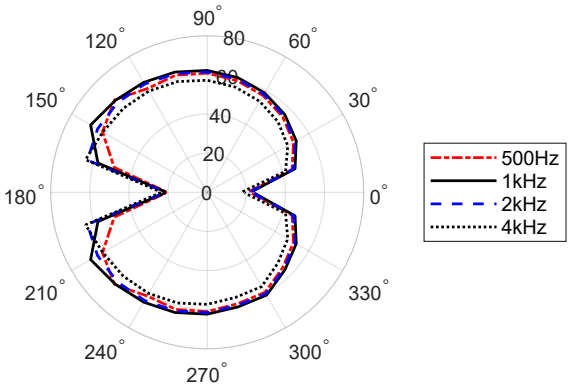

(a) SPL (dB) at various frequencies.

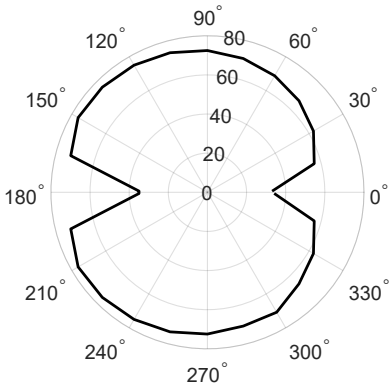

(b) Overall SPL (dB).

Figure C.6: Directivity of acoustic emission from trailing edge for case 1, predicted by Lee's WPS model and Amiet's model.

C.2 Validation against NASA experiments

As shown in Section C.1, the proposed reduced-order model matches well with BANC-III measurements at moderate to high Re flows. Since the Re of electronics cooling fans is typically very low, it is necessary to validate this model's performance at low Re

flows. Finding experimental wall pressure spectrum results for low Re airfoil flows in the literature is challenging. Therefore, the experimental noise data for various NACA 0012 airfoil test cases conducted by Brooks, Pope, and Marcolini [52] at NASA was chosen for validation. Assuming the chord length of an axial flow fan blade is usually 2.54 cm, the input velocity for a suitable test case can be estimated in the range of 28.8 - 57.5 m/s using the desired Reynolds number Re of $50,000 - 100,000$. Thus, this study selected NACA 0012 airfoil cases with a 2.54 cm chord at similar low Re, summarised in Tab. C.2.

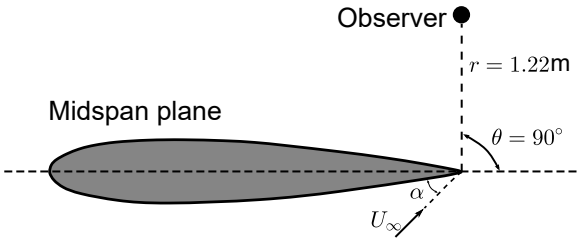

Figure C.7: The setup of NASA measurements.

Table C.2: Test conditions for NASA experiments.

Case	Airfoil	Chord length, m	U_∞, m/s	Re	α,°	Trans. position (x/c)
5	NACA 0012	0.0254	31.7	5.5×10^4	0	SS: 0.3, PS: 0.3
6	NACA 0012	0.0254	39.6	6.9×10^4	0	SS: 0.3, PS: 0.3
7	NACA 0012	0.0254	55.5	9.6×10^4	0	SS: 0.3, PS: 0.3
8	NACA 0012	0.0254	71.3	1.2×10^5	0	SS: 0.3, PS: 0.3

For acoustic experiments, the microphone is placed 1.22 m from the trailing edge, and the airfoil span is 0.4572 m. The microphone angle from the trailing edge is 90° for all cases. Figure C.7 shows the setup of the NASA measurements. More details about the experimental setup can be found in Ref. [52].

Figure C.8 shows comparisons of 1/3 octave band noise results between the measurement data, BPM predictions, and six WPS model predictions. The measurement and BPM prediction data were retrieved from Ref. [52]. For cases 5-7, each model captures the basic trend but underpredicts the noise levels at low and middle frequencies by more than 5 dB. Goody's model and Catlett's model significantly underpredict the noise levels, while Hu's model overpredicts at high frequencies. Rozenberg's model has identical prediction data to Lee's model, and they perform better for cases 5-7. For case 8, each model shows large discrepancies, especially at low and middle frequencies.

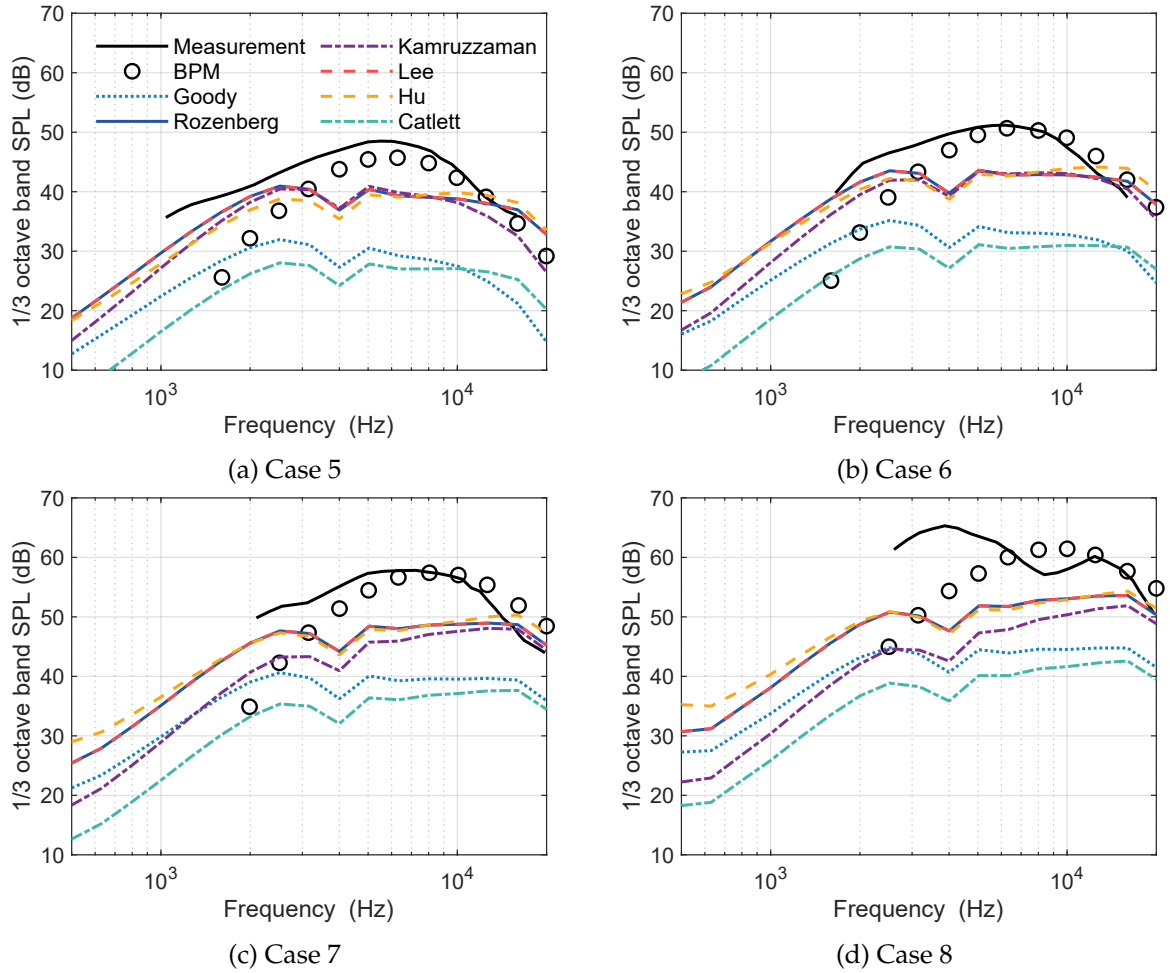

(a) Case 5

(b) Case 6

(c) Case 7

(d) Case 8

Figure C.8: Comparison between experimental data [52], BPM predictions [52], and six WPS models for far-field noise predictions in 1/3 octave bands.

Compared to BPM's prediction results, Amiet's model combined with Lee's/Rozenberg's WPS models performs better at low and high frequencies, while the BPM model aligns well with experimental data at middle frequencies.

Overall, the validation results show that the two low Re models (Rozenberg and Lee) closely match the measurement data but underpredict noise levels at middle frequencies. However, due to the lack of experimental data for wall pressure spectra at low Re flows, it is unclear whether these underpredictions are due to inaccuracies in the WPS models or the Amiet model. Further improvements could be made by gaining more insights into wall pressure spectra at low Re flows, either through experimental validations or high-fidelity CFD simulations.

Appendix D

ROM Code Validation for 3D UAV Rotor

This Appendix [1] presents the validation of the proposed reduced-order model (ROM) for noise prediction of open rotors. A benchmark case from Ref. [55] was selected to validate the 3D model for an open rotor. The rotor model consists of a two-bladed propeller operating at 5000 r/min, with a chord-based Reynolds number ranging from 4.6×10^4 to 10.6×10^4. The main design parameters for the rotor are listed in Tab. D.1, with a corresponding rotational tip Mach number of 0.23.

The structure of this open rotor case is slightly different from a typical cooling fan, but the flow conditions of the sectional airfoils are similar, as they operate at comparable Reynolds numbers. Therefore, this benchmark case, with detailed numerical and experimental studies in [55], is appropriate for validating Amiet's model and the FW-H method for noise prediction of open rotors with rotating blades. An exploded view of the propeller system is shown in Fig. D.1.

Figure D.1: The geometry of the two-bladed APC-96 UAV propeller (N = 5000 r/min, R_t = 150 mm), adapted from Ref. [55].

This rotor was redesigned based on an APC-96 model with the NACA 4412 sectional airfoil profile and a 150 mm tip radius. The computer-aided design (CAD) file of the

[1] This Appendix is based on the published conference paper [30]: W. Zhao, S. Wasala, and T. Persoons, "Reduced-order aeroacoustic modelling of electronics cooling fans," in Proceedings of the International Congress on Sound and Vibration, Society of Acoustics, 2022, pp. 1–8.

rotor geometry was obtained from the first author in Ref. [55]. The twist and chord distributions were retrieved from Ref. [55], as shown in Fig. D.2. The test condition selected for validating the numerical method is the 5000 r/min case with a jet exit velocity varying from 0 m/s to 20 m/s. By varying the jet wind tunnel velocity, a range of advance ratios $J = V_0/(nD)$ from 0 to 0.8 can be obtained, where V_0 denotes the freestream axial flow velocity, n is the number of rotor revolutions per second, and D is the rotor tip diameter. The benchmark results, including experimental data and high-fidelity lattice-Boltzmann method very large eddy simulation (LBM/VLES) data for this test condition and microphone location, were obtained from Ref. [55] for later validations. More details about the experimental setup and the LBM/VLES implementations can be found in Ref. [55].

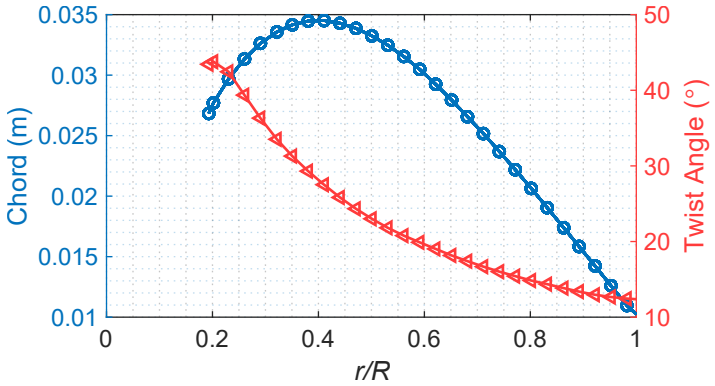

Figure D.2: Chord and twist distributions of the APC-96 UAV blades shown in Fig. D.1.

Table D.1: Design parameters for the APC-96 rotor.

Parameter	Value
Blade number B	2
Tip radius R_t [mm]	150
Hub radius R_h [mm]	12.5
Airfoil profile	NACA 4412
Rotational speed N [r/min]	5000
Free stream velocity U_∞, [m/s]	6
Rotational tip Mach number Ma	0.23
Tip Reynolds number Re	10.6×10^4

D.1 Aerodynamic validation

The conventional BEMT model described in Section 2.3.6 was used to calculate the rotor's flow field. The number of spanwise elements of a 3D blade is crucial when using the blade element theory-based method. Figure D.3 illustrates the chordwise and spanwise elements. The convergence of the aerodynamic results was checked by using various numbers of blade elements from 5 to 320, with a grid refinement ratio of 2. The test condition for validating convergence is the case with a jet exit velocity of 0.24 m/s, corresponding to the advance ratio $J = 0.24$. The force results were obtained by integrating the forces from $r/R_t = 0.3$ to 1. The thrust and torque coefficients C_T and C_Q are used to show the convergence trend, which are determined as:

$$\begin{aligned} C_T &= \frac{T}{\rho\Omega^2\pi R_t^4} \\ C_Q &= \frac{M}{\rho\Omega^2\pi R_t^5}. \end{aligned} \tag{137}$$

Figure D.4 shows the grid convergence trend of the thrust and torque coefficients. Grid independence of forces is clearly reached with 80 spanwise elements. The force results discrepancy between 80, 160, and 320 spanwise elements is under 1%. In terms of acoustic results convergence, Fig. D.5 shows the effect of the number of spanwise elements on the far-field noise. The acoustic power spectrum density was predicted by Rozenberg's model combined with the FW-H method. The predicted sound level for the 80 elements case is roughly 0.5 dB lower than that of the 160 elements case. Therefore, dividing a blade into 80 elements is determined as the best practice for this study, as a finer grid would be more time-consuming without being more accurate.

Figure D.6 shows the predicted thrust and torque coefficients compared to experiments and high-fidelity LBM/VLES results. The predicted thrust and torque agree well with the experimental data and LBM/VLES results, especially at higher advance ratios. For low advance ratios near hover conditions, BEMT is typically less accurate due to its inability to predict stall and post-stall behaviour of highly loaded blade sections near the hub [55]. Overall, the predicted thrust and torque values are in good agreement with the experimental data.

The 3D surface pressure distribution for the blade was obtained by calculating sectional pressure distributions using the integrated XFOIL code [97]. Figure D.7 shows the surface pressure distribution contour of one blade. This surface pressure data will be used by the acoustic models for steady loading noise prediction.

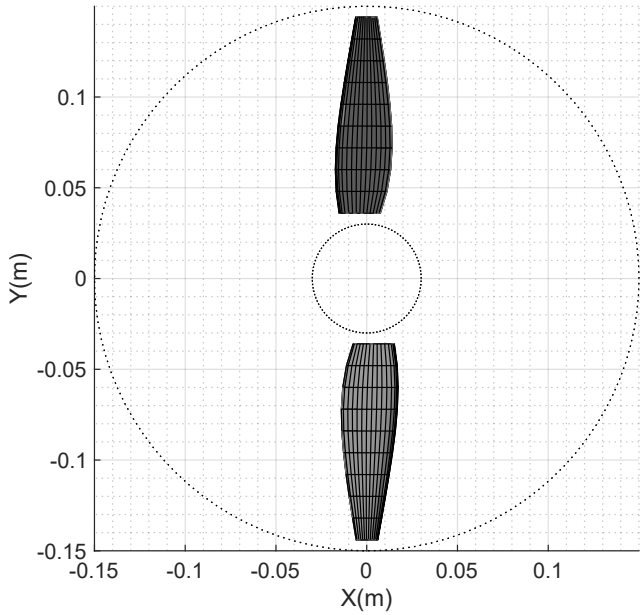

Figure D.3: Schematic of the chordwise and spanwise elements of the APC-96 rotor.

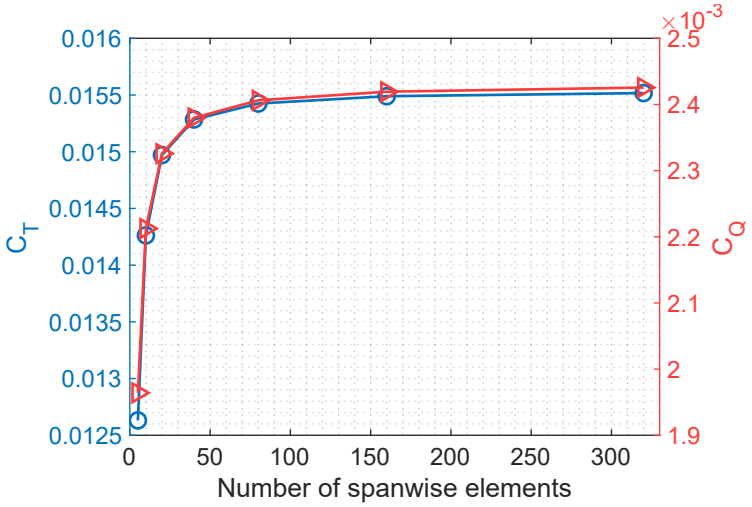

Figure D.4: Effect of the number of spanwise elements on the propeller forces.

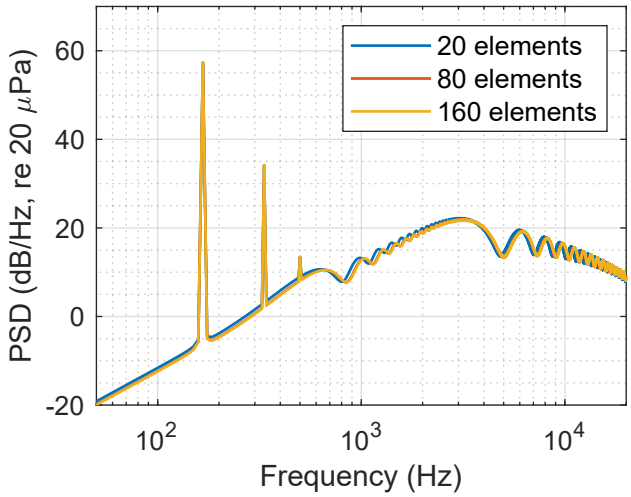

Figure D.5: Effect of the number of spanwise elements on the far-field noise predictions.

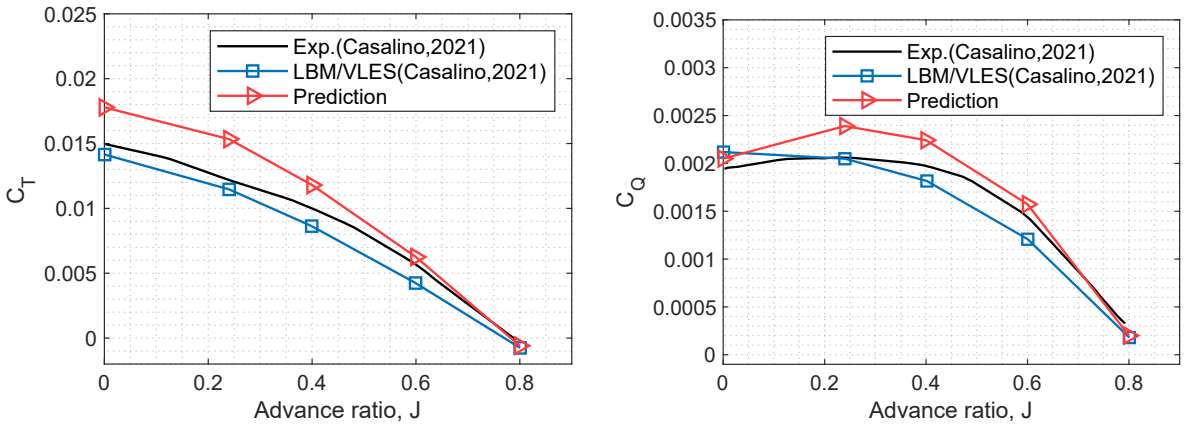

(a) Thrust coefficient (b) Torque coefficient

Figure D.6: Aerodynamic results comparison between measurements, LBM/VES and reduced-order model prediction.

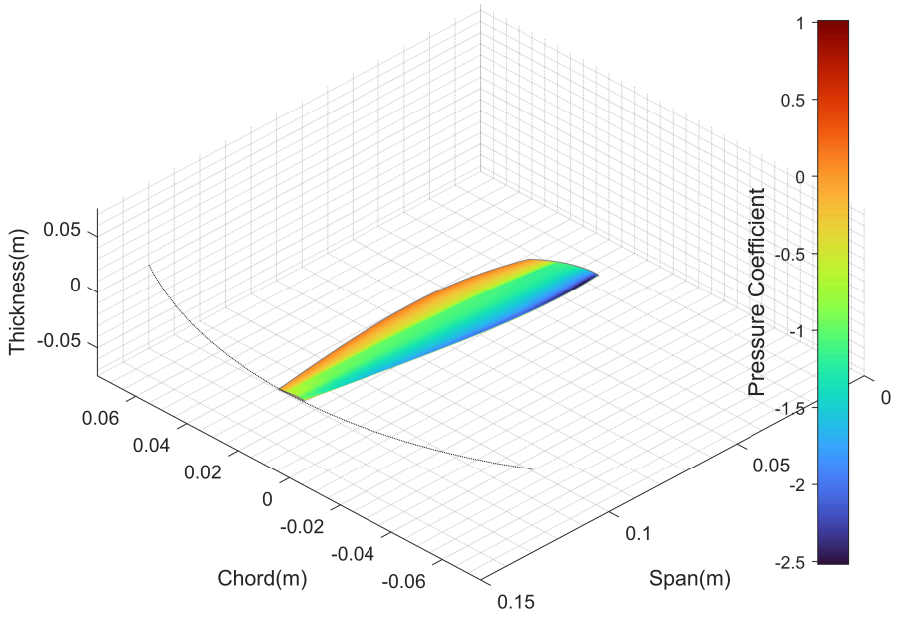

Figure D.7: Surface pressure distribution of one blade of the APC-96 UAV rotor.

D.2 Aeroacoustic validation

The test condition selected for validating the aeroacoustic method is the 5000 r/min case with a jet exit velocity of 6 m/s, corresponding to the advance ratio $J = 0.24$ in Ref. [55]. The far-field noise was calculated at a distance of 1.2 m in the rotor plane, matching the microphone location #7 illustrated in Ref. [55]. The wall pressure spectra were predicted by six different semi-empirical models, with the trailing edge boundary layer parameters estimated at 99% chord by the XFOIL code [97]. The broadband noise was calculated using Amiet's trailing edge model, and the tonal noise was obtained using PSU-WOPWOP.

Figure D.8 shows the comparison between the six WPS models and the benchmark results. Note that the ROM results in Fig. D.8 are only broadband noise predictions based on Amiet's model, while the benchmark results include both broadband and tonal noise. As shown in Fig. D.8, all models provided similar trends but with significantly different levels for the far-field noise prediction in the 1/3 octave band. These models perform better in the high-frequency range (above 3000 Hz), while underestimations occur in the low-frequency range. The low Re models (Rozenberg [119], Lee [123], Kamruzzaman [120]) have slightly better predictions than two of the high Re models (Goody [118] and Catlett [121]). Based on the results, Rozenberg's model shows slightly better performance for broadband noise prediction.

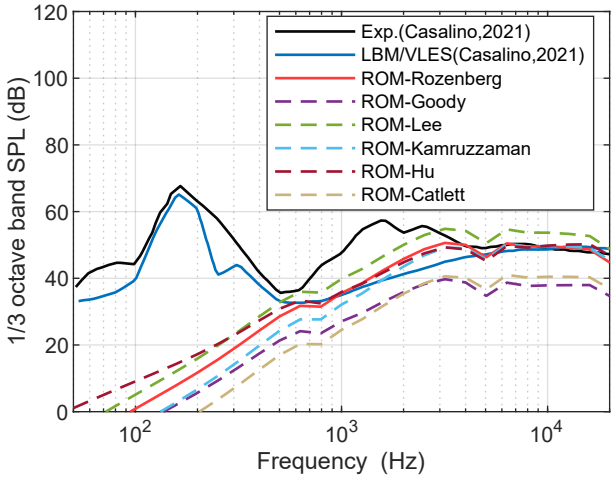

Figure D.8: Comparison between measurements [55], LBM/VLES [55] and predicted broadband results based on different wall pressure models.

Figure D.9 shows the comparison of noise power spectral density (PSD) between the prediction results and the benchmark results. The ROM's prediction data shows good agreement with the experimental data and the high-fidelity lattice-Boltzmann method very large eddy simulation (LBM/VLES) results. The proposed ROM accurately predicts the first two harmonics of blade passing frequency (BPF) and the broadband noise in the high-frequency range. Although the humps in the frequency range below

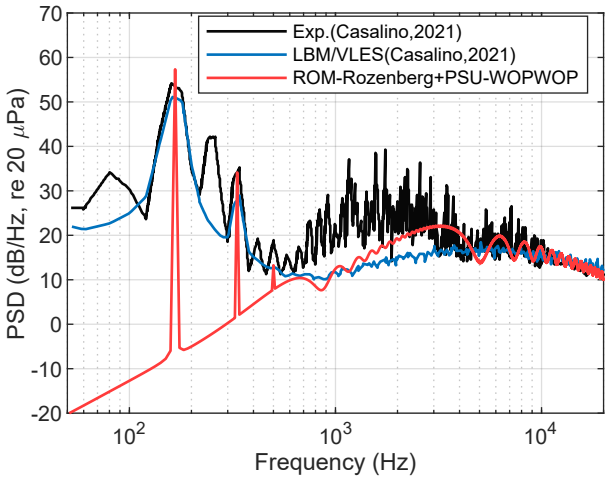

Figure D.9: Comparison between measurements [55], LBM/VLES [55] and predicted results based on Rozenberg's wall pressure model.

3000 Hz are not predicted in Fig. D.8, the underpredictions correspond to the pure tones in the third-octave band, as seen in Fig. D.9. Additionally, the electric motor noise likely contaminated noise levels below 3000 Hz, as reported in Ref. [55]. The background noise also plays an important role in frequencies below 200 Hz, since the cut-off frequency of the semi-anechoic chamber is around 200 Hz [55].

Appendix E

Derivations of the Source Vortex Panel Method for Airfoil Cascades

This section provides detailed derivations of the source vortex panel method (SVPM) for airfoil cascades. The derivations follow a similar approach to the source vortex panel method for an isolated airfoil introduced in Ref. [310].

E.1 Velocity components of potential flow

This Section derives flow velocities normal and tangential to the panel geometry. Equation 58 illustrates that the potential flow on each panel arises from both the upstream and downstream flow components, along with source and vortex terms from other panels. The contributions from the flow component in Eq. 58 on the i^{th} panel can be projected onto Cartesian coordinates, as given by:

$$\frac{\partial}{\partial x_{c_i}}\left\{\phi_{\text{flow}}(x_{c_i}, y_{c_i})\right\} = Vk_{x,i} + \frac{y_{c_i}}{(x_{c_i}-1)^2 + y_{c_i}^2}\sum_{i=1}^{m}\gamma l_i,$$

$$\frac{\partial}{\partial y_{c_i}}\left\{\phi_{\text{flow}}(x_{c_i}, y_{c_i})\right\} = Vk_{y,i} - \frac{x_{c_i}-1}{(x_{c_i}-1)^2 + y_{c_i}^2}\sum_{i=1}^{m}\gamma l_i.$$

The definitions for a simple panel are illustrated in Fig. 6.3. $Vk_{x,i}$ and $Vk_{y,i}$ are formulated as:

$$Vk_{x,i} = \frac{1}{2\pi}\left(Q_{\text{up}}\frac{x_{c_i}+1}{(x_{c_i}+1)^2+y_{c_i}^2} + \Gamma_{\text{up}}\frac{y_{c_i}}{(x_{c_i}+1)^2+y_{c_i}^2}\right) + \frac{1}{2\pi}\left(Q_{\text{down}}\frac{x_{c_i}-1}{(x_{c_i}-1)^2+y_{c_i}^2} - \Gamma_{\text{up}}\frac{y_{c_i}}{(x_{c_i}-1)^2+y_{c_i}^2}\right),$$

$$Vk_{y,i} = \frac{1}{2\pi}\left(Q_{\text{up}}\frac{y_{c_i}}{(x_{c_i}+1)^2+y_{c_i}^2} - \Gamma_{\text{up}}\frac{x_{c_i}+1}{(x_{c_i}+1)^2+y_{c_i}^2}\right) + \frac{1}{2\pi}\left(Q_{\text{down}}\frac{y_{c_i}}{(x_{c_i}-1)^2+y_{c_i}^2} + \Gamma_{\text{up}}\frac{x_{c_i}-1}{(x_{c_i}-1)^2+y_{c_i}^2}\right).$$

Converting Cartesian coordinates to panel coordinates, and expressing the velocity component normal to the i^{th} panel as:

$$\begin{aligned}\frac{\partial}{\partial n_i}\left\{\phi_{\text{flow}}(x_{c_i},y_{c_i})\right\} &= \frac{\partial}{\partial x_{c_i}}\left\{\phi_{\text{flow}}(x_{c_i},y_{c_i})\right\}\frac{\partial x_{c_i}}{\partial n_i} + \frac{\partial}{\partial y_{c_i}}\left\{\phi_{\text{flow}}(x_{c_i},y_{c_i})\right\}\frac{\partial y_{c_i}}{\partial n_i}\\ &= Vk_{y,i}\cos\Phi_i - Vk_{x,i}\sin\Phi_i + B_{s,i}^{\ n}\gamma. \end{aligned} \tag{138}$$

Here, the superscript n denotes the normal velocity component. $\frac{\partial x_{c_i}}{\partial n_i} = -\sin\Phi_i$, $\frac{\partial y_{c_i}}{\partial n_i} = \cos\Phi_i$, $\frac{\partial x_{c_i}}{\partial t_i} = \cos\Phi_i$ and $\frac{\partial y_{c_i}}{\partial t_i} = \sin\Phi_i$. They are obtained from the geometric relationships as shown in Fig. 6.3. The term $B_{s,i}^{\ n}$ takes the form of:

$$B_{s,i}^{\ n} = -\left(\frac{y_{c_i}}{(x_{c_i}-1)^2+y_{c_i}^2}\sin\Phi_i + \frac{x_{c_i}-1}{(x_{c_i}-1)^2+y_{c_i}^2}\cos\Phi_i\right)\sum_{i=1}^{m} l_i.$$

Similarly, the velocity component tangential to the i^{th} panel can be expressed as:

$$\begin{aligned}\frac{\partial}{\partial t_i}\left\{\phi_{\text{flow}}(x_{c_i},y_{c_i})\right\} &= \frac{\partial}{\partial x_{c_i}}\left\{\phi_{\text{flow}}(x_{c_i},y_{c_i})\right\}\frac{\partial x_{c_i}}{\partial t_i} + \frac{\partial}{\partial y_{c_i}}\left\{\phi_{\text{flow}}(x_{c_i},y_{c_i})\right\}\frac{\partial y_{c_i}}{\partial t_i}\\ &= Vk_{x,i}\cos\Phi_i + Vk_{y,i}\sin\Phi_i + B_{s,i}^{\ t}\gamma. \end{aligned} \tag{139}$$

where the superscript t denotes tangential velocity component. The term $B_{s,i}^{\ t}$ takes the form of:

$$B_{s,i}^{\ t} = \left(\frac{y_{c_i}}{(x_{c_i}-1)^2 + y_{c_i}^2} \cos\Phi_i - \frac{x_{c_i}-1}{(x_{c_i}-1)^2 + y_{c_i}^2} \sin\Phi_i \right) \sum_{i=1}^{m} l_i.$$

After deriving the flow component, the contribution from the panel component in Eq. 58 on the i^{th} panel can be determined. Express the contributions from all j^{th} panels to the velocity component normal to the i^{th} panel as:

$$\begin{aligned} \frac{\partial}{\partial n_i}\left\{\phi_{\text{panel}}(x_{c_i}, y_{c_i})\right\} = & \sum_{j=1, j\neq i}^{m} \frac{\sigma_j}{2\pi} \int_j \frac{\partial}{\partial n_i} \ln\left(\sqrt{(x_{c_i} - x_j(l_j))^2 + (y_{c_i} - y_j(l_j))^2}\right) \mathrm{d}l_j \\ & - \sum_{j=1, j\neq i}^{m} \frac{\gamma}{2\pi} \int_j \frac{\partial}{\partial n_i} \tan^{-1}\left(\frac{y_{c_i} - y_j(l_j)}{x_{c_i} - x_j(l_j)}\right) \mathrm{d}l_j \\ & + \frac{\sigma_i}{2}. \end{aligned} \tag{140}$$

For simplicity, the first integral expression from the contribution of panel sources in Eq. 140 is denoted as $A_{p,ij}^{\ n}$, and it can be expressed as:

$$\begin{aligned} A_{p,ij}^{\ n} &= \frac{1}{2\pi} \int_j \frac{\partial}{\partial n_i} \ln\left(\sqrt{(x_{c_i} - x_j(l_j))^2 + (y_{c_i} - y_j(l_j))^2}\right) \mathrm{d}l_j \\ &= \frac{1}{2\pi} \int_j \frac{\left(x_{c_i} - x_j(l_j)\right) \frac{\partial x_{c_i}}{\partial n_i} + \left(y_{c_i} - y_j(l_j)\right) \frac{\partial y_{c_i}}{\partial n_i}}{\left(x_{c_i} - x_j(l_j)\right)^2 + \left(y_{c_i} - y_j(l_j)\right)^2} \mathrm{d}l_j. \end{aligned}$$

Here, $x_j(l_j) = x_{b_j} + l_j \cos\Phi_j$ and $y_j(l_j) = y_{b_j} + l_j \sin\Phi_j$ are formulated based on the panel geometric relationships.

The last integral from the contribution of vortices is denoted as $B_{p,ij}^{\ n}$, which can be expressed as:

$$\begin{aligned} B_{p,ij}^{\ n} &= \frac{1}{2\pi} \int_j \frac{\partial}{\partial n_i} \tan^{-1}\left(\frac{y_{c_i} - y_j(l_j)}{x_{c_i} - x_j(l_j)}\right) \mathrm{d}l_j \\ &= \frac{1}{2\pi} \int_j \frac{\left(x_{c_i} - x_j(l_j)\right) \frac{\partial y_{c_i}}{\partial n_i} - \left(y_{c_i} - y_j(l_j)\right) \frac{\partial x_{c_i}}{\partial n_i}}{\left(x_{c_i} - x_j(l_j)\right)^2 + \left(y_{c_i} - y_j(l_j)\right)^2} \mathrm{d}l_j. \end{aligned}$$

Rewriting Eq. 140

$$\frac{\partial}{\partial n_i}\left\{\phi_{\text{panel}}(x_{c_i}, y_{c_i})\right\} = \sum_{j=1, j\neq i}^{m} A_{p,ij}^{\ n} \sigma_j - \sum_{j=1, j\neq i}^{m} B_{p,ij}^{\ n} \gamma + \frac{\sigma_i}{2}. \tag{141}$$

Similarly, the contributions from all j^{th} panels to the velocity component tangential to the i^{th} panel can be expressed as:

$$\begin{aligned}\frac{\partial}{\partial t_i}\left\{\phi_{\text{panel}}(x_{c_i}, y_{c_i})\right\} = &\sum_{j=1, j\neq i}^{m} \frac{\sigma_j}{2\pi} \int_j \frac{\partial}{\partial t_i} \ln\left(\sqrt{(x_{c_i} - x_j(l_j))^2 + (y_{c_i} - y_j(l_j))^2}\right) \mathrm{d}l_j \\ &- \sum_{j=1, j\neq i}^{m} \frac{\gamma}{2\pi} \int_j \frac{\partial}{\partial t_i} \tan^{-1}\left(\frac{y_{c_i} - y_j(l_j)}{x_{c_i} - x_j(l_j)}\right) \mathrm{d}l_j \\ &- \frac{\gamma}{2}. \end{aligned} \tag{142}$$

If the integrals are expressed in terms of the contributions of the panel sources ${A_{p,ij}}^{t}$ and vortices ${B_{p,ij}}^{t}$, the following relations can be found in [310]:

$${A_{p,ij}}^{t} = {B_{p,ij}}^{n} \quad \forall (i,j) \in \{1, \cdots, m\}^2$$

$${B_{p,ij}}^{t} = -{A_{p,ij}}^{n} \quad \forall (i,j) \in \{1, \cdots, m\}^2.$$

Hence, Eq. 142 can be given by:

$$\frac{\partial}{\partial t_i}\left\{\phi_{\text{panel}}(x_{c_i}, y_{c_i})\right\} = \sum_{j=1, j\neq i}^{m} {B_{p,ij}}^{n} \sigma_j + \sum_{j=1, j\neq i}^{m} {A_{p,ij}}^{n} \gamma - \frac{\gamma}{2}. \tag{143}$$

E.2 Flow tangency boundary condition

The flow tangency boundary condition (Eq. 61) is applied at i^{th} panel:

$$0 = \frac{\partial}{\partial n_i}\left\{\phi\left(x_{c_i}, y_{c_i}\right)\right\}.$$

Substituting with Eq. 138 and Eq. 141:

$$\begin{aligned} 0 &= \frac{\partial}{\partial n_i}\left\{\phi_{\text{flow}}(x_{c_i}, y_{c_i})\right\} + \frac{\partial}{\partial n_i}\left\{\phi_{\text{panel}}(x_{c_i}, y_{c_i})\right\} \\ &= V k_{y,i} \cos\Phi_i - V k_{x,i} \sin\Phi_i + {B_{s,i}}^{n} \gamma \\ &+ \sum_{j=1, j\neq i}^{m} {A_{p,ij}}^{n} \sigma_j - \sum_{j=1, j\neq i}^{m} {B_{p,ij}}^{n} \gamma + \frac{\sigma_i}{2}. \end{aligned} \tag{144}$$

Rewriting Eq.144, the following expression (identical to Eq. 62) can be given by:

$$\sum_{j=1,j\neq i}^{m} A_{p,ij}^{n}\sigma_j + \frac{\sigma_i}{2} - \sum_{j=1,j\neq i}^{m} B_{p,ij}^{n}\gamma + B_{s,i}^{n}\gamma = Vk_{x,i}\sin\Phi_i - Vk_{y,i}\cos\Phi_i.$$

Therefore, the linear system of equations (same as Eq. 64) can be built as:

$$\mathbf{A}\begin{bmatrix}\boldsymbol{\sigma}\\ \gamma\end{bmatrix} = \mathbf{b}.$$

In the context of the $(m+1)\times(m+1)$ matrix $\mathbf{A}$, a $m\times m$ source matrix and a $m\times 1$ vortex array storing the weights associated with the variable γ for each panel are given. Additionally, a $1\times(m+1)$ Kutta array representing the Kutta condition is yet to be incorporated, which will be derived in E.3.

E.3 Kutta condition

To satisfy the Kutta condition at the trailing edge, the pressure coefficient on the first panel must be the same as that on the last panel, which is given by:

$$C_{p_1} = C_{p_m}.$$

Using the definition of the pressure coefficient as shown in Eq. 66, the corresponding expression for the Kutta condition is derived as follows (identical to Eq. 63):

$$V_{t_1} = -V_{t_m}.$$

The tangential velocity for each panel can be written as:

$$V_{t_i} = \frac{\partial}{\partial t_i}\left(\phi\left(x_{c_i}, y_{c_i}\right)\right).$$

Substituting with Eq. 139 and Eq. 143, and rewriting as:

$$
\begin{aligned}
V_{t_i} &= \frac{\partial}{\partial n_i}\left\{\phi_{\text{flow}}(x_{c_i}, y_{c_i})\right\} + \frac{\partial}{\partial n_i}\left\{\phi_{\text{panel}}(x_{c_i}, y_{c_i})\right\} \\
&= Vk_{x,i}\cos\Phi_i + Vk_{y,i}\sin\Phi_i + B_{s,i}^{\ t}\gamma \\
&+ \sum_{j=1, j\neq i}^{m} B_{p,ij}^{\ n}\sigma_j + \sum_{j=1, j\neq i}^{m} A_{p,ij}^{\ n}\gamma - \frac{\gamma}{2}.
\end{aligned} \tag{145}
$$

Substituting Eq. 145 into Eq. 63, the Kutta condition can be expressed as:

$$
\begin{aligned}
&\begin{bmatrix}
(B_{p,11}^{\ n} + B_{p,m1}^{\ n}) \\
\vdots \\
(B_{p,1m}^{\ n} + B_{p,mm}^{\ n}) \\
\left(\sum_{j=1}^{m}(A_{p,1j}^{\ n} + A_{p,mj}^{\ n}) + B_{s,1}^{\ t} + B_{s,m}^{\ t}\right)
\end{bmatrix}^T
\begin{bmatrix}
\sigma_1 \\ \vdots \\ \sigma_m \\ \gamma
\end{bmatrix} \\
&= -(Vk_{x,1}\cos\Phi_1 + Vk_{y,1}\sin\Phi_1 + Vk_{x,m}\cos\Phi_m + Vk_{y,m}\sin\Phi_m).
\end{aligned} \tag{146}
$$

It provides an additional $1 \times (m+1)$ Kutta array for Eq. 64, completing the final derivation.

Appendix F

Geometrical Parameters of the Compact Micro-Slit Panel Absorbers (C-MSPAs)

Table F.1: Optimised geometrical parameters of the C-MSPAs under normal incidence. The parameters include the diameter of the micro-slit (d), the thickness of the micro-slit (t), the diameter of the micro-slit array (D), and the width of the micro-slit array (W). The optimised parameters are presented for three test cases: NI-1: 600 Hz, NI-2: 600 & 1200 Hz, and NI-3: 1000–2000 Hz. The overall absorber dimensions are 40 mm × 30 mm × 40 mm ($L_A \times D_A \times H_A$) and the wall thickness is h = 1 mm.

Case	d (mm)	t (mm)	D (mm)	ϕ (%) [W (mm)]
NI-1: 600 Hz	0.73	4.06	28.00	1.85 [38.00]
NI-2: 600 & 1200 Hz	0.62	2.21	28.00	5.07 [11.43]
	0.99	9.02	28.00	3.75 [25.57]
NI-3: 1000–2000 Hz	0.70	6.20	28.00	7.00 [9.00]
	0.50	4.70	28.00	6.25 [7.00]
	0.50	3.60	28.00	7.35 [5.70]
	0.50	2.80	28.00	8.62 [4.60]
	0.60	2.20	28.00	12.50 [3.80]
	0.60	1.50	28.00	15.00 [3.00]

Table F.2: Optimised geometrical parameters of the C-MSPAs under grazing incidence. The parameters include the diameter of the micro-slit (d), the thickness of the micro-slit (t), the diameter of the micro-slit array (D), and the width of the micro-slit array (W). The optimized parameters are presented for three test cases: GI-1: 600 Hz, GI-2: 1200 Hz, and GI-3: 900–1800 Hz. The overall dimensions of the annular rings are 60 mm length, 30 mm thickness (inner diameter of R_{in} = 77 mm and outer diameter of R_{out} = 117 mm).

Case	d (mm)	t (mm)	D (mm)	ϕ (%) [W (mm)]
GI-1: 600 Hz	1.00	10.00	28.00	3.84[19.00]
GI-2: 1200 Hz	1.00	3.60	28.00	8.09 [9.00]
GI-3: 900–1800 Hz	0.59	1.47	28.00	4.03 [10.72]
	0.64	1.69	28.00	6.48 [7.12]
	1.00	1.90	28.00	9.84 [7.39]
	1.00	4.57	28.00	5.69 [12.79]
	1.00	6.07	28.00	10.28 [7.10]
	1.00	7.86	28.00	9.27 [7.88]

Appendix G

Comparison of the Noise Level of the Baseline Fan Under Different Loading Conditions

This appendix compares the overall SPL (Fig. G.1 (a)) and noise spectral content (Fig. G.1 (b)) of the baseline fan under different flow rate coefficients, including free-delivery, maximum-efficiency, and stall points. It shows that fan loading has a more significant impact in stall conditions than in non-stall conditions. The spectral content of the noise under the free-delivery condition is similar to that under the maximum-efficiency condition, with a huge increase in the noise level at the stall point.

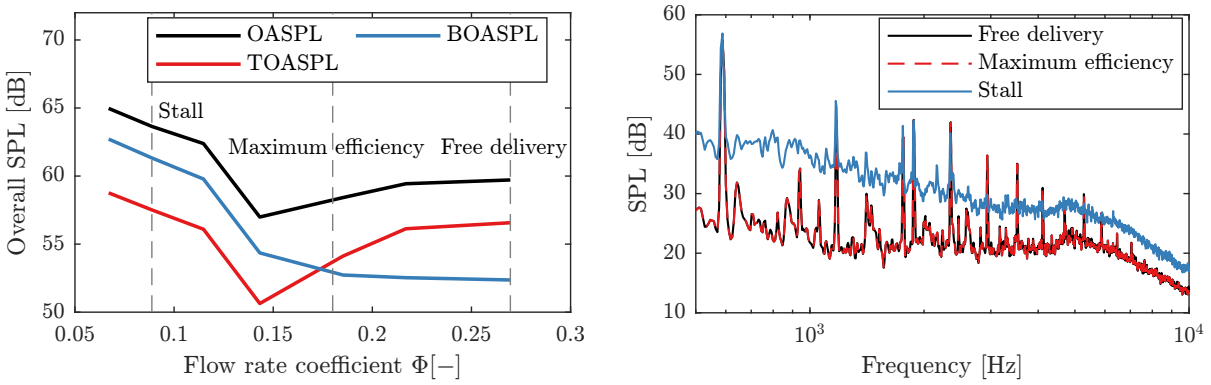

(a) (b)

Figure G.1: Comparison of the noise level of the baseline fan under different loading conditions: (a) Overall sound pressure level and (b) Narrowband sound pressure level.